

RIKEN **Accelerator** **Progress Report**

1987

vol. **21**

理化学研究所
the Institute of Physical and Chemical Research

RIKEN Accelerator Progress Report 1987
January-December

理化学研究所
the Institute of Physical and Chemical Research
Wako-shi, Saitama, 351-01 JAPAN

Editors

S. Ambe	K. Asahi
Y. Awaya	Y. Chiba
T. Inamura	S. Kitayama
I. Shimamura	I. Tanihata
E. Yagi	Y. Yano

This volume contains recent information of the accelerators at RIKEN (IPCR), informal reports and abstracts of papers which will be published at scientific meetings or in publications by staff members, guests, and visitors.

All rights reserved. This report or any part thereof may not be reproduced in any form (including photostatic or microfilm form) without written permission from the publisher.

CONTENTS

	Page
I. INTRODUCTION	1
II. OPERATION OF ACCELERATORS	
1. RIKEN Ring Cyclotron Operation	2
2. RILAC Operation	3
3. Cyclotron Operation	5
4. TANDETRON-Operation	6
III. RESEARCH ACTIVITIES	
1. Nuclear Physics	
1. The Intruder Deformed Band in ^{113}Sn	7
2. High Energy γ -Rays Observed in the $^{181}\text{Ta} + ^{40}\text{Ar}$ Reaction at 21 MeV/Nucleon	8
3. Angular Distribution of Fission Fragments Coincident with Projectile Fragments	9
4. Spin Alignment in Projectile Fragmentation at Intermediate Energies	11
5. Tensor Analyzing Powers of (d, ^2He) Reactions on ^1H and ^{12}C	13
6. Rotational Perturbation to the Natural Parity Rotational Band of ^{163}Dy	15
7. Study of Neutron-Rich Nuclei with Radio-Isotope Beams	17
8. Development of a Particle-Identification Technique and Search for New Isotopes	19
9. Total Reaction Cross Section Measurement of Unstable Nuclei	21
10. Effect of Final State Interactions on (π, γ) Reactions	23
11. Level Densities with Fixed Exciton Number for Pre-Equilibrium Nuclear Reaction	25
12. A High-Energy Scattering Approximation	27
13. Microscopic Analysis of the Hexadecapole Strength to the γ -Vibrational Bands	29
14. Derivation of the Global Equation of Motion for the Collective Variable	31
2. Atomic and Solid-State Physics	
1. Gauge Property for the Radiative Processes Induced by Ion-Atom Collision	32

	Page
2. Photon Angular Distributions of the Ultrarelativistic K-Shell Radiative Electron Capture Induced by Heavy-Ion Collision	35
3. Angular Distribution and Linear-Polarization of X Rays Induced by Radiative Electron Capture Process	37
4. Calculation of Electron-Stripping Cross Sections of Ne Ions in Proton Impact	39
5. Charge-Exchange Cross Sections and Equilibrium Charge States of Incident Uranium Ions with Relativistic Velocity	41
6. Electron Capture between Arbitrary Excited States in the Continuum Distorted Wave Approximation	43
7. Charge Transfer Collision between a Low Energy Ion and a Solid Surface	45
8. The Cross Section for $e^- + (e^+e^-)_{(1^3S_1)} \rightarrow (e^-e^+)_{(1^1S_0)} + e^-$	47
9. The Born Approximation to the Reactance Matrix in Low-Energy Electron-Molecule Collisions	49
10. Rotational Stopping Cross Sections for Collisions of Subexcitation Electrons with Dipolar Molecules: Dependence on the Temperature of the Molecular Gas	51
11. Doubly Excited Rydberg Series of Molecular Repulsive States: H_2	53
12. Continuum Multiple Scattering Method for Molecules	55
13. Hyper-Radial Adiabatic Expansion for a Muonic Molecule $dt\mu$	57
14. Deformed Atoms and Collective Rotational Motion of Electrons	59
15. Identification of Al X 2p3d-2p4f Transition of Beam-Foil Spectra	62
16. Tilted-Foil Method Using Extremely Thin Foils	63
17. Observation of Radiative Photons in the μ^- Transfer Process for Liquid D_2 with He Impurity	64
18. REC X-Rays from Collision System of 20.5 MeV/u Ar Ions on Be	67
19. Momentum Distribution of Be 2s Electron Measured by a Radiative Electron Capture Process	69
20. Resonant Transfer and Excitation (RTE) in Ge^{29-} on H_2 Collisions	71
21. Charge Equilibration Process of 50 MeV Ar Ions in C Foils	73
22. Broadening of Ar Projectile $K\alpha$ X-Ray Satellite Lines in Cu and Ni Target Foils	76
23. A Systematic Study of KL^n Multiple Vacancy Production for Ca Bombarded by 0.25–1.5 MeV/u Ne and Ar Ions	78

	Page
24. Impact Parameter Dependent Probabilities of Au L-Shell Ionization by Ar Ions	80
25. Charge-State Distribution Measurements of Ar Ions	82
26. Coincidence Measurements of Electron Capture and Target Ionization in 1.05 MeV/amu Ar ¹²⁺ + Ne Collision	84
27. High Charge Effects on Electron Excitations in Metal Targets for Ar ¹²⁺ Impact Compared with Those for He ²⁺ Impact	87
28. Energy Spectra of Al-LVV Auger Electrons Induced by Grazing Angle Incident Fast Heavy-Ion Impact	89
29. A Piezoelectric Bimorph Transducer for the Coulomb-Excitation Mössbauer Spectroscopy	92
30. ⁵⁷ Fe Mössbauer Study on YBa ₂ Cu _{3-x} Fe _x O _{7-y}	93
31. Emission Mössbauer Study of ¹¹⁹ Sb Ions Adsorbed on Ferrimagnetic Fe ₃ O ₄ Surfaces	96
32. TDPAC Study of Hyperfine Interactions at ¹¹¹ Cd(← ¹¹¹ In) in Li _{0.5} Fe _{2.5} O ₄ Single Crystal	98
33. Surface Structure of Krypton-Implanted Aluminum	101
34. Lattice Location Study on Krypton Atoms in Aluminum by Means of a Channeling Method	103
35. RBS Investigation of AlN _x Deposited on Glassy Carbon (I)	105
36. Lattice Location of Eu Ion in Eu-Implanted CaF ₂ Observed by Channeling Experiments	106
37. Lattice Disorder and the Behavior of Implanted Atoms in In-Implanted TiO ₂ (Rutile)	107
38. Hydrogen Trapping by Substitutional Impurities in Nb-3at%Mo Alloys as Observed by the Channeling Method	109
39. Evaluation of Structural Perfection by Rutherford Backscattering Spectroscopy (RBS) of 6H-SiC Single Crystal Grown with a Vapor Transport Method	112
40. Erosion of Graphite by Low Energy Atomic Hydrogen	114
41. The Channeling Analysis of Ge Epitaxial Growth on Si Substrate	116
42. Production of Fast Switching Power Thyristors by Proton Irradiation	118
43. Background in PIXE Spectra	120
 3. Radiochemistry and Nuclear Chemistry	
1. A New Nuclear Reaction Analysis of Nitrogen in Solids: Utilization of ¹⁵ N as an Activable Tracer	123
2. Study on Carbon and Boron in Gallium Arsenide	124

	Page
3. Analysis of Hydrogen in Plasma CVD SiO _x Films by an Elastic Recoil Detection Method	125
4. Heavy-Ion Rutherford 2 π -Scattering Analysis Applied to the Development of a Monitoring Detector for the Measurement of Water Reactivity	126
5. Application of PIXE to Medical and Environmental Science (II)	127
6. Application of PIXE and Diffraction Analysis to Ancient Remains (II)	129
7. <i>In Situ</i> Emission Mössbauer Studies of Solid/Solution Interface: ¹¹⁹ Sb ⁵⁺ and ⁵⁷ Co ²⁺ Ions Adsorbed on γ -Fe ₂ O ₃	131
8. Mössbauer Spectroscopic Studies of Ruthenium Trichlorides	133
9. Adsorption of No-Carrier-Added ¹¹⁹ Sb(V) Ions onto Metal Oxide Surfaces from Aqueous Solutions	135
 4. Radiation Chemistry and Radiation Biology	
1. High-Density Excitation by Heavy Ions: Measurement of Track-Depth Resolved Emission Spectra	137
2. Proton Irradiation Effects of Aliphatic Polymers	139
3. Dosimetry with a Cellulose-Triacetate Film for Proton Irradiation	141
4. Position Determination by Laser Marks of <i>B. subtilis</i> Spores Placed on a Plactic Track Detector and Inactivation of the Spores by a Single Heavy Ion	143
5. Mammalian Cell Inactivation and DNA Lesion Caused by Charged Particle Beams	145
6. Oncogenic Cell Transformation of Golden Hamster Embryo Cells by Heavy Ions	147
 5. Instrumentation	
1. Data Acquisition System at RIKEN Ring Cyclotron Facility	149
2. Cyclotron Calibration Test of Position Sensitive Detectors for Heavy Cosmic Ray Telescope in Space	152
3. Design of an Isotope Separator On-Line System at RIKEN Ring Cyclotron	155
4. An Ion-Guide Technique for On-Line Isotope Separation Coupled with a Gas-Filled Recoil Isotope Separator	158
5. Counter Development for Rotating Catcher System	161
6. Facilities for Studies on Nuclear Chemistry and Radiochemistry at RIKEN Ring Cyclotron	163
7. Further Study of Experimental Facilities for Light and Light-Heavy Ion Induced Reactions	164

	Page
8. Ray-Tracing Calculation of the Variable-Angle Beam Rotator	166
9. Design of the RIKEN Projectile-Fragment Separator RIPS	168
10. Design of a New Type of Low-Energy Radioisotope-Beam Channel "SLOW" for Surface Studies	170
11. Design of a Superconducting Secondary Beam Transport System with a Large Solid Angle (SLQ)	172
12. Apparatus for Resonance Ionization Spectroscopy of Atomic Nuclides	174
13. Resonance Ionization Spectroscopy of Neutral Atoms by a Laser Ablation Method	176
14. Observation of Two-Step Photoionization of a Na Atomic Beam Using cw and Pulsed Lasers	178
15. Development of the Parallel Plate Avalanche Counter for the Time-of-Flight Measurement	180
16. Pileup Rejecter for a Position-Sensitive Parallel-Plate Avalanche Counter	183
 IV. NUCLEAR DATA	
1. Status Report of the Nuclear Data Group	185
2. Present Status of $^{63}\text{Cu}(p, n)^{63}\text{Zn}$ and $^{65}\text{Cu}(p, n)^{65}\text{Zn}$ Monitor Reactions	186
3. Present Status of a Monitor Reaction $\text{Al}(p, x)^{24}\text{Na}$	190
4. On the Cross Sections for ^{77}Br Production Reactions	191
5. On the Cross Sections for $^{127}\text{I}(p, 5n)^{123}\text{Xe}$	195
 V. DEVELOPMENT OF ACCELERATOR FACILITIES	
1. Status of RIKEN Ring Cyclotron Project in 1987	196
2. Field Stability of the Sector Magnets	198
3. Applications of CIM-DIM in the Beam Diagnostic System of RIKEN Ring Cyclotron	201
4. Improvement of RF Amplifier of RIKEN Ring Cyclotron	203
5. Effects of Magnetic Fields on a Turbomolecular Pump of 5,000 l/s	205
6. Communication System for RIKEN Ring Cyclotron	207
7. Injector AVF Cyclotron for RIKEN Ring Cyclotron	210
8. ECR Ion Source for an Injector AVF Cyclotron	212
9. RF Amplifier System of the Injector Cyclotron for RIKEN Ring Cyclotron	214
10. Production of Multicharged Heavy Ions by PIG Source of RILAC	216

	Page
11. Development of an LCE Ion-Source	218
12. 6 GeV SOR Project	220
13. Design of the Booster Synchrotron Lattice	223
14. Lattice Design for a 6 GeV Storage Ring	225
15. Chromaticity Correction in the Low-Emittance Chasman-Green Lattice	228
16. Design Study of the Magnets for a Storage Ring	230
17. The Overall Beam Flow of the 6 GeV SOR	233
18. RF System for the 6 GeV SOR	235
19. Design of the RF Test Cavity for the 6 GeV SOR Ring	237
20. Vacuum Chamber for the 6 GeV Storage Ring	239
21. Pumping System for the 6 GeV SOR	241
22. Vacuum Test Device for Preliminary Experiments on the 6 GeV SOR	243
23. Synchrotron Radiation Power Distribution at the 6 GeV SOR	245
24. Crotch Design for the 6 GeV SOR	247
25. Design of the Front End of the Beam Line at the KEK Photon Factory	249
26. Construction of a Multipole Wiggler, B13MPW, at KEK-PF	252
VI. RADIATION MONITORING	
1. Leakage-Radiation Measurements in the Cyclotron Building	254
2. Routine Monitoring of the Cyclotron, RILAC, and TANDETRON	256
3. Radiation Monitoring at RIKEN Ring Cyclotron Facility	258
VII. LIST OF PUBLICATIONS	260
VIII. LIST OF OUTSIDE USERS AND THEIR THEMES	272
IX. LIST OF SEMINARS	273
X. LIST OF PERSONNEL	275
AUTHOR INDEX	

I. INTRODUCTION

H. Kamitsubo

During the past year the collaborative research work using heavy-ion beams has been carried out in the fields of atomic and nuclear physics, nuclear and radiation chemistry, material engineering, and radiation biology at the Institute of Physical and Chemical Research (RIKEN). The main facilities dedicated to the research work are a 160 cm cyclotron, a variable-frequency heavy-ion linac (RILAC), a 1 MV electrostatic accelerator (Tandatron), and a newly constructed separated sector cyclotron (RIKEN Ring Cyclotron, RRC).

The first beam was extracted successfully from RRC in December of 1986 and the inauguration was held on January 23, 1987, under the attendance of Ministry of State (Director of the Science and Technology Agency). From April RRC has been in routine operation, and test experiments on nuclear and atomic physics have been carried out. In 1987 we accelerated ions of ^{12}C , ^{14}N , ^{18}O , ^{40}Ar , and ^{65}Cu in the energy range of 20 to 44 MeV/u. Currently, only one experimental hall was available in this period. The construction of the second injector, an AVF cyclotron, and beam transport lines to other experimental halls started this year.

RRC is open equally to outside users and the collaboration with research groups of other institutions has been promoted in this period. International collaboration with IN2P3 of France, Academia Sinica of China, and other foreign institutions were also continued.

Studies on nuclear physics have been carried out using RRC. In addition to the usual heavy-ion experiments, new projects have started this year on the measurements of high energy γ rays and sub-threshold pion production cross sections, reaction cross sections by radio-active nuclei, and studies of nuclei far from the stability line.

Theoretical studies of heavy-ion reactions and fission process were performed on the basis of transport calculations. Nuclear structure studies of largely deformed nuclei were extensively performed, too. Theoretical research on atomic collision processes have been pursued in connection with various prob-

lems such as radiative electron capture at high energy, ionization processes in collision of highly stripped ions with atoms in gas and solid, and charge exchange collisions on solid surface. Structure of muonic molecular ions was also studied theoretically.

Experimental studies were carried out on atomic collision processes and on beam foil spectroscopy by measuring energy spectra of photons and Auger electrons, charge state distributions of colliding ions, and angular distributions X rays and electrons as well as scattered ions. Various kinds of ions accelerated at RILAC and RRC were used for these studies. The subnanosecond measurement of the light emission along the heavy-ion trajectory in gaseous materials has been continued in this year.

Mössbauer spectroscopy and perturbed angular correlation techniques have been applied to the studies on the properties of condensed matter and chemical processes on the surface of solid materials in liquid, by using γ rays emitted from Coulomb excited nuclei as well as from short-lived radioisotopes.

The analysis of the distributions of implanted or dissolved impurities in various materials has been continued by using a Rutherford back-scattering method, a Rutherford forward recoil detection method, and a nuclear reaction method. The activation analysis of light-element impurities in high-purity materials was continued as before. PIXE analysis was applied to the composition analysis of medical, environmental, and geological samples.

The construction of experimental equipments and devices has been continued. The design and fabrication of an on-line isotope separator (GARIS-IGISOL), a projectile fragment separator (RIPS), a BAF_2 2π spectrometer, a large scattering chamber, a large acceptance pion separator, and so on have been done in this period.

The R&D work on a high brilliance synchrotron light source started this year and the design study of a 6 GeV storage ring has pursued. The model study of a RF cavity and the R&D work on a vacuum chamber are in progress.

II. OPERATION OF ACCELERATORS

1. RIKEN Ring Cyclotron Operation

Y. Yano, K. Hatanaka, M. Kase, A. Goto, H. Takebe, H. Nonaka, H. Isshiki,*
R. Abe,* S. Otsuka,* H. Akagi,* and T. Ishikawa*

The routine operation of RRC (RIKEN Ring Cyclotron) began in April 1987. It has been made every other week: one week for the experiments and the other for the maintenance and improvements. April and May were devoted to the machine studies, and the beams were used to nuclear-physics and atomic-physics experiments since the end of May. The extensive overhauls were done this winter (January–March) and summer (August–September). Until the summer overhaul, RRC was operated with a harmonic number of 10 instead of 9 (normal operation). The use of this harmonic number came from a five-resonator operation of RILAC. The RF amplifier of its last (sixth) resonator was disassembled for the improvements. Since October, RILAC worked with six acceleration tanks, and accordingly RRC with normal harmonic number.

The following machine studies were performed to facilitate the operation of RRC and its beam transfer line: (1) automatic measurement of a charge-state distribution, (2) automatic beam alignment on the beam line, (3) optimization of the voltage and the phase of the RF buncher, (4) phase-setting optimization of the RF system, (5) beam injection and extraction procedures, (6) isochronization of sector fields, (7) transverse phase-space matching of RILAC beam with RRC acceptance, and (8) well-centered orbit acceleration. These items were successfully achieved by using our sophisticated computer control system and beam diagnostic system. Our original method with three long-stroke radial differential probes creates well-centered orbits inside RRC. In the beam-service runs, however, this operation is not performed, but off-centering acceleration is made to save the beam preparation time and to expand the turn separation in the extraction region as shown in Fig. 1. In this way, the single-turn extraction is established.

In this-year runs, five kinds of ion species were

used for experiments. The main characteristics of these beams are summarized in Table 1. A great number of improvements have been made in addition to above machine-operation techniques to start up the machine quickly, to keep the stable beam for a long time, and to provide high-quality beams for the users. It takes approximately a half day to prepare a beam. High-quality beams with transverse emmittances less than 3π mm·mrad, the energy resolution less than 0.1% and the time resolution less than 500 ps were used for experiments.

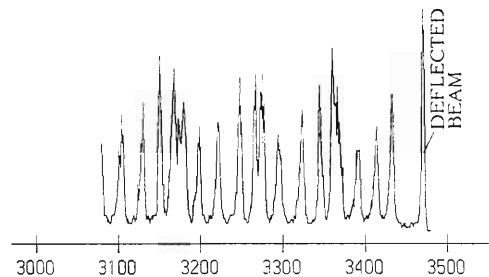


Fig. 1. Turn pattern measured with a radial differential probe in case of off-centering acceleration. Bottom figures represent radial distances from the machine center (mm in units).

Table 1. Characteristics of RRC beams in April–December, 1987.

		^{40}Ar	$^{14,15}\text{N}$	^{65}Cu	^{18}O	
RF frequency	MHz	28	28	35	25	35
RILAC						
Charge state		4+	4+	3+	5+	4+
Beam energy	MeV/u	1.28	1.58	2.00	1.01	2.48
Num. of tanks		5	6	5	5	6
RRC						
Charge state		12+	13+	6+	18+	7+
RF harmonic number		10	9	10	10	9
Beam energy	MeV/u	21.0	26.0	33.7	16.7	42.0
Intensity	enA	200	600	200	10	20
	(typical)					

* Sumijyu Accelerator service, Ltd.

II-2. RILAC Operation

Y. Miyazawa, M. Hemmi, T. Inoue, M. Yanokura, M. Kase,
E. Ikezawa, T. Aihara,* T. Ohki,* H. Hasebe,* and Y. Chiba

RILAC continues to supply various kinds of ion beams for many fields of research. Total beam time was reduced compared with the last year operation because of long-term shutdown to improve the RF oscillator and cooling system. Three days of the scheduled beam time were cancelled owing to accident in the RF cavities. A percentage of the beam time for RRC was about 42%; ions, ^{14}N , ^{15}N , ^{18}O , ^{40}Ar , and ^{65}Cu accelerated by RILAC were injected to RRC. Most of the users preferred Ar ions, and 75% of the total beam time was devoted to this ion.

The RILAC RF cavities had accident three times in this period with silver strips of 0.2 mm in thickness, which were inserted to make good RF-contact along a seam between the base block, supporting drift-tube, and the top of inner conductor of a coaxial resonator. Partially insufficient contact pressure caused RF-heating and protruding out of the position of the strips. The damaged contact strips in the cavities No. 5 and No. 6 were replaced with beryllium copper strips. A quadrupole doublet set in the injection beam line had an electric disconnection in its tape coil terminal; it was replaced.

Several improvements were put into six rf-power sources of RILAC. The virtual value of a grid damping resistor of the final amplifier was reduced to improve its stability in the high operating frequency region. Their alteration consequently required an additional driving power, which was achieved by modifying coupling elements between the final (vacuum tube RCA 4648) and the driving (EIMAC 3CX3000A7) stages and by providing a new plate

Table 1. Statistics of operation for the period of Jan. 1- Dec. 31, 1987.

	Days	%
Beam time	151	41.4
Frequency change	6	1.6
Overhaul and improvement	77	21.1
Periodic inspection and repair	24	6.6
Machine trouble	3	0.8
Scheduled shut down	104	28.5
Total	365	100

* Sumijyu Accelerator Service, Ltd.

Table 2. Percentage of beam time for research activities.

	Days	%
Atomic physics	36	23.8
Solid-state physics	15	9.9
Nuclear physics	1	0.7
Radiochemistry and nuclear chemistry	17	11.3
Radiation chemistry and radiation biology	8	5.3
Accelerator research	11	7.3
Beam transportation to RIKEN Ring Cyclotron	63	41.7
Total	151	100

Table 3. Statistics of ion used in this period.

Symbol	Mass	Charge state	Days
C	12	2	2
N	14	2	10
N	15	3	3
O	18	4	6
Ne	20	2	9
Si	28	3	1
Ar	40	4	113
Cu	65	4	4
Mo	92	7	2
Xe	132	9	1

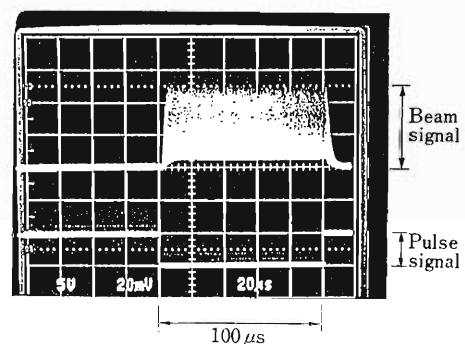


Fig. 1. A pulsed beam obtained by a repetition frequency of 5 kHz. Beam width is 100 μs .

power supply of 10 kW for the driving stage. A newly developed screen grid bypass capacitor of the final tube, having compact size but large capacitance (11 nF), replaced old one and contributed to stability of the amplifier also. Two-phase lock circuits to suppress fluctuation in phase of the accelerating

voltages were set for No. 1 and No. 2 resonators. The beam extracted from RILAC became stable by this improvement.

The main cooling tower operating for ten years was replaced with a new one. All water pumps and heat exchangers are overhauled this summer.

A beam chopper was installed at the injection beam line between bending magnets BM1 and BM2. This device has a rising time of beam pulsing of $10 \mu\text{s}$ and varies its pulse width from $20 \mu\text{s}$ to continuation. Figure 1 shows a pulsed beam obtained by this device at a repetition frequency of 5 kHz.

II-3. Cyclotron Operation

I. Kohno, K. Ogiwara, T. Kageyama, S. Kohara,
S. Fujita, K. Ikegami, and H. Takebe

The 160 cm cyclotron was operated on the 24 h a day basis during the period XXII from Jan. 1, 1987 to Dec. 31, 1987. The statistics of the machine operation time is shown in Table 1. The total net beam time in this period decreased compared with that of the last period because of a long scheduled shutdown.

Table 2 shows the beam-time allotment to various activities during this period. Table 3 shows the distribution of the scheduled beam-time among various particles.

Table 1. Cyclotron operation in the period XXII.

	Oscillator	Ion source	Beam
Reading of the time meter on			
Jan. 06 1987 (h)	93,985.8	99,050.2	59,334.9
Reading of the time meter on			
Jan. 06 1988 (h)	95,270.1	100,416.4	59,837.6
Difference (h)	1,284.3	1,366.2	502.7

Schedule in this period:

Beam-time	111 d
Overhaul and installation	30
Periodical inspection and repair	28
Scheduled shutdown	183
Machine troubles	13

Table 2. Scheduled beam-time and research subjects in the period XXII.

Subject	Heavy ion	Light ion	Total
RI production			
for nuclear physics	0 h	35 h	35 h
Nuclear chemistry	0	222	222
Radiation biology	50	62	112
Radiation chemistry	482	45	527
Radiation damage			
of polymer	0	68	68
Radiation damage			
of semiconductor	0	7	7
Test of radiation detector	120	54	174
Outside users			
Radiochemical analyses	0	89	89
Radiation damage			
of device for satellite	0	77	77
Test of single event upset	85	0	85
Proton irradiation			
on thyristor	0	86	86
Total	737 h	745 h	1,482 h
Percentage in total	49.7%	50.3%	100%

Table 3. Distribution of beam-time among particles accelerated.

Particle	(h)	(%)
p	452	30.5
d	0	0
$^3\text{He}^{2+}$	89	6.0
$^4\text{He}^{2+}$	204	13.8
$^{12}\text{C}^{4+}$	12	0.8
$^{14}\text{N}^{4+}$	651	43.8
$^{15}\text{N}^{5+}$	50	3.4
$^{20}\text{Ne}^{6+}$	24	1.6
Total	1,482	

II-4. TANDETRON-Operation

T. Kobayashi, H. Sakairi, E. Yagi, and T. Urai

The machine was operated for 182 days for one year from November, 1986. The species of accelerated ions were ^1H , ^3He , ^4He , and ^{11}B .

The exchanger, developed last year, of ion charge from positive to negative with lithium vapor, has been operating satisfactorily. The outline of this exchanger is described under another item of this report (p. 218).

No serious trouble occurred in the last period, but a time-worn multichannel pulse-height analyzer was replaced with new one controlled by a personal computer.

Experimental studies were carried out on following subjects:

(a) State of hydrogen in metals (Metal Phys. Lab. and Beam Analysis Center);

(b) Behavior of solid krypton in aluminum (Cyclotron Lab. and Metal Phys. Lab.);

(c) Solubility of D in Si (Nuclear Chem. Lab.);

(d) Lattice location of Eu in CaF_2 (Semiconductors Lab. and Beam Analysis Center);

(e) Characterization of epitaxial Ge on Si surface (Cyclotron Lab. and Metal Phys. Lab.);

(f) Lattice disorder and behavior of implanted impurities in ceramics (Metal Phys. Lab.);

(g) Evaluation of crystalinity of ceramics (Friction and Lubrication Lab. and Beam Analysis Center);

(h) Composition of AlN_x (Beam Analysis Center);

(i) Surface composition of Ar-implanted Kapton (Beam Analysis Center); and

(j) Basic study of PIXE and its application to medical, environmental, and archeological materials (Solid State Chem. Lab.).

III. RESEARCH ACTIVITIES

1. Nuclear Physics

1. The Intruder Deformed Band in ^{111}Sn

H. Harada, T. Murakami, K. Yoshida, J. Kasagi, T. Kubo, and T. Inamura

{ NUCLEAR REACTION $^{98}\text{Mo}(^{16}\text{O}, 3n)^{111}\text{Sn}$, $E = 76$ MeV; }
 { measured γ - γ coincidence, deduced levels. }

Spherical-deformed shape coexistence in Sn isotopes has been recognized since Bron *et al.* have discovered intruder bands in $^{112-118}\text{Sn}$.¹⁾ However, no experimental evidence for existence of the intruder bands in odd-mass Sn isotopes has been shown, mainly because the states investigated so far were only low-spin states. An investigation of the intruder bands in odd-mass Sn isotopes is desirable to examine a quasiparticle-core coupling scheme, which has been pointed out to be sensitive to the nature of the core.²⁾ The high spin states of ^{111}Sn were excited by the $^{98}\text{Mo}(^{16}\text{O}, 3n)^{111}\text{Sn}$ reaction with a beam energy of 76 MeV. The target used was a 98% enriched ^{98}Mo foil, 0.95 mg/cm² in thickness, and backed with a thin lead layer. Five sets of BGOACS were used for

γ - γ coincidence measurements. Experimental details were reported in Ref. 3.

The level scheme obtained in the present work is shown in Fig. 1, together with the relevant levels of ^{112}Sn (Ref. 3). The spin assignments are based on the γ - γ angular correlations. All transitions shown are of quadrupole character. As can be seen from Fig. 1, a distinct band structure is observed for the first time above the $23/2^-$ state. The band can be understood as originating from the coupling of the $h_{11/2}$ neutron to the deformed even core.

Transition energy ratio

$$E_{\gamma}(27/2^- - 23/2^-; ^{111}\text{Sn})/E_{\gamma}(8^+ - 6^+; ^{112}\text{Sn}) = 1.21$$

is obtained. The theoretical value for this ratio is 1.0 for a rotation aligned coupling scheme and 1.73 for a strong coupling scheme. Thus, the present result favors the rotation aligned coupling rather than the strong coupling. The present value is also close to the results^{2,4)} for Xe isotopes;

$$E_{\gamma}(27/2^- - 23/2^-; ^{117}\text{Xe})/E_{\gamma}(8^+ - 6^+; ^{116}\text{Xe}) = 1.21$$

and

$$E_{\gamma}(27/2^- - 23/2^-; ^{117}\text{Xe})/E_{\gamma}(8^+ - 6^+; ^{116}\text{Xe}) = 1.21.$$

This striking accordance on the energy ratio gives an another evidence for the similarity (Ref. 5) between the intruder bands in Sn isotopes and the g.s. bands in Xe isotopes.

References

- 1) J. Bron, W.H.A. Hesselink, A. van Poelgeest, J.J.A. Zalmsrta, M.J. Uitzinger, H. Verheul, K. Heyde, M. Waroquier, H. Vincx, and P. van Isacker: *Nucl. Phys. A*, **318**, 335 (1979).
- 2) P. Chowdhury, U. Garg, T. P. Sjoreen, and D. B. Fossan: *Phys. Rev. C*, **23**, 733 (1981).
- 3) H. Harada, T. Murakami, H. Tachibanaki, K. Yoshida, J. Kasagi, T. Kubo, and T. Inamura: *RIKEN Accel. Prog. Rep.*, **19**, 18 (1985).
- 4) V. P. Janzen, J. A. Cameron, A. J. Larabee, D. Rajnauth, and J. C. Waddington: *McMaster Acc. Lab. Annu. Rep.*, p. 54 (1984).
- 5) H. Harada, T. Murakami, K. Yoshida, J. Kasagi, T. Kubo, and T. Inamura: *Phys. Lett.* (in press).

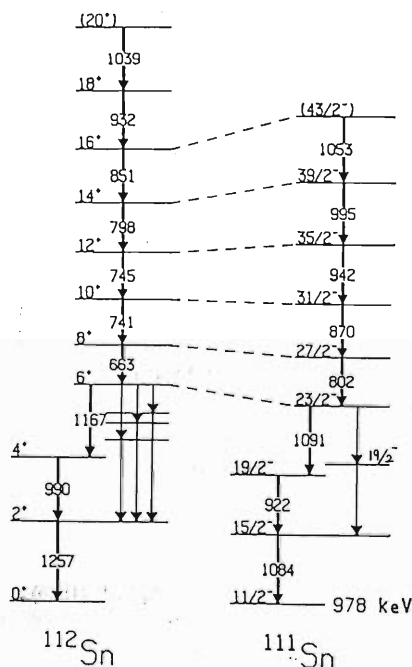


Fig. 1. Level scheme of ^{111}Sn of the present study. Inclusion of ^{112}Sn (from Ref. 3) is done for comparison as discussed in the text. Note that the $11/2^-$ state in ^{111}Sn is set at the same level as the 0^+ state in ^{112}Sn .

III-1-2. High Energy γ -Rays Observed in the $^{181}\text{Ta}+^{40}\text{Ar}$ Reaction at 21 MeV/Nucleon

K. Yoshida, H. Hama, H. Harada, H. Takeuchi, M. Sakurai,
J. Kasagi, K. Ieki, T. Kubo, and M. Ishihara

{ NUCLEAR REACTION $^{181}\text{Ta}+^{40}\text{Ar}$, 21 MeV/nucleon; }
{ measured γ -ray spectrum, statistical model calculation. }

Recently, high energy γ -rays with energies up to 100 MeV have been observed in heavy-ion collisions at bombarding energies above 20 MeV/nucleon. The reported γ -ray spectra exhibit following features: γ -ray yields fall exponentially with energies for $E_\gamma < 10$ MeV and $E_\gamma > 30$ MeV and the yields enhance in the region between 10 MeV and 30 MeV. It is suggested the high energy ($E_\gamma > 30$ MeV) exponentially falling component arises from the nucleon-nucleon or nucleus-nucleus bremsstrahlung emitted at an early stage of the collision.^{1,2)} The γ rays below 30 MeV have been described as the statistical GDR decay of highly excited reaction residues. In order to study these γ rays, we measured inclusive γ -ray spectrum in $^{181}\text{Ta}+^{40}\text{Ar}$ reaction at 21 MeV/nucleon.

The experiment was performed at RIKEN Ring Cyclotron. A foil of ^{181}Ta , 12 mg/cm² in thickness, was bombarded with ^{40}Ar beams of 21 MeV/nucleon. The high energy γ -rays were detected with a large BaF₂ detector, which consists of seven optically isolated elements (hexagonal, diameter = 7 cm, length = 20 cm). The detector was positioned at 15 cm from the target and at 90° with respect to the beam axis. Cosmic rays were rejected by the information of the ratio of the energy deposit between in the center element and in total. Gamma rays, light charged particles, and neutrons were identified by pulse-shape analysis³⁾ and time of flight with respect to the RF signal of the cyclotron. The detector response was calculated using a Monte Carlo simulation code.⁴⁾

Observed γ -ray spectrum is shown in Fig. 1. For $E_\gamma \geq 30$ MeV the spectrum can be fitted by an exponential function $\exp(-E_\gamma/E_0)$. The deduced slope parameter $E_0 = 7.0 \pm 1.1$ MeV is somewhat smaller than the systematics for bremsstrahlung spectra obtained from reactions at higher energies. On the other hand, the obtained cross section $670 \pm 200 \mu\text{b}$ for $E_\gamma \geq 30$ MeV is rather large.

For the energies below 30 MeV, we attempt to describe the spectrum as the statistical decay of highly excited residues dominated by the giant-dipole-resonance strength function. The γ rays from pro-

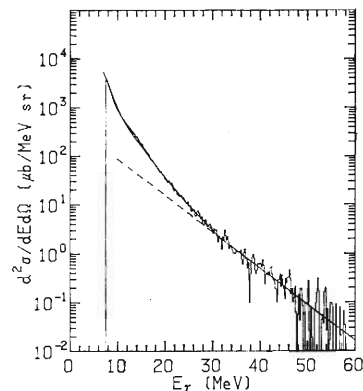


Fig. 1. γ -Ray spectrum observed for the reaction $^{181}\text{Ta}+^{40}\text{Ar}$ at 21 MeV/nucleon. The smooth line indicates statistical model calculation added a bremsstrahlung component. The dotted line indicates a bremsstrahlung component.

jectile-like fragments, target-like fragments, and fusion-fission fragments contribute to these γ rays. In calculation, only the γ rays from fusion-fission fragments were considered. The statistical model calculation using the code CASCADE was performed, and the results were folded by detector response to compare with the experimental spectrum. The excitation energies of the fission fragments (~ 170 MeV) are estimated by using the Viola systematics.⁵⁾ A Lorentzian shape was assumed as the GDR strength function. The experimental spectrum was reproduced with the resonance energy $E_G = 13$ MeV, width $\Gamma_G = 15$ MeV, and 100% sum rule strength. The resonance energy was rather small compared with the ground state systematics. To characterize these γ rays, measurements in coincidence with reaction residues are now in progress.

References

- 1) E. Grosse *et al.*: *Europhys. Lett.*, **2**, 9 (1986).
- 2) J. Stevenson *et al.*: *Phys. Rev. Lett.*, **57**, 555 (1986).
- 3) T. Murakami *et al.*: *Nucl. Instrum. Methods A*, **235**, 163 (1986).
- 4) T. Tachibanaki, T. Murakami, and J. Kasagi: *RIKEN Accel. Prog. Rep.*, **19**, 156 (1985).
- 5) V. E., Viola, K. Kwiatkowski, and M. Walker: *Phys. Rev. C*, **31**, 1550 (1985).

III-1-3. Angular Distribution of Fission Fragments Coincident with Projectile Fragments

K. Ieki, Y. Ando, H. Fujiwara, M. Ishihara, N. Iwasa, S. C. Jeong, S. M. Lee, T. Motobayashi, T. Mizota, H. Murakami, T. Murayama, Y. Nagashima, M. Ogiwara, S. Okumura, Y. H. Pu, Jian-zhi Ruan (Gen), S. Shibuya, and S. Shirato

{ NUCLEAR REACTION $^{209}\text{Bi} + ^{40}\text{Ar}$, $E(^{40}\text{Ar})/A = 26 \text{ MeV/u}$;
measured fission fragment angular distribution, projectile fragmentation, angular momentum transfer, spin alignment. }

For studies of heavy-ion reaction mechanisms, measurements of transferred angular momenta to the residual nuclei and their spin alignment have given important information. So far little is known about the angular momentum transfer for intermediate energy heavy-ion reactions. Therefore, we studied the angular momentum transfer and the spin alignment by measuring angular distribution of fission fragments coincident with projectile fragments for the $^{209}\text{Bi} + ^{40}\text{Ar}$ reaction at $E/A = 26 \text{ MeV/u}$. This method has been successfully applied for the studies of lower energy heavy-ion reactions.^{1,2)}

A self-supporting ^{209}Bi foil of about 1 mg/cm^2 in thickness was bombarded with a ^{40}Ar beam from RIKEN Ring Cyclotron. Projectile fragments were detected with two sets of counter telescopes located at 12° from the beam axis and at 40 cm from the target as shown in Fig. 1. The telescopes consist of $45 \text{ mm} \times 45 \text{ mm}$ Si $\Delta E(300 \mu\text{m})$ - $E(2 \text{ mm})$ - $E(2 \text{ mm})$ detectors. With these signals, particle identification (PI) was performed using a simple formula.³⁾ A sample PI spectrum is shown in Fig. 2. At this detection angle, α particles are mainly observed, and the yields for other particles become smaller as the particle mass increases. Coincident fission fragments were detected with 9 thin (30 or $50 \mu\text{m}$) Si detectors located at 10 cm from the target on the opposite side of the beam to the telescopes. The detection

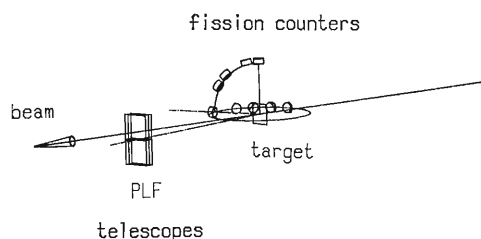


Fig. 1. Schematic view of the detector system.

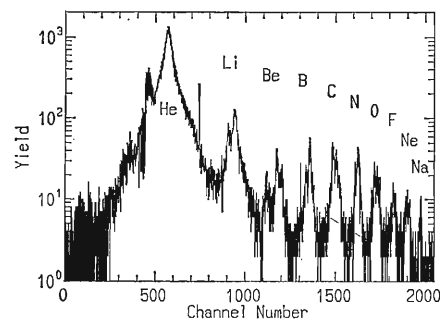


Fig. 2. Sample particle identification spectrum measured with the telescopes.

angles are $\phi = -70^\circ, -105^\circ, -125^\circ, -145^\circ, -165^\circ$ for inplane measurements and $\theta = 0^\circ, 15^\circ, 45^\circ, 60^\circ, \phi = -70^\circ$ for out of plane measurements, where θ and ϕ denote polar and azimuthal angles, respectively. The z axis and the x axis are defined by the reaction plane normal and the beam axis, respectively.

Typical fission-fragment spectra coincident with α particles in the laboratory frame are displayed in Fig. 3. The out of plane spectra (left-hand side) show a decrease in yield towards small polar angles. This large asymmetry of out-of-plane angular distribution suggests large angular momentum transfer and large spin alignment with respect to the reaction plane normal. The inplane spectra (right-hand side) show small variation in the yield. The spectra, however, differ from each other in shape, *i.e.*, the peak position moves as the detection angle changes. Assuming that fission-fragment energy spectra are the same in the rest frame of the fissile nuclei, the direction of which is found to be about -44° from the beam axis. On the other hand, the recoil angle of the fissile nucleus in the α particles obtained from

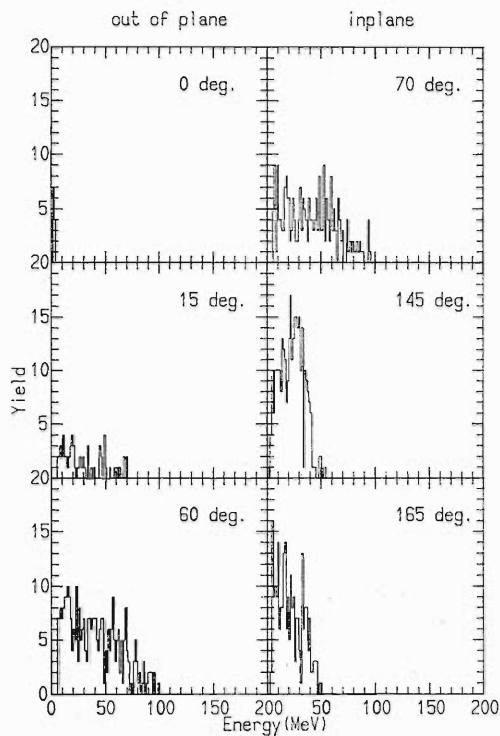


Fig. 3. Typical fission-fragment spectra coincident with α particles in the laboratory frame. On the left-hand side are shown the out-of-plane spectra with polar angles denoted; the azimuthal angle for them is 70° . The inplane spectra are shown on the right-hand side with azimuthal angles denoted.

the 2-body kinematics is much smaller. With these two facts combined, we can suppose that large missing momentum P_m exists in this reaction. Evaluating P_m from the momenta of the beam, α particle and fissile nucleus ($A \sim 200$), we found that the direction of P_m ($\phi \sim 6^\circ$) is near the grazing angle and the size of P_m corresponds to the projectile-like fragments ($A \sim 32$) emission at the beam velocity. Thus the observed large angular momentum transfer and the large spin alignment can be explained by peripheral collisions accompanied by sequential decays of the projectile-like fragments. Further analyses are now in progress.

References

- 1) P. Dyer, R. J. Puigh, R. Vandenbosch, T. D. Thomas, M. S. Zisman, and L. Nunnolley: *Nucl. Phys.*, **A322**, 205 (1979).
- 2) H. Utsunomiya, T. Nomura, M. Ishihara, T. Sugitate, K. Ieki, and S. Kohmoto: *Phys. Lett. B*, **105**, 135 (1981).
- 3) T. Nomura: *IPCR Cyclotron Prog. Rep.*, **11**, 81 (1977).

III-1-4. Spin Alignment in Projectile Fragmentation at Intermediate Energies

K. Asahi, M. Ishihara, T. Ichihara, M. Fukuda, T. Kubo, Y. Gono,
A. C. Mueller,* R. Anne,* D. Bazin,* D. Guillemaud-Mueller,*
R. Bombot,** W. D. Schmidt-Ott,*** and J. Kasagi

{ NUCLEAR REACTION $^{18}\text{O} + ^9\text{Be}$, $E(^{18}\text{O})/A = 60 \text{ MeV/u}$;
 β -delayed γ rays from ^{14}B , measured $W_\gamma(\theta)$; deduced spin
alignment of ^{14}B products, compared with theory. }

Recent progress in studies of nuclei far from stability, prompted by the advent of intermediate-energy heavy-ion accelerators, has proven that projectile fragmentation is a powerful tool for isotope production. The effectiveness of this method motivates further interest in whether these product nuclei are spin-oriented or not. In fact, more detailed spectroscopic investigations become possible if spin-oriented nuclei are available by this method. The measurement of the spin orientation in projectile fragmentation is also interesting, providing unique information on the reaction mechanisms. We thus performed a measurement of the spin alignment of projectile fragments using a LISE spectrometer at GANIL. Earlier part of this study has been reported.¹⁾

The spin alignment of ^{14}B nuclei produced in a $^{18}\text{O} + ^9\text{Be}$ reaction at $E(^{18}\text{O})/A = 60 \text{ MeV/u}$ was measured. The experimental setup is shown in Fig. 1. The spectrometer LISE was used for the isotope separation of the reaction products. A wedge-shaped energy degrader for a momentum-loss technique²⁾ was installed in the momentum-dispersive focal plane between the two dipole magnets of LISE. Produced ^{14}B was collected in a stopper foil (Pt) placed at the achromatic focal point. The static magnetic field $B_0 = 310 \text{ mT}$ parallel to the two dipole fields of LISE was applied to the stopper. γ Rays emitted after β decay of ^{14}B were detected with two NaI(Tl) detectors placed at 0° and 90° to the direction of B_0 . The ratio $R = N_\gamma(0^\circ)/N_\gamma(90^\circ)$ of the γ ray yields was measured both with B_0 on (*i.e.*, with the

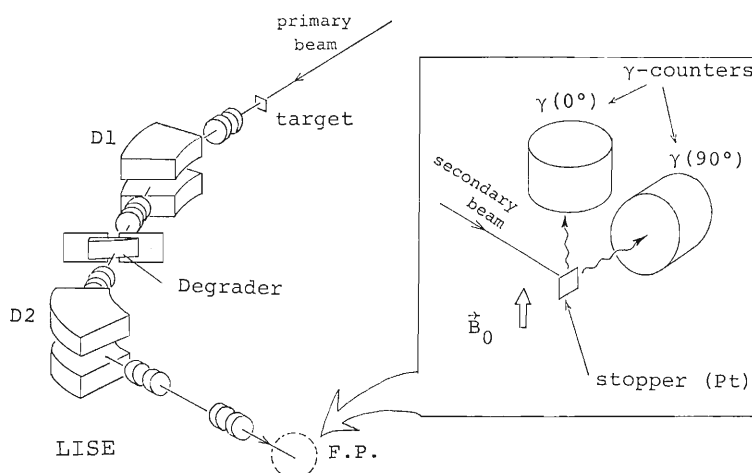


Fig. 1. Experimental setup.

* Grand Accelérateur National d'Ions Lourds (GANIL), Caen, France.

** Institut de Physique Nucleaire, Orsay, France.

*** Physikalisches Institut, Universität Göttingen, Göttingen, Fed. Rep. of Germany.

alignment preserved) and off (with the alignment destroyed).

The spin alignment A produced by the reaction in the beam axis is expressed in terms of the population probability a_m for the magnetic sublevel m as

$$A = (2a_{+2} - a_{+1} - 2a_0 - a_{-1} + 2a_{-2})/2$$

As a result of the spin precession in the dipole fields

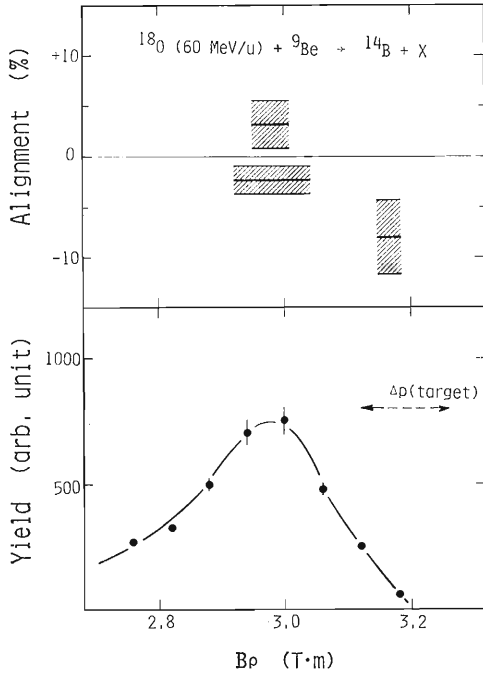


Fig. 2. Result for spin alignment A of ^{14}B produced in the reaction ^{18}O (60 MeV/u) + ^9Be ; the observed momentum distribution for ^{14}B is also shown. Value of A shown is the one averaged over the momentum bin which is indicated by horizontal bars.

of LISE and in B_0 , a new alignment $A' = -(1/2)A$ in the axis parallel to B_0 is established³⁾ after a short period of time characterized by the transverse spin relaxation time. Thus the initial alignment A was deduced from the change in R between the two conditions through

$$A = (-8/3)(R_{\text{ON}}/R_{\text{OFF}} - 1)$$

where ON and OFF refer to the measurement with B_0 on and off, respectively.

In Fig. 2 the result for the spin alignment is shown together with the momentum distribution measured for the ^{14}B particles. An interesting feature was observed: The alignment A is small in the momentum region corresponding to the peak in the yield, whereas A takes a large negative value for the high-momentum tail. The observed momentum variation in the alignment seems to agree with the prediction from a simple model of projectile fragmentation.⁴⁾

References

- 1) K. Asahi, M. Ishihara, T. Ichihara, Y. Gono, A. C. Mueller, R. Anne, D. Bazin, D. Guillemaud-Mueller, R. Bimbot, W. D. Schmidt-Ott, and J. Kasagi: *RIKEN Accel. Prog. Rep.*, **20**, 19 (1986).
- 2) D. Guillemaud-Mueller, R. Anne, D. Bazin, C. Detraz, J. Galin, D. Guerreau, A. C. Mueller, E. Roedel, M. G. Saint-Laurent, M. Bernas, V. Borrel, J. C. Jacmart, M. Langevin, F. Naulin, F. Pougheon, and E. Quiniou: *Proc. 5th Int. Conf. Nuclei Far from Stability* (Rosseau Lake, Canada, 1987), p. 757.
- 3) H. Morinaga and T. Yamazaki: *In-Beam Gamma-Ray Spectroscopy*, North-Holland, Amsterdam, Chap. 9 (1976).
- 4) K. Asahi and M. Ishihara: *RIKEN Accel. Prog. Rep.*, **20**, 21 (1986).

III-1-5. Tensor Analyzing Powers of (d, ^2He) Reactions on ^1H and ^{12}C

T. Motobayashi, M. Ishihara, H. Murakami, S. Satoh,* H. Sakai,** N. Matsuoka,**
T. Saito,** T. Noro,** K. Hosono,** A. Okihana,*** H. Okamura,**** and S. Hatori****

{ NUCLEAR REACTIONS ^1H , ^{12}C (polarized d, ^2He), $E = 70 \text{ MeV}$;
measured $A_{yy}(\theta)$ PWIA and DWBA analysis. }

The (d, ^2He) reaction, where ^2He denotes the two proton system in the relative S-state, is useful in studying spin-isospin excitation of nuclei. The importance of the measurements with a tensor polarized deuteron has been recently stressed by Wilkin and Bugg.¹⁾ We measured the tensor analyzing power A_{yy} for the targets of ^1H and ^{12}C using 70 MeV tensor polarized deuterons provided by the cyclotron of the Research Center for Nuclear Physics, Osaka University. Outgoing ^2He particles were detected by a silicon telescope array²⁾ or a magnetic spectrograph DUMAS,³⁾ the latter of which was used only for the measurements at forward angles. The results are shown in Figs. 1 and 2.

For the $^1\text{H}(d, ^2\text{He})n$ reaction the PWIA (Plane Wave Impulse Approximation) calculations were performed. The solid and dot-dashed curves in Fig. 1 represent the results using the N-N amplitudes of the Arndt's phase shift solution⁴⁾ with and without the D-state component of the deuteron wave function, respectively. The dashed curve shows the PWIA prediction including the deuteron D-state with the N-N amplitudes calculated from the Paris potential.⁵⁾

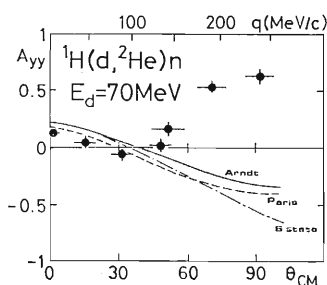


Fig. 1. Angular distribution of the tensor analyzing power A_{yy} of the $^1\text{H}(d, ^2\text{He})n$ reaction at $E_d = 70 \text{ MeV}$. The solid and dashed curves show the PWIA predictions with Arndt's phase shift solution and the Paris potential, respectively. The result without including the deuteron D-state is shown by the dot-dashed curve.

* Department of Physics, Rikkyo University.

** Research Center for Nuclear Physics, Osaka University.

*** Kyoto University of Education.

**** Department of Physics, Kyoto University.

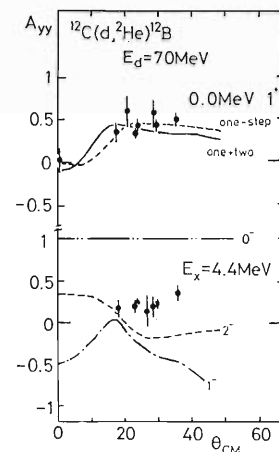


Fig. 2. Angular distributions of the tensor analyzing power A_{yy} for the (d, ^2He) reaction on ^{12}C . The results of the first- and second-order DWBA calculations are shown by the dashed and solid curves, respectively. For the $\Delta l = 1$ transition to the 2^- state of ^{12}B , the DWBA predictions assuming different spin values of 1^- and 0^- are also shown by the dot-dashed and double dot-dashed curves, respectively.

At forward angles, the calculations, especially that with the Paris potential, reproduce the tendency of the experimental data. This is inconsistent with the discrepancy between experimental data and PWIA predictions reported for the $K_{\frac{1}{2}}^{\frac{1}{2}}(0^{\circ})$ of the $^2\text{H}(p, n)-^2\text{He}$ reaction in the same energy range.⁶⁾ At backward angles the PWIA predictions deviate far from the data, suggesting the important contribution of a multiple scattering process in the high momentum transfer region.

The curves in Fig. 2 show the results of the one- and two-step DWBA (Distorted Wave Born Approximation) analysis for the $^{12}\text{C}(d, ^2\text{He})^{12}\text{B}$ reaction. The parameters used in the calculation are taken to be the same as those described in Ref. 7. The fits to the data for the ground state transition are good and the two-step effect is not so large as for the cross section.⁷⁾ For the $\Delta l = 1$ transition to the 2^- excited state of ^{12}B , the fits are poor, but the theoretical

curve is closer to the data than the ones for the $\Delta l=1$ transitions to the different spin states, 0^- and 1^- .

References

- 1) C. Wilkin and D. V. Bugg: *Phys. Lett. B*, **154**, 243 (1986).
- 2) T. Motobayashi, S. Satoh, H. Murakami, H. Sakai, and M. Ishihara: *RIKEN Accel. Prog. Rep.*, **20**, 125 (1986).
- 3) T. Noro, T. Takayama, H. Ikegami, M. Nakamura, H. Sakaguchi, H. Sakamoto, H. Ogata, M. Yosoi, T. Ichihara, N. Isshiki, M. Ieiri, Y. Takeuchi, H. Togawa, T. Tsutsumi, and S. Kobayashi: *J. Phys. Soc. Jpn.*, **55**, Suppl., 470 (1986).
- 4) R. A. Arndt and L. D. Roper: Scattering analysis interactive dial-in (SAID) program, Phase shift solution SP86, Virginia Polytechnic Institute and State University (unpublished).
- 5) M. Lacombe, B. Loiseau, J.M. Richard, R.V. Mau, J. Cote, P. Pires, and R. de Jureil: *Phys. Rev. C*, **21**, 861 (1980).
- 6) H. Sakai, N. Matsuoka, T. Saito, A. Shimizu, M. Tosaki, M. Ieiri, K. Imai, A. Sakaguchi, and T. Motobayashi: *Phys. Lett. B*, **177**, 155 (1986).
- 7) T. Motobayashi, M. Ishihara, H. Sakai, N. Matsuoka, K. Hosono, T. Saito, A. Okihana, S. Shimoura, and A. Sakaguchi: *RIKEN Accel. Prog. Rep.*, **20**, 29 (1986); T. Motobayashi, H. Sakai, N. Matsuoka, T. Saito, K. Hosono, A. Okihana, M. Ishihara, S. Shimoura, and A. Sakaguchi: *Phys. Rev. C*, **34**, 2365 (1986).

III-1-6. Rotational Perturbation to the Natural Parity Rotational Band of ^{163}Dy

T. Inamura, A. Hashizume, M. Oshima,* E. Minehara,* S. Kikuchi,*
M. Matsuzaki,** and H. Kusakari

(NUCLEAR STRUCTURE ^{163}Dy , energy levels, reduced transition probabilities, signature dependence, rotating shell model.)

As we reported previously,¹⁾ there is quite a strong signature dependent staggering of $B(M1)$ values in ^{163}Dy . This is an unexpected result because the ground-state rotational band of ^{163}Dy is based on the neutron $5/2[523]$ Nilsson orbital whose main components are low spin orbitals such as $h_{9/2}$ or $f_{7/2}$ and its energy levels show no signature dependence.

The rotational perturbation effect which causes signature dependent level energies and transition moments has been well established theoretically and experimentally for the case of high spin orbitals such as $i_{13/2}$.²⁻⁵⁾ This is because the Coriolis force strongly acts on high spin orbitals. However, no model calculations have ever suggested that there might be signature dependence in the nuclear structure of deformed nuclei with low spin orbitals. A new theoretical framework is needed to study such a nucleus as ^{163}Dy in question.

A rotating shell model with the γ degrees of freedom⁶⁾ seems to provide such a new framework. According to this model, we have calculated reduced transition probabilities and level energies. It turns out that one can neglect a static γ deformation, leaving the effect of a dynamical γ deformation (γ vibrations) significant; the static γ deformation is very small, being restricted to the region such that $0^\circ < \gamma < 5^\circ$.

Figure 1 shows quasineutron energy splitting $e'_{-1/2} - e'_{+1/2}$ as a function of the rotational frequency $\hbar\omega_{\text{rot}}$, where e'_α are quasineutron energies for the states with the signature $\alpha = \pm 1/2$. (The plot starts at the 2nd excited state $9/2^-$ at 167.3 keV.) Experimental splitting is shown by a bold line; and the splitting calculated with the γ vibrations are shown by a solid line, and the one without the γ degrees of freedom by a dotted line. Although there seems to be a room to study further for higher rotational frequencies, the agreement between the experimental

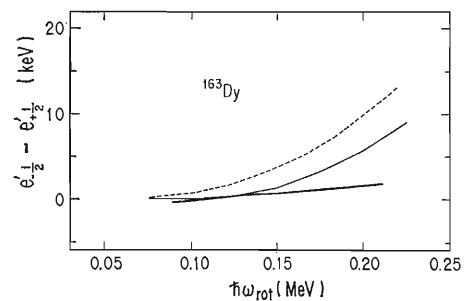


Fig. 1. Quasineutron energy splitting $e'_{-1/2} - e'_{+1/2}$ plotted as a function of the rotational frequency $\hbar\omega_{\text{rot}}$. The bold line denotes the experimental data. The solid line denotes the calculation with the γ vibrations, and the dotted one the calculation without the γ degrees of freedom.

and the calculation has significantly been improved by taking the γ vibrations into account. (Note that the quasineutron energy splitting, for instance in ^{167}Er , which is a typical nucleus with a high j orbital ($i_{13/2}$), are about ten times larger than that in ^{163}Dy .) It should also be pointed out that the improvement has been made without causing signature dependence in level energies, *i.e.*, quasiparticle energy splitting.

Figure 2 shows the signature dependence of the reduced M1 transition probabilities $B(M1)$ as a

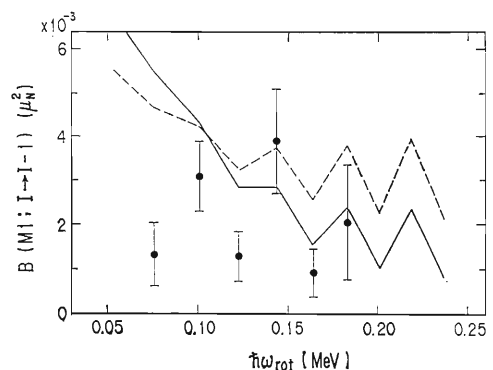


Fig. 2. $B(M1; I \rightarrow I-1)$ values for the ground-state rotational band of ^{163}Dy . The solid and dotted lines are the same as in Fig. 1.

* Tokai Research Establishment, Japan Atomic Energy Research Institute.

** Department of Physics, Kyoto University.

function of the rotational frequency $\hbar\omega_{\text{rot}}$. It is clearly seen that the signature dependent staggering is well reproduced in the present calculation. The calculation is a kind of cranked shell-model calculation. In general, the cranked shell model gets worse in the region of low rotational frequencies. This tendency appears in the present calculation, but this does not matter in the present study of signature dependence since only higher rotational frequencies concern the present study.

At present, it is hard to single out which is the main component, $h_{9/2}$ or $f_{7/2}$, but the $h_{9/2}$ orbital should be predominant in the $5/2[523]$ Nilsson orbital at the deformation parameter $\beta=0.285$;⁷⁾ the β value was estimated from the E2 transition probabilities between low spin members of the ground-state rotational band of ^{163}Dy . If the simple rule for signature dependence is applied to this case,⁶⁾ the phase of the staggering is different from the observed one: The experimental data appear as if the main component were the $f_{7/2}$ orbital. The signature dependent staggering has nothing to do with the γ degrees of freedom; but the absolute values of $B(M1)$ do have.

In the case of natural parity orbitals such as $f_{7/2}$ or $h_{9/2}$, one has to take into account j mixing,

which is automatically accommodated in the present calculation: The single particle space taken in the calculation is the $N_{\text{osc}}=4, 5, 6$ shells for neutrons; and the $N_{\text{osc}}=3, 4, 5$ for protons. Therefore, we conclude that the signature dependence of $B(M1)$ values in the natural-parity rotational band is sensitive to the j mixing effect.

In contrast, $B(E2; I \rightarrow I-2)$ and $B(E2; I \rightarrow I-1)$ values have no significant signature dependence.

References

- 1) E. Minehara, M. Oshima, S. Kikuchi, T. Inamura, A. Hashizume, and H. Kumahora: *Phys. Rev. C*, **35**, 855 (1987).
- 2) J. Kownacki, J. D. Garrett, J. J. Gaardhoje, G. B. Hagemann, B. Herskind, S. Jonsson, N. Roy, and W. Walus: *Nucl. Phys. A*, **394**, 269 (1983).
- 3) G. B. Hagemann, J. D. Garrett, B. Herskind, J. Kownacki, B. M. Nyako, P. L. Nolan, and J. F. Sharpey-Schafer: *Nucl. Phys. A*, **424**, 365 (1984).
- 4) M. Oshima, E. Minehara, M. Ishii, T. Inamura, and A. Hashizume: *Nucl. Phys. A*, **436**, 518 (1985).
- 5) I. Hamamoto and B. R. Mottelson: *Phys. Lett. B*, **132**, 7 (1983).
- 6) M. Matsuzaki, Y. R. Shimizu, and K. Matsuyanagi: *Prog. Theor. Phys.*, **77**, 1302 (1987).
- 7) A. Bohr and B. R. Mottelson: *Nuclear Structure*, Benjamin, Inc., New York, Vol. II, p.229 (1975).

III-1-7. Study of Neutron-Rich Nuclei with Radio-Isotope Beams

I. Tanihata, T. Kobayashi,* S. Shimoura,* K. Ekuni,**
K. Sugimoto,*** and H. Sato****

(Heavy-ion collision, Radioactive beam, High-energy collisions,
Interaction cross section, Nuclear radii, Isobaric dependence.)

It was shown that nuclear radii can be determined from the interaction cross sections of high-energy heavy-ion collisions.^{1,2)} In particular, the use of beams of radioactive nuclei provides a unique method for determining matter radii of unstable nuclei and enables us to make a direct comparison of radii between isobars. The isospin dependence of radii was difficult to study because, in most cases, only one stable isobar of the same mass number exists. In this report was present the isospin dependence of nuclear matter radii for isobars of mass numbers from 6 to 12.

The root-mean-square (*rms*) radii of nucleon distribution were deduced by a Glauber-type calculation. Details of the method are described in Ref. 2. The *rms* radii of nucleon distribution are plotted for isobars of mass number $A=6, 7, 8, 9, 11,$ and 12 in Fig. 1. A pair of nuclei with the same isospin (T) but different T_z , such as ${}^7\text{Li}$ - ${}^7\text{Be}$ or ${}^8\text{Li}$ - ${}^8\text{B}$, show equal radii. It suggests that the Coulomb effect on the radii is negligible for these light nuclei. On the other hand, a nucleus with a larger isospin shows a larger radius except for $A=9$ isobars. The isospin dependence of isobar radii thus obtained is compared with theoretical predictions as follows.

First, predictions from the droplet model³⁾ were shown by the dotted lines in Fig. 1. The predicted values are almost independent of isospin and fail to reproduce the experimental trend, *i.e.* the strong isospin dependence. The droplet model allows proton and neutron density distribution to vary so as to minimize the total nuclear energy, but it assumes constant surface diffuseness. The disagreement with the present data suggests that those changes are not enough to explain the observed isospin dependence.

Next, comparisons with the predictions from a Hartree-Fock (HF) calculation using the Skyrme potential⁴⁾ were made as shown in Fig. 1. Two different sets of potential parameters, SIII and SV,

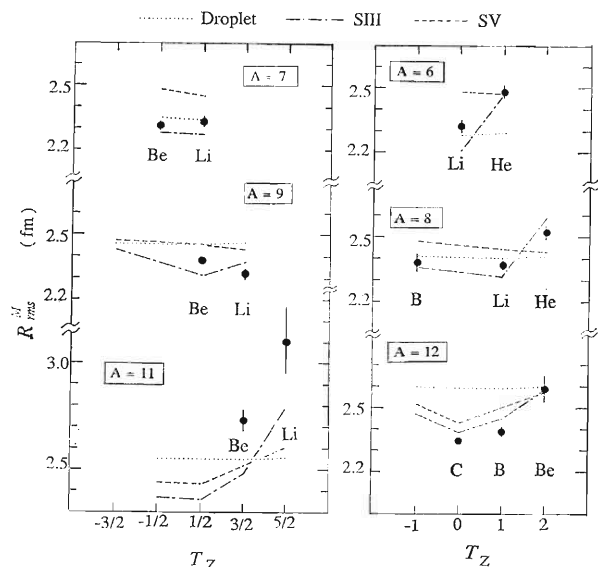


Fig. 1. Isospin dependence of the root-mean-square radii of nucleon distributions. Experimental values are shown by the solid circle. Dotted lines show results of the droplet model calculations. Results of the Hartree-Fock calculations with Skyrme potentials are shown by the dash-dotted line (for SIII potential) and by the dashed line (for SV).

were used.⁵⁾ These sets of parameters are basically different in the density dependence of effective interactions: SIII includes a strong density-dependent interaction, but SV does not. Both calculations are in fair agreement with the data to within 0.2 fm for most of the nuclei. The radii calculated with the SV potential, however, have the isospin dependence much weaker than that of observed. On the other hand, the radii obtained with the SIII potential agree well with the observed isospin dependence, except for $A=9$ isobars. The comparison of the data with the HF calculation, therefore, indicates the importance of the density dependent interaction in understanding the radii of exotic nuclei in the present framework. However, the other nuclear structure effects, such as deformation and clustering, have to be taken into account before obtaining the conclusive statement.

Isobars of $A=9$ show abnormal behavior in the

* National Laboratory for High-Energy Physics.

** Faculty of Science, Kyoto University.

*** Faculty of Science, Osaka University.

**** Institute for Nuclear Study, The University of Tokyo.

data, namely the isobar with smaller isospin (${}^9\text{Be}$) has a radius larger than the isobar with a larger isospin (${}^9\text{Li}$). It is known that the ${}^9\text{Be}$ nucleus has a broad charge distribution because of the strong configuration of two α clusters weakly bound by a neutron. This anomalous structure was not taken into account for the present HF calculation, therefore it is understandable that the calculation gave different isospin dependence of nuclear radii.

References

- 1) I. Tanihata, H. Hamagaki, O. Hashimoto, S. Nagamiya, Y. Shida, N. Yoshikawa, O. Yamakawa, K. Sugimoto, T. Kobayashi, D. E. Greiner, N. Takahashi, and Y. Nojiri: *Phys. Lett. B*, **160**, 380 (1985).
- 2) I. Tanihata, H. Hamagaki, O. Hashimoto, Y. Shida, N. Yoshikawa, K. Sugimoto, O. Yamakawa, T. Kobayashi, and N. Takahashi: *Phys. Rev. Lett.*, **55**, 2675 (1985); I. Tanihata, T. Kobayashi, O. Yamakawa, S. Shimoura, K. Ekuni, K. Sugimoto, N. Takahashi, T. Shimoda, and H. Sato: *Phys. Lett. B*, **206**, 592 (1988).
- 3) W. D. Myers and K.-H. Schmidt: *Nucl. Phys.*, **A410**, 61 (1983).
- 4) H. Sato and Y. Okuhara: *Phys. Rev. C*, **34**, 2171 (1986).
- 5) M. Beiner, H. Flocard, Nguyen Van Giai, and P. Quentin: *Nucl. Phys.*, **A238**, 29 (1975).

III-1-8. Development of a Particle-Identification Technique and Search for New Isotopes

W. P. Liu,* I. Tanihata, T. Kubo, T. Suzuki, M. Yanokura,
H. Kumagai, H. Murakami, T. Yanagimachi, T. Doke, N. Hasebe,
T. Nakagawa, J. Kikuchi, H. Yamaguchi, and T. Ito**

(NUCLEAR REACTIONS ${}^9\text{Be}$ (${}^{65}\text{Cu}$, ${}^{40}\text{Ar}$, ${}^{40}\text{Ca}$, x), $E=16.7, 25.75, 26.0$ MeV/A; measured time of flight, energy loss, total energy and magnetic rigidity; deduced mass number, atomic number, charge state and yield of fragments. Natural target.)

A problem of primary importance for all studies of nuclei far off stability is obviously to find suitable means to produce them in large quantities. As high intensity heavy ions are now available at intermediate energies (GANIL, LBL, SARA, CERN, RIKEN), the projectile fragmentation mechanism can be used to produce the exotic nuclei and the secondary beams of these nuclei can be produced by magnetic separation.

For this reason we have planned a set of experiments: ${}^{65}\text{Cu}$ (16.7 MeV/A) + Be, ${}^{40}\text{Ar}$ (25.75 MeV/A) + Be, and ${}^{40}\text{Ca}$ (26.0 MeV/A) + Be to establish an isotope identification technique and search for new isotopes:

The experimental setup is shown in Fig. 1. In RRC (Riken Ring Cyclotron) experiment room E1, the D (dipole) magnet bends the fragments of interest to 20 degree, and two Q (quadrupole) magnets focus them. In a focal plane, PPAC (parallel-plate avalanche counter), PSSD (position-sensitive silicon

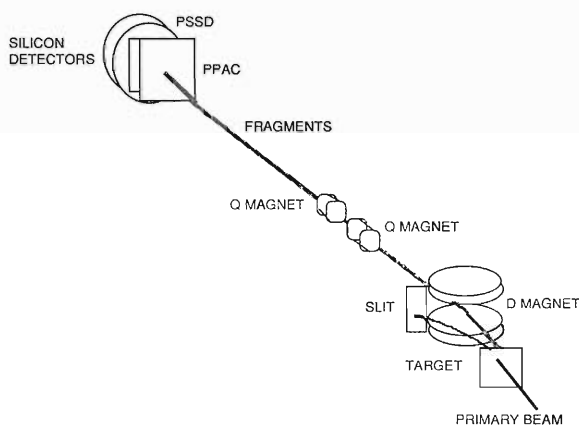


Fig. 1. Experiment setup. (See text for details.)

* Permanent Address: Institute of Atomic Energy, P.O. Box 275 (60), Beijing, China.

** Science and Engineering Research Laboratory, Waseda University.

detector) and silicon detectors constitute a ΔE - E -TOF (time of flight) isotope identification system. The start signal of TOF was given by an RF (radio frequency) signal of RRC. The probe inside the D magnet gave a reference for the selection of a $B\rho$ (magnetic rigidity) value. This system is rather simple compared with that of other laboratories, such as LISE (projectile fragments separator) in GANIL, but gave satisfactory results.

We present the results of these three experiments and the ideas evolved during the experiments.

${}^{65}\text{Cu}$ + Be run: A neutron-rich beam was chosen

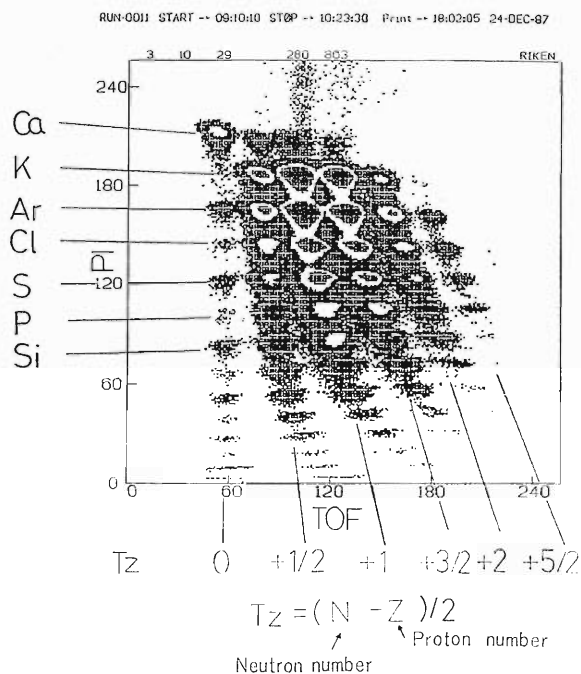


Fig. 2. TOF (time of flight)-PI (particle identification function) contour plot in $B\rho$ (magnetic rigidity) setting for $A/Z=2.0$ isotopes in an ${}^{40}\text{Ar}$ +Be run. The isospin T_z of each TOF branch and the element name of each PI line are indicated.

for searching ^{54}Sc . PSSD and PPAC were not used. Because of the momentum spread along the horizontal direction from the reaction mechanism, it was impossible to separate the mass with silicon detectors which have rather wide sensitive area (900 mm^2). Charge separation was achieved by using a PI function defined by $PI = (E + \Delta E)^{1.45} - E^{1.45}$, where ΔE is the energy loss in the first silicon detector and E is the residual energy in the second one.

$^{40}\text{Ar} + \text{Be}$ run: PPAC and PSSD were used. Isotope identification was achieved. By using the position signal of PSSD, all data without losing the time resolution were analyzed. Large cross sections for the production of K isotopes were observed. This results prompted us to use a ^{40}Ca beam to search for a new isotope ^{39}Sc and measure the cross sections of (^{40}Ca , ^{40}Sc) and (^{40}Ca , ^{40}K), which provide useful data for the transfer-reaction mechanism in this energy domain. Figure 2 gives a TOF- PI contour plot in a $B\rho$ setting appropriate for $A/Z=2.0$ isotopes. (The isospin T_z of each TOF branch and the element name of each PI line is indicated.)

$^{40}\text{Ca} + \text{Be}$ run: A proton-rich ^{40}Ca beam was chosen for searching for ^{39}Sc . By measuring the beam intensity through the secondary electron emission from the target, the absolute cross section can be deduced.

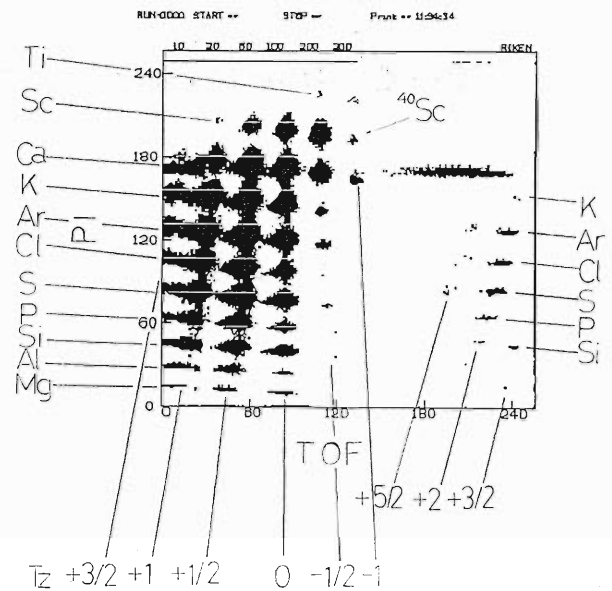


Fig. 3. The same plot as Fig. 2 in a $^{40}\text{Ca} + \text{Be}$ run; $B\rho$ setting for proton-rich isotopes.

^{40}Sc was observed on-line. Figure 3 shows a TOF- PI contour plot in a proton-rich $B\rho$ setting of the ^{40}Ca run.

The existence of ^{39}Sc and other results of these three runs are under analysis.

III-1-9. Total Reaction Cross Section Measurement of Unstable Nuclei

M. Fukuda, M. Ishihara, I. Tanihata, K. Asahi, T. Ichihara,
T. Kubo, M. Adachi, M. Koguchi, and H. Kumagai

{ Heavy-ion collisions, Radioactive beam, Projectile fragmentation, }
{ Total reaction cross section, ^{18}O . }

A total reaction cross section (σ_R) includes a variety of information on the properties of nuclei such as a nuclear size, reaction mechanism, or nuclear structure. However, it had not been possible to measure σ_R of unstable nuclei, until a projectile fragmentation reaction in the high or intermediate energy region provided a powerful tool to produce unstable nuclei as a beam. By using the projectile fragmentation, we can extend the field of the σ_R study to a broad unstable region. Another interest is in a point that in the intermediate energy region available at RIKEN Ring Cyclotron, a heavy-ion reaction mechanism may have a transitional feature between a low energy limit (collective aspect) and a high energy limit (nucleon-nucleon aspect). In addition, data on σ_R in this energy region is poor com-

pared with those in the lower or higher energy region.

Recently, Mittig *et al.* at GANIL reported the measurement of σ_R of unstable nuclei ($Z=5-12$) by detecting γ ray. They interpreted a detection of γ ray as a sign of an occurrence of a reaction. We also planned to measure σ_R in a different way—beam attenuation method—using Si-detectors and carried out a test experiment. One point of ours different from Mittig *et al.* is that as the method is different, and then the definition of ' σ_R ' is different, the physical meanings of measured value may also be different. Another point is a thin secondary target. The region of energy integration, therefore, becomes narrower (40–20 MeV/u) than theirs (60–0 MeV/u). Figure 1 shows a schematic drawing of the setup. A

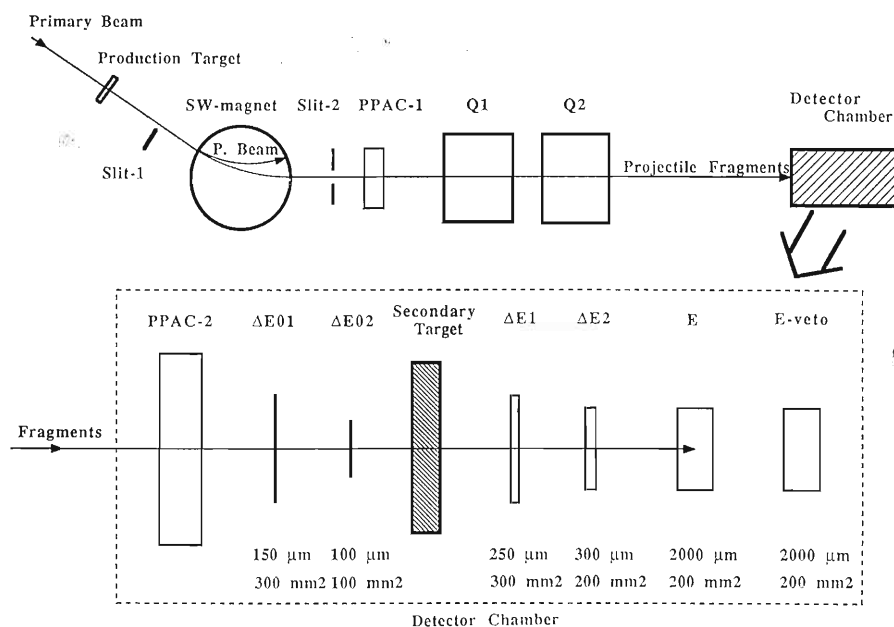


Fig. 1. Setup for σ_R measurement by a beam attenuation method in the test experiment. The production target was Be of 46 mg/cm^2 in thickness. The lower part shows a detector setup in the detector chamber. Six Si-detectors supplied from ORTEC were used. Figures under the Si-detectors are their thickness and active area. Secondary target was Be of 301 mg/cm^2 in thickness.

beam hitting a production target produces various kinds of nuclide coming out of the target with almost the same velocity as the beam. They are roughly separated by A/Z after passing through a switching (SW)-magnet. The beam is stopped at the exit of the SW-magnet, and only the projectile fragments are focussed on a detector position in the chamber. The detector setup is divided into two parts: one is for a first particle identification (PI) and the second is for PI after the secondary target. As the transported projectile fragments contain several kinds of nuclide, PI is needed at the first stage. The first PI consists of magnetic rigidity ($B\rho$), TOF, and ΔE measurements. $B\rho$ of a particle which can reach to the detector chamber is selected by the SW-magnet. The momentum dispersion at the second parallel plate avalanche counter (PPAC-2) is 8 mm/%. TOF and ΔE are measured with PPAC-1, PPAC-2 and $\Delta E01, 02$. In order to reduce wrong identification, we use two $\Delta E0$ counters to check their consistency. PPACs are position sensitive and PPAC-2 also plays a role as an active slit for Si-detectors.

The second PI is achieved by a ΔE - E counter telescope which consists of four Si-detectors. The second PI is for checking whether or not an incident

particle changes in the secondary target.

Two kinds of secondary target configurations, target-in-runs and target-out-runs, are needed. The target-out-run is for the correction for the missing of events by reaction in Si-detectors or pulse height defect. In the target-out-run, we put the secondary target just after the production target to adapt the energy at the entrance of the counter telescope to the one in the target-in-run and also to identify particles correctly.

The total reaction cross section is represented by

$$\sigma_R = (1/N_t) \cdot \ln(R_0/R)$$

where R and R_0 are the ratios (the number of unchanged events/the number of incident particle) for the target-in-run and the target-out-run, respectively, and N_t is the number of target nuclei per unit area.

A test measurement was carried out with an ^{18}O primary beam. (Fig. 2) The energy of the beam was 41.4 MeV/u, which was determined by an absolute TOF measurement with PPACs. The beam current was 0.1–1 enA. The production target was Be of 46 mg/cm² in thickness. At first, we measured σ_R of the primary beam itself as a test. The secondary target for the measurement was Be of 301 mg/cm². The probability of a reaction in the secondary target was about 2.5%. The preliminary result is σ_R (^{18}O - ^9Be) = 1,470 (80) mb. The main part of the error comes from the ambiguity in distinguishing unchanged events from reaction products due to the tailing peak in the energy spectra of ΔE counters. The production of unstable nuclei was also checked. Figure 3 shows several products identified by the first part of PI with SW- and Q-magnets adjusted to ^{16}C .

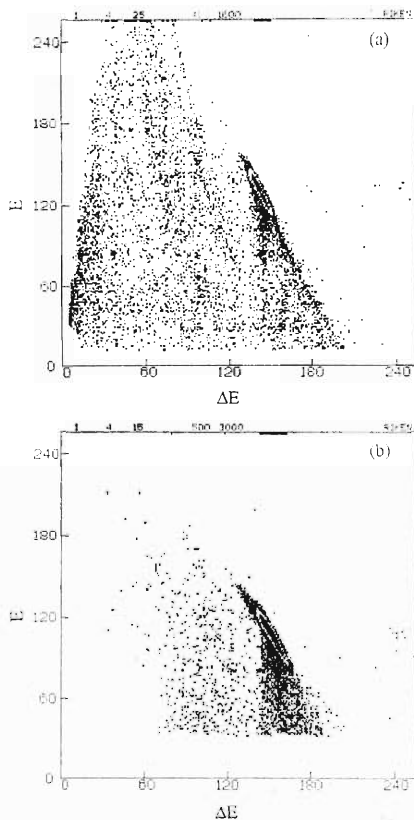


Fig. 2. ΔE - E plot of target-in-run (a), and target-out-run (b) for ^{18}O primary beam. ΔE is a sum of $\Delta E1$ and $\Delta E2$; E is an output of an E detector.

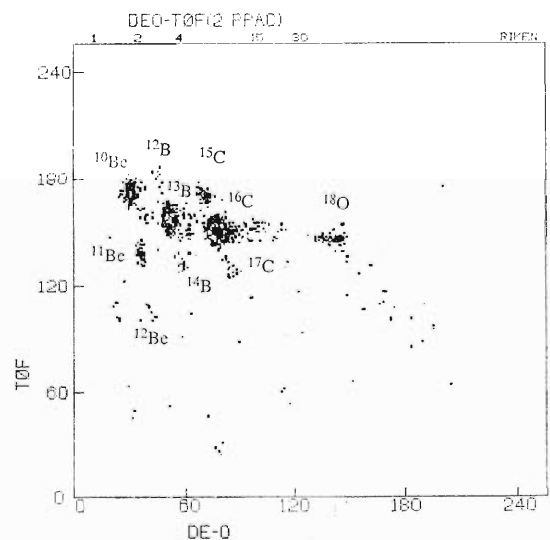


Fig. 3. $\Delta E0$ -TOF spectrum taken with a $B\rho$ condition adjusted to ^{16}C . The $B\rho$ resolution in this run was 1.9%; $\Delta E0$ is a sum of $\Delta E01$ and $\Delta E02$.

III-1-10. Effect of Final State Interactions on (π, η) Reactions

Y. Ohkubo and L. C. Liu*

{ NUCLEAR REACTION $^{12}\text{C}(\pi^+, \eta)$, $T_\pi = 555$ MeV; DWIA }
 { calculation with the eikonal approximation. }

The study of eta mesons is of fundamental interest because the so-called U(1) problem concerning eta mesons is still not fully understood. The simple SU(6) quark model cannot account for the mass difference between η and η' mesons. Studies of eta-nucleon interactions are expected to provide useful information that might shed light on the structures of eta mesons. Because it is nearly impossible to produce an eta beam, the nucleus is the only laboratory available for such studies. Recently, it has been shown by Liu and his collaborators that the low-energy S_{11} ηN interaction is attractive¹⁾ and that this attraction can bind the η into nuclear orbitals²⁾ in nuclei with a mass number $A > 10$. The existence of a mesic nucleus cannot be readily investigated with other mesons such as pions or kaons. As for pions, there is a strong cancellation between the isospin 1/2 and 3/2 πN s-wave scattering amplitudes such that the resultant low-energy s-wave pion-nucleus interaction is weak and even repulsive. The p-wave pion-nucleus interaction is attractive, but it turns out to be very small owing to the critical dependence of its strength on the local pion momentum. As for kaons, $K^+\text{N}$ interaction is repulsive at low energies. Although the low-energy $K^-\text{N}$ interaction is attractive, K^- preferentially forms mesic atoms because of strong Coulomb interactions. Liu and Haider^{3,4)} calculated and identified the signature for the formation of eta-mesic nuclei in the $^{16}\text{O}(\pi^+, p)^{16}_\eta\text{O}$ and $^{14}\text{C}(\pi^+, \pi^-)^{14}\text{O}$ (double isobaric analog state) reactions with the incident pion energy for the former case being about 610 MeV and that for the latter about 420 MeV.

We are planning to calculate the differential cross sections $d^2\sigma/dE_\eta d\Omega_\eta$ for the $A(\pi, \eta)$ reaction with $A = ^{12}\text{C}, ^{40}\text{Ca}, ^{208}\text{Pb}$, taking into account the attractive η -nucleus final state interaction. It is expected that this final state interaction enhances the cross sections at low energies of the outgoing η particle.⁵⁾ It is much of interest to know how significant the attractiveness in the η -nucleus final state interaction is. In this period, using the DWIA formalism with

the eikonal approximation⁶⁾ for the incident pion and with the plane wave approximation for the outgoing η , we calculated the differential cross section for the $^{12}\text{C}(\pi^+, \eta)$ reaction at $T_\pi = 554.6$ MeV to compare with its preliminary experimental data.⁷⁾ As we know, the eikonal approximation is simple and good for a high energy particle such as the incident pion in the present reaction, but is not considered as being good for a low energy particle such as the outgoing low energy η . For the η particle, as its momentum approaches zero, the optical potential approaches a nonzero value.¹⁾ Thus, the damping factor due to the distortion calculated by the eikonal approximation is expected to be unrealistically large for the low energy η . Moreover, the eikonal approximation cannot reflect the attractiveness in the η -nucleus interaction. It always diminishes the nuclear t matrix. We show in this work that we need seriously take into account the η -nucleus final-state interaction. Incidentally, we calculated using the eikonal approximation also for the outgoing η to see how the result due to this approximation looks like. We used the off-shell $\pi\text{N} \rightarrow \eta\text{N}$ t matrix for the basic scattering and the on-shell $\pi\text{N} \rightarrow \pi\text{N}$ and $\eta\text{N} \rightarrow \eta\text{N}$ t matrices for the initial and final state interactions, all of which were obtained by Bhalerao and Liu¹⁾ in a single calculation based on their coupled channels formalism. In Ref. 1 there are given two sets of numbers for coupling constants, range parameters, and bare masses, based on two sets of πN phase shift data. We used the values based on the πN phase shift given by Arndt *et al.* We calculated the invariant mass for the off-shell $\pi\text{N} \rightarrow \eta\text{N}$ t matrix in terms of kinematics for the outgoing particles. As nucleon wave functions for ^{12}C , we employed those based on a harmonic oscillator potential.⁸⁾ In calculating the inclusive differential cross sections, we took into account the 1s and 1p separation energy difference and thus represented the final state either as a system of an η , a proton, and a ground state of ^{11}C or that of an η , a proton, and an excited state of ^{11}C . The excitation energy of ^{11}C was calculated using harmonic oscillator parameters and is 15.1 MeV. Since the 1s neutron separation energy

* Isotope and Nuclear Chemistry Division, Los Alamos National Laboratory, New Mexico, USA.

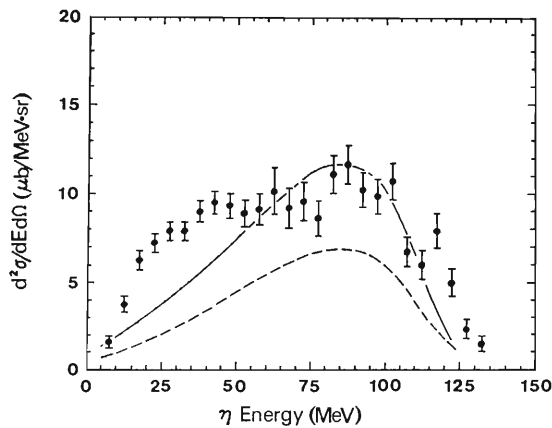


Fig. 1. Differential cross sections $d^2\sigma/dE_\eta d\Omega_\eta (0 < \theta_{lab} < 30^\circ)$ for the $^{12}\text{C}(\pi^+, \eta)$ reaction at $T_\pi = 554.6$ MeV. Solid circles with bars: preliminary experimental results;⁷⁾ solid curve: present calculation using the eikonal approximation for the incident pion, the outgoing η being treated as a plane wave; dashed curve: present calculation using the eikonal approximation for the incident pion and the outgoing η .

is larger than the $1p$ one, a phase space for the process with a $1s$ neutron off is smaller than that for the process with a $1p$ neutron off. We performed numerically 6-fold integrations with the help of the Gauss method. Figure 1 shows the preliminary experimental data obtained by Peng *et al.* (solid circles with error bars), our calculated results using the

eikonal approximation only for the incident pion, the outgoing η being treated as a plane wave (solid curve) and for the incident pion and the outgoing η (dashed curve). Our calculation with the eikonal approximation for the incident pion and outgoing η , as we expected, underestimated the differential cross sections at all η energies. Our calculation with the eikonal approximation for the incident pion and plane wave approximation for the outgoing η reproduces the cross sections at high η energies. However, even it underestimated the cross sections at low η energies. We speculate that the attractive s -wave ηN interaction enhances the cross sections very much at low η energies. This stimulates us to calculate reliable distorted η state functions. This program is undertaken.

References

- 1) R. S. Bhalerao and L. C. Liu: *Phys. Rev. Lett.*, **54**, 865 (1985).
- 2) Q. Haider and L. C. Liu: *Phys. Lett. B*, **172**, 257 (1986); **174**, 465 (E) (1986).
- 3) L. C. Liu and Q. Haider: *Phys. Rev. C.*, **34**, 1845 (1986).
- 4) Q. Haider and L. C. Liu: submitted to *J. Phys. G.*
- 5) J. R. Taylor: "Scattering Theory," John Wiley & Sons, Inc., New York, Chap. 21-b (1972).
- 6) Y. Ohkubo and L. C. Liu: *Phys. Rev. C.*, **30**, 254 (1984).
- 7) J. C. Peng: private communication.
- 8) L. C. Liu: *Phys. Rev. C*, **17**, 1787 (1978).

III-1-11. Level Densities with Fixed Exciton Number for Pre-Equilibrium Nuclear Reaction

K. Sato and S. Yoshida

(Level density with exciton number, Pre-equilibrium reaction,)
(Residual interaction.)

To evaluate pre-equilibrium reaction cross sections the level densities with fixed exciton numbers are necessary, and those of a well-known Ericson-Williams type have been widely used because of their simplicity. Recently Jacquemin and Kataria¹⁾ estimated, within the framework of an independent particle model, exact level densities by a recursive method using realistic single particle energies. However only a few studies have been carried out on the realistic level density which takes residual interaction explicitly into account.

Nishioka *et al.*²⁾ suggested the possibility of strong coupling between groups of the levels classified by exciton numbers. If such strong coupling is actually the case, the modification would be necessary for level densities with fixed exciton numbers having so far been used.^{2,3)} As for the total level density, which is given by the sum of such level densities, Jacquemin and Kataria anticipated the difficulty in fitting the experimental data at the thermal neutron resonances unless the residual interaction is taken into account.

In the present work we explicitly take the residual interaction in studying level densities classified by the exciton number m . It is done on the basis of the theory by Nishioka *et al.*²⁾ who introduced the Gaussian Distributed Ensemble (GDE). The GDE assumes many GOEs, which are specified with the exciton number m and have different centers h_m and variances M_{mm} and are coupled with one another by the off-diagonal GOE random interaction. Then the GDE is characterized by second moments M_{mn} .

First the nuclear second moments

$$M_{mn} = \frac{1}{N_m N_n} \sum_{\mu, \nu} |\langle m\mu | V^R | n\nu \rangle|^2 \quad (1)$$

are calculated on the basis of the same simple model as Ref. 3 by using realistic single particle states, but by adopting more general residual interactions, for ⁴⁰Ca and ²⁰⁸Pb as examples. In Eq. 1 N_m is the number of states which belong to the class of the exciton number m and V^R is the residual interaction.

The calculated result indicates that for such nuclei the strong interclass coupling proposed by Nishioka *et al.*²⁾ is nearly the actual case. Then level densities with an exciton number of ρ_m are obtained first by solving the saddle point equations³⁾ in the strong interclass coupling limit given by

$$\frac{\tau_m}{\lambda_m^2} = (E - h_m - \tau_m)^{-1} + \sum_{n(\neq m)} \frac{\lambda_{mn}^2}{\lambda_m^2} \sqrt{\frac{N_n}{N_m}} (E - h_n - \tau_n)^{-1} \quad (2)$$

using second moments as the input, and secondly by taking the imaginary part of the propagator as

$$\rho_m = -\frac{N_m}{\pi} \text{Im} (E - h_m - \tau_m)^{-1} \quad (3)$$

The partial level densities ρ_m ($m=2, 4, 6, \dots$) calculated for ²⁰⁸Pb are shown in Fig. 1. Dashed curves represent the semi-circle level densities obtained by switching off the interclass coupling. In Fig. 2 the total level density $\rho(E) = \sum_m \rho_m(E)$ is shown by a solid curve and is compared with the sum of semi-circle level densities; the total level

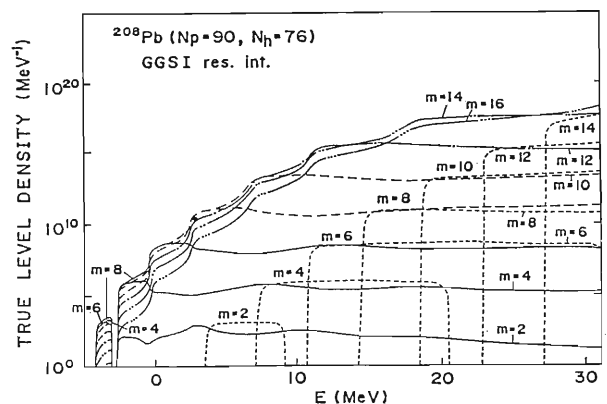


Fig. 1. Level densities with fixed exciton number for ²⁰⁸Pb. Dashed curves are semi-circles with exciton numbers m . In the weak interclass coupling limit level densities reduce to the values represented by semi-circles.

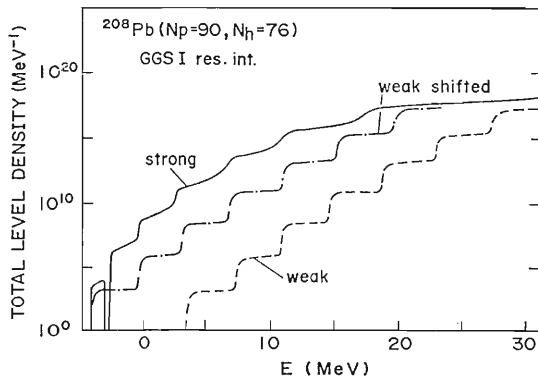


Fig. 2. Sum of level densities shown in Fig. 1.

density shifts to coincide with the solid curve at the threshold energy.

Essential results of the present study are (1) the enhancement in the low energy region, which would greatly improve the agreement with the experimental total level density at the thermal neutron resonances; (2) the general trend in shape change of level densities with fixed exciton number according to the strength of the coupling; (3) Wigner-like repulsion

between semi-circle level densities; and (4) the occurrence of the multimodal distribution, which was first found by French *et al.*⁴⁾ in another simple system.

Our results for level densities should be regarded as giving qualitative information concerning how the residual interaction changes their behavior. Because the present study includes unrealistic assumptions inherent in the pure GDE such as the degenerate spectrum of the one-body part of the Hamiltonian and the multi-body residual interaction. Actually unperturbed semi-circle partial level densities would be replaced by the Gaussian ones at least for large m if the two-body nature of the residual interaction is explicitly simulated. It is expected, however, that these results would be common features of level densities when the residual interaction is taken into account.

References

- 1) C. Jacquemin and S.K. Kataria: *Z. Phys. A*, **324**, 261 (1986).
- 2) H. Nishioka, J.J.M. Verveerschot, H. A. Weidenmüller, and S. Yoshida: *Ann. Phys.*, **172**, 67 (1986).
- 3) K. Sato and S. Yoshida: *Z. Phys. A*, **327**, 421 (1987).
- 4) J. B. French and V.K.B. Kota: *Phys. Rev. Lett.*, **51**, 2183 (1983).

III-1-12. A High-Energy Scattering Approximation

Y. Nishida,* T. Takemasa, and M. Shimauchi*

(High-energy, scattering, Glauber, amplitude, wave-function,)
 (Born, Gaussian potential, correction term.)

In previous work,^{1,2)} an approximation method was developed to describe the scattering of a high-energy Schrödinger particle from central potentials. In Refs. 1 and 2, the scattering wave function with an incident wave number k_0 was approximated by

$$\Psi(\mathbf{r}) = \exp[ik_0(\mathbf{s}_0 \cdot \mathbf{r})] + \int G(\mathbf{r}, \mathbf{r}') U(\mathbf{r}') \Psi_i(\mathbf{r}') d\mathbf{r}' \quad (1)$$

where $U(\mathbf{r}) = 2mV(\mathbf{r})/\hbar^2$, \mathbf{s}_0 is a unit vector along the incident direction, and $\Psi_i(\mathbf{r})$ the internal sphere wave function.¹⁾ Under the conditions that the strength of a potential is much smaller than the incident energy and its range is greater than the reduced wavelength, the method²⁾ can well give the scattering amplitude and the differential cross section in weak and intermediate coupling cases far beyond the angular validity criterion of the Glauber's formula.³⁾ However, the method includes a practically important problem of extending an allowed range of the coupling parameter.

In this note, an attempt is reported to improve the method by introducing manageable correction. The scattering wave function is taken here to be of the form

$$\Psi(\mathbf{r}) = \exp[ik_0(\mathbf{s}_0 \cdot \mathbf{r})] + \int G(\mathbf{r}, \mathbf{r}') U(\mathbf{r}') \exp[ik_0(\mathbf{s}_0 \cdot \mathbf{r}')] d\mathbf{r}' + \int G(\mathbf{r}, \mathbf{r}') U(\mathbf{r}') G(\mathbf{r}', \mathbf{r}'') U(\mathbf{r}'') \phi_i(\mathbf{r}'') d\mathbf{r}' d\mathbf{r}'' \quad (2)$$

which is obtained by adopting Eq. 1 in an iterative solution of the integral equation. The second and third terms of Eq. 2 can be transformed by means of the procedure developed in Ref. 2 into the single and double infinite series, respectively. The scattering amplitude $f(\theta)$ may correspondingly be written as

$$f(\theta) = f_{B1}(\theta) + \bar{f}_{B2}(\theta) + \sum_{m,n} \hat{f}_{mn}(\theta) \quad (3)$$

where $\bar{f}_{B2}(\theta)$ represents the second Born amplitude expressed as a single infinite series.

The main task is now to replace the infinite series included in Eqs. 2 and 3 by suitable finite series. Particularly in managing $\sum_{m,n} \hat{f}_{mn}(\theta)$, we adopt a procedure of choosing terms to be retained so as to approximate $f(\theta)$ and $d\sigma/d\Omega$ as good as possible over a wide range of scattering angles.

Numerical calculations are carried out for the Gaussian potential $U(r) = -A^2 \exp[-(r/b)^2]$. The

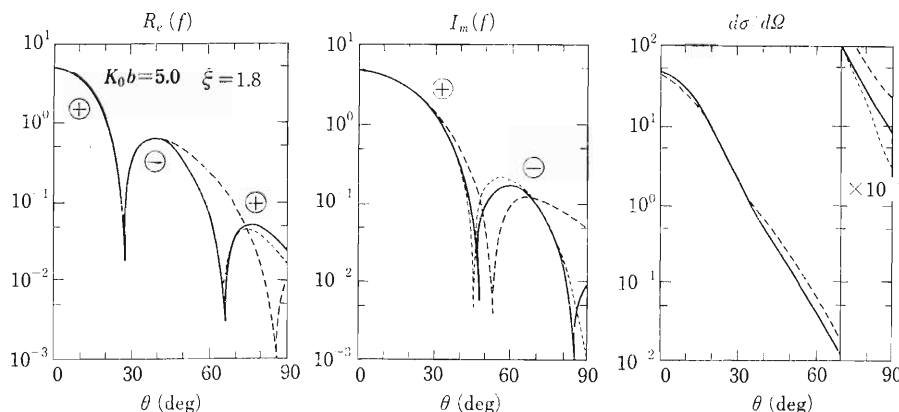


Fig. 1. Quantities $\text{Re}(f)$, $\text{Im}(f)$ and $d\sigma/d\Omega$ with $b=1.0$ (unit of length) at $k_0=5.0$ and $\xi=1.8$. The solid, dotted, and dashed curves show the results of the exact method, our procedure, and the eikonal approximation, respectively.

* Department of Physics, Saga University.

quantity $k_0 b$ is taken to be 5.0, and the coupling parameter $\xi = A^2 b / 2k_0$ is changed from 0.1 up to 2.0. The amplitude $\bar{f}_{B2}(\theta)$ can be written in a closed form for this potential. By comparison the corresponding infinite series proves to be well approximated by a sum of its first four terms, and the second term of Eq. 2 becomes thus manageable. By retaining the leading five and four terms in $\sum_{m,n} \hat{f}_{mn}(\theta)$ for $\xi = 1.0$ and 1.8, respectively, we found that the results obtained for the real and imaginary parts of $f(\theta)$ as well as $d\sigma/d\Omega$ can very well be approximated to those calculated by the exact method of partial waves. It is noteworthy that the results for $\xi = 1.0$ are much better in giving the change of signs of $f(\theta)$ than the corresponding ones in Fig. 1 of Ref. 2. For clarification and comparison, the results for $\xi = 1.8$ are shown in Fig. 1 together with those of the exact method and the eikonal approximation.⁴⁾ The range b is taken here to be a unit of length as in Refs. 2 and 4. Figure 1 confirms that

our method can markedly extend an allowed range of ξ . It also points out that the results of the eikonal approximation are much worse than ours for large scattering angles particularly on the change of signs of $f(\theta)$.

In summary, a method is developed to approximate the scattering wave function as a sum of the second Born form and correction terms. The present method very well reproduces the exact results for the coupling parameter larger as well as smaller than unity far beyond the conventional angular range of validity of Glauber's formula.

References

- 1) Y. Nishida, M. Shimauchi, and H. Tanaka: *Nucl. Phys.*, **50**, 403 (1964).
- 2) Y. Nishida and M. Shimauchi: *Prog. Theor. Phys.*, **76**, 143 (1986).
- 3) R. J. Glauber: *Lectures in Theoretical Physics*, Interscience, New York, Vol. 1, p. 315 (1959).
- 4) C. J. Joachain: *Quantum Collision Theory*, North-Holland, Amsterdam, Chap. 9 (1975).

III-1-13. Microscopic Analysis of the Hexadecapole Strength to the γ -Vibrational Bands

M. Matsuo

{ NUCLEAR STRUCTURE γ -vibrational bands, hexadecapole }
 transition probability, random phase approximation. }

The γ -vibration has been regarded as collective oscillation of a deformed nucleus with quadrupole multipolarity. Recent inelastic hadron scattering experiments, however, revealed that the hexadecapole transition strength to the γ -vibrational bands are considerably enhanced in some even-even rare earth nuclei^{1,2)} and that the strengths have strong dependence on nuclear species.⁴⁾

We theoretically investigate the origin of the observed features of the hexadecapole strength to the γ -bands. Although the enhancement may suggest a role of the two-body correlation of the hexadecapole type,³⁾ one has to be careful to draw the conclusion from this aspect. Since low-lying collective vibrations such as γ -motion are characterized strongly by the structure of the single-particle levels near the Fermi surface, the observed (N, Z) -dependence is also a key property in understanding the phenomena. One should also note the consistency of the hexadecapole correlation, while the authors of Ref. 3 do not.

We describe the γ -vibration microscopically by means of the random phase approximation (RPA). The Nilsson + BCS Hamiltonian h_{def} with quadrupole equilibrium deformation is employed as a single-particle basis. Two-body correlation we adopt consists of the doubly-stretched quadrupole-quadrupole ($Q_2''Q_2''$) and doubly-stretched hexadecapole-hexadecapole ($Q_4''Q_4''$) interactions:⁴⁾

$$H = h_{\text{def}} - \kappa_2 Q_{22}^\dagger Q_{22}'' - \kappa_4 Q_{42}^\dagger Q_{42}'' \quad (1)$$

where $Q_{LK}'' = (r^L Y_{LK})_{x \rightarrow x''}$ and the doubly-stretched coordinates x'' are those scaled according to the equilibrium deformation. The doubly-stretched multipole-multipole interactions satisfy consistency between the mean-field potential induced by the interactions and the matter density for deformed nuclei,⁴⁾ when the selfconsistent force strengths $\kappa_2 = \kappa_2^{(\text{self})}$ and $\kappa_4 = \kappa_4^{(\text{self})}$,⁵⁾ are used. Reduced isoscalar transition probabilities $B(1S_4, 0 \rightarrow 4\gamma)$ from the ground state to the 4^+ state in the γ -vibrational band are calculated in a usual manner using microscopically derived RPA phonon $X_\gamma^\dagger = \sum_{\mu\nu} \{ \psi(\mu\nu) a_\mu^\dagger a_\nu^\dagger + \phi(\mu\nu) a_\nu a_\mu \}$, where a_μ^\dagger is a quasiparticle operator for a single-

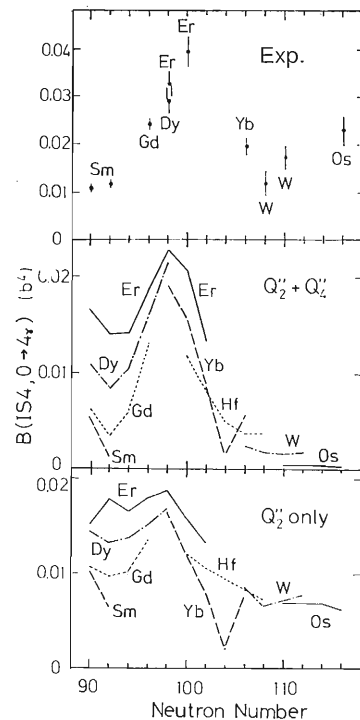


Fig.1. Observed and calculated reduced isoscalar hexadecapole transition probability $B(1S_4, 0 \rightarrow 4\gamma)$. Experimental data are taken from Ref.1. The theoretical results shown in the bottom figure is calculated without the hexadecapole interaction.

particle level μ .

Figure 1 shows the hexadecapole transition probabilities, $B(1S_4, 0 \rightarrow 4\gamma)$, evaluated from the (p, p') experiment¹⁾ and the calculated ones. It is seen that the characteristic (N, Z) -dependence of the experimental data is reproduced in the calculation. In order to see the effect of the hexadecapole correlation ($Q_4''Q_4''$), we show the result of calculation which takes into account only the quadrupole correlation ($Q_2''Q_2''$). The hexadecapole correlation is not found to play relevant roles in generating the (N, Z) -dependence of the γ -vibrations. On the other hand the absolute magnitude is underestimated by a factor of about two. It is hardly possible in our model to

enhance it with keeping the proper (N, Z) -dependence by increasing the hexadecapole correlation. The origin of this overestimation is unclear and should be investigated further.

The (N, Z) -dependence of B(IS4) is due to the property of the hexadecapole operator and the subshell structure of the single-particle levels. We can estimate the hexadecapole transition amplitude as

$$\begin{aligned} & \langle 0 | [X_\gamma, Q_{42}] | 0 \rangle \\ & \propto \sum_{\mu\nu} \frac{2E_{\mu\nu}}{E_{\mu\nu}^2 - E_\gamma^2} (u_\mu v_\nu + u_\nu v_\mu)^2 \\ & \quad \times \langle \mu | r^2 Y_{22} | \nu \rangle \langle \mu | r^4 Y_{42} | \nu \rangle \end{aligned} \quad (2)$$

by neglecting the hexadecapole correlation $Q_4''Q_4''$ (E_γ : γ -vibrational energy, $E_{\mu\nu} = E_\mu + E_\nu$: energy of quasiparticle pair, u_μ, v_μ : pairing factors). The contribution of quasiparticle pairs near the Fermi surface to the summation in Eq. 2 are influenced strongly by the subshell structure of the Nilsson single-particle levels. For dominant components satisfying the selection rule in the quadrupole matrix elements $\langle \mu | r^2 Y_{22} | \nu \rangle$, the matrix elements of the hexadecapole operator are expressed approximately as

$$\langle \mu | r^4 Y_{42} | \nu \rangle \propto (5n_3 - N_{\text{osc}}) \langle \mu | r^2 Y_{22} | \nu \rangle, \quad (3)$$

where $[N_{\text{osc}} n_3 A Q]$ is the asymptotic quantum number for a single-particle level μ . Since neutron single-particle levels with $N_{\text{osc}} = 5$ and $n_3 = 2$ dominate around the Fermi surface for $N \approx 98$, the contribution

of these levels to Eq. 2, gives positive coherence with respect to those of the core excitation. Thus B(IS4) enhances in this region. On the other hand, the situation is opposite for $N \geq 110$. Single-particle levels near the Fermi surface in this region belong to $N_{\text{osc}} = 5$ and $n_3 = 1, 0$, and their contributions cancel the other contribution in Eq. 2. The proton number dependence can be explained in a similar way.

Detail of this work is reported in Ref. 6.

References

- 1) T. Ichihara, H. Sakaguchi, M. Nakamura, T. Noro, F. Ohtani, H. Sakamoto, H. Ogawa, M. Yosoi, M. Ieiri, N. Isshiki, Y. Takeuchi, and S. Kobayashi: *Phys. Lett. B*, **149**, 55 (1984); T. Ichihara, H. Sakaguchi, M. Nakamura, M. Yosoi, M. Ieiri, Y. Takeuchi, H. Togawa, T. Tsutsumi, and S. Kobayashi: *Phys. Lett. B*, **182**, 301 (1986); *Phys. Rev.*, **36**, 1754 (1987).
- 2) I. M. Govil, H. W. Fulbright, D. Cline, E. Wesolowski, B. Kotlinski, A. Backlin, and K. Gridnev: *Phys. Rev. C*, **33**, 793 (1986).
- 3) V. O. Nesterenko, V. G. Soloviev, A. V. Sushkov, and N. Yu. Shirikova: *Sov. J. Nucl. Phys.*, **44**, 938 (1986) [*Yad. Fiz.*, **44**, 793 (1986)].
- 4) T. Kishimoto, J. M. Moss, D. H. Youngblood, J. D. Bronson, C. M. Rozsa, D. R. Brown, and A. D. Bacher: *Phys. Rev. Lett.*, **35**, 552 (1975); T. Kishimoto: Proc. Int. Symp. Highly Excited States in Nuclear Reactions, RCNP, Osaka, p. 145 (1980).
- 5) A. Bohr and B. R. Mottelson: *Nuclear Structure*, Benjamin, New York, Vol. 2 (1975).
- 6) M. Matsuo: *Prog. Theor. Phys.*, **78**, 609 (1987).

III-1-14. Derivation of the Global Equation of Motion for the Collective Variable

S. Yamaji, H. Hofmann,* and R. Samhammer*

[FISSION, linear response theory.]

We reported the calculation of selfconsistent transport coefficients.¹⁾ They were evaluated from the equation of the global motion for the collective variable $Q(t)$ at time t

$$\frac{\partial f(Q(t), T)}{\partial Q(t)} - \int_{-\infty}^{t_0} ds \tilde{\chi}(t-s)(Q(s) - Q(t)) = 0 \quad (1)$$

where, $f(Q, T)$ is a free energy of the temperature T , and $\tilde{\chi}(t-s)$ is a response function.

Equation 1 was derived in Ref. 2 by introducing a fixed Q_0 which represents Q at $t=t_0$. However, its derivation must be improved since each term was not treated consistently to order 1 in $(Q(s) - Q_0)$ in Ref. 2. In Ref. 3, Eq. 1 was given in its zero temperature limit.

Therefore, in this report, we give an extension to finite excitations, keeping terms of order 1 in $(Q(s) - Q_0)$ consistently. For that we expand the Hamiltonian like:

$$\begin{aligned} \hat{H}(\hat{x}_i, \hat{p}_i, Q) &\simeq H(Q_0) \\ &+ (Q - Q_0) \frac{\partial \hat{H}}{\partial Q_0} + \frac{1}{2} (Q - Q_0)^2 \frac{\partial^2 \hat{H}}{\partial Q_0^2} \end{aligned} \quad (2)$$

For the time interval $\delta t = t - t_0$ we then treat the influence of the local coupling

$$\delta \hat{V} = (Q - Q_0) \frac{\partial \hat{H}}{\partial Q_0} = (Q - Q_0) \hat{F}(Q_0) \quad (3)$$

on $\langle \partial H / \partial Q \rangle_t$ to order 1 in $(Q(s) - Q_0)$. We start from

$$\langle \hat{F} \rangle_t = \text{Tr} \hat{\rho}_{\text{eq}}(Q) \hat{F}(t) \quad (4)$$

where $\hat{F}(t)$ can be calculated to the first order as

$$\hat{F}(t) = \hat{F}^1(t) - i \int_{t_0}^t ds [\hat{F}^1(t), \hat{F}^1(s)] (Q(s) - Q_0) \quad (5)$$

with the interaction representation $\hat{F}^1(t)$ of $\hat{F}(Q_0)$ and $\hat{\rho}_{\text{eq}}(Q)$ is a equilibrium density operator given by $\exp(-\hat{H}(Q)/T) / \text{Tr} \exp(-\hat{H}(Q)/T)$. We expand Eq. 4 to the first order in $(Q - Q_0)$ and obtain

* Physik-Department der Technischen Universität München.

the following result:

$$\langle \hat{F} \rangle_t^Q = \langle \hat{F} \rangle_{Q_0} - \int_{-\infty}^{\infty} ds \tilde{\chi}(t-s)(Q(s) - Q) \quad (6)$$

with the response function $\tilde{\chi}(t-s)$ defined by

$$\tilde{\chi}(t-s) = i\theta(t-s) \langle [\hat{F}^1(t), \hat{F}^1(s)] \rangle \quad (7)$$

The detailed derivation of Eq. 6 is given in Ref. 4. Since the nucleus is an isolated system, its total energy must be a constant of motion. Since our Hamiltonian depends on the parameter $Q(t)$, this condition leads to

$$\frac{d}{dt} E_{\text{tot}} = \dot{Q} \left\langle \frac{\partial \hat{H}}{\partial Q} \right\rangle_t = 0 \quad (8)$$

In the equation of motion we must calculate $\langle \partial \hat{H} / \partial Q \rangle_t$. Within our perturbation approach, we obtain to the first order

$$\left\langle \frac{\partial \hat{H}}{\partial Q} \right\rangle_t = \langle \hat{F} \rangle_t^Q + \left\langle \frac{\partial^2 \hat{H}}{\partial Q_0^2} \right\rangle_{Q_0} (Q - Q_0) \quad (9)$$

Inserting Eq. 6 into Eq. 9 yields

$$\begin{aligned} \left\langle \frac{\partial \hat{H}}{\partial Q} \right\rangle_t &= \langle \hat{F} \rangle_{Q_0} + \left\langle \frac{\partial^2 \hat{H}}{\partial Q_0^2} \right\rangle_{Q_0} (Q - Q_0) \\ &\quad - \int_{-\infty}^{\infty} \tilde{\chi}(t-s)(Q(s) - Q) ds \end{aligned} \quad (10)$$

The first two terms represent static forces, which can be expressed by the partial derivative with respect to Q about the free energy $f(Q, T)$ defined by

$$f(Q, T) = -T \ln \text{Tr} \exp \left(-\frac{\hat{H}(Q)}{T} \right) \quad (11)$$

Thus we finally obtain Eq. 1 in the non-static case.

References

- 1) S. Yamaji and H. Hofmann: *RIKEN Accel. Prog. Rep.*, **20**, 33 (1986).
- 2) H. Hofmann: *Phys. Lett. B*, **61**, 423 (1976).
- 3) P. J. Siemens: *Nucl. Phys.*, **A387**, 247 (1982).
- 4) S. Yamaji, H. Hofmann, and R. Samhammer: *Nucl. Phys.*, **A475**, 487 (1987).

III-2. Atomic and Solid-State Physics

1. Gauge Property for the Radiative Processes Induced by Ion-Atom Collision

K. Hino and T. Watanabe

In order to solve the problem of inconsistency which lies in the formulation for radiative processes induced by three-particle collisions,^{1,2)} we investigate the property of gauge invariance of the formula for a radiative process. As a preliminary discussion before we treat the three-body system, we consider the gauge invariance property on the occasion of two-body collisions. The photon emission processes induced by the acceleration of an active electron in two-body collisions are

$$a+b \rightarrow a+b+\gamma \quad (1)$$

(free-free transition, *i.e.*, Bremsstrahlung; a is a nucleus, b an electron, and γ a photon) and

$$a+b \rightarrow (a, b)+\gamma \quad (2)$$

(free-bound transition, *i.e.*, radiative recombination). For two-body scattering, the problem of photon emission processes was already treated in 1930 and has set from the theoretical point of view.³⁾ Because we know the exact formulas of a scattering state as well as a bound state, we can see that the gauge invariance property of photon emission S matrix holds in these processes as already known.³⁾

When the initial and final scattering states of process 1 are expanded as

$$\psi_i = \psi_{i0} + G_0 V \psi_{i0} + G_0 V G_0 V \psi_{i0} + \dots \quad (3)$$

$$\psi_f = \psi_{f0} + G_0 V \psi_{f0} + G_0 V G_0 V \psi_{f0} + \dots \quad (4)$$

where $G_0 = (E - H_0 + i\epsilon)^{-1}$, $H_0 = \frac{-\hbar^2}{2\mu} \nabla^2$, is a reduced mass of a and b , and V is the interaction potential between a and b , and S matrix for the radiative process can be written as

$$\begin{aligned} & \langle \psi_i | \sum_j H_j' | \psi_f \rangle \rho_f \\ &= \langle \psi_{i0} | \sum_j H_j' | \psi_{f0} \rangle \rho_f + \langle \psi_{i0} | V G_0 \sum_j H_j' \\ & \quad + \sum_j H_j' G_0 V | \psi_{f0} \rangle \rho_f \\ & \quad + \langle \psi_{i0} | V G_0 V G_0 \sum_j H_j' + V G_0 \sum_j H_j' G_0 V \\ & \quad + \sum_j H_j' G_0 V G_0 V | \psi_{f0} \rangle \rho_f + \dots \end{aligned} \quad (5)$$

where $H_j' = \frac{-ie}{2M_j} \mathbf{A} \cdot \mathbf{p}_j$, \mathbf{A} is the vector potential of radiation field, and \mathbf{p}_j is the linear momentum of particle j . ψ_{i0} and ψ_{f0} of particles and photons are unperturbed wavefunctions (plane waves).

The property of gauge invariance is examined by the following procedure. Let us consider the case where the initial state of a particle with no photon $\psi_i(\mathbf{y})$ (\mathbf{y} : the four-component vector, *i.e.*, three dimensional position vector \mathbf{y} and the time t) changes into the final state of a particle with one photon $\psi_f(x)$ (x : the four-component vector) due to the interaction $A_\mu(z)$ $\Omega_\mu(z; x, y)$ as shown in Fig. 1. The S matrix for a photon emission process between these states can be written by

$$S_{fi} = \langle \psi_f(x) | A_\mu(x) \Omega_\mu(z; x, y) | \psi_i(y) \rangle \quad (6)$$

where $A_\mu = (\mathbf{A}, \Phi)$, $\Omega_\mu = (\mathbf{\Omega}, \Omega_0)$, \mathbf{A} is the vector potential of radiation fields, Φ its scalar potential. $\mathbf{\Omega}$ is the vertex function (the current operator) of a particle and is given by

$$\begin{aligned} \mathbf{\Omega}(z; x, y) = & -\frac{ie}{2M} [\delta^{(4)}(x-z) \vec{\nabla}_z \delta^{(4)}(z-y) \\ & - \delta^{(4)}(x-z) \vec{\nabla}_z \delta^{(4)}(z-y)] \end{aligned} \quad (7)$$

and Ω_0 is the charge of a particle and is given as

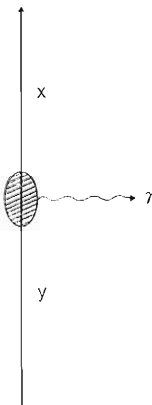


Fig. 1. Schematic diagram for the photon emission process due to the acceleration of a charged particle with the interaction of radiation fields.

$$\Omega_0(z; x, y) = \varepsilon \delta^{(4)}(x-z) \delta^{(4)}(z-y) \quad (8)$$

Now the S matrix is rewritten by a gauge transformation from $A_\mu(z)$ to $A'_\mu(z)$ using a relation

$$A'_\mu(z) = A_\mu(z) + \partial_\mu \lambda(z), \quad (9)$$

namely,

$$A'(z) = A(z) + \nabla \lambda(z) \quad (10)$$

$$\Phi'(z) = \Phi(z) + \dot{\lambda}(z) \quad (11)$$

where $\lambda(z)$ is an arbitrary function and $\dot{\lambda}$ is the derivative with respect to time. Under this transformation, a new S matrix S_{fi}' is written as

$$S_{fi}' = S_{fi} + \langle \phi_f(x) | \partial_{\mu^z} \lambda(z) \Omega_\mu(z; x, y) | \psi_i(y) \rangle \quad (12)$$

If we write $\Delta S = S_{fi}' - S_{fi}$, ΔS is given by

$$\Delta S = \int dx dy \int dz \phi_f^*(x) (\partial_{\mu^z} \lambda(z)) \Omega_\mu(z; x, y) \psi_i(y) \quad (13)$$

Making use of Green's theorem, we can obtain ΔS as

$$\Delta S = \int dx dy \left[\int dS_{\mu^z} \{ \phi_f^*(x) \lambda(z) \Omega_\mu(z; x, y) \psi_i(y) \} - \int dz \phi_f^* \{ \partial_{\mu^z} \Omega_\mu(z; x, y) \} \lambda(z) \psi_i(y) \right] \quad (14)$$

where dS_{μ^z} is the surface area element in the integration on the boundary. Because $\lambda(\pm\infty) = 0$ on the boundary, the first term of the right-hand side of Eq. 3 can be deleted. We have

$$\Delta S = - \int dx dy \int dz \partial_{\mu^z} \{ \phi_f^*(x) \Omega_\mu(z; x, y) \psi_i(y) \} \lambda(z) \quad (15)$$

Because $\lambda(z)$ is an arbitrary function, in order to obtain $\Delta S = 0$, *i.e.*, to hold the gauge invariance of S matrix, it is necessary that we have

$$\partial_{\mu^z} J_\mu(z) = 0 \quad (16)$$

where

$$J_\mu(z) = \langle \phi_f(x) | \Omega_\mu(z; x, y) | \psi_i(y) \rangle \quad (17)$$

Namely, a current defined by

$$J(z) = - \frac{ie}{2m} \langle \phi_f(x) | \delta^{(4)}(x-z) \vec{\nabla}_z \delta^{(4)}(z-y) - \delta^{(4)}(x-z) \vec{\nabla}_z \delta^{(4)}(z-y) | \psi_i(y) \rangle \quad (18)$$

$$J_0(z) = e \langle \phi_f(x) | \delta^{(4)}(x-z) \delta^{(4)}(z-y) | \psi_i(y) \rangle = e \phi_f^*(z) \psi_i(z) \quad (19)$$

in the usual form, should be conserved before and after the interaction. For various $\psi_i(y)$ and $\phi_f(x)$, we can examine the gauge invariance property on the basis of Eq. 16, *i.e.*, the current conservation requirement.

In the case of Bremsstrahlung, we can see that the gauge invariance property holds in every order of perturbation expansions of the S matrix. However, if we make a perturbation expansion according to Eq. 3, in the continuum wavefunction for the radiative recombination process and employ ψ_f an exact bound-state wavefunction, the gauge invariance property does not hold in every order of perturbation expansion of the S matrix.

For photon emission by electron acceleration in the three-body system, we also examine the gauge

Table 1. Validity of gauge invariance in various approximations.

Systems and processes	Approximation	Gauge invariance
Two-body + fields $a + b \rightarrow a + b + \gamma$ $\rightarrow (a, b) + \gamma$	Exact solution for Bremsstrahlung and for radiative recombination	Hold
Two-body + fields $a + b \rightarrow a + b + \gamma$	Perturbation expansion in terms of $V_{a,b}$	Hold
Two-body + fields $A + b \rightarrow (a, b) + \gamma$	— // —	Does not hold
Three-body + fields $a + (b, c) \rightarrow a + (b, c)^* + \gamma$ $a + (b, c)^* \rightarrow a + (b, c) + \gamma$	Perturbation expansion in terms of $V_{a,b} + V_{a,c}$	Hold
Three-body + fields REC process $a + (b, c) \rightarrow (a, c) + b + \gamma$	Perturbation expansion in terms of $V_{a,c}$ or $V_{b,c}$ using non-potential Green's function (Brinkman-Krammers approximation)	Does not hold
— // —	Perturbation expansion in terms of $V_{a,c} + V_{a,b}$ or $V_{b,c} + V_{a,b}$ using non-potential Green's function (Born approximation)	Does not hold
— // —	Perturbation expansion in terms of $V_{a,c}$ with Green's function under $V_{a,c}$ potential (Impulse approximation)	Approximately hold
— // —	Strong potential Born approximation application	Approximately hold

invariance property in the same way. The gauge invariance holds for radiative excitation and radiative de-excitation such as

$$a+(b, c) \rightarrow a+(b, c)^* + \gamma \quad (20)$$

and

$$a+(b, c)^* \rightarrow a+(b, c) + \gamma \quad (11)$$

if we expand the scattering state in terms only of $V_{a,c}$ and not of $V_{a,b}$ (here we assume a and b are bare nuclei and c is an electron). However, for REC such as

$$a+(b, c) \rightarrow (a, c) + b + \gamma, \quad (22)$$

the gauge invariance property does not necessarily hold.

In the Brinkman-Kramers approximation (that ignores $V_{a,b}$ and expands the S matrix in terms of $V_{a,c}$ or $V_{b,c}$ with a no-potential Green's function) and in the Born approximation (that expands the S matrix in terms of $V_{a,b} + V_{b,c}$ or $V_{a,b} + V_{a,c}$ with a no-potential Green's function), the gauge invariance does not hold. The impulse approximation and the strong-potential Born approximation (that expands the S matrix in terms of $V_{a,c}$ with Green's function under $V_{a,c}$ without and with off-shell contribution, respectively) satisfy the gauge invariance approximately in every order of perturbation expansions.

The same results are found in the relativistic theory. Table 1 summarizes the gauge invariance property of the S matrices for radiative processes in various theories.

Inferring from the gauge properties of two-body radiative processes the Bremsstrahlung and the radiation recombination, we would expect that the gauge invariant S matrix given by using a certain approximation method does not depend on the reference frame employed for the three-body radiative process. Furthermore, by taking the degree of accuracy of the gauge invariance into consideration, we can make a judgement of the coordinate-dependence of the S matrix obtained by a certain perturbation expansion for scattering states.

In the case of the REC S matrix by the perturbation expansion, for instance, the gauge invariance holds more exactly in the projectile frame than in the laboratory one.

References

- 1) J. S. Briggs and K. Dettmann: *Phys. Rev. Lett.*, **33**, 1123 (1974).
- 2) R. Shakeshaft and L. Spruch: *Phys. Rev. Lett.*, **38**, 175 (1977).
- 3) H. Bethe and E. E. Salpeter: *Quantum Mechanics of One- and Two-Electron Atoms*, Springer, Heidelberg, p. 320 (1957); Plenum, New York (1977).

III-2-2. Photon Angular Distributions of the Ultrarelativistic K-Shell Radiative Electron Capture Induced by Heavy-Ion Collision

K. Hino and T. Watanabe

In 1979, Spindler *et al.*¹⁾ observed that the radiation pattern of the radiative electron capture (REC; hereafter, we refer to REC into the projectile K shell merely as REC) exhibits the forward-backward symmetry. This feature is mainly due to the cancellation between the retardation effect of the emitted photon and the aberration of the emission angle of photons from moving light source, *i.e.*, the relativistic effect cancels with the Lorentz transformation effect from the moving frame into the laboratory frame. Here, the moving frame and the laboratory frame mean that the origin of the coordinates are centered on the incident projectile ion and on the center of mass of the target atom, respectively. The cancellation effect of the REC photon angular distributions can be shown using the first Born approximation as follows. The angular distribution of the REC photon estimated in the moving frame

$$(d\sigma/d\Omega_M) \propto \sin^2 \theta_M (1 + \beta \cos \theta_M)^{-4} \quad (1)$$

is Lorentz-transformed into the laboratory frame to provide the form:

$$(d\sigma/d\Omega_L) \propto \sin^2 \theta_L \quad (2)$$

where θ_M and θ_L represent the emission angles of photons measured from the direction of the incident velocity in the moving frame and in the laboratory frame, respectively, Ω_M and Ω_L stand for the associated solid angles, and $\beta = v/c$ where v and c are the relative velocity and the velocity of light, respectively. Equation 1 includes the photon retardation effect in the second term in parentheses; however, this effect is cancelled by the aberration effect given by Eq. 2.

Anholt *et al.*²⁾ experimentally justified the $\sin^2 \theta_L$ dependence of REC photons in bombardment of Be atoms with 197 MeV/u Xe⁵⁴⁺ ions ($\beta = 0.56$). Recently, Pacher *et al.*³⁾ theoretically confirmed such behavior of the REC photon angular distribution by using the non-relativistic impulse approximation (IA) method with retardation corrections. Furthermore, Hino and Watanabe⁴⁾ calculated the REC angular distribution by virtue of the relativistically extended strong-potential-Born (SPB) approximation and verified the experimental results of Anholt *et al.* In addition, they indicated that the $\sin^2 \theta_L$ dependence

is deviated to some extent in the backward angle region in the case of bombardment of Be atoms with 422 MeV/u U⁹²⁺ ions ($\beta = 0.72$) because of the strong distortion effects between the incident projectile ion and the active electron. But there are no experimental studies of REC photon angular distributions in the mass and energy region above 197 MeV/u Xe ions.

We are concerned with the ultrarelativistic behavior of REC photon angular distributions, where β is nearly equal to or above 0.9. Recently, we⁵⁾ evaluated the radiation pattern of REC angular distributions induced by U⁹²⁺ colliding on a Be atom at several ultrarelativistic incident velocities as depicted in Fig. 1. For calculations, two types of Feynman diagrams are taken into consideration to explain the ultrarelativistic behavior of the REC process as shown in Fig. 2. The first diagram is the conventional one and the other involves an internal conversion process, that is, the e^+e^- pair creation and the successive e^+e^- pair annihilation. In the ultrarelativistic energy region, the contributions of the second diagram to the REC process become comparable to that of the first one. In Fig. 1, it is found that the peak positions of the REC angular distributions are shifting to the forward angle region, and their shapes deviate significantly from the $\sin^2 \theta_L$ dependence as the incident velocity approaches the velocity of light. In the high energy

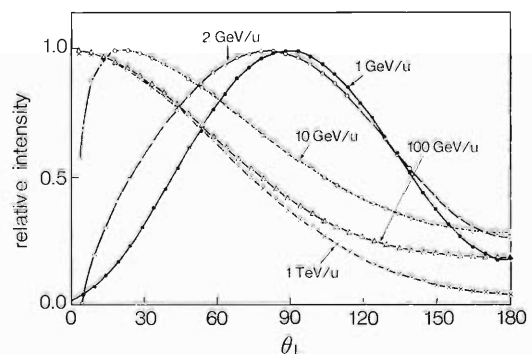


Fig. 1. Angular dependence of REC photon intensity for U⁹²⁺ ions on Be systems. The intensity of photons is normalized to the maximum value. Incident energy of ions are indicated in the figure. θ_L denotes the angle in the laboratory system.

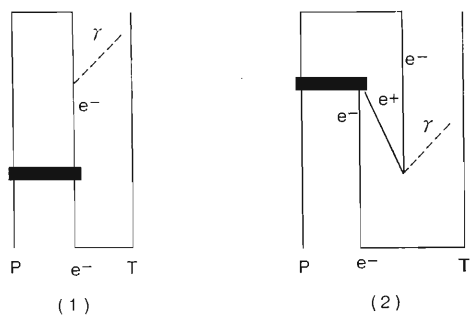


Fig. 2. Feynman diagrams for the relativistic radiative electron capture process. P, a projectile ion; T, a target nucleus; e^- , an active electron; e^+ , a positron; γ , an emitted photon. A black bold block represents the Coulomb interactions.

limit ($\beta=1$), the REC photon angular distribution is deduced to

$$\left(\frac{d\sigma}{d\Omega_L}\right) \propto \cos^2(\theta_L/2), \quad (3)$$

which is very different from the $\sin^2\theta_L$ dependence given by Eq. 2. The behavior represented by Eq. 3 is due mainly to the higher-order photon retardation corrections.

We investigate the possibility of experimental measurement along the line of radiative process due

to ion-atom collisions. When the incident energy of projectiles is more than 2 GeV/u , that is, the REC photon energy exceeds $2mc^2$, a pair of e^- and e^+ is produced. Since pair creation occurs in the moving frame, the emitted e^- and e^+ are concentrated in the forward angle in the laboratory system. A permanent magnet will be used to extract e^- or e^+ to detect them with surface barrier detectors. When the pair creation is carried out by the radiative electron capture to continuum, an additional electron will be detected at the forward angle in coincidence with a pair or e^- and e^+ . This ultrarelativistic effect of REC angular distribution will be detected by coincidence measurements of simultaneously emitted two electrons and one positrons.

References

- 1) E. Spindler, H.-D. Betz, and F. Bell: *Phys. Rev. Lett.*, **42**, 832 (1979).
- 2) R. Anholt, S. A. Andriamonje, E. Morenzoni, Ch. Stoller, J. D. Molitoris, W. E. Meyerhof, H. Bowman, J.-S. Xu, Z.-Z. Xu, J. O. Rasmussen, and D. H. H. Hoffmann: *Phys. Rev. Lett.*, **53**, 234 (1984).
- 3) M. C. Pacher, A. D. González, and J. E. Miraglia: *Phys. Rev. A*, **35**, 4108 (1987).
- 4) K. Hino and T. Watanabe: *Phys. Rev. A*, **36**, 581 (1987).
- 5) K. Hino and T. Watanabe: unpublished.

III-2-3. Angular Distribution and Linear Polarization of X Rays Induced by Radiative Electron Capture Process

K. Hino and T. Watanabe

Calculations using the Born approximation are made for X-ray emission process on the ion-atom collisions. The physical quantities treated here are the angular distribution of the X-ray intensity due to radiative electron capture (REC) into L-shells and the linear polarization correlation of photons induced by REC to the K shell in the range of relativistic incident velocities.

Spindler, Betz, and Bell¹⁾ found for the first time by measuring the REC spectra caused by light-ion atom collisions that the radiation pattern of REC to the K shell capture (K-REC) exhibits the forward-backward symmetry independent of the projectile velocity. They attributed this effect to the cancellation between electron retardation effects and the Lorentz transformation from the projectile frame to the laboratory frame.

Recently, it has become possible experimentally to measure the angular distribution for photons induced by REC to the L shell (L-REC) with the increase of beam intensities of high-energy, heavy-ion accelerators. As far as we know, however, from theoretical point of view, there is not even a simple prediction for the angular distribution so far. It is expected that the measurements of the polarization effects of the REC photons shed light on the REC process from other viewpoints. In the present report, we discuss the angular distributions for L-REC photons²⁾ and further for the linear polarization effects for K-REC photons²⁾ by using the simple formulae for the photoelectric effect (PE) given by the Born approximation³⁾ and by Lorentz-transforming the formulae to the laboratory frame. Hereafter, by the projectile frame, the origin of the coordinate system is centered on an incident projectile ion, and by the laboratory frame, the origin is chosen at the center of mass of an initial target atom.

Recently we investigated the validity of the quantum mechanical theory on REC from the viewpoint of the gauge invariance property.⁴⁾ For the heavy projectile ion impact on a light target, the projectile coordinate system is found to be most proper or, in other words, call least errors under the condition of electro-magnetic current conversion. Thus, the coordinate system for PE is always defined in the projectile frame. Herein, we use L-REC for

the radiative electron capture to the 2p state of a final projectile atom unless otherwise stated. We have little interest in the radiation pattern for REC to the 2s state because the pattern is almost the same as that for K-REC. Furthermore, REC is assumed nothing but the inverse process of PE, namely, the (two-body) radiative recombination process.³⁾

Firstly, we consider the shapes of the angular distributions for L-REC. By Lorentz-transforming to the laboratory frame the angular distribution for PE from the 2p states (L PE) given by using the Born approximation including the lowest-order retardation corrections,^{5,6)} this can be obtained as

$$\left(\frac{d\sigma_{\text{II+III}}}{d\Omega}\right) = (\sigma_{\text{II+III}}/4\pi) \cdot [1 - 2\beta \cos\theta \sin^2\theta] \quad (1)$$

where subscript I stands for 2s state and II+III for 2p $P_{1/2}$ as well as 2p $P_{3/2}$ states, $\beta = v/c$ (v and c are velocities of an ejected electron and light, respectively), θ and Ω denote the emission angle of a photon and the associated solid angle in the laboratory frame, respectively, and $\sigma_{\text{II+III}}$ represents the total L(II+III) cross section for L-REC. If the retardation is negligible, *i.e.*, if the second term in the square brackets of Eq. 1 can be dropped, the angular distributions for L-REC become isotropic as shown by Bethe and Salpeter.³⁾ It is easily found from Eq. 1 that the retardation effects of L-REC are not completely cancelled by the Lorentz-transformation, while those of K-REC are done.¹⁾

The observed photon spectra are given as the summation of both contributions of REC into 2s states and 2p states.⁷⁾ The photon angular shape of REC into a projectile 2s state (L(I)-REC) is essentially the same as for K-REC. Further, we use L(II+III)-REC to mean the capture into the projectile 2p states. On the assumption that the REC process is the inverse one of corresponding photoionization, the angular distributions of X rays for L(II+III)-REC must be isotropic as pointed out by Bethe and Salpeter.³⁾ However, we know the fact that the angular distributions of an ejected electron for the photoionization deviate from the isotropic behavior with the increase in the importance of the photon retardation effect.

By Lorentz-transforming the angular distributions for the photoionizations from the 2s and the 2p state from the projectile (moving) frame into the laboratory frame, we can obtain the photon angular distributions in the relativistic velocity region of L(I)- and L(II+III)-REC as:

$$(d\sigma_I/d\sigma_L) = (3/8\pi)\sigma_I \sin^2 \theta_L \quad (2)$$

where σ_I and σ_{II+III} represent the total cross sections for REC into the projectile 2s and 2p states, respectively and are given by

$$\sigma_I = \nu_p^5 (1 + 4\nu_p^2) (1 + \nu_p^2)^{-3} F(\nu_p) \quad (3)$$

and

$$\sigma_{II+III} = \nu_p^7 (3 + 11\nu_p^2) (1 + \nu_p^2)^{-4} F(\nu_p) \quad (4)$$

Here,

$$F(\nu_p) = (2^{10}\pi r_0^2 / 3\alpha) \cdot 4\pi \times \nu_p [1 - \exp(-4\pi\nu_p)]^{-1} \exp(-8\nu_p \cot^{-1}\nu_p) \quad (5)$$

with r_0 the classical electron radius where $\nu_p = Z_p\alpha/n\beta$, Z_p is the charge of projectile ion in units of electronic charge, α is the fine structure constant, and n is a principal quantum number ($n=2$).

In fact, one observes the L-REC angular distributions as the summation of the contributions from both L(I)-REC (Eq. 3) and L(II+III)-REC (Eq. 4). Thus, it is important to know the ratios of σ_I to σ_{II+III} with respect to the only one parameter ν_p . They are given in Table 1. It is expected that deviations of the L-REC angular distributions from $\sin^2\theta_L$ -dependence can be measured clearly in the large ν_p regions. In Fig. 2, we depict some normalized L-REC angular distributions for the projectile charges $Z_p=54$ and the incident velocities $v/c=0.2$ and 0.4 , respectively.

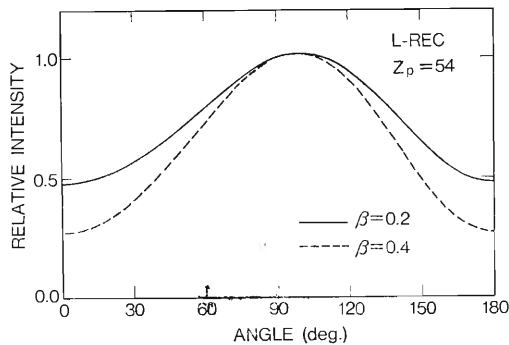


Fig. 1. Normalized photon angular distributions of L-REC (L(I) + L(II+III)) for the projectile charge $Z_p=54$.

Table 1. Ratios of σ_I to σ_{II+III} vs. the Coulomb parameters ν_p .

ν_p	0.1	0.2	0.3	0.4	0.5	0.6	0.7	0.8	0.9	1.0
σ_I/σ_{II+III}	32.0	8.8	4.1	2.5	1.7	1.3	1.1	0.9	0.8	7.0

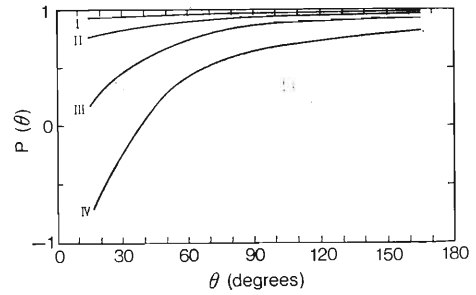


Fig. 2. Linear polarization correlation $P(\theta)$ for radiative electron capture to the K-shell for several velocities. I, $\beta=0.6$ (235 MeV/amu); II, 0.7 (376 MeV/amu); III, 0.8 (626 MeV/amu); and IV, 0.9 (1.22 MeV/amu).

Next, the linear polarization correlations for the K-REC photon are taken into consideration. The differential cross section for PE from the K shell (K PE) is of the form^{8,9)}

$$(d\sigma_{PE^K}/d\Omega') = 2^{-1}(d\sigma_{PE^K}/d\Omega')_{unpol}(1 + P'(\theta') \cos 2\phi) \quad (6)$$

where θ' and Ω' stand for the emission angle and the solid angle in the projectile frame, respectively, $(d\sigma_{PE^K}/d\Omega')_{unpol}$ means the K PE angular distribution for the unpolarized photon, $P'(\theta')$ represents the linear polarization correlation for K PE, ϕ is the angle between the scattering plane and the polarization plane constructed by \mathbf{k} and \mathbf{e} .

We can obtain the linear polarization correlation for K-REC, $P(\theta)$:

$$P(\theta) = \frac{-(\gamma-1) + 2\gamma(1-\beta \cos \theta)}{[(\gamma-1)(\gamma-2) + 2\gamma(1-\beta \cos \theta)]} \quad (7)$$

where $\gamma^{-1} = (1-\beta^2)^{1/2}$, $P(\theta)$ represents the polarization correlation for the linear polarized K-REC photon in the laboratory frame, average over initial target electron spin states and summed over final projectile electron spin states. $P(\theta)$ is depicted in Fig. 2.

References

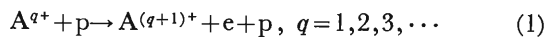
- 1) E. Spindler, H.-D. Betz, and F. Bell: *Phys. Rev. Lett.*, **42**, 832 (1979).
- 2) K. Hino and T. Watanabe: *Phys. Rev. A*, **36**, 5862 (1987).
- 3) H. A. Bethe and E. E. Salpeter: *Quantum Mechanics of One- and Two-Electron Atoms*, Springer-Verlag, Heidelberg (1957); Plenum, New York (1977).
- 4) K. Hino and T. Watanabe: unpublished.
- 5) G. Schur: *Ann. Phys. (Leipz.)*, 5 Folge, **4**, 433 (1930).
- 6) H. K. Tseng, R. H. P. Simon Yu, and A. Ron: *Phys. Rev. A*, **17**, 1061 (1978).
- 7) Y. Awaya, K. Hino, A. Hitachi, K. Kanai, K. Kawatsura, K. Kuroki, H. Vogt, Y. Yamazaki, and T. Watanabe: *High-Energy Ion-Atom Collisions, Lecture in Physics*, No. 294 (eds. D. Berényi and G. Hock), Springer-Verlag, Heidelberg, p. 185 (1988).
- 8) B. C. H. Nagel: *Ark. Fys.*, **18**, 1 (1960).
- 9) R. H. Pratt, R. D. Levee, R. L. Pexton, and W. Aron: *Phys. Rev.*, **134**, A898 and A916 (1964).

III-2-4. Calculation of Electron-Stripping Cross Sections of Ne Ions in Proton Impact

X. Fang,* X. Zhang,* Q. Ma,* and Y. Liu,* and T. Watanabe

Inelastic collision processes involving multi-charged ions and atomic hydrogen are of considerable interest, not only from theoretical viewpoints but also in relation to the practical aspects of electron stripping processes of accelerated projectile ions by accelerators. Among them, the processes of charge stripping (ionization) and charge exchange (electron capture) have received a great deal of attention in the study of charge balancing mechanism.

In this work, we treat the problem of electron stripping processes:



We use a binary encounter approximation (BEA) to describe collisions between an incident proton and electrons of a target ion and use the Roothaan-Hartree-Fock method to obtain velocity distributions for the electrons.

Theoretical work on the electron stripping process of a multicharged ion was reported recently by Karashima *et al.*¹⁾ They calculated the electron stripping cross sections of C and Ne ions in proton impact based on BEA and velocity distributions of the Thomas-Fermi model. The main purpose for their calculation is to obtain the cross section for electron stripping of a multicharged incident ion by a hydrogen target atom. In some cases, the theory can be replaced by that for the ionization processes by proton impact.

A main advantage of the binary encounter theory²⁾ is that it gives, in a direct and simple way, reasonable estimates of cross sections for a wide variety of physical processes. In general it is most satisfactory to apply the binary encounter theory to the ionization process in comparison with charge exchange and excitation processes. The Hartree-Fock method generally involves a great deal of calculations and gives numerical results for atomic orbitals and energy levels. Analytic fitting to numerical solutions of the Hartree-Fock equations is very useful for practical purposes. The Roothaan-Hartree-Fock method³⁾ can be used to obtain analytic orbitals for atomic systems. According to the Roothaan-Hartree-Fock formalism, Clementi and Roetti⁴⁾ calculated and tabulated the parameters to determine analytic orbitals for a series

of atoms and ions in the ground and some excited states. We will use relevant data given by Clementi *et al.*⁴⁾ to calculate the electron velocity distributions of target ions.⁵⁾

The BEA cross section for the ejection of an electron with the velocity w and binding energy U by an incident proton of the velocity v was derived²⁾ as follows:

$$\begin{aligned} \sigma_{\text{BEA}}(w, v, U) &= \frac{2\pi e^4}{mv^2} \left[\frac{1}{U} + \frac{mw^2}{3U^3} - \frac{1}{2m(v^2 - w^2)} \right] \\ &\quad \text{for } w \leq v - \frac{U}{2mv} \\ &= \frac{\pi e^4}{mv^2} \left[\frac{1}{2mw(v+w)} + \frac{1}{U} + \frac{m}{3wU^2} \right. \\ &\quad \left. \times \left\{ 2v^3 - w^3 - \left(\frac{2U}{m} + w^2 \right)^{3/2} \right\} \right] \\ &\quad \text{for } w \geq v - \frac{U}{2mv} \\ &= 0 \text{ for } w \leq \frac{U}{2mv} - v \end{aligned} \quad (2)$$

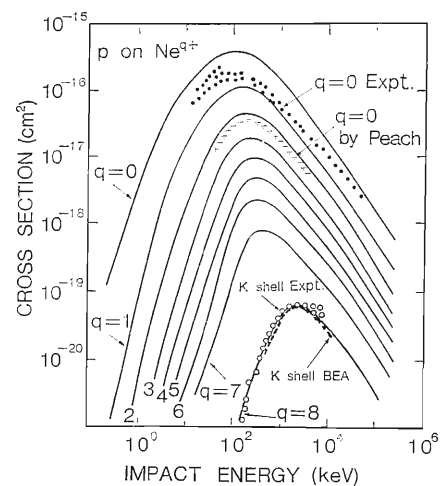


Fig. 1. Electron stripping cross sections of Ne ions in proton impact, calculated by the BEA and RHF velocity distributions. The comparisons are made for $q=0$ and $q=8$ with experimental as well as other calculated data. For $q=0$ ($p + \text{Ne}$), experiments are from many authors⁶⁻¹⁰⁾ and calculation is using the Born approximation by Peach.¹¹⁾ For $q=8$, comparison is made by the scaled cross sections for K-shell ionization by proton impact on neutral target, not for Ne^{8+} target. Particularly the K-shell ionization cross section for neutral atomic target can generally be reduced from the scaled cross sections.

* Department of Modern Physics, University of Science and Technology of China, Hefei, Anhui, China.

where m is the mass of the electron.

The average cross section for process (1) is given by

$$\sigma(v) = \sum_{i\lambda} \int \sigma_{\text{BEA}}(w, v, U_{i\lambda}) f_{i\lambda}(w) dw \quad (3)$$

$$= \sum_{i\lambda} w_{i\lambda} \int \sigma_{\text{BEA}}(w, v, U_{i\lambda}) w^2 \sum_k C_{i\lambda k} F_{\lambda k}(w)^2 dw \quad (4)$$

where we have identified the binding energies of the electron shell (i), U_i with the magnitude of the orbital energy given by Clementi *et al.*⁴⁾

According to expression 3, we performed calculation for collisions between proton and Ne^{q+} ($q = 0, 1, 2, \dots, 8$) in the ground state. Figure 1 shows the results.

References

- 1) S. Karashima, T. Watanabe, Y. Awaya, and Y. Liu: *Nucl. Instrum. Methods A*, **240**, 505 (1985).
- 2) L. Vriens: *Case Studies in Atomic Collisions Physics*, (eds. E. W. McDaniel and M. R. C. McDowell) North-Holland, Amsterdam, Vol. I, Chap. 6 (1967).
- 3) C. C. J. Roothaan: *Rev. Mod. Phys.*, **23**, 69 (1951); J. Hinze and C. C. J. Roothaan: *Prog. Theor. Phys. Suppl.*, **40**, 37 (1967).
- 4) E. Clementi and C. Roetti: *At. Data Nucl. Data Tables*, **14**, 177 (1974).
- 5) X. Fang: M.S. Thesis, USTC, Hefei, Anhui, China (1986).
- 6) J. W. Hooper, D. S. Harmer, D. W. Martin, and E. W. McDaniel: *Phys. Rev.*, **125**, 2000 (1962).
- 7) F. J. de Heer, J. Schutten, and H. Moustafa: *Physica* **32**, 1766 (1966).
- 8) H. B. Gilbody and J. B. Hasted: *Proc. R. Soc. A*, **240**, 382 (1957); H. B. Gilbody and A. R. Lee: *Proc. R. Soc. A*, **274**, 365 (1963).
- 9) L. I. Pivovar and Yu. Z. Levchenko: *Zh. Eksp. Teor. Fiz.*, **52**, 42 (1962) [*Sov. Phys. JETP*, **25**, 27 (1967)].
- 10) E. S. Solov'ev, R. N. Il'in, V. A. Oparin, and N. Y. Fedorenko: *Zh. Eksp. Teor. Fiz.*, **52**, 42 (1962) [*Sov. Phys. JETP*, **15**, 459 (1962)].
- 11) G. Peach: *Proc. Phys. Soc.*, **85**, 709 (1965); G. Peach: *J. Phys. B*, **1**, 1088 (1968).

III-2-5. Charge-Exchange Cross Sections and Equilibrium Charge States of Incident Uranium Ions with Relativistic Velocity

S. Karashima, K. Hino, and T. Watanabe

Knowledge of the charge states of relativistic heavy ions and of their charge-exchange processes in low and high atomic-number (Z_T) materials is of great theoretical and experimental interest from the viewpoint of fundamental science and the applications such as to the fields of heavy-ion beam inertial confinement fusion and of accelerator science.

The equilibrium charge states and linear energy transfer, LET, of Ne and Ar ions in hydrogen gas were calculated¹⁾ in non-relativistic velocity region. In this paper, the charge-exchange processes and charge-state distributions of uranium ions with a relativistic velocity impacted in mylar, Al, Cu, Ag, and Ta are treated by the relativistic formalism, and the calculations are compared with experimental values.

The fundamental processes in charge exchange are electron loss from a projectile ion and electron capture from a target atom into a projectile atomic level. We develop a relativistic Born approximation for the calculation of electron-loss cross sections. For electron capture processes, radiative electron capture (REC) dominates rather than non-radiative electron capture (non-REC) in the high impact velocity range. The REC cross sections into a projectile K-shell fall off as v^{-5} with increasing relative velocity, while the non-REC decays as v^{-12} . The non-REC and the REC cross sections are calculated by the relativistically extended eikonal and strong-potential Born approximation.

On the occasion where a projectile ion with a charge q collides with atoms in a target, the ion may capture or lose one or more electrons at each encounter. From now on, for simplicity, single-charge-exchange processes are assumed to be dominant for relativistic heavy-ion impacts. The equilibrium charge state distributions of the ion with an atomic number Z are determined from the ratios²⁾ of the electron capture and loss cross sections. The average equilibrium charge \bar{q} is obtained from a fraction F_q of charge state q :

$$\bar{q} = \sum_q q F_q, \quad \text{with} \quad \sum_q F_q = 1 \quad (1)$$

We consider two processes for electron capture in relativistic velocity range: REC process and non-REC

process. REC is the inverse of a photoelectric process. A bound target-electron is captured into a vacant state of the projectile and can directly radiate the energy gained by this transition as an X-ray photon. Charge exchange in matter for sufficiently high incident energies is due predominantly to the REC process.

The non-REC cross sections are calculated using Eichler's formula³⁾ based on a relativistic eikonal approach. The eikonal approach is an asymmetric theory with respect to projectile and target. When the active-electron-projectile and the active-electron-target interaction are treated nonperturbatively, one obtains different results. This is inherent in the eikonal theory and is called the post-prior discrepancy. Concerning these two theoretical versions on the treatment of non-REC process, we properly use the prior form if $Z_p \leq Z_T$, and the post form if $Z_p \geq Z_T$, where Z_p is the projectile atomic number.

For the REC, Hino and Watanabe⁴⁾ developed a strong-potential Born approximation⁵⁾ relativistically for the process depicted in the Feynman diagram shown in Fig. 1(a). Projectile (P), target (T), and active electron (e^-) move along arrows through P- e^- and e^- -T interactions. In addition to this usual photon emission process, the present calculation includes the contribution from the internal conversion process shown in Fig. 1(b); that is, in the first place,

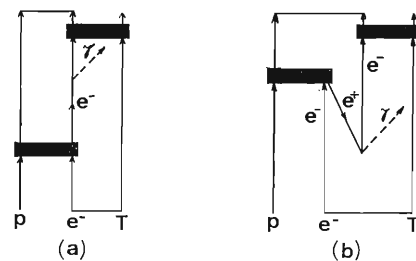


Fig. 1. (a) Feynman diagram for the usual REC photon emission process. P denotes a projectile ion, e^- an active electron, and T a target atom. e^- -T makes an initial bound state and P- e^- a final bound state. Photon (γ) is emitted through an electron capture process from a target into the projectile. (b) Feynman diagram including the internal conversion process for the REC. e^+ denotes a positron, the direction of particles are indicated by arrows and a black bold block represents Coulomb interactions.

the final electron and the virtual positron are produced at the same time when the photon emission occurs and then the positron is pair-annihilated with the initial electron under the Coulomb potential between the electron (e^-) and the projectile (P). When the relative velocity v is higher than 0.5 nu (nu: natural units, $\hbar = c = 1$), the internal conversion contributions take an important part in the REC process. This effect becomes remarkable particularly for collision of highly charged ions such as U^+ ion.

The electron-loss cross sections from projectile atomic states are formulated by the Born approximation with some relativistic modifications. The modifications to the formalism include the consideration of the bi-spinor contribution of respective particles as well as the full employment of the relativistic kinematics. The Coulomb distortion effect between a projectile and an active electron as well as the Coulomb interaction between a projectile electron and a target nucleus is taken into account, whereas the loss cross sections due to the Bethe theory⁶⁾ used by Gould *et al.*^{7,8)} only include the latter contribution. We can write the total electron loss cross section in the form:

$$\begin{aligned} \sigma_i = & \frac{8\pi(Z_T^2 + Z_T)e^4}{v^2} \\ & \times \int k^2 d\vec{k} \int \frac{d\vec{q}}{q^3} \left(\frac{1 + \gamma_k^{-1}}{2} \right) \\ & \times \left[1 - \frac{m\gamma_k}{M_T\gamma} + \frac{m^2\gamma_k^2 - q^2}{(2M_T\gamma)^2} \right] \\ & \times \left| \langle \phi_{pe}^{(-)}(\vec{k}, \vec{r}) | e^{i\vec{q}\cdot\vec{r}} | \phi_{pe}(\vec{r}) \rangle \right|^2 \end{aligned} \quad (2)$$

where $\phi_{pe}(\vec{r})$ and $\phi_{pe}^{(-)}(\vec{k}, \vec{r})$ are the initial bound-stage wave function of an electron in the projectile nucleus and the continuum-state Coulomb wave function of an ejected electron with a momentum \vec{k} , respectively, M_T and m are the masses of a target atom and an electron, $\gamma_k = (1 + (k/m)^2)^{1/2}$, $\gamma = 1/(1 - v^2)^{1/2}$ and \vec{q} denotes the momentum change of a target atom.

We calculated the charge state fractions F_q under the condition of local charge equilibrium by

$$F_q = \prod_{j=1}^q P_j / \left[1 + \sum_{q=1}^Z \prod_{j=1}^q P_j \right] \quad (3)$$

with

$$F_q / F_{q-1} = \sigma_{q-1, q} / \sigma_{q, q-1} = P_j$$

where $\sigma_{q, q'}$ is the capture (or loss) cross section from charge state q to q' .

For comparison with the experimental data obtained by Gould *et al.*, we calculated the value of the equilibrium charge state distributions for 200 MeV/nucleon ($v = 0.57$ nu), 437 MeV/nucleon ($v = 0.73$ nu) and 962 MeV/nucleon ($v = 0.87$ nu) uranium ions and found that the overall tendency is explained on the basis of our calculation, although small discrepancies could be found. For accounting for the target Z_T -dependence of cross sections more precisely, it is necessary to accumulate the cross section values as a function of the target atomic number. In high- Z_T targets, the non-REC process into excited states of the projectile would be dominant, although not considered in the present calculations.

References

- 1) S. Karashima and T. Watanabe: *Radiat. Res.*, **99**, 476 (1984).
- 2) S. Karashima and T. Watanabe: *Jpn. J. Phys.*, **22**, 895 (1983).
- 3) J. Eichler: *Phys. Rev. A*, **32**, 112 (1985).
- 4) K. Hino and T. Watanabe: *Phys. Rev. A*, **36**, 581 (1987).
- 5) J. Macek and R. Shakeshaft: *Phys. Rev. A*, **22**, 1441 (1980); J. Macek and S. Alston: *Phys. Rev. A*, **26**, 250 (1982); S. Alston: *Phys. Rev. A*, **27**, 2342 (1983).
- 6) H. A. Bethe: *Ann. Phys. (Leipzig)*, **5**, 325 (1930).
- 7) H. Gould, D. Greiner, P. Lindsrom, T. J. M. Symon, M. Grawford, P. Thieberger, and H. Wegner: *Phys. Rev. Lett.*, **52**, 180 (1984); Errata: *Phys. Rev. Lett.*, **52**, 654 (1984).
- 8) H. Gould, D. Greiner, P. Lindstrom, T. J. M. Symons, M. Grawford, P. Thieberger, and H. Wegner: *Nucl. Instrum. Methods B*, **10/11**, 32 (1985).

III-2-6. Electron Capture between Arbitrary Excited States in the Continuum Distorted Wave Approximation

S. C. Mukherjee* and T. Watanabe

The cross sections for electron capture between arbitrary excited states of a target and a projectile have been calculated by Omidvar¹⁾ in the Oppenheimer-Brinkman-Kramers (OBK) approximation. The 'Full Born approximation' has been used by Toshima²⁾ for the calculation of a few selected transitions between high-lying states of atomic hydrogen. The charge exchange calculations between arbitrary excited hydrogenic states, nl and $n'l'$ of a target and a projectile in the high energy region have been reported by Eichler³⁾ in the eikonal approximation. Ho *et al.*⁴⁾ extended the eikonal calculations to cover nlm contributions.

In the study of charge exchange process, at high incident velocities the classical capture occurs through a two-step process and thus the inclusion of the

second-order term is necessary in the quantum mechanical calculation.⁵⁾ The continuum distorted wave approximation (CDW) is known as an adequate second-order method for the calculation of charge exchange cross sections.⁶⁾ In the present paper, we study the charge-transfer cross sections from arbitrary initial excited states to final excited states in the CDW approximation. The procedure we follow here has been developed in a recent publication.⁷⁾ The Coulomb integrals involved in the CDW approximation are evaluated in a closed form in terms of a terminating Gauss-Hyper Geometric function. This approach is found to be (quite) suitable for application to any arbitrary excited states and also appears to be of much convenience for numerical computation.

Table 1. Charge transfer cross-sections, $\sigma_{nlm-n'l'm'} \times 10^{-16}$ in cm^2 , calculated for the reactions $\text{H}^+ + \text{H}(2l) \rightarrow \text{H}(3l') + \text{H}^+$ as a function of energy. The numbers in parenthesis denote the powers of ten, by which the numbers are multiplied.

Lab. energy of H^+ (keV)	σ_{2s-3s}	σ_{2s-3p}	σ_{2s-3d}	σ_{2p-3s}	σ_{2p-3p}	σ_{2p-3d}
25	1.30(-1)	1.55(-1)	5.09(-2)	1.41(-1)	3.51(-1)	2.05(-1)
50	1.56(-2)	1.26(-2)	2.63(-3)	6.12(-3)	1.31(-2)	8.10(-3)
100	9.74(-4)	5.03(-4)	6.62(-5)	1.86(-4)	3.57(-4)	2.23(-4)
250	1.23(-5)	3.47(-6)	2.88(-7)	1.20(-6)	2.46(-6)	1.65(-6)
500	3.28(-7)	6.01(-8)	4.43(-9)	2.15(-8)	5.71(-8)	3.82(-8)
800	2.56(-8)	3.63(-9)	2.73(-10)	1.33(-9)	4.42(-9)	2.95(-9)
1,000	7.49(-9)	9.58(-10)	7.68(-11)	3.65(-10)	1.32(-9)	6.90(-10)

Table 2. Charge transfer cross-sections, $\sigma_{nlm-n'l'm'} \times 10^{-16}$ in cm^2 , calculated for the reactions $\text{H}^+ + \text{H}(2l) \rightarrow \text{H}(4l') + \text{H}^+$ as a function of energy. The numbers in parenthesis denote the powers of ten, by which the numbers are multiplied.

Lab. energy of H^+ (keV)	σ_{2s-4s}	σ_{2s-4p}	σ_{2s-4d}	σ_{2s-4f}	σ_{2p-4s}	σ_{2p-4p}	σ_{2p-4d}	σ_{2p-4f}
25	5.69 (-2)	6.63 (-2)	2.62 (-2)	8.12 (-3)	7.6 (-2)	1.90 (-1)	1.50 (-1)	1.09 (-1)
50	7.00 (-3)	5.80 (-3)	1.54 (-3)	2.80 (-4)	3.03 (-3)	6.48 (-3)	4.41 (-3)	3.44 (-3)
100	4.29 (-4)	2.31 (-4)	4.01 (-5)	5.57 (-6)	8.50 (-5)	1.63 (-4)	1.06 (-4)	9.20 (-5)
250	5.30 (-6)	1.58 (-6)	1.74 (-7)	2.32 (-8)	5.26 (-7)	1.08 (-6)	7.21 (-7)	6.72 (-7)
500	1.40 (-7)	2.74 (-8)	2.97 (-9)	4.12 (-10)	9.24 (-9)	2.46 (-8)	6.16 (-9)	1.01 (-8)
800	1.08 (-8)	1.67 (-9)	1.90 (-10)	2.44 (-11)	6.3 (-10)	1.84 (-9)	1.23 (-9)	7.90 (-10)
1,000	3.18 (-9)	4.40 (-10)	5.46 (-11)	6.76 (-12)	1.68 (-10)	5.58 (-10)	3.50 (-10)	3.63 (-10)

* Permanent address: Indian Association for the Cultivation of Science, Jadavpur, Calcutta-700032, India.

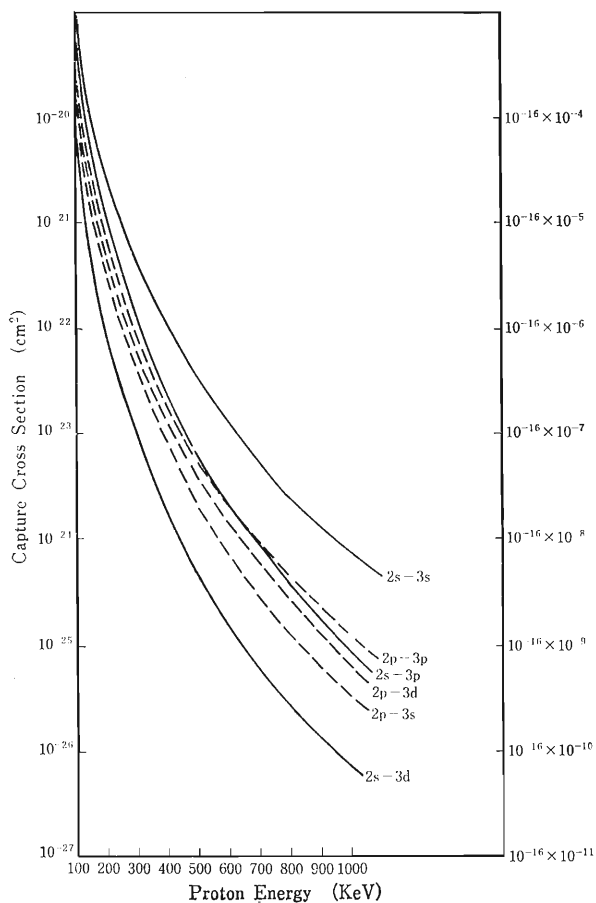


Fig. 1. Cross sections for charge transfer between the $n=2$ and $n'=3$ level of hydrogen atom as a function of proton laboratory energy. — present CDW results for initial 2s states, --- present CDW results for initial 2p states.

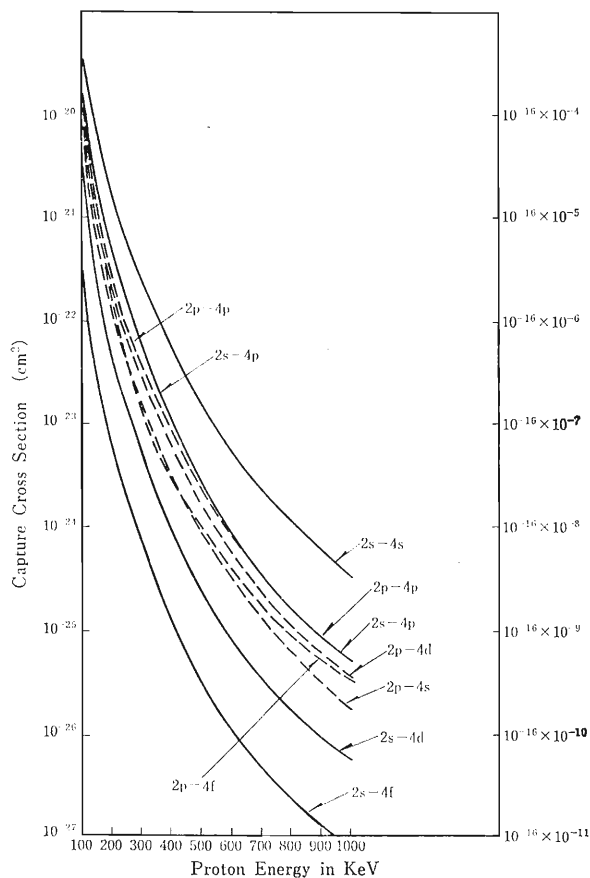


Fig. 2. Cross sections for charge transfer between the $n=2$ and $n'=4$ level of hydrogen atom as a function of proton laboratory energy. — present CDW results for initial 2s states --- present CDW results for initial 2p states.

References

- 1) K. Omidvar: *Phys. Rev.*, **153**, 121 (1967).
- 2) N. Toshima: *J. Phys. Soc. Jpn.*, **46**, 927 (1979); **46**, 1295 (1979).
- 3) J. K. M. Eichler: *Phys. Rev. A*, **23**, 498 (1981).
- 4) T. S. Ho, D. Umberger, R. L. Day, M. Leiber, and F. T. Chan: *Phys. Rev. A*, **24**, 705 (1981).
- 5) D. Ž. Belkić: *J. Phys. B*, **10**, 3491 (1977).
- 6) D. Ž. Belkić and R. McCarroll: *J. Phys. B*, **10**, 1933 (1977).
- 7) G. C. Saha, S. Datta, and S. C. Mukherjee: *Phys. Rev. A*, **36**, 1656 (1987).

III-2-7. Charge Transfer Collision between a Low Energy Ion and a Solid Surface

K. Fujima, H. Adachi,* and M. Kimura

In a previous report¹⁾ we calculated the charge transfer cross section between He^+ and Si to simulate Ion Neutralization Spectra. This model calculation in a diatomic model is the simplest, but it is desirable to extend our calculation into a more realistic case.

To investigate the charge-transfer cross section between a low energy ion and a solid surface, we take a simple but still realistic cluster model.

We selected the Si (100) surface as a target and took a cluster shown in Fig. 1 to represent the surface. This cluster is made of seven silicon atoms including the central and second nearest neighbor atoms. A He^+ ion approaches along the Z-axis and captures an electron from the target cluster. We employed a basis set consisting of 1s for the He^+ ion and 1s to 3d for the Si cluster for most calculations. Selected calculations were performed for larger basis sets including additional 2s and 2p orbitals for the He^+ ion to examine the issue of convergence.

Figure 2 illustrates the level diagram of the system of $\text{He}^+ + \text{Si}_7$. In the united atom limit, this system becomes a Si_6S cluster. The orbital energies of this neutral cluster are shown on the left-hand side of Fig. 2. Shown on the right-hand side of the figure are the orbital energies in the separated atom limit, *i.e.*, an isolated Si surface plus a free He^+ ion. Since the 2s and 2p of the Si atoms are inner shell orbitals, these orbitals do not mix with each other except for the central Si atom. The 3s and 3p orbitals make an sp valence band. The 3d orbitals of the Si atom are not occupied and therefore make an unoccupied band, which is not indicated in Fig. 2. The 1s level of He^+ is located in the middle of the L and M

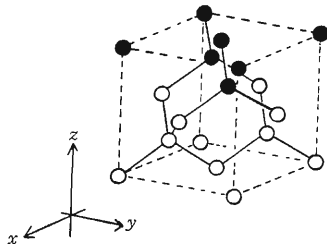


Fig. 1. A target cluster of Si atoms (solid circles) used in the calculations.

shell levels of the Si atoms, as in the diatomic case in the separated atom limit. When a He^+ ion approaches the surface at distances larger than 1 a.u.,

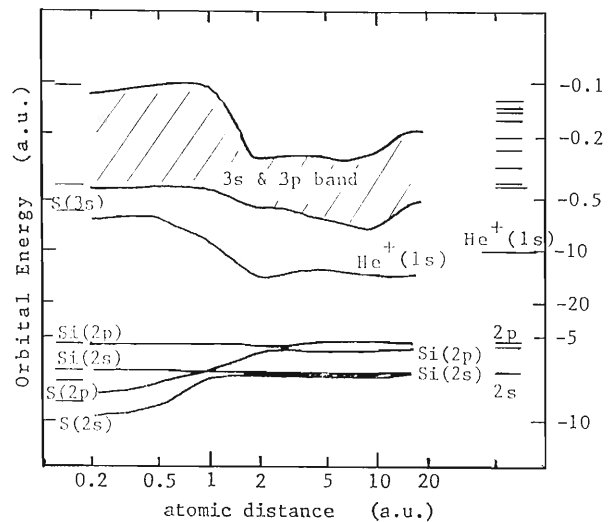


Fig. 2. Energy diagram of the $\text{He}^+ + \text{Si}_7$ system. The 1s orbital energies of the Si atoms are not plotted. Only the top and bottom of the Si 3s-3p band are indicated.

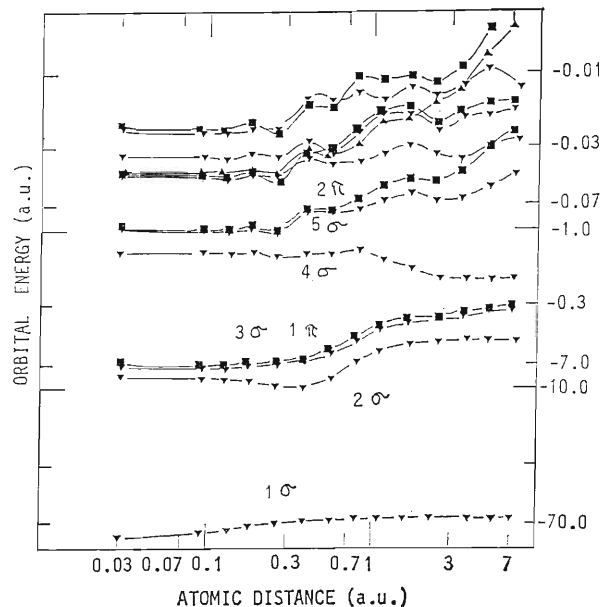


Fig. 3. Energy diagram of the $\text{He}^+ + \text{Si}$ system. Orbitals belonging to σ , π , and δ irreducible representations are plotted with \blacktriangledown , \blacksquare , and \blacktriangle , respectively.

* Hyogo University of Teacher Education.

the orbital energies of the cluster do not change drastically. When the He^+ comes closer to the surface, the 2 s and 2 p levels of the central Si atom start to lower because of the attractive core potential of the He^+ ion. Owing to this lowering of the inner shell levels, the 3 s and 3 p orbitals of the central Si atom make molecular orbitals with the 1 s orbital of the He^+ ion. The bottom of the 3 s-3 p band rises in energy. The energy of the 1 s orbital of the He^+ ion increases. The energy difference between the bottom of the 3 s-3 p valence band of the Si surface and the 1 s level of He^+ becomes smaller. In fact, the 1 s level is known to merge into the 3 s-3 p band in the united atom limit, though the present calculations are too inaccurate close to this limit to be included in Fig. 2.

This feature is quite similar to that of the $\text{He}^+ + \text{Si}$ system previously reported¹⁾ and indicates the large amplitude of picking up an electron from the bottom

of the Si 3 s-3 p band. The energy diagram of the $\text{He}^+ + \text{Si}$ system is shown in Fig. 3. Since the general trend of the energy diagram of the $\text{He}^+ + \text{Si}_7$ system is very similar to that of the $\text{He}^+ + \text{Si}$ system, the charge-transfer cross sections of both systems are thought to be of the same order of magnitude.

However, our calculation suggests that if the 2 s and 2 p vacant orbitals of He^+ are taken into account, these orbitals will mix with the 3 s and 3 p orbitals of the central Si atom. These orbitals will also mix with those of neighboring silicon atoms making a band. This would result in a quite different charge-transfer cross section from the 3 s-3 p band of the Si surface to the L shell orbitals of the He^+ ion as compared with the case of the diatomic model.

Reference

- 1) K. Fujima and H. Adachi: *RIKEN Accel. Prog. Rep.*, **20**, 37 (1986).

III-2-8. The Cross Section for $e^- + (e^+e^-)_{(1^3S_1)} \rightarrow (e^-e^+)_{(1^1S_0)} + e^-$

Q. Ma,* X. Zhang,* Y. Liu,* and T. Watanabe

The lifetime of positronium is influenced greatly by its spin state. The singlet spin state (*para*-positronium) decays radiatively emitting two γ -rays with a lifetime of 1.25×10^{-10} s¹⁾ and the triplet spin states (*ortho*-positronium) decays emitting three γ -rays with a lifetime of 1.41×10^{-7} s.²⁾ The conversion cross section is important in measuring the lifetimes of the positronium. In this paper we calculated and obtained an analytical formula for the *para-ortho* conversion cross section using the first Born approximation (FBA). Difficulty appears in evaluating the matrix element by using the Jacobi coordinate system which has been treated in a $\mu^+ + (\mu^-p)$ scattering problem.³⁾ The numerical results are compared with the classical trajectory Monte Carlo (CTMC) calculation.⁴⁾

Let us consider the case where electron 1 collides with a positronium composed of electron 2 and positron 3 to result in a new positronium composed of electron 1 and positron 3, as shown in Fig. 1. We use two-state approximation

$$\Psi = F_i(\vec{R})\phi_i(\vec{r})S_i(1,2,3) + F_f(\vec{R}')\phi_f(\vec{r}')S_f(2,1,3) \quad (1)$$

where $\phi_i(\vec{r})$ and $\phi_f(\vec{r}')$ are the eigenfunctions of bound states in the initial and the final states, $F_i(\vec{R})$ and $F_f(\vec{R}')$ are the wavefunctions for the travelling states of $e^- + (e^-e^+)$ in the initial and final states, respectively, and $S_i(1,2,3)$ and $S_f(2,1,3)$ are the initial and the final spin-state wavefunctions, respectively.

The scattering amplitude for the process in the first Born approximation is written as

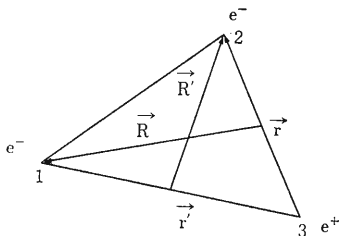


Fig. 1. Schematic colliding system and its coordinates.

$$g(\theta) = -\frac{\mu}{2\pi\hbar^2} \int d\vec{R}'' e^{-i\vec{k}_f \cdot \vec{R}''} \times \langle \phi_f(\vec{r}') | H_1' | F_i(\vec{R}) \phi_i(\vec{r}) \rangle \times \langle S_f(2,1,3) | S_i(1,2,3) \rangle \quad (2)$$

where \vec{k}_f is a vector of k_f with $k_f^2 = \frac{2\mu}{\hbar^2}(E - \epsilon_f)$, $F_i(\vec{R}) = e^{i\vec{k}_i \cdot \vec{R}}$ and \vec{k}_i is a vector of k_i with $k_i^2 = \frac{2\mu}{\hbar^2} \times (E - \epsilon_i)$, θ is the angle between \vec{R}_f and \vec{k}_i , H_1' is the interaction potential in the initial state, and S_i and S_f are the initial and the final spin-state wavefunctions, respectively. The differential cross section is obtained as

$$\frac{d\sigma}{d\Omega}(\theta, \phi) = \frac{k_f}{k_i} |g(\theta)|^2 \quad (3)$$

and the total cross section is given by

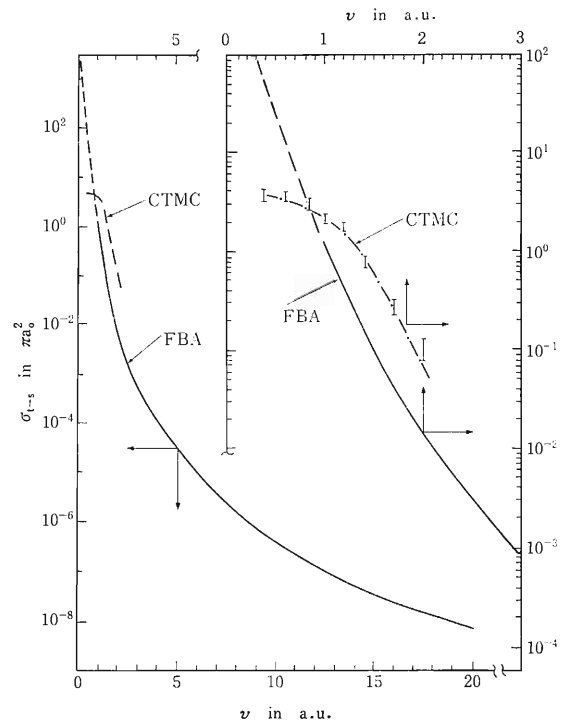


Fig. 2. Total cross section for $e^- + (e^+e^-)_{(1^3S_1)} \rightarrow (e^-e^+)_{(1^1S_0)} + e^-$ (*ortho-para* conversion) as a function of relative impact velocity in atomic units. FBA, the present FBA calculation; CTMC, the classical trajectory Monte Carlo calculation (Ref. 4); -----, poor approximation region in FBA.

* Department of Modern Physics, University of Science and Technology of China, Hefei, Anhui, China.

$$\sigma = 2\pi \frac{k_f}{k_i} \int_0^\pi |g(\theta)|^2 \sin \theta d\theta \quad (4)$$

$$\cos \theta = \frac{\vec{k}_i \cdot \vec{k}_f}{k_i k_f}$$

The total cross sections for the *para-ortho* conversion process as a function of an incident relative velocity are given in Fig. 2. These data are compared with the results by CTMC.⁴⁾

Comparison with the CTMC calculations for the total cross section (TCS) shows that TCS by FBA has the same velocity dependence and is somewhat smaller than that by CTMC above 1.5 a.u., contrary to the cases of μ^+ on (μ^-p) and of positron on H scattering. It is evident that the first-order calculation overestimates TCS at low velocities particularly in a particle transfer process.

Differential cross sections (DCS's) have a quite different tendency of the scattering-angle dependence

from those of μ^+ on (μ^-p) and e^+ on H by FBA. This is due to the same mass of the particles concerned. In the high velocity limit, the cross section for the break-up channel $e^- + (e^-e^+) \rightarrow e^+ + e^- + e^-$ will dominate. The exchange channel is limited to the cases where the final momenta of the projectile e^- and e^+ are confined to a small three-dimensional domain, making a new positronium possible. This is the reason why DCS in the high velocity limit is concentrated on 180° whereas DCS for $\mu^+ + (\mu^-p)$ and for $e^+ + H$ is concentrated on 0° .

References

- 1) S. DeBenedetti and H. C. Corben: *Ann. Rev. Nucl. Sci.*, **4**, 191 (1954).
- 2) A. Ore and J. L. Powell: *Phys. Rev.*, **75**, 1696 (1949).
- 3) Q.-C. Ma, X.-X. Zhang (Cheng), Z.-H. Liu, Y.-Y. Liu, and T. Watanabe: *Phys. Rev. A*, **32**, 2645 (1985).
- 4) K. Nakanishi, K. Iguchi, A. Ohsaki, and T. Watanabe: submitted to *Phys. Rev. A*.

III-2-9. The Born Approximation to the Reactance Matrix in Low-Energy Electron-Molecule Collisions

C. T. Whelan and I. Shimamura

The calculation of accurate collisional parameters for electron-impact excitation of the rotational levels of polar molecules is greatly complicated by the large number of angular-momentum values (that correspond to impact parameters) that must be included.

It has been suggested that by using the Born approximation to the reactance matrix^{1,2)} and retaining the full unitarity of the S matrix (*i.e.*, the Born-II approximation) the contribution from intermediate to large values of the angular momentum may be estimated accurately.

This approach parallels quite closely the use of the Bethe approximation to the reactance matrix in the study of the intermediate-energy scattering of electrons from neutral atoms.³⁾

In this note we remark on how the mathematical and computational methods developed for the neutral-atom problem may be applied to advantage in the molecular case.

We will be concerned with rotational excitation of molecules and will work in a space-fixed frame of reference. We will assume that the multipole expansion of the electron-molecule electrostatic potential has its asymptotic form

$$\sum_{\lambda} V_{\lambda} r^{-\lambda-1} P_{\lambda}(\hat{\mathbf{r}} \cdot \hat{\mathbf{R}}) \quad (1)$$

where V_1, V_2, \dots , are the dipole, quadrupole, \dots , moments of the charge distribution. P_{λ} is a Legendre function of the cosine of the angle between the molecular axis and the position vector of the electron. In these circumstances the Born reactance matrix for the transition from an initial rotational state j to a final rotational state j' is given by⁴⁾

$$R_{jj'}^{J(B)} = -2 \sum_{\mu \geq 1} f_{\mu}(j'l'jl; J) V_{\mu} I_0(k_j, l, k_{j'}, l'; \mu) \quad (2)$$

where f_{μ} is defined in Ref. 1, (k_j, l) and $(k_{j'}, l')$ are,

respectively, the wave number and the angular momentum of the scattered electron before and after the collision, and J is the vectorial sum of the two angular momenta j and l . I_0 is an integral³⁾

$$I_0(k_j, l, k_{j'}, l'; \mu) = \sqrt{(k_j k_{j'})} \int_0^{\infty} j_{l'}(k_{j'} r) j_l(k_j r) r^{-\mu+1} dr \quad (3)$$

with j_l and $j_{l'}$ spherical Bessel functions.

All scattering cross sections may be written in terms of the transition matrix. For example, the total cross section is given by

$$\sigma(j', j) = \pi / \{k_j^2 (2j+1)\} \sum_{J, l'} (2J+1) |T_{J, j'l'}|^2 \quad (4)$$

We distinguish two approximations

$$T^J(\text{Born II}) = -2i \mathbf{R}^{J(B)} / \{1 - i \mathbf{R}^{J(B)}\} \quad (5)$$

and

$$T^J(\text{Born I}) = -2i \mathbf{R}^{J(B)} \quad (6)$$

The strong-coupling approximation, Born II, conserves probability current and preserves the unitarity of the S matrix, while the weak-coupling approximation, Born I, does not. When summed over J the Born-I approximation is identical to the first-Born approximation as derived from standard perturbation theory. It should be emphasized that the Born-II approximation follows from the variational principle for electron scattering, and is not merely a "unitarized" form of the first-order perturbation theory.^{3,5)} In Padial *et al.*²⁾ the utility of the Born-II approximation for high J was demonstrated, but their calculations were carried out in the body-fixed frame with the fixed-nuclei approximation, *i.e.*, $k_j = k_{j'}$. In this case the Born matrix element is easy to compute, since, as is well known,

$$I_0(k, l, k', l'; \mu) = \frac{\pi k^{\lambda-1} \Gamma(\lambda) \Gamma(\{l+l'-\mu+2\}/2)}{2^{\mu+1} \Gamma(\{l-l'+\mu+1\}/2) \Gamma(\{l'-l+\mu+1\}/2) \Gamma(\{l+l'+\mu+2\}/2)} \quad (7)$$

In the general case $k_j \neq k_{j'}$, however, the numerical evaluation of $I_0(k_j, l, k_{j'}, l'; \mu)$ is more difficult.

In Ref. 3 it is shown that, for $k_j \neq k_{j'}$,

$$I_0(k_j, l, k_{j'}, l'; \mu) = \sum_{L} Q_{\mu L}(k_j, l, k_{j'}, l') Q_L(\lambda) \sqrt{(\pi/k_j k_{j'})} / 2^{\mu} \Gamma\left(\mu + \frac{1}{2}\right) \quad (8)$$

where the sum over L is finite, $Q_{\mu L}(k_j, l, k_{j'}, l')$ is given in Ref. 1, and $Q_L(\chi)$ is a Legendre function of the second kind with

$$\chi = (k_j^2 + k_{j'}^2) / (2k_j k_{j'}) \quad (9)$$

In this form I_0 can be computed to arbitrary accuracy at only a small cost in computer time.⁶⁾

We will shortly make available a molecular version of the computer program BETRT⁶⁾ that has been developed based on Eqs. 7 and 8 and used for electron scattering by neutral atoms.

The basic philosophy of the approximation adopted is to assume that, because of the centrifugal barrier, we may take progressively simpler approximations for the transition matrix as l (and hence J) increases.

So we might, for example, take a sophisticated static-exchange calculation, *e.g.*, R-matrix or close-coupling, for the first few J , and then, when

$$|\mathbf{R}^{(B)}|^2 \ll |\mathbf{R}^{(B)}| \quad (10)$$

we could use the Born-I approximation for J_0 to infinity. In the particular case of dipolar molecules, however, a very large number of terms of the Born-I form may be needed, because of the long-range nature of the interaction, if we are to sum to convergence. It is therefore useful to be able to sum for $J \geq J_0$ in a closed analytic form.

When $\mu = 1$ we have the $l'lJ$ contribution³⁾

$$\sigma_{l'lJ}^{\text{Born I}}(j', j) = 16(2J+1) |f_1(j'l'jl; J)|^2 V_1^2 |I_0|^2 \quad (11)$$

Now, just as in Ref. 3, we may sum this over J such that

$$\sigma_{l'l}^{\text{Born I}}(j', j) = (16/3) V_1^2 j_{>l} I_0^2(k, l, k', l'; 1), \quad (12)$$

where $j_{>} = \max(j, j')$, $l_{>} = \max(l, l')$, and $l' = l \pm 1$.

It can be shown, however, that⁴⁾

$$\begin{aligned} \sum_{l=l_0}^{\infty} \sum_{l'=l \pm 1} l_{>} I_0^2(k_j, l, k_{j'}, l'; 1) \\ = (l_0/4) (k_j/k_{j'}) \{Q^2_{l_0-1}(\chi) - Q^2_{l_0}(\chi)\} \end{aligned} \quad (13)$$

and hence, we know

$$\sum_{l=l_0}^{\infty} \sum_{l'=l \pm 1} \sigma_{l'l}^{\text{Born I}}(j', j)$$

and can deduce

$$\sum_{j=J_0}^{\infty} \sum_{l'} \sigma_{l'lJ}^{\text{Born I}}(j', j)$$

References

- 1) M. J. Seaton: *Proc. Phys. Soc.*, **77**, 174 (1961).
- 2) N. T. Padiyal, D. W. Norcross, and L. A. Collins: *J. Phys. B*, **14**, 2901 (1981).
- 3) C. T. Whelan: *J. Phys. B*, **19**, 2343 (1986).
- 4) N. Chandra: *Phys. Rev. A*, **16**, 80 (1977).
- 5) C. T. Whelan, A. Burgess, and M. A. Hayes: submitted for publication.
- 6) A. Burgess and C. T. Whelan: *Comput. Phys. Commun.*, **47**, 295 (1987).

III-2-10. Rotational Stopping Cross Sections for Collisions of Subexcitation Electrons with Dipolar Molecules: Dependence on the Temperature of the Molecular Gas

I. Shimamura

Secondary electrons produced by high-energy charged particles or by ionizing radiations lose their energies, as they penetrate matter, by exciting atoms or molecules. When the energies E of the secondary electrons become lower than a few electron volts and below the threshold for electronic excitation, the main energy-loss mechanism is vibrational and rotational excitation in electron-molecule collisions. We refer to such low-energy electrons as subexcitation electrons.

The cross section $\sigma(v\mathbf{J} \rightarrow v'\mathbf{J}'; E)$ for electron-impact excitation of a molecule from a well-defined vib-rotational state $v\mathbf{J}$ to a well-defined vib-rotational state $v'\mathbf{J}'$ at a collision energy E is difficult to measure directly. This is due to the small rotational level spacings; an electron spectrometer with extremely good energy resolution is required for resolving rotational lines in electron energy-loss spectra. On the other hand, reliable theoretical calculations of the vib-rotational-excitation cross sections are usually cumbersome.

Molecules in a gas at thermal equilibrium are normally distributed among many high rotational states because of the small rotational energies. Therefore, transitions from many different \mathbf{J} to many different \mathbf{J}' are taking place in the gas as subexcitation electrons penetrate it. Calculations of the cross sections for all of these transitions are almost impossible.

The mean energy loss by subexcitation electrons due to a particular vibrational transition $v \rightarrow v'$ is determined by the stopping cross section $S(E)$ defined by an average of the quantity

$$\sum_{\mathbf{J}} (E_{v\mathbf{J}'} - E_{v\mathbf{J}}) \sigma(v\mathbf{J} \rightarrow v'\mathbf{J}'; E) \quad (1)$$

over the degenerate initial states, where $E_{v\mathbf{J}}$ is the energy level of the state $v\mathbf{J}$. For application to a real gas, $S(E)$ is to be further averaged over the rotational distribution that depends on the gas temperature T ; the stopping cross section of the gas against electrons may be written as $S(E, T)$.

Because $S(E)$ depends on the initial rotational state in general, $S(E, T)$ is a function of both E and T . I proved a theorem some years ago, however, that $S(E)$ is independent of the initial rotational state if

E is much higher than the rotational-excitation energy.¹⁻³⁾ In other words $S_J(E)$ for any value of the magnitude J of the initial \mathbf{J} is equal to $S_{J=0}(E)$. This leads to an important theorem that $S(E, T)$ is independent of T (so that $S(E, T) = S(E, 0) = S_{J=0}(E)$), if E is much higher than the thermal energy $k_B T$ corresponding to the temperature T . I used a commutation relation involving the rotational Hamiltonian to prove this theorem for linear, symmetric-top, and asymmetric-top rotators.¹⁾ Later, different proofs by use of some relations between Clebsch-Gordan coefficients were shown for linear and symmetric-top rotators,^{4,5)} but not for asymmetric-top rotators.

In fact this theorem was proved on the assumption that the collision time is much shorter than the rotational period of the molecule. This assumption is valid for nonpolar molecules if E is much higher than the rotational-excitation energy. For polar molecules, however, this assumption is invalid for small-angle scattering even at high E , because of the long effective collision time for distant collisions that correspond to small-angle scattering.

In distant collisions the interaction between an electron and a polar molecule is weak, and a perturbation theory is applicable. Furthermore, only the long-range charge-dipole interaction survives at large distances between an electron and a molecule. Therefore, we may safely apply the first-Born approximation to scattering at angles below, say, θ_c , assuming only the charge-dipole interaction. Then, we may use a known formula for the differential cross section for rotational excitation. At angles higher than θ_c we may assume that the collision time is much shorter than the rotational period, and may apply the theorem of Ref. 1 mentioned above. By summing the contributions from the two angular regions, we obtain the following results.

For molecules that may be regarded as linear rotators it follows that

$$S_J(E) = S_{J=0}(E) - 2B\sigma_m^p a(J) \quad \text{for small } B/E \quad (2)$$

where B is the rotational constant of the molecule,

$a(J)$ is defined by

$$a(0)=0 \quad (3a)$$

and

$$a(J) = [(J+1)^2 \ln(J+1) - J^2 \ln J] / (2J+1) \\ \text{for } J \neq 0 \quad (3b)$$

and σ_m^B is the momentum-transfer cross section in the Born approximation and is expressible as

$$\sigma_m^B = \frac{4\pi D^2}{3E} \text{ a.u.} \quad (4)$$

in terms of the dipole moment D .

The rotational energy of a symmetric-top rotator depends not only on the magnitude J of the rotational angular momentum \mathbf{J} but also on its projection K onto the symmetry axis. For such a molecule we have

$$S_{J,K}(E) = S_{J,K=0}(E) - 2B\sigma_m^B b(J,K) \\ \text{for small } B/E \quad (5)$$

where

$$b(0,0) = 0 \quad (6a)$$

and

$$b(J,K) = a(J) - [K^2/(2J+1)] \ln [(J+1)/J] \\ \text{for } J \neq 0 \quad (6b)$$

Note that both Eqs. 2 and 5 are independent of the choice of the critical angle θ_c . From these equations it follows for both linear and symmetric-top rotators that

$$S(E,T) = S(E,0) - B\sigma_m^B \ln(k_B T/B) \\ \text{for small } B/k_B T \quad (7)$$

In conclusion I have extended a theorem on the gas-temperature dependence of the rotational stopping cross section for collisions of dipolar molecules with electrons. For gas temperatures much higher than the rotational excitation energy, the way the stopping cross section depends weakly on the temperature is explicitly expressible in a simple form.

References

- 1) I. Shimamura: *Phys. Rev. A*, **23**, 3350 (1981).
- 2) I. Shimamura: *Electron-Molecule Collision* (eds. I. Shimamura and K. Takayanagi), Plenum, New York, Chap. 2 (1984).
- 3) I. Shimamura: *Electronic and Atomic Collisions, Invited Papers, XIVth Int. Conf. the Physics Electronic and Atomic Collisions, Stanford, July 1985* (eds. D. C. Lorents *et al.*), North-Holland, Amsterdam, p. 93 (1986).
- 4) I. Shimamura: *J. Phys. B: At. Mol. Phys.*, **15**, 93 (1982).
- 5) D. W. Norcross: *Phys. Rev. A*, **25**, 764 (1982).

III-2-11. Doubly Excited Rydberg Series of Molecular Repulsive States: H_2

I. Shimamura, C. J. Noble,* and P. G. Burke**

Most doubly excited states lie energetically above the threshold of ionization, and they ionize when a sufficient energy is transferred from one to the other of the two excited electrons through the electron-electron interaction. The lifetime of a doubly excited state is inversely proportional to the energy width of the profile that appears in a spectrum due to this state. A doubly excited molecule may dissociate, if a sufficient energy is transferred to the vibrational motion before it ionizes. Thus, ionization and dissociation are competing processes for a doubly excited molecule to break up.

Doubly excited states of molecules play an important role in many kinds of dynamic processes, such as dissociative attachment and recombination, associative detachment, and competing photoionization and photodissociation.

Doubly excited molecules may be formed in collisions of neutral molecules with photons, electrons, or ions. Alternatively, they may be formed in collisions of molecular ions with electrons as compound resonance states. Therefore, doubly excited states of molecules may be studied by calculating electron-ion collisions at varying collision energies and by observing structures in the cross section. We have carried out such calculations using the R-matrix method.

The R-matrix method, proposed by Wigner and Eisenbud to study nuclear reactions, was introduced into the field of atomic collisions by Burke and others. We generalized the method for dealing with electron-molecule collisions.¹⁾ The successful applications of this method to a wide variety of atomic and molecular processes were reviewed in Refs. 2, 3, and 4.

In the R-matrix method we pay particular attention to the difference in the physics prevailing in two different regions of the configuration space. The inner region is where the scattered electron is inside the molecular electron cloud. Here, all electrons in the collision system interact strongly, and both the exchange and correlation effects are important. The

whole system is treated by the configuration-mixing method. The outer region, where the scattered electron is outside the molecular electron cloud, is infinitely large. Here, the scattered electron is distinguishable from the molecular electrons. There is no exchange potential that the scattered electron feels. Thus the Schrödinger equation reduces to second-order coupled ordinary differential equations. Fast and stable numerical methods for solving these equations exist in the literature. The whole scattering problem is solved, if the wave functions in both regions are connected smoothly across the boundary.

The essential physics of the doubly excited resonance states lies in the strong electron correlation in the inner region. The configuration-mixing method is appropriate for describing this effect. The most time-consuming part of the inner-region calculations need be carried out only once for all collision energies. The outer-region calculations must be carried out separately at each energy, but they are simple and short in terms of the computer time. Thus the R-matrix method is suitable for calculations at many energy points and for detection of narrow resonance structures in the cross section as a function of the energy.

We have applied the R-matrix method to electron scattering by the hydrogen molecular ion to study doubly excited states of the hydrogen molecule in the $^1\Sigma_g^+$ symmetry.

In the adiabatic-nuclei approximation, in which the internuclear distance is fixed, we have calculated the eigenphase sum by taking into account six channels ($1\sigma_g$) (El_g) and ($1\sigma_u$) (El_u) with $l_g=0, 2, 4$ and $l_u=1, 3, 5$, and configurations representing the correlation effect in the inner region. Whenever a structure is found in the eigenphase sum, we fit it to the Wigner resonance formula to determine the energy level and the width of the doubly excited state corresponding to the structure.

Although only three resonances of this symmetry are reported in the literature, we have found more than fifteen resonances at each internuclear distance. These resonances may be classified into two groups, ($1\sigma_u$) ($np\sigma$) and ($1\sigma_u$) ($nf\sigma$) Rydberg series, the previously known resonances being the first three

* Daresbury Laboratory, SERC, England.

** Department of Applied Mathematics and Theoretical Physics, the Queen's University of Belfast, Northern Ireland.

Table 1. Doubly excited Rydberg states of the hydrogen molecule in the $^1\Sigma_g^+$ symmetry at an internuclear distance of 2 a.u. E : Resonance energy in Rydberg units. Γ : Energy width in Rydberg units. n : Principal quantum number. μ : Quantum defect. $1.0(-2)=1.0\times 10^{-2}$.

$(1\sigma_u)(np\sigma)$				$(1\sigma_u)(nf\sigma)$			
n	E	Γ	μ	n	E	Γ	μ
2	0.40836	1.0(-1)	0.526				
3	0.73093	1.0(-2)	0.305				
4	0.79621	3.8(-3)	0.285	4	0.80635	2.4(-5)	-0.006
5	0.82382	1.8(-3)	0.278	5	0.82877	1.8(-5)	-0.006
6	0.83816	1.0(-3)	0.274	6	0.84095	1.2(-5)	-0.007
7	0.84657	6.4(-4)	0.272	7	0.84829	8.5(-6)	-0.007
8	0.85192	4.2(-4)	0.271	8	0.85307	6.0(-6)	-0.007
9	0.85554	2.9(-4)	0.270	9	0.85634	4.4(-6)	-0.007
10	0.85810	2.1(-4)	0.270	10	0.85868	3.3(-6)	-0.007

members of the former series. The former series couples strongly with the continuum, and is broader and has a larger quantum defect than the latter.

Table 1 shows the calculated parameters for the doubly excited Rydberg states at a representative internuclear distance.

In conclusion this work presents the first *ab-initio* calculations of doubly excited molecular Rydberg series, and proves the power of the R-matrix method for such studies.

References

- 1) P. G. Burke, I. Mackey, and I. Shimamura: *J. Phys. B: At. Mol. Phys.*, **10**, 2497 (1977).
- 2) I. Shimamura: Invited Papers, Xth Int. Conf. the Physics of Electronic and Atomic Collisions, Paris, July 1977 (ed. G. Watel), North-Holland, Amsterdam, p.213 (1978).
- 3) I. Shimamura: *Electron-Molecule Collisions* (eds. I. Shimamura and K. Takayanagi), Plenum, New York, Chap. 2 (1984).
- 4) P. G. Burke: *Atomic Physics 10* (eds. H. Narumi and I. Shimamura), North-Holland, Amsterdam, p.243 (1987).

III-2-12. Continuum Multiple Scattering Method for Molecules

H. Sato, M. Kimura,* and K. Fujima

Continuum wavefunctions of molecules play an important role in studies of electron scattering, photoionization and others. A continuum multiple scattering CMS) method^{1,2)} is a very useful method for calculation of continuum states.

In the CMS method the coordinate space is partitioned into three types of regions (see Fig. 1):

- I atomic: the inner regions of atomic spheres;
- II molecular: the region between atomic spheres and an outer sphere;
- III outer: the outer region of outer sphere.

The atomic spheres are centered at the constituent atoms and do not overlap each other. The outer sphere includes all the atomic spheres and is selected so as to minimize a size of the sphere. A molecular field regulating motion of a continuum electron is assumed to be spherically symmetric in the regions I and III and to be constant in the region II.

When a continuum electron having kinetic energy E is in the i -th atomic sphere, a wavefunction is expressed as

$$\phi^{I_i} = \sum_{lm} a_{ilm}^I f_i^{I_i}(r_i) Y_{lm}(\theta_i, \phi_i)$$

where r_i , θ_i , and ϕ_i are spherical coordinates of a position vector \mathbf{r}_i having an origin on the i -th nucleus. The function $f_i^{I_i}(r)$ is a solution of the one-electron Schrödinger equation

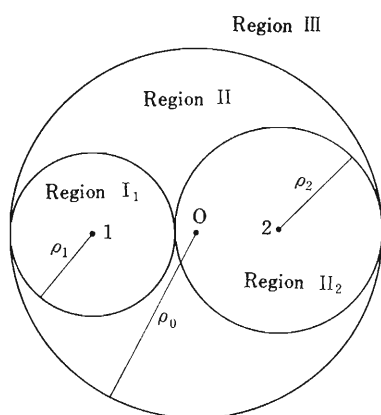


Fig. 1. Partition of the coordinate space.

$$\left[-\frac{1}{2r^2} \frac{d}{dr} \left(r^2 \frac{d}{dr} \right) + \frac{l(l+1)}{2r^2} + V_{I_i}(r) - E \right] \phi_l(r) = 0$$

and is finite at $r=0$. Atomic units are used unless otherwise stated.

Since the potential in the region II is constant, the wavefunction is expanded in terms of the spherical Bessel and Neumann functions j_l and k_l ,

$$\begin{aligned} \phi^{II} = & \sum_{lm} a_{lm}^{II} j_l(\kappa r_0) Y_{lm}(\theta_0, \phi_0) \\ & + \sum_i \sum_{lm} a_{ilm}^{II} n_l(\kappa r_i) Y_{lm}(\theta_i, \phi_i) \\ & \kappa = [2(E - V_{II})]^{1/2} \end{aligned}$$

where \mathbf{r}_0 is a position vector originated at the center of the outer sphere and V_{II} the value of the constant potential.

If the electron is in the region III, we can write the wavefunction as

$$\begin{aligned} \phi^{III} = & \sum_{lm} b_{lm}^{III} f_l^{III}(r_0) Y_{lm}(\theta_0, \phi_0) \\ & + \sum_{lm} a_{lm}^{III} g_l^{III}(r_0) Y_{lm}(\theta_0, \phi_0) \end{aligned}$$

Here the functions $f_l^{III}(r)$ and $g_l^{III}(r)$ are solutions of the equation

$$\begin{aligned} \left[-\frac{1}{2r^2} \frac{d}{dr} \left(r^2 \frac{d}{dr} \right) + \frac{l(l+1)}{2r^2} \right. \\ \left. + V_{III}(r) - E \right] \begin{pmatrix} f_l^{III}(r) \\ g_l^{III}(r) \end{pmatrix} = 0 \end{aligned}$$

and have the following asymptotic forms

$$\begin{aligned} f_l^{III}(r) & \rightarrow \frac{1}{kr} \sin \left(kr - \frac{1}{2} l\pi + \omega \right) \\ g_l^{III}(r) & \rightarrow -\frac{1}{kr} \cos \left(kr - \frac{1}{2} l\pi + \omega \right) \end{aligned}$$

where ω is the phase due to long-range behavior of the potential $V_{III}(r)$.

For a given set of b_{lm}^{III} we can determine the coefficients a_{ilm}^I , a_{lm}^{II} , a_{ilm}^{II} , and a_{lm}^{III} by connecting these functions smoothly at the boundaries of the regions.^{1,2)} Therefore, we can construct a continuum wavefunction of a molecule which has a given asymptotic form at $r \rightarrow \infty$.

Electron elastic scattering by $\text{H}_2\text{O}^3)$ and several organic molecules have been investigated by applying the CMS method. The potentials for continuum electrons are generated by using the discrete variable

* Argonne National Laboratory, Argonne, Illinois 60439, USA and Rice University, Department of Physics, Houston, Texas 77251, USA.

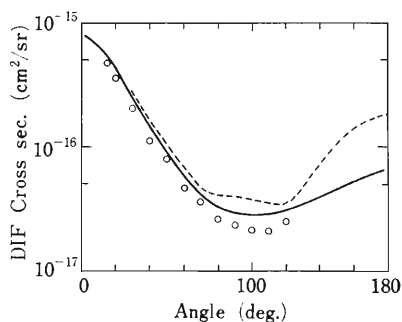


Fig. 2. Differential cross section for electron elastic scattering by H_2O at $E=20$ eV. Theory: solid line, Ref. 3; broken line, Ref. 7. Experiment: circle, Ref. 5.

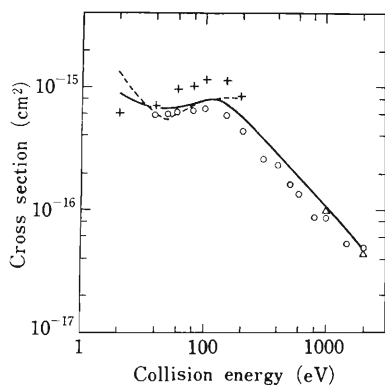


Fig. 3. Total momentum transfer cross section for electron elastic scattering by H_2O . Theory: solid line, Ref. 3; broken line, Ref. 7. Experiment: circle, Ref. 5; cross, Ref. 6; triangle, Ref. 8.

$X\alpha$ method.⁴⁾ The Hartree-Fock-Slater approximation is adopted for the exchange interaction in this method.

The total and differential cross sections for electron scattering by H_2O were calculated for collision energies E from 2 to 200 eV. The overall trend of the present results is in good agreement with recent measurements.^{5,6)} The differential cross section at $E=20$ eV³⁾ is shown in Fig. 2, and the total momentum transfer cross section in Fig. 3. Results for organic molecules will be published soon.

References

- 1) K.H. Johnson: *Adv. Quantum Chem.*, **7**, 143 (1973).
- 2) J.L. Dehmer and D. Dill: Argonne Natl. Lab. Radiol. Environ. Res. Div. Ann. Rep., July 1972-June 1973, ANL-8060, part I, p.119 (1973).
- 3) H. Sato, M. Kimura, and K. Fujima: *Chem. Phys. Lett.*, **145**, 21 (1988).
- 4) F.W. Averill and D.E. Ellis: *J. Chem. Phys.*, **59**, 6412 (1973).
- 5) A. Danjo and H. Nishimura: *J. Phys. Soc. Jpn.*, **54**, 1224 (1985).
- 6) T.W. Shyn and S.Y. Cho: *Phys. Rev. A*, **36**, 5138 (1987).
- 7) L.M. Brescansin, M.A.P. Lima, T.L. Gibson, V. McKoy, and W.M. Huo: *J. Chem. Phys.*, **85**, 1854 (1986).
- 8) A. Katase, K. Ishibashi, Y. Matsumoto, T. Sakae, S. Maezono, E. Murakami, K. Watanabe, and H. Maki: *J. Phys. B*, **19**, 2715 (1986).

III-2-13. Hyper-Radial Adiabatic Expansion for a Muonic Molecule $dt\mu$

S. Hara, H. Fukuda,* T. Ishihara,* and A. V. Matveenko**

It is well known that the wave function expanded in terms of basis functions which are adiabatic in hyper-radius satisfies correct boundary conditions for a general three body problem. In practical application of such approach, five coordinates other than hyper-radius can be chosen in many ways. Macek¹⁾ and Lin²⁾ have successfully used hyper-spherical coordinates to treat atomic three body problems where one particle is heavy and two are light. Recently Matveenko³⁾ and Matveenko and Abe⁴⁾ proposed to use hyperspheroidal coordinates for more general cases. In this report we calculate, with sufficient accuracy, the adiabatic potential curves and non-adiabatic interactions for low lying states of $dt\mu$ system using these two sets of coordinates. We also calculated the bound states with total angular momentum $J=0$ by solving the three-state coupled equations.

The hyper-radius R for the system of a triton t , a deuteron d and a negative muon μ is defined by

$$M_0 R^2 = MX^2 + m x^2 \quad (1)$$

where M and m are reduced masses of systems (t, d) and ($t+d, \mu$),

$$1/M = 1/m_t + 1/m_d \quad (2)$$

$$1/m = 1/(m_t + m_d) + 1/m_\mu \quad (3)$$

\mathbf{X} is the position vector of d relative to t , and \mathbf{x} is that of μ with respect to the centre of mass of ($t+d$). M_0 is an arbitrary mass constant; we choose $M_0 = M$ in the following.

The Hamiltonian for our system is given by using the hyper-radius by^{1,3)}

$$H = -\frac{1}{2M} \frac{1}{R^5} \frac{\partial}{\partial R} R^5 \frac{\partial}{\partial R} + h(\mathcal{Q}; R) \quad (4)$$

where h is the adiabatic Hamiltonian operator which includes R as a parameter and \mathcal{Q} represents five dimensionless variables. The eigenfunctions $\phi_n(R; \mathcal{Q})$ and eigenvalues $\varepsilon_n(R)$ of the operator h for a given R are obtained by solving the Schrödinger equation

$$[h - \varepsilon_n(R)]\phi_n(\mathcal{Q}; R) = 0 \quad (5)$$

In hyper-spherical coordinates, a set of variables

* Institute of Applied Physics, University of Tsukuba.

** Joint Institute for Nuclear Research, Moscow.

\mathcal{Q} is chosen to $(\alpha, \hat{\mathbf{X}}, \hat{\mathbf{x}})$, where $\hat{\mathbf{X}}$ and $\hat{\mathbf{x}}$ are polar and azimuthal angles of vectors \mathbf{X} and \mathbf{x} , respectively, and

$$\alpha = \arctan(\sqrt{M} X / \sqrt{m} x) \quad (6)$$

The explicit form of the h is given in these coordinates¹⁾

$$h = \frac{A^2}{2MR^2} + V \quad (7)$$

where

$$\begin{aligned} A^2 = & -\frac{1}{\sin \alpha \cos \alpha} \cdot \frac{\partial}{\partial \alpha} \left(\sin \alpha \cos \alpha \frac{\partial}{\partial \alpha} \right) \\ & + \frac{1}{\cos^2 \alpha} \left(-i\mathbf{X} \times \frac{\partial}{\partial \mathbf{X}} \right)^2 \\ & + \frac{1}{\sin^2 \alpha} \left(-i\mathbf{x} \times \frac{\partial}{\partial \mathbf{x}} \right)^2 \end{aligned} \quad (8)$$

and V is the Coulomb interaction between three particles

$$V = 1/X - 1/r_t - 1/r_d \quad (9)$$

where r_t and r_d are the positions of t and d relative to the muon.

In hyper-spheroidal coordinates, \mathcal{Q} is a set of variables $(\xi, \eta, \varphi, \hat{\mathbf{X}})$, where

$$\xi = (r_t + r_d)/X, \quad \eta = (r_t - r_d)/X \quad (10)$$

and φ , the azimuthal angle for \mathbf{x} around \mathbf{X} axis, are the spheroidal coordinates for \mathbf{x} . In this coordinate system, h is given explicitly by³⁾

$$h = -\frac{\rho^2}{2m} V_r^2 + \frac{\rho}{2MR^2} (J^2 - B - J_z^2) + V + \frac{\rho q}{MR^2} \quad (11)$$

where \mathbf{J} is the angular momentum of the system, and J_z its component along \mathbf{X} ,

$$p = 1 + \frac{m x^2}{MX^2} \quad (12)$$

$$q = \frac{1}{\rho} \mathbf{x} \cdot \frac{\partial}{\partial \mathbf{x}} \quad (13)$$

$$\begin{aligned} V_r^2 = & \frac{4}{R^2} \left[\frac{1}{(\xi^2 - \eta^2)} \left\{ \frac{\partial}{\partial \xi} (\xi^2 - 1) \frac{\partial}{\partial \xi} + \frac{\partial}{\partial \eta} (1 - \eta^2) \frac{\partial}{\partial \eta} \right\} \right. \\ & \left. + \frac{1}{(\xi^2 - 1)(1 - \eta^2)} \frac{\partial^2}{\partial \varphi^2} \right] \end{aligned} \quad (14)$$

The operator B is the Coriolis interaction operator given in the paper of Matveenko and Abe.⁴⁾ In the above expressions, the units $e = \hbar = m = 1$ are used.

We have calculated $\varepsilon_n(R)$ and $\phi_n(R; \Omega)$ for the $dt\mu$ system with $J=0$ by variational method. The form of the trial function adopted in hyper-spherical coordinates is

$$\phi_n = \sum_i a_{in} \varphi_i \quad (15)$$

$$\varphi_i = (\cos \alpha)^{l_i} (\sin \alpha)^{l_i} F \left(n_i, 2l_i + 2 + n_i, l_i + \frac{3}{2}, \sin^2 \alpha \right) P_{l_i}(\hat{\mathbf{x}} \cdot \hat{\mathbf{X}}) \quad (16)$$

where φ_i is an eigen-function⁵⁾ of \mathcal{L}^2 , F the hypergeometric function, and P_l the Legendre polynomial.

In hyper-spheroidal coordinates, we adopt

$$\Phi_n = \sum_i b_{in} \phi_i \quad (15')$$

$$\phi_i = \sqrt{\rho} \xi^{n_i} e^{-\beta_i R \xi} P_{l_i}(\eta) \quad (17)$$

for small R and

$$\phi_i = \sqrt{\rho} \xi^{n_i} e^{-\beta_i R \xi} \eta^{l_i} e^{\gamma_i R \eta} \quad (18)$$

for large R .

For the trial function in hyper-spheroidal coordinates, we use 77 basis functions. We obtained $\varepsilon_n(R)$ for the lowest three states ($n=1, 2$, and 3) with sufficient accuracy in the region $R > 0.3$. Inaccuracy for small R region is caused partly by the numerical integration carried out over ξ and η . If we use the trial function in hyper-spherical coordinates, convergence is very slow except for small R . Using 91-term trial functions, we have obtained satisfactory results only for $R < 0.01$. This is because our ($dt\mu$) system is more like a molecule rather than an atom. For $0.01 < R < 0.3$ the results are unsatisfactory, but better than the hyper-spheroidal results. In the following we use hyperspheroidal results for $R > 0.3$ and hyper-spherical results for $R \leq 0.3$.

The total wave-function Ψ is expanded by ε_n

$$\Psi = R^{-5/2} \sum_n \Phi_n(\Omega; R) \chi_n(R) \quad (19)$$

Thus the radial wave-function χ_n satisfies a set of coupled equations

$$\left[-\frac{1}{2M} \frac{d^2}{dR^2} + V_n(R) - E \right] \chi_n - \sum_{m \neq n} \left[W_{nm} + 2U_{nm} \frac{d}{dR} \right] \chi_m = 0 \quad (20)$$

where

$$V_n(R) = \varepsilon_n(R) + \frac{15}{8MR^2} - W_{nn}(R) \quad (21)$$

$$W_{nm}(R) = \frac{1}{2M} \left(\Phi_n \frac{\partial^2}{\partial R^2} \Phi_m \right) \quad (22)$$

$$U_{nm}(R) = \frac{1}{2M} \left(\Phi_n \frac{\partial}{\partial R} \Phi_m \right) \quad (23)$$

Table 1. Bound state energies (in eV) of the $dt\mu$ molecule with $J=0$.

n	$v=0$	$v=1$
1	-317.75	-31.99
2	-317.80	-33.46
3	-318.7	-34.4
Variation ⁷⁻⁹⁾	-319.14	-34.83

and E is the total energy.

The coupling terms U_{nm} are calculated by numerical differentiation of ψ_n and by using the Hellmann and Feynman theorem. Both results agree at least 3 digits in the calculation in hyper-spheroidal coordinates. W_{nm} are obtained by numerical differentiation. It is confirmed that the numerical calculation in hyper-spheroidal coordinates well reproduces the correct asymptotic forms of V_n ⁶⁾

$$V_1(R) = -2.4190/MR^4 \quad (24)$$

$$V_2(R) = 0.0087 - 2.6454/MR^4 \quad (25)$$

where 0.0087 is the difference in the binding energies between the $d\mu$ and $t\mu$ atoms in the $1s$ -state in our energy units. Energy is measured relative to the ground state of $t\mu$. In the potential curve $\varepsilon_2(R)$, there is a shallow minimum of about 5 eV at $R = 7.0$. This causes the peak in U_{12} in that region of R . This dip almost disappears when the coupling term W_{22} is added to $\varepsilon_2(R)$.

We have solved Eq. 20 and obtained the bound state energies of $dt\mu$ molecule with $J=0$. Calculations are carried out both variationally and by solving coupled differential equations numerically⁶⁾ for one and two state cases and variationally for the three state case. In the variational calculation, $12 \times n$ ($n=1, 2, 3$, are numbers of states) basis functions are adopted. The results are shown in Table 1. By the three-state calculation, we have obtained -318.7 eV and -34.4 eV, for vibrational quantum numbers $v=0$, and 1 , respectively. These values are compared with -319.14 eV and -34.83 eV obtained by full variational calculations⁷⁻⁹⁾ using several hundred to more than one thousand trial functions.

References

- 1) J. Macek: *J. Phys. B: At. Mol. Phys.*, **1**, 831 (1968).
- 2) C. D. Lin: *Phys. Rev. A*, **10**, 1986 (1974).
- 3) A. V. Matveenko: *Phys. Lett.*, **129**, 11 (1983).
- 4) A. V. Matveenko and Y. Abe: *Few-Body Systems*, **2**, 127 (1987).
- 5) P. M. Morse and H. Feschbach: *Methods in Theoretical Physics*, McGraw-Hill Book Co., New York, p.1730 (1954).
- 6) H. Fukuda, S. Hara, and T. Ishihara: to be published.
- 7) S. Hara, T. Ishihara, and N. Toshima: *J. Phys. Soc. Jpn.*, **55**, 3229 (1986).
S. Hara, T. Ishihara, and N. Toshima: *Muon Catalyzed Fusion*, **1**, 277 (1987).
- 8) L. I. Ponomarev: *At. Phys.*, **10**, 197 (1987).
- 9) M. Kamimura: *Muon Catalyzed Fusion*, **2**, in press.

III-2-14. Deformed Atoms and Collective Rotational Motion of Electrons

M. Iwai

Recently, there has been considerable interest in collective motion of atomic electrons. Many theoretical models have been proposed to analyze the joint motions of electrons. The group theoretical method¹⁾ which leads to a molecular model and the adiabatic hyperspherical coordinate approach²⁾ are the most typical ones. In the present paper we present a new interpretation of collective rotational motion of electrons. Using the symmetry-violating mean field approach³⁾ and the Peierls-Yoccoz projection method,⁴⁾ developed in nuclear many-body problem, we shall analyze the collective rotational motions of electrons in Be-like ions.

Let us first consider the possibility of deformation in the atomic Hartree-Fock fields in comparison with the quadrupole deformation of nuclei.³⁾ An important feature of the nuclear shell structure is that the $SU(3)$ multiple structure of single-particle levels, inherent in a three dimensional isotropic harmonic oscillator, is realized to a good approximation. That is, single-particle levels with the same parity form a quasi-degenerate manifold. The 'quadrupole' deformation of nuclei with a half-filled shell originates from this symmetry property.³⁾ The expectation value of the quadrupole tensorial operator is regarded as an order parameter of the deformation. Our question is how this picture of nuclear deformation is modified in the case of atomic systems. The high degeneracy in hydrogen atom, which reflects the $O(4)$ symmetry, is broken in many-electron atoms. However, even in many-electron atoms the quasi-degeneracy among the Hartree-Fock levels with the same principal quantum number n still remains. With increasing azimuthal quantum number l , the orbital energy usually becomes higher. Let us focus on a system with a closed subshell and with the ground state of the ${}^1S^e$ symmetry, such as alkaline earth atoms. In such a system, the lowest single-particle excitation occurs between the orbitals whose azimuthal quantum numbers differ only by unity. This suggests a 'dipole' deformation of atoms. Since electron-electron interaction is repulsive, it is energetically more favorable to break a singlet electron pair in the same orbital. This is the origin of the well-known fact that the lowest excited state of an alkaline each atom has the ${}^3P^o$ symmetry. With increasing

strength of electron correlation, or equivalently, with decreasing nuclear charge Z , the RPA^{3,5)} frequency from the ground to the lowest ${}^3P^o$ state could be negative. In such a case, we obtain, in analogy to nucleus, a deformed Hartree-Fock ground state with the energy lower than the spherical solution. In this ${}^3P^o$ -type deformation, one notices that the order parameter is given by the expectation value of the operator $\mathbf{T}_{\text{space}}^{(1)} \mathbf{O}_{\text{spin}}^{(1)}$ whose spatial and spin parts behave as a rank one tensor under spatial rotation.

We have carried out the ground state Hartree-Fock calculations for Be-like ions, employing the discrete cartesian Gaussian-type functions contracted to 21 basis orbitals. First we obtain a solution under the restriction that the ground state has the ${}^1S^e$ symmetry. By using the single-particle states generated by this calculation, stability of the ${}^1S^e$ ground state was investigated by the RPA method. Negative excitation energy to the ${}^3P^o$ excited state is observed for ions with $Z < 4.4$. We next try to find the most stable non spherical Hartree-Fock solution for Be and Li^- . An effective method to do this is the linear constraint method³⁾ explained below. First the following mean field calculation is performed in the presence of the symmetry-violating operator $\mathbf{T}_{\text{space}}^{(1)} \mathbf{O}_{\text{spin}}^{(1)}$:

$$\delta \langle \Psi(\boldsymbol{\lambda}) | H - \lambda_{\mu\nu} (\mathbf{T}_{\text{space}}^{(1)})_{\mu} (\mathbf{O}_{\text{spin}}^{(1)})_{\nu} | \Psi(\boldsymbol{\lambda}) \rangle = 0 \quad (1)$$

where $\lambda_{\mu\nu}$ is the Lagrange multiplier corresponding to a condition,

$$\langle \Psi(\boldsymbol{\lambda}) | H | \Psi(\boldsymbol{\lambda}) \rangle = q_{\mu\nu} \quad (2)$$

The value of $q_{\mu\nu}$ plays a role of the order parameter. The Hellmann-Feynman theorem gives

$$\lambda_{\mu\nu} = d \langle \Psi(\boldsymbol{\lambda}) | H | \Psi(\boldsymbol{\lambda}) \rangle / dq_{\mu\nu} \quad (3)$$

This means that the symmetry breaks down spontaneously without help of the symmetry-violating operator at extrema of the energy hypersurface spanned by the order parameters, $q_{\mu\nu}$. Such symmetry violating Hartree-Fock solutions were found for Li^- . The most stable such a state is realized when $q_{00} = 0$ and all other $q_{\mu\nu} = 0$.

Figure 1 shows the energy difference between the Hartree-Fock state of the ${}^1S^e$ symmetry and that of

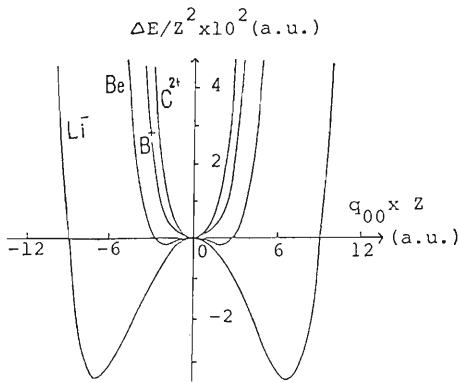


Fig. 1. The ground state Hartree-Fock energy change due to deformation as function of order parameter.

this broken symmetry as a function of the order parameter,

$$q_{00} = \langle \Psi(\lambda) | \sum_j z(j) s_z(j) | \Psi(\lambda) \rangle \quad (4)$$

where $z(j)$ and $s_z(j)$ are the z components of the position vector and the spin angular momentum vector of the j -th electron, respectively. The z axis is chosen to coincide with the quantization axis of electron spin. The 'second-order phase transition' to symmetry-violating state is seen at around Be. The $^1S^e$ solution becomes a saddle point in this case.

Electron density is plotted in Fig. 2 for Hartree-Fock state of Li^- . From this figure, the deformation seems to be like the ordinary quadrupole deformation

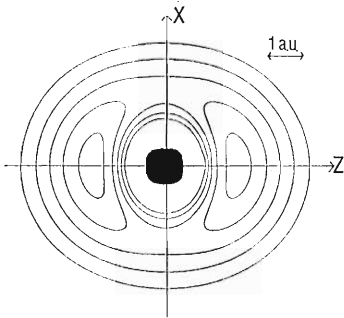


Fig. 2. Total density of two valence electrons of the most stable deformed state of Li^- .

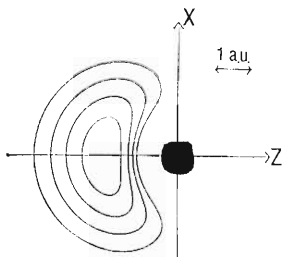


Fig. 3. One valence electron density of the most stable deformed state of Li^- . Electron distribution of the other electron is just a mirror-reflection of this with respect to x - y plane.

of nucleus.³⁾ However, this is not true, because each electron orbital experiences the 'dipole' deformation as is seen from Fig. 3. Two electrons with opposite spin angular momenta repel each other, keeping the reflection symmetry with respect to the x - y plane. Since each electron is localized separately in space, its kinetic energy increases, but the mutual coulombic repulsion energy is reduced.

This deformed state violates the rotational symmetry, except for the rotation about the z -axis. Time reversal symmetry and parity are also broken. Thus the deformed ground state includes the components of states with symmetry, different from $^1S^e$. Take, for instance, the restricted case of $n=2$. Then, the deformed ground state can be given approximately as

$$\begin{aligned} & |(2s + \epsilon 2p_0)\chi_{+1/2}, (2s - \epsilon 2p_0)\chi_{-1/2}| \\ & \sim (|2s^2\ ^1S^e\rangle - \epsilon^2/\sqrt{3} |2p^2\ ^1S^e\rangle) \\ & - \sqrt{2} \epsilon |2s2p^3\ ^P^o\rangle - \sqrt{6} / 3 \epsilon^2 |2p^2\ ^1D^e\rangle \end{aligned} \quad (5)$$

where $\chi_{\pm 1/2}$ is the spin function. Here one sees that the states of the $^3P^o$ and $^1D^e$ symmetries mix into the ground state wave function. Then the projection of the deformed ground state onto the eigenfunction of the total 'orbital' angular momentum is sufficient to restore the spin and parity symmetries.

Collective rotational motions are clearly extracted through the angular momentum projection, as is explained below.^{3,4)} An energy expectation value of the deformed state is independent of its orientation relative to the space-fixed frame. Superposing the wave functions of states deformed in all orientations \mathcal{Q} and variationally determining the corresponding weight function $f(\mathcal{Q})$, we can obtain more accurate wave function and restore the broken symmetry.⁴⁾ In the present case, the deformed state is axially symmetric and is the eigenstate with the eigen value $K=0$, where K is the projection of the angular momentum on this symmetric axis. Then $f(\mathcal{Q})$ is determined only by the symmetry requirement, and we have

$$|\Psi_{LM}\rangle = \int d\mathcal{Q} D_{M0}^{*L}(\mathcal{Q}) R(\mathcal{Q}) |\Phi\rangle \quad (6)$$

where $|\Phi\rangle$ is the wave function of the state deformed in an arbitrarily chosen orientation. L and M are the total orbital angular momentum and its z component, respectively. $R(\mathcal{Q})$ is the rotation operator acting on the spatial part of wave function. D_{M0}^L is the rotation matrix. It should be noted that this procedure is just the angular momentum projection operation. If we assume that the deformation is sufficiently large, the energy spectrum has the rotor-like series with the cut-off: $E_L \sim L(L+1)$.³⁾

Figure 4 shows the energy levels calculated by the configuration interaction (CI) method and the pro-

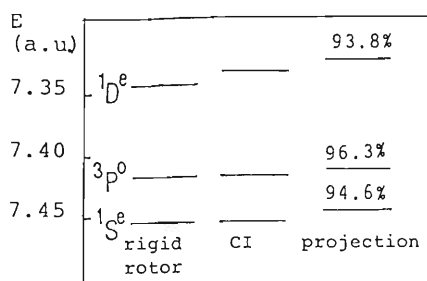


Fig. 4. Energy levels of ground and low-lying excited states of L_1^- calculated by the configuration interaction (CI) method and projection method. The numbers attached to the level of projection method indicate the overlap between the two wave functions obtained by CI and the projection method. The first and second level of rigid rotor are adjusted to the $1S^e$ and the $3P^0$ states of the CI method.

jection method. The figures attached to the projected levels in Fig. 4 represent the percentage contribution of the CI wave function to the corresponding projected one. We notice that their overlaps are fairly

large. The rigid rotor levels are also presented in Fig. 4 for comparison. It is seen from this figure that the following picture holds quite well: the strong correlation between electrons brings about the symmetry violation in the mean field and then the collective rotational motion of electrons restore the broken symmetry.

The dipole character of the deformation and repulsive nature of the interaction which leads to the breaking of singlet electron pair are reflected in the rotational series $1S^e$, $3P^0$, $1D^e$,

References

- 1) D. R. Herrick and M. E. Kellman: *Phys Rev. A*, **21**, 418 (1980).
- 2) C. D. Lin: *Phys. Rev. A*, **29**, 1019 (1984).
- 3) P. Ring and P. Schuck: *The Nuclear Many-Body Problem*, Springer-Verlag (1980).
- 4) R. E. Peierls and J. Yoccoz: *Proc. Phys. Soc. (London)*, **A70**, 381 (1957).
- 5) D. J. Thouless: *Nucl. Phys.*, **21**, 225 (1960); **22**, 78 (1961).

III-2-15. Identification of Al X 2p3d-2p4f Transition of Beam-Foil Spectra

K. Ando, S. Kohmoto, Y. Awaya, H. Kumagai, T. Tonuma, and S. Tsurubuchi

The transition array of 2p3d-2p4f has been observed only for carbon, nitrogen, and oxygen ions, but not for other ions. We have newly identified that of 2p3d-2p4f for Al X.

The identification of the Al X 2p3d-2p4f transition array was carried out as the following procedure. The average energy, Slater direct- and exchange-radial integrals, and spin-orbit interactions were estimated by the Hartree-Fock program code of MCHF77¹⁾ for the 2p3d and 2p4f configurations. The above values and configuration interactions of the 2p3d are determined as parameters from the observed energy levels by means of the least-squares fits.²⁾ Using these parameters for the 2p3d and 2p4f configurations and configuration interactions of 2p3d, we calculated a theoretical spectrum of this transition array by the program code of Cowan.²⁻⁴⁾ The parameters for the 2p4f configuration were determined by comparing the experimental spectrum with the theoretically calculated one. In this procedure, the uncertainty of the energy values of the lower levels of 2p3d 3F was found to affect the position of the calculated spectral lines, especially of the strongest line. Therefore, the energy value of the lower level 2p3d 3F_4 was adjusted so as to fit the position of the calculated line to the experimental one.

The theoretically calculated spectra fits almost completely with the experimental spectrum as shown in Fig. 1. The identification and classification of spec-

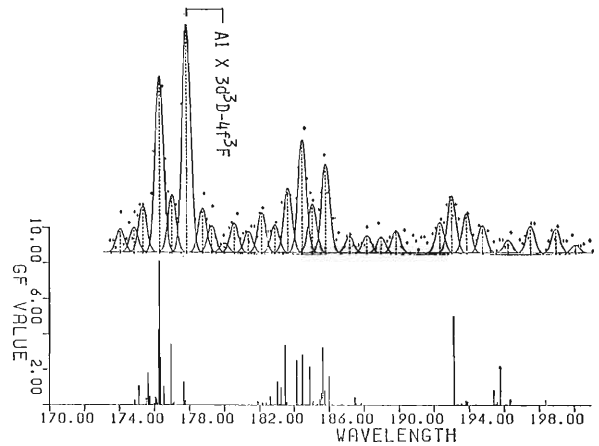


Fig. 1. Observed spectrum (upper) and theoretically calculated one (lower) of the Al X 2p3d-2p4f transition array.

tral lines are given in Table 1, in which the coupling scheme of 2p3d is the LS-coupling, and that of 2p4f is the jj-coupling because the purity of the jj-coupling is higher than the LS-coupling.

References

- 1) C. F. Fischer: *Comput. Phys. Commun.*, **14**, 145 (1978).
- 2) R. D. Cowan: *The Theory of Atomic Structure and Atomic Spectra*, Univ. of California Press, California (1981).
- 3) R. D. Cowan: *Phys. Rev.*, **163**, 54 (1967).
- 4) R. D. Cowan and D. C. Griffin: *J. Opt. Soc. Am.*, **66**, 1010 (1976).

Table 1. Identification of lines of the 2p3d-2p4f transition array in Al X. Level designation is given in the LS-coupling scheme for 2p3d and in the jj-coupling for 2p4f.

No.	Observed		Calculated		O-C (Å)	Classification	
	(Å)	I	(Å)	gf		lower	upper
1	174.86	98	175.09	1.10	-0.23	3F_3	$(3/2, 5/2)_4$
2	175.77	148	175.64	1.82	0.13	3F_3	$(3/2, 7/2)_4$
3	176.35	400	176.24	4.28	0.11	3F_2	$(1/2, 5/2)_3$
			176.30	8.13	0.05	3F_4	$(3/2, 7/2)_5$
			176.35	2.60	0	1D_2	$(3/2, 5/2)_3$
4	177.06	165	176.95	3.44	0.11	3F_3	$(1/2, 7/2)_4$
5	177.82*		177.68	1.34	0.14	1D_2	$(1/2, 7/2)_3$
6	183.02	84	183.04	1.32	-0.02	3D_2	$(3/2, 5/2)_3$
7	183.56	121	183.48	3.39	0.08	3D_3	$(3/2, 7/2)_4$
8	184.33	287	184.15	2.52	0.18	3D_1	$(1/2, 5/2)_2$
			184.47	2.87	-0.14	3D_2	$(1/2, 7/2)_3$
9	184.86	178	184.91	2.16	-0.05	3D_3	$(1/2, 7/2)_4$
10	185.67	177	185.65	3.26	0.02	3P_2	$(3/2, 7/2)_3$
11	193.08	159	193.15	5.01	-0.07	1F_3	$(3/2, 5/2)_4$
12	195.79	39	195.76	2.19	0.03	1P_1	$(3/2, 7/2)_2$

rms deviation=0.11Å

*blended with Al X 2s3d 3D -2s4f 3F 177.80Å

III-2-16. Tilted-Foil Method Using Extremely Thin Foils

S. Kohmoto, K. Ando, and M. Ishihara

The generation mechanism of atomic polarization of an ion beam passing through tilted foil is not fully clarified. We carried out tilted-foil experiments to see whether there exists any influence of the early stage of passage in a tilted-foil, *i.e.* a charge-non-equilibrium stage, on the atomic polarization state of ions which emerge from the foil. For this purpose, we used carbon foils of $0.7 \mu\text{g}/\text{cm}^2$ in thickness. The experiments were performed at the RILAC with a $^{14}\text{N}^{3+}$ beam of a 29 MeV incident energy. The tilt angle was 45° . Photons which are emitted from the beam ions excited by the tilted foil successively pass a phase plate, a polarizer, and a monochromator and are detected finally with a photomultiplier. The photon intensity is measured as a function of the

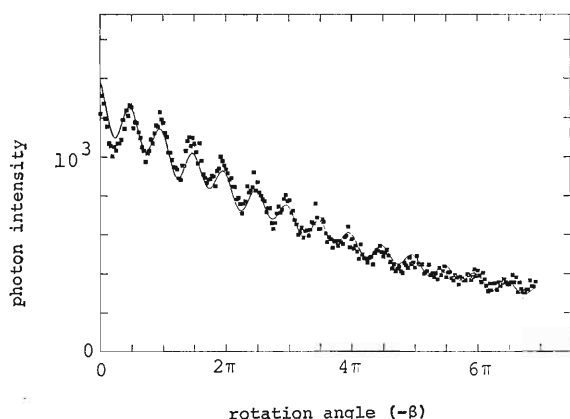


Fig. 1. Light intensities measured (dots) and calculated (continuous line) as a function of phase plate angle. The absolute values of the relative Stokes parameters extracted from the fitting are $M/I = (-16.9 \pm 12.9)\%$, $C/I = (-6.2 \pm 13.0)\%$ and $S/I = (2.2 \pm 3.2)\%$.

rotation angle (β) of the phase plate. This angle was advanced by 5° for each ion currents of $6 \mu\text{C}$ accumulated in the Faraday cup. Figure 1 shows an example of the intensity curve for NV $\lambda = 493 \text{ nm}$ line. On the whole, the intensity decreases gradually as β increases or the irradiation time of the foil increases. This is probably because the charge state of ions after passing through a carbon foil changes from the non-equilibrium one to equilibrium one due to the foil thickening under the bombardment of ions owing to the insufficient vacuum. The continuous line in Fig. 1 was calculated by assuming a functional form $I'(\beta; I, M, C, S) \exp(-a\beta)$, where function $I'(\beta; \dots)$ is usually used one¹⁾ to express the photon intensity in charge-equilibrium state with the Stokes parameters I , M , C , and S . Although the exponential term is introduced to simulate the foil thickening effect, the fitting is not good in the small β region. It should be reminded that, the incident-beam ions being N^{3+} , the charge fraction ϕ_4 of $4+$ ions is 0 at the zero foil-thickness. It seems that our starting foil-thickness ($\sim 0.7\sqrt{2} \mu\text{g}/\text{cm}^2$) is not far from the maximum of ϕ_4 . For the N IV $\lambda = 341 \text{ nm}$ line,¹⁾ where also an ion beam of N^{3+} was used, one exponential term was sufficient to simulate the foil-thickening effect and a set of relative Stokes parameters seems to be common both in charge-non-equilibrium and equilibrium stages. Further analysis is in progress.

Reference

- 1) S. Kohmoto, K. Ando, and M. Ishihara: *RIKEN Accel. Prog. Rep.*, **19**, 64 (1985).

III-2-17. Observation of Radiative Photons in the μ^- Transfer Process for Liquid D_2 with He Impurity

T. Matsuzaki, K. Ishida, Y. Hirata,* R. Kadono,** and K. Nagamine

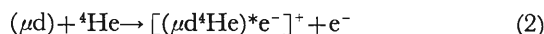
The recent experiments on the muon catalyzed fusion (MCF) in a D_2/T_2 mixture carried out at muon facilities are focussing to measure the muon sticking probability, which is defined to be a muon loss by the muon sticking to ^4He nucleus, where ^4He is a fusion product of the MCF process. Under a practical experimental condition, we should take into account the other possibility of the muon loss. The one of other serious muon loss processes is considered to be an effect of ^3He in the D/T target which is a decay product of the tritium. As is experimentally known, the muon easily transfers from muonic hydrogen atoms to helium nuclei to terminate the MCF cycle. Therefore, it is very important to investigate the μ^- transfer process from muonic hydrogen atoms to helium nuclei ($^3,^4\text{He}$). In the first stage, we studied the muon transfer mechanism from muonic hydrogens to ^4He . We will then extend our experiment to ^3He in order to compare both results.

From the theoretical point of view, a Leningrad theoretical group has proposed a picture of the μ^- transfer mechanism *via* the formation of the intermediate mesomolecule.¹⁾ They calculated energy levels and the formation rate of mesomolecules which is the order of $10^8/\text{s}$. On the other hand, according to the earlier theoretical calculation, the rate of the direct charge exchange process (1) is of the order of $10^6/\text{s}$.²⁾

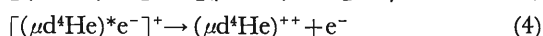
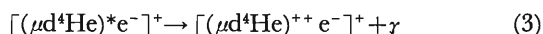


But the recent experimental transfer rates support the prediction assuming the molecular charge exchange process.

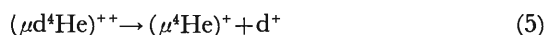
In the present system, we can consider the molecular charge exchange reaction as follows.



where the excited state of mesomolecule is formed as an intermediate state, accompanying a conversion electron emission. The excited state can decay to the ground state of the mesomolecule through radiative transition or Auger electron emission from the molecular ion.



where the contribution of the Auger process to the deexcitation was calculated to be less than 15%. Since there exists no bound ground-state of the mesomolecule, it will dissociate into a muonic helium atom and a deuteron.



The whole molecular charge exchange process does imitate the direct charge exchange process (1). The schematic picture of the energy levels for the proposed model is shown in Fig. 1. There appears the excited

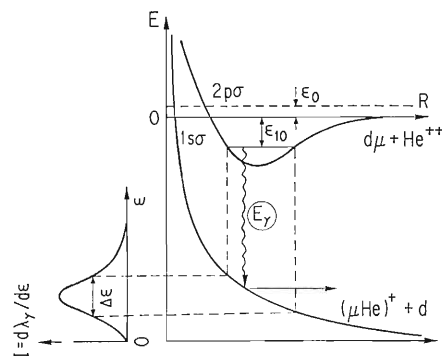


Fig. 1. Schematic picture for the radiative decay photons in the proposed μ^- transfer mechanism.¹⁾

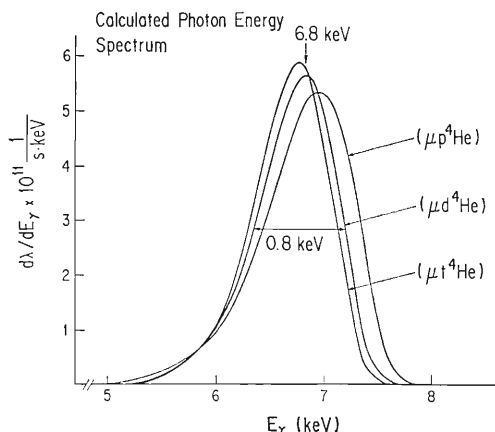


Fig. 2. Photon energy spectra accompanying the μ^- transfer processed from muonic hydrogen isotope atoms to ^4He nuclei.²⁾

* Nuclear Engineering Research Laboratory, University of Tokyo.

** Meson Science Laboratory, University of Tokyo.

bound state for the ($\mu^-d^4\text{He}$) mesomolecule. This excited bound state is very interesting from the viewpoint of the three body system bound by the Coulomb force. The radiative transition occurs from the excited state to the unbound ground-state. Kravtsov *et al.*³⁾ also calculated the photon energy spectra accompanying the muon transfer process from the muonic hydrogen atom to ^4He nucleus; their results are shown in Fig. 2. For the ($\mu d^4\text{He}$) system, the central energy and the width of expected photons were calculated to be 6.8 keV and 0.8 keV, respectively. The predicted photon line-shape is not a Gaussian but asymmetric with a low energy tail.

In order to observe an evidence of the predicted transfer mechanism and obtain an accurate transfer rate, we measured an energy and a time distribution of the emitted photons from a liquid deuterium target containing a small amount of ^4He impurity after injection of μ^- beams. So far, no one has ever measured the photon spectrum accompanying the deexcitation of mesomolecule. The delayed photon observation will be direct evidence for the mesomolecular formation.

The present experiment was performed at the superconducting muon channel of the pulsed muon facility of the Meson Science Laboratory, the University of Tokyo, located at KEK.⁴⁾ This facility produces a sharply pulsed muon beam (50 ns width and 50 ms interval) and enable us to carry out a low background measurement of the delayed phenomena associated with muon pulses. The 60 MeV/c backward negative muon beam was injected into the liquid deuterium target (20 K) with a ^4He concentration of 430 ppm. The liquid deuterium target was placed in the gap of Superconducting Helmholtz Coil setup (SHC). We used a Si(Li) detector to observe a low-energy photon; a Si(Li) detector was also placed in the gap of SHC. The photon energy signal and the timing signal relative to the muon beam arrival were recorded onto magnetic tapes event by event. The whole experimental setup is similar to that utilized in the MCF experiment⁵⁾ and is described elsewhere.⁶⁾

The delayed events in a time range between 0.28 and 7.5 μs were analyzed. In the delayed photon energy spectrum, we clearly observed a broad photon peak around 6.85 keV. In order to examine a detailed structure of the photon peak, backgrounds due to a pure deuterium target was subtracted; the results are shown in Fig. 3. The observed line-shape is not a Gaussian but asymmetric with a low energy tail. The experimental photon energy and the line shape itself show fairly good agreement with the predicted spectrum as shown in Fig. 2. The time distribution of the 6.86 keV photon was also analyzed and is shown in Fig. 4. The decay rate was deduced to

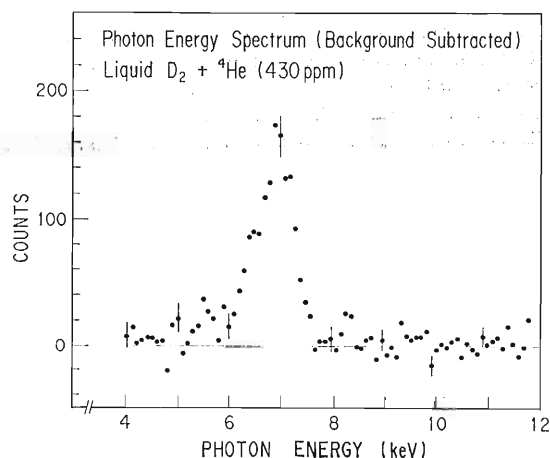


Fig. 3. Observed delayed photon energy spectrum. The delayed photon background was subtracted. The base line is shown by a fine solid line.

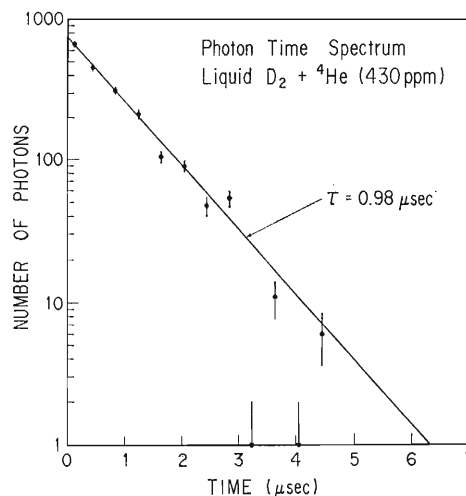


Fig. 4. Time spectrum of the delayed 6.85 keV photon peak. The contribution of delayed photon background was subtracted.

be $0.98 \pm 0.05 \mu\text{s}$ and the μ^- transfer rate at 20 K from (μ^-d) to ^4He was determined to be $13.1 \pm 1.2 \times 10^8/\text{s}$, where the contribution of Auger process is not taken into account.

Recently, the transfer rates have been calculated for the muonic hydrogen atoms with helium nuclei by means of various theoretical methods.⁷⁾ The rates were calculated as a function of the energy of relative motion which depends on the temperature of the system. We compare the obtained experimental rate with these theoretical predictions and found they are in good agreement. The detailed comparison was described in Ref. 6.

References

- 1) Yu. A. Aristov, *et al.*: *Yad. Fiz.*, **33**, 1066 (1981).
- 2) S. S. Gershtein: *Zh. Eksp. Teor. Fiz.*, **43**, 706 (1962) [Sov.

- Phys. JETP*, **16**, 501 (1963)].
- 3) A. V. Kravtsov, *et al.*: *Phys. Lett. A*, **83**, 379 (1984).
 - 4) K. Nagamine: *Hyperfine Interact.*, **8**, 787 (1981); UT-MSL Newsletter No. 1-6 (1981-1986) (eds. K. Nagamine and T. Yamazaki) (unpublished).
 - 5) K. Nagamine, *et al.*: *Muon Catalyzed Fusion*, **1**, 137 (1987).
 - 6) T. Matsuzaki, *et al.*: *Muon Catalyzed Fusion*, **2**, 217 (1988).
 - 7) A. V. Kravtsov, A. I. Mikhailov, and N. P. Popov: *J. Phys. B: At. Mol. Phys.*, **19**, 2579 (1986).

III-2-18. REC X-Rays from Collision System of 20.5 MeV/u Ar Ions on Be

Y. Awaya, A. Hitachi, Y. Kanai, K. Kawatsura,
K. Kuroki, H. Vogt, and Y. Yamazaki

When an energetic highly charged heavy ion directly captures a bound electron of a target atom to its inner shell orbit and the excess energy is emitted as a photon, this process is called radiative electron capture (REC).¹⁾ The photon thus emitted is called as REC X-rays. When one wants to describe the process more precisely, expressions of K REC, L REC and so forth are used according to the inner shell of the projectile by which the electron is captured.

We have measured the REC X-rays emitted from the 20.5 MeV/u Ar ions colliding with Be target atoms at newly constructed RIKEN Ring Cyclotron (RRC) in the course of testing the experimental conditions, such as the background caused by nuclear reactions in this energy range and the setup at this accelerator. The final purpose is to obtain the angular dependence of the L REC because the relativistic effects appear more clearly than the K REC.^{2,3)} We report here the preliminary results of this work.

Ar¹²⁺ ions accelerated by RRC were led to a target chamber,²⁾ which was installed on a so-called E1-b test experiment beam line to which beams come straight from RRC. The energies of Ar ions were estimated from the acceleration conditions and also from the amount of the Doppler shift of REC K X-rays as a function of the detection angle with respect to the beam direction. The values of energy estimated by both methods agreed well with each other within the limits of error.

Since the thickness of a Be target foil was 25 μm (4.6 mg/cm²), the charge of about 90% of Ar ions turns to 18+ after passing through about 1 mg/cm² of the target. The target foil was placed at the center of the target chamber. The ports for the measurement of X rays were covered with 50 μm Be foils. Two Si(Li) detectors were used; one for the measurement of angular dependence of X rays and the other as a monitor set at 90° with respect to the beam direction. The measurements of X rays were made at 45°, 90°, 135°, and 155° with respect to the beam direction. The size of the beam spot on the target was about 3 mm \times 3 mm. The diameter of the Si(Li) was 6 mm and the distance between the target and the detector was about 20 cm.

X-ray spectra are shown in Fig. 1. Main con-

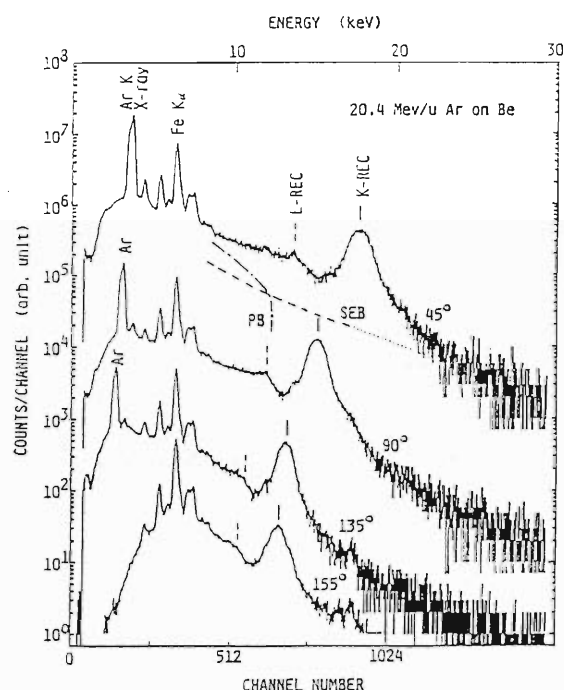


Fig. 1. Angular dependence of X rays emitted on collision of 20.5 MeV/u Ar ions on a Be target. The detection angles with respect to the beam direction are shown. A 25 μm aluminum absorber was used for the measurement at 155°.

tributions to the spectrum are attributed to K REC, L REC, secondary electron bremsstrahlung (SEB), and primary bremsstrahlung (PB). Peaks corresponding to the characteristic X rays of Ar ions, to those of some elements contaminating the Be foil, and to those of material of target holder induced by the stray beams are also observed in the spectra. The energy of X rays from the projectile is changed according to the Doppler shift as is seen in Fig. 1. The SEB and PB contributions evaluated by the Born approximation are shown in Fig. 1 for the spectrum taken at 45°.⁴⁾

The component of SEB is subtracted from the spectra by assuming that the pattern of SEB is an exponential function and by normalizing to the experimental data at energies higher than the K REC peak. It was found that the K REC peak consists of two components: one comes from the capture of

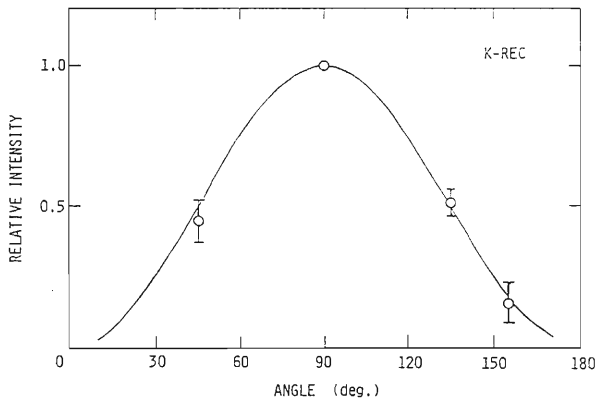


Fig. 2. Angular dependence of K REC X-ray yields as a function of the detection angle with respect to the beam. The solid curve shows the pattern of $\sin^2\theta_L$, and is normalized to the experimental data at $\theta_L=90^\circ$, where θ_L is the photon emission angle in the laboratory frame.

a 2 s Be electron and the other from that of a 1 s Be electron. This will be discussed precisely in the succeeding report.⁵⁾ The angular dependence of K REC X-ray yield is shown in Fig. 2. The experimental results fit to the curve of $\sin^2\theta_L$ predicted by the theory; θ_L is the photon emission angle in the laboratory frame.

The shape of the L REC peak is evaluated by using the Gaussian curve with the same width as

the K REC peak. In this case, the K REC peak was fit to a single Gaussian curve, because that L REC peak is difficult to resolve into two components corresponding to the captures of 2 s and 1 s electrons of the Be target. The result obtained in the present preliminary experiments agrees with theoretical prediction^{2,3)} within experimental uncertainties, though insufficient for further discussion. We plan an experiment with the larger value of Bohr's criterion, $\nu_p = Z_p\alpha/n\beta$, where the contribution of REC by the 2 p shell relative to the 2 s shell becomes larger than the present experimental condition, where, Z_p is the electric charge of the projectile, α is the fine-structure constant, n is the principal quantum number of the projectile atomic orbit by which an electron is captured, and β is the velocity of a projectile in units of the light velocity.

References

- 1) K. W. Schnopper, H. D. Betz, J. P. Delvaille, K. Kalata, A. R. Sohval, K. W. Jones, and H. E. Wegner: *Phys. Rev. Lett.*, **29**, 898 (1972).
- 2) Y. Awaya, K. Hino, A. Hitachi, Y. Kanai, K. Kawatsura, K. Kuroki, H. Vogt, Y. Yamazaki, and T. Watanabe: *Lecture Note on High-Energy Ion-Atom Collision Process*, Springer-Verlag, p.185 (1988).
- 3) K. Hino and T. Watanabe: p.37 in this report.
- 4) K. Ishii: private communication, 1987.
- 5) Y. Awaya, K. Hino, Y. Kanai, A. Hitachi, H. Vogt, K. Kuroki, and Y. Yamazaki: p.69 in this report.

III-2-19. Momentum Distribution of Be 2s Electron Measured by a Radiative Electron Capture Process

Y. Awaya, K. Hino, Y. Kanai, A. Hitachi,
H. Vogt, K. Kuroki, and Y. Yamazaki

The radiative electron capture (REC) is the process in which a highly ionized projectile ion directly captures an orbital electron of a target atom and the excess energy is emitted as a photon. The photon is called the REC X-ray and has energy of $(1/2)mv_p^2 + U_n - u_n$, where m is the electron mass, v_p the velocity of a projectile, U_n the binding energy of the n orbital of projectile ions that capture an electron and u_n is the binding energy of the n orbital electron to be captured in the target atoms. The width of the REC X-ray peak is roughly proportional to $mv_p v_n$, where $u_n = (1/2)mv_n^2$.

Since Schnopper *et al.* observed REC X-rays,¹⁾ it has been urged that one can determine the momentum distribution of a captured electron in a target atom from the peak width of the REC X-rays; however, only a few experimental studies have been reported. Kambara *et al.*²⁾ compared the width of the K REC X-rays emitted on collision of Ne ions and various gas targets with that calculated by assuming the hydrogenic wave functions for outermost electrons of the gas targets. In this calculation, the effect of the inner-shell electrons of the target atoms were neglected for the elements with $Z > 2$. They found relatively good agreement for the target of $Z = 1$ to 10, but some ambiguity was left concerning the absolute value.

The contribution of capturing core-electrons of the target atoms has been discussed by Betz *et al.*³⁾ and Spindler *et al.*⁴⁾ for the target elements heavier than carbon. They have pointed out that the width of the momentum distribution of an outermost shell electron obtained from the K REC X-ray peak is larger than that obtained by the Compton scattering method.

We will report for the first time that the momentum distribution of the outermost shell electron obtained from the REC X-rays agrees well with that obtained by the Compton scattering method. We have measured the REC X-rays from the 20.5 MeV/u Ar ions colliding with target Be atoms. The details of the experiments and the X-rays spectra are given separately in this volume.⁵⁾ Since a Be atom has only 2s and 1s electrons, we could separate the contribution of the outermost shell electrons (2s) and the

core-shell electrons (1s).

The component of secondary electron bremsstrahlung (SEB) is subtracted from the spectra by assuming that the pattern of SEB is an exponential function and by normalizing to the experimental data in the energy region of spectra higher than the K REC peak. It is considered that the K REC peak consists of two main components: one owing to the capture of a 2s electron of Be and the other the capture of a 1s electron of Be.

The full width half maximum (FWHM), Δ , of the REC X-rays estimated by the relativistic Born approximation is given by⁶⁾

$$\Delta = 2(2^{1/3} - 1)^{1/2} \lambda v (1 - v \cos \theta_L)^{-1} \quad (1)$$

in natural units ($\hbar = c = 1$), where $\lambda = mZ_T\alpha$, m is the electron mass, Z_T is the screened nuclear charge which is felt by an orbital electron captured by the projectile, α is the fine structure constant, v is the velocity of projectile, and θ_L is the angle in the laboratory system where the REC X-rays are measured. The shape of the K REC X-rays emitted by

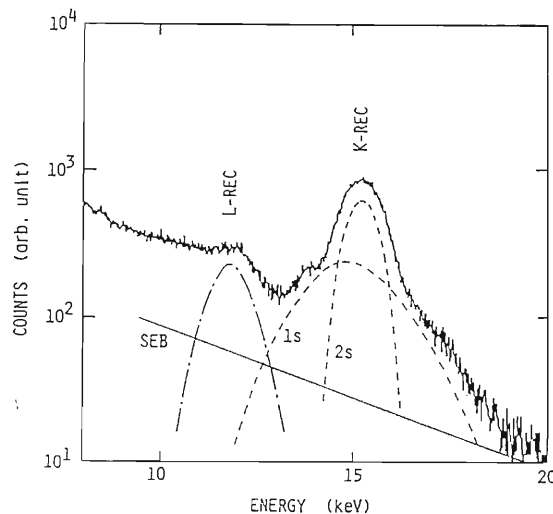


Fig. 1. Contributions of SEB (solid line), K REC (broken line), and L REC (dot-dashed line) to the experimentally obtained spectrum. 1s and 2s denote the contribution from Ar^{18+} ion capturing 1s and 2s electrons of the Be target. The spectrum was obtained at 90° with respect to the beam.

capturing a 1s electron of Be is assumed to be Gaussian with Δ , where Z_T is taken as 3.7 according to Slater. The Gaussian curve thus obtained was subtracted from the spectrum by fitting the low and the high energy region of the K REC peak. The remainder is considered to be the component due to the capture of the Be 2s electron. Small contribution of Ar^{17+} ions is neglected in this analysis. The resolved spectrum obtained at 90° with respect to the beam is shown in Fig. 1. Δ of the K (2s) REC at 90° was estimated to be 1.14 keV.

On the other hand, the momentum distribution of orbital electrons was studied precisely by the Compton scattering of photons. To check whether the momentum distribution obtained for Be 2s electron in this work agrees with the values obtained by the Compton scattering, we compared our result with that obtained by Carrant *et al.*⁷⁾ They measured the Compton profile of Be by Compton scattering of Mo $K\alpha$ X-rays. By subtracting the contribution of the 1s electron, the value of 315 eV is obtained for the FWHM of the Compton profile, D , for the 2s electron at Compton shift of 850 eV.

In order to compare these two values, we should consider the definition of the FWHM of a peak in

each case. In REC Δ is nearly equal to $A\lambda V/c$, whereas in Compton scattering D is nearly equal to $A\lambda(2\omega^{(0)}/m)^{1/2}$, where A is a constant, $V=vc$, $\omega^{(0)}$ is the Compton shift, and m is the electron mass in keV. Then the $A\lambda$ values of 5.4 and 5.5 were obtained for the REC peak and the Compton scattering, respectively; that is, the width of the REC X-ray peak gives truly the momentum distribution of outermost shell electrons.

References

- 1) H. W. Schnopper, H.-D. Betz, J. P. Delvaille, K. Kalata, A. R. Sohval, K. W. Jones, and H. E. Wegner: *Phys. Rev. Lett.*, **29**, 898 (1972).
- 2) T. Kambara, Y. Awaya, A. Hitachi, M. Kase, I. Kohno, and T. Tonuma: *J. Phys. B: At. Mol. Phys.*, **15**, 3759 (1982).
- 3) H.-D. Betz, M. Kleber, E. Spindler, F. Bell, H. Panke, and W. Stehling: Proc. Xth Int. Conf. Physics of Electronic and Atomic Collisions, p.520 (1977).
- 4) E. Spindler, H.-D. Betz, and F. Bell: *J. Phys. B: At. Mol. Phys.*, **10**, L561 (1977).
- 5) Y. Awaya, A. Hitachi, Y. Kanai, K. Kawatsura, K. Kuroki, H. Vogt, and Y. Yamazaki: p.67 in this report.
- 6) This equation is obtained by one of authors, K. Hino.
- 7) R. Carrant, P. D. DeCicco, and R. Kaplow: *Phys. Rev. B*, **3**, 243 (1971).

III-2-20. Resonant Transfer and Excitation (RTE) in Ge^{29+} on H_2 Collisions

S. Reusch,* Y. Awaya, T. Kambara, D. J. McLaughlin,**
P. H. Mokler,* A. Müller,*** R. Schuch, and M. Schulz****

In ion-atom collisions, it is possible that an excitation of an electron in the projectile ion and a transfer of an electron from the target atom to the projectile occur simultaneously in one process induced by an electron-electron interaction. This process which is called as resonant transfer and excitation (RTE) can be active if the total energy gained by the target electron during the capture to the projectile coincides with the excitation energy of the bound electron in the projectile. As a consequence of the RTE, the projectile ion is in a doubly-excited state with the charge state smaller by one than the initial state. This state can decay *via* photon emission or auto-ionization.

Figure 1 shows the RTE mechanism in the case of Li-like germanium ion (Ge^{29+}) incident on a hydrogen target at energy of 13 MeV/amu. The resonance condition shown here is marked as a KLL process which corresponds to K-to-L excitation and target-to-L capture. If the target electron is free and monoenergetic, this process is called dielectronic recombination (DR) which is described as the inverse process of Auger-electron emission. The width of the resonances in DR is expected to be ≤ 1 eV. However, the target electron to be captured is not

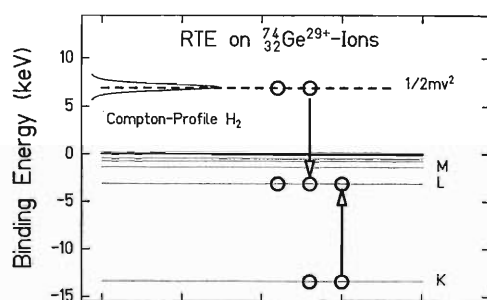


Fig. 1. Schematic description of the KLL-RTE process in the case of 13 MeV/amu Ge^{29+} and H_2 collision.

* GSI, D6100 Darmstadt, F. R. Germany.

** Physics Department, University of Hartford, Hartford CT06117, USA.

*** Strahlencentrum, Universität Gießen, D6300 Gießen, F. R. Germany.

**** Physikalisches Institut, Universität Heidelberg, D6900 Heidelberg, F. R. Germany.

free but bound in a hydrogen atom and in motion, the velocity distribution of the target electron (Compton profile) makes the width of the observed resonance broader. In the example shown here, the observed width of RTE is in the order of keV by the effect of the Compton profile, which is also indicated in Fig. 1.

We have investigated the $\text{KL}n$ ($n \geq 2$) resonances of the RTE process in collisions between Ge^{29+} ions and a H_2 target. We worked with a beam of Ge^{29+} ions from the UNILAC facility at GSI in Darmstadt in the energy range between 12 and 18.5 MeV/amu. In order to get a reasonable narrow Compton profile for the target electrons to be captured, we should use a target with a small electron momentum distribution, in other word, a small electron binding energy. In the experiment, we used a differentially-pumped gas target of H_2 . We measured characteristic K X rays of Ge-ions from the target region in coincidence with charge-analyzed Ge^{28+} projectiles after a magnet downstream of the target. The primary beam was monitored by a Faraday cup for normalization. A single-collision condition in the target was checked by varying the target gas pressure.

The cross sections for RTE which are obtained from the experiment are shown in Fig. 2. The data show three clearly separated structures. The peak at

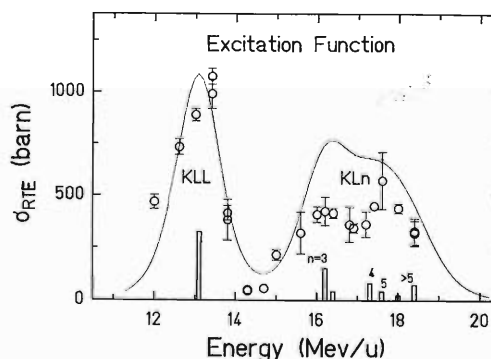


Fig. 2. RTE cross sections. Dots show experimental data. The error bars are of statistical origins only. Vertical bars at the bottom show the position and relative cross section of DR resonances. Solid curve shows the DR cross sections folded with the Compton profile of H_2 . The experimental data are normalized to the maximum of the curve.

13 MeV/amu is due to the KLL processes, where the target electron is captured to the L-shell of the projectile, predominantly resulting to the $1s2s2p^2$ state. This doubly-excited state can stabilize *via* an emission of a $K\alpha$ X-ray photon. The second maximum at around 16.2 MeV/amu corresponds to KLM processes with final states of Ge^{28+} which have one electron in the M shell. The third one at around 17.5 MeV/amu corresponds to $\text{KL}n$ ($n > 3$) processes. This is the first measurement of RTE where a separation between KLM and higher resonances was observable.

The data points are compared with *ab-initio* calculated DR cross sections which are indicated as

vertical bars at the bottom of Fig. 2. The positions of the resonances are deduced using the multi-configuration code of Grant *et al.*¹⁾ Folding the contributions of different DR resonances with the Compton profile of H_2 , one yields the solid curve of Fig. 2. The data points are adjusted in absolute height to this curve in the maximum of the KLL resonance. The general agreement between the theory and the experiment is quite fair.

Reference

- 1) I. P. Grant, B. J. McKenzie, P. H. Norrington, D. F. Mayers, and N. C. Pyper: *Comput. Phys. Commun.*, **21**, 207 (1980).

III-2-21. Charge Equilibration Process of 50 MeV Ar Ions in C Foils

T. Mizogawa, Y. Awaya, T. Kambara, Y. Kanai,
M. Kase, H. Kumagai, and K. Shima

It is well known that an effective projectile K X-ray emission cross section, *i.e.* the K X-ray yield per ion divided by the target thickness, depends on the target thickness in collisions between heavy ions and solid targets.¹⁾ This occurs when the mean interval of relevant collisions and the lifetime of K-hole bearing states are of the same order of magnitude. On the other hand, when the target thickness becomes thin enough, another thickness dependence of the K X-ray cross section appears owing to the variation of the L-shell configuration, affecting the K-hole formation cross section. In both cases the experiment on target-thickness dependence of K X-ray yield is useful to obtain the information about the collision processes concerning projectile inner shells in solid. In the latter case, however, the analysis based solely on the data of X-ray measurements may be unsuccessful because of the complication owing to the large number of concerning states of projectiles.

We have performed the experiments on the target-thickness dependence of 50 MeV Ar ion charge-state distribution (CSD) after passing the ions through thin carbon foils. With the aid of these data, an analysis of our previous results on K X-ray measurements in the L-shell nonequilibrium region for the same collision system²⁾ can be made. In this paper the description is restricted to this analysis, and the present data of CSD measurements will be fully discussed elsewhere.

In the K X-ray measurements²⁾ we found that the projectile K-hole formation cross section depends on the number of the L-holes in the initial state of a projectile. The effective K-hole formation cross section can be approximated as

$$\bar{\sigma}_V = \sigma_I + \sigma_E \bar{n}_L \quad (1)$$

where σ_I is the ionization cross section and σ_E is the K-L excitation cross section per one L-hole, and

$$\bar{n}_L = \frac{1}{d} \int_0^d n_L dx \quad (2)$$

where n_L is the average number of L-holes at the depth x . If the value \bar{n}_L is known from the CSD data, the ratio σ_E/σ_I can be deduced from the experimental data of $\bar{\sigma}_V$.

Carbon foil target (2–20 $\mu\text{g}/\text{cm}^2$) were bombarded

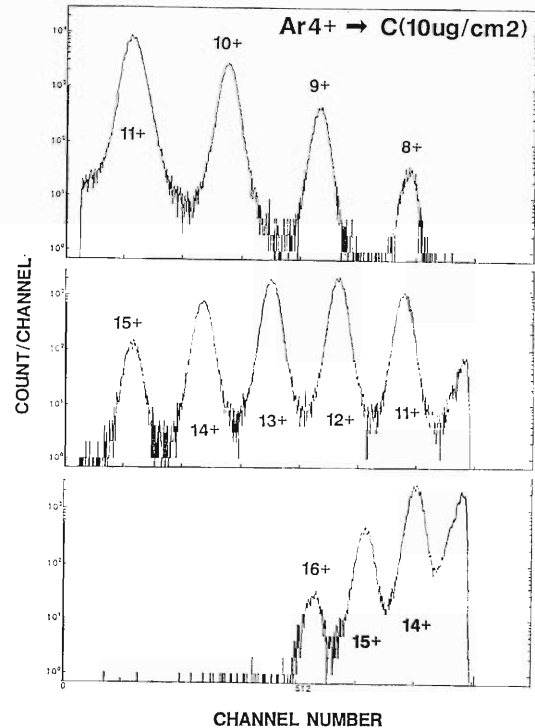


Fig. 1. Typical charge spectrum of Ar ions after passing through C foils.

with 50 MeV $\text{Ar}^{4+,12+}$ from the RIKEN linear accelerator (RILAC). The CSD was measured with a magnetic charge analyzer and a position-sensitive parallel-plate avalanche counter. The target thicknesses were measured after the CSD measurements by a recoil-detection method described in Ref. 2. The beam intensity during each CSD measurement was low enough and caused no deterioration of the target. A typical charge spectrum is shown in Fig. 1. The charge-state fractions determined from such spectra are shown as a function of target thickness in Figs. 2(a) and (b).

The target-thickness dependence of CSD for gaseous targets can be analyzed by a parameter-fitting technique using coupled rate equations containing a suitable number of adjustable charge-changing cross sections.³⁾ For solid targets, however, such an approach is hardly applicable, mainly because of the difficulty in preparing the target thin enough to

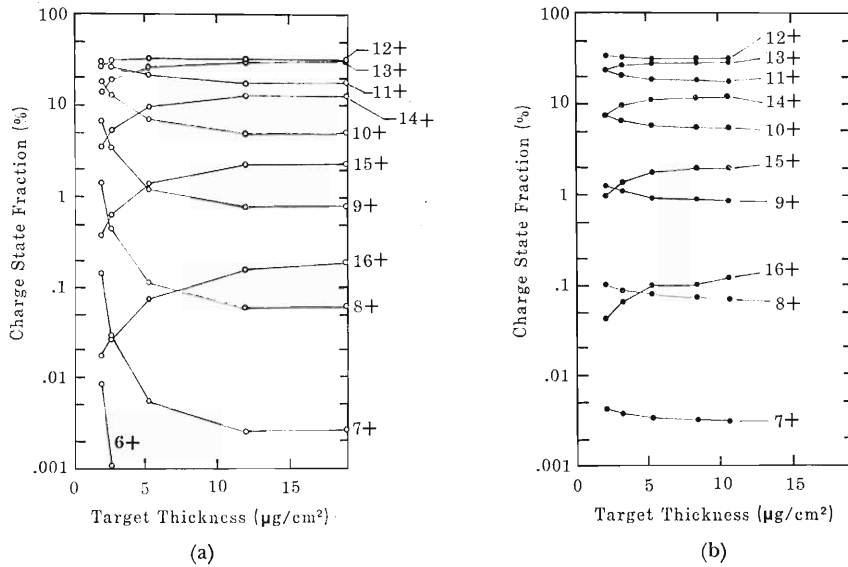


Fig. 2. Target thickness dependence of Ar-ion charge-state fractions after passing through C foils. (a), Ar⁴⁺ impact; (b), Ar¹²⁺ impact.

extract the meaningful information. A more simplified model is desirable for solids. In this paper we assume firstly that the distribution of ions over the number of M-holes immediately reaches an equilibrium after passing the entrance surface of the target regardless of L- and K-shell configurations. Secondly, we assume that the fraction of K-hole bearing ions is negligibly small. Then our problem reduces to the development of L-holes in solid. The problem can be described by 9-component rate equations,

$$\frac{d}{dx} Y_i = \sum_j \sigma_{ij} Y_j - (\sum_j \sigma_{ji}) Y_i \quad (3)$$

where Y_i denote the fractions of ions having i L-holes ($0 \leq i \leq 8$) at the depth x , and σ_{ij} are the cross sections for changing the L-hole number from j to i . The value σ_{ij} can be approximated as

$$\sigma_{ij} = \int P_{ij}(b) (2\pi b) db \quad (4)$$

where $P_{ij}(b)$ is the impact-parameter dependent probability for changing the L-hole number from j to i . Here we adopt further approximations that

(a) each orbital in the L-shell occupied by an electron has a constant probability p_1 to lose the electron regardless of the other orbitals and

(b) each unoccupied orbital in the L-shell has also a constant probability p_c to capture a target electron regardless of the other orbitals.

Assumption (b) may not be unrealistic if the average number of captured electrons in a single collision is small enough compared with the Z number of the target atom. Then

$$P_{ij} = \sum_k \binom{8-j}{k} p_1^k (1-p_1)^{8-j-k} \binom{j}{i-k} p_c^{j-i+k} (1-p_c)^{i-k} \quad (5)$$

The average increase in L-holes after the collision for the initial state j is

$$\sum_i (i-j) P_{ij} = (8-j)p_1 - j p_c \quad (6)$$

After integrating over the impact parameter,

$$\sum_i (i-j) \sigma_{ij} = (8-j)\sigma_1 - j\sigma_c \quad (7)$$

where

$$\sigma_1 = \int p_1(b) (2\pi b) db, \quad \sigma_c = \int p_c(b) (2\pi b) db \quad (8)$$

Using Eq. 7 we obtain a differential equation for the average L-hole number n_L as a function of the depth,

$$\frac{d}{dx} n_L = \sigma_1 (8 - n_L) - \sigma_c n_L \quad (9)$$

where

$$n_L = \sum_j j Y_j \quad (10)$$

The parameters σ_1 and σ_c can be deduced by a least-square fitting of the solution of Eq. 9 to the experimental average L-hole number. To analyze the full CSD data, however, we need the knowledge of the impact-parameter dependence of p_1 and p_c , but it is out of the range of this report.

In Fig. 3 the thickness dependence of the average charge q computed from the CSD data is shown. According to the Eq. 9, the data can be fitted by the form

$$q = n_L^{(eq)} + n_M^{(eq)} + (n_L(0) - n_L^{(eq)}) \exp(-\lambda x) \quad (11)$$

where $n_L^{(eq)}$ and $n_M^{(eq)}$ are the equilibrium numbers of the L- and M-holes, and

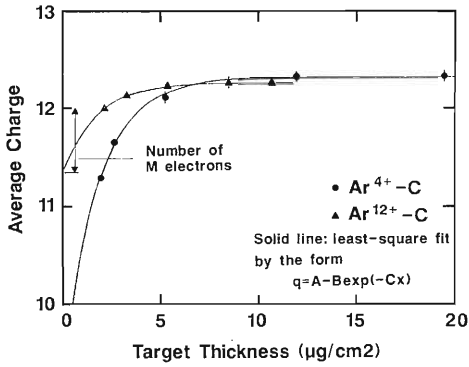


Fig. 3. Average charge as a function of the target thickness.

$$\lambda = 1/(\sigma_I + \sigma_E) \quad (12)$$

To evaluate the values in Eq. 2, we tentatively adopt the $n_M^{(eq)}$ obtained by the fitting to Ar^{12+} data, because the value evaluated from Ar^{4+} data is too sensitive to the experimental errors. Then average L-hole number n_L is

$$n_L = q - n_M^{(eq)} \quad (13)$$

The equilibrium M-hole number is

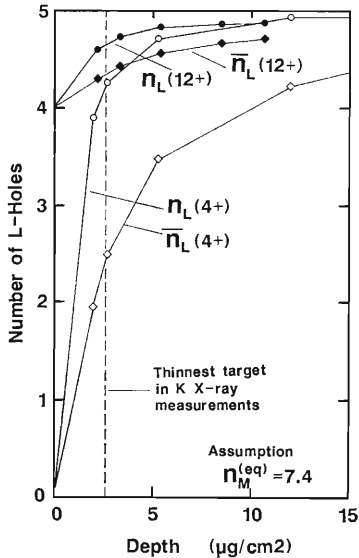


Fig. 4. Average L-hole number. See Text.

$$n_M^{(eq)} = 7.4 \quad (14)$$

In Fig. 4 n_L is plotted. Interpolating the n_L data and the given zero-thickness value by straight lines, integration was performed. Resulted \bar{n}_L is also plotted in Fig. 4. With the aid of these \bar{n}_L and Eq. 1, σ_E/σ_I can be evaluated.

$$\bar{\sigma}_V[12+] = \sigma_I + \sigma_E \bar{n}_L[12+] \quad (15)$$

$$\bar{\sigma}_V[4+] = \sigma_I + \sigma_E \bar{n}_L[4+] \quad (15)$$

Then

$$\sigma_E/\sigma_I = \frac{\bar{\sigma}_V[12+] - \bar{\sigma}_V[4+]}{\bar{n}_L[12+] \bar{\sigma}_V[4+] - \bar{n}_L[4+] \bar{\sigma}_V[12+]} \quad (16)$$

From the data for the thinnest target of the K X-ray measurements,

$$\sigma_E/\sigma_I = 0.23 \text{ per one L-hole}$$

The most serious error source in above evaluation would be the equilibrium number of M-holes. However ± 0.5 error in $n_M^{(eq)}$ causes only 10% error in above ratio. Another error source is σ_V itself, which we deduced from K X-ray emission cross sections by neglecting the electron capture to K-hole.²⁾ For thin target this effect is small and tends to cancel in the ratio $\bar{\sigma}_V[12+]/\bar{\sigma}_V[4+]$. In conclusion, the contribution of K-L excitation to the total K-hole formation cross section is approximately given by

$$\frac{0.23 \times (\text{L-hole number})}{1 + 0.23 \times (\text{L-hole number})}$$

This means that about 50% of the K-hole formation cross section for the charge-equilibrated Ar beam (of which average L-hole number is at least 4.3) is due to the K-L excitation.

References

- 1) See for example, H. D. Betz, F. Bell, H. Panke, G. Kalkoffen, M. Welz, and D. Evers: *Phys. Rev. Lett.*, **33**, 807 (1974).
- 2) T. Mizogawa, Y. Awaya, T. Kambara, Y. Kanai, M. Kase, H. Kumagai, P. H. Mokler, and K. Shima: *Nucl. Instrum. Methods Phys. Res. A*, **262**, 141 (1987).
- 3) S. Datz, H. O. Lutz, L. B. Bridwell, C. D. Moak, H. D. Betz, and L. D. Ellsworth: *Phys. Rev. A*, **2**, 430 (1970).

II-2-22. Broadening of Ar Projectile $K\alpha$ X-Ray Satellite Lines in Cu and Ni Target Foils

H. Vogt, Y. Awaya, Y. Kanai, M. Kase, and T. Mizogawa

We have investigated the widths of $K\alpha$ satellite X-ray lines of 33 MeV Argon projectiles induced in Cu and Ni foils of various thicknesses. Previous measurements,^{1,2)} where thick target foils have been used, have shown a strong dependence of the projectile satellite line widths on the atomic number Z of the target foil material. For target materials like *e.g.* Cu, Ni, and Fe the satellite line widths are severely broader than in cases where C or Al targets have been used. In Ref. 2 it was shown that this broadening of the satellites lines may be correlated to the electron density Zn_a of the target material, where n_a is the atomic density. The line width can not be explained fully by Doppler broadening due to multiple scattering of the projectiles and due to the spectrometer resolution. In targets of higher electron density the rate of interactions of the projectile with the target electrons is higher and may lead to a lifetime shortening effect of the excited projectile similar to pressure broadening in optical spectra. Here different types of interaction are however possible. The highly ionized Ar projectile (mean charge state here $\approx 11+$) can capture or lose K, L, and M shell electrons or may scatter elastically. The influence of these processes on the satellite line widths is not well understood.

The aim of these measurements is to determine if the line broadening is still present in very thin targets, where the projectile X-rays are emitted mainly outside the target. For typical K-hole lifetimes of about

10^{-14} s a target thickness of much less than $0.1 \mu\text{m}$ is required to obtain X-rays from projectiles decaying outside the target. Measurements using gas targets of the same atomic number would be very interesting, however, in this case technical problems to get a gas target of sufficient intensity and small target length arise. We carried out measurements of the Ar $K\alpha$ X-ray spectra using target foils of Cu and Ni with thicknesses ranging from $0.03 \mu\text{m}$ up to $1 \mu\text{m}$ (27 – $890 \mu\text{g}/\text{cm}^2$). The Ar $K\alpha$ X-rays were measured using a broad range crystal spectrometer (Ge crystal, $2\theta = 74 \text{ deg}$)³⁾ at an observation angle of 90 deg . The experimental setup is shown in Fig. 1.

In order to have a definite mean charge-state even inside the thinnest targets, an Ar^{4+} beam of the RIKEN linear accelerator was passed through a C foil of $10 \mu\text{g}/\text{cm}^2$ in thickness located about 10 cm in front of the target. The target thickness was estimated by measuring the Rutherford scattered projectiles and recoil atoms with a surface barrier detector at 45 deg . The satellite line widths are

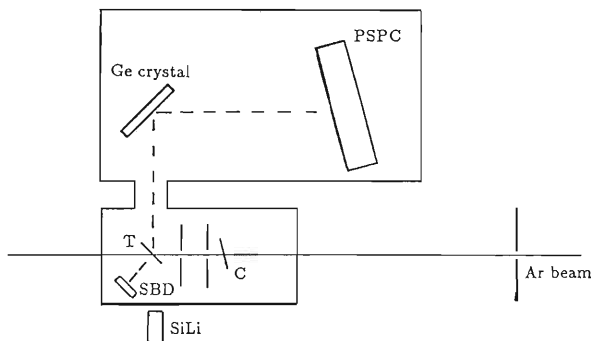


Fig. 1. Experimental setup. PSPC, position sensitive proportional counter; T, target; C, carbon foil; SBD, surface barrier detector. Distances, target-Ge crystal: 315 mm, Ge crystal-PSPC: 187 mm.

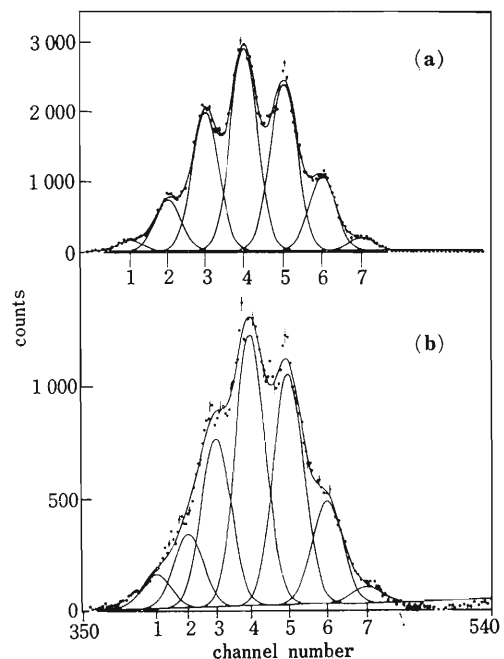


Fig. 2. Measured Ar $K\alpha$ X-ray spectra in a) Al foil $0.8 \mu\text{m}$ and in b) Ni foil $0.5 \mu\text{m}$ in thickness. Solid line: Result of the Gaussian line fits.

estimated by fitting Gaussian curves to the observed satellite spectra.

The fitting procedure was carried out under the assumption that each satellite component KL^n has same line width. Figure 2 shows results of the $K\alpha$ spectra and the Gaussian line fit obtained with an Al foil and with a Ni foil. The measured line widths as a function of the target thickness are shown in Fig. 3 for Cu targets and in Fig. 4 for Ni targets. In Figs. 3 and 4 are shown error bars of the line width calculated by the fitting program. Not shown are the errors of the target thickness measurements which are up to 50% because of the small distance of 4 cm between the SBD, which was used to count the Rutherford scattered particles, and the target. For a direct comparison of the results, which were obtained in different beam times and thus with slightly different Ar beam profiles, measurements using Al target foils, where the line broadening is much smaller,

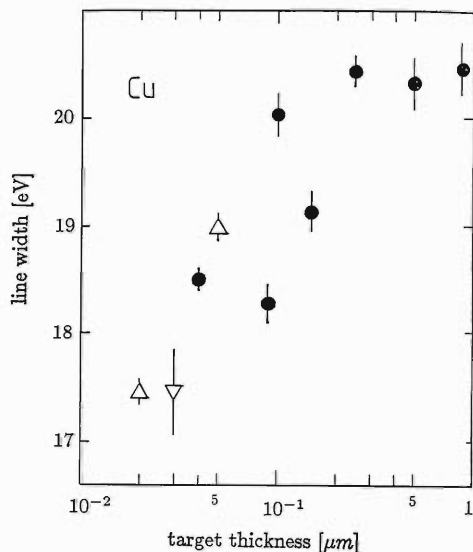


Fig. 3. Line width (FWHM) of the Gaussian line fits of the KL^α satellite components as function of the Cu target foil thickness. \bullet , selfsupported Cu foil; Δ , Cu foil on $3 \mu\text{g}/\text{cm}^2$ C foil; ∇ , Cu foil on $1 \mu\text{g}/\text{cm}^2$ C foil.

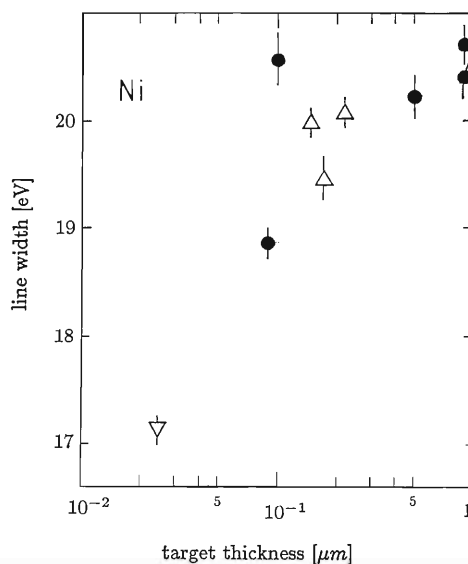


Fig. 4. As Fig. 3 for Ni target foils. \bullet , selfsupported Ni foil; Δ , Ni foil on $4 \mu\text{g}/\text{cm}^2$ C foil; ∇ , Ni foil on $3 \mu\text{g}/\text{cm}^2$ C foil.

were carried out at the beginning and end of each beam time. (The line width here with Al foil $0.8 \mu\text{m}$ is 18.0 eV , with C foil $3 \mu\text{g}/\text{cm}^2$ is 15.3 eV).

Figures 3 and 4 show that the satellite line widths are small at very low target thicknesses up to $0.05 \mu\text{m}$ and increase in the thickness range of 0.05 to $0.1 \mu\text{m}$ to a constant value. During the K-hole lifetime the 33 MeV Ar ion travels roughly a length of $0.1 \mu\text{m}$. Therefore, these measurements support the conclusion that the line broadening arises only if the projectile ion decays inside the target.

References

- 1) Y. Awaya, T. Kambara, M. Kase, H. Shibata, H. Kumagai, K. Kujima, J. Urakawa, T. Matsuo, and J. Takahashi: *Nucl. Instrum. Methods B*, **10/11**, 53 (1985).
- 2) R.L. Watson, J.R. White, A. Langenberg, R.A. Kenefick, and C.C. Bahr: *Phys. Rev. A*, **22**, 582 (1980).
- 3) A. Hitachi, H. Kumagai, and Y. Awaya: *Nucl. Instrum. Methods*, **195**, 631 (1982).

III-2-23. A Systematic Study of KL^n Multiple Vacancy Production for Ca Bombarded by 0.25–1.5 MeV/u Ne and Ar Ions

B. Sulik, Y. Awaya, T. Kambara, Y. Kanai, and T. Mizogawa

We studied the KL^n multiple vacancy production of Ca target atoms by measuring the relative K satellite X-ray yields. For an Ar projectile the colliding system is almost symmetric ($Z_1=18$, $Z_2=20$), whereas for a Ne projectile it is asymmetric. The scaled projectile velocity, *i.e.*, the projectile velocity divided by the characteristic velocity of the target L-shell electrons, is less than unity in the whole projectile energy region.

Experiments were carried out on the beams of RILAC. Energies of the Ne^{2+} projectiles were 0.54, 0.83, 1.03, 1.31, and 1.54 MeV/u and those of Ar^{4+} projectiles were 0.25, 0.54, 0.80, 1.04, 1.30, and 1.57 MeV/u. The target was $70 \pm 10 \mu g/cm^2$ Ca exaporated to a $10 \mu g/cm^2$ carbon backing. K_α satellites, K_α hypersatellites, and a part of K_β satellites were measured by using a broad-range crystal spectrometer¹⁾ consisting of a flat crystal and a position sensitive proportional counter. The beam was focused and collimated to a 1 mm size spot on the target surface. The target was placed at 60° with respect to the beam. The carbon backing of the target was faced to the beam in order to ensure the almost equilibrium charge state distribution of the projectile ions inside the Ca part. A Ge(111) crystal was placed at 90° with respect to the beam and with inclination of $2\theta = 58.8^\circ$ at the center of the crystal,

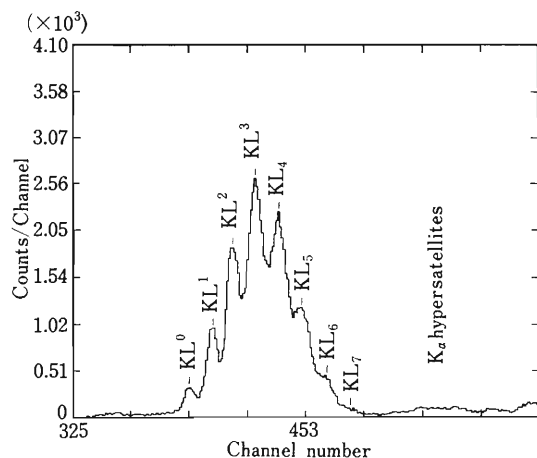


Fig. 1. Typical Ca K X-ray spectrum. KL^n denotes the initial vacancy configuration. The projectile is 1.30 MeV/u Ar ions.

where θ is the Bragg angle. Simultaneously a Si(Li) detector was used partly for monitoring the beam and the target, partly for measuring an X-ray spectrum in a wide energy range.

A typical Ca K spectrum is given in Fig. 1. A preliminary evaluation of the intensities of the K_α diagram and satellite lines was carried out. The experimental values of the L-shell ionization probabilities per electron, P_L , are plotted as a function of the scaled projectile energy $E/\lambda U$ in Figs. 2 and 3 for Ne ions on a Ca target and Ar ions on a Ca target, respectively, where E is the projectile energy, λ is the ratio of the projectile rest mass to the rest mass of the electron, and U is the binding energy of the L-shell electron of the target. In these figures, calculated curves are also shown for comparison; the dotted line and dashed one show the prediction of the binary encounter approximation (BEA)^{2,3)} and the solid line shows that of the geometrical model (GM).⁴⁾ For the BEA calculations no accepted method is available in the literature to determine an effective projectile charge Z_{eff} ; therefore, we presented the predictions of this theory using both the

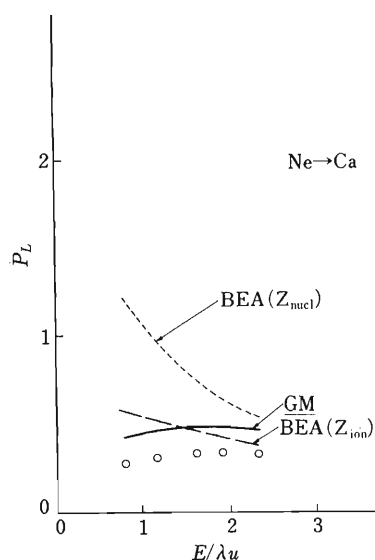


Fig. 2. Energy dependence of P_L for Ne-ion bombardment. Open circles, experiment (present work); dotted line, BEA with $Z_{eff}=Z_{nuclear}$; dashed line, BEA with $Z_{eff}=Z_{ionic}$; solid line, GM.

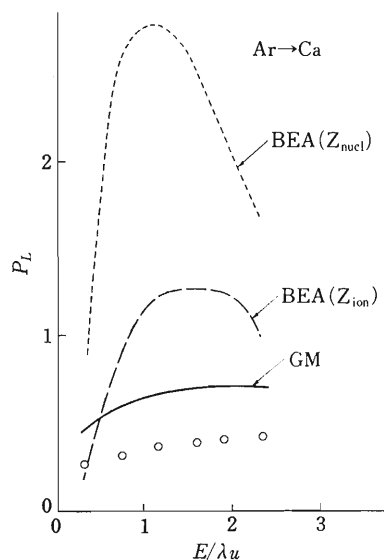


Fig. 3. Energy dependence of P_L for Ar-ion bombardment. For details, see the caption of Fig. 2.

nuclear charge (dotted line) and the average (equilibrium) ionic charges (dashed line) of the projectiles as possible upper and lower limits of the BEA descrip-

tion. The equilibrium ionic charges were determined by the scaling formula of Ref. 5. In the process of the GM calculations the determination of Z_{eff} is included. Both theories are given in their simplest forms: binding correction, charge transfer and rearrangement process prior to the K-vacancy decay are not taken into account. In comparison with the experimental data, both theories overestimate the P_L values, but among them, the GM prediction seems to fit the experimental data better than the BEA one and also reproduce the experimental tendencies. A more detailed analysis is under work.

References

- 1) A. Hitachi, H. Kumagai and Y. Awaya: *Nucl. Instrum. Methods*, **195**, 631 (1982).
- 2) J.H. McGuire and P. Richard: *Phys. Rev.*, **A8**, 1374 (1973).
- 3) Y. Awaya: Proc. XI-th Int. Conf. on Physics of Electronic and Atomic Collisions, Kyoto, 1979 (eds. N. Oda and K. Takayanagi), North Holland, p.325 (1980).
- 4) B. Sulik, I. Kadar, S. Ritz, D. Varga, J. Vegh, G. Hock, and D. Berenyi: *Nucl. Instrum. Methods B*, **28**, 509 (1987).
- 5) K. Shima, T. Mikumo and H. Tawara: *At. Data Nucl. Data Tables*, **34**, 357 (1986).

III-2-24. Impact Parameter Dependent Probabilities of Au L-Shell Ionization by Ar Ions

T. Kambara, T. Mizogawa, Y. Awaya, Y. Kanai,
K. Shima, and R. Schuch

The ionization processes in asymmetric ion-atom collisions have often been compared with perturbation theoretical descriptions. In these cases, a so-called binding effect is often introduced to the first-order perturbation theories like a plane-wave Born approximation (PWBA) and a semi-classical approximation (SCA). When the two nuclei of the projectile and the target approach closer than the radius of the electron orbit, the initial state wavefunction of the bound electron in the target is changed by the influence of the field of the projectile. This is called a binding effect.

To investigate the binding effect in a heavy ion-atom collision, the target L_{III}-shell ionization probability as a function of impact parameter was measured in a collision system of 1 MeV/amu Ar on Au. The result is compared with calculations of a semi-classical approximation (SCA) with relativistic electronic wavefunctions.

The measurement was performed at RILAC by using almost the same experimental setup as that reported previously.¹⁾ An Ar beam with energy of 40.6 MeV was collimated to 1 mm × 1 mm and divergence of 0.02 deg by a double slit system and was led to a target. The target was Au with thickness of about 30 μg/cm² evaporated on a thin C foil. The characteristic L X-rays of Au were detected with a Si(Li) detector placed at 90 deg to the beam at 16.5 mm of distance. Scattered projectiles were detected with a parallel-plate avalanche detector (PPAD) placed at 193.5 cm from the target to the forward direction. The anode of the PPAD is divided into 16 rings corresponding to 16 different scattering angles ranging from 0.14 to 1.4 deg. The coincidence events between the X rays and the scattered projectiles at different scattering angles are recorded in event mode by a computer. At the same time the total number of scattered particles at each ring of the PPAD was counted with scalers and was used for the normalization to obtain the probability of the target L X-ray emission at each scattering angle.

The L_{III}-ionization probability was estimated from the measurement of the Lα X-ray which emits from the transition of an M electron to an L_{III} hole. The

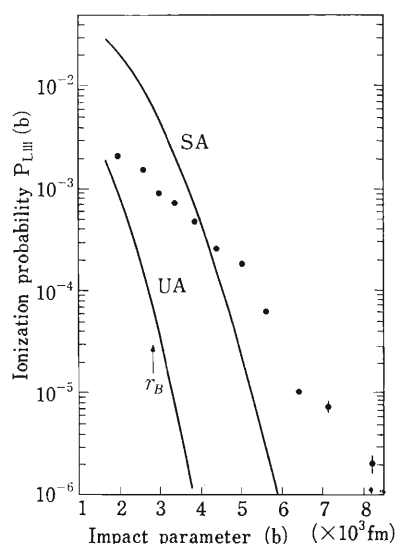


Fig. 1. Impact parameter dependence of the ionization probability of Au L_{III} shell. Dots show the experimental data and lines show the SCA calculation results; SA is for separated atom wavefunction for the initial state of the ionized electron and UA is for the united atom one. r_B shows the Bohr radius of Au L shell.

obtained Lα X-ray emission probabilities were corrected for the fluorescence yield of the neutral atom to obtain the L_{III}-vacancy production probability $P_{L_{III}}(b)$. The effect of the Coster-Kronig transition was not considered. The results are shown in Fig. 1. The impact parameter b was calculated from the scattering angle by a screened Coulomb potential. The Bohr radius of the Au L shell is about 2,800 fm.

The lines in Fig. 1 represent the probabilities predicted by SCA calculation.²⁾ In the calculations, relativistic wavefunctions were used for the L_{III} electrons of the target Au and the recoil effect was considered. To see the contribution of the binding effect, we compared the results of calculations for different effective nuclear charges which determines the initial electron wavefunction in the target: one is the target nuclear charge (SA) and the other is the sum of the projectile and the target (UA) nuclear charge. The screening by the inner shell electrons was taken into account according to Slater. The full line shows the result of the calculation with the SA

assumption and the dashed lines show that with UA.

At impact parameter larger than the Bohr radius of the Au L shell, the experimental $P_{LIII}(b)$ has values close to or larger than the SA calculation. At smaller impact parameter, it becomes considerably smaller than the SA calculation and tends to be close to the UA values. We have observed the same effect in the $P(b)$ of the target K-shell ionization of He-Ca collision system.¹⁾ It supports the applicability of the SCA calculation with the binding effect for ionization in different collision systems.

The effect of multi-scattering in the solid target may affect the shape of the $P_{LIII}(b)$ especially at smaller scattering angles. According to a table given

by Sigmund and Winterbon,³⁾ the half width of the angular distribution of the multiple scattering is estimated to be smaller than 0.06 deg in our case. It may cause the flattening of the shape of $P_{LIII}(b)$ at large impact parameters. Detailed analysis is in progress.

References

- 1) R. Schuch, Y. Awaya, T. Kambara, T. Mizogawa, Y. Kanai, H. Shibata, and K. Shima: *Z. Phys. D-At. Mol. Clusters*, **4**, 339 (1987).
- 2) D. Trautmann: Private communication.
- 3) P. Sigmund and K. B. Winterbon: *Nucl. Instrum. Methods*, **119**, 541 (1974).

III-2-25. Charge-State Distribution Measurements of Ar Ions

Y. Kanai, Y. Awaya, T. Kambara, M. Kase,
H. Kumagai, T. Mizogawa, and K. Shima

We measured the charge-state distributions of projectile Ar ions after single close collisions with gas targets to investigate the heavy ions-atom violent collisions. We used Ar ions (1.27 MeV/u) from RILAC. Our experimental setup is as same as shown in previous papers.^{1,2)} A gas cell was set at the target position and was differentially pumped to maintain the beam line in good vacuum. The pressure of the target gas was monitored with a capacitance manometer (MKS Baratron). Though difficult to measure from the value indicated with the Baratron gauge, the gas pressure at the beam position was considered proportional to the value of the gauge.

The target gas pressure dependence of the charge-state fractions of Ar ions after collisions was measured in the pressure range between 10^{-2} and 10^{-3} Torr (at the Baratron gauge), since the single-collision condition is maintained in this range as shown in Fig. 1. Typical charge-state distributions of Ar ions in the $\text{Ar}^{4+} + \text{Ar}$ collisions are shown in Fig. 2, in which open and closed circles are for the scattering angle of $0^\circ \pm 0.066^\circ$ and $0.13^\circ \pm 0.066^\circ$, respectively.

The mean charge states $\bar{q}_1(Z_2)$ measured for Ar ions (1.27 MeV/u) are shown as a function of the target atomic number (Z_2) in Fig. 3. The values

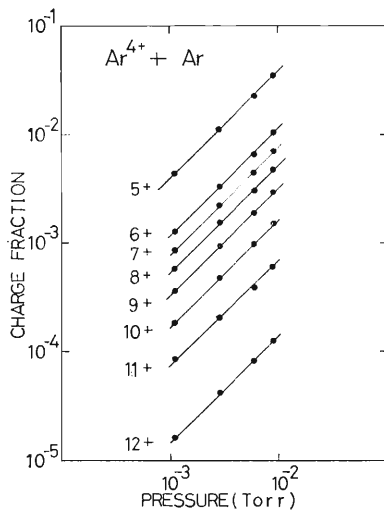


Fig. 1. Pressure dependence of the charge-state fraction of argon ions after the $\text{Ar}^{4+} + \text{Ar}$ collisions.

plotted in this figure are for Ar ions with almost the same impact parameter: $0.6 \pm 0.1 \times 10^{-9}$ cm for a Ne target, $0.8 \pm 0.1 \times 10^{-9}$ cm for an Ar target and $1.0 \pm 0.1 \times 10^{-9}$ cm for a Kr target. The results for Ar^{12+} are also plotted. Our results seem to show that the value of the mean charge state converges to a certain

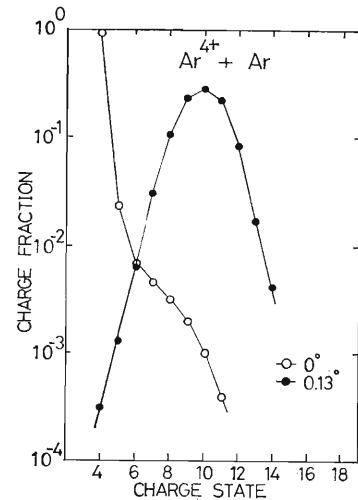


Fig. 2. Charge-state distributions of Ar ions after the $\text{Ar}^{4+} + \text{Ar}$ collision. Energy of Ar^{4+} is 1.27 MeV/u. Open and closed circles are for charge-state distributions of Ar ions scattered into $0^\circ \pm 0.066^\circ$ and $0.13^\circ \pm 0.066^\circ$, respectively. Target Ar gas pressure is 5.9 mTorr.

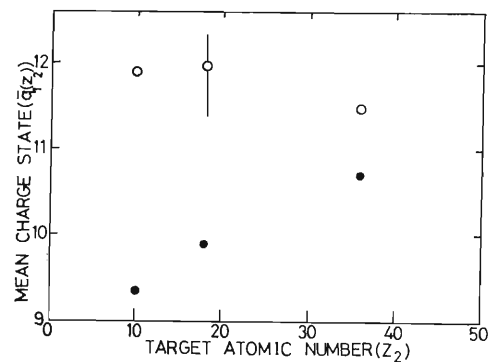


Fig. 3. Target atomic number (Z_2) dependence of the mean charge state of Ar ions after single close collisions. The impact parameter is 0.6×10^{-9} cm for the Ne target, 0.8×10^{-9} cm for the Ar target, and 1.0×10^{-9} cm for the Kr target. The energy of Ar ions is 1.27 MeV/u. Closed circles are for Ar^{4+} impact; open circles for Ar^{12+} impact.

value as Z_2 becomes large. Rosner and his group reported similar results as ours.^{3,4)} In their cases, the K-shell vacancies have influence on the mean charge values of ions, since the impact parameter (b) is much smaller than the K-shell radius (r_k) of the projectile ions. In our case, the impact parameter is larger than the K-shell radius of Ar, *i.e.*, 0.45×10^{-9} cm. Considering the impact-parameter dependence of the K-shell-vacancy production probability $P_k(b)$ for 1 MeV/u S ions on Kr and Xe by Maor *et al.*⁵⁾: (1) the values of $P_k(b)$ for $b > r_k$ are smaller than those for $b < r_k$, (2) the values of $P_k(b)$ for S on Kr are smaller than those for S on Xe, we may say that the values of $P_k(b)$ for the Ar (1.27 MeV/u)-Ne, Ar Kr collisions are so small that the effect of

production of K-shell vacancies is negligible. The Z_2 dependence of the mean charge state of Ar (1.27 MeV/u) after single close collisions, shown in Fig. 3, would be determined by the behavior of the L-shell (and outershell) electrons.

References

- 1) Y. Kanai, Y. Awaya, T. Kambara, M. Kase, H. Kumagai, T. Mizogawa, and K. Shima: *RIKEN Accel. Prog. Rep.*, **20**, 56 (1986).
- 2) Y. Kanai, Y. Awaya, T. Kambara, M. Kase, H. Kumagai, T. Mizogawa, and K. Shima: *Nucl. Instrum. Methods A*, **262**, 128 (1987).
- 3) B. Rosner and D. Gur: *Phys. Rev. A*, **15**, 70 (1977).
- 4) B. Rosner and W. Brandt: *Phys. Lett. A*, **61**, 97 (1977).
- 5) D. Maor, B. Rosner, M. Meron, H. Schmidt-Bocking, and R. Schuch: *J. Phys. B*, **14**, 693 (1981).

III-2-26. Coincidence Measurements of Electron Capture and Target Ionization in 1.05 MeV/amu Ar^{12+} + Ne Collision

T. Tonuma, T. Matsuo, H. Kumagai, S. H. Be, and H. Tawara

We report experimental studies of target ionization and projectile electron capture processes, studies which were carried out through coincidence measurements between a charge-analyzed projectile and target ion for 1.05 MeV/amu Ar^{12+} projectiles colliding with Ne targets.

A 1.05 MeV/amu Ar^{4+} beam was provided by RILAC. Ar^{12+} beams were selected with a switching magnet by passing through a carbon foil and directed into a target cell. A target-gas cell and a recoil ion detection system are shown in Fig. 1. Ionized recoil target ions were charge-analyzed on a time-of-flight (TOF) spectrometer. This spectrometer separates recoil ions with respect to their flight times, which determine their charge state. The bottom plate (ion repeller) and the grid inside the target cell were on a positive potential of +700 V and +300 V, respectively. An Einzel lens plate was on a negative potential of -300 V, and a channeltron-detector cone was to -2.5 kV. The distance between the interaction region and the channeltron detector was about 14 cm. After allowed to pass the target cell, the projectile ions were charge-analyzed with an electrostatic analyzer and detected with a position-sensitive parallel

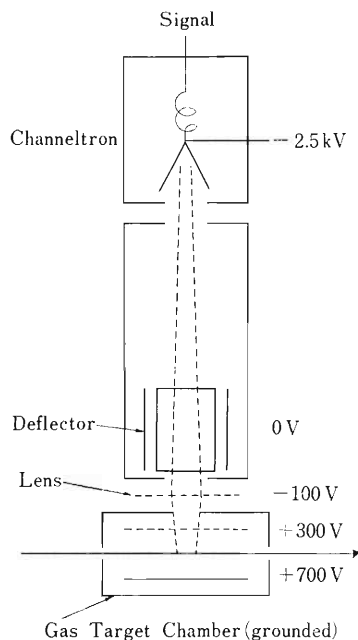


Fig. 1. Target gas cell with a time-of-flight spectrometer.

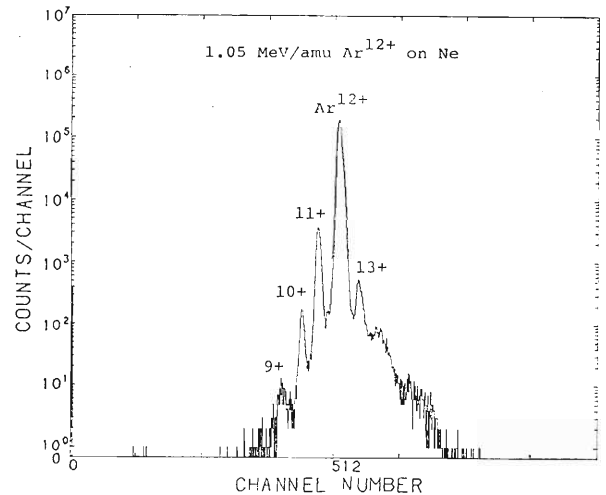


Fig. 2. Charge distribution spectrum of the projectile in $\text{Ar}^{12+} + \text{Ne}$ collision.

plate avalanche counter (PPAC) (see Fig. 2 which shows a typical charge distribution spectrum of the projectile in $\text{Ar}^{12+} + \text{Ne}$ collision).

The experimental setup is shown schematically in Fig. 3. The energy signal from the PPAC was used as a stop signal to a time-to-pulse height converter, and the signal from the channeltron counting recoil ions was used as a start signal, with which a TOF spectrum (*i.e.*, a recoil-ion charge-state spectrum) was obtained. The projectile charge-state spectrum was recorded *via* the position information from the PPAC. On the basis of a list mode option,¹⁾ the spectra, which represent coincidences with a given gate in other spectrum (for example, a particular projectile charge shown in Fig. 2), could later be obtained. It should be noted from PPAC spectra (see Fig. 2) that the relative cross sections of electron capture for the projectile are much larger than those of electron loss in the present collision system.

Figure 4 shows typical coincidence spectra for Ar^{12+} on Ne. Figure 4(a) shows the TOF spectrum taken in coincidence with beam particles which do not change their charge (pure ionization). On the other hand, Fig. 4(b) shows the spectrum taken in coincidence with beam particles which have captured two electrons. A little shift of peak positions at the same

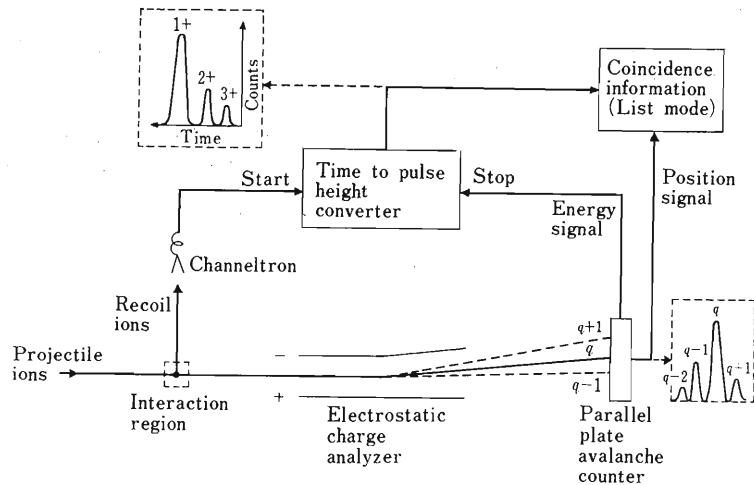


Fig. 3. Schematic diagrams of the coincidence experiment.

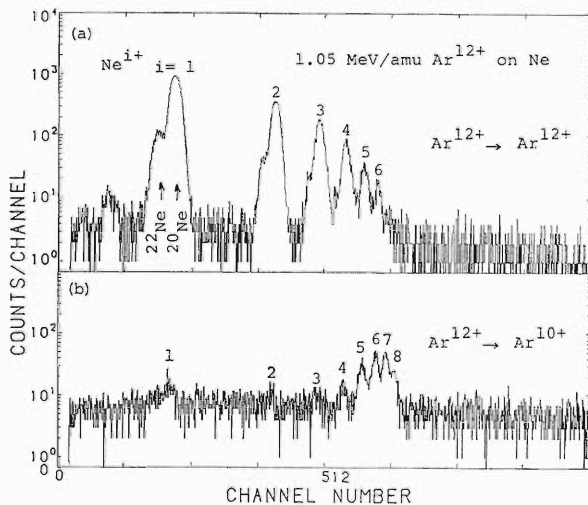


Fig. 4. Time-of-flight spectra for 1.05 MeV/amu $\text{Ar}^{12+} + \text{Ne}$ collision. (a), Spectrum was taken in coincidence with beam particles which do not change their charge (pure ionization spectrum); (b), Spectrum was taken in coincidence with beam particles which captured two electrons (transfer-ionization spectrum).

charge state between (a) and (b) spectra was caused by the electric circuit system. As can be seen from these spectra, for a given incident-projectile charge state, the charge-state distribution of the recoil ions is strongly correlated to the final charge state of the projectiles. The double-electron capture events by the incident ions during collision are found to cause significant shifts in recoil ion charge-state distribution toward high charge states. We concluded from these observations that the direct multiple ionization is a dominant process for the production of low charge-state recoil ions, whereas the production of high charge-state recoil ions is accompanied by electron capture into projectile ions from target atoms (transfer ionization).

The observed charge-state distribution of recoil Ne^{i+} ions summed over single- and double-electron capture events of projectiles is compared with the compound atom model²⁾ whose main assumption is that during close collision some electrons of both projectile and target atoms, whose electrons are not altogether thrown out of the system, create a common structureless electron cloud. The electrons in this electron cloud are later redistributed between both ions depending upon their nuclear charge, which in turn determines the final charge-state distribution of recoil ions produced in close collision as well as that of projectile ions. The results are shown in Fig. 5 where both the experimental and theoretical values at recoil-ion charge state $i=5$ are normalized to unity. Figure 5 indicates that the compound atom model well reproduces the observed (relative) charge distribution of recoil ions with $i \geq 5$ whereas the model underestimates those for $i \leq 4$. It is not clear why the observed values for low charge recoil ions, which are

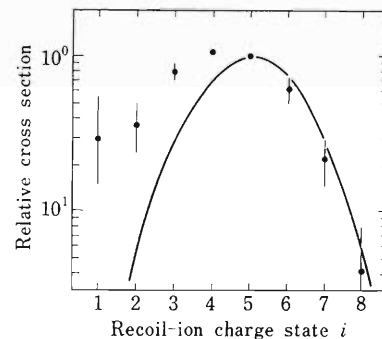


Fig. 5. Charge-state distribution of recoil Ne ions in collision of 1.05 MeV/amu Ar^{12+} with a Ne target as a function of the recoil-ion charge state i . Solid points represent the experimental data summed over single- and double-electron capture events. Solid line represents the distribution calculated by the compound atom model. Both values are normalized to unity at $i=5$.

related with single- and double-electron capture, are far larger than the calculation. This might be due in part to electron capture of recoil ions before acceleration. It should be also noted that intense projectile beams were used when spectrum shown in Fig. 4(b) was taken, while the main incident projectile beams without change in charge were stopped in a Faraday cup. As discussed in a previous paper,³⁾ the contribution of direct ionization to low charge

recoil ions is two or three orders of magnitude larger than the values estimated from the compound model.

References

- 1) H. Kumagai, M. Sasagase, and T. Wada: *RIKEN Rep.*, **62**, 114 (1986) (in Japanese).
- 2) M. Meron and B. Rosner: *Phys. Rev. A*, **30**, 132 (1984).
- 3) T. Tonuma, T. Matsuo, M. Kase, T. Kambara, H. Kumagai, S. H. Be, I. Kohno, and H. Tawara: *Phys. Rev. A*, **36**, 1941 (1987).

III-2-27. High-Charge Effects on Electron Excitations in Metal Targets for Ar^{12+} Impact as Compared with Those for He^{2+} Impact

A. Koyama, H. Ishikawa, Y. Sasa, O. Benka,* and M. Uda**

In the present paper, energy spectra of low energy Auger electrons (AE) from Al, and Cu metals induced by Ar^{12+} are compared with those for He^{2+} in order to examine the excitation of inner-shell-electrons with binding energies lower than 100 eV by high-charge projectiles. Experimental results were obtained which suggest that the screening of projectile's charge by other target electrons is important also in the excitation of those inner-shell-electrons.

The apparatus and experimental conditions are the same as those described in a previous paper.¹⁾ Velocities of Ar^{12+} and He^{2+} are equal and correspond to 1.1 MeV/amu. Al and Cu targets are vacuum-evaporated *in-situ* on polished stainless-steel substrates. Targets are set at the earth potential. The beam is incident on a target at an angle of 39° relative to the surface.

Figure 1 shows the angular resolved energy spectra, $E \cdot N(E)$, of LVV-AE from Al on the background of continuous SE; (a) is for Ar^{12+} and (b) for He^{2+} . Hyper-satellite peaks, L^*VV and $L^{**}VV$, are seen in (a),²⁾ but only L^*VV is seen in (b).

Figure 2 shows the ratio of the yields of electrons (AE plus SE) for Ar^{12+} to those for He^{2+} . At 70 eV, the ratio decreases stepwise from 33 to 25. In the energy ranges below 30 eV and above 80 eV, the

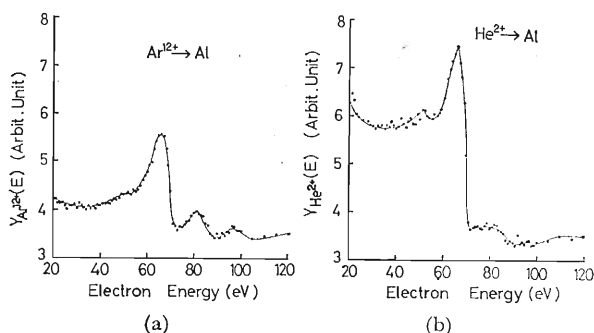


Fig. 1. Energy spectra of Al-LVV Auger electrons on the background of continuous secondary electrons induced by Ar^{12+} impact (a), and by He^{2+} impact (b). Energy of the projectiles correspond to 1.1 MeV/amu.

* Universität Linz, A-4040 Linz, Austria.

** Present address: Department of Materials Science, Waseda University, Tokyo.

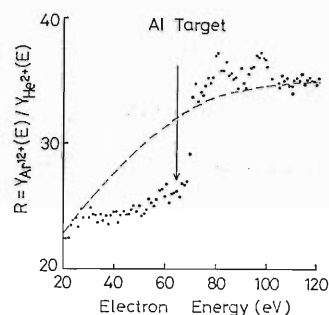


Fig. 2. Ratios of the yields of electrons (Auger plus secondary electrons) for Ar^{12+} impact to those for He^{2+} impact. The arrow indicates the energy at which the Auger peak takes its maximum. The dotted line shows the values of the ratios only for the yields of secondary electrons, in the energy range below 30 eV or above 100 eV. In the intermediate region, the dotted line shows the values of the ratios only for continuous SE as estimated from interpolation.

ratios are relevant only to SE. In the energy region 30–100 eV, the ratio for background SE were estimated from interpolation and shown by the dotted curve in Fig. 2. At the energy of the AE peak (marked by an arrow), the value of the ratio of the yields of electrons (AE plus SE) is 25, fairly small compared with the estimated value of the ratio for SE, 32. From these values for the ratios, it follows that

$$Y_{\text{AE}}(\text{Ar})/Y_{\text{SE}}(\text{Ar}) \cong 0.8 Y_{\text{AE}}(\text{He})/Y_{\text{SE}}(\text{He}) \quad (1)$$

where Y_{AE} and Y_{SE} are the yields of AE and SE, respectively.

Figure 3 shows similar energy spectra of MVV-AE from Cu on continuous SE. Hyper-satellite peaks are not distinguished even for Ar^{12+} . Figure 4 shows the similar ratio for the yields of electrons (AE plus SE) induced by Ar^{12+} to those induced by He^{2+} . A pronounced dip can be seen around the energy of the AE peak. In the energy regions below 50 eV and above 70 eV, the ratios are relevant only to SE. In the energy region 50–70 eV, the dotted line shows the ratio only for SE as estimated by interpolation. At the energy of the Auger peak,

$$Y_{\text{AE}}(\text{Ar})/Y_{\text{SE}}(\text{Ar}) \cong 0.88 Y_{\text{AE}}(\text{He})/Y_{\text{SE}}(\text{He}) \quad (2)$$

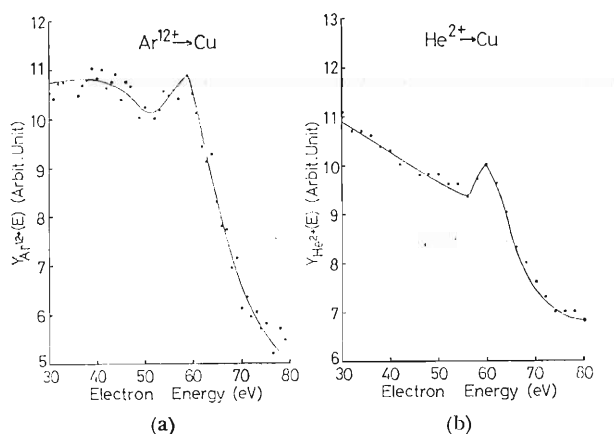


Fig. 3. Energy spectra of Cu-MVV Auger electrons on the background of continuous secondary electrons induced by Ar^{12+} impact (a), and by He^{2+} impact (b).

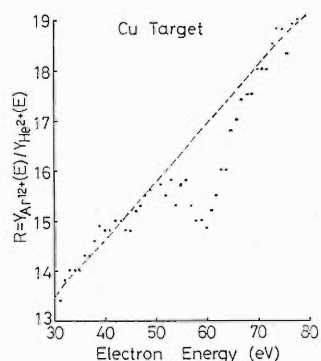


Fig. 4. Ratio of the yields of electrons (Auger plus secondary electrons) for Ar^{12+} impact to those for He^{2+} impact. The dotted line is obtained by the same procedure as in Fig. 2.

Fluorescence yields are usually negligibly small, when the binding energy of the concerned inner-shell is low, and when there are not too many holes in the outer-shells. In metal targets, holes in outer-shells are refilled by outer electrons of surrounding atoms in a very short time compared with the lifetime of the hole in the inner-shell. In fact, no satellite peaks have been observed in the spectra of low energy AE from lattice atoms.³⁾ Thus it is reasonable to consider that the peak heights of these AE with the contribution from hyper-satellite peaks

are proportional to the ionization cross-sections of the respective inner-shells. By the correction for the contribution from the hyper-satellite peaks, the ratio for Al in Fig. 2 increases from 25 to 27 at the peak energy of the AE. This correction is small and will be small also for the case of a Cu target. Then it is said that the ratio of the ionization cross-section of the inner-shells, L-shell of Al, or M-shell of Cu targets, by Ar^{12+} impact to that by He^{2+} impact is smaller than the ratio of the production probability of continuous SE with corresponding energies by Ar^{12+} impact to that by He^{2+} impact. Continuous SE will be mainly contributed from valence electrons. The following equation can therefore be obtained from Eqs. 1 and 2,

$$\frac{P_{\nu}(\text{Ar})}{P_{\nu}(\text{Ar})} \cong 0.85 \frac{P_{\nu}(\text{He})}{P_{\nu}(\text{He})} \quad (3)$$

where P_{ν} is the ionization probability of ν -shell, and P_{ν} is the excitation probability of valence electrons into continuous states with corresponding energies.

Such depression of the ionization probability of inner-shell electrons relative to the excitation of valence electrons for Ar^{12+} compared with that for He^{2+} can be tentatively explained in terms of the screening of the Coulomb force of high-charge projectiles by other target electrons. In the case of He^{2+} , the impact parameter is small, and only very few electrons are present between the projectile and an electron concerned; thus screening will be ignored. However, in the case of Ar^{12+} , the impact parameter is large, and more electrons will be present between the projectile and the target electron in an inner-shell than in an outer-shell. This will result in more effective screening for inner-shell electrons than for outer-ones.

References

- 1) A. Koyama, O. Benka, Y. Sasa, and M. Uda: *Nucl. Instrum. Methods Phys. Res. B*, **13**, 637 (1986).
- 2) W. Schmidt, P. Muller, V. Brucker, F. Loffler, G. Saemann-Ishenko, and W. Schukert: *Phys. Rev. A*, **24**, 2420 (1981).
- 3) G. Saemann-Ishenko and W. Schmidt: *Nucl. Instrum. Methods Phys. Res.*, **218**, 757 (1983).

III-2-28. Energy Spectra of Al-LV Auger Electrons Induced by Grazing Angle Incident Fast Heavy-Ion Impact

A. Koyama, H. Ishikawa, and Y. Sasa

In the present experiment, projectile dependence of the AL-L_{2,3}VV Auger line is precisely examined for incident energies corresponding to about 1 MeV/amu, and for incident angles of 39° and 4° relative to the surface of a target. Although projectile dependence is negligible for 39° incidence, clear projectile-dependence was observed for 4° incidence; the peak energy of the L_{2,3}VV Auger electrons decreases as the atomic number of projectiles increases. This paper reports these new observations.

An Al target was *in-situ* vacuum deposited on a polished stainless-steel substrate with a 1 cm × 1 cm area at a pressure lower than 10⁻⁸ Torr. The pressure of the target chamber was kept below 2 × 10⁻¹⁰ Torr when a beam was incident on a target. The beam diameter was 1.5 mm, and beam current was less than 5 nA. Incident energies for N⁶⁺, Ar¹²⁺, and Ar¹²⁺ correspond to 1.3 MeV/amu, and that for Xe⁹⁺ 0.98 MeV/amu. Only electrons emitted back-

ward from the target are concerned here. The apparatus was described previously.¹⁾ The angle resolution of the parallel plate analyzer was 1°. Furthermore, only electrons emitted from a fine spot (0.5 mm × 0.5 mm) on the target are energy-analyzed and detected. Contamination by secondary electrons emitted from the edge of the target or other places outside the target can thereby be ignored, and spectra are energy- and angle-resolved ones. The reproducibility of the data was confirmed by independent measurements.

Figure 1 shows energy spectra of electrons emitted at an angle of 90° relative to the surface of the target induced by the various projectiles in the energy range from 54 to 69 eV. Figure 1(1) is for large incident angles: (a) for 1 keV e⁻ with an incident angle of 24° relative to the surface, (b) for N⁶⁺, (c) for Ar¹²⁺, and (d) for Xe⁹⁺. The incident angles for N⁶⁺, Ar¹²⁺, and Xe⁹⁺ are all 39° rel-

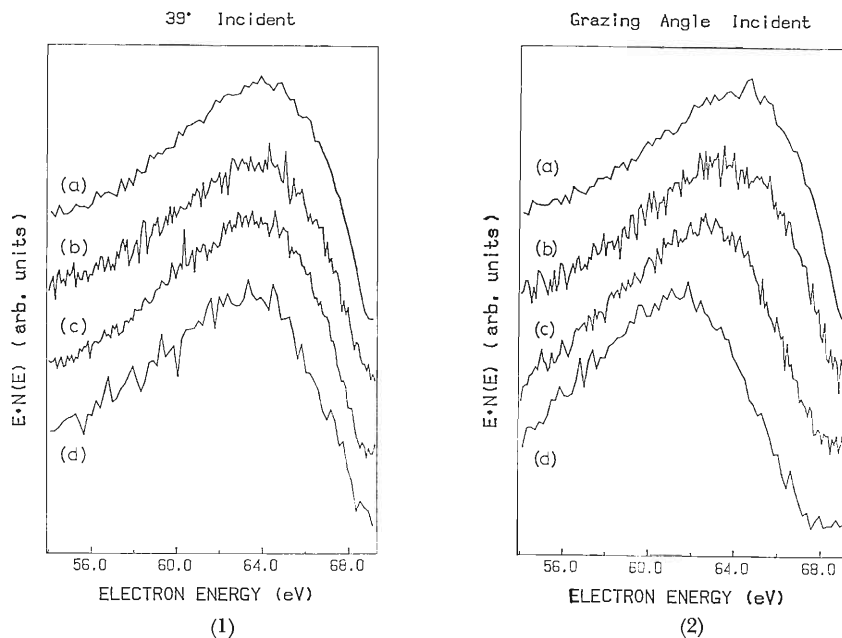


Fig. 1. Energy spectra of electrons emitted at an angle of 90° relative to the surface of the Al target induced by various projectiles. Spectra are normalized to give the same peak height. (1), for large angle incidence: (a), for 1 keV e⁻ incident at 24° relative to the surface; (b), for N⁶⁺; (c), for Ar¹²⁺; and (d), for Xe⁹⁺. Incident angles for N⁶⁺, Ar¹²⁺, and Xe⁹⁺ are all incident at 39° relative to the surface. (2), for grazing angle (4°) incidence: (a), for e⁻; (b), for N⁶⁺; (c), for Ar¹²⁺; and (d) for Xe⁹⁺.

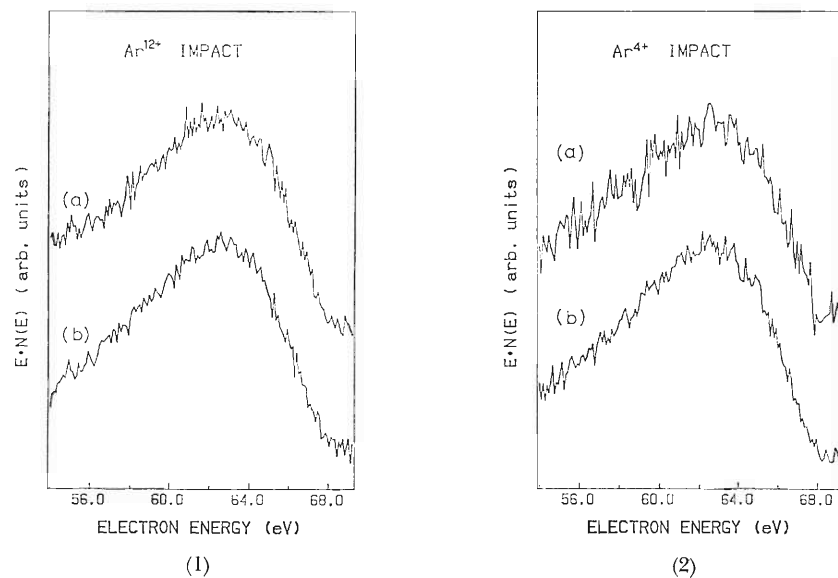


Fig. 2. Emission angle dependence of the Auger spectra induced by the grazing angle (4°) incidence of Ar ions. Spectra are normalized to give the same peak height. (1), for Ar^{12+} impact: (a), for an emission angle at 129° , and (b), for 94° , relative to the beam. (2), for Ar^{4+} impact: (a) for an emission angle of 34° , and (b) for 94° , relative to the beam.

ative to the surface. Figure 1(2) is for the grazing angle incidence of 4° relative to the surface: (a) for e^- , (b) for N^{6+} , (c) for Ar^{12+} , and (d) for Xe^{9+} . The spectra are normalized to give the same height for all the projectiles. When incident angles are large, the projectile-dependence of the peak energy is almost negligible. On the other hand, for the grazing angle incidence the peak energy of the $\text{Al-L}_{2,3}\text{VV}$ Auger electrons shows clear projectile-dependence: the peak energy is shifted to a lower value, as the atomic number of the projectile increases; this is the first observation to authors' knowledge. The amount of the energy decrease for Xe^{9+} is as large as 3–4 eV compared with for e^- . It should also be noted that, in Figs. 1(1) and 1(2), the widths of the Auger peaks are independent of the projectiles.

Figure 2 shows the emission-angle dependence of the peak energy for grazing angle (4°) incidence of Ar ions. Figure 2(1) is for Ar^{12+} impact: (a) is for an emission angle of 129° , and (b) for an emission angle of 94° , relative to the beam direction. The peak energies for (a) and (b) are almost the same. Figure 2(2) is for Ar^{4+} impact: (a) is for an emission angle of 34° , and (b) for an emission angle of 94° , relative to the beam direction. The peak energies are also the same for (a) and (b). It is thus concluded that there is no emission-angle dependence in the energy of the Auger electrons.

For grazing angle incidence of heavy projectiles, a frequent hard collisions will occur in a thin surface region compared with for a larger angle incidence.

Sputtered atoms in flight will play an important role for Auger emission, consequently. An Auger line of Al atoms in flight will show atom-like features,²⁾ and also show emission-angle dependence or peak broadening due to the Doppler effect. The Auger peaks for the grazing angle incidence obtained here, however, show neither atom-like features, emission angle dependence, nor peak broadening, as shown in Figs. 1 and 2. Thus the peak shift observed here is not due to the Doppler effect.

When outer-shell electrons are excited together with an inner-shell electron, the energy level of the outer-shell is lowered, and it is well known that the energy of the satellite Auger line is lower than that of the diagonal line. Then, if the lifetime of the electron holes in the outer-shell is longer than that of the electron hole in the inner-shell, such decrease in the energy of the Auger line will be observed even for metal targets.

According to Saemann-Ishenko and Schmidt, the $\text{Ni-M}_{2,3}\text{VV}$ Auger peak shows projectile dependence even for a large-angle incidence of 50° relative to the surface.³⁾ They suggested that the projectile dependence of the Auger line is due to the long lifetime of electron holes in the d-band of Ni produced in multiple excitation of target electrons by heavy projectiles. They also suggested that the projectile independence of the $\text{Al-L}_{2,3}\text{VV}$ Auger line is due to the short lifetime of electron holes in the valence band of Al targets. In the case of grazing angle incidence of heavy projectiles with incident energies concerned here, the lifetime of electron holes is

suspected to be prolonged owing to a kind of a surface effect even for the Al valence band. A great number of low energy electrons are excited by projectiles and emitted almost perpendicularly to the beam direction. In the case of large angle incidence, however, excited electrons are only "replaced" from the path region of the projectiles: most of excited electrons will be inside the target. Thus, the electron density averaged in time for the projectile's path region will be nearly equal to that in the other region. In the case of grazing angle incidence, how-

ever, excited electrons will be directly emitted from the surface, and the electron density averaged in time for the path region will be really lower, causing a longer lifetime of electron holes.

References

- 1) A. Koyama, O. Benka, Y. Sasa, and M. Uda: *Nucl. Instrum. Methods Phys. Res. B*, **13**, 637 (1986).
- 2) C. Benazeth, N. Benazeth, and L. Viel: *Surf. Sci.*, **78**, 625 (1978).
- 3) G. Saemann-Ishenko and W. Schmidt: *Nucl. Instrum. Methods Phys. Res.*, **218**, 757 (1983).

III-2-29. A Piezoelectric Bimorph Transducer for the Coulomb-Excitation Mössbauer Spectroscopy

N. Sakai, F. Ambe, and K. Asai

Previously, we have verified^{1,2)} that a Mössbauer transducer composed of piezoelectric bimorph (PB) actuators is very useful for the Coulomb-excitation Mössbauer spectroscopy. We have further developed the transducer which can be applied not only to ordinary measurements but also to in-beam experiments. The improved driving unit is illustrated schematically in Fig. 1. The size of the PB plate (purchased from NGK Spark Plug Co., Ltd. in Japan) is 40 mm in length, 15 mm in width, and 0.5 mm in thickness. Two PB plates are connected to a holder for an absorber or a source with V-shaped metallic plates, which are necessary to release the slight change in the horizontal length of the PB

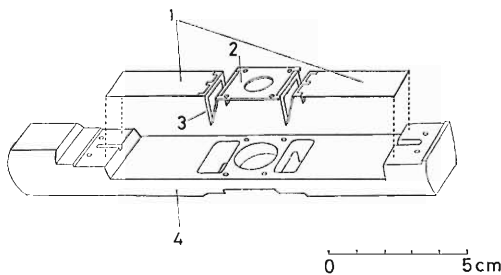


Fig. 1. Schematic drawing of the piezoelectric bimorph transducer: 1, piezoelectric bimorph actuator plates; 2, holder; 3, V-shaped Cu-metal connectors; 4, base.

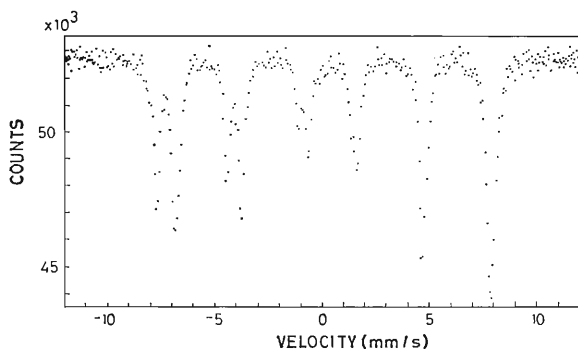


Fig. 2. Test spectrum of magnetite Fe_3O_4 at room temperature.

plates during their vibration. The reason for using a pair of PB plates instead of one is to achieve uniformity in velocity over the entire holder. The actuators are activated by sinusoidal voltage from a digital function generator at 97.65 Hz which corresponded to 10- μs dwell time per channel of a 1,024 channel MCA. For the room-temperature operation, the applied peak voltage was about ± 0.9 V for a velocity of ± 15 mm/s. Slightly different voltages but with the same phase were applied to the two actuators to make their mechanical amplitudes identical. Good stability of the motion of the transducer was found without any negative feedback sensor on the source holder. The observed FWHM of the absorption peaks ($\pm 1/2 \rightarrow \mp 1/2$) of natural Fe metal accumulated for 16 hours was 0.256 ± 0.005 mm/s, which was comparable to the value obtained with a conventional electromechanical transducer. The observed symmetry of the Fe-metal spectrum indicates that there is no hysteresis effect of the piezoelectricity, because of the small amplitude of displacement (about 0.1 mm) of the PB plate. The Mössbauer spectrum of Fe_3O_4 at room temperature, shown in Fig. 2, demonstrates good velocity resolution in the high velocity region. Clear separation of the two peaks around -8 mm/s shows that the PB driving unit is reliable in the measurement up to 10 mm/s. It is easy to increase the maximum velocity of this driving system up to several hundreds of millimeters per second by applying higher voltage with a higher frequency to the actuators.

Contrary to a usual electromechanical driving unit, this PB plate has the advantage of operation at low temperatures down to the liquid-He temperature. The construction of a liquid-He cryostat for this purpose is now in progress.

References

- 1) N. Sakai, F. Ambe, and K. Asai: *RIKEN Accel. Prog. Rep.*, **19**, 159 (1985).
- 2) N. Sakai, F. Ambe, and K. Asai: *RIKEN Accel. Prog. Rep.*, **20**, 65 (1986).

III-2-30. ^{57}Fe Mössbauer Study on $\text{YBa}_2\text{Cu}_{3-x}\text{Fe}_x\text{O}_{7-y}$

T. Okada, N. Sakai, K. Asai, Y. Toba, and T. Yamadaya

Since Bednorz and Müller found a clue to a high T_c copper oxide superconductor,¹⁾ many studies have been intensively performed seeking a new material having a high T_c . The oxide $\text{YBa}_2\text{Cu}_3\text{O}_{7-y}$ is a typical superconductor with $T_c = 90$ K found among these oxides.²⁾ The high T_c of this material is far beyond the upper limit predicted by the BCS theory, and the mechanism of the superconductivity of this material is yet unrevealed. Some crystallographic, electric, and magnetic studies have been made, but only a few microscopic studies on the electronic structures of this material using hyperfine techniques have been reported to our knowledge and thus are highly desired. In the present study, we report the ^{57}Fe Mössbauer study on the system $\text{YBa}_2\text{Cu}_{3-x}\text{Fe}_x\text{O}_{7-y}$ with the Fe content x between 0.03 and 1.0.

Specimens were prepared by calcination of Y_2O_3 , BaCO_3 , CuO , and $^{57}\text{Fe}_2\text{O}_3$ powders at 950°C in the oxygen-gas flow. By means X-ray analysis, we verified that they were of an orthorhombic ($x \geq 0.03$) or a tetragonal ($0.1 \leq x < 1.0$) phase. The lattice constant c decreased slightly with an increase in the Fe content x , but the lattice constant a in the tetragonal phase remained almost unchanged. Detailed results of the crystallographic, electric, and magnetic studies on this system will be reported elsewhere. Mössbauer spectra were taken at temperatures between 1.7 K and room temperature with a conventional or a newly developed driving system.³⁾

Figure 1 shows the typical Mössbauer spectra of ^{57}Fe in this system at room temperature. The spectrum changes drastically with the Fe content x , and each spectrum consists of several broad lines. After a number of trials, we found that all the spectra can be analyzed with three slightly asymmetric doublets, which means that the sites occupied by Fe ions can be classified into three groups: the isomer shifts and the quadrupole splittings of ^{57}Fe on the sites in the same group resemble each other, but are distributed to some extent. The isomer shifts relative to Fe metal, the quadrupole splittings, and the relative intensities of the doublets for these three groups are listed in Table 1. We call these groups I, II, and III, according to the magnitude of the quadrupole splitting. The quadrupole splittings for the groups I and II are considerably large, and their isomer shifts are nearly zero. On the other hand, the

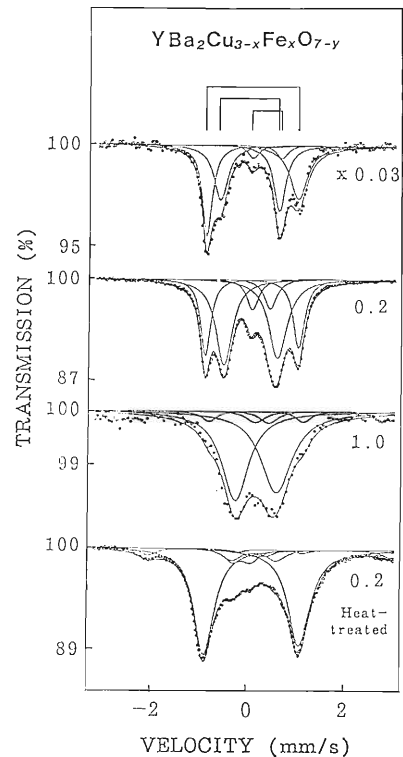


Fig. 1. Typical Mössbauer spectra of ^{57}Fe in $\text{YBa}_2\text{Cu}_{3-x}\text{Fe}_x\text{O}_{7-y}$ ($0.03 \leq x \leq 1.0$) at room temperature. The bottom one (d) shows the spectrum of a specimen ($x=0.2$) heat-treated at 550°C in vacuum for 20 h.

quadrupole splitting for the group III is small, and its isomer shift is near the one for Fe^{3+} on the octahedral sites in highly covalent oxides.⁴⁾ Apparently, these hyperfine parameters for these groups change little, but their relative intensities change systematically with the Fe content x . The population of Fe ions of each group per one chemical formula can be determined from the product of its relative intensities and the total Fe content x under the assumption that the recoilless fractions for these three groups are equal; the populations of the Fe ions of each group are shown in Fig. 2 as a function of x . In a small x region ($x \leq 0.1$), the populations of these groups increases with an increase in x . On the other hand, in the larger x region ($x > 0.1$), only the population of the group II increases with an increase in x , and the populations in the groups I and III remain nearly

Table 1. Mössbauer parameters for the three groups in $\text{YBa}_2\text{Cu}_{3-x}\text{Fe}_x\text{O}_{7-y}$ at room temperature. The isomer shift is relative to Fe metal.

x	IS (mm/s)			QS (mm/s)			Relative area			Other phase
	I	II	III	I	II	III	I	II	III	
0.03	+0.04	-0.03	+0.34	1.91	1.22	0.60	0.50	0.42	0.08	
0.1	+0.05	+0.01	+0.22	1.92	1.17	0.44	0.52	0.38	0.10	
0.2	+0.04	+0.02	+0.24	1.93	1.12	0.37	0.30	0.56	0.14	
0.3	+0.04	+0.03	+0.17	1.95	1.09	0.28	0.21	0.67	0.12	
0.4	+0.04	+0.04	+0.23	1.96	1.05	0.27	0.17	0.70	0.13	
0.5	+0.05	+0.05	+0.20	1.88	0.96	0.21	0.11	0.79	0.10	
1.0	+0.12	+0.12	+0.23	1.85	0.85	0.24	0.03	0.65	0.04	0.28
0.2*	+0.11	—	+0.21	1.95	—	0.21	0.70	0	0.04	0.26

* Heat-treated at 550°C in vacuum.

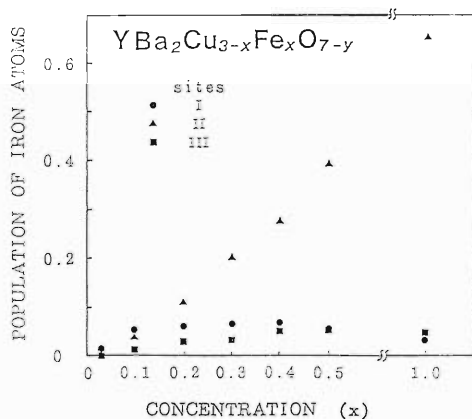


Fig. 2. Populations of the three Fe groups per one chemical formula as a function of the total Fe content x .

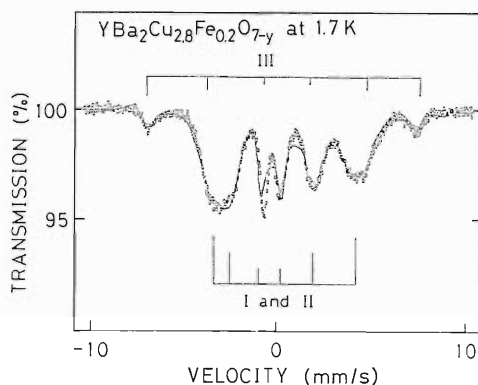


Fig. 3. Mössbauer spectra of ^{57}Fe in $\text{YBa}_2\text{Cu}_{2.8}\text{Fe}_{0.2}\text{O}_{7-y}$ at 1.7 K. S_1 is the difference between the first peak position and the second one, S_2 between the fifth and the sixth.

constant. Figure 3 shows the Mössbauer spectrum for the specimen with $x=0.2$ at 1.7 K. This spectrum can be ascribed to the superposition of two magnetically split sextets: The major one ($\approx 80\%$) has a distributed hyperfine magnetic field around 240 kOe, a quadrupole splitting parameter, S_1-S_2 (for the

definition, see Fig. 3), of about 1.48 mm/s and the isomer shift of 0.04 mm/s, and the minor one ($\approx 20\%$) has a hyperfine field of 442 kOe and the isomer shift of 0.26 mm/s. The quadrupole splitting of the latter is found to be small. From the values of the isomer shifts and the relative populations, the major sextet can be attributed to the ^{57}Fe of the groups I and II, and the minor sextet to that of the group III. Figure 1(d) shows the Mössbauer spectrum of the specimen with $x=0.2$ at room temperature obtained after a heat treatment at 550°C in vacuum for 20 h. The doublet for the group I remains almost unchanged. On the other hand, the intensities of the doublets for the other groups, especially for the group III, diminish drastically, and a magnetically split sextet ($H_{\text{hf}}=270$ kOe) appears in the spectrum.

The Fe ions are considered to occupy the Cu sites substitutionally. Thus, the chemical formula of this system can be written as $\text{YBa}_2(\text{Cu}_{1-\xi}\text{Fe}_\xi)[\text{Cu}_{1-\gamma}\text{Fe}_\gamma]_2\text{O}_{7-y}$. The ions denoted in () are on the 1a site which is the center of a plane formed by four O^{2-} ions, and those in [] are on the 2q site which is the center of the basal plane of a O^{2-} pyramid. In the present paper, we refer to the former sites as the planar sites and the latter as the pyramidal ones. It has been reported that the O^{2-} ions on the 1b sites neighboring the planar (1a) sites are partially removed by the above-mentioned heat-treatment in vacuum, but the O^{2-} ions neighboring the pyramidal (2q) sites are not affected.⁵⁾

Our explanation of the present results is as follows: Iron ions belonging to the group I, remaining after the heat treatment in vacuum, occupy the pyramidal sites, and those belonging to the group II occupy the planar sites, and those belonging to the group III, minor in population for any concentration x , occupy some octahedral sites.

There are two points to be noted. One relates to the hyperfine parameters for the groups I and II.

The isomer shifts and the hyperfine magnetic fields for these groups are remarkably smaller than Fe^{3+} or Fe^{4+} found in other oxides. This result means that the electronic states of the Fe ions of I and of II in this oxide are much different from those ordinarily realized in other oxides. We propose that the valence states of the Fe ions of these groups are the Fe^{5+} . The hyperfine parameters for the Fe^{5+} found in $(\text{Sr}, \text{Ca})\text{FeO}_{3-x}$ ($IS \simeq 0$ mm/s, and $H_{\text{hf}} \simeq 280$ kOe at low temperatures)⁶⁾ are relatively close to those in the present study. Another point is the occurrence of the magnetic order of the Fe ions occupying the Cu sites in this superconductor. In magnetic susceptibility measurements, the present specimen with $x=0.2$ shows a fairly sharp transition at $T_c = 53$ K. Whether the coexistence of magnetic order and superconduc-

tivity shown in the present study is intrinsic or due to an inhomogeneity of the specimen is not clear at present.

References

- 1) J.G. Bednorz and K.A. Müller: *Z. Phys. B*, **64**, 189 (1986).
- 2) M.K. Wu, J.R. Ashburn, C.J. Torng, P.H. Hor, R.L. Meng, L. Gao, Z.L. Huang, Y.Q. Wang, and C.W. Chu: *Phys. Rev. Lett.*, **58**, 908 (1987).
- 3) N. Sakai: *Hyperfine Interact.*, **42**, 1165 (1988).
- 4) K. Asai and H. Sekizawa: *J. Phys. Soc. Jpn.*, **49**, 90 (1980).
- 5) S. Izumi, H. Asano, T. Ishigaki, E. Takayama-Muramachi, Y. Uchida, N. Watanabe, and T. Nishikawa: *Jpn. J. Appl. Phys.*, **26**, L649 (1987).
- 6) M. Takano, N. Nakanishi, Y. Takeda, S. Naka, and T. Takeda: *Mater. Res. Bull.*, **12**, 923 (1977).

II-2-31. Emission Mössbauer Study of ^{119}Sb Ions Adsorbed on Ferrimagnetic Fe_3O_4 Surfaces

T. Okada, S. Ambe, F. Ambe, and H. Sekizawa*

Application of emission Mössbauer spectroscopy to the study of the chemical states of ions adsorbed on the surfaces of ferrites has been proved to be very useful.¹⁻³⁾ In these studies the so-called “no-carrier-added” parent nuclide ions are hydrolytically adsorbed onto the surfaces of powdered magnetic oxides, and the γ -rays emitted by the daughter Mössbauer nuclide ions are collected to be analyzed. The ionic states of the ions are reflected in the resulting Mössbauer spectrum through the hyperfine magnetic and electric fields acting on the corresponding nuclei of the ions.

We have been studying the ionic states of $^{119}\text{Sb}^{5+}$ ions hydrolytically adsorbed on the surfaces of various ferrimagnetic spinel type oxides such as $\gamma\text{-Fe}_2\text{O}_3$, NiFe_2O_4 , and CuFe_2O_4 . In this paper we report the temperature dependence of the “as adsorbed” ionic states of ^{119}Sb ions hydrolytically adsorbed on the surfaces of Fe_3O_4 by means of emission Mössbauer analysis of the daughter nuclide.

Experimental procedures were described in previous reports.¹⁻³⁾ The source nuclide ^{119}Sb was produced by the cyclotron. No-carrier-added $^{119}\text{Sb}^{5+}$ ions were hydrolytically adsorbed on the surfaces of the ferrimagnetic spinel oxide powders of Fe_3O_4 , the Néel temperature of which is about 575°C . The powders were filtered out and dried in vacuum over P_2O_5 . Emission Mössbauer analysis was applied to the daughter nuclide $^{119\text{m}}\text{Sn}$ arising from $^{119}\text{Sb}^{5+}$ by means of a conventional spectrometer in absorber-drive mode with a BaSnO_3 absorber at room temperature.

The Mössbauer spectra of $^{119}\text{Sb}^{5+} (\rightarrow ^{119}\text{Sn})$ ions hydrolytically adsorbed on the surfaces of the ferrimagnetic oxide powders of Fe_3O_4 measured at room temperature and liquid nitrogen temperature are shown in Figs. 1(B) and (C), respectively, along with the computer-fitted curves. The upper reference spectrum shown in Fig. 1(A) is that of Cr_2O_3 taken at room temperature, which is characteristic of diamagnetic Sn ions on a material with a negligibly small hyperfine magnetic field and also a negligibly small electric field gradient. It is noteworthy that no sharp central peak due to ^{119}Sn in the absence of a magnetic field (the so-called “para- or diamagnetic peak” with a width of about 1.0 mm/s) was observed in the spectra of Fig. 1(B) and (C). From the

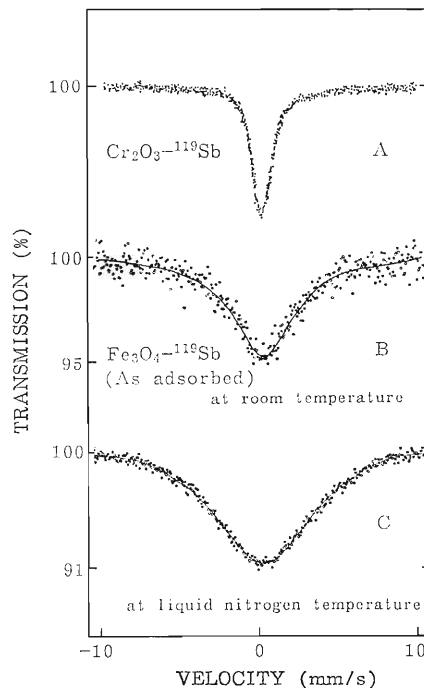


Fig. 1. (A) Mössbauer spectrum of $\text{Cr}_2\text{O}_3\text{-}^{119}\text{Sb}$ at room temperature. (B) Mössbauer spectrum of “as adsorbed” $\text{Fe}_3\text{O}_4\text{-}^{119}\text{Sb}$ at room temperature, and (C) at liquid nitrogen temperature.

values of the isomer shift ($0.0 \pm 0.3\text{ mm/s}$ relative to BaSnO_3), it is certain that the ^{119}Sn ions resulting from the adsorbed ^{119}Sb ions are tetravalent. As can be seen from Fig. 1, even in the “as adsorbed” specimen the emission line is considerably broadened compared with that of diamagnetic $^{119}\text{Sn}^{4+}$ ions. We attribute the origin of the broadening to the STHF magnetic interactions of the $^{119}\text{Sn}^{4+} (\leftarrow ^{119}\text{Sb}^{5+})$ ions with the magnetically ordered Fe^{3+} and Fe^{2+} ions in the Fe_3O_4 substrates. The distribution of the hyperfine magnetic field (H_{hf}) was computed by analyzing the spectra by means of Hesse-Rübartsch method,⁴⁾ and the obtained distribution function $P(H)$ of the hyperfine magnetic field H_{hf} is shown in Fig. 2.

In ferrimagnetic Fe_3O_4 with a spinel structure, the tetrahedral (A) sites are occupied by the Fe^{3+} ions, and the octahedral (B) sites by Fe^{3+} , Fe^{2+} , and Sb^{5+} ions. There are the $\text{Fe}^{3+}(\text{A})\text{-O-Sb}^{5+}(\text{B})$ pathways in this structure, where O is an oxygen anion. The

* Chiba Institute of Technology.

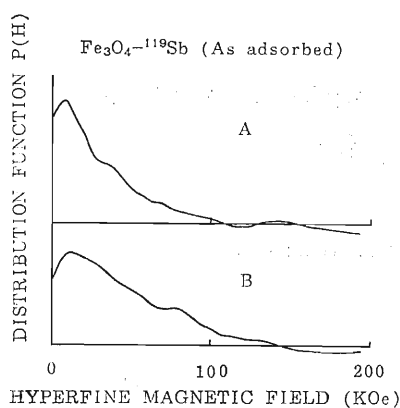


Fig. 2. (A) Distribution function $P(H)$ of the hyperfine magnetic fields of "as adsorbed" $\text{Fe}_3\text{O}_4\text{-}^{119}\text{Sb}$ at room temperature and (B) at liquid-nitrogen temperature.

magnetic hyperfine fields observed at diamagnetic nuclei, $^{119}\text{Sn}^{4+}(\leftarrow^{119}\text{Sb}^{5+})$ in Fe_3O_4 and other spinel ferrites, are supertransferred hyperfine fields, which arise as a result of the transfer of electronic spin density from the magnetic nearest neighbors (the Fe ions). This STHF interaction between Fe^{3+} (A) and Sb^{5+} (B) ions can be divided into two processes. The first is the polarization of the ligand electrons of O^{2-} ions by the 3d electrons of the Fe^{3+} (A) ions, and the second is the polarization of s electrons of the Sb^{5+} (B) ions by these ligand electrons. These two processes are caused by the overlap and the transfer mechanisms in the relevant chemical bonds (Fe^{3+} (A)- O^{2-} for the first process, O^{2-} - Sb^{5+} (B) for the second), and it is known that the magnitude of the total STHF interaction increases with an increase in the covalency of either bond.

Indices of dominant free crystal surfaces of powdered Fe_3O_4 is unsettled yet, but (111) seems to be the most plausible one. Thus, the description of the spinel type crystal structure based on an image of alternative stacking of (111) oxygen layers and metal layers given by Iida⁵⁾ seems suitable for our purpose. According to this model, various types of adsorbed $^{119}\text{Sb}^{5+}$ ions can be discriminated. The distribution of the hyperfine magnetic fields at the $^{119}\text{Sb}^{5+}$ ions is being analyzed on the basis of this model. Establishment of a conclusive model which can explain all the experimental findings for Fe_3O_4 and other various ferrites is in progress.

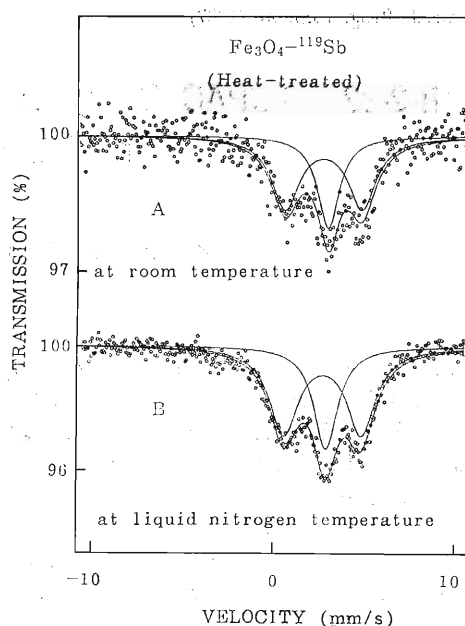


Fig. 3. (A) Mössbauer spectra of $\text{Fe}_3\text{O}_4\text{-}^{119}\text{Sb}$ heat-treated at $1,100^\circ\text{C}$ for 2 h in soft vacuum and measured at room temperature, and (B) at liquid-nitrogen temperature.

The Mössbauer spectra of a $\text{Fe}_3\text{O}_4\text{-}^{119}\text{Sb}$ specimen heat-treated at $1,100^\circ\text{C}$ for 2 h in soft vacuum are taken at room temperature and liquid nitrogen temperature; the results are shown in Fig. 3. The spectra consist of a singlet and a doublet. The singlet has a large positive value of isomer shift. The doublet has a large quadrupole splitting, and a large positive value of isomer shift. From isomer shift ($+2.8$ mm/s) determined by analyzing the spectra, the valence state of the Sn ions in heat-treated Fe_3O_4 is concluded to be divalent.

The full accounts of the results on a group of similar materials such as $\gamma\text{-Fe}_2\text{O}_3$, NiFe_2O_4 , and CuFe_2O_4 , along with the results on the effect of heat-treatment after adsorption, will be published.

References

- 1) T. Okada, S. Ambe, F. Ambe, and H. Sekizawa: *J. Phys. Chem.*, **86**, 4726 (1982).
- 2) F. Ambe, T. Okada, S. Ambe, and H. Sekizawa: *J. Phys. Chem.*, **88**, 3015 (1984).
- 3) F. Ambe, S. Ambe, T. Okada, and H. Sekizawa: *ACS Symp. Ser.*, **86**, 403 (1986).
- 4) J. Hesse and A. Rübartsch: *J. Phys. E*, **7**, 526 (1974).
- 5) S. Iida: *J. Phys. Soc. Jpn.*, **12**, 222 (1957).

III-2-32. TDPAC Study of Hyperfine Interactions at $^{111}\text{Cd}(\leftarrow^{111}\text{In})$ in $\text{Li}_{0.5}\text{Fe}_{2.5}\text{O}_4$ Single Crystal

K. Asai, T. Okada, T. Yamadaya, and H. Sekizawa

We have been systematically investigating the supertransferred hyperfine (STHF) magnetic field, H_{STHF} , at $^{111}\text{Cd}^{2+}$ in ferrimagnetic oxides with the spinel structure by means of the time differential perturbed angular correlation (TDPAC) of 171–245 keV cascade γ -rays emitted from $^{111}\text{Cd}(\leftarrow^{111}\text{In})$.^{1,2)} In the spinel oxides, the parent nuclei ^{111}In occupy the A (tetrahedral) sites [denoted by $^{111}\text{In}(\text{A})$], and the daughter nuclei $^{111}\text{Cd}(\text{A})$ feel H_{STHF} transferred from the magnetic ions on the nearest neighbor B (octahedral) sites. In a previous study on the system $\text{M}_x\text{Fe}_{3-x}\text{O}_4$ ($\text{M}=\text{Ni}$ or Co ; $0.0 \leq x \leq 1.0$),²⁾ we clarified the contributions of individual B site ions to the H_{STHF} 's. Their magnitudes are 11.0 and 8.0 kOe for $\text{Fe}^{3+}(\text{B})$ and $\text{Fe}^{2+}(\text{B})$ ions, respectively, and about 4 kOe both for $\text{Co}^{2+}(\text{B})$ and for $\text{Ni}^{2+}(\text{B})$ ions at room temperature.

This year, we studied H_{STHF} at $^{111}\text{Cd}^{2+}(\text{A})$ in lithium ferrite. This ferrite is a completely inverted spinel ($\text{Fe}^{3+})_{\text{A}}[\text{Li}_{0.5}^{1+}\text{Fe}_{1.5}^{3+}]_{\text{B}}\text{O}_4$, in which $\text{Li}^{1+}(\text{B})$ and $\text{Fe}^{3+}(\text{B})$ ions form an ionic order in the B sites.³⁾ It should be noted that this ferrite has the highest Curie temperature ($T_c=943$ K) among all the spinel ferrites,³⁾ although one fourth of the B sites are occupied by diamagnetic ions $\text{Li}^{1+}(\text{B})$. An aim of the present study is to clarify the mechanism producing the high T_c of this ferrite.

The probe nuclei $^{111}\text{Cd}^{2+}(\text{A})$ in this ferrite feel an axially-symmetric electric field gradient (EFG) in addition to H_{STHF} because of the trigonal symmetry of the A sites of this ferrite. When EFG coexists with the hyperfine magnetic field H_{hyp} , there are, generally, unavoidable ambiguities in the analysis of the TDPAC spectra for polycrystalline samples. (The field H_{hyp} includes both the field H_{STHF} and the external field H_{ext} .) Thus, we measured the TDPAC spectra of ^{111}Cd in the single crystals.

We carried out measurements at room temperature in a magnetic field, H_{ext} , of 10 kOe applied perpendicularly to the detectors plane in order to polarize the magnetization of the specimens completely in this direction. We define the normalized anisotropy, $R(t)$, of the angular correlation $N(\theta, t)$ by

$$R(t) = \frac{[N(-3\pi/4, t) - N(+3\pi/4, t)]}{[N(-3\pi/4, t) + N(+3\pi/4, t)]}$$

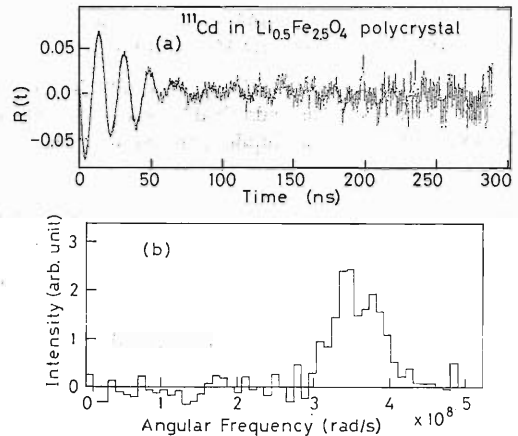


Fig. 1. (a) Normalized anisotropy $R(t)$ of the angular correlation of γ -rays emitted from $^{111}\text{Cd}(\leftarrow^{111}\text{In})$ in polycrystalline $\text{Li}_{0.5}\text{Fe}_{2.5}\text{O}_4$ at room temperature. The solid curve is the fitted one with the Fourier spectrum shown in (b). (b) The Fourier spectrum of $R(t)$.

where θ and t are the angle and the time interval between the cascade γ -rays. The Fourier component of $R(t)$ corresponds to the twice of the Larmor frequency unless EFG exists.

The anisotropy $R(t)$ for polycrystalline $\text{Li}_{0.5}\text{Fe}_{2.5}\text{O}_4$ and its Fourier spectrum are shown in Figs. 1(a) and 1(b), respectively, in which the Fourier spectrum has a considerably broad intensity distribution around 3.5×10^8 rad/s. However, we could not determine whether this distribution is caused by a distribution of H_{hyp} , or otherwise caused by an EFG coexisting with H_{hyp} .

The anisotropies $R(t)$ for single crystalline $\text{Li}_{0.5}\text{Fe}_{2.5}\text{O}_4$ measured in two different geometries are shown in Figs. 2(a) and 2(b): (a) in the one geometry with $[111] \parallel H_{\text{ext}}$ and $[11\bar{1}]$ in the x - z plane, and (b) in the other geometry with $[100] \parallel H_{\text{ext}}$ and $[111]$ in the x - z plane. Here, the x - and z -axes are defined by the directions of the first γ -ray (171 keV) and H_{ext} , respectively. A remarkable difference between these two spectra indicates that an appreciable magnitude of EFG acts on $^{111}\text{Cd}^{2+}(\text{A})$ in addition to the hyperfine magnetic field H_{hyp} .

We derived an explicit expression of $R(t)$ for the intermediate state ($5/2+$) of ^{111}Cd under $H_{\text{hyp}} (\parallel z)$, combined with an axially-symmetric EFG, and then

analyzed the observed spectra in Figs. 2(a) and 2(b) using this expression. Both spectra are reproduced well with a common set of the Larmor frequency and the quadrupolar frequency, and with the orientations of the principal axes of EFG expected from the crystalline geometries. The fitted curves and their Fourier spectra are shown in Figs. 2 and 3, respectively. The derived H_{hyp} is 122 kOe parallel to H_{ext} , and the magnitude of EFG is 90×10^{13} esu. The fairly large widths of the Fourier components are

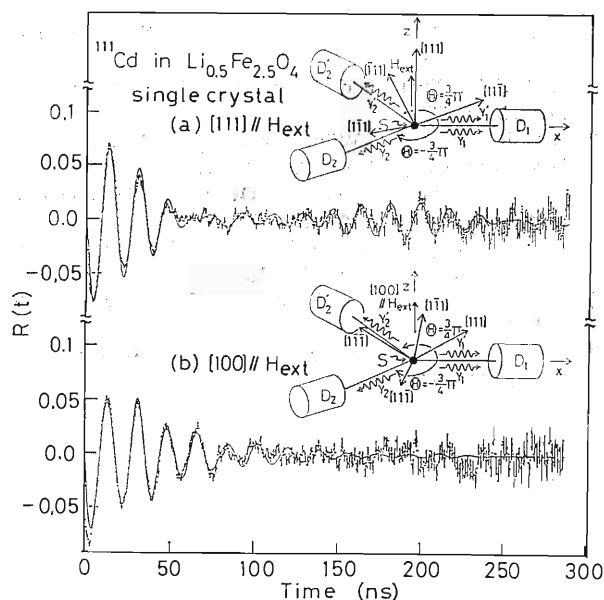


Fig. 2. Normalized anisotropies, $R(t)$, of the angular correlations of γ rays emitted from $^{111}\text{Cd} (\leftarrow ^{111}\text{In})$ in a single crystalline $\text{Li}_{0.5}\text{Fe}_{2.5}\text{O}_4$ at room temperature. The solid curves are the fitted ones with the Fourier spectra shown in Fig. 3. Geometries of the single crystal, detectors, and the externally applied magnetic field are shown in the insets: (a) $[111] // H_{\text{ext}}$ and $[11\bar{1}]$ in the x - z plane; (b) $[100] // H_{\text{ext}}$ and $[111]$ in the x - z plane.

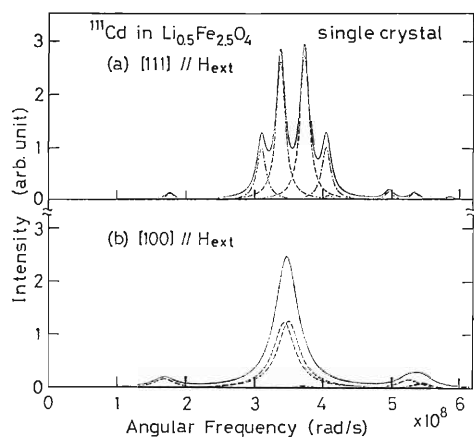


Fig. 3. Fourier spectra of $R(t)$ for a single crystalline $\text{Li}_{0.5}\text{Fe}_{2.5}\text{O}_4$ at room temperature. Dotted lines represent individual Fourier components and solid lines the total of them: (a) $[111] // H_{\text{ext}}$ and $[11\bar{1}]$ in the x - z plane; (b) $[100] // H_{\text{ext}}$ and $[111]$ in the x - z plane.

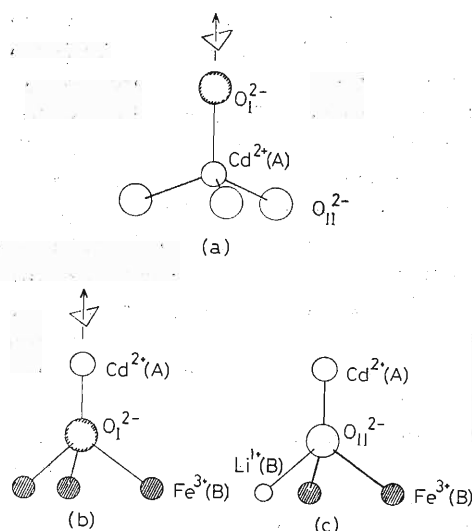


Fig. 4. Local ionic configurations of $\text{Li}_{0.5}\text{Fe}_{2.5}\text{O}_4$: (a) O^{2-} ions around $\text{Cd}^{2+}(\text{A})$. The trigonal axis lies along $\text{Cd}^{2+}(\text{A}) - \text{O}_1^{2-}$ bond. (b) Cations around O_1^{2-} ions. (c) Cations around O_{11}^{2-} ions.

ascribed to the after-effects of the EC decay of $^{111}\text{In} \rightarrow ^{111}\text{Cd}$.⁴⁾

The field H_{STHF} then derived is 112 kOe. Figure 4 shows the ionic configurations in $\text{Li}_{0.5}\text{Fe}_{2.5}\text{O}_4$. The probe ion $^{111}\text{Cd}^{2+}(\text{A})$ is surrounded by four O^{2-} ions of two kinds denoted by O_1^{2-} and O_{11}^{2-} ; through O_1^{2-} ion, three $\text{Fe}^{3+}(\text{B})$ ions are linked to the $\text{Cd}^{2+}(\text{A})$; on the contrary through O_{11}^{2-} ion, two $\text{Fe}^{3+}(\text{B})$ and one $\text{Li}^{1+}(\text{B})$ ions are linked. Thus, the magnitude of the field from one $\text{Fe}^{3+}(\text{B})$ ion through O_1^{2-} or O_{11}^{2-} [denoted by $h(\leftarrow \text{Fe}^{3+})$] is 12.4 kOe on average.

The value of 12.4 kOe for $\text{Li}_{0.5}\text{Fe}_{2.5}\text{O}_4$ is more than 10% larger than the one (11.0 kOe) reported for $\text{M}_x\text{Fe}_{3-x}\text{O}_4$ ($\text{M} = \text{Ni}$ or Co) system.²⁾ By comparing crystallographic parameters of $\text{Li}_{0.5}\text{Fe}_{2.5}\text{O}_4$ and $\text{M}_x\text{Fe}_{3-x}\text{O}_4$, it is concluded that this large value of $h(\leftarrow \text{Fe}^{3+})$ in the former as compared with that in the latter system cannot be explained by the difference of either the lattice constants or the oxygen (u) parameters between them,^{3,5)} but should be attributed to the presence of $\text{Li}^{1+}(\text{B})$ in the former. Then, we consider the influence of $\text{Li}^{1+}(\text{B})$ to the STHF interactions between $\text{Cd}^{2+}(\text{A})$ and $\text{Fe}^{3+}(\text{B})$ in $\text{Li}_{0.5}\text{Fe}_{2.5}\text{O}_4$.

The electronegativities of Li^{1+} and 3d transition metal ions are listed in Table 1.⁶⁾ The electronegativity of Li^{1+} ions is markedly smaller than those of 3d transition metal ions. In $\text{Li}_{0.5}\text{Fe}_{2.5}\text{O}_4$, it will occur as a result of this smaller electronegativity of

Table 1. Electronegativities of Li and some 3d transition metal ions.⁶⁾

Ion	Li^{1+}	Fe^{2+}	Fe^{3+}	Co^{2+}	Ni^{2+}
Electronegativity	0.95	1.7	1.8	1.7	1.7

$\text{Li}^{1+}(\text{B})$ that the ligand electrons of $\text{O}_{\text{II}}^{2-}$ are polarized towards the $\text{Cd}^{2+}(\text{A})$ and the two $\text{Fe}^{3+}(\text{B})$ ions to some extent since the electrons are less attracted towards the $\text{Li}^{1+}(\text{B})$. Therefore, the covalencies of the chemical bonds $\text{Cd}^{2+}(\text{A})-\text{O}_{\text{II}}^{2-}$ and $\text{Fe}^{3+}(\text{B})-\text{O}_{\text{II}}^{2-}$ are expected to be larger than the corresponding bonds with no adjacent $\text{Li}^{1+}(\text{B})$ in $\text{Li}_{0.5}\text{Fe}_{2.5}\text{O}_4$ or in other ferrites. This influence of the $\text{Li}^{1+}(\text{B})$ ion on the neighboring bonds is expected also from the extended electrostatic valence principle.⁷⁾ It holds generally in ionic crystals that the STHF interaction between the cations increases with an increase in the covalency of the chemical bond connecting these cations through the intervening oxygen ion. Thus, we conclude $h(\leftarrow\text{Fe}^{3+})$ through $\text{O}_{\text{II}}^{2-}$ is enhanced by the neighboring $\text{Li}^{1+}(\text{B})$. If we assume that $h(\leftarrow\text{Fe}^{3+})$ through O_{I}^{2-} is 11.0 kOe as in $\text{M}_x\text{Fe}_{3-x}\text{O}_4$, $h(\leftarrow\text{Fe}^{3+})$ through $\text{O}_{\text{II}}^{2-}$ must be 13.3 kOe, about 20% larger than the former.

The markedly large axially-symmetric EFG observed at $\text{Cd}^{2+}(\text{A})$ in $\text{Li}_{0.5}\text{Fe}_{2.5}\text{O}_4$ is explained as a result of the difference in the covalency between one $\text{Cd}^{2+}(\text{A})-\text{O}_{\text{I}}^{2-}$ and three $\text{Cd}^{2+}(\text{A})-\text{O}_{\text{II}}^{2-}$ bonds around $\text{Cd}^{2+}(\text{A})$ in this crystal [see Fig. 4(a)].

The STHF and superexchange interactions have noticeable similarity: Both increase with an increase in the covalency of the relevant chemical bond. The superexchange interactions between $\text{Fe}^{3+}(\text{A})$ and $\text{Fe}^{3+}(\text{B})$ through $\text{O}_{\text{II}}^{2-}$ must be enhanced by the presence of the neighboring $\text{Li}^{1+}(\text{B})$ ions. This enhancement of the superexchange interactions by $\text{Li}^{1+}(\text{B})$ is considered to be an origin of the high T_c of $\text{Li}_{0.5}\text{Fe}_{2.5}\text{O}_4$.

References

- 1) K. Asai, T. Okada, and H. Sekizawa: *J. Phys. Soc. Jpn.*, **54**, 4325 (1985).
- 2) K. Asai, T. Okada, and H. Sekizawa: *Hyperfine Interact.*, **34**, 435 (1987).
- 3) J. Smit and H. P. J. Wijn: *Ferrites*, John Wiley & Sons, New York, Chap. 8, pp. 136-175 (1959).
- 4) K. Asai, F. Ambe, S. Ambe, T. Okada, and H. Sekizawa: *Hyperfine Interact.*, **34**, 277 (1987).
- 5) The oxygen positions are described well by the oxygen parameter u even in $\text{Li}_{0.5}\text{Fe}_{2.5}\text{O}_4$.
- 6) W. Gordy and W. J. O. Thomas: *J. Chem. Phys.*, **24**, 439 (1956).
- 7) I. D. Brown and R. D. Shannon: *Acta Crystallogr. Sect. A*, **29**, 266 (1973).

III-2-33. Surface Structure of Krypton-Implanted Aluminum

I. Hashimoto,* H. Yamaguchi,* E. Yagi, and M. Iwaki

Extensive experimental information on the evolution of surface structure of metals due to implantation of gas ions has been accumulated in the last decade. Especially, a great number of data have been obtained on implantation of light ions (H and He) in solids and summarized, for example, in a review paper by Scherzer.¹⁾ The study on implantation of heavy ions has been made also for neon, argon, krypton, and xenon in various metals.²⁻⁸⁾

We have studied recently the thermal extraction of krypton atoms from krypton-implanted aluminum by a constant rate heating method and shown that krypton atoms are extracted in the temperature range from 540 to 1,100 K.⁹⁾ It is to be noted that no detectable amount of krypton atoms was extracted below 540 K. We have also determined that the diffusion coefficients of krypton in aluminum obtained by the extraction experiment are between 10^{-15} and 10^{-14} cm²/s in the temperature range from 713 to 813 K.⁹⁾ Furthermore, as already pointed out in a previous paper,¹⁰⁾ the implanted krypton atoms form solid bubbles. These bubbles are stable at temperatures lower than 618 K and melt at about 620 K. These results indicate that the structural changes of implanted specimen would have occurred during annealing. It is thus interesting to observe the change of an implanted surface during annealing.

In the present study, we examined the surface-structure change of krypton-implanted aluminum by means of scanning electron microscopy (SEM).

The material used was single crystal aluminum foils of 99.99% purity, grown by a strain annealing procedure. Specimens suitable for electron microscopy were prepared by conventional chemical- and electrolytical-polishing and implanted at an energy of 50 keV with a dose of 10^{16} ions/cm².

To examine the effect of annealing on the implanted surface, we carried out SEM observation after annealing at various temperatures for 10 min outside the electron microscope. The results are shown in Figs. 1(a)–(f) and the features observed after each annealing are as follows.

Some circular fractures on the surface are observed at 723 K (Fig. 1(a)). In addition, small irregular shaped surface pits are observed as shown by small

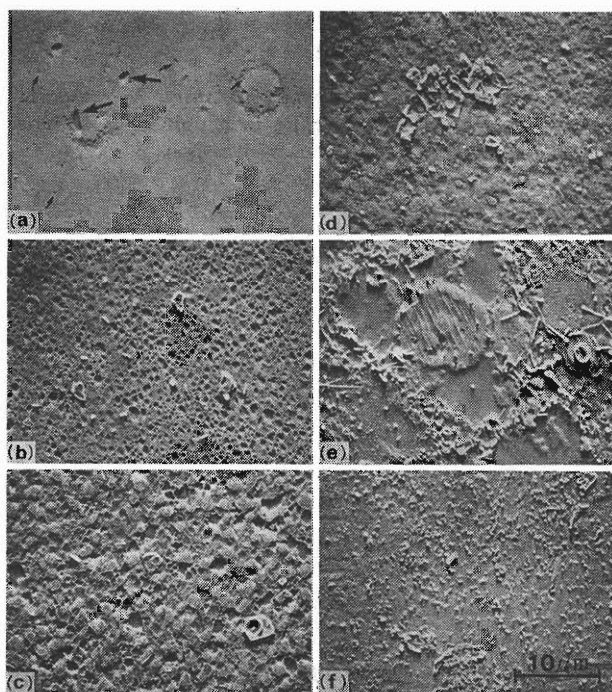


Fig. 1. Surface features after annealing at various temperatures for 10 min outside an electron microscope. (a), 723 K; (b), 748 K; (c), 773 K; (d), 873 K; (e), 923 K; (f), 933 K. Small and large arrows in (a) show surface pits and blister craters, respectively.

arrows, and larger and deeper holes (blister craters) are shown by large arrows. Between 723 and 823 K, the change of the surface structure occurs abruptly. The number of blister craters (observed as images with a large black contrast in Fig. 1(b)) increases rapidly at 748 K, and the whole area is covered with spongy structures (observed as a white contrast containing small black spots). Blister craters and some flakes are observed at 773 K (Fig. 1(c)). Size distributions of spongy structures and blister craters at several annealing temperatures are shown in Figs. 2(a), 2(b), and 3, respectively. Here, although the spongy structures and the blister craters have irregular shape, their diameters are estimated by assuming that they are equal to those of circles having the same area. On the basis of the difference between Figs. 2(a) and 2(b), it can be concluded that smaller sponges disappear more rapidly than larger ones with increasing temperature. From Fig. 3, the size distributions of the blister craters change markedly be-

* Department of Physics, Faculty of Science, Science University of Toyko.

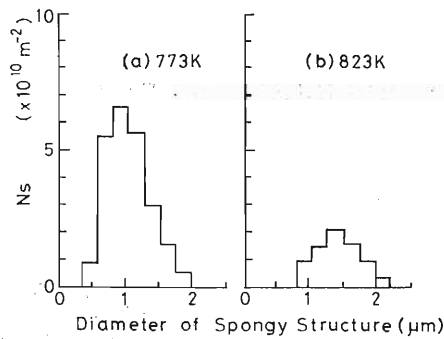


Fig. 2. Size distributions of spongy structures. N_s shows the number of the spongy structure in a unit area. It is to be noted that the smaller ones disappear more rapidly than the larger ones.

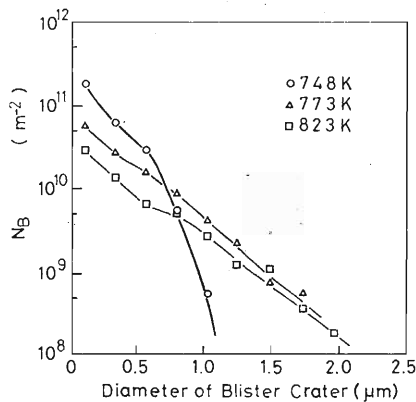


Fig. 3. Size distributions of blister craters. N_B in logarithmic scale shows the number of the blister craters in a unit area. The number of small ones decreases rapidly during annealing, while that of large ones increases.

tween 748 and 773 K, and smaller ones decrease with increasing temperature, while larger ones increase. It is to be noted that the surface covered with the spongy structures and with the blister craters peel off from the specimen at 823 K and a flatter surface appears at 873 K (Fig. 1(d)).

When temperature rises above 873 K, a marked structural change occurs again on the specimen surface.

In this case, the driving force for the fracture formation would be given by bubbles having very high pressure owing to the high temperature annealing.

After annealing at 923 K, the same types of defects shown in Figs. 1(a), (b), and (c) are observed again together with new fine blisters and needle-shaped structures as shown in Fig. 1(e). The formation of the needles is considered to occur by the curling of remaining flakes or by remaining blister boundaries.

Finally, after annealing at 933 K, the specimen which was partially melting was examined. Large fractures are almost eliminated, while there remain some small blisters (Fig. 1(f)). This result shows that even above the melting point of aluminum some of krypton atoms remain in an aluminum matrix; this result is consistent with the result reported in a previous paper.⁹⁾ More detailed descriptions on these phenomena are given in Ref. 11.

References

- 1) B. M. U. Scherzer: *Top. Appl. Phys.*, **52**, 271 (1983).
- 2) N. Marachov and P. J. Goodhew: *Radiat. Eff. Lett.*, **85**, 61 (1984).
- 3) R. J. Cox, P. J. Goodhew, and J. H. Evans: *J. Nucl. Mater.*, **126**, 117 (1984).
- 4) A. vom Felde, J. Fink, Th. Müller-Heinzerling, J. Pflüger, B. Scheerer, G. Linker, and D. Kaletta: *Phys. Rev. Lett.*, **53**, 922 (1984).
- 5) D. J. Mazey and J. H. Evans: *J. Nucl. Mater.*, **138**, 16 (1986).
- 6) P. Lukac and V. Jesenak: *Phys. Status Solidi A*, **55**, 647 (1979).
- 7) R. C. Birtcher and W. Jäger: *Nucl. Instrum. Methods Phys. Res. B*, **15**, 435 (1986).
- 8) R. C. Birtcher and W. Jäger: *J. Nucl. Mater.*, **135**, 274 (1985).
- 9) K. Takaishi, T. Kikuchi, K. Furuya, I. Hashimoto, H. Yamaguchi, E. Yagi, and M. Iwaki: *Phys. Status Solidi A*, **95**, 135 (1986).
- 10) I. Hashimoto, H. Yorikawa, H. Mitsuya, H. Yamaguchi, K. Takaishi, T. Kikuchi, K. Furuya, E. Yagi, and M. Iwaki: *J. Nucl. Mater.*, **149**, 69 (1987).
- 11) I. Hashimoto, H. Yorikawa, H. Mitsuya, H. Yamaguchi, K. Furuya, E. Yagi, and M. Iwaki: *J. Nucl. Mater.*, **150**, 100 (1987).

III-2-34. Lattice Location Study on Krypton Atoms in Aluminum by Means of a Channeling Method

E. Yagi, K. Tanaka, and M. Iwaki

Recently it has been demonstrated that the heavier inert gases (Ar, Kr, and Xe) precipitate in bubbles at ambient temperature into a solid phase epitaxially with a host matrix.^{1,2)} Such behavior of inert gas atoms has been investigated mostly by electron microscopy. In the present study, this effect was investigated more microscopically on Kr-implanted Al by use of an ion channeling method.

The specimens used were Al single-crystal slice of 99.999% purity. They were chemically and electrolytically polished and then annealed at 10^{-6} Torr at 823 K for 7 h. The Kr⁺-implantation was carried out at room temperature and at 50 keV at a dose rate of $3.2 \times 10^{12}/\text{cm}^2 \text{ s}$ to two different doses, $1 \times 10^{15}/\text{cm}^2$ and $1 \times 10^{16}/\text{cm}^2$. To study the lattice location of implanted Kr atoms, we investigated the axial channeling effect at room temperature with respect to $\langle 100 \rangle$, $\langle 110 \rangle$, and $\langle 111 \rangle$ axes by means of backscattering with a 1 MeV He⁺ beam accelerated by a tandem accelerator. Channeling angular profiles for the as-implanted specimens are shown in Fig. 1.

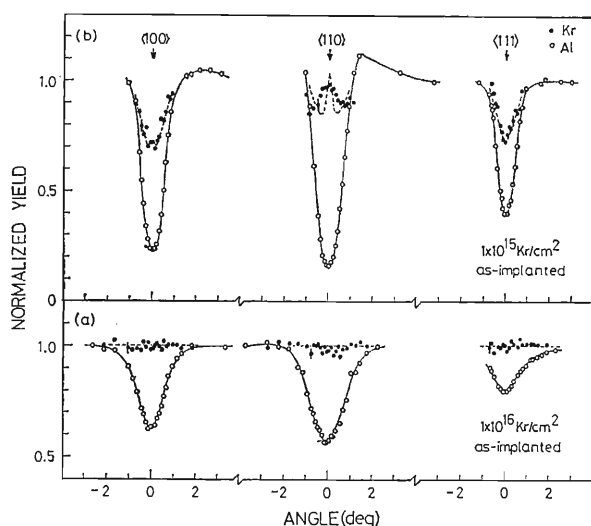


Fig. 1. Channeling angular profiles of backscattering yields of He ions from Al and implanted Kr atoms on the as-implanted specimens for (a) $1 \times 10^{16} \text{ Kr}/\text{cm}^2$ and (b) $1 \times 10^{15} \text{ Kr}/\text{cm}^2$ implantations. The dotted curves are calculated ones for the distribution with (a) 100% of Kr atoms at random sites and (b) 57% of Kr atoms at random sites, 23% at substitutional sites, 3% at tetrahedral sites, and 17% at octahedral sites.

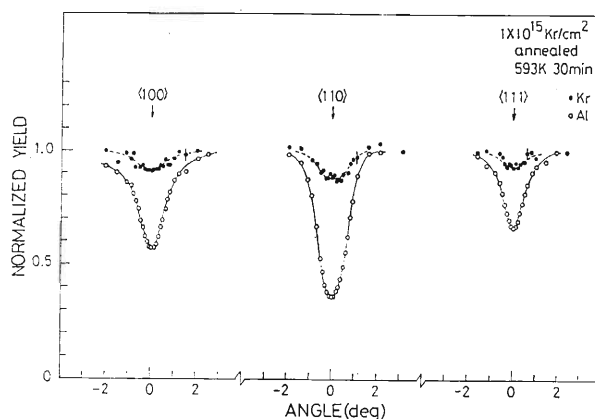


Fig. 2. Channeling angular profiles for a specimen implanted with a dose of $1 \times 10^{15} \text{ Kr}/\text{cm}^2$ and annealed at 593 K for 30 min. The dotted curves are calculated ones for the distribution with 80% of Kr atoms at random sites and 20% at substitutional sites.

For the $1 \times 10^{15} \text{ Kr}/\text{cm}^2$ implantation, post-implantation annealing was carried out at 593 K for 30 min; the result is shown in Fig. 2.

For the $1 \times 10^{16} \text{ Kr}/\text{cm}^2$ implantation, the normalized scattering yields from Kr atoms (Kr-yields) were the same independent of the incident angle for the $\langle 100 \rangle$, $\langle 110 \rangle$, and $\langle 111 \rangle$ channels, indicating that most of the Kr atoms are located at random (R) sites, *i.e.* in the form of precipitates. Studies by electron microscopy revealed that the precipitates are in the solid phase epitaxial with a host Al crystal to have an fcc structure with a lattice constant of 0.534 nm, which is larger by 30% than that of the Al crystal.³⁾

For the $1 \times 10^{15} \text{ Kr}/\text{cm}^2$ implantation, the $\langle 100 \rangle$ and $\langle 111 \rangle$ channeling angular profiles of Kr-yield on the as-implanted specimen exhibited a shallow dip with a half width approximately the same as that of the corresponding Al-profile. On the $\langle 100 \rangle$ Kr-profile a small central peak was superposed. The $\langle 110 \rangle$ Kr-profile consisted of a large central peak and a wide shallow dip. The fractions of Kr atoms at various sites were estimated by fitting the calculated angular profiles to the observed ones. The observed profiles were well fitted by a distribution with 55–57% of the Kr atoms at R-sites, 23–25% at substitutional (S) sites, 3–5% at tetrahedral (T)

sites, and 15–17% at octahedral (O) sites. Examples of calculated profiles are indicated by dotted curves in Fig. 1. Figure 2 shows that, upon annealing, the fine structures in the Kr-profiles disappear and a simple shallow dip with the same half-width as the corresponding Al-dip is observed for the $\langle 100 \rangle$, $\langle 110 \rangle$, and $\langle 111 \rangle$ channels. This result indicates that the T- and O-site occupancies have disappeared and that the Kr atoms are located at R- and S-sites. The observed profiles were well fitted with calculated ones for the distribution with 80% of Kr atoms at R-sites and 20% at S-sites (dotted curves in Fig. 2). Therefore, the T- and O-site occupancies are interpreted as a result of the strong interaction of Kr atoms with vacancies introduced by Kr implantation to form Kr-vacancy complexes

having configurations similar to those of a trivacancy and a pentavacancy.

More detailed descriptions are given in Refs. 4 and 5.

References

- 1) A. vom Felde, J. Fink, Th. Müller-Herzering, J. Pflüger, B. Scheerer, G. Linker, and D. Kaletta: *Phys. Rev. Lett.*, **53**, 922 (1984).
- 2) C. Templier, C. Jaouen, J.-P. Rivière, J. Delafond, and J. Grilhè: *C. R. Acad. Sci. Paris*, **299**, 613 (1984).
- 3) I. Hashimoto, H. Yorikawa, H. Mitsuya, H. Yamaguchi, K. Takaishi, T. Kikuchi, K. Furuya, E. Yagi, and M. Iwaki: *J. Nucl. Mater.*, **149**, 69 (1987).
- 4) E. Yagi: *Phys. Status Solidi A*, **104**, K13 (1987).
- 5) E. Yagi, M. Iwaki, K. Tanaka, I. Hashimoto, and H. Yamaguchi: *Nucl. Instrum. Methods Phys. Res. B*, in press.

III-2-35. RBS Investigation of AlN_x Deposited on Glassy Carbon (I)

K. Kobayashi, S. Namba, T. Fujihana, Y. Dai,
T. Kobayashi, and M. Iwaki

Recently aluminium nitride (AlN) is of particular interest because it has a large energy gap, good thermal conductivity, and stability up to very high temperature, as well as chemical inertness.¹⁾

We investigated the composition of AlN_x films deposited by the activated reactive evaporation (ARE) by Rutherford backscattering (RBS).

The AlN_x films were deposited on glassy carbon by means of ARE in a nitrogen atmosphere. The base pressure was 2×10^{-6} Torr and the partial pressure of the nitrogen during deposition was 1×10^{-4} Torr by N_2 gas feeding into a chamber. Substrates were water-cooled and a bias voltage was not supplied between the substrates and the evaporation source. The power of the electron shower for ionizing the nitrogen was about 3.6 W. Two kinds of films were obtained by two deposition rates: at about 70 Å/min and at about 7 Å/min. The thickness of the former film was about 750 Å and that of the latter was about 1,250 Å. The composition of the

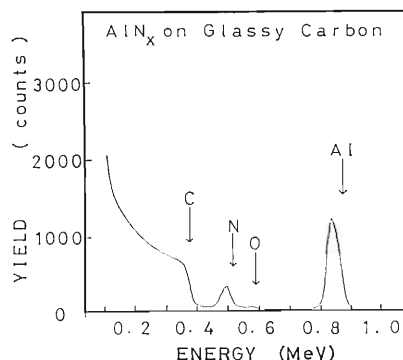


Fig. 1. Rutherford backscattering (RBS) spectrum for an AlN_x film deposited on the glassy carbon by the activated reactive evaporation (ARE) at a deposition rate of about 70 Å/min. The arrows indicate the edges of Al, O, and N on the AlN_x film.

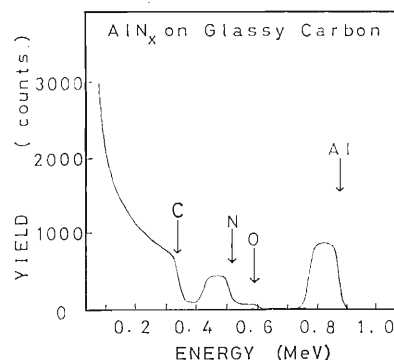


Fig. 2. Rutherford backscattering (RBS) spectrum for an AlN_x film deposited on the glassy carbon by the activated reactive evaporation (ARE) at a deposition rate of about 7 Å/min. The arrows indicate the edges of Al, O, and N on the AlN_x film.

film deposited on the glassy carbon was evaluated from RBS with 1.5 MeV He^+ beams.

Figures 1 and 2 show the spectra of RBS. The arrows indicate the edges of Al, O, and N on the AlN_x film surface. A small amount of O-atoms found in the film were not identified whether they had migrated from the glassy carbon or had been absorbed from the nitrogen atmosphere. On the basis of the first order approximation of the RBS analysis, the ratio, Al/N, for the film at a deposition rate of about 70 Å/min was about 1.3 and that at a rate of about 7 Å/min was about 0.6. These results indicate that the stoichiometric AlN films on glassy carbon would be gained at a deposition rate of about 43 Å/min.

Reference

- 1) A. Fathimulla and A. Lakhani: *J. Appl. Phys.*, **54**, 4586 (1983).

III-2-36. Lattice Location of Eu Ion in Eu-Implanted CaF_2 Observed by Channeling Experiments

K. Aono, M. Iwaki, and S. Namba

A study has been carried out of luminescence from CaF_2 during ion-implantation with Eu, Cr, or Fe ions as a function of the implantation-dose. In this report, the radiation damage caused in Eu-implanted CaF_2 was studied from the transmission changes in the optical density and by a He^+ backscattering-channeling technique using the TANDETRON.

Specimens used were colorless, transparent single CaF_2 crystals with the surface parallel to the (111) cleavage plane. The Eu^+ -implantation was performed to the doses from 10^{12} to 10^{16} ions/ cm^2 at room temperature at a relatively low dose rate of about $0.2 \mu\text{A}/\text{cm}^2$ in a direction misoriented by a few degrees from crystal axis with ions having an energy of 100 keV. The ion implantation caused no change in color of CaF_2 ; this result differs from that of implantation into any other insulators. In general, we could see coloring of the specimens in the visible region due to radiation damage caused by 100 keV ion-implantation. The optical transmittance was $\sim 94.7\%$ and $\sim 95.5\%$ for CaF_2 implanted with 1×10^{16} ions/ cm^2 and un-implanted, respectively, over a wide visible wavelength range. These results indicate that 100 keV-ion implantation hardly results in radiation damage.

Channeling measurements were carried out using 1.5 MeV He ions with a fluence of $10 \mu\text{C}$. Back-scattered particles were detected at an angle of 150° , and random and $\langle 111 \rangle$ or $\langle 110 \rangle$ aligned spectra were determined for estimation of compositions, damage, and Eu-lattice sites in the implanted layers. As reported elsewhere,¹⁾ no out-diffusion of Ca and F atoms occurs through the surface. These spectra also show no out-diffusion of Eu atoms implanted in CaF_2 , and the aligned spectrum for the

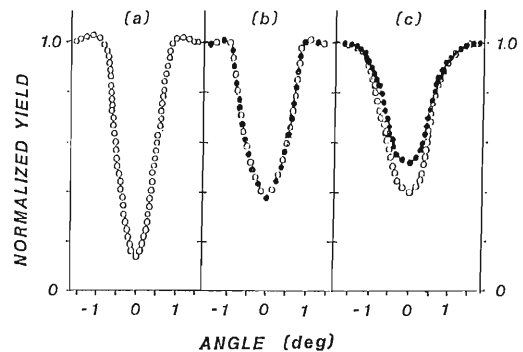


Fig. 1. Close-encounter probability (normalized yield) as a function of angle from $\langle 111 \rangle$ axis for Ca- (\circ) and Eu- (\bullet) atoms in Eu-implanted $\langle 111 \rangle$ CaF_2 . a, un-implanted; b, 1×10^{15} Eu/cm^2 ; and c, 1×10^{16} Eu/cm^2 .

implanted specimen with 1×10^{16} ions/ cm^2 shows little damage near the surface. For implantation with 1×10^{15} and 1×10^{16} ions/ cm^2 the scattering yield of the aligned Eu-spectrum decreased markedly in comparison with that of the random spectrum. This result suggests that implanted Eu-atoms occupied the lattice sites of CaF_2 . The results of angular scans for the host Ca and impurity Eu yields near the $\langle 111 \rangle$ direction are shown in Fig. 1. For a relatively low dose of 1×10^{15} ions/ cm^2 , Eu has the same angular profile as Ca; we also obtained the same results for an angular scan near the $\langle 110 \rangle$ direction.

In conclusion Eu-atoms implanted in CaF_2 mainly occupy the Ca substitutional sites.

Reference

- 1) K. Aono, M. Iwaki, and S. Namba: *Nucl. Instrum. Methods Phys. Res. B*, in press.

III-2-37. Lattice Disorder and the Behavior of Implanted Atoms in In-Implanted TiO₂ (Rutile)

S. Nakamura, E. Yagi, T. Osaka,* and M. Iwaki

Rutile (TiO₂) is an insulator; upon reduction and doping impurities it becomes a semiconductor. Although ion implantation is a useful technique for such doping, the interaction of implanted atoms with defects during implantation plays an important role in determining the properties of implanted materials. Studies of such interactions are required, therefore, for elucidation of the mechanism by which the material is modified.

In the present study of TiO₂ implanted with In atoms, which act as acceptors, the lattice disorder and lattice location of implanted atoms were investigated by an RBS-channeling method.

In⁺-implantation was carried out for TiO₂ (rutile) single crystal slices of 99.99% purity at room temperature at 100 kV to various doses from 10¹⁴ to 10¹⁵/cm². Channeling measurements were performed with a 1.5 MeV ⁴He⁺ beam collimated to give a divergence of less than 0.07°. The area irradiated at a beam current of 1–2 nA was 0.78 mm². The backscattered He⁺ ions were detected with an SSD at a scattering angle of 155°.

Typical aligned spectra for the [0 0 1] and [1 0 0] channels are shown in Fig. 1. The maximum disorder in both Ti and O sublattices saturated at a dose of around 2 × 10¹⁵ In/cm², below which the [0 0 1] Ti disorder peak consisted of two subpeaks, *i.e.*, peak A around the depth of 150 Å from the surface and peak B around 300 Å. The depth of peak B coincides within the experimental error with the measured implantation depth of the In atoms

($R_p = 270$ Å), therefore, peak B is attributed to the disorder caused by the presence of the In atoms. Since the depth of peak A is shallower than R_p , peak A is considered to be due to the damage caused by In-irradiation. The presence of two peaks has also been observed in In-implanted Al₂O₃.¹⁾ On the other hand, in the [1 0 0] spectra, no separate peaks were observed, because peak B is much higher than that in the [0 0 1] case, and the height of peak A is not very different between the two cases. Thus peak A has small anisotropy and peak B large anisotropy at low doses. The anisotropy disappeared at a dose of saturation.

The recovery of lattice disorder in the Ti sublattice proceeded through two annealing stages at around 650 K and at above 1,000 K. In the 650 K stage, the recovery was a little at the depth of the peak B; in the second stage, the recovery was extensive and the disorder peak shifted towards the surface. Simultaneously, In atoms diffused towards the surface. After annealing at 1,173 K, about 15% of the implanted In atoms diffused out. Such out-diffusion of implanted impurity atoms after the recovery of lattice disorder has been observed in Pb- or Xe-implanted Al₂O₃.²⁻⁴⁾

In order to investigate the lattice location of In atoms, we performed channeling angular scans through the [1 0 0] and [0 0 1] axes, and a (0 0 1) plane on the specimens implanted with 5 × 10¹⁴, 1 × 10¹⁵ and 5 × 10¹⁵ In/cm². Figure 2 shows the [1 0 0] and [0 0 1] angular profiles for the 5 × 10¹⁴ In/cm² implantation. The [0 0 1] angular profile of In-yields (In-profile) exhibited the same dip as the Ti-profile, which was wider than the O-dip. The [1 0 0] In-dip had approximately the same half-width, but was about 12% shallower than the Ti-dip. Therefore, in the 5 × 10¹⁴ In/cm² case, most of the In atoms substitute Ti sites but some of them are located at interstitial sites along the *c*-axis of a Ti sublattice. In the 1 × 10¹⁵ In/cm² implantation (angular profiles are not shown), the In profile coincided with the Ti-dip for the [0 0 1] channel, but was about 25% shallower than the Ti-dip for the [1 0 0] channel. Further, this [1 0 0] In profile clearly exhibited a fine structure with double peaks at about ±0.15°.

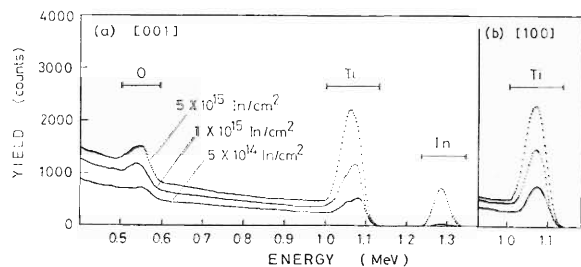


Fig. 1. Aligned [0 0 1] and [1 0 0] spectra of backscattered He⁺ ions in TiO₂ crystal implanted with 100 keV In.

* The School of Science and Engineering, Waseda University.

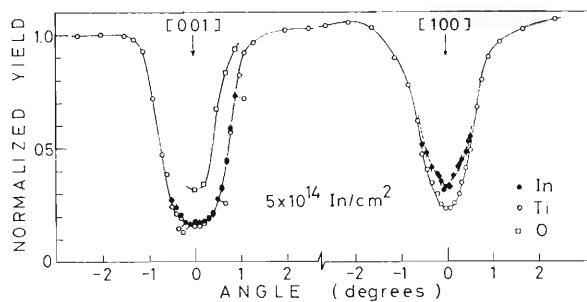


Fig. 2. Channeling angular profiles on the 5×10^{14} In/cm² implanted TiO₂. Broken lines represent the calculated profiles.

From these results, some fraction of the In atoms are anticipated to be located at $00\frac{1}{4}$ sites. The results on the (001) channel agreed with this site occupation.

The distribution of In atoms at various kinds of sites can be examined by comparing the observed In-angular profiles with calculated ones. The calculation was performed using a multi-string model by considering three kinds of site occupancy: Ti substitutional (S) sites, $00\frac{1}{4}$ interstitial sites, and random (R) sites. The distributions of In atoms were estimated as follows: 88% at S-sites, 11% at $00\frac{1}{4}$ sites, and 1% at R-sites for the 5×10^{14} In/cm² implantation, as shown by the broken curves in Fig. 2, and 72% at S-sites, 24% at $00\frac{1}{4}$ sites, and 4% at R-sites for the 1×10^{15} In/cm² implantation.

With increasing dose to 5×10^{15} In/cm², the minimum yield of In-dip increased drastically to 1–0.9, suggesting that most of the In atoms precipitated as In clusters or some other type of second phase. Nevertheless, the $00\frac{1}{4}$ site occupancy was still observed. Annealing at 973 K eliminated the $00\frac{1}{4}$ site occupancy and increased the fraction of substitutional site occupancy.

The increase in the $00\frac{1}{4}$ site occupancy with increasing dose, and its disappearance after annealing at 973 K suggest that the $00\frac{1}{4}$ site occupancy of In atoms results from the interaction of In atoms with defects formed during implantation, i.e., In-defect complexes. Considering the symmetry around the c -axis of the $00\frac{1}{4}$ site and the close-packing of the Ti atoms along the c -axis, an In-Ti vacancy pair and an In-Schottky trio complex are proposed as the In-defect complex. These configurations are shown in Fig. 3.

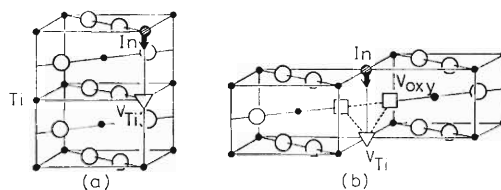


Fig. 3. The In atom-defect complex models in which an In occupies $00\frac{1}{4}$ site; (a) In-Ti vacancy pair, and (b) In-Schottky trio complex.

When a larger In atom replaces a Ti atom, or when an In atom is located at the $00\frac{1}{4}$ site by trapping a Ti vacancy or a Schottky trio, the Ti atoms neighboring the In atom, or the Ti vacancy, respectively would relax. The magnitude of relaxation is larger in the [001] direction than in the [100] direction, because the separation of neighboring Ti atoms in the [100] direction is 1.5 times larger than that in the [001] direction. The lattice disorder in a Ti sublattice due to this effect would be observed more conspicuously in the [100] channeling than in the [001] channeling. The anisotropy of peak B is thus explained qualitatively.

The In-implantation produces a large number of point defects. At low doses, mainly Ti interstitials and their clusters would be responsible for peak A in the aligned Ti spectra. Ti interstitials are considered to be located at $0\frac{1}{2}\frac{1}{4}$ or $0\frac{1}{2}\frac{1}{2}$ sites.^{5,6} These sites produce flux peaks in both [100] and [001] channeling angular profiles. Therefore, Ti interstitials produce no large anisotropy in the lattice disorder as observed for peak A. More detailed descriptions are given in Ref. 7.

References

- 1) A. P. A. Mouritz, D. K. Sood, D. H. St. John, M. V. Swain, and J. S. Williams: *Nucl. Instrum. Methods Phys. Res. B*, **19/20**, 805 (1987).
- 2) A. V. Drigo, S. Lo Russo and P. Mazzoldi, P. D. Goode, and N. E. W. Hartley: *Radiat. Eff.*, **33**, 161 (1977).
- 3) H. J. Matzke and J. L. Whitton: *Canad. J. Phys.*, **44**, 995 (1966).
- 4) A. Tuross, H. J. Matzke, and P. Rabette: *Phys. Status Solidi A*, **64**, 565 (1981).
- 5) J. B. Wachtman, Jr. and L. R. Doyle: *Phys. Rev. A*, **135**, 276 (1964).
- 6) E. Yagi, A. Koyama, H. Sakairi, and R. R. Hasiguti: *J. Phys. Soc. Jpn.*, **42**, 939 (1977).
- 7) S. Nakamura, E. Yagi, T. Osaka, and M. Iwaki: *Nucl. Instrum. Methods Phys. Res.*, in press.

III-2-38. Hydrogen Trapping by Substitutional Impurities in Nb-3at%Mo Alloys as Observed by the Channeling Method

E. Yagi, T. Kobayashi, S. Nakamura, F. Kano,
K. Watanabe,* Y. Fukai,* and T. Matsumoto**

The effect of alloying on the terminal solubility for hydrogen (TSH) in group Va metals (V, Nb and Ta) has been investigated for various alloying elements. It has been known that for undersized metal solutes the TSH increases rapidly with metal solute concentration. For the enhancement of TSH a trapping model has been proposed:¹⁾ a strong attractive interaction between substitutional solute atoms and hydrogen. If such a strong interaction is effective, it might result in the change of the lattice location of hydrogen. Hence, the observation of lattice location of hydrogen will give the useful information on the existence of the attractive interaction, and, therefore, the mechanism of the enhancement of TSH.

In the present study the lattice location of hydrogen was investigated in Nb-3at%Mo alloys, where Mo atoms are undersized solutes, by means of a channeling method utilizing the nuclear reaction ${}^4\text{H}({}^{11}\text{B}, \alpha)\alpha$, a method which is effective for the detection of lattice location change as reported in previous papers.^{2,3)}

Experiments were performed with a 2.03 MeV ${}^{11}\text{B}^{2+}$ beam, and channeling angular profiles of back-scattered ${}^{11}\text{B}$ and emitted α -particles were obtained for $\langle 100 \rangle$, $\langle 110 \rangle$, and $\{100\}$ channels.

The angular profiles obtained at room temperature on the specimens Nb-3at%Mo-2at%H and Nb-3at%Mo-5at%H are shown in Fig. 1 as a function of an incident angle ψ with respect to the channeling direction. When the hydrogen concentration is lower than that of Mo (Nb-3at%Mo-2at%H, Fig. 1(a)), the angular profiles of α particle yields (α -angular profiles) are very different from those for the tetrahedral (T) site occupancy as observed in the Nb-H system.⁴⁾ In the α phase of the Nb-H system the α -angular profiles exhibited a large central peak at $\psi=0^\circ$ for the $\langle 100 \rangle$ channel, a large central peak consisting of three subpeaks at $\psi=0^\circ$ and $\pm 0.35^\circ$ for the $\langle 110 \rangle$ channel, and a shallow dip superposed with a small central peak for the

$\{100\}$ channel.⁴⁾ In the Nb-3at%Mo-2at%H alloy the α -angular profiles exhibited no peak at $\psi=0^\circ$ for all the three channels, but a small peak at $\psi \cong 0.1^\circ$ for the $\langle 100 \rangle$ channel, much smaller peak around $\psi = \pm 0.2^\circ$ and -0.6° for the $\langle 110 \rangle$ channel, and a shallow dip for the $\{100\}$ channel.

When the hydrogen concentration becomes higher than that of Mo (Nb-3at%Mo-5at%H, Fig. 1(b)), the α -angular profiles change significantly. The $\langle 100 \rangle$ α -angular profile exhibited a higher central peak at $\psi=0^\circ$. In the $\langle 110 \rangle$ channel, much higher subpeaks appeared at $\psi=0^\circ$ and about $\pm 0.35^\circ$, the small peak around -0.6° being still observed. The $\{100\}$ α dip became deeper and a small central peak appeared, being superposed on the dip. These newly observed subpeaks are located at the same angular positions as observed in the α phase of the Nb-H system.⁴⁾ These results suggest that some fraction of H atoms are located at T-sites in the Nb-3at%Mo-5at%H alloy.

The angular profiles obtained at 373 K on the specimen Nb-3at%Mo-5at%H are shown in Fig. 2. The α -angular profiles exhibited a much higher central peak at $\psi=0^\circ$ for the $\langle 100 \rangle$ channel, and a shallow dip superposed with a central peak for the $\{100\}$ channel. They are characteristic of the T-site occupancy.⁴⁾ This result indicates that H atoms are located at T-sites at 373 K.

These results can be interpreted as follows. In the Nb-3at%Mo-2at%H alloy most of the H atoms are trapped by Mo atoms and located at sites different from T-sites (trapped sites) at room temperature. In the Nb-3at%Mo-5at%H alloy some fraction of H atoms are located at trapped sites and the remaining H atoms are at T-sites at room temperature, while at 373 K the trapped H atoms are detrapped to be located at T-sites.

The lattice location of the trapped site was determined by fitting the calculated angular profiles to the observed ones. The calculation was made on the basis of the multi-string model by using the Erginsoy formula for a continuum potential. From this analysis it is concluded that in the Nb-3at%Mo-2at%H alloy

* Faculty of Science and Engineering, Chuo University.

** National Research Institute for Metals.

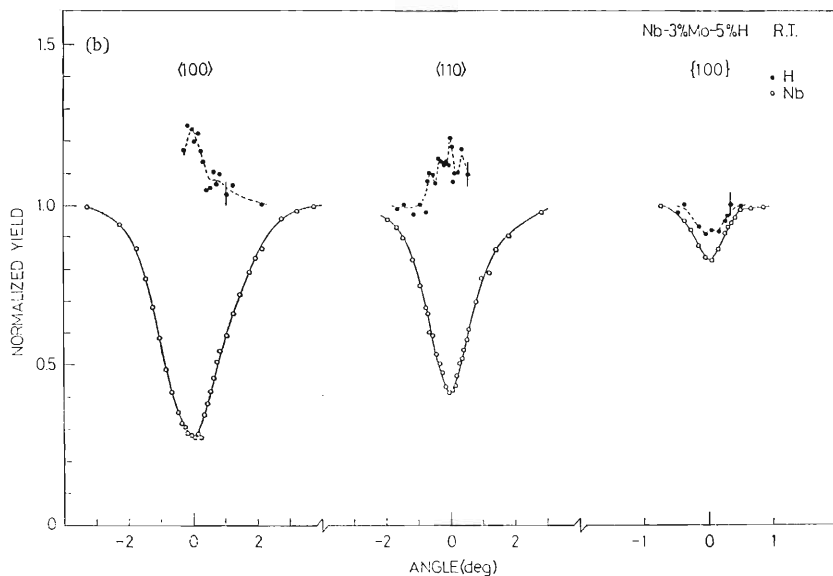
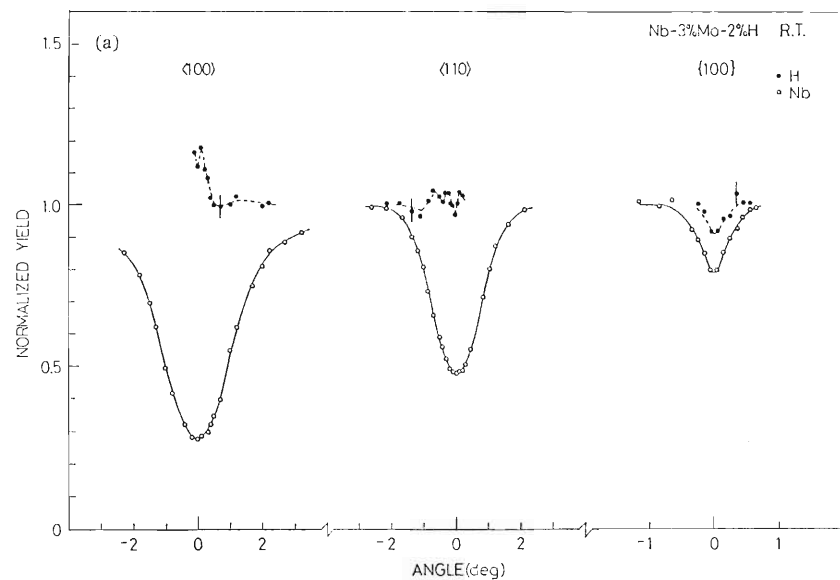


Fig. 1. Channeling angular profiles of ^{11}B - and α -yields obtained at room temperature for (a) the Nb-3at%Mo-2at%H alloy, and (b) the Nb-3at%Mo-5at%H alloy. The full curves and the dashed curves were drawn to guide the eye.

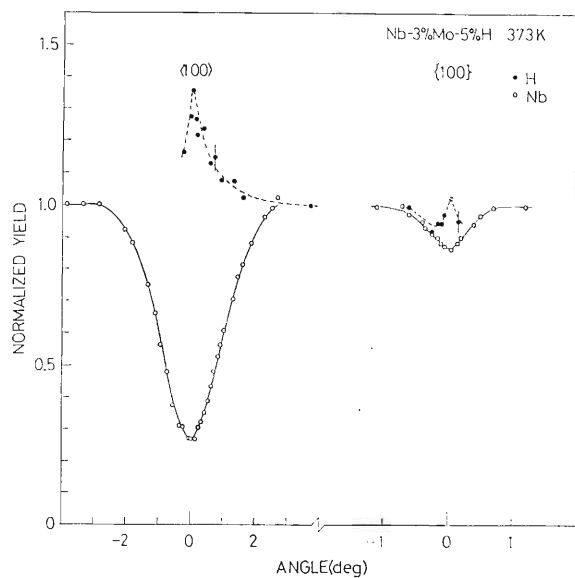


Fig. 2. Channeling angular profiles of ^{11}B - and α -yields obtained at 373 K for the Nb-3at%Mo-5at%H alloy. The full curves and the dashed curves were drawn to guide the eye.

all H atoms are trapped by Mo atoms to be located at sites displaced from T-sites by about 0.6 Å towards the nearest neighbor Mo atoms and at 373 K they are detrapped to be located at T-sites. The present results give the direct evidence for the existence of attractive interaction between substitutional solute atoms and hydrogen in the Nb-3at%Mo alloys.

References

- 1) T. Matsumoto, Y. Sasaki, and M. Hihara: *J. Phys. Chem. Solidis*, **36**, 215 (1975).
- 2) E. Yagi, T. Kobayashi, S. Nakamura, Y. Fukai, and K. Watanabe: *J. Phys. Soc. Jpn.*, **52**, 3441 (1983).
- 3) E. Yagi, T. Kobayashi, S. Nakamura, F. Kano, K. Watanabe, Y. Fukai, and S. Koike: *Phys. Rev. B*, **33**, 5121 (1986).
- 4) E. Yagi, S. Nakamura, T. Kobayashi, K. Watanabe, and Y. Fukai: *J. Phys. Soc. Jpn.*, **54**, 1855 (1985).

III-2-39. Evaluation of Structural Perfection by Rutherford Backscattering Spectroscopy (RBS) of 6H-SiC Single Crystal Grown with a Vapor Transport Method

T. Kobayashi, M. Iwaki, H. Sakairi, and M. Aono

Single crystal of 6H-SiC of $3\text{ mm} \times 3\text{ mm} \times 4\text{ }\mu\text{m}$ was prepared by the vapor transport method in which silicon vapor from molten silicon is transported to a growth cavity made of graphite at the National Institute for Research in Inorganic Materials.¹⁾ X-ray diffraction revealed that the largest face of the crystal is parallel to the (0001) plane. The crystal was chemically polished at room temperature with HF and HNO₃ mixed at a volume ratio of 1:1.

The RBS experiments were carried out with a beam of ⁴He⁺ accelerated to 1.5 MeV with a Cockcroft-Walton-type tandem accelerator (Tandetron) and collimated to a 1 mm diameter; the intensity was 0.7 nA in total. The specimen was mounted on a three-axis goniometer, with which the orientation of the specimen could be set with $\pm 0.004^\circ$. The energy of backscattered ⁴He particles was analyzed with a surface-barrier solid-state detector placed at a scattering angle of 150° connected with a 1,024-channel pulse-height analyzer. The energy resolution and the solid angle of the solid state detector were 20 keV (FWHM) and 0.03 sr, respectively. During the RBS experiments, the temperature of the specimen was kept at room temperature.

Figure 1 shows typical RBS spectra of 6H-SiC measured with a 1.5 MeV ⁴He⁺ beam. The energies

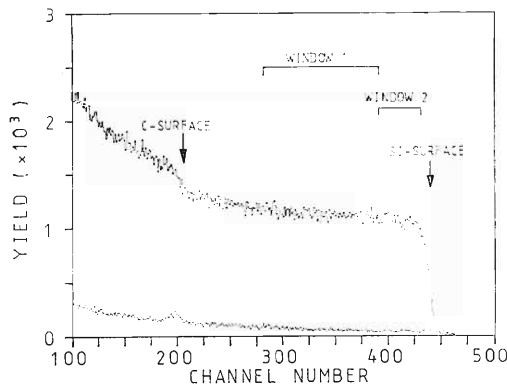


Fig. 1. Typical RBS spectra of 6H-SiC crystal measured with a 1.5 MeV ⁴He⁺ beam. Energies of scattered ⁴He particles are plotted *vs.* channel numbers. The lower and upper spectra were measured in the [0001] channeling axis and in a random direction, respectively.

of scattered ⁴He particles are plotted *vs.* the channel numbers. The lower and upper spectra were measured for the incidence parallel to the $\langle 0001 \rangle$ axis and to a random direction, respectively. Both spectra are ascribed only to silicon and carbon and show no impurity present within the detection limits of the present technique. In the lower spectrum a carbon-surface peak is clearly observed at an energy corresponding to a channel number of 196. The width of the carbon-surface peak, 22 keV in FWHM, is close to the energy resolution of the detector (20 keV). Although a silicon-surface peak is also observed at a channel number of 437, its intensity is much smaller than that of the carbon-surface peak despite the fact that the Rutherford scattering cross section of silicon is larger than that of carbon by a factor of 6.5. This indicates that the (0001) surface is mostly terminated with carbon atoms or that, although the surface is more or less terminated with silicon atoms, they are covered with carbon or hydrogen atoms which give no spectral features because of their smaller mass than that of ⁴He⁺ but shadow the silicon atoms.

Figure 2 shows the angular dependence of the

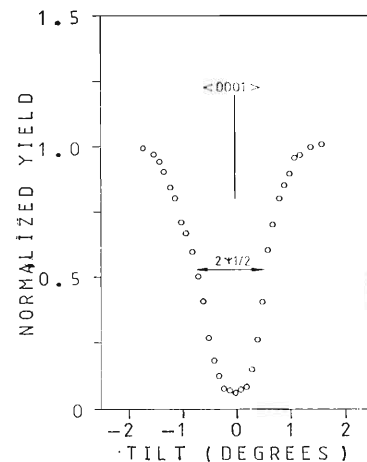


Fig. 2. Angular dependence of the intensity of ⁴He particles scattered from silicon atoms in 6H-SiC crystal. The dependence was measured by changing the direction of the incident ⁴He⁺ beam around the [0001] channeling axis.

intensity of ^4He particles scattered from silicon atoms; the dependence was measured by changing the direction of the incident $^4\text{He}^+$ beam around the $\langle 0001 \rangle$ channeling axis normal to the surface. The energy window used in this measurement is shown in Fig. 1 as 'window 1.' This considerably wide energy window was used to reduce the statistical error in the intensity of scattered ^4He particles and to measure the axial half-angle with high accuracy. The axial half-angle, $\psi_{1/2}$, is defined to the half angle of the channeling dip observed in the angular dependence of the intensity of scattered ^4He particles as indicated in Fig. 2, and is estimated to be $0.64^\circ \pm 0.07^\circ$. Theoretically, $\psi_{1/2}$ is given by²⁾

$$\psi_{1/2} = 0.246 F_{\text{RS}}(\xi) (Z_1 Z_2 / Ed)^{1/2} \text{ (in degrees)} \quad (1)$$

where Z_1 and Z_2 are the atomic numbers of projectile ion and target atom, respectively, E the incident energy of projectile ion (in MeV), d the atomic spacing along the axial direction (in Å), F_{RS} proportional to the square root of the continuum Moliere potential, and $\xi = 1.2u_1/a_{\text{TF}}$ (u_1 and a_{TF} are the one-dimensional rms vibration amplitude and the Thomas-Fermi screening radius, respectively). The values of F_{RS} vs. ξ are given in Ref. 2.

In the present case, $\psi_{1/2}$ is calculated and found to be 0.61° from Eq. 1. This theoretical value, which is estimated by assuming that the 6H-SiC crystal has a perfect structure, is close to the experi-

mental value mentioned above, $0.64^\circ \pm 0.07^\circ$.

An experiment similar to that of Fig. 2 was carried out by using another energy window just below the silicon surface peak indicated in Fig. 1, as 'window 2.' From the result of the measurement (not shown), we estimated the value called the minimum yield χ_{min} . The value of χ_{min} for the 6H-SiC specimen determined in this way is 0.040 ± 0.001 . Theoretically, χ_{min} is given by²⁾

$$\chi_{\text{min}} = Nd\pi(2u_1^2 + a_{\text{TF}}) \quad (2)$$

where N is the atomic density and the meanings of other notations were the same as above. In the present case, where $N = 0.0861$ atoms/Å³, χ_{min} is obtained to be 0.040 from Eq. 2. This theoretical value for the perfect structure is again in agreement with the corresponding experimental value mentioned above, 0.040 ± 0.001 .

Thus, both $\psi_{1/2}$ and χ_{min} determined by the RBS experiments for the 6H-SiC specimen are found to agree with the corresponding theoretical values estimated by assuming that the crystal has a perfect structure. The vapor transport method is considered promising in preparing a good crystal of 6H-SiC.

References

- 1) Y. Inomata: *J. Cryst. Growth*, **12**, 57 (1972).
- 2) J. W. Mayer and E. Rimini: "Ion Beam Handbook for Material Analysis," Academic Press Inc., New York (1977).

III-2-40. Erosion of Graphite by Low Energy Atomic Hydrogen

K. Yano, H. Oyama, Y. Sakamoto, and M. Yanokura

Materials covered with graphite tiles or coated with carbon film are promising for first wall of fusion devices, because carbon has the low atomic number and is heat-resistant. In fusion devices, a cold plasma of electron temperature of ~ 10 eV is present near the first wall, surrounding a hot core plasma. Franck-Condon hydrogen neutral atoms are produced mostly in this region by a dissociative excitation process. These chemically active atoms with energies of ~ 5 eV react with carbon atoms on the surface and cause erosion of the wall. Therefore, we need data concerning the erosion of carbon wall, especially of graphites, because the practical wall is composed essentially of graphite tiles. An ECR (Electron Cyclotron Resonance) plasma forms considerably high flux of Franck-Condon neutrals in simulation experiments and neutrals impinge on graphite surfaces without collision with molecules, because the resonant energy absorption by electrons allows low pressure ($\sim 10^{-2}$ Pa) operation.

Figure 1 shows the experimental setup described in detail elsewhere.¹⁾ A graphite sample (SA) is situated 13 cm apart from the discharge tube axis to assure elimination of influx of energetic ions which intensify erosion. Before erosion experiments, dis-

charge cleaning with hydrogen plasmas was carried out carefully to reduce impurity contamination, especially oxygen and/or water having very large erosion rates.

Three kinds of graphite samples ($40 \times 40 \times 0.5$ mm) were used:

- | | |
|-----------------------|--|
| I) Isotropic graphite | |
| 1) ISO-880U | apparent density $\rho = 1.90 \text{ g cm}^{-3}$ |
| 2) IG-110U | $\rho = 1.77$ |
| II) Molded graphite | |
| 3) YPD-K | $\rho = 2.00$ |

Irradiation plasma was produced under the following conditions.

- | | |
|--------------------------------|-----------------------|
| 1) H_2 flow rate | 2 SCCM |
| pressure in the discharge tube | 4×10^{-2} Pa |
| 2) microwave power | 200 W cw |

The plasma had the electron density of $2.7 \times 10^{10} \text{ cm}^{-3}$ and the temperature of 10 eV. From these plasma parameters, the Franck-Condon neutral flux was estimated²⁾ and found to be $2.3 \times 10^{15} \text{ cm}^{-2} \text{ s}^{-1}$. We irradiated the samples with the above neutral flux for 100 h at 50°C . We determined the erosion rates from weight loss measurements using a microbalance:

- | | |
|-------------|--|
| 1) ISO-880U | 3.0×10^{-8} C atoms/ H^0 |
| 2) IG-110U | 4.2×10^{-8} |
| 3) YPD-K | 2.6×10^{-8} |

From these results, the erosion rate was found to decrease with increase in the apparent density. Since these values lie in between those for energetic ions ($\sim 10^{-2}$ C/ H^+) and thermal atomic hydrogens ($\sim 10^{-4}$ C/ H^0), our results are probably reasonable. It is well known that the erosion rate depends on the surface concentration of hydrogen; accordingly, an ERD method by using RILAC was employed for measuring the near-surface concentration. Graphite samples for the ERD measurement were irradiated with D_2 plasmas, because graphites contain hydrogen by nature. The depth profiles of H and D near surfaces at different sample temperatures are shown in Figs. 2(a) and (b). Figure 2 shows that the concentration of D in the surface heated at 385°C is low compared with that at 50°C . This result indicates that the erosion rate increases with increasing surface temperature, because recombination of near-surface atoms with incident atoms decreases with increasing temperature.³⁾

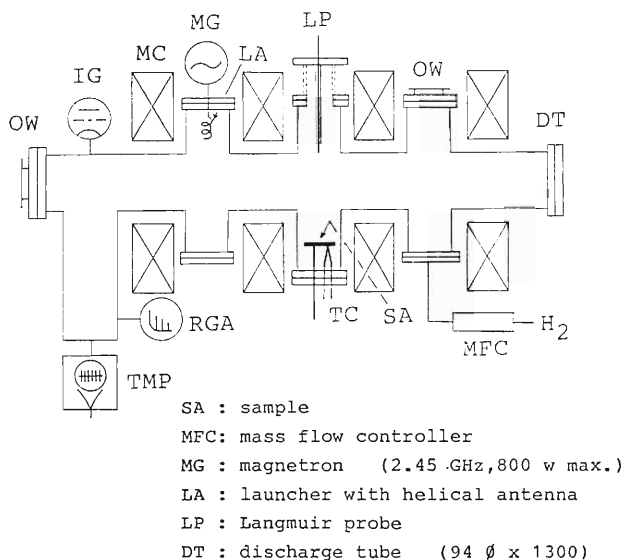


Fig. 1. Schematic arrangement of the ECR plasma irradiation apparatus.

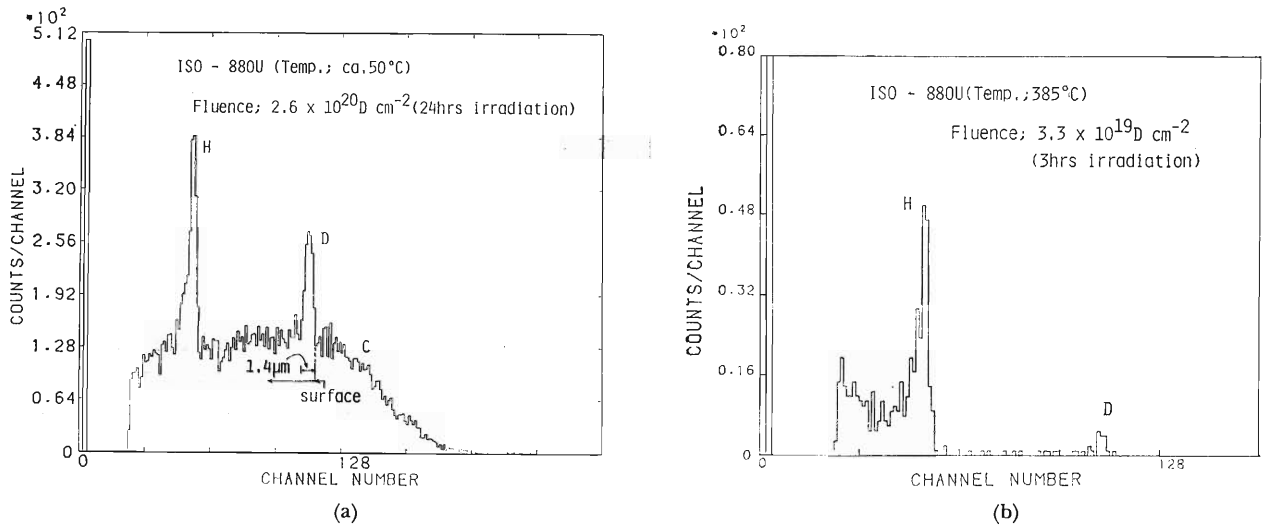


Fig. 2. Depth profiles of H and D near graphite surfaces irradiated with D atoms at (a) 50°C and (b) 385°C .

References

- 1) Y. Sakamoto, Y. Ishibe, K. Okazaki, H. Oyama, K. Yano, M. Yanokura, and I. Kohno: *RIKEN Accel. Prog. Rep.*, **19**, 98 (1985).
- 2) K. Yano, H. Oyama, Y. Sakamoto, K. Okazaki, and Y. Ishibe: *Jpn. J. Appl. Phys.*, **20**, 1765 (1981).
- 3) J. Roth: *J. Nucl. Mater.*, **145-147**, 87 (1987).

III-2-41. The Channeling Analysis of Ge Epitaxial Growth on Si Substrate

K. Tanaka, E. Yagi, and H. Kamitsubo

The heteroepitaxial layer of Ge on a Si substrate can be applied to an infrared sensor or a suitable buffer layer for the subsequent growth of GaAs. For these purposes, a Ge epitaxial layer of high crystalline quality is required. Cross-sectional transmission electron microscopy (TEM) and an X-ray diffraction method have been used to investigate the crystalline quality of deposited layers. However, for cross-sectional TEM observation a skilful technique is indispensable for preparation of thin foils from the samples without introducing defects. The information on the crystalline quality as a function of depth cannot be obtained from the X-ray diffraction method. An Rutherford backscattering (RBS) ion channeling method nondestructively provides quantitative information on surface layers as a function of depth. In the present study, therefore, we used the RBS method to investigate the crystalline quality of the Ge epitaxial layers on Si substrates.

Ge layers were grown on Si (100) substrates by using a molecular beam epitaxy method. As shown in Fig. 1, Ge was grown by a two-step procedure:¹⁾ the first Ge layer was grown at lower temperature than that for the second layer formation in order to form an interlayer to reduce the lattice mismatch between Ge and Si. In this work the growth temperature of the second layer was kept constant at 600°C and that of the first layer was changed. Table 1 shows growth conditions of Ge layers.

Characterization of the Ge epitaxial layers was carried out by RBS with a 1.5 MeV ⁴He beam.²⁾

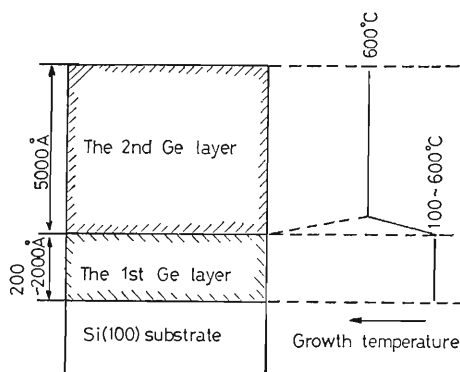


Fig. 1. Schematic illustration of the growth method of a Ge epitaxial layer on Si (100) by a two-step procedure.

The beam diameter was 1 mm and the beam divergence was less than 0.076°; the current was approximately 1 nA. The backscattered ⁴He ions were detected with a surface barrier solid state detector at a scattering angle of 155°. The sample was mounted on a three-axis goniometer and the <100> axis of the sample was aligned in the direction of a beam

Table 1. Growth conditions of Ge layers on Si (100) substrates by a two-step procedure growth method. The growth temperature of the second layer was kept constant at 600°C and the thickness of the second layer was 5,000 Å. Sample 7 was prepared by a one-step procedure.

Sample number	1	2	3	4	5	6	7
1st layer thickness (Å)		200		2,000			—
1st layer growth temperature (°C)	135	310	480	300	400	500	600

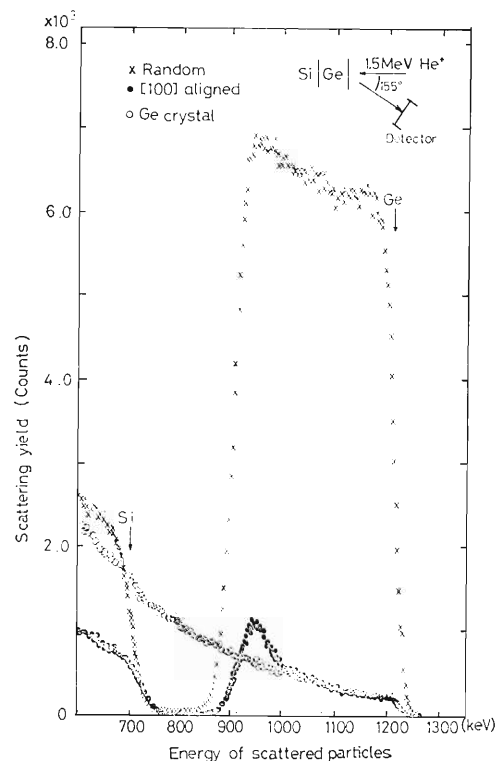


Fig. 2. Rutherford backscattering spectra of a Ge epitaxial layer on Si (Sample 2 in Table 1).

incidence. Figure 2 shows typical energy spectra of the backscattered ^4He ions for $\langle 100 \rangle$ aligned and random incidences. The $\langle 100 \rangle$ aligned spectrum for a Ge single crystal was also shown in Fig. 2. The dechanneling from the Ge epitaxial layer was greater than that in the Ge single crystal and an additional peak was observed at the Ge/Si interface. As crystallinity degrades the dechanneling increases. As a measure for the perfection of the Ge epitaxial layer, the value A was defined as:

$$A = \frac{\chi_s - \chi_r}{1 - \chi_r} \quad (1)$$

where χ_s is the backscattering yield from the Ge epitaxial layer for the $\langle 100 \rangle$ aligned incidence normalized to that for the random incidence; χ_r is the backscattering yield from a Ge single crystal for the $\langle 100 \rangle$ aligned incidence normalized to that for the random incidence.³⁾

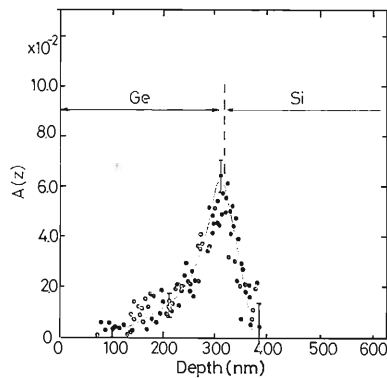


Fig. 3. Plot of A versus depth in a Ge epitaxial layer on a Si substrate (Sample 2 in Table 1). A is defined by Eq. 1 and is directly proportional to the dislocation density.

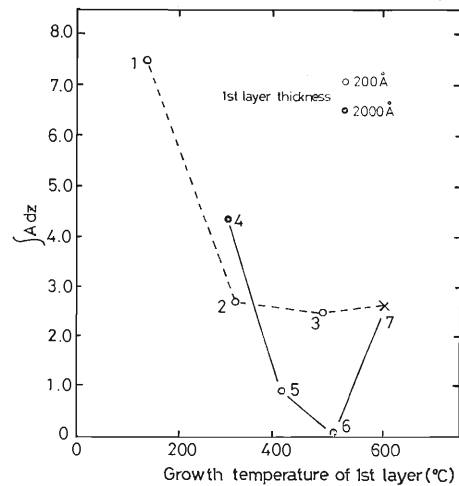


Fig. 4. Plot of A versus growth temperature of the 1st layer.

Figure 3 shows an example of the plot of A vs. depth (z) in the Ge layer. The depth (z) was derived from the energies of backscattered ^4He ions. The integrated values of A over the thickness of the Ge epitaxial layer are plotted as a function of the growth temperature in Fig. 4. We concluded that the best crystalline quality of heteroepitaxially grown Ge/Si is obtained when the first layer is grown at 400–500°C, and the second layer is grown subsequently at 600°C.

References

- 1) Y. Fukuda and Y. Kohama: *J. Cryst. Growth*, **81**, 451 (1987).
- 2) E. Yagi, F. Kano, S. Nakamura, M. Iwaki, and T. Osaka: *RIKEN Accel. Prog. Rep.*, **20**, 80 (1986).
- 3) A. Kyoshima: *J. Phys. Soc. Jpn.*, **50**, 2395 (1981).

III-2-42. Production of Fast Switching Power Thyristors by Proton Irradiation

I. Kohno

The thyristor features quick switching. When used for a high-frequency power source, it can exert its full advantages. Even thyristors with short turn-on and turn-off times, a tail current is generated when it is used for a high-frequency power source. The tail loss due to this tail current determines the upper limit of the working frequency of the devices. Therefore, how to minimize the tail current is an essential problem for thyristors when used for high-frequency power source. For thyristors, it is necessary to control the life time of carriers in the base layer to reduce the tail current. In order to control the life time of carriers we used defects produced by proton irradiation.

Figure 1 shows various ways of proton irradiation on thyristors. When (1) the surface of thyristor was

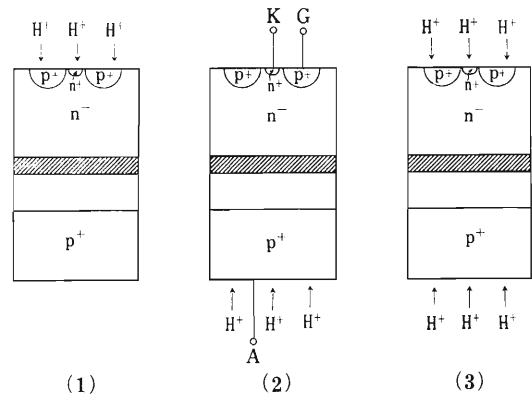


Fig. 1. Various ways of proton irradiation on the thyristor, A, K and G stand for an anode, cathode, and gate of the thyristor, respectively.

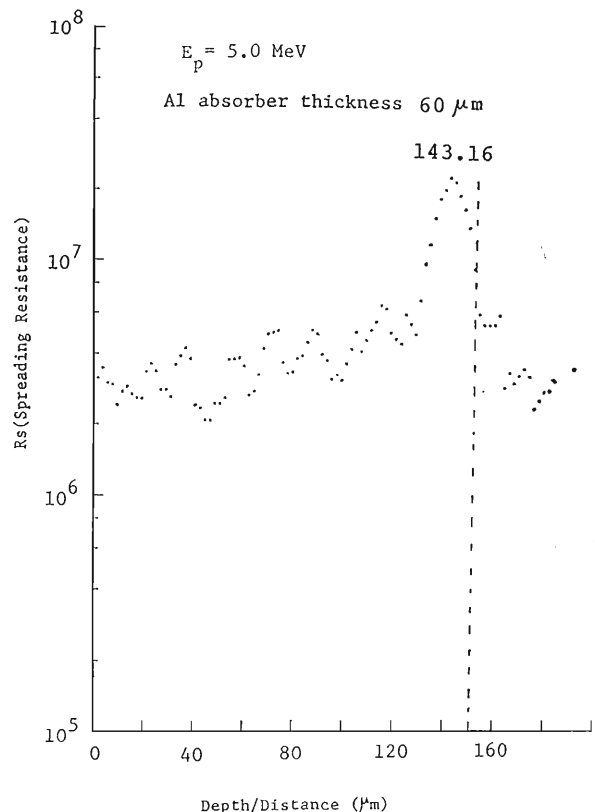
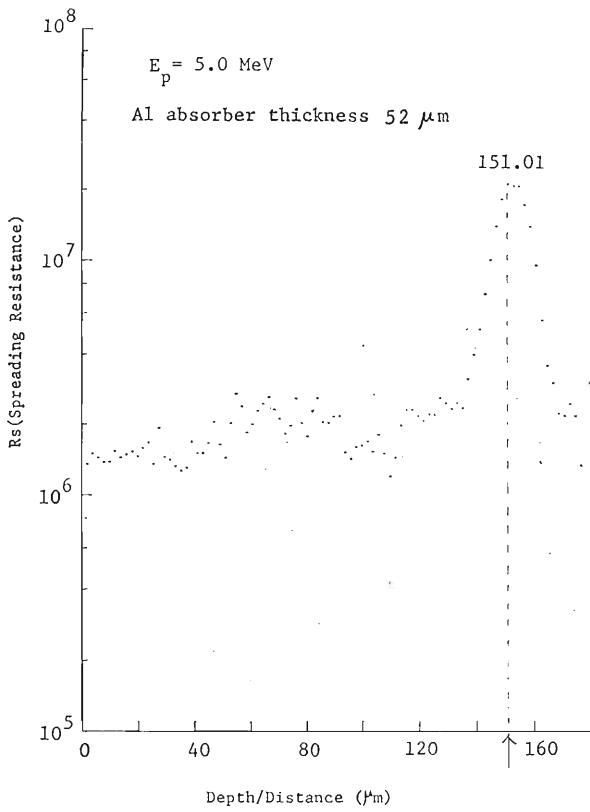


Fig. 2. R_s (spreading resistance) profile. Ordinate is arbitrary.

irradiated with protons at the energy to produce vacancies in the n^- region. When (2) the back surface was irradiated with proton, and when (3) the both surfaces was irradiated with proton.

Figure 2(a) shows an example of the depth profile of the R_s (spreading resistance) of silicon irradiated with 5 MeV protons with fluence $5 \times 10^{12} \text{cm}^{-2}$ through a $52 \mu\text{m}$ thick Al absorber (case (1)). An R_s crest created by the defect production appeared at $151 \mu\text{m}$ from the silicon surface with an extensive width of about $27 \mu\text{m}$. This R_s profile indicates that the proton irradiation produces defects at a narrow depth region in the n^- layers. Figure 2(b) shows a depth profile of the P_s of silicon irradiated with 5 MeV protons through a $60 \mu\text{m}$ thick Al absorber.

Figure 3 shows the relationships between a proton fluence Φ and T_{OFF} (turn-off time) which stands for the time during which anode current decreases from 90% value of peak to 10%. When Φ is increased to above $0.5 \times 10^{12} \text{cm}^{-2}$, T_{OFF} can be decreased drastically. On the other hand, when Φ is increased the electric resistance between the anode A and the cathode K was increased.

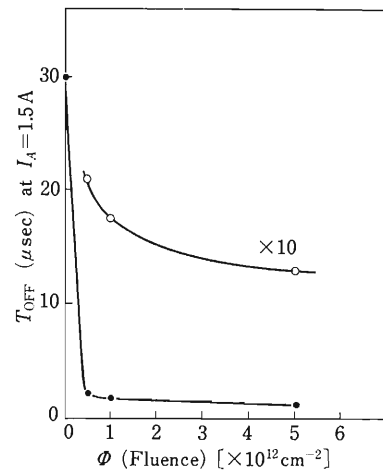


Fig. 3. Relationship of Φ (proton fluence) vs. T_{OFF} (turn-off time).

From these experimental results we can find that the proton irradiation of proper fluences for the production of vacancies in the n^- layer is effective to reduce turn off time of the thyristor when used for a high-frequency power source.

III-2-43. Background in PIXE Spectra

K. Maeda, Y. Sasa, and M. Uda*

For quantitative elemental analysis by PIXE (particle induced X-ray emission), the exact evaluation of background is indispensable. Most of the background in PIXE spectra comes from continuous X rays emitted from the target itself. The intensities of continuous X rays decrease rapidly with increasing X-ray energy. Thus, appropriate X-ray absorbers are often used to attenuate low energy X rays for achieving sufficient sensitivity. To investigate the influence of absorbers on the profiles of background in PIXE spectra, we measured continuous X-ray spectra emitted from a Kapton ($(\text{H}_{10}\text{C}_{22}\text{N}_2\text{O}_5)_n$) film through different kinds of absorbers. We chose Kapton as a target material because it emits no high-energy characteristic X rays that complicate the analysis of background.

X-ray spectra emitted from a $7.5 \mu\text{m}$ Kapton film were measured through five different absorbers: 3.9 mg/cm^2 aluminum, 6.0 mg/cm^2 titanium, 9.9 mg/cm^2 vanadium, 5.2 mg/cm^2 silver, and 94 mg/cm^2 polyethylene films. X rays were detected with an ECON-2 Si(Li) detector with a $7.5 \mu\text{m}$ -thick beryllium window. An 8 MeV helium ion beam of 3 mm in diameter was used for excitation. The details of the spectrometer geometry were described elsewhere.¹⁾

A thin ($1 \mu\text{m}$) polypropylene film was placed to protect the detector window from the attack of scattered ions when absorbers were not used. The spectrum observed through this thin film may be presumed to be the spectrum without an absorber, because the absorption of X rays by the film is not so significant (less than 10% at the energies higher than 1.25 keV).

Figure 1 shows PIXE spectra obtained from a Kapton film with and without X-ray absorbers. The spectra detected through the Al, Ti, V, and Ag absorbers seem as if they have broad peaks at the low energy sides of the absorption edges of the absorbers. A similar peak was also seen in a spectrum obtained with a polyethylene absorber. Appearance of such broad peaks is due mainly to the presence of low-energy signals, the intensities of which were not reduced to the extent that expected from the absorption effects of the absorbers. If only the absorption effects are taken into accounts, the spectra measured through absorbers should have sharp curvatures such as those represented by dashed lines in Fig. 1.

γ rays must contribute at least in part to the low-energy background, since the main component of high-energy background is caused by the Compton

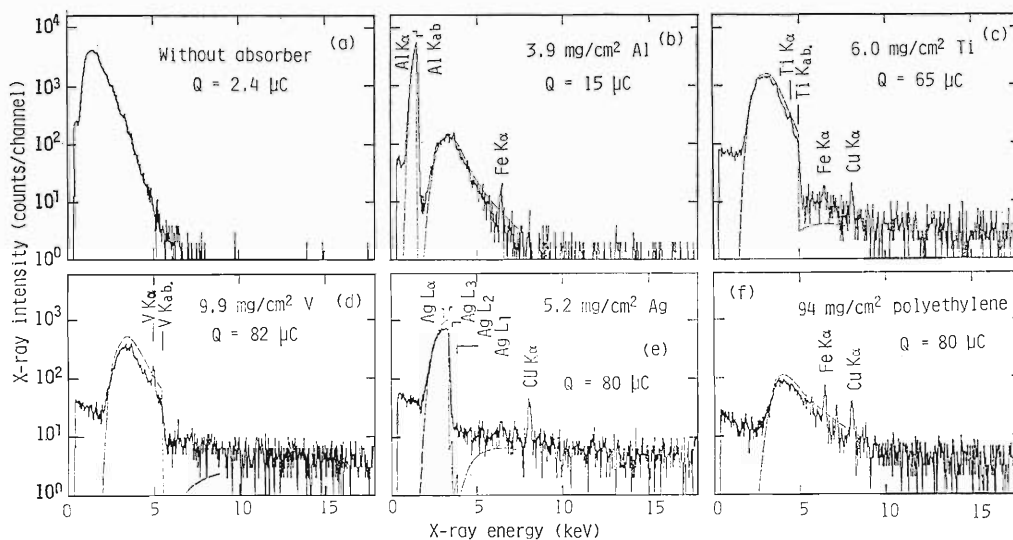


Fig. 1. PIXE spectra obtained from a Kapton film with and without X-ray absorbers: dashed lines were estimated by multiplying the spectrum without absorber (a) by the transmissivities²⁾ of the absorbers.

* Present address: Department of Materials Science, Waseda University, Tokyo.

scattering of nuclear γ rays, and the γ -ray background increases slowly with decreasing pulse-height energy.³⁾ This component should be almost unaffected by absorption in the typical X-ray energy region. However, as it can be seen from Fig. 1, counts of low-energy signals are essentially different from a spectrum to another. To account for entire profile of the spectra, other effects which give rise to low energy signals should be taken into consideration.

It is known that when monochromatic X rays are detected with a Si(Li) detector, many kinds of signals modified by the internal processes in the detector (*e.g.*, Si $K\alpha$ escape and incomplete charge collection) are found in the resulting pulse-height spectrum. The major contributors to the low-energy signals are the Si $K\alpha$ escape peak, the truncated flat continuum, and the truncated exponential tail on the low energy side of the full energy peak.⁴⁾ For continuous X-ray

spectra, the contributions from these modified signals to the background are to be determined by integration of the intensity distributions of incident (*i.e.*, original) spectra operated with the response function of the detector for X rays of each energy. We have attempted here to evaluate how much the modified signals contribute to the measured continuous spectra by complementary use of the known data concerning the response functions of Si(Li) detectors.⁵⁻⁷⁾ The profile of the continuous X-ray spectrum was numerically estimated for each absorber used in this experiment, based on an assumption that the spectrum is composed of real continuous X rays, low-energy signals modified from these X rays by the internal processes in the detector, and the γ -ray background. The spectrum of the Kapton film measured without absorber (Fig. 1 (a)) was used as an original one, after subtraction of small amounts of the γ -ray background and multiplication by the transmissivity of the

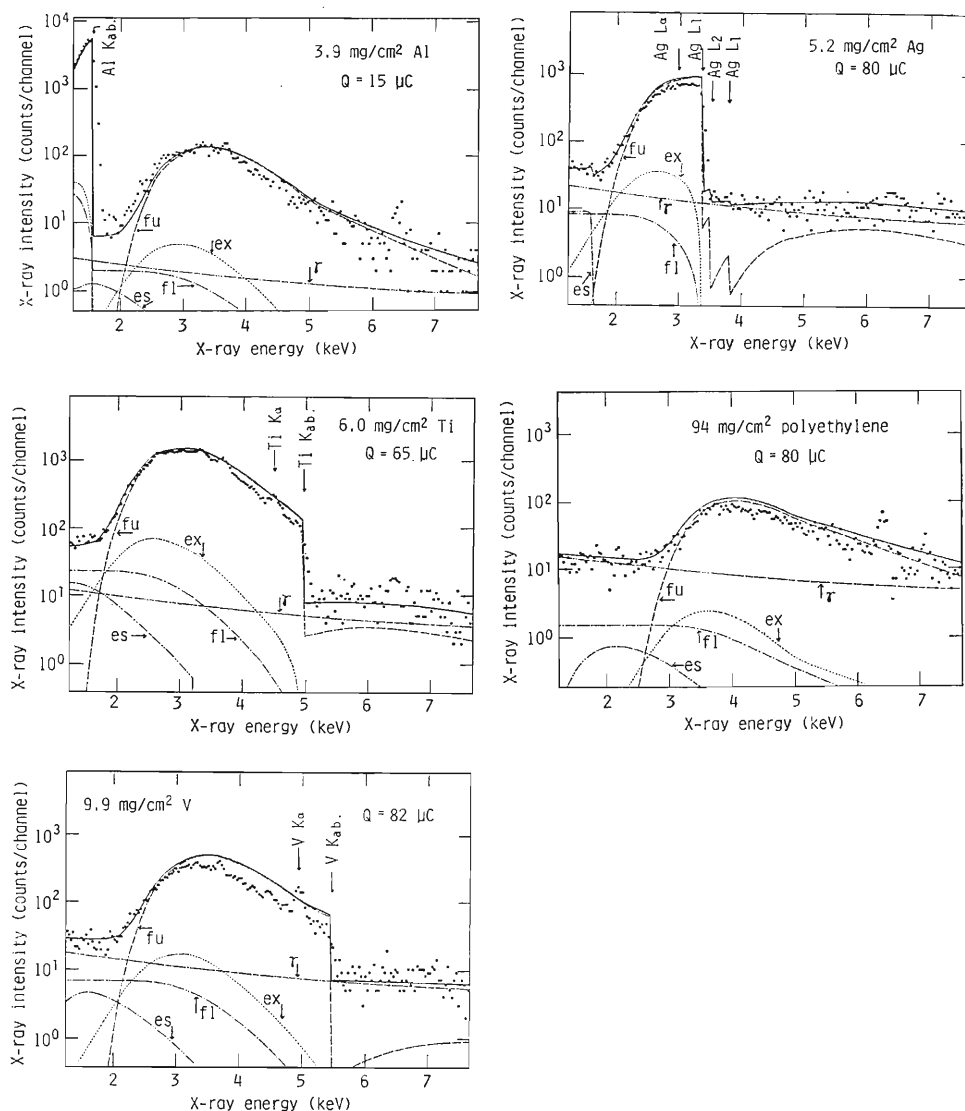


Fig. 2. Observed and estimated PIXE spectra of a Kapton film. ●, observed; —, estimated total signals; ---, full energy component; - - - - -, escape component; ·····, flat continuum component; - · - · - ·, low-energy exponential tail component; — · · · —, γ -ray component.

absorber.

The escape fraction was obtained from Eq. 2 in Ref. 5. The energy dependency of the tail fraction was reported by Shima *et al.*⁶⁾ The tail fraction depends on detectors used. Therefore, we measured the tail fractions at S $K\alpha$ and Ti $K\alpha$ for our detector and used them to estimate the tail fractions at other energies by assuming that the energy dependency is the same as that given by Shima *et al.* The flat continuum fraction was reported to be 1 to 5% in the energy range of 1.5–5.9 keV,⁷⁾ but its energy dependency was not clear. Thus, we adopted the average value of 3% for the flat continuum fraction. The contribution from the γ -ray background $S_\gamma(\epsilon)$ was estimated by using a model³⁾ given by $S_\gamma(\epsilon) = a[\exp(-b\epsilon) + c]$, where a , b , and c are the fitting parameters, and ϵ the pulse height energy. We used as the parameters, b and c , those deduced from the pulse-height spectrum of Dotite (its main component is carbon) detected through a very thick absorber (170 mg/cm² polyethylene), assuming that the shape of the γ -ray background for Kapton is similar to that for Dotite. The parameter, a , was determined for each spectrum using the average of signals in

the high energy region (15–18 keV).

The spectra thus estimated are shown in Fig. 2 together with their components and observed data. The profiles of the observed spectra are well interpreted on the basis of the effects of the absorption factors of the absorber, the response function of the detector, and the nuclear γ -ray background. The components produced by the internal processes in the detector were not too small to be neglected in the evaluation of background in PIXE analysis, especially in the low energy region.

References

- 1) K. Maeda, Y. Yokode, Y. Sasa, H. Kusuyama, and M. Uda: *Nucl. Instrum. Methods B*, **22**, 188 (1987).
- 2) V.M. J. Veigle: *At. Data Tables*, **5**, 51 (1973).
- 3) H.C. Kaufmann, K.R. Akselsson and W.J. Courtney: *Adv. X-Ray. Anal.*, **19**, 355 (1976).
- 4) R.P. Gardner and J.M. Doster: *Nucl. Instrum. Methods*, **198**, 381 (1982).
- 5) P.J. Staham: *J. Phys. E*, **9**, 1023 (1976).
- 6) K. Shima, S. Nagai, T. Mikumo, and S. Yasumi: *Nucl. Instrum. Methods* **217**, 515 (1983).
- 7) W. Maenhaut and H. Raemdonck: *Nucl. Instrum. Methods B*, **1**, 123 (1984).

III-3. Radiochemistry and Nuclear Chemistry

1. A New Nuclear Reaction Analysis of Nitrogen in Solids: Utilization of ^{15}N as an Activable Tracer

Y. Itoh, H. Fukushima, T. Nozaki, Y. Mochizuki, and E. Arai*

Determination of a trace amount of nitrogen contained in metals and semiconductors is one of the most important subjects in solid state sciences. Nitrogen is abundant in nature, and the determination of its trace contents is likely to be interfered with contaminations on the surface and from environment; thus, the use of ^{15}N is meaningful as an activable tracer. We reported the determination of nitrogen in bulk silicon (130 μm depth from the surface; the incident energy of 20 MeV) by activation with the $^{15}\text{N}(\alpha, n)^{18}\text{F}$ reaction.¹⁾ This method is sensitive over deeper portions; shallower parts of a sample can be analyzed by the following d-induced reaction. We used the $^{15}\text{N}(\text{d}, \text{p})^{16}\text{N}$ reaction to determine nitrogen on and near the solid surface. Our ultimate

interest is to examine whether any enhanced solubility and diffusion be observed in the portion near the surface as compared with the deeper portion.

We used silicon wafers covered with ^{15}N nitride films formed by epitaxy from $^{15}\text{NH}_3$ (^{15}N 50%) and SiH_4 and Si_3N_4 (^{15}N 0.365%) plate. The analysis was carried out by cyclic activation. Each bombardment used a deuteron beam of <5 nA for 15 s. After the beam was cut off pneumatically, the high energy γ -rays from the excited states of the ^{16}O ($E_\gamma = 6.13, 7.12$ MeV) were measured for 15 s with a BGO scintillator placed close to the sample. The cycle of 15 s bombardment—15 s measurement was repeated automatically for 500–1,000 s.

The spectra of typical samples are shown in Fig. 1 together with a normal background spectrum of nitrogen-free silicon. The region integrated for quantitative determination is also shown. Since these γ rays are of so high energies, the interferences with all lower energy γ rays can be removed by discrimination. The thick target yield of this reaction is shown in Fig. 2. This method indicates the sensitivity of 10^{18} at. cm^{-3} . Further studies are in progress.

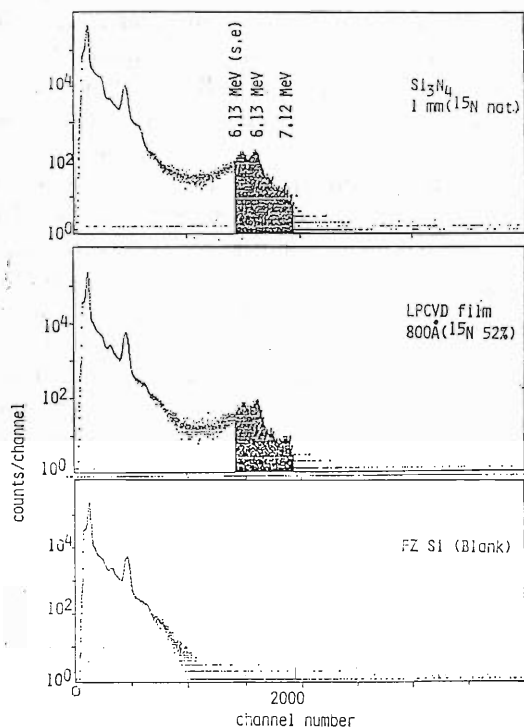


Fig. 1. Typical energy spectra for γ rays in silicon nitride samples induced by $^{15}\text{N}(\text{d}, \text{p})^{16}\text{N}$ with a background of silicon.

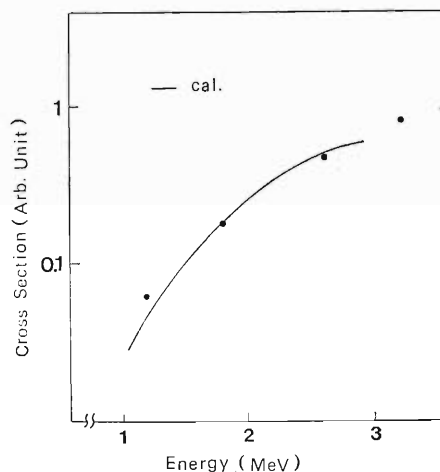


Fig. 2. Thick target yields of the $^{15}\text{N}(\text{d}, \text{p})^{16}\text{N}$ reaction.

Reference

- 1) Y. Itoh, T. Nozaki, Y. Ohkubo, and Y. Mochizuki: *RIKEN Accel. Prog. Rep.*, 20, 92 (1986).

* Nuclear Reactor Research Laboratory, Tokyo Institute of Technology.

III-3-2. Study on Carbon and Boron in Gallium Arsenide

Y. Itoh, T. Nozaki, H. Fukushima, and Y. Kadota*

Accurate determination of ultra trace carbon in high purity gallium arsenide is required to clarify the effect of carbon on the semi-insulated matrix. We reported on the determination of carbon by means of the deuteron activation analysis with the $^{12}\text{C}(d, n)^{13}\text{N}$ reaction.¹⁾ The relationship between the infrared (IR) absorption coefficient and the carbon concentration obtained by this method was also reported.²⁾ Since IR spectrophotometry is used for the routine analysis of carbon in gallium arsenide in semiconductor industries, it is urgently required to determine the calibration curve as reliably as possible for general use. Japan Electronic Industry Development Association organized a committee for the determination of the calibration curve. As a member laboratory of the committee, we have continued the charged particle activation analysis of carbon in samples prepared by the committee. These samples were already submitted to round robin IR measurement by 16 laboratories belonging to the committee. The results are under treatment by the committee.

To prove the reliability of the analysis, we analyzed many sample wafers cut from a presumably uniform portion of a single ingot before the committee's work.

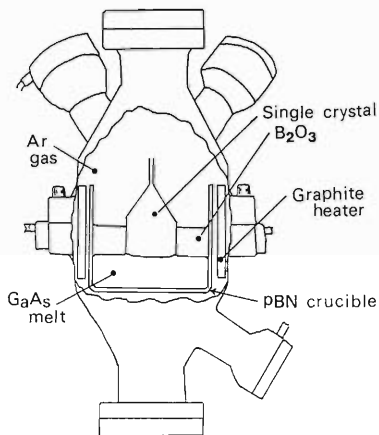


Fig. 1. Crucible for growing LEC GaAs ingots.

* Electronics Materials Laboratory, Sumitomo Metal Mining Co., Ltd.

Table 1. Concentrations of carbon and boron in GaAs crystals grown in different ambiances.

Sample No.	Atmosphere	Solid fraction (%)	Carbon ($\times 10^{15}\text{cm}^{-3}$)	Boron ($\times 10^{16}\text{cm}^{-3}$)
A	Ar	0.17 (top)	0.93	2.5
		0.64 (tail)	0.51	1.9
B	Ar+1% O ₂	0.14	16	3.6
		0.76	18	3.4
C	Ar+1% CO	0.1	6.4	1.7
		0.77	6.4	1.5
D	Ar+1% CO (long duration)	0.17	6.0	2.8
		0.78	6.1	1.9

Graphite plates were used as the activation comparator. In this method boron can be analyzed simultaneously with carbon by the $^{10}\text{B}(d, n)^{11}\text{C}$ reaction. The reproducibility of analysis is shown by the following results; for 30 graphite plates, $(3.68 \pm 0.044) \times 10^8$ cpm as saturation activity for $1 \mu\text{C min}^{-1}$ bombardment; for 18 samples 24.6 ± 2.62 ppb.wt of carbon and 48.8 ± 4.2 ppb.wt of boron, where the sign \pm indicates standard errors.

Since the ingot was grown from GaAs melt covered with B_2O_3 encapsulant in a pyrolytic boron nitride crucible, as shown in Fig. 1, the crystal is thought to inevitably contain a noticeable concentration of boron. These samples actually were found to contain 10^{16} to 10^{18} atoms cm^{-3} boron. Table 1 shows the concentrations of carbon and boron in 8 samples cut from top and tail positions of 4 ingots grown in different ambiances. Further experiments are planned to get more information about correlation among the concentrations of carbon, oxygen and boron.

References

- 1) Y. Itoh, T. Nozaki, Y. Ohkubo, T. Kimura, H. Fukushima, Y. Kadota, and K. Sakai: *RIKEN Accel. Prog. Rep.*, **20**, 91 (1986).
- 2) Y. Kadota, K. Sakai, T. Nozaki, Y. Itoh, and Y. Ohkubo: *Semi-Insulating III-V Materials*, Ohmusha, Ltd., Tokyo, p. 201 (1986).

III-3-3. Analysis of Hydrogen in Plasma CVD SiO_x Films by an Elastic Recoil Detection Method

K. Saito, H. Yamaguchi,* M. Aratani, and M. Yanokura

A plasma CVD (chemical vapour deposition) SiO_x film is a promising insulation material for surface passivation or isolation of multilayer metallization on integrated circuit (IC). Since the electrical property of IC is affected by the composition of the SiO_x film, it is indispensable to find the relationship between the value of film growth conditions and the film composition on IC production process. Especially hydrogen remaining in the SiO_x films after CVD growth using SiH_4 gas for the reactant material affects physical strength or electrical leakage of films. In the present study, the hydrogen contents in the SiO_x films grown under different conditions were measured by an ERD (elastic recoil detection) method using an Ar-ion beam from RILAC. SiO_x films were grown to 1 μm in thickness on single silicon substrates under various conditions:

- (1) Flow rate of reactant gasses ($\text{SiH}_4/\text{N}_2\text{O}$): flow rate of SiH_4 was changed from 110 sccm to 160 sccm, while that of N_2O was kept constant.
- (2) Plasma power: 1 A to 3 A.
- (3) Substrate temperature: 250°C to 350°C.

Geometrical arrangement of the ERD measurement is shown in Fig. 1 with an example of hydrogen peak profiles. The sample surface was bombarded with a 50 MeV Ar^{4+} -ion beam at an incident angle of 30°, and recoiled hydrogen ions were measured at a detection angle of 33°. Scattered silicon ions or

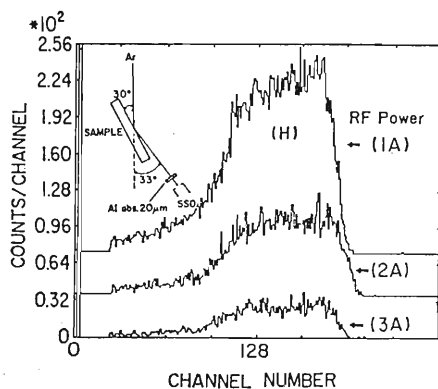


Fig. 1. Geometrical arrangement of ERD measurement and ERD spectra of hydrogen in SiO_x films.

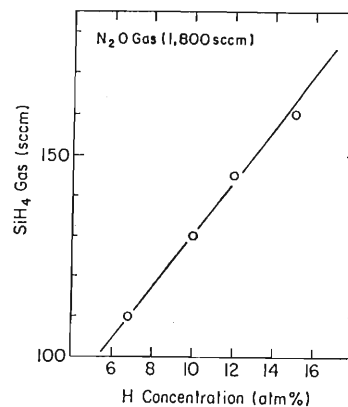


Fig. 2. Relation between the hydrogen content and the SiH_4 flow rate.

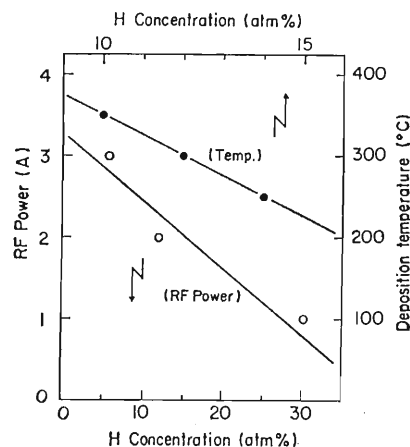


Fig. 3. Relation between the hydrogen content and the substrate temperature and RF (radio frequency) power.

oxygen ions, which form a background at the hydrogen peak, were absorbed with a 20 μm thick aluminum film placed in front of the detector.

The results of analysis are shown in Figs. 2 and 3, which indicate that the hydrogen content increases in proportion to the SiH_4 flow rate and decreases in inverse proportion to the substrate temperature and the plasma power. From these results, the hydrogen content of a CVD SiO_x film was found sensitive to film growth conditions.

* R & D Center, Toshiba Corporation.

III-3-4. Heavy-Ion Rutherford 2π -Scattering Analysis Applied to the Development of a Monitoring Detector for the Measurement of Water Reactivity

T. Nozaki,* M. Aratani, M. Yanokura, and B. G. Yu

Heavy-ion Rutherford 2π -scattering (HIR2 π S) analysis was used to develop a monitoring detector for the water reactivity. The principle is as follows. Soda-lime-silica glass plates are treated with a CsCl solution¹⁾ or D₂O for the replacement of cations near the surface (up to a few micrometer depth) with Cs⁺ or D⁺, and then exposed to the environment. The extent of Cs-to-H or D-to-H exchange with environmental water is measured by heavy-ion Rutherford 2π -scattering analysis. Information is also obtained on salts contained in the water simultaneously.

Soda-lime-silica glass plates treated with a boiling CsCl solution, or sealed with D₂O or D₂O-H₂O in quartz ampules and heated to 100°C for 4 to 5 days, were kept in contact with sand containing water, or exposed to air or water for various times. Table 1 shows some preliminary results on the D/H ratio of the total area covered by a D Peak to that by a H peak in HIR2 π S spectra^{2,3)} which were obtained under the same geometrical arrangement. The total area covered by a H peak of as-obtained glass samples, which is regarded as due to background surface hydrogen, was subtracted from every measurement

Table 1. D-for-Na substitution and D-by-H replacement for glass plate under various conditions.

Sample No.	Pretreatment	Treatment	D/H Ratio	
1	None	D ₂ O 100°C, 120 h	0.266	
2		D ₂ O-H ₂ O(10:1) D ₂ O-H ₂ O(3:1) D ₂ O-H ₂ O(1:1)	0.294	
3			100°C, 98 h	0.195
4				
5	D ₂ O	Sand 26°C, 216 h	0.279	
6		Sand+15% H ₂ O	0.190	
7	100°C, 120 h	Sand+ 7% H ₂ O	60°C, { 24 h	0.181
8			{ 72 h	0.091
9		Room Air	(26°C), 216 h	0.214

* Present address: School of Hygienic Sciences, Kitasato University, Kitasato, Sagami-hara, 228, Japan.

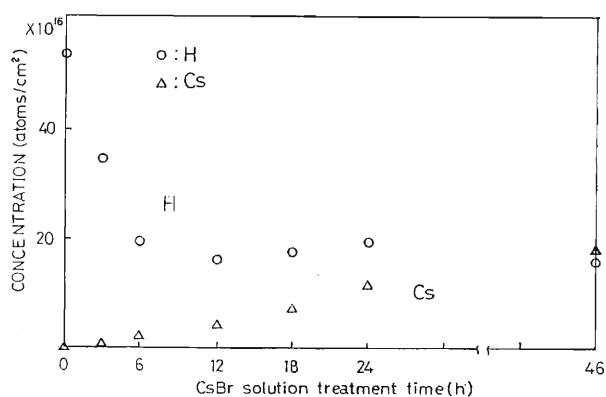


Fig. 1. Preparation of Cs-substituted glass plates for a monitoring detector of water reactivity.

value. The background surface hydrogen was rather constant in the order of 10^{15} H atoms/cm² among various samples.²⁾ The water content of sand is given by the weight fraction of water added to the sand which had been dried at 100°C for several days.

Correlations seen in Table between the ease of the D-to-H replacement and environmental condition are thought to be reasonable, though qualitatively at the present stage. The D/H ratio is always less than 1, mainly because H was not replaced by D in the D₂O treatment at 100°C in the depth beneath micrometer. The uncertainty in the value of D/H would be 10% due to statistical error.

Cs-substituted glass plates are also promising as a monitoring detector of water reactivity. We obtained preliminary results on exposing experiments. The results are shown in Fig. 1.

We intend to utilize this method for the study on water in nature.

References

- 1) B. G. Yu, M. Aratani, M. Yanokura, T. Nozaki, and E. Arai: *RIKEN Accel. Prog. Rep.*, **20**, 100 (1986).
- 2) H. Nagai, S. Hayashi, M. Aratani, T. Nozaki, M. Yanokura: *Nucl. Instrum. Methods B*, **28**, 59 (1987).
- 3) M. Aratani: *Radioisotopes*, **37**, 43 (1988).

III-3-5. Application of PIXE to Medical and Environmental Science (II)

K. Maeda, Y. Sasa, H. Kusuyama, K. Yoshida,*
M. Maeda,** and M. Uda***

Growing interest has developed in a balance of element concentrations in biological organs and environmental materials affecting human health. Rapid, sensitive multielemental analyses are required for investigating this problem. PIXE is one of the most advanced methods which meet such a requirement. We have continued a study on the application of PIXE to medical and environmental science.¹⁻⁴⁾ We report here the PIXE analysis made on (1) human spermatozoa and seminal plasma and (2) seaweeds.

(1) Spermatozoa and seminal plasma

Recently many papers have been presented on correlations between trace element concentrations in semen and human sperm quality relating infertility. It is attractive to investigate element concentrations in spermatozoa themselves. PIXE is quite suitable for such small amounts of samples. We have analyzed human spermatozoa and seminal plasma taken from three patients of infertility and a normal man. Spermatozoa were separated from seminal plasma by centrifugation. The samples were deposited on 1 μm thick polypropylene film, dried in a vacuum desiccator and then used as targets without any other pre-treatments. An 8 MeV He^+ ion beam of 1 mm in diameter was used as an excitation source. X rays generated

from the targets were detected with a Si(Li) detector through an X-ray absorber made of 1.5 μm thick polypropylene or 1.0 mm thick polyethylene film.

Typical PIXE spectra obtained in this experiment are shown in Fig. 1. The elements, Na, Mg, P, S, Cl, K, Ca, Fe, Cu, Zn, and Br were detected in both spermatozoa and seminal plasma. The K concentration in dried weight was almost the same in all samples examined here. For all of the sample pairs, S and Fe are richer in spermatozoa than in seminal plasma. The Fe content in spermatozoa taken from the normal man was higher than those from the infertile men. We are now searching for a technique for preparing spermatozoa samples which are not contaminated with seminal plasma, without changing their composition, in order to obtain more reliable data.

(2) Seaweeds

Seaweeds, favorite healthy food for Japanese, are important sources of iodine and so-called mineral components essential for living. Numerous analyses have been made on concentrations of individual elements contained in marine organisms.⁵⁾ There are, however, few reports on simultaneous multielemental analyses of seaweeds. We studied here the variations in element compositions with species, growing dis-

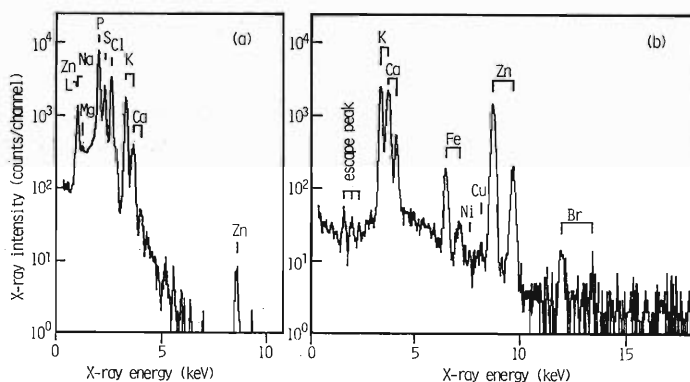


Fig. 1. PIXE spectra of spermatozoa taken from a normal man. (a) with 1.5 μm polypropylene and (b) with 1 mm polyethylene absorbers.

* Saitama Medical Center, Saitama Medical School.

** Tokyo University of Fisheries.

*** Present address: Department of Materials Science, Waseda University, Tokyo.

tricts, and the distributions of elements in a specimen. Commercially available edible seaweeds, a sea

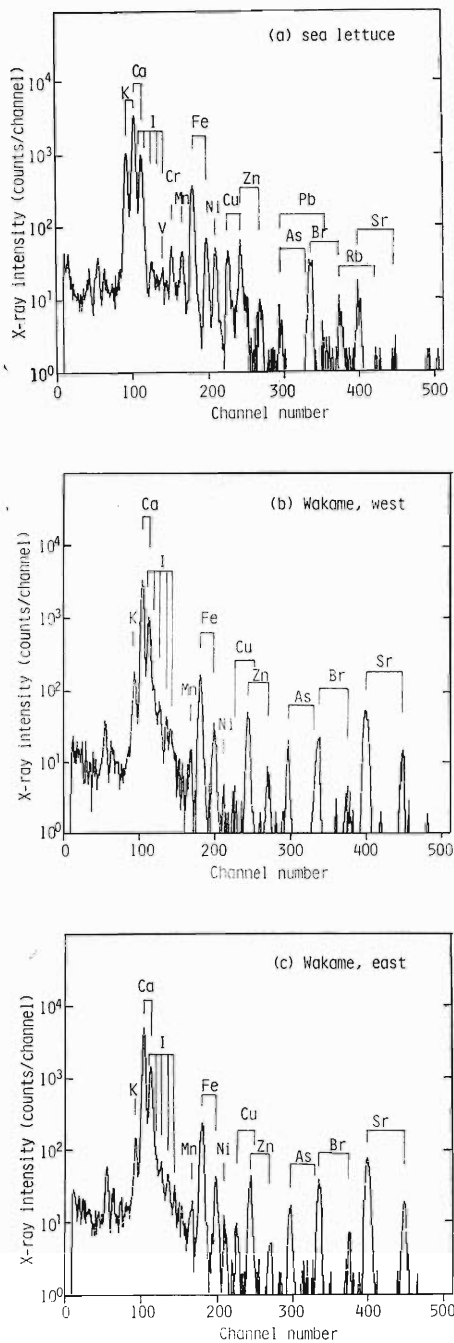


Fig. 2. PIXE spectra taken from dried seaweeds. (a) sea lettuce obtained from Noto district at the west coast of Japan; (b) *wakame* obtained from Noto district; and (c) *wakame* obtained from Sanriku district at the east coast of Japan. 1.6 MeV H^+ impact, 1 mm polyethylene absorber.

Table 1. $K\alpha$ peak intensities^{a)} of PIXE spectra for a fresh sea tangle: 5.0 MeV H^+ impact.

	Cl	K	Ca	Zn	Br	Sr	I
Outer region of stick	200	2.9	1.2	0.028	0.19	0.06	0.032
Inner region of stick	160	7.4	3.8	0.024	0.09	0.06	0.006
Leaf	110	6.5	8.0	0.037	0.08	0.06	0.005

^{a)} Peak intensities are normalized by use of the background intensities at 3.0 keV.

lettuce (*Ulva* sp., green algae) grown at the west coast of Japan and two *wakames* (*Undaria* sp., brown algae) from the east and the west coasts of Japan, were analyzed. The sample materials were reconstituted from dried seaweeds with distilled water. Figure 2 shows the PIXE spectra taken from these samples excited with 1.6 MeV H^+ ions. The element compositions of *wakames* obtained from different districts were almost the same. The *wakames* (brown algae) contained a large amount of As, I, and Sr; the sea lettuce (green algae) were rich in Cr, Ni, and Cu. Brown algae are well known to accumulate I and As in high concentrations.⁵⁾ PIXE is expected to be a convenient and effective method to seek for such accumulator organisms because of its ability to detect fugacious elements together with other elements simultaneously without any chemical pre-treatments.

Three parts of a fresh sea tangle (*Laminaria* sp., brown algae), the leaf, and the outer and the inner regions of stick, were analyzed with 5.0 MeV H^+ ions. The sample was washed with tap water and cut with a stainless steel knife. The results are shown in Table 1, where the $K\alpha$ peak intensities are normalized with the background at 3.0 keV. Iodine is concentrated in the outer region of stick compared with the leaf and the inner region of stick. The Ca level was highest in the leaf.

References

- 1) M. Uda, K. Maeda, Y. Sasa, H. Kusuyama, and Y. Yokode: *Nucl. Instrum. Methods B*, **22**, 184 (1987).
- 2) K. Maeda, Y. Yokode, Y. Sasa, H. Kusuyama, and H. Uda: *Nucl. Instrum. Methods B*, **22**, 188 (1987).
- 3) K. Maeda, Y. Sasa, M. Maeda, and M. Uda: *Nucl. Instrum. Methods B*, **22**, 456 (1987).
- 4) K. Maeda, Y. Sasa, H. Kusuyama, M. Maeda, H. Ishikawa, Y. Yokode, and M. Uda: *RIKEN Accel. Prog. Rep.*, **20**, 94 (1986).
- 5) R. Eisler: *Trace Metal Concentrations in Marine Organisms*, Pergamon Press, New York (1981).

III-3-6. Application of PIXE and Diffraction Analysis to Ancient Remains (II)

Y. Sasa, K. Maeda, and M. Uda*

For the analysis of ancient remains, non-destructive and highly sensitive measuring methods are indispensable. PIXE is one of the most effective methods to gain our ends in view of elemental analyses. Several PIXE data have been reported on ancient coins and jewelries.¹⁻⁹⁾ Crystallographic analyses also bring us highly reliable information on structures and chemical constituents of archaeological samples. This paper reports chemical and crystallographic surveys of coins from different districts and ages. Concentrations of minor constituent elements in these ancient remains might give us keys to understanding of exchange or diffusion of cultures. These data will also contribute to the elucidation of technological backgrounds in ancient periods.

The samples analyzed were coins made at different districts and ages: 1) Pakistan coins and their dark grey casting molds obtained from the Banbhor ruin in Pakistan dated back to 0-7th centuries; 2) ancient Chinese coins casted at Tang and Song era, 7-11th centuries, of China (referred to as ancient Chinese coins); 3) a coin minted at the Qing era (1841) of China (referred to as a Qing coin). Target materials were irradiated with 1.3-2.1 MeV/amu He⁺ ions obtained from the linear accelerator and 1.6 MeV H⁺ ions from the RIKEN TANDETRON. X rays generated from the targets were detected with a Si(Li) detector through a 7.5 μm Be window. High energy X-rays emitted from the trace amounts of elements were measured through a thick polyethylene absorber (1 mm) or thin Co absorber (8 μm) inserted between the target and the detector in order to depress the pile-up phenomenon in the detector. Signals from the detector were stored in a multi-channel analyzer, and then processed on a micro-computer and transferred to magnetic discs. Background X-ray spectra were subtracted.

X-ray diffraction data were taken with an automated X-ray diffractometer equipped with a Cu radiation source, a graphite monochromator, and a NaI scintillation counter. Operation conditions of goniometer scanning speed ($2\theta^\circ/\text{min}$) = 2 and time constant = 1 s were used, and diffraction data were

recorded on strip charts and magnetic floppy discs.

Figure 1 shows the PIXE spectrum obtained from Banbhor coin. The chemical compositions correspond to bronze including a relatively high contents of iron and lead (Fe K α /Cu K α = ~0.08 and Pb L α /Cu K α = ~0.05). The X-ray diffraction analysis also confirmed a bronze phase. From the coin casting mold with a dark grey color α -quartz, ferro-alumino-

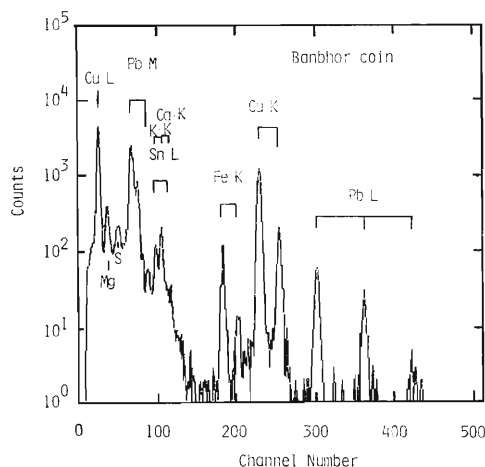


Fig. 1. PIXE spectrum from the Banbhor coin (dated 0-7th century) bombarded with a 2.1 MeV/amu He⁺ beam.

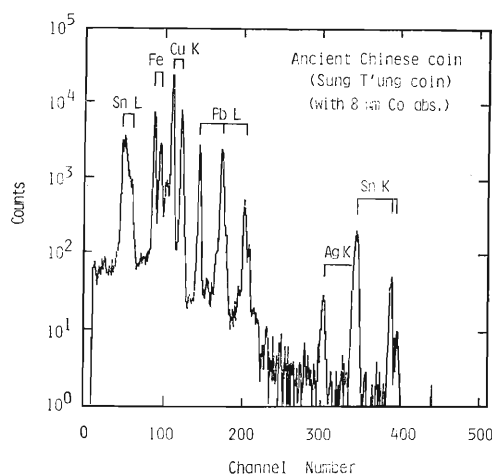


Fig. 2. PIXE spectrum from the ancient Chinese coin (Song Tang coin) bombarded with a 1.6 MeV proton beam; on 8 μm Co absorber was used.

* Present address: Department of Materials Science, Waseda University, Tokyo.

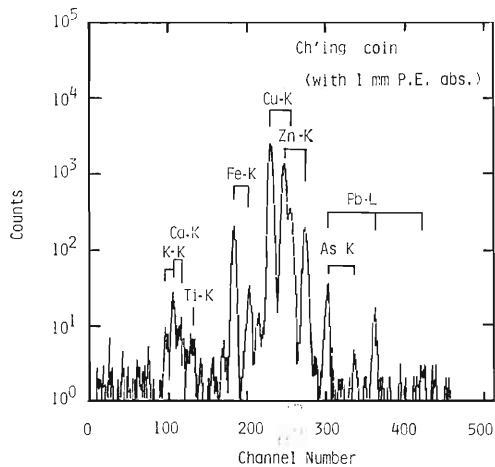


Fig. 3. PIXE spectrum from the Qing coin (1941) bombarded with a 2.1 MeV/amu He^+ beam; a 1,000 μm polyethylene absorber was used.

silicates and calcite were detected by X-ray diffraction. The PIXE data shows that the main components of the mold are Si, Ca, and Al (Ca $K\alpha$ /Si $K\alpha$ =0.30 and Al $K\alpha$ /Si $K\alpha$ =0.26), indicating that results from PIXE are consistent with those from X-ray diffraction.

A typical PIXE pattern of an ancient Chinese coin is displayed in Fig. 2. All coins studied were grouped into bronze from elemental and structural analysis. Detailed technological or archaeological analyses on

these coins are now in progress.

PIXE spectrum from Qing coin is seen in Fig. 3. On the basis of the PIXE analyses the coin was made of brass (Zn $K\alpha$ /Cu $K\alpha$ = \sim 0.55). Lead was also found from this sharply grooved coin (Pb $L\alpha$ /Cu $K\alpha$ =0.08–0.18), suggesting that the coin was casted in a mold and then letters or figures on the coin were finished up by knife cutting. Ancient craftsmen seem to have already known that Pb in brass is very effective to improve machinability; modern metallurgy uses Pb-brass for fine machinery.

References

- 1) H. Mommsen and T. Schmittinger: *Archaeometry*, **23**, 71 (1981).
- 2) G. P. Ferreira and F. B. Gil: *Archaeometry*, **23**, 189 (1981).
- 3) C. P. Swan: *Nucl. Instrum. Methods*, **197**, 237 (1982).
- 4) G. Demortier, B. van Dystaeyer, and A. Boullor: *Nucl. Instrum. Methods B*, **3**, 339 (1984).
- 5) Z. Smit and P. Kos: *Nucl. Instrum. Methods B*, **3**, 416 (1984).
- 6) S. J. Fleming and C. P. Swan: *Nucl. Instrum. Methods A*, **242**, 626 (1986).
- 7) Proc. Int. Workshop on IBA in the Arts and Archaeology, Pont-à-Mousson, *Nucl. Instrum. Methods B*, **14** (1986).
- 8) J. W. Palmer, M. G. Hollander, P. S. Z. Roger, C. J. Duffy, and T. M. Benjamin: *Nucl. Instrum. Methods B*, **22**, 419 (1987).
- 9) Y. Sasa, K. Maeda, and M. Uda: *Nucl. Instrum. Methods B*, **22**, 426 (1987).

III-3-7. *In Situ* Emission Mössbauer Studies of Solid/Solution Interface: $^{119}\text{Sb}^{5+}$ and $^{57}\text{Co}^{2+}$ Ions Adsorbed on $\gamma\text{-Fe}_2\text{O}_3$

F. Ambe, S. Ambe, and T. Okada

In spite of the development of physicochemical techniques for surface analysis, spectroscopic methods applicable to the study of chemical bonding at interfaces between solid and aqueous phases are limited. We previously demonstrated that the *ex* and *in situ* emission Mössbauer measurements are useful in clarifying the chemical environment of dilute metal ions adsorbed on magnetic metal oxide surfaces.¹⁻³⁾ When ^{119}Sn or ^{57}Fe ions arising from $^{119}\text{Sb}^{5+}$ or $^{57}\text{Co}^{2+}$ are bonded through oxide ions to the ordered surface metal ions of a magnetic oxide, the ^{119}Sn or ^{57}Fe nuclei feel the hyperfine magnetic fields induced by interaction with the ordered magnetic metal ions of the substrate. The hyperfine magnetic fields are observed as broadening or splitting in the emission Mössbauer spectra. In this report, application of this technique to $^{119}\text{Sb}^{5+}$ and $^{57}\text{Co}^{2+}$ ions at the interface between $\gamma\text{-Fe}_2\text{O}_3$ and aqueous solutions is described.

The source nuclide ^{119}Sb was produced by the cyclotron.⁴⁾ About 10 cm^3 of an aqueous solution containing $^{119}\text{Sb}^{5+}$ or $^{57}\text{Co}^{2+}$ was put in a Teflon

vessel equipped with a 0.5 mm-thick Teflon window at the bottom. About 30 mg of $\gamma\text{-Fe}_2\text{O}_3$ powders was added to the solution. The suspension was shaken thoroughly at room temperature. The amounts of antimony and cobalt coexisting with the nuclides are estimated to have been less than 400 ng and 300 ng, respectively, *i.e.*, to have been much smaller than that required for monolayer coverage of 30 mg of the $\gamma\text{-Fe}_2\text{O}_3$ sample.

The $\gamma\text{-Fe}_2\text{O}_3$ with adsorbed $^{119}\text{Sb}^{5+}$ or $^{57}\text{Co}^{2+}$ along with the solution was subjected to the emission Mössbauer measurement at $24 \pm 1^\circ\text{C}$. The absorbers employed were ^{57}Fe -enriched potassium ferrocyanide ($0.5\text{ mg }^{57}\text{Fe}/\text{cm}^2$) and barium stannate (0.9 mg

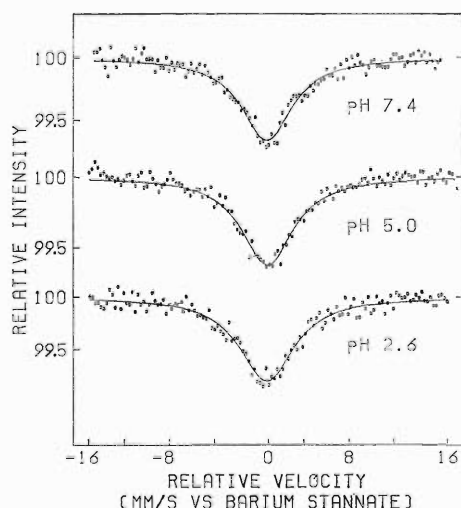


Fig. 1. *In situ* emission Mössbauer spectra of $^{119}\text{Sn}^{4+}$ arising from $^{119}\text{Sb}^{5+}$ at the $\gamma\text{-Fe}_2\text{O}_3/0.25\text{ mol dm}^{-3}$ LiCl solution interface at pH 7.4, 5.0, and 2.6 (measurement at room temperature). The isomer shift is given relative to barium stannate at room temperature and the sign of relative velocity is defined as in ordinary absorption spectra. The curves are the results of least-squares fitting with a Lorentzian.

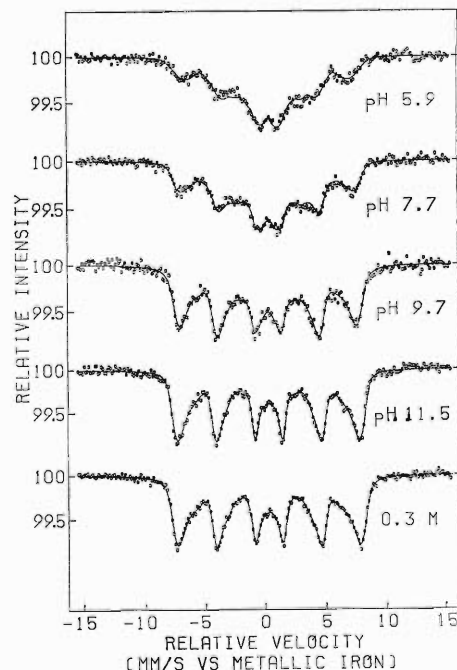


Fig. 2. *In situ* emission Mössbauer spectra of $^{57}\text{Fe}^{2+}$ arising from $^{57}\text{Co}^{2+}$ at the $\gamma\text{-Fe}_2\text{O}_3/0.1\text{ mol dm}^{-3}$ NaCl solution or 0.3 M NaOH interface for various pH values of the aqueous phase (measurement at room temperature): (A) pH 5.9, (B) pH 7.7, (C) pH 9.7, (D) pH 11.5, (E) 0.3 M NaOH. The isomer shift is given relative to metallic iron at room temperature and the sign of relative velocity is defined as in ordinary absorption spectra. The curves are constituted based on the results of Hesse-Rübartsch analysis assuming no relaxation.

$^{119}\text{Sn}/\text{cm}^2$). The Mössbauer γ -rays of ^{57}Co and ^{119}Sb were detected respectively with a Kr (+3% carbon dioxide)-filled proportional counter and with a 2 mm-thick NaI (Tl) scintillation counter through a $65\ \mu\text{m}$ -thick Pd critical absorber for Sn K X-rays.

The *in situ* emission Mössbauer spectra of $^{119}\text{Sn}^{4+}$ arising from $^{119}\text{Sb}^{5+}$ ions adsorbed on $\gamma\text{-Fe}_2\text{O}_3$ from $0.25\ \text{mol}/\text{dm}^3$ LiCl solutions of different pH values at room temperature are shown in Fig. 1. As seen from Fig. 1, the spectra are essentially symmetric lines centered at the zero relative velocity against a barium stannate absorber. This demonstrates that ^{119}Sn at the interface is exclusively in the tetravalent state. The width of the lines is much larger than that for $^{119}\text{Sn}^{4+}$ arising from $^{119}\text{Sb}^{5+}$ on dia- or paramagnetic oxide surfaces (about $1.3\ \text{mm s}^{-1}$). We conclude, therefore, that most of the adsorbed $^{119}\text{Sb}^{5+}$ ions on $\gamma\text{-Fe}_2\text{O}_3$ particles have a certain magnetic interaction with the ordered ferric ions of the substrate at the pH value. The pH dependence of the line width is, however, much less pronounced for $\gamma\text{-Fe}_2\text{O}_3$ than the case of $^{119}\text{Sb}^{5+}$ on $\alpha\text{-Fe}_2\text{O}_3$.³⁾

The emission Mössbauer spectra of ^{57}Fe arising from $^{57}\text{Co}^{2+}$ ions at the interface between $\gamma\text{-Fe}_2\text{O}_3$ particles and $0.1\ \text{mol}/\text{dm}^3$ NaCl solutions of different pH as well as a $0.3\ \text{M}$ NaOH solution at room temperature are shown in Fig. 2. As can be seen

from Fig. 2, the emission spectra show a marked dependence on the pH of the aqueous phase in contrast to the case of $^{119}\text{Sb}^{5+}$ described above. No emission lines ascribable to paramagnetic iron species are recognized in the spectra within the experimental uncertainties. The isomer shift indicates that ^{57}Fe ions arising from $^{57}\text{Co}^{2+}$ at the interface are predominantly in the trivalent state. At pH 5.9 and 7.7, the spectra consist of a partly resolved sextet of broad lines. With increase in pH of the aqueous phase the splitting of the sextet increases and simultaneously the width of each line diminishes. These observations are essentially in parallel with those for $\alpha\text{-Fe}_2\text{O}_3$ reported previously.³⁾

The results of detailed analysis of the experimental data and discussion in terms of the surface structure of the oxides will be described elsewhere.

References

- 1) T. Okada, S. Ambe, F. Ambe, and H. Sekizawa: *J. Phys. Chem.*, **86**, 4726 (1982).
- 2) F. Ambe, T. Okada, S. Ambe, and H. Sekizawa: *J. Phys. Chem.*, **88**, 3015 (1984).
- 3) F. Ambe, S. Ambe, T. Okada, and H. Sekizawa: *Geochemical Processes at Mineral Surface* (eds. J. A. Davis and K. F. Hayes), ACS Symp. Ser. 323; Am. Chem. Soc., Washington, D.C., p. 403 (1986).
- 4) S. Ambe: *J. Radioanal. Nucl. Chem. Artic.*, **81**, 77 (1984).

III-3-8. Mössbauer Spectroscopic Studies of Ruthenium Trichlorides

Y. Kobayashi, M. Katada, H. Sano,* T. Okada,
K. Asai, N. Sakai, S. Ambe, and F. Ambe

We previously reported the ^{99}Ru Mössbauer spectroscopic investigation using the cyclotron-produced ^{99}Rh in ruthenium powders as a source.¹⁾ In this period, the ^{99}Ru Mössbauer effect and the magnetic susceptibility were studied on anhydrous ruthenium trichlorides.²⁾

It is known that anhydrous ruthenium trichlorides occur in two forms; black $\alpha\text{-RuCl}_3$ with the $P3_112$ space group and brown $\beta\text{-RuCl}_3$ with the trigonal $P3c1$. In both forms, trivalent ruthenium ions have a low-spin $4d^5$ configuration lying in a distorted octahedra of chloride ions. It was also reported that α - and $\beta\text{-RuCl}_3$ became antiferromagnetic below 13 K and about 870 K, respectively, on the basis of magnetic susceptibility data.³⁾ No Mössbauer spectrum of $\alpha\text{-RuCl}_3$ has been published yet. The spectrum of $\beta\text{-RuCl}_3$ is reported to show only a quadrupole splitting,⁴⁾ in contradiction to the above magnetic susceptibility result.

The method of source preparation was similar to that previously reported,¹⁾ except that 97%-enriched ^{99}Ru metallic powders (83 mg cm^{-2}) were used for proton irradiation to improve the S/N ratio of Mössbauer γ rays. Magnetic susceptibility measurement was carried out using a vibrating-sample magnetometer (the Foner type) with a magnetic field up to 20 kOe for $\alpha\text{-RuCl}_3$ and 16 kOe for $\beta\text{-RuCl}_3$ between 4 K and room temperature. The sample of $\alpha\text{-RuCl}_3$ was commercially obtained, $\beta\text{-RuCl}_3$ was prepared by a new method developed by us: by heating triruthenium dodecacarbonyl, $\text{Ru}_3(\text{CO})_{12}$, in a chlorine stream at 360°C for 4 h. Our method is more convenient and yields purer $\beta\text{-RuCl}_3$ compared with the previous one.⁵⁾ Neither unreacted carbonyl nor by-products (such as $\alpha\text{-RuCl}_3$, other chlorides and ruthenium metal) were detected from the X-ray diffraction pattern of the obtained product.

The typical Mössbauer spectra obtained with the source and absorber, 1.02 g cm^{-2} of $\alpha\text{-RuCl}_3$ and 0.34 g cm^{-2} of $\beta\text{-RuCl}_3$, at 5 K are shown in Figs. 1(a) and (b), respectively. The susceptibility of $\alpha\text{-RuCl}_3$ is essentially in agreement with the previous result³⁾ and follows the Curie-Weiss law in the temperature range 120–300 K. The magnetic susceptibility of $\beta\text{-RuCl}_3$ was found to obey the Curie law

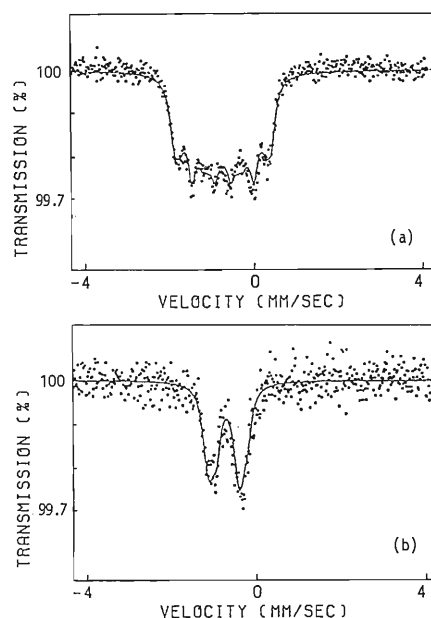


Fig. 1. Mössbauer spectra at 5 K of (a) $\alpha\text{-RuCl}_3$ and (b) $\beta\text{-RuCl}_3$ against the $^{99}\text{Rh-Ru}$ metal source at the same temperature ((a) a total of 5.4×10^7 counts per channel and (b) a total of 1.1×10^7 counts per channel).

over the temperature range studied.

In the analysis of the Mössbauer spectra, we adopted Kistner's value of 2.7 for the E2/M1 mixing ratio, δ^2 , together with the ratio of the quadrupole moment of the nuclear excited state ($I_e=3/2$) to that of the ground state ($I_g=5/2$), $Q_e/Q_g=2.89$.⁶⁾ Symmetric 18 lines appear in a spectrum under a pure magnetic field, while an asymmetric doublet appears in the presence of an electric field gradient of ordinary magnitude.

As seen from Fig. 1(a), the Mössbauer spectrum of $\alpha\text{-RuCl}_3$ has a hyperfine structure with little asymmetry. This observation suggests the presence of a considerably strong magnetic field and the absence of a significant electric field gradient at the ^{99}Ru nuclei in this compound. In fact, the experimental data can be analyzed with a reasonable χ^2 -value assuming no electric field gradient. The obtained Mössbauer parameters are summarized in Table 1. The value of the isomer shift is in the range typical for trivalent ruthenium compounds.⁷⁾ The magnitude of H_{hf} , 209 kOe, is about 2/3 of those in trivalent

* Department of Chemistry, Tokyo Metropolitan University.

Table 1. Mössbauer parameters for anhydrous ruthenium trichlorides.

Compound	δ (mm s ⁻¹) ^a	$\frac{e^2qQ_s}{2}$ (mm s ⁻¹) ^b	H_{hf} (kOe)	Ref.
α -RuCl ₃	-0.74	0	209	this work
β -RuCl ₃	-0.71	0.75	0	this work
β -RuCl ₃	-0.71	0.85	—	4

a, relative to ruthenium metal; b, the quadrupole splitting for the excited state.

ruthenium oxides with the perovskite structure, in which Ru ions are also in the low-spin 4d⁵ state. Isomorphous iron trichloride, FeCl₃, has a large hyperfine magnetic field of 495 kOe extrapolated to 0 K, because Fe³⁺ is in a high-spin 3d⁵ state. On the basis of the present result of Mössbauer measurements, we conclude that α -RuCl₃ is in a magnetically ordered state at 5 K. The temperature dependence of the magnetic susceptibility supports this conclusion. The absence of an appreciable quadrupole interaction implies that the distortion of six Cl⁻ octahedron around trivalent Ru ions is small in the layer structure of α -RuCl₃.

The Mössbauer spectrum of β -RuCl₃ (Fig. 1(b)) is a doublet with a small asymmetry. The spectrum was analyzed satisfactorily on the assumptions of zero magnetic field and an axially symmetric electric field gradient expected from a crystallographic study.³⁾ The determined Mössbauer parameters of β -RuCl₃

are shown in Table 1. Our refined data are not so different from those reported by Clausen *et al.*⁴⁾ The occurrence of the antiferromagnetic ordering below about 870 K proposed by Fletcher *et al.* based on their magnetic susceptibility measurement is obviously inconsistent with the Mössbauer spectroscopic results. On the other hand, our measurement shows that the magnetic susceptibility follows the Curie law down to 4 K, indicating that β -RuCl₃ is paramagnetic at 5 K where the Mössbauer spectrum was obtained. The electric field gradient is attributed to the distortion of RuCl₆ octahedron with a relatively close Ru-Ru spacing in the chain structure of this compound.³⁾

References

- 1) Y. Kobayashi, M. Katada, H. Sano, T. Okada, K. Asai, S. Ambe, and F. Ambe: *RIKEN Accel. Prog. Rep.*, **20**, 111 (1986).
- 2) Y. Kobayashi, M. Katada, H. Sano, T. Okada, K. Asai, N. Sakai, S. Ambe, and F. Ambe: *Hyperfine Interact.*, **41**, 487 (1988).
- 3) J. M. Fletcher, W. E. Gardner, A. C. Fox, and G. Topping: *J. Chem. Soc. (A)*, 1038 (1967).
- 4) C. A. Clausen, R. A. Prados, and M. L. Good: *Chem. Phys. Lett.*, **8**, 565 (1971).
- 5) K. R. Hyde, E. W. Hooper, J. Waters, and J. M. Fletcher: *J. Less-Common Metals*, **8**, 428 (1965).
- 6) O. C. Kistner: *Phys. Rev.*, **144**, 1022 (1966).
- 7) D. C. Foyt, T. H. Siddall, C. J. Alexander, and M. L. Good: *Inorg. Chem.*, **13**, 1793 (1974).

III-3-9. Adsorption of No-Carrier-Added $^{119}\text{Sb(V)}$ Ions onto Metal Oxide Surfaces from Aqueous Solutions

S. Ambe

We previously studied the adsorption kinetics of cyclotron-produced $^{119}\text{Sb(V)}$ onto $\alpha\text{-Fe}_2\text{O}_3$ surfaces by a radiotracer method.¹⁾ The adsorption was found to proceed at pH 4, at the highest rate from a solution and with the second-order kinetics with respect to the concentration of antimony (V) and the surface area of $\alpha\text{-Fe}_2\text{O}_3$. These findings were discussed in connection with the chemical structure of adsorbed $^{119}\text{Sb(V)}$ investigated by emission Mössbauer spectroscopy.^{2,3)} The results motivated us to study the adsorption of $^{119}\text{Sb(V)}$ onto other metal oxides with different crystal structures. This report describes the pH dependence of the adsorption of no-carrier-added $^{119}\text{Sb(V)}$ ions onto Cr_2O_3 , $\alpha\text{-Al}_2\text{O}_3$, $\gamma\text{-Fe}_2\text{O}_3$, $\alpha\text{-FeOOH}$, CoF_2O_4 , and NiFe_2O_4 as well as respective adsorption kinetics.

The adsorbent was added to a 0.25 mol dm^{-3} LiCl solution containing no-carrier-added $^{119}\text{Sb(V)}$ ions. The suspension was shaken in a definite 8-shape motion with a mechanical shaker at given temperature. An aliquot of the suspension was taken at a given intervals for determination of the fraction of ^{119}Sb adsorbed. The adsorbent suspended in the aliquot was filtered out with a glass fiber filter. The 23.9 keV γ rays and Sn KX rays of ^{119}Sb in each filtrate were counted with an NaI scintillation counter.

Adsorption of $^{119}\text{Sb(V)}$ ions was analyzed on the basis of a rate equation:

$$dx/dt = k(a-x)^n \quad (1)$$

where a is the initial radioactivities of $^{119}\text{Sb(V)}$ in the solutions, x the radioactivities of $^{119}\text{Sb(V)}$ adsorbed, k the rate constant, and n the order of adsorption. The surface areas of the adsorbents used are sufficiently large to assume that the areas are invariable on adsorption of Sb(V) ions.

The percentages of $^{119}\text{Sb(V)}$ ions adsorbed on Cr_2O_3 are shown in Fig. 1. A part of the ^{119}Sb ions were adsorbed by Cr_2O_3 in the acid pH range after 60 min shaking at 60°C , though the yield was low. In the alkaline pH range no adsorption was observed. Marked increase in the adsorption was observed at pH 2-4 after 170 min stirring at 100°C , the adsorbed fraction amounting to 80-90% of the total $^{119}\text{Sb(V)}$

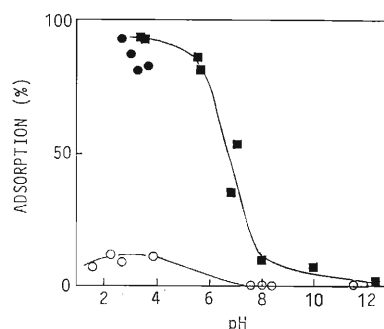


Fig. 1. Percentage adsorption of no-carrier-added $^{119}\text{Sb(V)}$ ions from 0.25 mol dm^{-3} LiCl solutions onto (O) Cr_2O_3 after 60 min shaking at 60°C , (●) Cr_2O_3 after 170 min shaking at 100°C and (■) $\gamma\text{-Fe}_2\text{O}_3$ after 30 min shaking at 20°C .

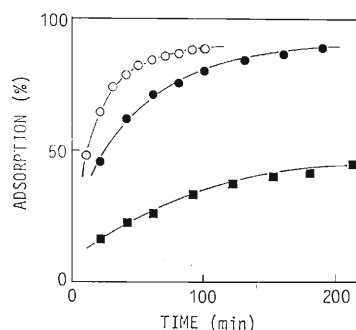


Fig. 2. Adsorption kinetics of no-carrier-added $^{119}\text{Sb(V)}$ ions onto (●) Cr_2O_3 from a 0.25 mol dm^{-3} LiCl solution of pH 3.0 at 100°C , onto (O) $\alpha\text{-Al}_2\text{O}_3$ from the solution of pH 2.0 at 100°C , and onto (■) CoFe_2O_4 from the solution of pH 2.3 at 50°C .

ions. The kinetic plot obtained for a solution at pH 3.0 at 100°C is shown in Fig. 2. The adsorption increased steadily with time of stirring. The result of analysis of the data by an integral form of Eq. 1 ($n=2$) shows that the relation between $1/(a-x)$ and t is linear, indicating that the order of reaction is 2.

About 30% of $^{119}\text{Sb(V)}$ was adsorbed by $\alpha\text{-Al}_2\text{O}_3$ from solutions at pH 1-3 and 10-20% at pH 6-10 after 60 min shaking at 50°C . At 100°C , 80-90% of ^{119}Sb was adsorbed at pH 2.0 in 80 min. An adsorption kinetic study carried out with a solution of pH 2.0 at 100°C shows that the adsorption yield

of $^{119}\text{Sb}(\text{V})$ increased with time (Fig. 2). The relation of $1/(a-x)$ vs. t was represented as a line with a bent on the half way, that is, a steep line followed by a less steep one.

$^{119}\text{Sb}(\text{V})$ ions were adsorbed rapidly by $\gamma\text{-Fe}_2\text{O}_3$ in the acid pH range at 20°C and the percentage adsorption amounted to 90% in 30 min as shown in Fig. 1. The adsorption decreased abruptly at pH's higher than 7. The kinetic data obtained from a solution of pH 4.0 at 50°C are shown in Fig. 3. The relation of $1/(a-x)$ vs. t obtained from the data is linear, suggesting that the adsorption is of the second order.

The adsorption of $^{119}\text{Sb}(\text{V})$ onto $\alpha\text{-FeOOH}$ at pH 4.0 proceeded rapidly, resulting in more than 90% of adsorption in 4 min at 50°C (Fig. 3). The data are analyzed in accordance with the third-order kinetics.

The adsorption of $^{119}\text{Sb}(\text{V})$ onto CoFe_2O_4 powder was found to be affected greatly by the pH of the solutions. Maximum adsorption was observed around

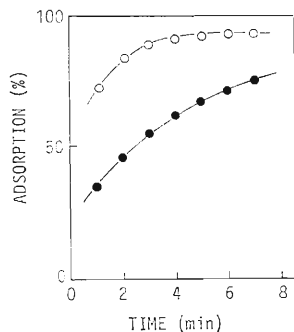


Fig. 3. Adsorption kinetics of no-carrier-added $^{119}\text{Sb}(\text{V})$ ions onto (●) $\gamma\text{-Fe}_2\text{O}_3$ and onto (○) $\alpha\text{-FeOOH}$ from 0.25 mol dm^{-3} LiCl solutions of pH 4.0 at 50°C .

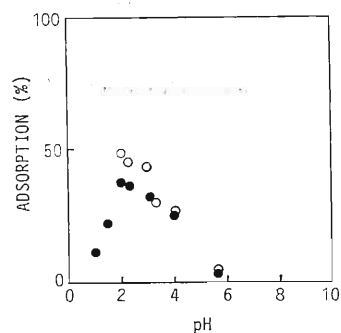


Fig. 4. Percentage adsorption of no-carrier-added $^{119}\text{Sb}(\text{V})$ ions from 0.25 mol dm^{-3} LiCl solutions onto (●) CoFe_2O_4 and (○) NiFe_2O_4 at 50°C after 60 min shaking.

pH 2 as shown in Fig. 4. From a solution at pH 2.5, about 80% of $^{119}\text{Sb}(\text{V})$ was adsorbed in 1 h at 100°C . The amount of $^{119}\text{Sb}(\text{V})$ adsorbed at pH 2.3 and 50°C increased with time (Fig. 2). However, the kinetic data failed to fit the integral form of Eq. 1 with $n=1, 2$, or 3. Adsorption of $^{119}\text{Sb}(\text{V})$ onto NiFe_2O_4 powder showed also pH dependence similar to that for CoFe_2O_4 (Fig. 4). About 90% of $^{119}\text{Sb}(\text{V})$ was adsorbed at 100°C at pH 2.4 in 2 h.

The above findings suggest that not only the surface structure of the oxides but also the kinds of chemical elements involved are important in determining the order of the adsorption rate.

References

- 1) S. Ambe: *Langmuir*, **3**, 489 (1987).
- 2) T. Okada, S. Ambe, F. Ambe, and H. Sekizawa: *J. Phys. Chem.*, **86**, 4726 (1982).
- 3) F. Ambe, S. Ambe, T. Okada, and H. Sekizawa: *Geochemical Processes at Mineral Surface* (eds. J. A. Davis and K. F. Hayes), ACS Symp. Ser. 323; Am. Chem. Soc., Washington, D.C., p. 403 (1986).

III-4. Radiation Chemistry and Radiation Biology

1. High-Density Excitation by Heavy Ions: Measurement of Track-Depth Resolved Emission Spectra

K. Kimura, T. Yoshida, S. Imai, T. Nakamura, and N. Hamada

One of the most characteristic irradiation effects of heavy ions is, in condensed matter, the high-density excitation of electrons in an outermost shell. Most of the high-energy states such as ions and excited states of inner-shell electrons can be converted into lower excited states of the outermost shell. Energy deposition of an ion varies along the path of the ion, as illustrated by the curve of stopping power dE/dx vs. range (x), and the maximum energy-deposition for heavy ion possibly amounts to as large as a few thousand electron volts per Angstrom. Since energy deposition should be expressed by $dE/(r^2dx)$ (r stands for the track radius) rather than in dE/dx , it should increase in much larger extent near its maximum than that estimated from dE/dx , considering that a radius of the "core"-part is approximately proportional to the ionic velocity, v , and the "halo"-part, $v^{2.7}$. Furthermore, $dE/(r^2dx)$ may be expressed formally as $1/v$, since dE/dx in a vicinity of its maximum can be approximated to v . The high-density effect is, therefore, much larger than that estimated by dE/dx especially near termination of an ion and its maximum should be shifted to the track end. In addition, charge-exchange and Coulomb-explosion, which are not included explicitly in stopping power calculation, become important in the region mentioned above. What is actually caused in matter by such high-density excitation is unknown yet and is considered to be an important problem to be resolved.

Previously, we measured the track depth-resolved emission spectra and their decays along the path of ion track in dense helium gas to obtain detailed information of specific emission dL/dx and its efficiency dL/dE . Since rare gases give relatively high emission yields under high-density excitation, they are most appropriate to our aims. Previous experiments¹⁻³⁾ on dense helium gas at 400 Torr and 5 K irradiated with 5 MeV/amu N-ions (track length of 11 mm) showed several interesting results. One of them is that dL/dE along the track continues increasing in the region of decreasing stopping power after its maximum value. Is this result explicable

by $dE/(r^2dx)$ or by increase in the probability of direct excitation and charge exchange? Is this correlated with the new emission bands observed? They all are essential problems in the initial physico-chemical stage of radiation effects in matter. On the other hand, excited states may be quenched at much higher density of excitation than the above conditions. We are also interested in such a quenching process. The depth-resolution of the previous measurements was, however, about 0.1 mm, which is too crude to analyze the region near the maximum stopping power.

Then, we developed a new simple track-scope for the precise observation of UV- and VUV-emission intensities with much denser samples. The scope is

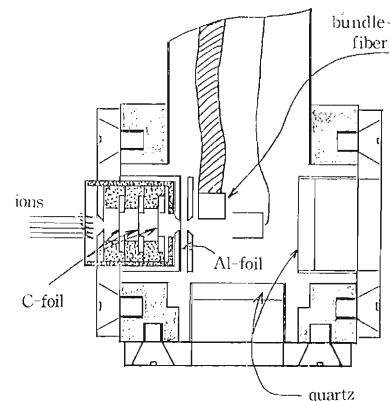


Fig. 1. Experimental arrangement of a track-scope, an ion detector, and the cold part of a cryostat.

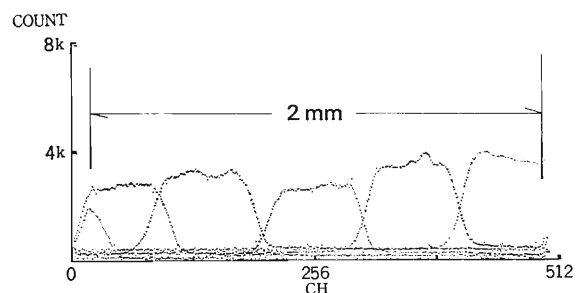


Fig. 2. Photosensitivities of the track scope along ion-tracks, measured by sliding 2,537 Å light of 0.3×10.0 mm.

composed of a square bundle of 2×2 mm of 10,000 quartz fibers. The terminal of the array is coated with sodium salicylate to convert VUV light to UV with a peak at 420 nm and was set close (< 0.1 mm) laterally to the ion-tracks shaped with a cross section of 0.1×2 mm by collimation with a slit. Light from another terminal was focused on the photoplate of an OMA (Optical Multichannel Analyzer by Princeton Applied Research) for simultaneous counting of photons from each fiber. Thus, the UV or VUV track-image has a resolution of 20 μ m and can be integrated for time without disturbance due to

instability of ion current. To calibrate photosensitivity of the track scope along the direction of ions, 2,537 Å light (0.33×10 mm) was projected on different sections of a VUV-sensitive plane of the track-scope. Figure 2 illustrates a superposition of typical 6 OMA-spectra, showing nearly constant photosensitivity. Experimental data are under analysis.

References

- 1) K. Kimura: *J. Chem. Phys.*, **84**, 2002 (1986).
- 2) K. Kimura: *J. Chem. Phys.*, **84**, 2010 (1986).
- 3) K. Kimura, M. Kataoka, K. Hara, and T. Iida: *RIKEN Accel. Prog. Rep.*, **19**, 141 (1985).

III-4-2. Proton Irradiation Effects on Aliphatic Polymers

T. Sasuga, S. Kawanishi, T. Seguchi,* and I. Kohno

Polymers used in space as the components and equipments of artificial satellites are subjected to irradiation of high-energy electrons, protons, and heavy ions. The radiation effects are presumed to be different between ion beams and electron or γ rays because of the difference in energy deposition. Irradiation effects of electron and/or γ rays on organic polymers have been extensively studied at the request of utilization around nuclear power facilities, but those of heavy ions are a few, especially on mechanical properties.¹⁻³⁾ The main reason for such a few data would be due to the lack in irradiation techniques and equipments to evaluate the mechanical properties of polymers.

The study was planned to measure the practical properties of organic polymers irradiated with high energy protons in comparison with those irradiated with electron. A special chamber was constructed to allow a wide area of polymer films to irradiate uniformly, and the radiation-induced changes in mechanical properties were studied by tensile tests.

Polyethylene, polypropylene, ethylene-vinylacetate copolymer, polyvinylidene fluoride, and tetrafluoroethylene-propylene copolymer, and Nylon 6 were used in a form of film with 100 μm thickness. Proton irradiation was performed with a beam of 8 MeV from the cyclotron in the specially constructed chamber shown in Fig. 1. The specimen mounted on an aluminum rotor of 50 mm in diameter was rotated and moved repeatedly along the rotation axis. By using this apparatus, the specimen can be irradiated uniformly over the area of $157 \times 36 \text{ mm}^2$,

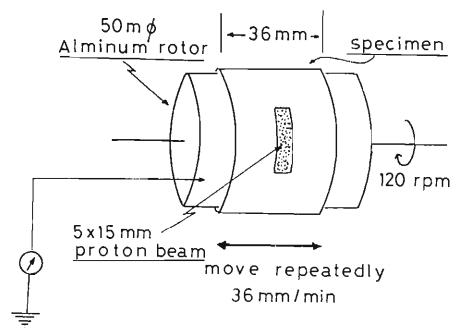


Fig. 1. Schematic drawing of the irradiation method.

which is enough for the measurement of the tensile properties.

Specimens were irradiated under vacuum with a proton beam adjusted to the size of 5 mm horizontal and 15 mm vertical. Eight MeV for proton is enough to pass through a polymer film of 100 μm thickness, because the range of 8.06 MeV proton was reported⁴⁾ to be 1.353 mg/cm². The current of the incident beam was about 1 μA , and was monitored during irradiation. The total charge was obtained by integrating the beam current passing through the specimen. The average fluence rate was about 13 nC/cm²/s. The temperature during irradiation was monitored by a thermo-color indicator put on the rotor and the temperature of specimen was confirmed to be below 60°C.

Electron irradiation was carried out under helium gas flow with a 2 MeV electron beam from the accelerator installed in JAERI Takasaki; the electron fluence rate was 1.07 $\mu\text{C}/\text{cm}^2/\text{s}$. The radiation effects were measured by a tensile test under the testing conditions of a cross head speed of 200 mm/min at 25°C for the specimens cutting into an ASTM 1822 type dumbbell.

For polyethylene the ultimate elongation is shown as a function of the fluences of 8 MeV proton and

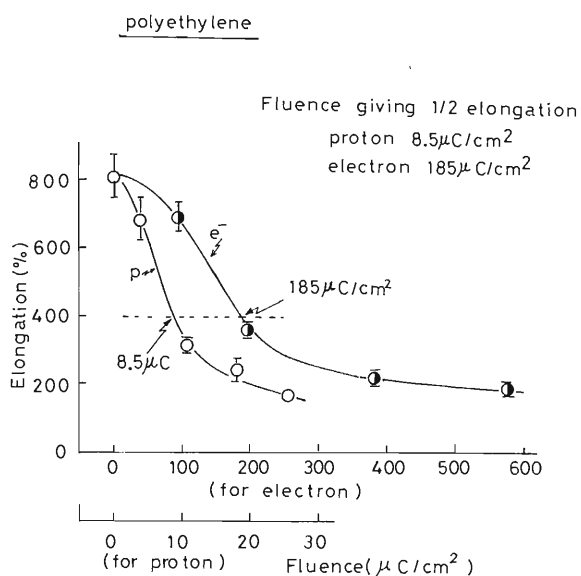


Fig. 2. Ultimate elongation against fluence for polyethylene films irradiated with electrons and protons.

* Takasaki Radiation Chemistry Research Establishment, Japan Atomic Energy Research Institute.

2 MeV electron in Fig. 2. The fluence giving the half value of the initial elongation is $8.5 \mu\text{C}/\text{cm}^2$ for proton and $185 \mu\text{C}/\text{cm}^2$ for electron, respectively, indicating that the ratio of radiation effects per one proton to that per electron is 26.

An absorbed dose D (kGy) of charged particles for organic compounds is given:

$$D = S \times Q \quad (1)$$

where S ($\text{MeV cm}^2/\text{g}$) is the mass collision stopping power of the incident particle and Q ($\mu\text{C}/\text{cm}^2$) is the fluence. The stopping power was calculated by using Bethe's equation:

$$S = (-dE/dx) = k Z [\ln(2m_0v^2/I(1-\beta)) - \beta^2] \quad (2)$$

where m_0 is the rest mass of electron, v and c are the velocities of an incident particle and light, β is v/c , and Z and I are mean atomic number and mean excitation energy of the target material, respectively. I can be calculated by an additive rule from the excitation energy of each element constituting the material.⁵⁾ I and S of polyethylene for 8 MeV proton are 56.51 eV and $53.00 \text{ MeV cm}^2/\text{g}$.

The absorbed dose (D_e) in electron irradiation was calculated by:

$$D_e = D_c \times (S \text{ of polyethylene} / S \text{ of CTA}) \quad (3)$$

where D_c is the dose measured with a CTA (cellulose-triacetate) film dosimeter. The stopping power for electron was calculated by Seltzer and Berger method⁵⁾ to be $1.77 \text{ MeV cm}^2/\text{g}$ for polyethylene.

The tensile strength, yield strength and elongation are shown in Fig. 3 as a function of the dose calculated by Eqs. 1 and 3. The changes in the tensile strength with dose is slightly different between proton and electron, but those of the yield strength and elongation are completely coincident. The other polymers used in this study showed no marked difference in the dose dependence of mechanical properties between proton and electron irradiation.

The changes in the mechanical properties of polymer are ascribed mainly to chemical reactions like chain scission and/or crosslinking through excitation, ionization, free radical formation, and reactions of active species. It can be seen from the stopping powers for protons and electrons that the linear energy transfer (LET) of proton is about 30 times higher than that of electron. Since difference in LET causes the difference in the distribution of ionization

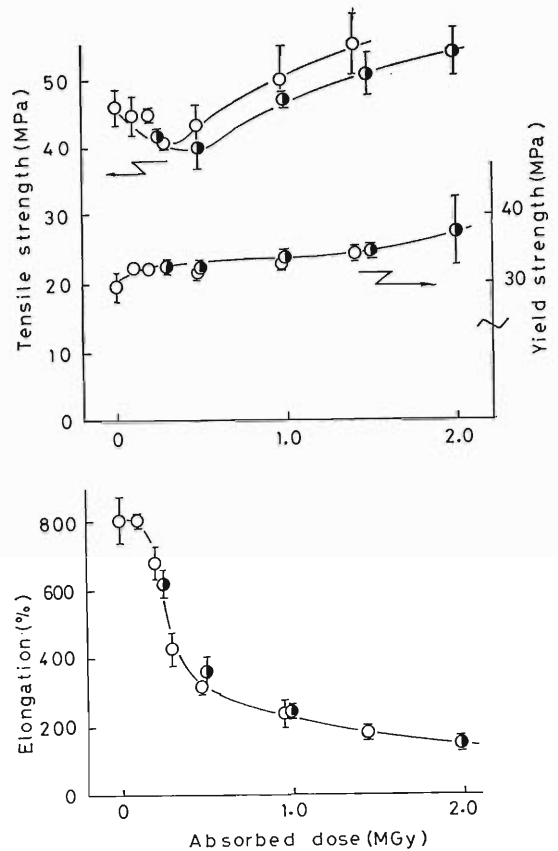


Fig. 3. Tensile properties as a function of dose for polyethylene films irradiated with electrons (●) and protons (○).

sites even though the total energy deposition is same, the mechanical properties are expected to be different among the irradiation sources. In contrast with this consideration, the findings for several aliphatic polymers showed that there is little or no LET effects observed in the changes of mechanical properties between proton and electron irradiation.

References

- 1) B. Santos and G.F. Sykes: Proc. 13th Natl. SAMPE Tech. Conf., p.256 (1981).
- 2) G. Wang, X. Li, Y. Zhu, Q. Liu, N. Hu, X. Gu, and Q. Wang: Nucl. Instrum. Methods Phys. Res. B, 7/8, 497 (1985).
- 3) D.R. Coulter, Ma. V. Smith, F. Tsay, and A.V. Gupta: J. Appl. Polym. Sci., 30, 1753 (1985).
- 4) L.C. Northcliffe and R.F. Scilling: Nucl. Data Table, A7, 255 (1970).
- 5) S.M. Seltzer and M.J. Berger: Int. J. Radiat. Isot., 33, 1189 (1982).

III-4-3. Dosimetry with a Cellulose-Triacetate Film for Proton Irradiation

H. Sunaga, T. Agematsu,* R. Tanaka,* K. Yoshida,* and I. Kohno

Recent application of ion-beam irradiation for studies on material science and radiation chemistry requires an ion-beam dosimetry for high doses and high dose-rates.

Ionization chambers have been used so far mainly for proton-beam dosimetry in the field of radiation therapy, but are difficult to apply to the higher dose-rate region for studies of material science.

Film dosimeters widely used for radiation processing with electron beams and γ rays are suitable for this purpose because of the high spatial resolution and simplicity of the measurement. We tried to apply a cellulose-triacetate (CTA) film dosimeter¹⁾ used mainly for electron-beam dosimetry to proton irradiation and compared the basic dosimetric characteristics for proton beams with those for electron beams.²⁾

A commercial CTA film dosimeter, FTR-125 of Fuji Photo Film Co., Ltd. of 125 μm in thickness, was used. The dosimetry is based on the linear dose response of radiation-induced optical densities at 280 nm. The dose response was measured mainly with a CTA film dose reader FDR-01, and two-dimensional dose distribution was measured with a double-scanning micro-spectrophotometer. CTA films were irradiated in vacuum with protons of 5, 8, and 15 MeV from the cyclotron.

A rotation-type irradiation apparatus was attached to the beam course No. 2 for the uniform irradiation over a wide area to give the same dose. It provides a cylindrical film holder made of aluminum of 50 mm in diameter, which is rotated 120 rpm and simultaneously scanned mechanically between two points separated by 36 mm at a speed of 36 mm/min along the rotation axis perpendicular to the direction of the proton beam. The total charge impinging on the sample holder is measured with a current integrator.

The proton fluence was calculated from the total charge and the effective irradiation area given by the product of the circumference of the cylindrical holder and the scan width on the rotation axis. The absorbed dose of the CTA sample exposed to the

proton beam was given from the product of the mass stopping power in CTA and the proton fluence onto the sample. The stopping power was calculated by using "OSCAR 84" developed by Hata. The calculated values for 5, 8, and 15 MeV protons are 75.0, 51.8, and 31.3 ($\text{MeV}\cdot\text{g}^{-1}\cdot\text{cm}^2$), respectively.

Figure 1 shows the relationship between the absorbed dose and the radiation induced optical density (ΔOD) in the CTA film (FTR-125) in comparison with the result obtained with electron beams. The radiation induced optical density for proton beams increases linearly with dose up to 300 kGy. The value of ΔOD per unit dose (K value) is 0.063 ($10\text{ kGy})^{-1}$

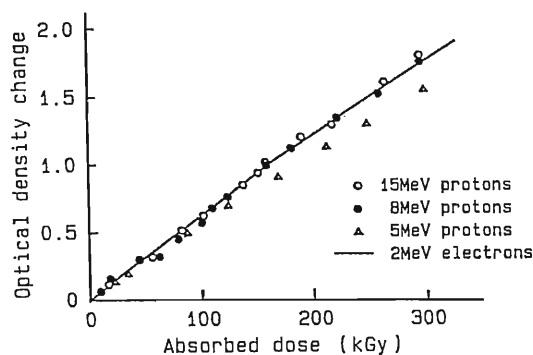


Fig. 1. Relation between the absorbed dose and the radiation induced optical density at 280 nm of a CTA dosimeter exposed to 5, 8, and 15 MeV protons.

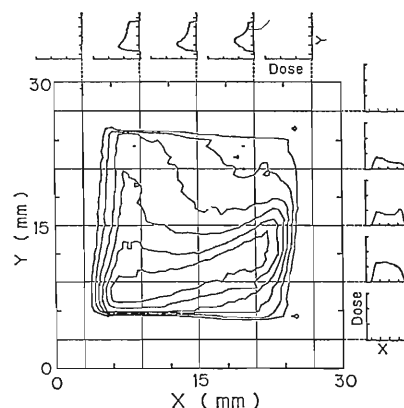


Fig. 2. An example of the two-dimensional dose distribution in a CTA sheet exposed to 8 MeV protons.

* Takasaki Radiation Chemistry Research Establishment, Japan Atomic Energy Research Institute.

for 8 and 15 MeV, which is the same as the value for electron beams. The K value for 5 MeV is smaller than the value for 8 and 15 MeV by about 10%.

The above result suggests that there is no difference in LET effect between a high-energy proton beam and an electron beam, but the LET dependence may be appreciable in a CTA film dosimeter for protons lower than 5 MeV. A similar LET dependence was observed in a Radiachromic film dosimeter.⁹⁾

Figure 2 shows a typical example of equi-dose maps in the cross-section of proton beams obtained with a CTA film exposed to an 8 MeV proton beam passed through a beam aperture (20 mm × 20 mm). The result shows that it is necessary to uniformize the lateral dose distribution in the film sample for a dosimetric study.

Figure 3 shows the depth-dose distribution in a stack of CTA films exposed to a 15 MeV proton beam. Precision in determining the depth-dose profile will be enhanced by using thinner CTA films.

From the results described above, the CTA film dosimeter is found to be useful for dosimetry and dose mapping for proton irradiation in the high dose range from 10 to 300 kGy. It will be necessary to study the dosimetric characteristics on higher LET

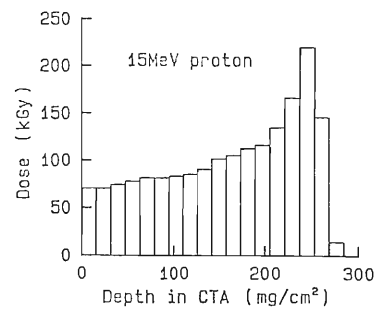


Fig. 3. An example of the depth-dose distribution in a stack of CTA sheets exposed to 15 MeV protons.

radiations, such as heavy ions and low energy protons, with thinner CTA films.

References

- 1) R. Tanaka, S. Mitomo, H. Sunaga, K. Matsuda, and N. Tamura: JAERI-M (in Japanese), 82-033, Japan Atomic Energy Research Institute (1982).
- 2) H. Sunaga, T. Agematsu, R. Tanaka, K. Yoshida, and I. Kohno: *Radioisotopes* (in Japanese), 37(2), 83-86 (1988).
- 3) J.W. Hansen and M. Wille: *Radiat. Phys. Chem.*, 23, 455 (1984).

III-4-4. Position Determination by Laser Marks of *B. subtilis* Spores Placed on a Plastic Track Detector and Inactivation of the Spores by a Single Heavy Ion

T. Takahashi, F. Yatagai, T. Katayama, S. Konno,
K. Izumo, I. Kaneko, and T. Kasuya

For better understanding of the mechanism of cell inactivation induced by heavy ions, we carried out experiments to characterize the microscopic structure of the radiation action nearby a single heavy ion. This has been done by measuring the fraction of dead spores as a function of the distance between the center of the path of an ion and spores around it, but the precise position of the spores in relation to an ion track is very difficult to determine. Few years ago we succeeded in marking scratches on a plastic detector by using a micromanipulator. The technique has been intensively employed by Bückner and his group for the marking on cellulose nitrate (CN) track detectors.¹⁾ Recently, a further improvement has been made in laser marking on CR-39-type plastic detectors, providing etch pits clearer than those of CN detectors. The CR-39 track detectors were dyed to be opaque to 355 nm, the third harmonics of a YAG laser. *B. subtilis* spores were fixed with a 5% polyvinyl alcohol solution on the plastic detector, and then reference grid-like marks were printed with a UV laser beam on the dyed detector. After irradiated with Ar ions from the RILAC, the spores were covered with a nutrient agar film. A photograph was taken to check the outgrowth for the spore after incubation at 37°C. The detectors were immersed in a 6N-NaOH solution at 70°C. Etch pits were found to be sufficiently developed in 30 min for ~25 MeV Ar ions and in 2 h for ~60 MeV N ions. The position of the spores in relation to the track etch pits was determined sometimes to better than 0.2 μm , but was estimated on the average to about 0.5 μm . For the constant accuracy to 0.2 μm , further improvement is necessary. The present technique will be applied to investigate the effects of high *Z* and high-energy particles on living cells during the space flight (IML-1 mission) in 1991.

The fraction of dead spores is shown in Fig. 1 as a function of the distance from the particle track of Ar ions and in Fig. 2 for N ions. To date, we cannot decide whether or not there is a statistically meaningful increase in the fraction of dead spores in the range of 0.5–1.0 μm compared with the control level (see Fig. 1(A) and (B)). If the fraction of

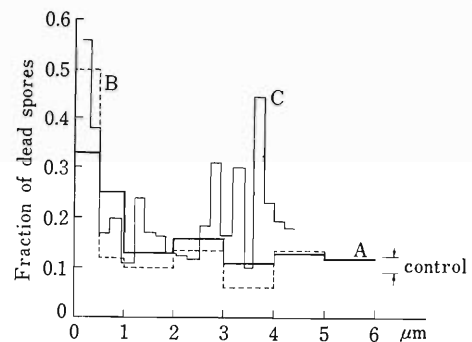


Fig. 1. Fraction of dead spores as a function of the distance from the etch pit of an Ar ion. (A) Bold solid line, ~25 MeV Ar observed by A; (B) Dotted line, ~25 MeV Ar observed by B corrected by T; (C) Thin solid line, ~56 MeV Ar from Ref. 3.

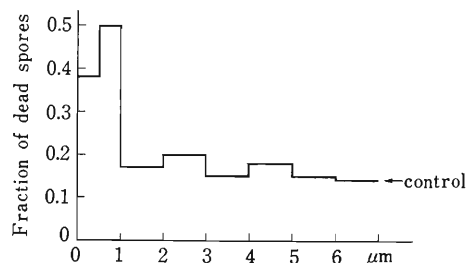


Fig. 2. Fraction of dead spores as a function of the distance from the etch pit of an N ion. Scratched marks were used for the determination of the position of spores.

dead spores really exceeds the control level, thermal spikes or shock waves produced by a heavy ion²⁾ may be responsible for the inactivation since the range of δ -electrons from ~25 MeV Ar ions in the plastic is less than 0.2 μm . As shown in Fig. 1(C), Schäfer *et al.*³⁾ observed a conspicuous increase in the fraction of dead spores at 2.5–4.0 μm for ~56 MeV Ar-ion irradiation, in contrast to our result; the discrepancy might be due to the different experimental conditions. They³⁾ also claim that the inactivation probability is considerably lower than unity at small impact parameters. Here, the impact parameter means the distance between the center of the spore and the path of an ion and the present experiment is in accordance with their result. However, the small impact parameter does not always mean a direct

hit. In case of direct hit, the amount of energy deposited by an Ar-ion traversal corresponds to a dose whereby at least 90% of the spores will be inactivated. For distinguishing a direct hit from the hits at small impact parameters, the accuracy of the position must be less than $0.2 \mu\text{m}$, because radius of the spore core in which DNA is contained is considered to be about $0.25\text{--}0.3 \mu\text{m}$. Furthermore, it is not always guaranteed that the spore core is located at the center of the spore coat whose shape is visible under the microscope, whereas the spore core is not. If yeast is used in such an experiment, it would be easy to distinguish a direct hit, because yeast is

much larger in size than the spore. A preliminary test for yeast (*Saccharomyces cerevisiae*) is now in progress.

References

- 1) M. Schäfer, R. Facius, K. Baltschkat, and H. Bückner: 7th Symp. on Microdosimetry (1980).
- 2) T. Takahashi, F. Yatagai, T. Katayama, Y.H. Kang, S. Tamada, I. Kaneko, and S. Okada: *RIKEN Accel. Prog. Rep.*, **17**, 11^s (1983).
- 3) M. Schäfer, R. Facius, and H. Bückner: Proc. 10th Int. Conf. Solid State Nuclear Track Detectors, p.1055 (1980).
- 4) M. Schäfer, R. Facius, and H. Bückner: 8th Symp. on Microdosimetry (1983).

III-4-5. Mammalian Cell Inactivation and DNA Lesion Caused by Charged Particle Beams

K. Eguchi-Kasai, T. Kosaka, I. Kaneko, T. Takahashi,
A. Maruhashi, and K. Nakano

Mammalian cells are more sensitive to charged particle beams than to γ rays or X rays. The absorbed dose required to reduce the cell survival fraction to 37% (D_{37}) is in the range of 2–5 Gy in ^{60}Co γ rays and about 1 Gy in charged particles. Moreover, the dose-survival curve (natural log of surviving fraction as a function of radiation dose) for charged particles is nearly linear whereas it is convex for γ rays. Ritter *et al.* insisted that non-repairable DNA breaks resulted in cell death because an excellent correlation was held between the efficiency of single-hit cell killing and the induction of non-repairable DNA strand breaks over a linear energy transfer (LET) range of 1–1,953 keV/ μm .¹⁾ The non-repairable DNA breaks assayed in their work, however, cannot be directly related to the cell death, because they used heavy ions of fairly higher doses (up to 450 Gy) than the dose to examine survival (up to 15 Gy) to induce DNA breaks. A recent study showed a similar relationship of DNA breaks between LET and the relative biological effectiveness (RBE) at low doses (20 Gy).²⁾ These results did not explain the difference in the

Table 1. LET of radiations in water.

radiation	LET (keV/ μm)
α particles (HMV-I)	77
(HA-1)	36
N ions	530
^{60}Co γ -rays	0.3

shape of dose-survival curves for low- and high-LET radiations and did not show even the nature of non-repairable DNA breaks. We have shown that a N-ion beam induces more single strand breaks and DNA-protein crosslinks than X rays.³⁾ Here we examined the DNA double strand breaks (DSB) induced by α particles and N ions in comparison with the cell killing in 2 mammalian cell lines which show a different radiosensitivity to ^{60}Co γ rays.

We used HMV-I cells derived from human melanoma (tumor cells) and HA-1 cells derived from chinese hamster cells ("normal" cells). Nitrogen ions and α particles (0.8–2 Gy/min) from RIKEN Cyclotron and ^{60}Co γ rays (1.4 Gy/min) were used. The irradiation procedure for particle beams was previously described.³⁾ Beam currents were

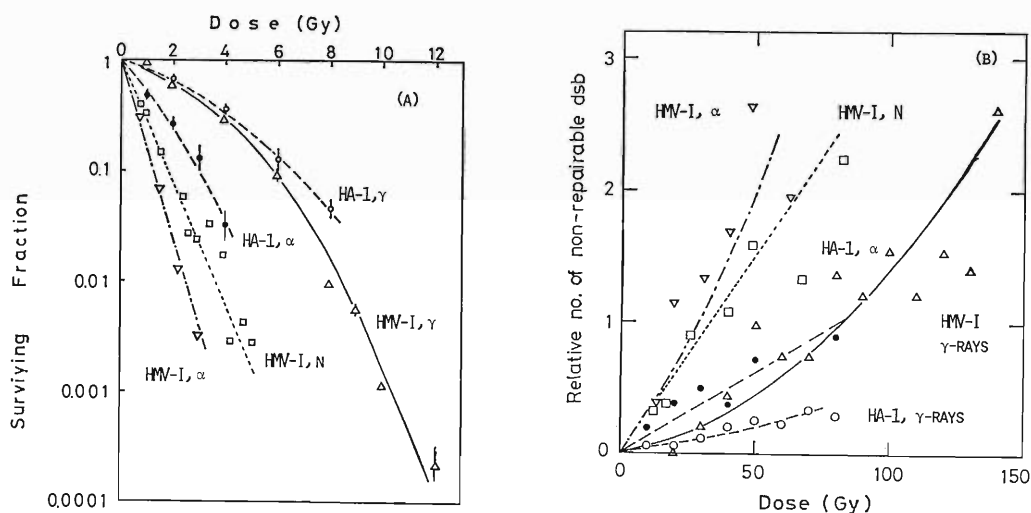


Fig. 1. Dose-survival curves (A) and a relative number of non-repairable DNA double strand breaks in mammalian cells (B). \circ , HA-1 cell after γ -ray irradiation; \bullet , HA-1 α -particles; Δ , HMV-I γ -rays; \square , HMV-I N-ions; ∇ , HMV-I α -particles. The lines in figures were fitted by least-squares method. One unit of the ordinate in (B) corresponds to approximately 600 non-repairable DNA dsb per cell.

monitored with a Faraday cup and transmission ionizing chambers during irradiation. The LET values in water were listed in Table 1. Cells were irradiated at room temperature in most cases except for the test on DSB induced immediately after irradiation where cells were irradiated on ice. DSB was detected by a neutral elution technique,⁴⁾ which detects DNA breaks very sensitively. The relative numbers of DSB are plotted against the absorbed dose and the curves were fitted to a linear-quadratic relationship by a least-squares method.

The number of DSB induced by γ ray was compared between 2 cell lines which have different γ ray sensitivities; HMV-I cells were more sensitive to γ rays than HA-1 cells. The number of DSB was found independent from the radiation sensitivity of cell, because DSB was induced as much as or slightly more in HA-1 cells than in HMV-I cells (data not shown). However, about 60–90% of the total DSB was rejoined during post-irradiation incubation at 37°C. Remainder can be considered to be non-repairable. It was shown that more number of non-repairable DSB was induced in HWV-I cells than in HA-1 cells by γ rays (Fig. 1(B)). Number of non-repair-

able DSB in both cells increased quadratically with the dose of γ rays, whereas it increased linearly with the dose of charged particle radiation. These results correspond to data of cell survival curves (Fig. 1(A)) and also indicate that a non-repairable DSB is induced by a single hit of a charged particle, whereas two hits on duplex DNA at the same or a 'quite near' point are necessary for γ rays.

We found that the amounts of non-repairable DSB in the two cell lines at the same survival levels are almost same without regard to cell lines and to the quality of radiation. These results show a close relationship between the cell inactivation and the non-repairable DNA DSB.

References

- 1) M. A. Ritter, J. E. Cleaver, and C. A. Tobias: *Nature*, **266**, 653 (1977).
- 2) R. Roots, T. C. Yang, L. Craise, E. A. Blakely, and C. A. Tobias: *Radiat. Res.*, **78**, 38 (1979).
- 3) K. Eguchi, T. Inada, M. Yaguchi, S. Satoh, and I. Kaneko: *Int. J. Radiat. Biol.*, **52**, 115 (1987).
- 4) M. O. Bladely and K. W. Kohn: *Nucl. Acid Res.*, **7**, 793 (1979).

III-4-6. Oncogenic Cell Transformation of Golden Hamster Embryo Cells by Heavy Ions

M. Watanabe, M. Suzuki, K. Suzuki, and I. Kaneko

The major objective of the present study is to understand the potential carcinogenic effects of cosmic rays and the mechanisms of radiation-induced cell transformation. During the past several years, we have studied the induction of oncogenic transformations by X rays in primary cultures of golden hamster embryo (GHE) cells and established the relationship between absorbed dose and the frequency of transformation over the dose range from 0.01 to 6 Gy.¹⁾ This study is designed to examine the efficiency of radiations by heavy ions in producing oncogenic cell transformations.

We used diploid GHE cells cultured for 13 to 14 day-old embryos. The tissue culture techniques for obtaining GHE cells was modified from that previously described.¹⁾ Cells were grown in Eagle's minimum essential medium supplemented with 10% fetal bovine serum. The transformation assay used in this study was reported previously.¹⁻³⁾ Briefly, after irradiation, about 60 viable cells per dish of 60 mm in diameter were inoculated into dishes containing feeder cells and were grown for 10-12 days, before being fixed and stained with a Giemsa solution. Although a heterogeneous population of colonies was observed in this system, the end point used for determining the transformational change was the appearance of morphologically altered colonies, which were observed only a very low frequency in control ($<5 \times 10^{-4}$). Transformed colonies were readily distinguished by their morphological change according to the criteria that the cells in the transformed colony piled up to from densely stained colonies with a characteristic criss-cross pattern at the periphery (type B colonies).¹⁾ Cells derived from type B colonies were tumorigenic. In parallel to the transformation study, a survival study was carried out by using the colony-forming method. The transformation frequency was determined by dividing the number of transformed colonies by the number of surviving colonies.

The survival curves for cells exposed to various kinds of radiations are shown in Fig. 1, which indicates that N ion (95 MeV) and α particles (22 MeV) give curves exponential to the dose over the entire dose range examined (0-6 Gy). In contrast the survival curves for X rays and γ rays from

^{137}Cs have broad shoulders at low doses, but approximate to exponential functions of dose at high doses. Figure 2 shows RBE for cell killing of various radiations relative to X rays (182 kVp). RBE for heavy ions apparently vary with the cell killing level at which the comparison is made. RBE for heavy ions decrease with increasing cell killing. However, the RBE of γ rays from ^{60}Co and ^{137}Cs to X rays are not greatly different in cell killing. The data for cell transformation as a function of dose following exposure to X rays or γ rays from ^{137}Cs are presented

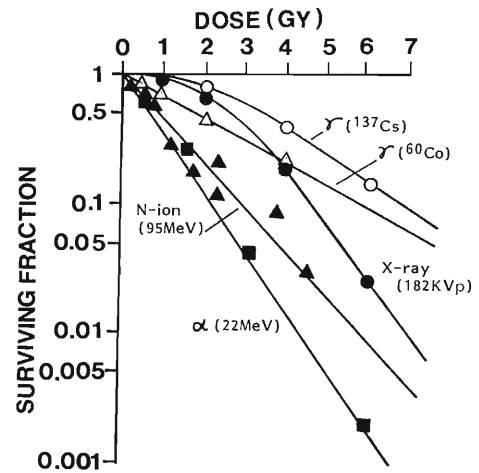


Fig. 1. Dose-response curves for GHE cells irradiated with various radiations. The data points plotted are the means of replicate experiments.

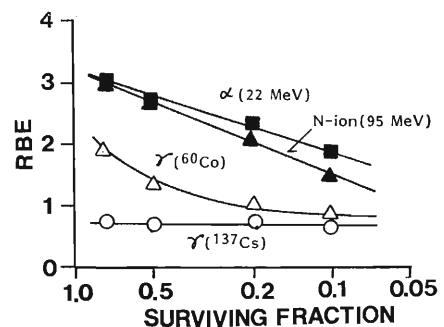


Fig. 2. RBE relative to X rays for cell killing of GHE cells by various radiation.

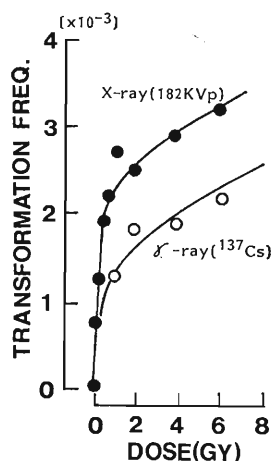


Fig. 3. Dose-response curves for cell transformation by X rays and γ rays from ^{137}Cs . The data points plotted are the means of replicate experiments.

in Fig. 3. The general shapes of induction curves of transformants were almost the same for X rays and γ rays from ^{137}Cs . At shoulder doses (<2 Gy),

the transformation frequencies increased steeply with increasing dose. At doses higher than 2 Gy the frequencies of transformants increased only slightly. When the transformation frequency per survivor induced by an X rays dose that gives a 50% lethality is taken at the reference point, the RBE for γ rays from ^{137}Cs was found to be about 0.78 ($2.3 \times 10^{-3} / 2.0 \times 10^{-3}$). This value is about same for both cell killing and oncogenic transformation for X rays.

We continue to investigate the oncogenic transformation effects of heavy ions. An understanding of the carcinogenic potential at low doses of a variety of radiations is of great help in assessing the cancer risk to environmental and occupational exposures.

References

- 1) M. Watanabe, M. Horikawa, and O. Nikaido: *Radiat. Res.*, **98**, 274 (1984).
- 2) M. Watanabe, O. Nikaido, and T. Sugahara: *Int. J. Cancer*, **33**, 483 (1984).
- 3) M. Watanabe, N. Suzuki, S. Sawada, and O. Nikaido: *Carcinogenesis*, **5** 1293 (1984).

III-5. Instrumentation

1. Data Acquisition System at RIKEN Ring Cyclotron Facility

T. Ichihara, T. Wada, and T. Inamura

The project of the construction of the data acquisition system at RIKEN Ring Cyclotron Facility started in spring 1985. In the beginning of 1986, we prepared a test bench system consisting of a DEC Micro VAX II computer and a CES 2180 Auxiliary Crate Controller. The basic design was settled also during the same period. In August 1987, the half part of the system was installed (VAX computers), and in January 1988 the remaining part of the system (FACOM M-380 computer) was installed. The overall turning of the system is now in progress.

Figure 1 shows the configuration of the data acquisition system. This system is a hierarchical multi-processor system: CAMAC interface, fast front-end processors (CES 2180 ACC), local processors (VAX), and a host processor (FACOM M-380). Each data from the counters is digitalized by the CAMAC modules. Data from the CAMAC module are read by the front-end processor event by event and buffered. When the buffer is full, the buffered data are transferred to the local processor by the Direct Memory Access (DMA). At the local processor, data are monitored and analyzed in real time and

recorded in magnetic tapes. Furthermore, the data are transferred to host processor.

- (1) Front end processor—CES 2180 Auxiliary Crate Controller (ACC)

CES 2180 ACC is a single-span CAMAC module. This module reads data from CAMAC modules event by event, triggered by the interrupt signal. Typical CAMAC read time is about 2 μ s for 16 bit data including the software. When the buffer is full, this module sends an interrupt signal (LAM) to the local processor and changes the buffer and continues the data acquisition. The data is then transferred to the local processor by DMA.

Figure 2 shows a block-diagram of CES 2180 ACC. This module consists of DEC J11 CPU (one chip PDP-11 micro processor), 128 kB static RAM, and some interface circuits to CAMAC bus and external Q22 bus. The overhead of the interrupt service routine is very small (about 10 μ s including saving all the registers) to minimize the dead time.

In order to extract the maximum performance, the data acquisition program on this front-end processor is written in PDP-11 Macro Assembler. The development of the program on this processor and assemble and link is carried out on the local processor (VAX/Micro VAX) using VAX/RSX (PDP11 emulator) software. The task image is on-line down-line loaded from the VAX computer to the memory of the 2180 ACC *via* the CAMAC data way. This

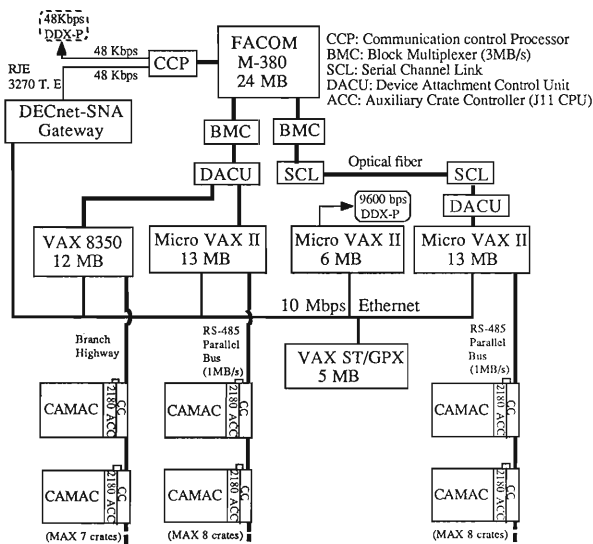


Fig. 1. Data acquisition system at RIKEN Ring Cyclotron. 5 February 1988.

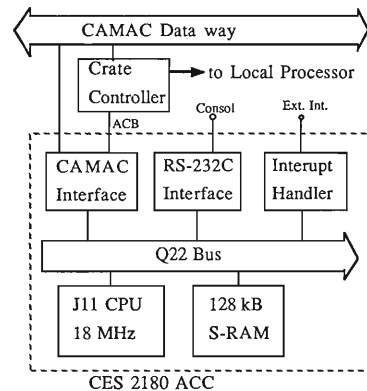


Fig. 2. Block diagram of CES 2180 ACC.

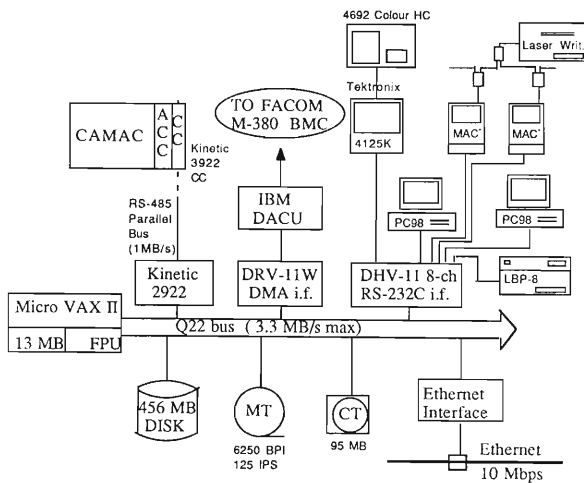


Fig. 3. Configuration of the Micro VAX II based local processor system.

on-line down-loading mechanism enlarges the flexibility of the data acquisition.

- (2) Local processor—DEC Micro VAX II/VAX 8350 computer

Buffered data from the front end processor are transferred to the local processor in DMA via the CAMAC crate controller; the data transfer rate is about 1 MB/s. We prepared three local-processor systems (two Micro VAX II system and one VAX 8350 system) to enable two experiments and program

development or experimental preparation simultaneously.

On-line data monitoring and data recording are carried out in the local processor. Finally, raw data are recorded in 6250 BPI magnetic tapes. Data can be also transferred to the host processor in DMA via the DR(V)-11W interface, a Device Attachment Control Unit (DACU), and Block Multiplexer (BMC).

Raw data are analyzed and displayed on a color graphic display (Tektronix 4125K, 4207), and color hard copies are available (Tektronix 4692 and 4696). Many personal computers (Macintosh and PC9801) are also used as graphic terminals.

The operating system on the local processor is VAX/VMS which supports the real-time and time sharing system simultaneously. Most of the programs are written in FORTRAN. The on-line data taking and analyzing tasks are consisted of

- (1) DMA control (data transfer) task;
- (2) Command interpretation and execution task;
- (3) On-line data analyzing task; and
- (4) Data display tasks.

These are running in a real-time multi-task environment with proper priorities. Figure 3 shows a typical configuration of the Micro VAX II.

- (3) Host processor—FACOM M-380 Main frame computer

A host processor is used for the on-line very com-

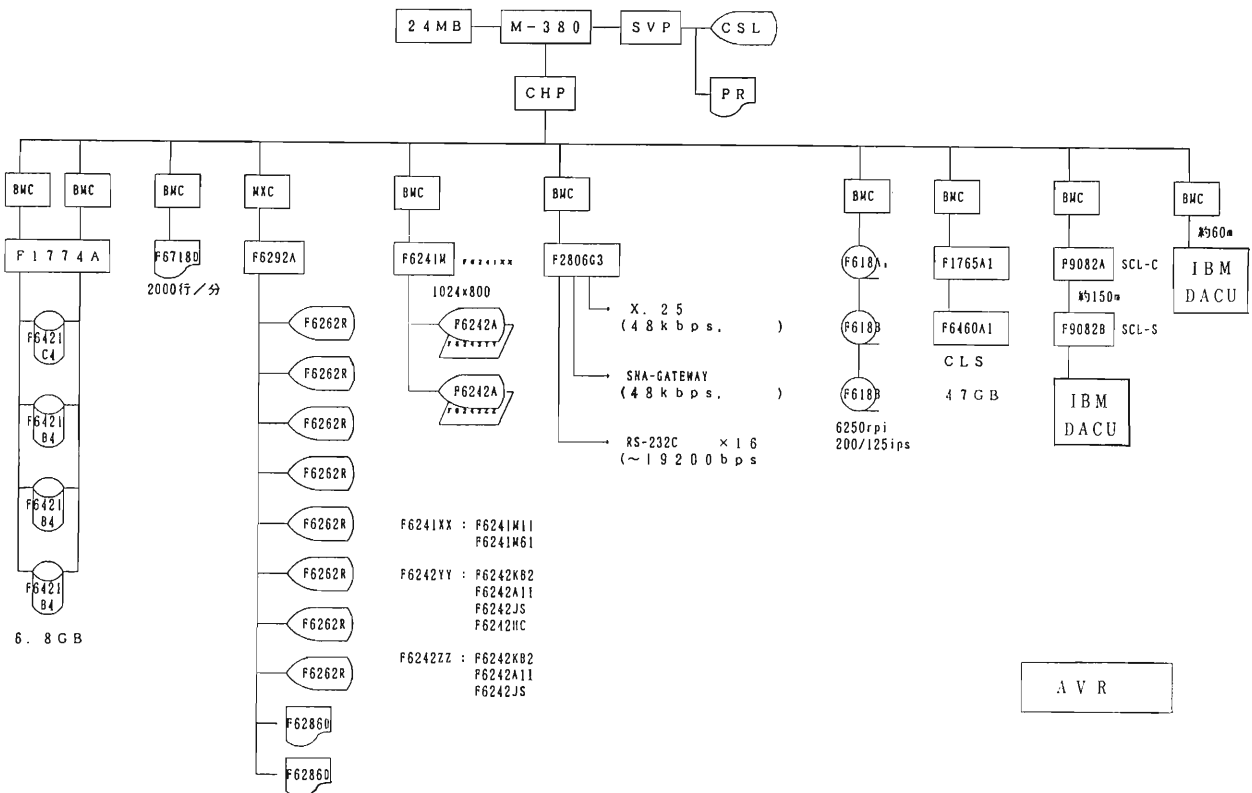


Fig. 4. Configuration of the host processor (FACOM M-380).

plicated data analysis as well as for the off-line data analysis. The speed of this CPU is about 23 million instructions per second (MIPS). Figure 4 shows the configuration of this system. During experiments, raw data from the local processor (VAX/Micro VAX) are transferred to the channel adapter (BMC) of the host processor *via* Device Attachment Control Unit (DACU), which is a standard interface between VAX and an IBM main frame computer. The effective data transfer rate is 400 kB/s.

This computer has a hierarchical mass storage: 24 MB main memory, 6.8 GB disk system, 48 GB cartridge library system (CLS), and three 6250-BPI

200-IPS magnetic tape drivers. The data transferred from the local processor are stored in a disk and analyzed in real time. The CLS are used as the secondly disk system. The file transfer between the standard disk and CLS are carried out automatically.

DECnet-SNA gateway enables the network connection between host and local processors *via* ethernet. File transfer using the remote job entry (RJE) and remote login using a 3270 terminal emulator are available. Packet switching data network link using an X.25 protocol (NTT DDX-P, KDD VENUS-P) is also available at 48 kbps.

III-5-2. Cyclotron Calibration Test of Position Sensitive Detectors for Heavy Cosmic Ray Telescope in Space

T. Kohno, T. Imai, K. Munakata, T. Doke, J. Kikuchi,* T. Kashiwagi, H. Murakami, T. Motobayashi, A. Nakamoto, T. Yanagimachi, N. Hasebe, and K. Nagata

Techniques of a $\Delta E-E$ telescope of silicon solid state detectors are useful for the observations of elemental and isotopic compositions of cosmic ray heavy particles. A large geometric factor of the telescope plays an essential role in the observations in space.

A wide acceptance angle, as well as a large detection area, is necessary to realize a large geometric factor of the telescope. Slant incidences in a telescope having a wide acceptance angle, however, smear the ΔE information by broad pathlength distribution. In order to have a large acceptance angle without smearing the ΔE information, we need to know the particle incident angle by getting the positions at appropriately separated two detectors. Recently new large position sensitive detectors (we call PSD hereafter) with good linearity became available from Hamamatsu Photonics Company, and its characteristics are examined with cyclotron beams.

The PSD is of an ion-implanted type with a sensitive area of $45\text{ mm} \times 45\text{ mm}$, thickness of $400\text{ }\mu\text{m}$

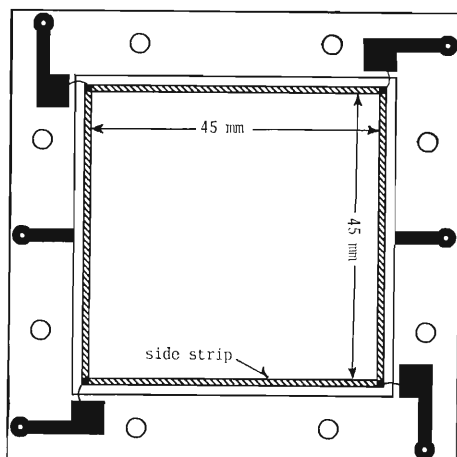


Fig. 1. Schematic view of the PSD. The surface resistivity of $18\text{ k}\Omega$ is surrounded by side strips of $1.5\text{ k}\Omega$ each resistivity. Four signals can be taken out from the four corners while the energy signal can be taken from rear side. The effective area is $45\text{ mm} \times 45\text{ mm}$ and the thickness is $400\text{ }\mu\text{m}$.

* Science and Engineering Research Laboratory, Waseda University.

and junction capacitance of 500 pF ; the shape is shown in Fig. 1. The position signals are taken out from the electrodes at the four corners of an ion-implanted anode side, where the surface resistivity and the line resistivities of the strips at the four sides are formed.¹⁾ The position of the incident particle can be expressed by

$$X = \frac{(A+B)-(C+D)}{A+B+C+D} \cdot \frac{L}{2} \quad (1)$$

$$Y = \frac{(B+C)-(A+D)}{A+B+C+D} \cdot \frac{L}{2} \quad (2)$$

where $A, B, C,$ and D are the charge signals from electrode and L is the length of one side. The origin of the coordinate $(0, 0)$ is set at the center of the

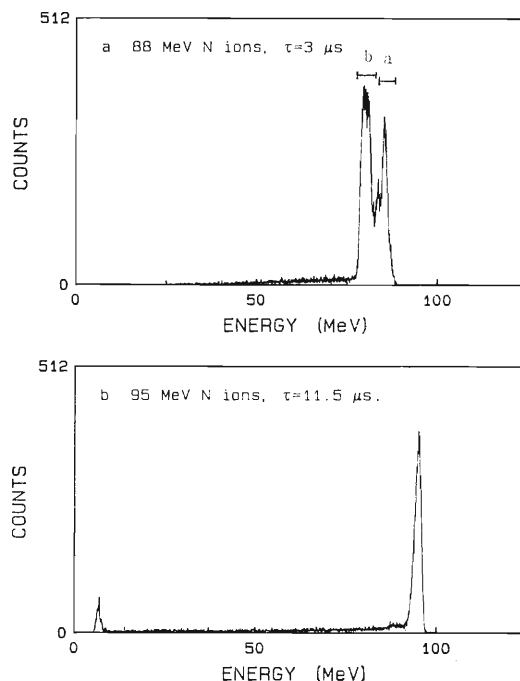


Fig. 2. Energy spectra in N ion experiments. a, Accumulated data of four position signals for 88 MeV . The pulse shaping time is $3\text{ }\mu\text{s}$; b, Energy signals from rear the side for 95 MeV beam. Shaping time is $11.5\text{ }\mu\text{s}$. The pulse height ranges indicated by two horizontal bars named a and b correspond to the data groups used in a and b of Fig. 3, respectively. All N ions with these energies will be stopped in PSD.

detector. We used a He beam with energy of 40 MeV and N beams with 88 MeV and 95 MeV. While N ions of both energies will be stopped in PSD, He ions can penetrate it, therefore, we used a Si(Li) detector of 1 mm in thickness and 3" in diameter as an energy detector behind PSD. In front of PSD, we put a multi-slit collimator consisting of 9×9 holes of $0.5 \text{ mm} \phi$ disposed in a checkerboard pattern having a 5 mm adjacent distance. The material of the collimator is 0.6 mm thick phosphor bronze.

A main beam was scattered with a $4 \mu\text{m}$ Au foil target, and the detector system was set at a 30° scattering angle and at 30 cm apart the target. Each signal was recorded on a micro computer through a CAMAC system. Four different pulse shaping time constants of $1.8 \mu\text{s}$, $3 \mu\text{s}$, $5 \mu\text{s}$ and $11.5 \mu\text{s}$ were tested.

Figure 2 shows the energy spectra of N ions in the PSD for two shaping time constants of $3 \mu\text{s}$ and $11.5 \mu\text{s}$. The spectrum with $3 \mu\text{s}$ shaping time is complicated and shows a broad distribution, but that with $11.5 \mu\text{s}$ shaping time shows a narrow single peak with FWHM of 2.3 MeV. With such a large detector, the time necessary to collect the whole charge varies with the incident position of particles. That is to say, the closer the ion position to the side strip or the electrode itself, the faster the charge collection to the electrode. If the pulse shaping time constant is smaller than the time scale which we need to collect the whole charge, the obtained pulse height

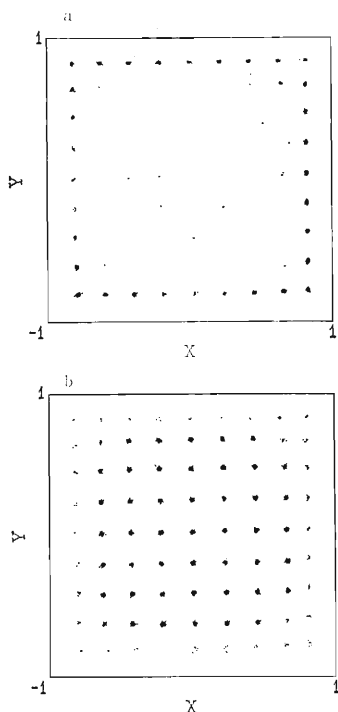


Fig. 3. Positions calculated by Eqs. 1 and 2 for the two data groups indicated by the horizontal bars in Fig. 2a. The L of Eqs. 1 and 2 is assumed tentatively to be 2.

will be lower than that from the larger shaping time constant. We can obviously see this effect in Fig. 3, where the pulse heights from nearest particles to the each side strips or each electrode itself are clearly higher than those from the other positions. The reason why the spectrum has a two distinct peaks instead of broad distribution may be attributed to the difference in the distance from the side strip to the first row and the second row is discrete.

Two examples of the position data for He ions are shown in Fig. 4, which also shows the position resolution dependence on the shaping time constant. Since we used Si(Li) detector behind PSD in the He-beam experiment, the data taking system was triggered with a pulse from the Si(Li) detector. The detector size of 3" in diameter cannot cover the whole PSD, and this effect can be seen in Fig. 4 as the data absence at each corner of the PSD.

We obtained the quantitative position resolution of each measurement from the average of FWHM of Gaussian fitting of each slit data. The resultant position resolutions of all measurement are listed in Table 1.

The position non-linearity (deformation of the multi-slit image on the position data plots) is also important for our final purpose of cosmic-ray observation. Here we define the position non-linearity as

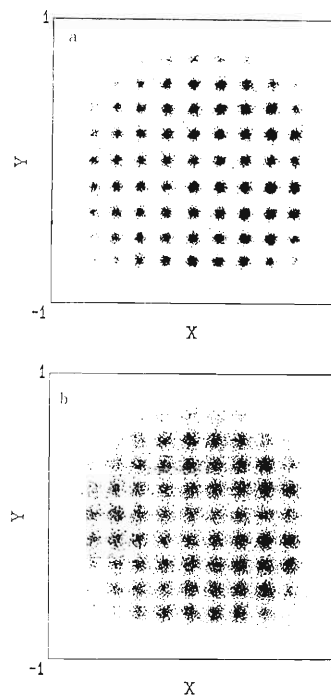


Fig. 4. Position data (same as Fig. 3) for He ions. Pulse shaping time is $1.8 \mu\text{s}$ for a and $5.6 \mu\text{s}$ for b. The energy deposition of the ions in the PSD is 15 MeV. The data taking system is triggered with a pulse from a Si(Li) detector located behind the PSD. The size of the Si(Li) detector of 3" in diameter cannot cover the whole PSD; hence there are no data at the corners.

Table 1. Summary of position resolutions and non-linearities.

Ion	Energy (MeV)	Shaping time (μ s)	Position res. (FWHM in mm)	Non-linearity (rms in mm)
N	88	3.0	0.42 ± 0.12	0.097
N	95	11.5	0.71 ± 0.13	0.054
He	15*	1.8	1.03 ± 0.55	0.109
He	15*	5.6	1.97 ± 0.71	0.086
He	15*	11.5	3.35 ± 1.01	0.134

* Energy deposited in the detector by He ions with an initial energy of 40 MeV.

the root mean squares of the distances from the real slit position to the measured position plotted in Fig. 4, for example. Above defined non-linearities obtained from all measurements are also shown in Table 1.

From a series of cyclotron experiments, we reach the first conclusion that the newly developed PSDs have good enough characteristics for our final purpose of cosmic-ray observation in space.

Reference

- 1) T. Doke, J. Kikuchi, H. Yamaguchi, S. Yamaguchi, and K. Yamamura: *Nucl. Instrum. Methods A*, **261**, 605 (1987).

III-5-3. Design of an Isotope Separator On-Line System at RIKEN Ring Cyclotron

K. Morita, T. Inamura, K. Valli,[†] T. Nomura, J. Tanaka, H. Miyatake, K. Sueki, Y. Hatsukawa,* M. Fujioka, T. Shinozuka, K. Taguchi,** H. Kudo, Y. Nagai, T. Toriyama,*** H. Hama, M. Yoshii,**** and K. Furuno

An isotope separator on-line (ISOL) system is now under construction at the E1 experimental hall at RIKEN Ring Cyclotron (RRC) facility. The aims of constructing this ISOL system are to search for new isotopes which will be produced with high-energy heavy-ion beams from RRC and to get new structural information of such unstable nuclei. We report here the characteristics of RIKEN ISOL system.

This ISOL consists of two parts. One is a gas-filled recoil isotope separator (GARIS) and the other is an ion-guide isotope separator on-line (IGISOL). The main role of GARIS is to separate reaction products from beam particles and to transmit them to IGISOL with a high efficiency. GARIS can also be used by itself as an isotope separator with a moderate resolving power. The principle of GARIS is as follows. Reaction products recoiled out of a target have broad distributions both in charge and in momentum. When they enter a dipole magnet filled with low pressure gas, they follow average trajectories corresponding to their momenta and an average charge (\bar{q}) defined by their multiple collision with gas atoms. Because \bar{q} is roughly proportional to the velocity, the average trajectory is almost independent of the initial distributions of momentum and charge states, but depends only on their mass (A) and atomic number (Z). That is

$$\bar{q} \propto \frac{v}{v_0} \times Z^\alpha \quad (1)$$

in which v is the velocity of a recoiled atom and v_0 is the Bohr velocity ($v_0 = c/137$). The value of α is 1/3 according to the theoretical consideration by Bohr, but Miyatake *et al.*¹⁾ give the value of 0.57 from their experimental study. The magnetic rigidity ($B\rho$) can be written as

$$B\rho = 0.084 \times \frac{A}{Z^{0.57}} (\text{T} \cdot \text{m}) \quad (2)$$

The IGISOL technique was developed by Årje *et al.*²⁾ as a new method of ISOL for the light-ion induced reactions, and then developed to apply to the heavy-ion induced reactions by Morita *et al.*³⁾ A prominent advantage of IGISOL is that its operation is almost independent of the chemical and physical properties of elements and, therefore, it can be applied to study all elements equally well. A principle of IGISOL is as follows: the reaction products recoiled out of a target are stopped in a chamber (thermalization chamber) filled with helium gas (~ 100 Torr) and go out through a small exit hole of the chamber. Atoms of the reaction product are singly charged for some time even after they are thermalized in the helium gas. These singly charged atoms are extracted through the exit hole by a gas flow and transported to an accelerating region where the pressure is low enough ($\sim 1 \times 10^{-4}$ Torr) through a skimmer having a negative potential of several hundreds of volts relative to the thermalization chamber.

The effect of the plasma formed along the path of the incident beam in the thermalization chamber was studied by Morita *et al.*³⁾ and found that the efficiency decreases with the increase in the density of the plasma. Therefore we decide to couple GARIS to IGISOL in order to eliminate the incident beam and to get a high collection efficiency for the study of rare events. This combination, GARIS + IGISOL, was tested by Nomura *et al.*⁴⁾ and proved to work well even when large ($\sim 40 \text{ cm}^3$) thermalization chambers are used. From this result it can be deduced that the lifetime of singly charged ^{28}Al ions in helium gas is more than 50 ms.

1) GARIS

GARIS consists of a D-Q-Q configuration as shown in Fig. 1; the characteristics are listed in Table 1 together with those of the dipole magnet of IGISOL. We have two target positions in GARIS. One is placed at the input pole boundary of the dipole magnet and the other is placed at 0.7 m in front of the boundary. Experimentalists can choose

[†] On leave from Jyväskylä University, Finland.

* Institute for Nuclear Study, University of Tokyo.

** Cyclotron and Radio-Isotope Center, Tohoku University.

*** Photon Factory, KEK.

**** Tandem Accelerator Center, University of Tsukuba.

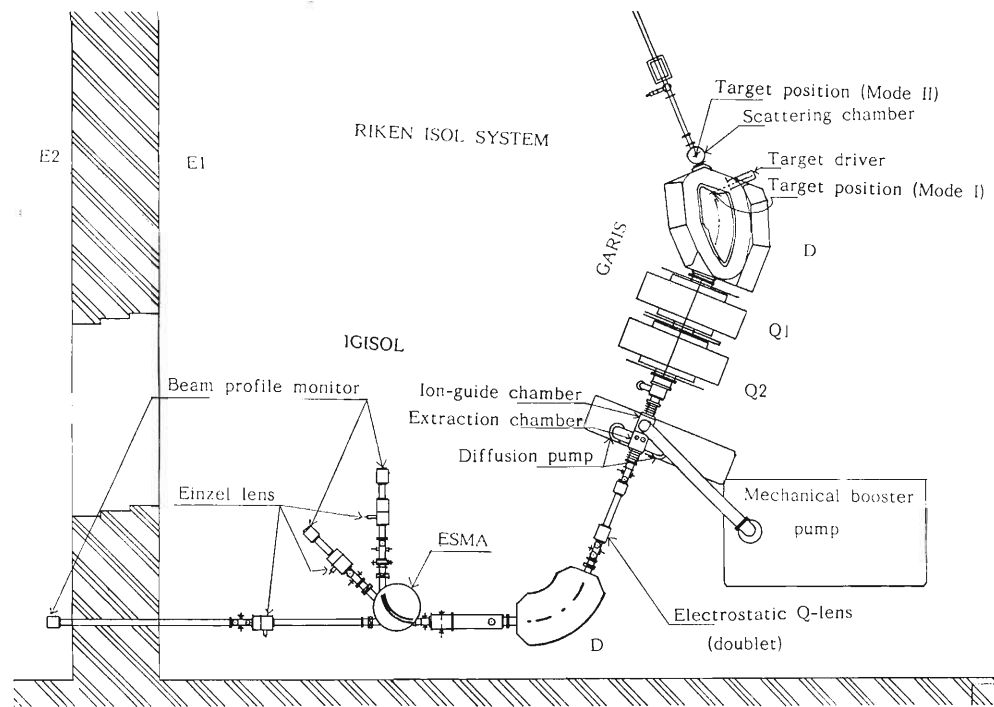


Fig. 1. Schematic view of the RIKEN ISOL system.

Table 1. Characteristics of magnets.

	GARIS		IGISOL
	D	Q1, Q2	D
Deflecting angle (degree)	45	—	68
Maximum field (T)	1.5	—	0.75
Maximum field gradient (T/m)	—	5.2	—
Pole length (mm)	942.5	500	1,186.8
Pole gap or bore radius (mm)	150	150	55
Radius of central ray (mm)	1,200	—	1,000
Pole tilt angle (degree) input	45	—	0
Pole tilt angle (degree) output	-45	—	0
Radius of pole boundary (mm) input	-400	—	—
Radius of pole boundary (mm) output	1,200	—	—
Maximum ampere-turn/pole (A-turns)	115,000	57,000	18,300
Number of turn/pole (turns)	210	179	60
Maximum current (A)	548	319	309
Total residence of coil at 20°C(Ω)	0.231	0.47	0.053
Maximum power dissipation (kW)	79	53.9	5.4
Flowing rate of cooling water (l/min)	47.6	40	9.8

Table 2. Comparison between two modes.

	MODE I	MODE II
Distance from the target to pole boundary (mm)	0	700
Angular acceptance (mr), horizontal	±85	±80
Angular acceptance (mr), vertical	±80	±70
Solid angle (msr)	13.6	11.2
Dispersion (cm/%)	0.20	0.78
Total length (mm)	4,070	4,770
Magnification, horizontal	-0.57	-0.74
Magnification, vertical	-1.47	-1.51

the target position according to their aims of the experiments. Differences of the characteristics between these two modes are listed in Table 2.

The region where the gas is filled is separated from the vacuum region by thin metal foils.

2) IGISOL

The total IGISOL system is also shown in Fig. 1 schematically. The central parts of an ion-guide chamber and an extraction chamber are shown in Fig. 2. The ion-guide chamber is evacuated with a mechanical booster pump having a large pumping speed (6,000 m³/h). The extraction chambers are separated by a skimmer with a 1.5 mm ϕ hole and evacuated by two oil diffusion pumps of a 1,500 l/s pumping speed. The ion-guide chamber, the extraction chamber, and the pumps mentioned above are electrically insulated from the ground potential to apply 80 kV potential for acceleration.

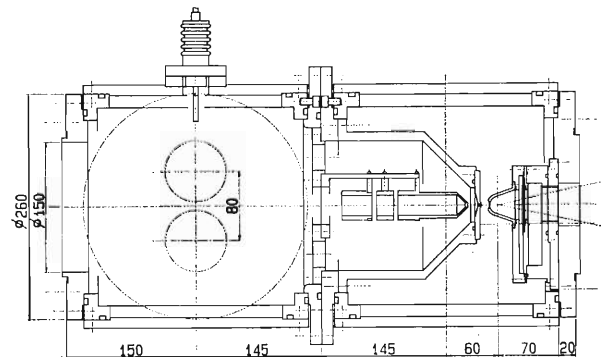


Fig. 2. Central part of IGISOL. The ion-guide chamber and the extraction chamber.

Table 3. Characteristics of the electrostatic analyzer.

Form of electrodes	Spherical condenser
Radius of central ray (mm)	500
Focal length (mm)	1,000
Gap between electrodes (mm)	40
Height of the electrodes (mm)	60
Deflecting angle (degree)	90

We have one einzel lens and electrostatic Q-lens (doublet) before the analyzer magnet, one einzel lens after the magnet, and four sets of electrostatic deflectors (both horizontal and vertical) for successful beam transportation. The characteristics of the analyzer magnet are listed in Table 1. We have three lines for a momentum analyzed beam. The straight line leads the beam to the next experimental hall E2. The 90°-bent line has an electrostatic mass

analyzer (ESMA) to get better mass resolution. The characteristics of the ESMA are listed in Table 3.

All the equipments will be set by the end of June, 1988.

References

- 1) H. Miyatake, T. Nomura, H. Kawakami, J. Tanaka, M. Oyaizu, K. Morita, T. Shinozuka, H. Kudo, K. Sueki, and Y. Iwata: *Nucl. Instrum. Methods B*, **26**, 309 (1987).
- 2) J. Ärje, J. Äystö, H. Hyvönen, P. Taskinen, V. Koponen, J. Honkanen, K. Valli, A. Hautojärvi, and K. Vierinen: *Nucl. Instrum. Methods A*, **247**, 431 (1986).
- 3) K. Morita, T. Inamura, T. Nomura, J. Tanaka, H. Miyatake, M. Fujioka, T. Shinozuka, M. Yoshii, H. Hama, K. Taguchi, K. Sueki, Y. Hatsukawa, K. Furuno, and H. Kudo: *Nucl. Instrum. Methods B*, **26**, 406 (1987).
- 4) T. Nomura, J. Tanaka, M. Oyaizu, Y. Iwata, N. Ikeda, K. Valli, K. Morita, Y. Nagai, T. Toriyama, Y. Murakami, Y. Yorii, and S. Harada: submitted for publication in *Nucl. Instrum. Methods*.

III-5-4. An Ion-Guide Technique for On-Line Isotope Separation Coupled with a Gas-Filled Recoil Isotope Separator

K. Morita, K. Valli,[†] T. Nomura, J. Tanaka, M. Oyaizu, N. Ikeda,^{*}
Y. Nagai, T. Toriyama,^{**} Y. Murakami,^{**} Y. Torii,^{**} and S. Harada^{**}

The ion-guide technique for on-line isotope separation is based on the fact that nuclear reaction products recoiled out of a target and stopped in helium gas are still singly-charged sometimes with high probabilities. Those ions are quickly transported to a low-pressure region with a gas-jet through a small exit hole of a gas chamber and accelerated in the same way as in an usual isotope separator on-line (ISOL). The ion-guide ISOL (IGISOL) has advantages that it works very stable for all elements because no ion source is used, and that it can be applied to radio-activities with half-lives as short as 0.1 ms.

IGISOL has been successfully applied to the products in light-ion induced reactions. However, it is still questionable whether IGISOL works sufficiently well in heavy-ion induced reactions because of a following reason: The velocity of the reaction products formed in heavy-ion reactions is generally larger than that in light-ion reactions, so that higher gas pressure is needed to stop the products in the helium gas chamber. Thus, dense plasma must be formed in the gas along a beam path due to collisions of beam particles with helium atoms and may result in quick neutralization of charged reaction products since they are mostly recoiled out in the same direction. Note that the plasma density is proportional to the energy loss of beam particles, gas pressure, and beam intensity. In fact, we have recently observed a considerable decrease of the IGISOL efficiency due to the plasma effect in heavy-ion reactions when the beam intensity becomes high.¹⁾

The difficulty mentioned above can be avoided by permitting only the reaction products separated from the beam particles to the gas chamber. This will be realized when we put the gas chamber of IGISOL at the focal point of the recoil isotope separator with a high collection efficiency. A purpose of this work is to study characteristics of such hybrid type IGISOL, especially ionic-state probability of reaction products thermalized in helium gas.

The present experiment has been carried out using

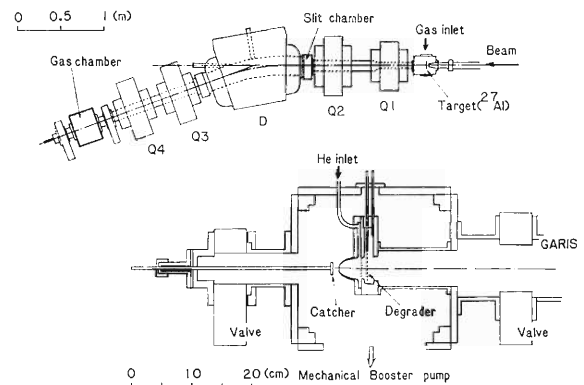


Fig. 1. A schematic view of the present experimental set-up.

radioactive ^{28}Al produced in the $^{27}\text{Al}(\alpha, 2p_n)$ reaction at $E_\alpha = 38$ MeV. The experimental setup is shown in Fig. 1. A gas-filled recoil isotope separator (GARIS)²⁾ set at the cyclotron laboratory at the Institute for Nuclear Study, University of Tokyo, was used to transport ^{28}Al recoiled out of a target foil (1 mg/cm^2 Al) from the target position to the focal plane of GARIS. The entire region of GARIS was filled with helium gas of about 1.7 mbar. The collection efficiency of the system was about 20%.

The kinetic energy E_R of ^{28}Al ions ejected from the target ranged from 160 keV/u to zero, since the thick target was used. ^{28}Al lost its energy through successive collisions with helium atoms, its maximum E_R at the focal plane being estimated by use of the range-energy relation given in Ref. 3. Polyester foils of various thicknesses could be placed 1 cm before the focal plane to degrade E_R when necessary. In order to obtain a rough estimate of a distribution of E_R values at the focal plane, we measured the yield of ^{28}Al as a function of the degrader thickness. For this purpose a round catcher foil of 35 mm in diameter was set at the focal plane to collect ^{28}Al . The 1.78 MeV γ -ray yield following the β decay of ^{28}Al ($t_{1/2} = 2.2$ min) was measured off-beam by use of a 120 cm^3 Ge(Li) detector after the target was irradiated for 5 min with a $1\ \mu\text{A}$ α beam; the result is shown in Fig. 2. It turned out that the yield at a $1.5\ \mu\text{m}$ degrader foil was equal to that without the degrader, indicating that there was the minimum

[†] On leave from Jyväskylä University, Finland.

^{*} Institute for Nuclear Study, University of Tokyo.

^{**} Faculty of Science, Tokyo Institute of Technology.

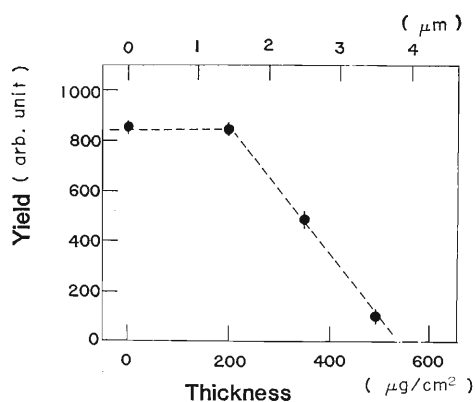


Fig. 2. Measured yields of the 1.78 MeV γ rays following the β decay of ^{28}Al at various degrader thickness. The measurement started 2.25 min after the 5 min irradiation of the target with a $1\ \mu\text{A}$ α beam as explained in text and continued for 5 min.

value of E_R in ^{28}Al reaching the focal plane. The range of ^{28}Al in polyester was found to be about $530\ \mu\text{g}/\text{cm}^2$ at $E_R = 160\ \text{keV}/u$. Assuming that the range-energy curve of ^{28}Al in polyester is similar to that of ^{27}Al in mylar given in Ref. 3, we estimated the minimum value of E_R of 23 keV.

The efficiency of IGISOL was measured by setting a gas chamber of a conical shape at the focal plane of GARIS (see Fig. 1). A window of the gas chamber consists of $1.5\ \mu\text{m}$ polyester foil attached onto a stainless mesh, which is round in shape and 35 mm in diameter. The transmission of the mesh is 85%. The ^{28}Al activity transported from the target enters the gas chamber filled with helium of 200–300 mbar and is extracted through an exit hole of 1.1 mm in diameter. The gas chamber was placed in a larger cubic vacuum chamber, which was pumped with a mechanical booster pump of a $2,070\ \text{m}^3/\text{h}$ pumping speed. An aluminum catcher foil was set about 1 cm behind the exit hole to collect the ^{28}Al radioactivity extracted through the hole. In order to distinguish positive ions of ^{28}Al from neutral ones, we applied positive or negative voltage onto the catcher foil relative to the gas chamber. An example of the yield of the 1.78 MeV γ ray as a function of the applied voltage (V) is shown in Fig. 3. The measured yield decreases drastically by changing the sign of V , indicating that there is a considerable amount of positive ^{28}Al ions. The yield of positive ions (n^+) is deduced from $n^+ = N_- - N_+$, where N_- and N_+ are the yields at negative and positive voltages, respectively. We assume here that the yield of negative ions is negligibly small. Since the yield is almost independent of the absolute values of the applied voltage, we usually apply ± 50 volts to obtain N_{\pm} .

The efficiency measurements were made for various conditions summarized in Fig. 4. For I, we

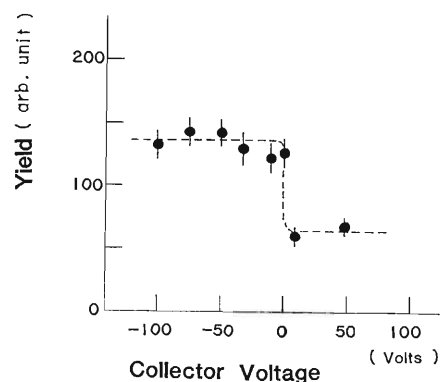


Fig. 3. Measured yields of 1.78 MeV γ rays versus the applied voltage of the catcher foil placed 1 cm behind the exit hole of conical shape gas chamber taken in the similar way to Fig. 2.

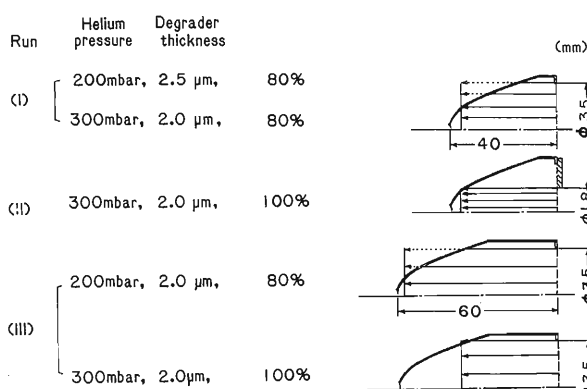


Fig. 4. Schematic presentation of the present experimental conditions of the gas chamber of IGISOL. The maximum range of ^{28}Al in helium under the given conditions is indicated by arrows. The degrader thickness, helium pressure, and fraction of ^{28}Al which can be stopped in helium relative to ^{28}Al entering the gas chamber are given.

used an original conical gas chamber to stop reaction products (^{28}Al) in helium. For II, we changed the opening of the window of the gas chamber by setting a thick slit of 18 mm in diameter on the window, so that ^{28}Al could enter only the central part of the chamber. In this case, a proportion of ^{28}Al entering the chamber was measured to be about 36% as compared with the case I. For III, the gas chamber was enlarged in length by putting a 2 cm cylindrical extension behind the window. The maximum range of ^{28}Al corresponding to the maximum kinetic energy of ^{28}Al after the $1.5\ \mu\text{m}$ polyester foil was estimated by use of the range-energy relation given in Ref. 3. Assuming that the distribution in kinetic energy of ^{28}Al is uniform, we estimated a fraction of ^{28}Al stopped in helium for each case. This fraction (f) is also indicated in Fig. 4.

The measurements were carried out in the following way. The target was irradiated for 5 min with $2\ \mu\text{A}$ α beam; the catcher foil was then taken out

Table 1. Results of present experiment. $n^+ = N_- - N_+$ and $n^{\text{tot}} = N_-$. n_{stop} is the yield of γ ray corresponding to the number of ^{28}Al atoms stopped in helium (see text and figure caption for Fig. 2).

Run	Helium pressure (mbar)	Degradation thickness (μm)	n_{stop} (counts)	n^+ (counts)	n^+/n^{tot} (%)	n^+/n_{stop} (%)
I	200	2.5	666	49 ± 9	48 ± 9	7.2 ± 1.4
I	300	2	884	78 ± 8	63 ± 7	8.8 ± 0.9
II	300	2	411	33 ± 4	57 ± 8	8.0 ± 1.0
III	200	2	884	45 ± 7	44 ± 7	5.1 ± 0.8
III	300	2	1,105	72 ± 8	52 ± 5	6.5 ± 0.7

from the vacuum chamber and was put just in front of the surface of a Ge(Li) counter, which was placed in a low background room.

The results are summarized in Table 1. Note that

the absolute values of ^{28}Al (denoted by n_{stop} in the table) were estimated by use of the results shown in Fig. 2 and the fractions f indicated in Fig. 4. It turned out that about 12–16% of ^{28}Al stopped in helium were extracted, and that about a half of them remained charged.

References

- 1) K. Morita, T. Inamura, T. Nomura, J. Tanaka, H. Miyatake, M. Fujioka, T. Shinozuka, M. Yoshii, H. Hama, K. Taguchi, K. Sueki, Y. Hatsukawa, K. Furuno, and H. Kudo: *Nucl. Instrum. Methods B*, **26**, 406 (1987).
- 2) H. Miyatake, T. Nomura, H. Kawakami, J. Tanaka, M. Oyaizu, K. Morita, T. Shinozuka, H. Kudo, K. Sueki, and Y. Iwata: *Nucl. Instrum. Methods B*, **26**, 309 (1987).
- 3) L. C. Northcliffe and R. F. Schilling: *Nucl. Data Tables A*, **7**, 4 (1970).

III-5-5. Counter Development for Rotating Catcher System

M. Koguchi, M. Fukuda, K. Asahi, H. Kumagai,
M. Adachi, and M. Ishihara

We previously reported the design of a rotating catcher system (CAROT) for studies of β decay of nuclei far from stability.¹⁾ Briefly, CAROT aims at observation of decay particles (including β rays and β -delayed particles) from identified mother nuclides produced in projectile fragmentation reactions. Because of the general slowness of β transitions (half-lives known so far are longer than several milliseconds for β decays) a conventionally employed coincidence technique is not applicable to correlating of detected decay particles with the isotope identification signals obtained from an SSD telescope. CAROT employs a novel method using a rotating disc in which reaction products are implanted after passing through the SSD telescope. β Rays from the disc are detected by position-sensitive detectors. Details and the geometry of the system are presented in Ref. 1.

The mechanical part of the system and a control unit with a microprocessor have been constructed in the Technology Division. A catcher disc made of aluminum (80 cm in diameter and 0.10 cm in thickness) was installed, and the maximum rotating speed of 10 rounds/s was attained.

Below in this report we describe the development of a β counters for CAROT. A position-sensitive detector consisting of 100 strips of a plastic scintillator (each 1 mm thick, 2 mm wide, and 27 mm long) has been developed. Both ends of each strip are optically coupled to plastic lightguides of 1 mm in diameter which transport scintillation light separately to two photomultipliers. Twenty photomultipliers, each accepting the light from ten scintillator strips, constitute a 10×10 matrix and thus provide the position information of detected β ray. Pulse-height spectra obtained for β rays from a ^{90}Sr source indicated that the β -ray signals are large enough to be discriminated from noise, as shown typically in Fig. 1. This transmission type detector is placed close to the rotating disc, and is used for determination of the position in the disc from which β ray is emitted.

A sector-shaped plastic scintillation counter was assembled for measurement of the β -ray energies. This counter consists of six segments, each being a trapezoid of 8 cm in thickness, 15 cm in length and 7 cm in average width. A photomultiplier of 5 cm

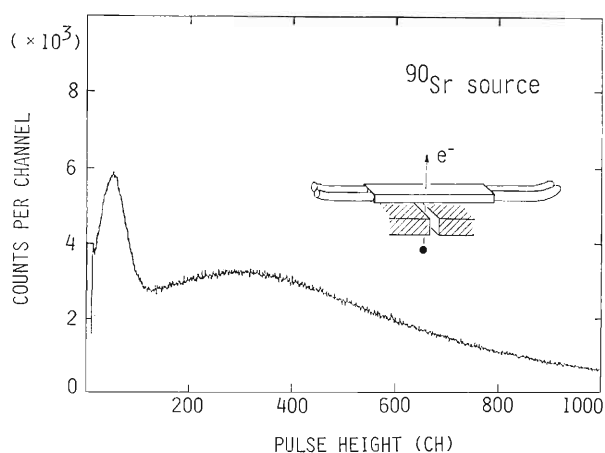


Fig. 1. Typical pulse-height spectrum obtained from a plastic scintillator strip of the position-sensitive β -ray detector. A β -ray source of ^{90}Sr was placed at a distance of 2 mm from the strip.

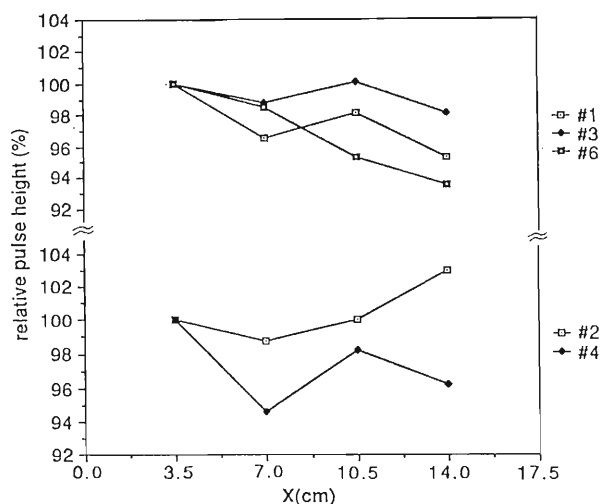
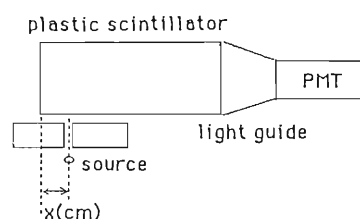


Fig. 2. Measured position dependence of the signal pulse height from each segment of a β -ray energy counter. Abscissa represents the position of the source as illustrated in the upper part of the figure.

in diameter is attached to each segment of the counter. In order to make the position dependence of the signal pulse heights as small as possible, several methods for wrapping the scintillators (for light reflection) were carefully examined. After several trials we chose Teflon film as a wrapping material. In Fig. 2 the position dependence observed for each scintillator segment is shown.

Development of a computer software for data processing and control will be started shortly.

Reference

- 1) M. Fukuda, T. Kubo, K. Asahi, I. Tanihata, M. Ishihara, H. Kumagai, Y. Oikawa, T. Abe, and H. Taketani: *RIKEN Accel. Prog. Rep.*, **20**, 146 (1986).

III-5-6. Facilities for Studies on Nuclear Chemistry and Radiochemistry at RIKEN Ring Cyclotron

M. Yanokura, Y. Ohkubo, S. Ambe, and F. Ambe

For a variety of chemical studies making use of RIKEN Ring Cyclotron, a unique irradiation system and laboratory equipment for chemical handling of radioisotopes have been designed and are to be constructed in the near future.

The main part of the "Falling-ball Irradiation System" will be installed in the E3 irradiation room. The system has been selected, because the transportation with a conventional pneumatic tube is not suitable for targets irradiated in vacuum and has the risk of bringing contaminated air with targets. Our system assures safe and rapid transportation of the irradiated targets to the hot laboratory. This system also has an advantage, because the laboratory lies downstairs just beneath the irradiation room.

Targets are mounted in hollow metallic balls, which are set in a standby tube connected to the

irradiation chamber. They are sent to an irradiation position one by one. After irradiation, the target is moved down to a monitoring site under the chamber, where its radioactivity is measured with an ionization chamber. If the radiation level of the target is suitable for safe handling in the hot laboratory, the ball is rolled down to a hood installed in the laboratory through a stainless steel tube. In the midway of the tube, a deceleration device is installed to avoid a violent collision of the ball against the end of the tube. After closing a gate valve near the end of the tube, the terminal lid of the tube is open and the target is taken out from the ball for chemical studies.

In the hot laboratory are to be installed hoods, sinks, workbenches, and glove boxes. The details of the facilities and the results of test experiments will be reported.

III-5-7. Further Study of Experimental Facilities for Light and Light-Heavy Ion Induced Reactions

H. Ohnuma, K. Hatanaka, S. Hayakawa,* T. Ichihara, K. Ieki, M. Ishihara, S. Kato, T. Kubo, S. Kubono, K. Maeda,** T. Motobayashi, T. Nakamura,*** H. Orihara, H. Shimizu, H. Toyokawa,**** M. Yasue, and H. Yoshida****

Further study of a particle detection system to be used in experiments with light- and light-heavy ion beams from RIKEN Ring Cyclotron is in progress.

Continuous efforts have been made to optimize the whole system reported in the RRC Annual Report last year.¹⁾ Figure 1 shows an example of the results of the first-order beam optics calculation for the twister-beam swinger system. General discussion of the optics of beam twisters is given elsewhere.²⁾

Extensive ray tracing calculations for the proposed cascade-type magnetic spectrometer have been carried out. A typical result is shown in Fig. 2. It is intended that the combined system can be used in dispersion matching mode.

The structural design of magnets is also under way. Figure 3 shows an example of the field calculation of a split-type quadrupole magnet for the spectrometer. Such a quadrupole magnet is needed to

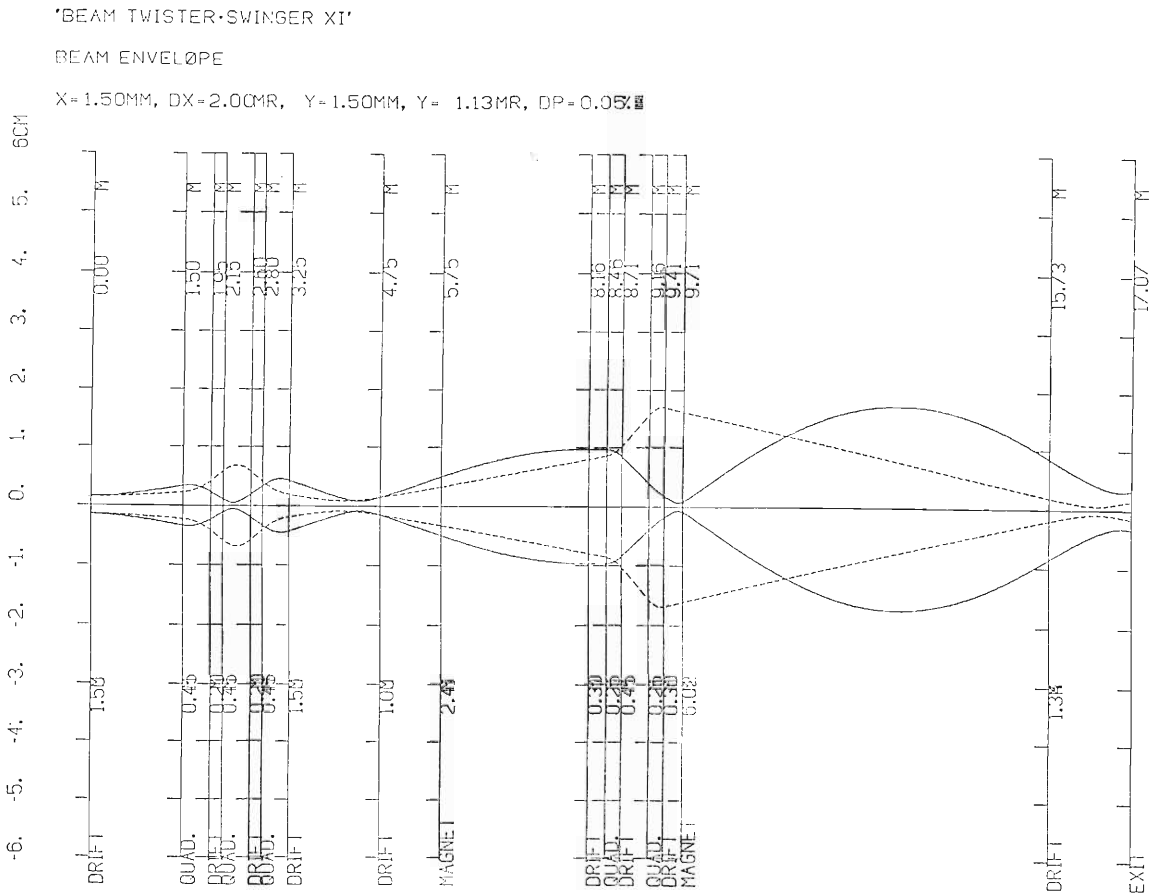


Fig. 1. Beam optics for the twister-swinger system.

* Ashikaga Institute of Technology.

** College of General Education, Tohoku University.

*** Cyclotron and Radioisotope Center, Tohoku University.

**** Department of Physics, Tokyo Institute of Technology.

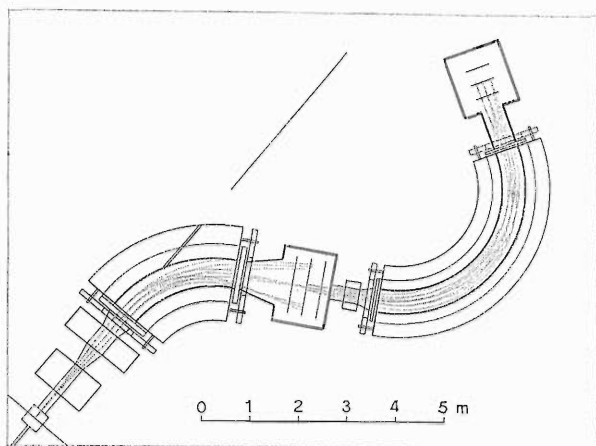


Fig. 2. Sample ray-tracing calculation for a cascade-type spectrometer.

facilitate small angle measurements with the present large solid-angle (20 msr) spectrometer.

In addition, two types of neutron detectors of a rectangular type (5 cm \times 10 cm \times 100 cm) and a cylindrical type (5 cm thick and 20 cm in diameter), were designed. They are to be used in neutron TOF measurements as well as in the detection of emitted neutrons in heavy-ion induced reactions.

Estimates of radiation doses due to the beam and

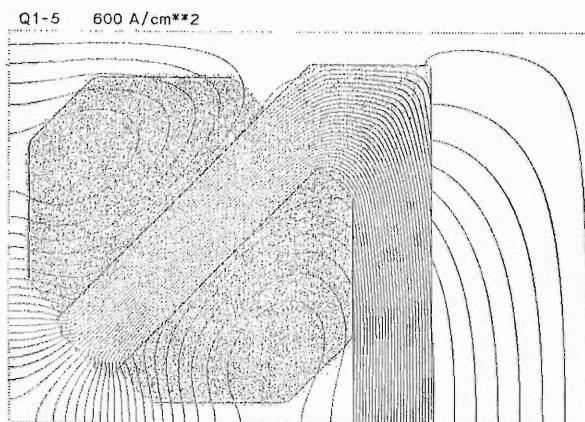


Fig. 3. Magnetic field calculation of a split-type quadrupole magnet.

to residual activities have been obtained, and used to carry out shield calculations under various experimental conditions.

References

- 1) H. Ohnuma, T. Ichihara, K. Ieki, M. Ishihara, S. Kato, T. Kubo, K. Maeda, T. Motobayashi, H. Orihara, and H. Shimizu: *RIKEN Accel. Prog. Rep.*, **20**, 134 (1986).
- 2) S. Kato: *Nucl. Instrum. Methods A*, **254**, 487 (1987); p.166 in this report.

III-5-8. Ray-Tracing Calculation of the Variable-Angle Beam Rotator

S. Kato

The high resolution magnetic spectrometer to be constructed will not be rotated even for measurements of angular distribution.¹⁾ Instead, the beam will be transported through a rotate-type beam swinger²⁻⁴⁾ to the target from various incident angles. The reaction plane becomes perpendicular. The median plane of the swinger magnet is not in coincidence with that of the upstream transport system. There are many merits in such a spectrometer. But we must overcome a serious demerit of it. The symmetry with respect to the horizontal plane which has been conserved by the upstream beam transport system will be destroyed by the rotated swinger. Without the symmetry, the beam character at the target will no longer possess the condition of the dispersion matching between the beam transport system and the spectrometer.

In order to retain the symmetry, we must rotate the beam image around the beam direction by any angle before the swinger so that a new symmetry plane of the beam coincides with the median plane of the rotated swinger magnet. A detailed analytical discussion how to rotate the beam images has been described in Ref. 5 by use of the first order transfer matrices. In the present report we briefly survey how we can rotate the beam image and illustrate the results of ray-tracing calculations.

In the point-to-point transportation, an ordinary triplet of quadrupole magnets, whose geometrical arrangement possesses a symmetry with respect to the direction of the motion of the beam, transfers beams with unit magnifications in both the transverse directions. One of the signs of these magnifications is positive and the other is negative. The signs can be interchanged by changing the polarity of the current. The triplet plays a role of an inverter of the beam images with respect to the plane which corresponds to the negative magnification.

If we rotate the symmetry plane around the axis, which is defined by the direction of the beam, the beam image will be inverted with respect to the rotated symmetry plane. The result can be regarded as the inversion with respect to the original symmetry plane and the rotation by twice the rotated angle of the magnets. The inversion of the beam images does not matter because the system in the upstream is symmetric with respect to the median plane. Thus

we can rotate the beam images by rotating an inverter.

The remaining problem is that the symmetric triplet of quadrupole magnets is not the ideal inverter because the triplet transfers only the coordinate components, leaving the angular ones transferred improperly. The matrix elements $(x' | x)$ and $(y' | y)$ which should be equal to 0 do not vanish.

In order to eliminate these two elements, we must add two degree of freedom. The simplest symmetric set of quadrupole magnets with additional two parameters is a symmetric septet of quadrupole magnets. We can obtain the full inverter of the beam images by the symmetric septet of quadrupole magnets. It will rotate the beam image by twice the geometrically rotated angle with accompanying beam inversion which is not the aim of the system.

The difference between the full inverter and the ordinary triplet is difficult to understand from the discussion of the elements of transfer matrices. We illustrate the difference between them by the ray-tracing calculations. We traced the motion of beams in the fields of triplet and the septet of quadrupole magnets. The lengths of the quadrupole magnets were assumed to be 0.20 m. The length of the free spaces were set as 0.30 m with the exceptions of 0.40 m at the both ends. The strengths of the quadrupole magnets of the triplet were searched so that $(x | x')$ and $(y | y')$ vanished and the numbers of intermediate nodes became 0 and 1 for the horizontal and the vertical directions, respectively. Then the conditions of $(x | x) = (x' | x') = 1$ and $(y | y) =$

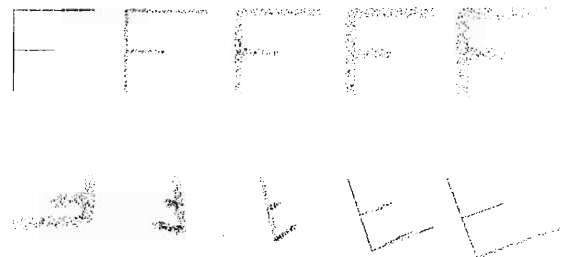


Fig. 1. Beam images for the triplet of quadrupole magnets. Upper five figures are images at and near the starting point with 0.04 m (tenth of the length of the free space) intervals. The lower ones show those near and at the focus point.

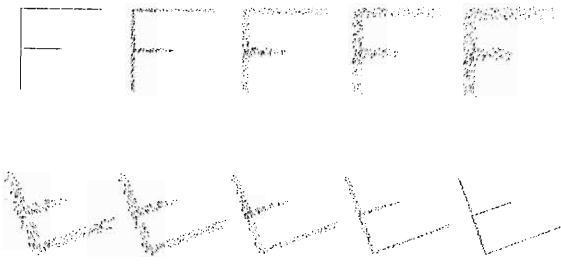


Fig. 2. Beam images for the septet of quadrupole magnets. The other conditions are same as those of the Fig. 1.

$(y' | y') = -1$ were automatically fulfilled. Those of the septet were searched so that the additional conditions of $(x' | x) = (y' | y) = 0$ were also satisfied.

In Figs. 1 and 2, we show the beam images at several spots near the starting point and the focusing point of 0.04 m steps for the triplet and for the septet, respectively. The systems were rotated by 10 degrees. We can expect the beam images to be rotated by 20 degrees and inverted. Although there is no remarkable difference between the images of the triplet and the septet at the focusing point, the

difference between them off the focusing point is remarkable. This means that although the beam image can be transferred by both the triplet and the septet, the angle of incidence cannot be properly transferred by the triplet. In order to rotate the beam images with the full phase space unchanged, we must use a symmetric septet of quadrupole magnets.

References

- 1) H. Ohnuma, K. Hatanaka, S. Hayakawa, T. Ichihara, K. Ieki, M. Ishihara, S. Kato, T. Kubo, S. Kubono, K. Maeda, T. Motobayashi, T. Nakamura, H. Orihara, H. Shimizu, H. Toyokawa, M. Yasue, and H. Yoshida: p. 164 in this report.
- 2) D. A. Lind, R. F. Bentley, J. D. Carlson, S. D. Schery, and C. D. Zafiratos: *Nucl. Instrum. Methods*, **130**, 93 (1975).
- 3) R. K. Bhowmik, R. R. Deoring, L. E. Young, S. M. Austin, A. Galonsky, and S. D. Schery: *Nucl. Instrum. Methods*, **143**, 63 (1977).
- 4) H. Orihara and T. Murakami: *Nucl. Instrum. Methods*, **188**, 15 (1981).
- 5) S. Kato: *Nucl. Instrum. Methods Phys. Res. A*, **254**, 487 (1987).

III-5-9. Design of the RIKEN Projectile-Fragment Separator RIPS

T. Kubo, M. Ishihara, K. Asahi, and I. Tanihata

Experimental studies of nuclei far from stability are one of the most interesting subjects pursued by using heavy-ion beams from RIKEN Ring Cyclotron. The construction of the projectile-fragment separator RIPS (RIKEN Projectile-fragment Separator) has been proposed¹⁾ in order to facilitate the experiments on such exotic nuclei.

The ion-optical design of RIPS has been completed. The layout is schematically shown in Fig. 1, and the basic characteristics are given in Table 1. The ion optics of RIPS has been designed to have a high collection efficiency compared with a similar separator LISE at GANIL.²⁾ The solid angle of RIPS is about 25 times larger than that of LISE. This large acceptance should enable us to collect more than half of fragmentation yields.

The separator RIPS forms an achromatic beam transport line, which can be divided by focal planes

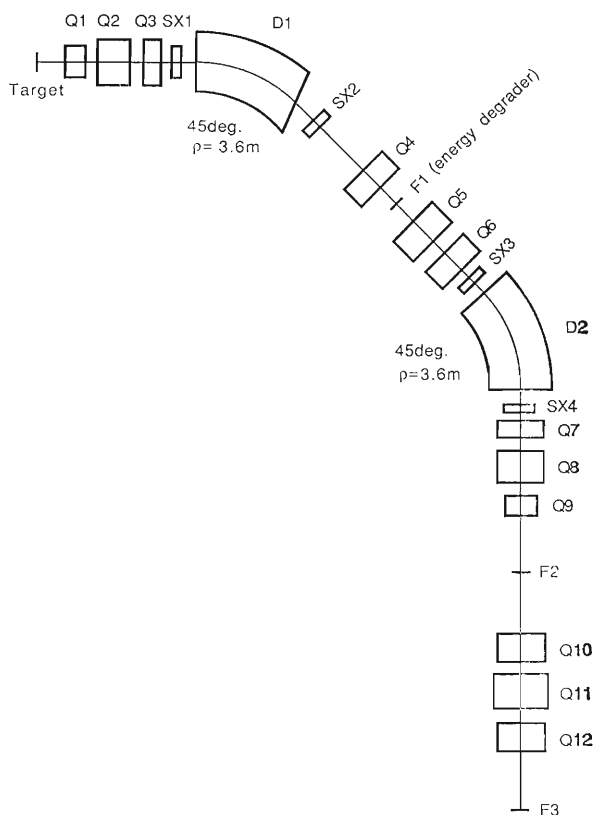


Fig. 1. Layout of the separator RIPS.

Table 1. Design characteristics of RIPS.

Configuration	Q-Q-Q-SX-D-SX-Q (first stage) Q-Q-SX-D-SX-Q-Q-Q (second stage) Q-Q-Q (third stage)
Aperture	± 40 mr, circle
Solid angle	5 msr
$B\rho$ acceptance	$\pm 3\%$
Maximum $B\rho$	5.76 Tm
Focal planes	F1, dispersive, end of first stage F2, achromatic, end of second stage F3, achromatic, end of third stage
Isotope separation	A/Z and energy loss selection
Energy degrader (F1)	wedge-shaped (achromatic degrader)
Goal of mass resolution (F2)	$A/\Delta A \sim 100$ for full acceptance
Correction for aberration	by four sextupole magnets

into three stages. The first stage consists of a Q-Q-Q-SX-D-SX-Q configuration, where Q, D, and SX represent quadrupole, dipole, and sextupole magnets, respectively. The momentum-dispersive focusing at the first focal plane (F1) is obtained by quadrupole magnets on this stage. An energy degrader foil, which permits isotopes to be separated, is set at F1. The second stage consists of a Q-Q-SX-D-SX-Q-Q-Q configuration, by which the achromatic focusing at the second focal plane (F2) is achieved. The role of sextupole magnets on these two stages is to minimize optical aberration.

The principle of isotope separation is the same as that of LISE. The first stage allows coarse separation according to A/Z of fragments, because projectile fragmentation approximately conserves a beam velocity. Fine separation by the energy degrader is made on the second stage. The isotope dependence of energy loss, expressed as $dE/dx \propto A^{2.5}/Z^{1.5}$, generates isotope dispersion at F2, which enables us to select a specific isotope. The wedge-shaped degrader²⁾ will be used, which does not affect the first-order optics on the second stage.

The final stage, which consists of triplet quadrupole magnets, transports a selected isotope to experimental devices at the final focal plane (F3).

In the ion-optical design, the minimization of aberration is necessary especially for F2 where the isotope separation is made. This is because RIPS

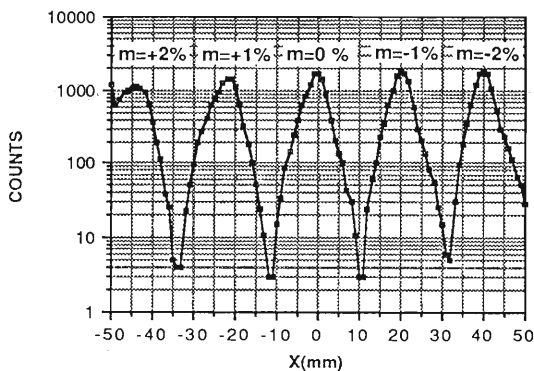


Fig. 2. Typical mass spectrum at F2 simulated using optical parameters obtained by ORBIT2. Full acceptance and degrader thickness of $d/R^{23}=0.5$ are assumed. Each peak corresponds to isotopes whose fractional mass differences ($m=(A-A_0)/A_0$) are -2 , -1 , 0 , $+1$, and $+2\%$, respectively.

is required to have large acceptance. Effects of degrader on optics have been also taken into account because the presence of degrader is found to affect aberration. We have used the code ORBIT2³⁾ developed for this purpose. The code ORBIT2 allows the ion-optical treatment of degrader⁴⁾ and calculates aberration coefficients up to the third order.

By using ORBIT2, we have made the ion-optical design as follows: 1) the first-order optics is designed so that it may produce small aberration; 2) then, each strength of four sextupole magnets is searched for so as to minimize major aberration such as $(x/\theta\delta)$, $(x/\theta m)$, (x/δ^2) , (x/θ^2) , and (x/θ^3) . Figure 2 shows an example of the mass spectra at F2 simulated using optical parameters thus obtained. This figure shows that a mass resolution greater than the design goal ($A/\Delta A \sim 100$) is achieved.

The detailed design of magnets, vacuum chambers, and beam monitoring system is now in progress toward the completion in the spring of 1989.

References

- 1) T. Kubo, K. Asahi, T. Ichihara, T. Matsuzaki, M. Fukuda, K. Nagamine, I. Tanihata, and M. Ishihara: *RIKEN Accel. Prog. Rep.*, **20**, 136 (1986).
- 2) J. P. Dufour, R. Del Moral, H. Emmermann, F. Hubert, D. Jean, C. Poinot, M. S. Pravikoff, A. Fleury, H. Delagrangé, and K. H. Schmidt: *Nucl. Instrum. Methods A*, **248**, 267 (1986).
- 3) By S. Morinobu at RCNP, Osaka University: private communication.
- 4) S. Morinobu: Proc. RIKEN-IN2P3 Symp. Heavy-Ion Collisions, Shimoda, Oct. (1987), p. 91.

III-5-10. Design of a New Type of Low-Energy Radioisotope-Beam Channel "SLOW" for Surface Studies

T. Matsuzaki, K. Ishida, and K. Nagamine

We are constructing a low-energy radioisotope-beam channel "SLOW" in the E7 experimental area of RIKEN Ring Cyclotron (RRC). "SLOW" is used for the study of emission mechanisms of various slow radioactive atoms from characterized metal surfaces treated carefully and is also for the extraction of useful radioisotopic ions for solid-state physics studies.

High-energy heavy-ion beams available at RRC will be injected into a metal target, whose temperature could reach 2,000 K. By a nuclear reaction, many kinds of radioisotopes are produced and moderated in the target. The moderated atoms reach the metal surface by diffusion and could evaporate into a vacuum outside the target surface. In particular, the atoms of alkaline, alkali earth, and rare earth metals evaporate from the surface with a thermal energy and autoionize partly by a surface ionization effect. The surface ionization occurs only when the evaporating atom has the ionization potential smaller than the work function of the target metal surface. The other atoms with higher ionization potentials are emitted from the target surface and will be ionized by an ionizing device separately prepared near the target surface. Thus, around the target surface, the low-energy radioisotopic ions are generated with a uniform kinetic energy. By means of "SLOW" beam channel, these ions are extracted, accelerated, energetically analyzed, and transported to focussing points.

In Fig. 1, a proposed design of the "SLOW" beam

channel is shown. All beam lines are composed of electrostatic lenses with no magnetic field. Thus, the ions with an equal charge state can be transported and focussed under the same beam-line conditions. The masses will be identified by means of a TOF (Time Of Flight) method. The ions are then extracted and accelerated (<10 kV) by SOA electric aperture/tube lenses located in a ultra-high vacuum chamber and are focussed at the first focussing point (F1) with a pair of electric quadrupole lenses (EQ). The ions starting from F1 are transported with 4 sets of EQ's and bent in an electric bend (EB) by 90 degrees. Finally, the ion beams are focussed again at the second focussing point (F2). The electrode of EB is troidal-shaped. The troidal electrode is capable of focussing ion beams not only horizontally but also vertically relative to the transporting plane. The EQ has 4 spherical shaped electrodes, and the bore diameter for the beam is 80 mm. The "SLOW" beam line has also an adjustable slit (SXY and SX) and an electrostatic X-Y deflector (ED.) All electrical lenses are designed to be insulated up to ± 10 kV.

Prior to experiment, an electron source will be used to tune a beam line and to examine the optical properties of the "SLOW" beam line, when the polarity of all electric lenses are reversed. The high voltage supplied from a main high-voltage power supply (10 kV, 10 mA) is applied to each terminal through a voltage divider. The radioisotopic ions are detected at F1 and F2 with a micro channel

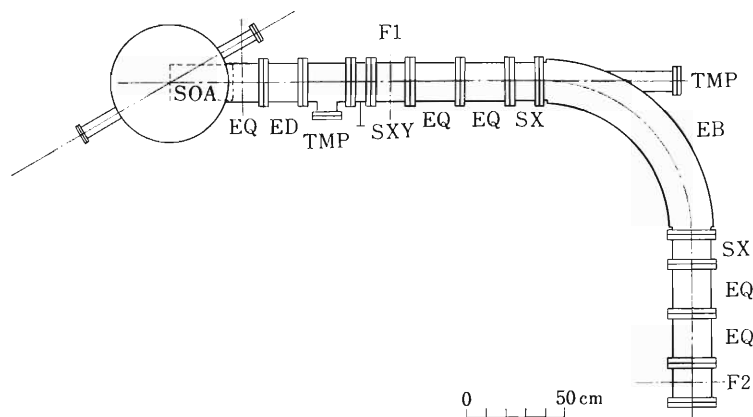


Fig. 1. Proposed design of a "SLOW" beam channel.

plate and a Si(Li) particle detector. To define the time zero of radioisotopic beams, the applying voltage for the second electrode of an SOA lense is rectangular-pulsed. The TOF is measured as a time difference between the time zero and the stop pulse obtained by particle detectors. In addition to the TOF analysis, the lifetime and energy for β - or γ -rays from stopped ions at F2 are measured for nuclear assignment.

For a high vacuum (10^{-8} Torr) of the beam line to be kept, the whole beam line is designed to be bakable up to 150°C . The vacuum space of the beam line is evacuated with two sets of turbo molecular pumps (TMP, 300 l/s). At the head of the "SLOW" beam line, there is a large ultra-high vacuum (UHV) chamber evacuated with a cryo-pump (1,500 l/s). The inside vacuum of the UHV chamber is aimed to reach as high as 10^{-10} Torr after outgasing by elaborate baking. In addition to a vacuum gauge, an electric quadrupole mass analyzer is equipped to analyze a residual gas component in a vacuum. The residual gas is known to affect the metal surface; therefore, its analysis is essential to control the metal surface. Above the UHV chamber, we put an additional vacuum chamber, with which we can treat and characterize the metal surface of targets. The 5 kV argon-ion gun is equipped to carry out an ion etching on the metal surface. A LEED/AUGER spectrometer installed in the chamber is used for crystallographic measurements and

analysis of the components on the metal surface.

In order to investigate the emission mechanisms of various ions from the characterized metal surface, we should observe a variety of the emitted radioisotopic ions and their yields under various conditions (surface treatment, coating materials, crystallographic axis, surface temperature, target thickness, target materials, incoming heavy-ion beams, and incident energy). The present method is superior to an ion-scattering or an ion-implantation method, because various ions are generated inside the metal and will be emitted from the surface after thermal diffusion. By selecting a combination of an incoming heavy-ion beam, an incident energy and a target material, we can choose radioisotopic atoms produced inside the target metals through various nuclear reactions.

The second goal of this work, in addition to the study of emission mechanism, is to obtain radioactive ^6He and ^8He beams. They are very useful to study microscopic diffusion properties of helium atoms in metals, because they are β -ray emitters with lifetimes of 808 and 122 ms, respectively. We can trace the diffusion of helium atoms in/on metals by observing the β rays from them with an aid of a multi wire proportional counter array. The properties of helium in metals have not yet been well investigated; therefore the radioactive helium beams will be of a great importance for the study on the behavior in metals.

The detailed optical calculations and design work are now in progress.

III-5-11. Design of a Superconducting Secondary Beam Transport System with a Large Solid Angle (SL Ω)

K. Ishida, T. Matsuzaki, and K. Nagamine

A new type of beam transport system for light charged particles (Superconducting Large Ω) has been designed and is under construction at E7 port of RIKEN Ring Cyclotron. It makes use of the focusing properties of an axially symmetric magnetic field of 0.8 T (at maximum value) produced by three superconducting coils. The main purpose of the beam channel is to collect the secondary particles as much as possible with a moderate momentum and mass separation.

In an axially symmetric magnetic field, a charged particle emitted from a point source on the axis is refocused onto the axis after one Larmor period of a helical orbit. In order to gain a high flux, it is desirable for the rays of a number of trajectories to intersect at the same point along the same axis. The rays should be characterized by a large spread in emission angle α and a small spread in momentum p . It is well known that a suitably shaped concave magnetic field ($d^2B/dz^2 > 0$) has this property due to the following reasons:^{1,2)} the concave field produces intermediate ring focus; by means of an annular slit situated at this intermediate image the momentum spread can be selected for the particles collected at the focus; moreover, only a small spherical aberration is produced at the focus.

A schematic diagram of the proposed system is shown in Fig. 1. The system makes use of two Larmor periods in an axisymmetric field. The basic concept is as follows: the first part from T to F1 selects the momentum to a resolution of $\pm 2\%$; the second part from F1 to F2 separates the particles according to the energy loss at the degrader.

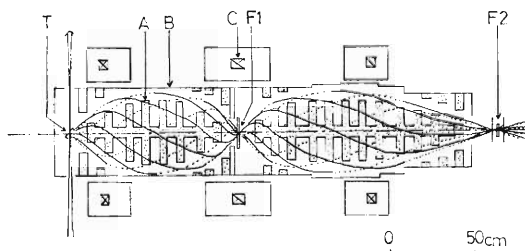


Fig. 1. Schematic diagram of the large Ω beam course: T, production target; F1, energy degrader at first focus; F2, experimental target and detectors at second focus; A, annular slits; B, vacuum chamber; C, superconducting coils.

Calculations were performed by using an M780 computer at RIKEN. The field calculating program and the ray tracing program calculate the ray tracks in the magnetic field. In determining the coil parameters, we placed the following requirements: the spherical aberration at F2 should be small; the rays should be nearly parallel at F2; the solid angle should be as large as possible; the momentum resolution should be below 2%; the magnification should be so small that the size or the position of the primary beam at the target is not essential; the stray field at F2 should be small.

In Tables 1 and 2 we present the optical properties

Table 1. Optical properties of large Ω .

Production target location T	$z = 0$ cm
First focus location (F1)	$z = 100$ cm
Second focus location (F2)	$z = 255$ cm
Angular acceptance	$35^\circ \sim 47^\circ$
Solid angle	860 msr
Maximum momentum	30 MeV/c
Resolution of momentum	$\pm 2\%$
Maximum distance of the rays from the axis	27 cm

Table 2. Technical characteristics of large Ω (designed values).

Coil parameters	Coil 1	Coil 2	Coil 3
Inner diameter (cm)	74.1	74.1	74.1
Outer diameter (cm)	85.9	85.9	85.9
Coil length (cm)	4.8	7.3	4.8
Location of coil centers (cm)	20.0	100.0	180.0
Coil weight (kg)	143	200	143
Number of turns	1,980	3,036	1,980
Inductance (H)	6.1	13.5	6.1
Mutual inductance (H)	0.36	0.36	
Current per wire (A)	152	159	83
Current/coil (kAT)	300	484	164
Current density (A/mm ²)	106	112	58
Hoop force (t)	25.5	59.5	8.7
Attractive force between coils (t)		2.33	1.32
Cryostat parameters			
Total weight	2.0 t		
Stored energy	260 kJ		
Inner bore diameter	60 cm		
Outer diameter	102 cm		

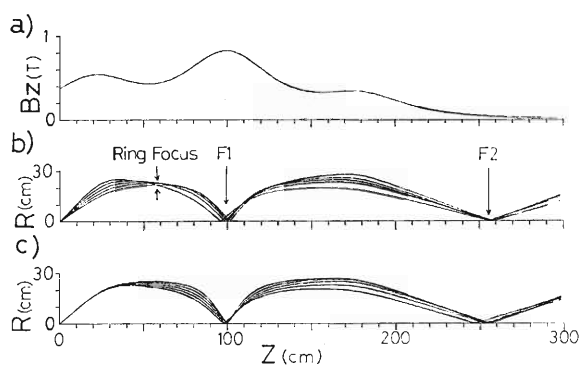


Fig. 2. (a) The axial field produced by the set of coils in Table 2. (b) Trajectories with $p=30$ MeV/c and emission angles $\alpha_0=35, 38, 41, 44,$ and 47° with respect to the system axis. (c) Rays with emission angle $\alpha_0=41^\circ$ and momenta $p=28.8, 29.4, 30.0, 30.6,$ and 31.2 MeV/c.

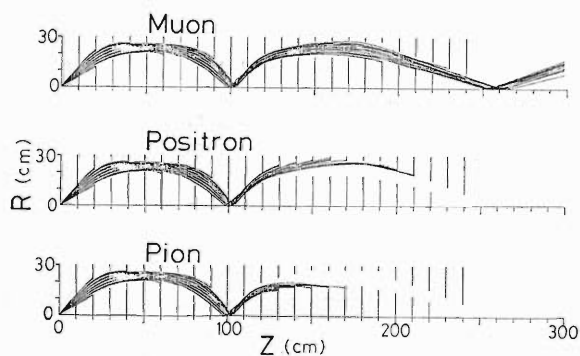


Fig. 3. Trajectories of muons, positrons, and pions for all combinations of emission angles $\alpha_0=32, 35, 38, 41, 44, 47,$ and 50° and momenta $p=28.8, 29.4, 30.0, 30.6,$ and 31.2 MeV/c. The currents of coil 2 and coil 3 are reduced compared with that of Fig. 2(a) to match the reduced momenta of muons after the degrader.

and coil parameters thus determined. The axial field produced by this coil configuration is presented in Fig. 2(a). The ray tracks for a point source on the axis at $z=0$ cm are presented in Figs. 2(b) and 2(c) for various angles and momenta, respectively.

One of the main purposes of the beam course is to collect surface muons obtained as products of positive pions decay at the skin of the production target, where the pions were produced by high energy heavy ions. Figure 3 shows the trajectory of muons, positrons and pions emitted from the axis at $z=0$ cm for various angles and momenta. Annular slits are located at $z=10, 20, \dots, 230,$ and 240 cm. An energy degrader of 50 mg/cm² in thickness is placed at $z=100$ cm. We can expect the angular acceptance of 800 msr and momentum acceptance of $\pm 2\%$ with a full separation of muons from positrons and pions. The system can be also applied to collect slow heavy ions. For a particle with mass number A and charge state q , the maximum accepted momentum is $30q$ MeV/c and the maximum accepted energy is $0.48 q^2/A$ MeV.

The field produced by this superconducting coil system is moderate. Instead, it has the following characters. The cryostat has a large room temperature access to the central region. The current of the three coils can be changed independently with the use of six current leads to guarantee the flexibility needed for various types of application of this celebrated system.

References

- 1) K. Siegbahn: Alpha-, Beta- and Gamma-Ray Spectroscopy, North-Holland, Amsterdam, Vol. 1, p. 145 (1965).
- 2) I. Lindgren and W. Schneider: *Nucl. Instrum. Methods*, **22**, 48 (1963).

III-5-12. Apparatus for Resonance Ionization Spectroscopy of Atomic Nuclides

T. Murayama, M. Takami, Y. Matsumoto, and T. Inamura

A resonance ionization technique is one of the most powerful methods of spectroscopy of elements in trace amounts. Its high selectivity and sensitivity for all of the elements (except He and Ne) have well been recognized in the last decade.¹⁾ Recently, a method of high sensitive detection of pairs of ions and electrons has been developed for resonance ionization spectroscopy (RIS).²⁾ To make use of this novel technique for nuclear spectroscopy, lasers were installed and an interaction chamber was constructed; the chamber is equipped with an ion gun to produce neutral atoms.

Figure 1 shows an arrangement of the lasers, the interaction chamber, and optics. The specifications of the lasers are listed in Table 1. Two laser systems are used for the multistep excitation in RIS: One is a ring dye laser pumped by an Ar-ion laser, which is important especially for the first step excitation to give the selectivity of elements; and the other is a dye laser pumped by a copper-vapor laser. Laser beams are guided along with each other by using

Table 1. Specifications of the lasers for nuclear spectroscopy.

(1) Ring Dye Laser System
High Resolution Dye Laser: Ring Dye Laser (Coherent 699-29)
Wavelength 400-600 nm
Pumping Laser: Ar-Ion Laser (Spectra Physics 171-19)
Output 18 W, CW
(2) Copper Vapor Laser System
High Power Dye Laser: Lambda Physik FL3002E
Copper Vapor Laser: Plasma Kinetics 351-HR
Frequency 6-10 kHz
Output Power average 24 W
peak 180 W at 8 kHz
(pulse width 17 ns)
Wavelength 511 nm (60%), 578 nm (40%)

mirrors and interact with atomic beams in the chamber. A frequency doubler BBO (β -BaB₂O₄) crystal is useful to expand the region of elements available for RIS; its conversion efficiency is expected to be more than 60%.

In Fig. 2 is presented a photograph of the chamber.

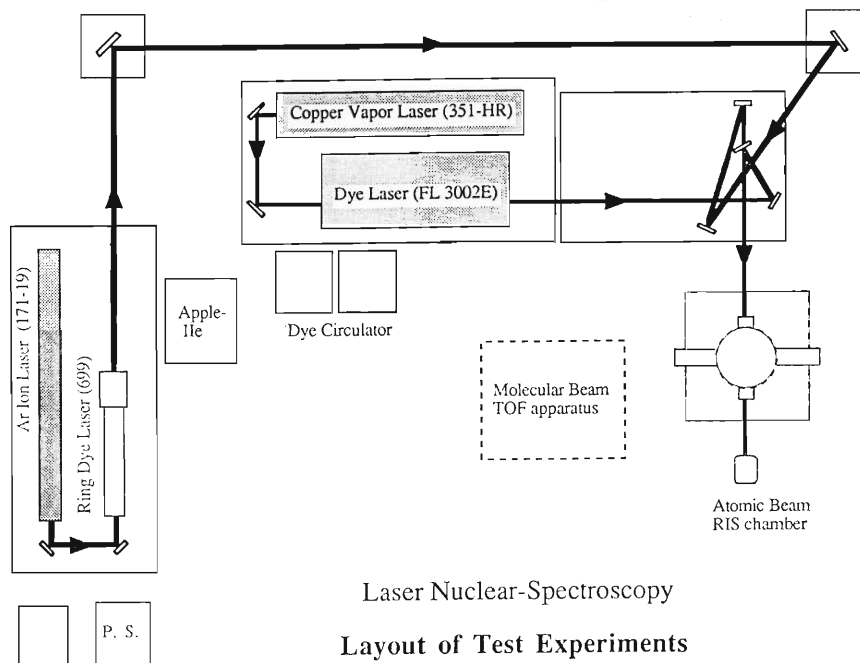


Fig. 1. Schematic arrangement of the apparatus.

Figure 3 shows the schematic presentation of the RIS experiment using the apparatus. Atomic beams are

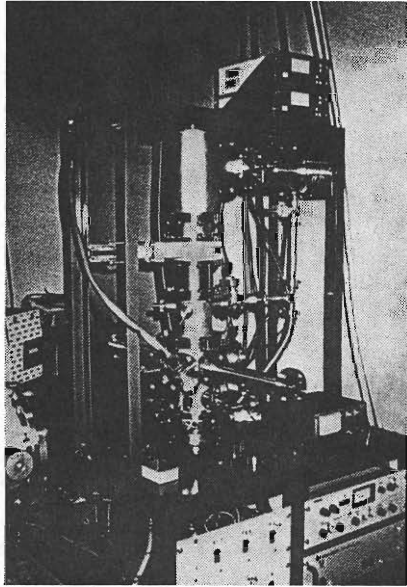


Fig. 2. Photograph of the interaction chamber for RIS. Lasers come into the resonance cell through a long guide. Ar beams from the ion gun bombard the target at the bottom of the chamber, producing neutralized target atoms.

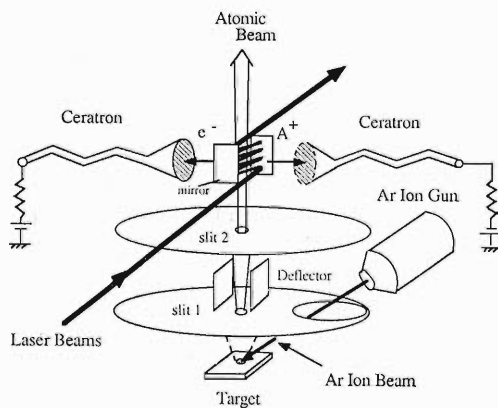


Fig. 3. Schematic presentation of our method.

produced by sputtering a target material by Ar-ion beams from an ion gun (ANELVA 5 kV Ion Gun). Sputtering has the following advantages in producing atomic beams: i) The sputtering process occurs almost independently of the chemical properties of elements; ii) Sputtering has nothing to do with volatility; and iii) most of the sputtered particles are neutral atoms (more than 99%). Ar beams bombard the surface of the target with an angle of 65° to the normal so as to obtain maximum yields.

Test experiments off-line are now in progress. First we make spectroscopy of stable nuclei of rare earth elements. Our method also enables us easily to make spectroscopy of elements Ta and W whose melting points are prohibitively high to vaporize. Next we proceed to spectroscopy of radioactive isotopes. Radioactive atomic beams can be generated by sputtering the target onto which they are implanted: Radioactive species are produced in the heavy-ion induced nuclear reactions such as target fragmentation. In the end we aim to measure hyperfine structure to determine spins and moments of nuclei far from the stability line and also to measure isotope shifts to deduce the change in charge radius as a function of the number of neutrons or protons.

We will extend the present method for the on-line spectroscopy with a hybrid isotope separator, GARIS³⁾ and IGISOL,⁴⁾ and a projectile isotope separator RIPS.⁵⁾ Lastly, mention should be made that the devices will shortly be installed for RADOP (radiation detect optical pumping).

References

- 1) C. S. Hurst: *Resonance Ionization Spectroscopy 1984* (eds. G. S. Hurst and M. G. Payne), The Institute of Physics, Bristol and Boston, p. 7 (1984).
- 2) T. Minowa, H. Katsuragawa, K. Nishiyama, M. Shimazu, and T. Inamura: *J. Appl. Phys.*, **61**, 436 (1987).
- 3) H. Miyatake, *et al.*: *Nucl. Instrum. Methods B*, **26**, 309.
- 4) K. Morita, *et al.*: *Nucl. Instrum. Methods B*, **26**, 406 (1987).
- 5) T. Kubo, H. Ishihara, K. Asahi, and I. Tanihata: p. 168 in this report.

III-5-13. Resonance Ionization Spectroscopy of Neutral Atoms by a Laser Ablation Method

M. Otsuki,* T. Minowa, H. Katsuragawa, M. Shimazu,* and T. Inamura

We have employed a laser ablation method to carry out resonance ionization spectroscopy (RIS) of Al, Sr, Na, and Cu because this method is capable of generating neutral atoms from almost all the matter. The laser ablation method is based on nonlinear phenomena caused by a laser with a high output power. A laser beam with an extremely strong field intensity generates plasma on the surfaces of metal samples to produce large amount of neutral atoms as well as ions.

The schematic diagram of the experimental setup is shown in Fig. 1. The half of the output energy (60 mJ per laser pulse) of a XeCl excimer laser was used to generate neutral atoms. The laser beam was focused on the surface of a metal sample (Al, Sr, Na, or Cu) placed in a proportional counter filled with a pure Ar gas (1 atm) to multiply ionization signals and to prevent neutral atoms from chemical reactions. Neutral atoms generated were ionized resonantly by irradiation of single or two pulses of a dye laser according to the ionization scheme of atoms concerned. A chopper cut off the output beam of the XeCl laser every two shots. Photoionization signals were detected with a proportional counter when the XeCl laser beam was not in the counter. The output

signals from the proportional counter were amplified and averaged by using a boxcar integrator. The intensity of the averaged signal was recorded against the output wavelength of the dye-laser pulse (1 mJ/pulse).

Spectra observed are shown in Fig. 2.

(1) Aluminum

Peaks I and II are due to the coincidence of the laser frequency with the $4S_{1/2}-3P_{3/2}$ and $4S_{1/2}-3P_{1/2}$ transition frequencies of Al, respectively. Dependence of the intensity of peak II on the output energy of the dye-laser pulse was measured. From this measurement almost all the Al atoms in the ionization area are ionized at output energies above 0.1 mJ. The intensity ratio of peak I to peak II is 0.6 and agreed with the population ratio of the $3P_{3/2}$ state to the $3P_{1/2}$ state at room temperature.

(2) Strontium

Peak III is due to the coincidence of the laser frequency with that of the $5P_1-5S_0$ transition of Sr.

(3) Sodium

Peaks IV and V are due to the coincidence of the laser frequency with the $3P_{1/2}-3S_{1/2}$ and the $3P_{3/2}-3S_{1/2}$ transition frequencies of Na, respectively. The intensity of peak IV is not equal to that of peak V.

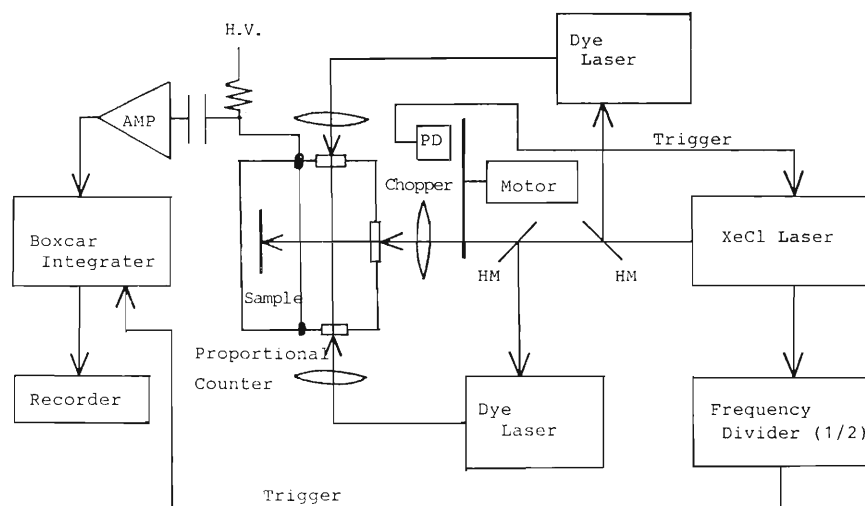


Fig. 1. Schematic diagram of an experimental setup.

* Department of Physics, Faculty of Science, Toho University.

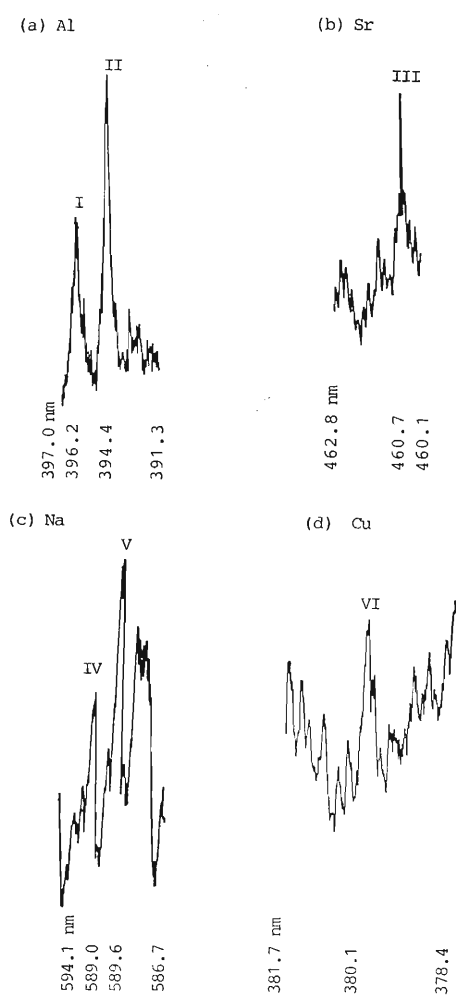


Fig. 2. Observed spectra for Al, Sr, Na, and Cu atoms.

This result suggests that the output power of the pulsed dye-laser was not enough for almost complete ionization of Na atoms in the ionization area.

(4) Copper

Peak VI is due to the coincidence of two times the laser frequency with the $6S_{1/2}$ - $4S_{1/2}$ transition frequency of Cu. Two-photon absorption takes place.

Using the sensitivity of the proportional counter, we estimated the densities of neutral atoms at 10^{10} cm^{-3} .

III-5-14. Observation of Two-Step Photoionization of a Na Atomic Beam Using cw and Pulsed Lasers

T. Minowa, H. Katsuragawa, and M. Shimazu*

Recently we have carried out highly sensitive resonance ionization spectroscopy (RIS) of a Tl atomic beam by a time-of-flight (TOF) method¹⁾ and were able to detect Tl atoms of a density of 20 cm^{-3} . As next step we observed two-step photoionization of a Na atomic beam to demonstrate the applicability of the technique used in RIS of a Tl atomic beam and the possibility to construct high-resolution laser spectrometers with high sensitivity.

The schematic diagram of an experimental setup is shown in Fig. 1. The output beam of a cw dye-laser was admitted into a vacuum chamber containing a Na atomic beam source, the two beams being collinear. The cw dye-laser had an output power of 10 mW and the width of the output wavelength of 0.1 nm at 590 nm and was used to excite Na atoms from the ground electronic state ($3S_{1/2}$) to the $3P_{3/2}$ state; emission due to the $3P_{3/2}$ - $3S_{1/2}$ transition is well known as the D_2 line (589.0 nm). Na atoms were evaporated from a Na sample by heating and collimated through two baffles having holes (3 mm in diameter) at centers.

The output beam of a pulsed dye-laser pumped by a XeCl excimer laser was focused on the Na atomic beam in a crossed way. Because the wavelength of the output beam of the pulsed dye-laser is 390 nm (3.18 eV) and the ionization potential of Na is 5.14 eV, Na atoms in the ground electronic state were ionized by two-photon absorption. The

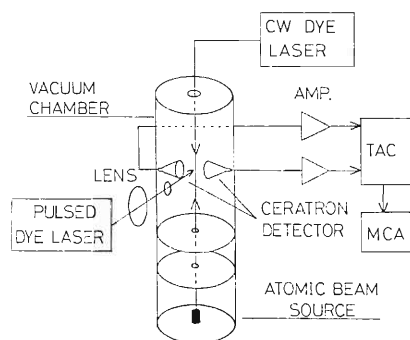


Fig. 1. Schematic diagram of an experimental setup. TAC, time to amplitude converter; MCA, multichannel analyzer.

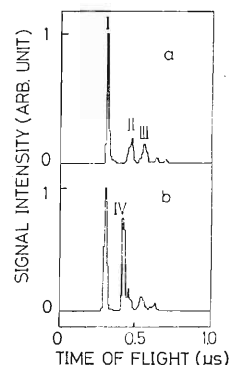


Fig. 2. Time-of-flight spectra, (a) Na atomic beam source is not heated. (b) Na atomic beam source is heated.

Na atoms populated in the $3P_{3/2}$ level with the resonant cw dye-laser beam can be ionized by single photon (390 nm) absorption.

Na ions and electrons generated by irradiation of the pulsed dye-laser beam were detected with a pair of CERATRON detectors (MURATA EMW-6081B). The arrangement of electronic devices for detecting ions and electrons were described in detail in Ref. 1. Electron signals were used as the time origin for the TOF measurement because the TOF of electrons was negligibly short compared with the time resolution of the electronic devices. Only ion signals having the TOF corresponding to Na ions were recorded in order to reduce the background noise.

The TOF spectra obtained are shown in Fig. 2; (a) the Na atomic beam source is not heated, and (b) the source is heated. Peaks I, II, and III in (a) appear to correspond to C , C_2 , and C_3 ions, respectively. These ions would be generated by dissociation and ionization of molecules of diffusion pump oil. When the Na atomic beam source reaches a temperature enough for Na to be evaporated, TOF signals due to Na ions appear on the TOF spectrum (peak IV in (b)). Signal intensities due to Na ion were recorded against output energies of the pulsed dye-laser. This result suggests that the saturation condition is fulfilled at energies above 1 mJ per pulse. The peak power density at the ionization area is estimated at 10^9 W/cm^2 at the output energy of

* Department of Physics, Faculty of Science, Toho University.

1 mJ per pulse.

Intensities of Na ion signals under both conditions, where (a) the output beam of the cw laser is tuned to the $3P_{3/2}$ - $3S_{1/2}$ transition of Na (on resonance) and (b) it is detuned (off resonance), were recorded. The signal intensity under the condition (a) was larger than that under the condition (b) by a factor of about 3. The output energy of the pulsed dye-laser was kept at about 0.4 mJ per pulse in these measurements. The increase in Na ion signal intensity

is due to excitation of Na atoms by the resonant cw dye-laser beam. This result means that a highly sensitive laser spectrometer with high resolution can be constructed by using the combination of a high resolution cw laser and a high power pulsed laser.

Reference

- 1) H. Katsuragawa, T. Minowa, M. Shimazu, and T. Inamura: *Nucl. Instrum. Methods B*, **26**, 440 (1987).

III-5-15. Development of the Parallel Plate Avalanche Counter for the Time-of-Flight Measurement

H. Kumagai, M. Fuse, E. Gotoh, M. Fukuda,
K. Asahi, and M. Ishihara

We have been investigating for these three years the characteristics of a parallel plate avalanche counter (PPAC)¹⁾ and constructed several different types of PPAC. Taking advantage of the high-counting rate capability and the high resistance against radiation damages, these counters have proven to be very useful as heavy-ion detectors. Several counters designed for the angular distribution measurements have been successfully used in the atomic physics^{2,3)} and nuclear physics⁴⁾ experiments. Here we report a recent application of the PPAC to the time-of-flight (TOF) measurement for heavy ions. PPAC is a low pressure gas detector with small thickness, it can be used for timing measurements without causing substantial change in the energy of detected particles.

The structure of the PPAC currently constructed for the TOF measurement is shown in Fig. 1. The counter has an effective area of 50 mm × 50 mm and comprises an anode and two cathodes. The anode is made of a 2 μm thick Mylar film, on both sides of which 40 μg/cm² thick gold layers are deposited. Each of the two cathodes, one providing the position sensitivity for the *x*-direction and the other for the *y*-direction, consists of ten strips of a gold layer of 4.5 mm wide and 40 μg/cm² thick with 0.5 mm inter-strip spacing, which are formed by evaporating gold on a 2 μm thick Mylar film. The anode and the two cathodes are aligned parallel to one another with 3 mm spacing, as shown in Fig. 1. They are installed in a chamber filled with the isobutane (10 Torr). Each strip in the cathodes is electrically connected to the two neighboring strips through 2 ns delay lines. Signals from the strips are read out from both ends of the strip chain, and thus the time difference between the two pulses propagating through the different paths is used to identify the strip in which the particle is detected.

Figure 2 shows the position spectrum obtained with α particles from an ²⁴¹Am source. In this measurement a shielding plate with holes of 1 mm in diameter was placed in front of the detector. The α particles were collimated with these holes so that they were incident at the central part of each strip. The full

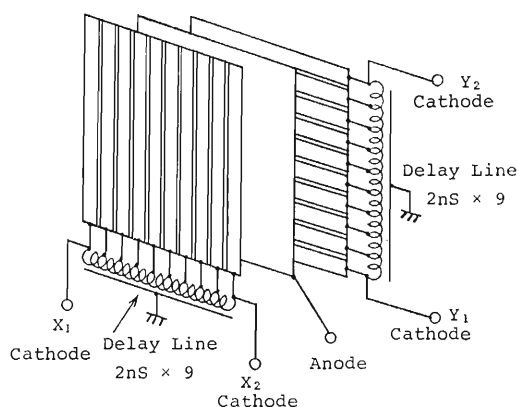


Fig. 1. Structure of the PPAC developed for the TOF measurement.

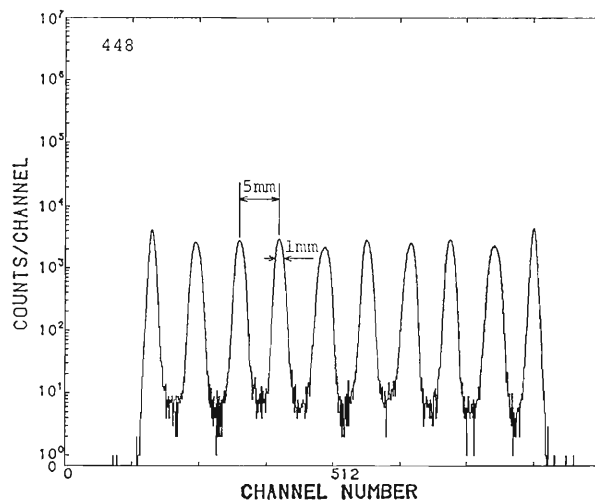


Fig. 2. Position spectrum obtained with α particles from an ²⁴¹Am source. The α particles are collimated so as to be incident at the central part of each cathode strip.

width at half maximum (FWHM) of about 1 mm was obtained, showing that the timing property was good enough for the identification of the strip.

A TOF measurement using two PPACs of this type was performed in December 1987 during an experiment⁴⁾ on the total reaction cross sections for unstable nuclei. Arrangement of the counters and a target is schematically shown in Fig. 3. Use of the

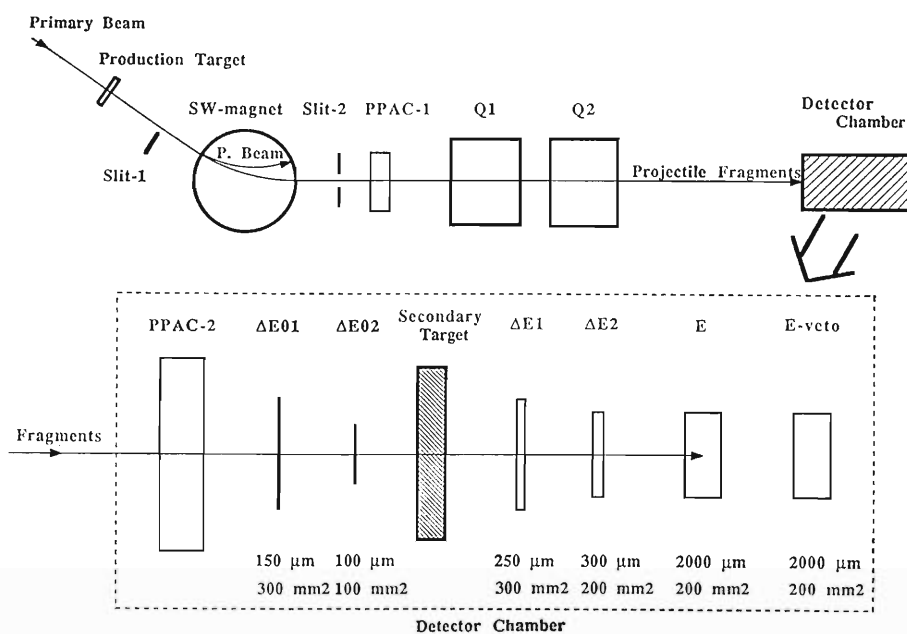


Fig. 3. Schematic view of the arrangement for the target, PPAC1, PPAC2, and solid state detectors (SSD) used in the experiment on total reaction cross section for unstable nuclei. Particles from the target are deflected with a dipole magnet, pass through a slit, and are focused at the focal point inside a detector chamber, in which PPAC2 and the six SSDs are installed.

position sensitive counters not only provided a means to monitor the beam profile, but also greatly reduced the uncertainty in flight time determination due to the position dependence of the propagation delay for the anode signal. In fact, without position detection the uncertainty would amount to ± 0.13 ns (taking the value⁵⁾ of 19 cm/ns for the signal propagating speed along the electrode), corresponding to ± 2.5 cm uncertainty in the propagation path (determined by the size of the anode). By simply detecting the position to ± 0.25 cm uncertainty (the cathode strip size), this ambiguity was reduced by a factor of 10.

A simplified block diagram of the electronics used for the TOF measurement is shown in Fig. 4. The trigger signal for the data acquisition was obtained from the 3-fold coincidence among the anode signal of PPAC2 and timing signals of two solid state detectors ($\Delta E1$ and $\Delta E2$). Pulse durations of the $\Delta E1$ and $\Delta E2$ signals fed to the coincidence circuit were chosen to be so long that the leading edge of the trigger signal was solely given by that of the PPAC2 signal. Cathode signals of PPAC1 and PPAC2 were fed into an 8-ch Time-to-Digital Converter (TDC), thus providing the position information in the way described above. The TOF measurement for detected particles was made by using a Time-to-Amplitude Converter (TAC). The start and stop signals were obtained from the anode signals of PPAC2 and PPAC1, respectively. TAC was care-

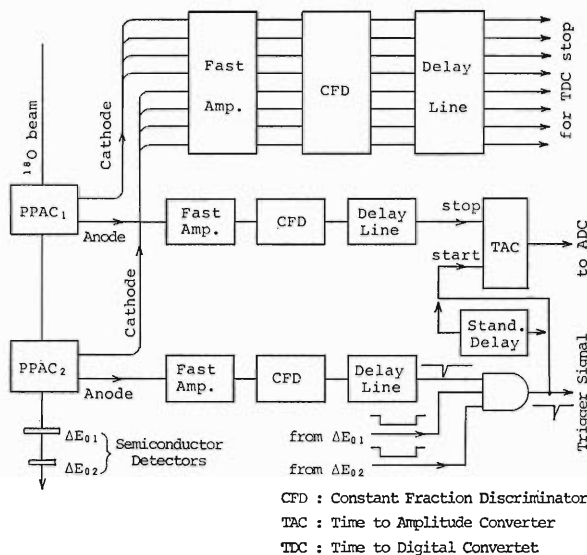


Fig. 4. Block diagram of the electronics used for the TOF measurement.

fully calibrated by using an ORTEC 462 Time Calibrator. Furthermore, in order to minimize the error originating from possible non-linearity of the TAC, a reference peak in the TAC spectrum was recorded by replacing the PPAC1 and PPAC2 signals with a standard pulser signal and by inserting a standard delay line whose delay time was accurately known (to ± 0.03 -ns accuracy) before the stop input.

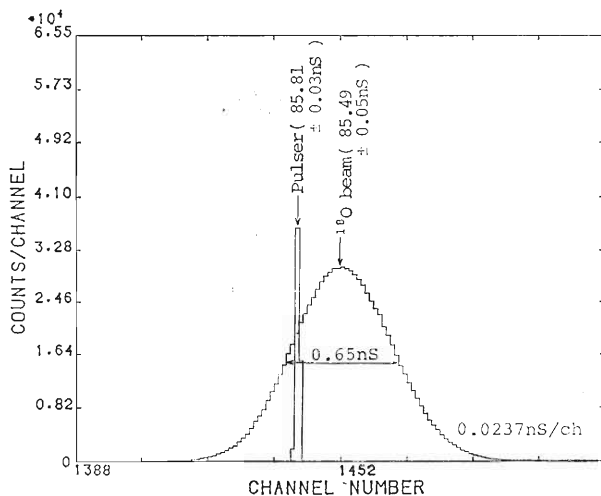


Fig. 5. Time spectrum obtained for the ^{18}O beam from RIKEN Ring Cyclotron. Reference peak recorded by replacing the PPAC signals for TAC inputs with a pulser signal and by inserting the standard delay line before the stop signal is also shown.

The absolute value for the TOF was obtained by comparing the observed peak for the particles with the reference peak.

Figure 5 shows the time spectrum obtained for the ^{18}O beam from RIKEN Ring Cyclotron. From the observed difference in peak position between the detected particles and the reference signals, the TOF

for the ^{18}O particles was deduced to be 85.56 ± 0.06 ns. This value includes a correction for the difference (measured to be 0.06 ns) between the signal propagation times in the anodes of the two PPACs. Combined with the measured length of 739.7 ± 0.2 cm for the flight path from PPAC1 to PPAC2, the kinetic energy of the ^{18}O particles

$$E/A = 41.32 \pm 0.08 \text{ MeV/u}$$

was obtained. Taking into account the energy loss in PPAC1 (0.08 MeV/u), the E/A value thus obtained indeed agrees very well with that calculated from the employed values of parameters for the beam acceleration. The excellent accuracy (0.2%) obtained in the energy determination demonstrates the usefulness of the position-sensitive PPAC in heavy-ion TOF measurements.

References

- 1) H. Kumagai, S. Sasagase, and T. Wada: *Reports I.P.C.R.*, **62**, 114 (1986) (in Japanese).
- 2) Y. Kanai, Y. Awaya, T. Kambara, M. Kase, H. Kumagai, T. Mizogawa, and K. Shima: *Nucl. Instrum. Methods A*, **262**, 128 (1987).
- 3) T. Tonuma, T. Matsuo, H. Kumagai, S.H. Be, and H. Tawara: p.84 in this report.
- 4) M. Fukuda, M. Ishihara, I. Tanihata, K. Asahi, T. Ichihara, T. Kubo, M. Adachi, M. Koguchi, and H. Kumagai: p.21 in this report.
- 5) H. Stelzer: *Nucl. Instrum. Methods*, **133**, 409 (1976).

III-5-16. Pileup Rejecter for a Position-Sensitive Parallel-Plate Avalanche Counter

H. Kumagai

We have constructed¹⁾ a parallel-plate avalanche counter (PPAC) capable of one-dimensional position detection. This counter has been extensively used in the studies of atomic physics.²⁾ The position analysis³⁾ was made by using an ORTEC Model 464 position-sensitive detector analyzer (PSDA). In these measurements, however, the obtained position spectra exhibited a broad peak presumably ascribed to an improper operation of analyzing circuits. Although the signals contributing to this spurious peak appeared with only small probabilities (1% or less in typical), it turned out to become a severe difficulty in certain experimental situations.

The position analysis in PSDA involves peak-sensitive detection of a pulse height, and thus the spurious peak above can arise from two sources: i) the pileup due to the overlap of two successive pulses and ii) the misassignment of the peak which occurs when the peak part of a pulse is gated off during processing time needed for a preceding pulse. The probability for these events to occur increases with increasing counting rate, and this spoils the advantage of the high-counting capability⁴⁾ of PPAC. To cope with this problem we developed a pileup rejecter. The essential function of this module is to block the signals which are preceded or followed by other pulses with time intervals of $3 \mu\text{s}^*$ or less.

The electric circuit for the pileup rejecter shown in Fig. 1 consists of three basic sections. The first section, shown in lower part of Fig. 1, includes six integrated circuits (IC_1 to IC_6), and monitors a time interval between two successive pulses. A gate pulse is generated when intervals of longer than $3 \mu\text{s}$ are detected. The minimum separable interval between two successive pulses is 20 ns. Actually this limitation introduces no difficulty in applying this circuit to experiments at RIKEN Ring Cyclotron or RILAC, since the beams from these accelerators are bunched with the intervals longer than 20 ns. The second section (shown in the middle part of Fig. 1) consisting of IC_9 to IC_{11} generates a gate pulse with $3 \mu\text{s}$ duration. This pulse opens a linear gate (IC_{13})

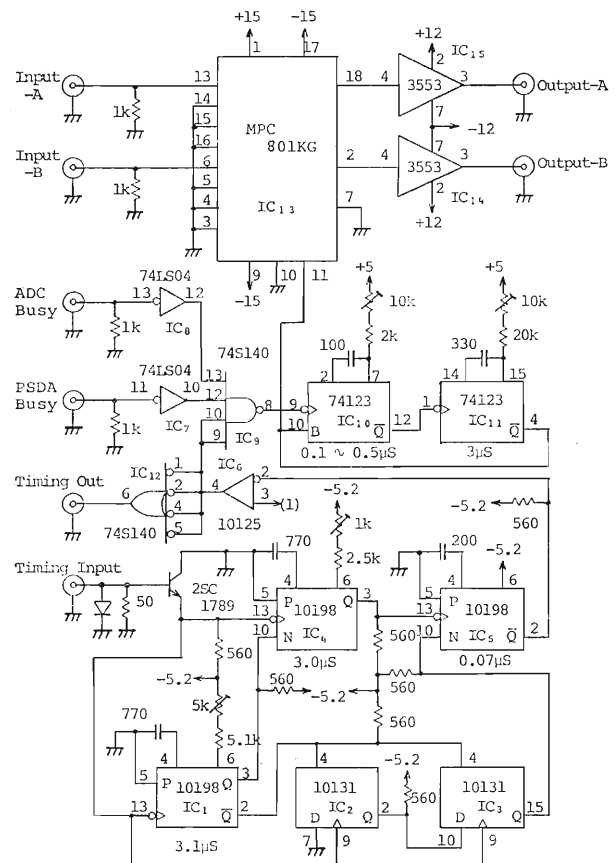


Fig. 1. Circuit diagram of the pileup rejecter.

of the last section shown in the upper part. The last section also includes an output driver stage with unit gain (IC_{14} and IC_{15}).

Figure 2 shows the block diagram of the electronics used for the measurement of position by using the pileup rejecter and PSDA. A timing signal for the pileup rejecter was extracted from the anode. In order to remove the events classified above as ii), the pileup rejecter was gated by BUSY signals from PSDA and from ADC.

In Fig. 3 a position spectrum obtained with pileup rejection is compared with that without rejection. Two collimated α sources (^{241}Am) with different intensities were placed near the right- and left-hand ends of the detector window. The total counting

* This value is chosen so as to make the pileup effect be negligible for the pulse shaping time of $0.5 \mu\text{s}$ as recommended in the PSDA instruction manual.

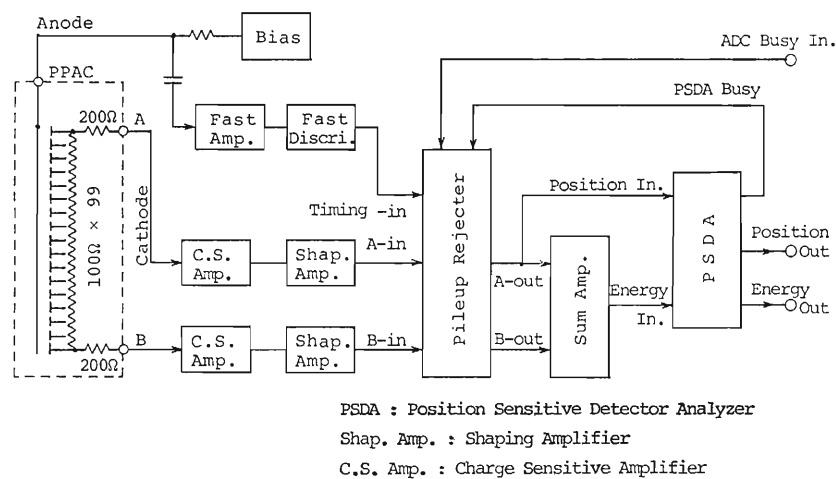


Fig. 2. Block diagram of the electronics used in the position measurement.

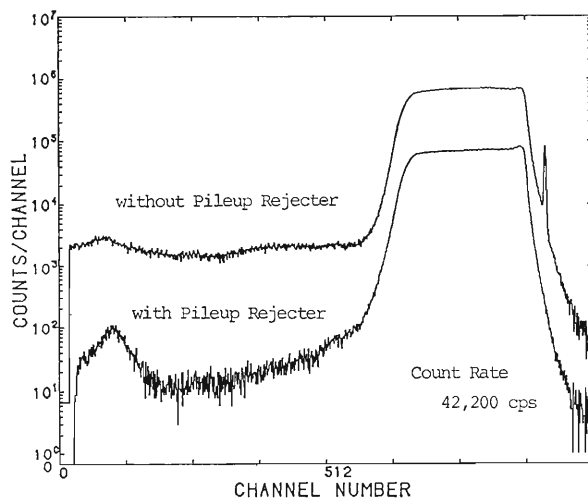


Fig. 3. Position spectra obtained with (lower curve) and without (upper curve) using a pileup rejecter.

rate was 42.2 kcount/s. A peak originating from a weaker source is identified much clearly in the pileup-rejected spectrum (lower) compared with the spectrum without pileup rejection, thus demonstrating the effectiveness of the present pileup rejecter for observation of weak contributions. A narrow peak on the right-hand side in the upper spectrum originates from the saturated signals due to pileup and is completely absent in a pileup rejected spectrum.

References

- 1) H. Kumagai, T. Kubo, M. Ishihara, M. Fuse, and E. Gotoh: *RIKEN Accel. Prog. Rep.*, **19**, 148 (1985).
- 2) Y. Awaya, M. Kase, T. Kambara, H. Kumagai, Y. Kanai, T. Mizogawa, K. Shima, and T. Chiba: *RIKEN Accel. Prog. Rep.*, **20**, 132 (1986).
- 3) H. Kumagai, S. H. Be, M. Ishihara, Y. Ikegami, M. Fuse, and E. Gotoh: *RIKEN Accel. Prog. Rep.*, **18**, 164 (1984).
- 4) H. Stelzer: *Nucl. Instrum. Methods*, **133**, 409 (1976).

IV. NUCLEAR DATA

1. Status Report of the Nuclear Data Group

A. Hashizume, Y. Tendow, Y. Ohkubo, K. Kitao, K. Sueki, and T. Nozaki

In this period efforts were continued on the two items. The first is related to the nuclear data activity concerning with the charged particle induced reactions. In this connection we cooperated with Nuclear Data Section in International Atomic Agency (IAEA) and the Consultants' Meeting and 'Data Requirements for Medical Radioisotope Production' was held at Kyoiku Kaikan in Tokyo from 20 to 24 in April 1987. The objectives of the meeting are: to make a survey of the medical radioisotopes in use and their production methods, to optimize the production methods, to list reliable and generally available computer codes suitable for the calculation of excitation functions of radioisotopes, to develop guidelines and priorities for the compilation of available excitation functions, to prepare an outline of the planned IAEA Handbook Computer File, to consider the standard monitor reactions, and to enquire into the availability of the appropriate target material.

The second is the mass-chain evaluation work of nuclear structure for the implement of Evaluated Nuclear Structure Data File (ENSDF) and compilation of reference files originated in Japan.

(1) The work for the compilation of new EXFOR (Exchange Format for Experimental Data) files of nuclear reaction cross sections has been continued. The reactions which we mainly interested in are those whose products are utilized for mediobiological applications. The cross sections of the reactions producing the following isotopes have been compiled in the EXFOR file. The isotopes are ^{11}C , ^{13}N , ^{15}O , ^{18}F , ^{28}Mg , ^{52}Fe , ^{67}Ga , ^{68}Ge , ^{68}Ga , ^{74}As , ^{77}Br , ^{82}Br , ^{77}Kr , ^{81}Rb , $^{82\text{m}}\text{Rb}$, ^{111}In , ^{129}Xe , ^{127}Xe , ^{123}I , ^{124}I , and ^{125}I nuclei.¹⁾ We have also compiled the reaction cross-sections for various combinations of which the above primary interested reactions were investigated.

The compilation of the integrated nuclear reaction cross-section data originated in Japan in the EXFOR files is also continued. The main sources of recent data are annual reports published by universities and institutes having accelerator facilities.

We are planning to publish a Data Book of excitation functions for the reaction which produce radioisotopes above mentioned. For this purpose, we are now collecting complete cross section data from EXFOR Files and/or from original reports. For the listing of excitation functions, the use of flexible graph

describing program completed last year is previewed.

As explained in the status report of the last year,²⁾ it is important to make clear the present status of the cross sections of standard monitor reactions. There are more than 17 reactions which have been used for this purpose. We collected the data on the $^{12}\text{C}(p, pn)^{11}\text{C}$, $^{27}\text{Al}(p, 3pn)^{24}\text{Na}$, $^{63}\text{Cu}(p, 2n)^{62}\text{Zn}$, and $^{65}\text{Cu}(p, n)^{65}\text{Zn}$ reactions.^{3,4)}

The computer code ALICE to calculate nuclear reaction cross sections in compound and precompound processes can be now used. This code will be served for the evaluation of experimental data. The parameter search of the code has been done for the reaction $^{127}\text{I}(p, 5n)^{123}\text{I}$ and other reactions.^{5,6)}

The center host computer M-780/10s has been replaced with an M-780/10 which economize about 10% for cpu time. We have also used a micro-computer PC9801.

(2) For the mass chain evaluation of nuclear structure data, the proofreading on the mass 120 had been made, compiled in the ENSDF (Evaluated Nuclear Structure Data File) of NDC at Brookhaven National Laboratory and published in the Nuclear Data Sheets from Academic Press. The evaluation work on the nuclear structure of the $A=177$ mass chain has been continued.

The recent reference files published periodically by Brookhaven National Laboratory should cover all references in the field of nuclear physics, but the reports in Japan were not completely filed. The references of annual reports and quarterly reports published in Japan were compiled and were sent to the BNL Data Center. In connection with this work, all reference files of Nuclear Data Sheets were received from Japan Atomic Energy Research Institute.

References

- 1) A. Hashizume, Y. Tendow, Y. Ohkubo, T. Nozaki, and K. Kitao: *RIKEN Accel. Prog. Rep.*, **20**, 152 (1986).
- 2) "Report on the 8th IAEA Consultants' Meeting of the Nuclear Reaction Data Centers," Oct. 1985, INDC (NDS)-178.
- 3) A. Hashizume, Y. Tendow, Y. Ohkubo, and K. Kitao: p. 186 in this report.
- 4) A. Hashizume, Y. Tendow, Y. Ohkubo, and K. Kitao: p. 190 in this report.
- 5) K. Kitao, A. Hashizume, Y. Tendow, Y. Ohkubo, and K. Sueki: p. 191 in this report.
- 6) K. Sueki and A. Hashizume: p. 195 in this report.

IV-2. Present Status of $^{63}\text{Cu}(p, n)^{63}\text{Zn}$ and $^{65}\text{Cu}(p, n)^{65}\text{Zn}$ Monitor Reactions

A. Hashizume, Y. Tendow, Y. Ohkubo, and K. Kitao

The $^{63}\text{Cu}(p, n)^{63}\text{Zn}$ and $^{65}\text{Cu}(p, n)^{65}\text{Zn}$ reactions have been frequently used for monitor reactions to obtain integral reaction cross sections in activation method. The threshold energies of these reactions are 4.21 and 2.17 MeV for $^{63}\text{Cu}(p, n)$ and $^{65}\text{Cu}(p, n)$ reactions, respectively. Since these values are lower than that of the $^{11}\text{C}(p, n)$ or $\text{Al}(p, x)^{24}\text{Na}$, a copper target can be used as the monitor in the low energy region. Copper with a natural isotopic abundance can be used as the target, because the half-life of

^{63}Zn is relatively short (38.1 m) and that of ^{65}Zn is long (244.1 d) and that their γ rays which are used as determinations of activities can be separated in a γ -ray spectrum. Many studies have been made on excitation functions comparing other kinds of reactions.

$^{63}\text{Cu}(p, n)^{63}\text{Zn}$ reaction: This reaction has been investigated since 1950.¹⁾ The range of incident proton energies used for bombardment lies from the threshold to 11.5 GeV; however, the data are scarce

Table 1. Reaction list of $^{63}\text{Cu}(p, n)^{63}\text{Zn}$.

First author	Place	Ref.	Target (mg/cm ²)*	Beam energy (MeV)	Detector	Errors and comment
S.N. Ghoshal	(Berkeley)	1)	—	3.2-26	GM	typical error: 9%, $T_{1/2}=38$ m, $I_{\beta^+}=93\%$, $I_{\text{ECC}}=7\%$.
J.-P. Blaser	(Zurich)	2)	8.3, 0.85	6.45 ± 0.03	GM	not reported, $T_{1/2}=38$ m
J.W. Meadows	(Massachusetts)	3)	0.01''	100, 70 ± 1	GM	relative to $^{27}\text{Al}(p, 3pn)^{24}\text{Na}$
H.A. Howe	(California)	4)	40	20 ± 0.40 10 ± 0.53 5 ± 0.94	NaI $\times 2$	3% (uncertainty of EC correction is not included), (det. eff.: $< 1\%$, stand. source: 2%), $T_{1/2}=38.3$ m $I_{\beta^+}=89.3\%$ 7% (the detail is not reported)
R.D. Albert	(California)	5)	1.5	9.85	n long counter	$< 10\%$, $T_{1/2}=38.3$ m, $I_{\beta^+}=93\%$
J. Wing	(Argonne)	6)	5	10.5-4.5 10 ± 0.15 5 ± 0.5	ppc, NaI $\times 2$	6% (T^{***} thick: 3%, $I_{\text{beam}}: < 3\%$, det. eff.: 3%), $I_{\beta^+}=89.8\%$
H. Taketani	(Rochester)	7)	69.09%: 4.26, 5.03 99%: 4.43	4.1-6.5 0.1	NaI $\times 2$	7% (A long counter was calibrated by MnSO_4)
L.F. Hansen	(California)	8)	1.5-8	5.2-11	n long counter	4.2% (stand. source: 2%, beam integrator: 1%)
K. Chackett	(Birmingham)	9)	0.001 in.	$9.3 \pm 0.3^{**}$	NaI $\times 2$	5.4% (the detail is not reported)
R.M. Humes	(Ohio)	10)	not given	6.75	ppc, NaI $\times 2$	5.4%, $T_{1/2}=38$ m, $I_{\beta^+}=90\%$
G.F. Dell	(Ohio)	11)	$2.5 \mu\text{m}$	6.75	NaI $\times 2$	13% (det. eff.: 5%)
J.E. Cline	(Idaho)	12)	50-1000	590	Ge(Li)	relative to $^{27}\text{Al}(p, 3pn)^{24}\text{Na}$
M. Hille	(München)	13)	$10 \mu\text{m}$	8.7-16 8.7 ± 0.2	Ge(Li)	6% (det. eff.: 3%, statistical: $< 1\%$, photo peak area: 3%, T thick.: 3% $I_{\text{beam}}: 2\%$, $T_{1/2}: 1-3\%$)
E.P. Steinberg	(Argonne)	14)	several	1.5-11.5 GeV	ppc, chem. sep.	5-10%, monitor $^{27}\text{Al}(p, 3pn)^{24}\text{Na}$
R. Colle	(BNL)	15)	5-15	2.86-25 0.10	Ge(Li)	7-12% ($I_{\text{beam}}: 1\%$, number of T atoms: 1-1.5%, T thick.: 1-1.5%, statistical: $< 3\%$ $T_{1/2}: 3\%$, det. eff.: 5-10%, $I_T: 1-4\%$)
Y. Yoshizawa	(Hiroshima)	16)	$10 \mu\text{m}$	25-50	GM	10% (detail is not reported) Isotope Separator on Line was used.

Table 1. (Continued)

First author	Place	Ref.	Target (mg/cm ²)*	Beam energy (MeV)	Detector	Errors and comment
A. Grutter	(Wurenlingen)	17)	0.1 0.05	16.1-69.8 70±0.53 16±1.6	Ge(Li)	3-5%, relative to ⁶⁵ Cu(p,n) ⁶⁵ Zn $T_{1/2}=38.47$ m, $I_{\gamma}(669.6)=8.40\%$
M. E. Sevier	(Melbourne)	18)	99.89%	4.21-4.86	BF ₃ in paraf.	11% (I_{beam} : 2%, number of T atoms: 2%, n detection: 10%)

* If unit is not given, the thickness is represented by mg/cm².

** Energy spread due to target is included.

*** T: target

Table 2. Reaction list of ⁶⁵Cu(p,n)⁶⁵Zn.

First author	Place	Ref.	Target (mg/cm ²)*	Beam energy (MeV)	Detector	Errors and comment
J.-P. Blaser	(Zurich)	2)	8.3, 0.85	6.5±0.25	GM	not reported, $T_{1/2}=250$ d
J. W. Meadows	(Harvard)	3)	0.01''	5-100 70±1	GM	relative to ²⁷ Al(p,3pn) ²⁴ Na
H. A. Howe	(California)	4)	uniform. <0.5%	10±0.53 5±0.94	NaI	3% (uncertainty of EC correction is not included), (det. eff.: <1%, stand. source: 2%), $T_{1/2}=38.3$ m, $I_{\beta^+}=0.893$
R. D. Albert	(California)	5)	1.5	9.85	n long counter	7% (the detail is not reported)
B. W. Shore	(Massachusetts)	19)	0.25 mil	7.5	NaI, CsI	3.7% (weighing: 1%, statistical: 1%, coin.: 3%, I_{beam} : 1%, beam integrator: <1%, $T_{1/2}$: 0.5%)
K. F. Chackett	(Birmingham)	9)	0.001''	9.3±0.3**	NaI, ppc chem. sep.	3.9% (calib. source: 2%, I_{beam} : 1%) $I_{\text{EC}}=98.3+0.1\%$
J. Wing	(Argonne)	6)	5	10.5±0.15 5±0.5	NaI×2	<10%, $T_{1/2}=245$ d, $I_{\gamma}(1120)=0.49$
R. M. Humes	(Ohio)	10)	—	6.75	NaI, ppc	6.5% (the detail is not reported)
G. F. Dell	(Ohio)	11)	2.5 μm	6.75	NaI, ppc	5% (the detail is not reported)
I. R. Williams	(Oakridge)	20)	0.005-0.02''	60±0.35 40±0.55	Ge(Li)	$T_{1/2}=248.5$ d, $I_{\gamma}(1114)=0.49$ 30%, I_{beam} : 1%
M. W. Greene	(BNL)	21)	7	16-32.8	Ge(Li)	$T_{1/2}=245$ d, $I_{\gamma}(1114)=0.45$ 10%, (T*** thick.: 1%, statistics: 3%, det. eff.: 3%)
R. Colle	(BNL)	15)	5-15	2.86-25 0.10	Ge(Li)	9% agreement to ¹² C(p,n) ¹¹ C 7-12% (I_{beam} : 1%, T: 1-1.5%, T thick.: 1-4%, statistics: <3%) Decay: 3%, det. eff.: 5-10%) $I_{\gamma}(1114)=0.506±0.004$
E. Gadioli	(Milano)	22)	30.91% 42.52 mg	10.2-44.3 18±0.25 10±0.35	Ge(Li)	<10%, $T_{1/2}=246$ d, $I_{\gamma}(1115)=0.49$
Z. E. Switkowski	(Melbourne)	23)	—	2.15-4.0	BF ₃ with paraf.	normalized to 73Co001 data
A. Grutter	(Wurenlingen)	17)	0.1, 0.05	16.1-70 70±0.53 16±1.6	Ge(Li)	3-5% (errors caused by decay data are not included), $I_{\gamma}(1115)=0.5075$
M. E. Sevier	(Melbourne)	18)	5 keV at 2.2 MeV	2.2-3.2	BF ₃ in paraf.	11% (det. for n: 10%, det. for γ : 9%) I_{beam} : 2%, T: 5%, I_{γ} : 2.5%)
P. Kopecky	(Rez, Czeck.)	24)	22.8	4.42-32.4 32.7±0.2 14.5±0.45 13.0±0.2 4.42±0.4	Ge(Li)	5-8% (beam integrator: 0.5%, T thick.: 1%, det. eff.: 4%, statistics: <2%, γ peak area=1.9-6.8%)

* If unit is not given, the thickness is represented by mg/cm².

** Energy spread due to target is included.

*** T: target

above 70 MeV. Authors, target thicknesses, incident beam energies, detectors employed, errors, and others are listed in Table 1. In 1950s, activities were determined by counting positions with GM counters based on an emitting probability of 89.3 or 90%, which is lower than the commonly adopted value of 93% by Auble.²⁵⁾ Therefore, a correction of about 3% should be made for the difference. The data of 14 experiments up to 70 MeV of incident energies are plotted in Fig. 1. In the figure the plots were not corrected to show the differences. The results of Meadows³⁾ deviate toward high values. The data of Albert⁵⁾ and Chackett⁹⁾ is also about 35% higher than Colle's¹⁵⁾ data at 9.3 MeV. The agreement between Colle's¹⁵⁾ and Grutter's¹⁷⁾ results, which were obtained from the most recent precise

measurements, is good. Yoshizawa's results obtained by using ISOL were interpreted tentatively as $^{63}\text{Cu}(p, n)$ and not $^{nat}\text{Cu}(p, n)$, because by this interpretation, the data are reasonably normalized to Medows' results at 25 MeV as explained by the authors. However the disagreement between Grutter's and Yoshizawa's results are apparent; a precise measurement above 22 MeV is needed.

$^{65}\text{Cu}(p, n)^{65}\text{Zn}$: All experiments done for this reaction are shown in Table 2, and 17 experimental results were plotted in Fig. 2. One observes the deviation toward high values for the results obtained during 1950 and the beginning of 1960 (Howe,⁴⁾ Chackett,⁹⁾ Humes,¹⁰⁾ Williams.²⁰⁾ The agreements among the data of Colle,¹⁵⁾ Kopecky²⁴⁾ and Grutter¹⁷⁾ are good, though there is a systematic trend that

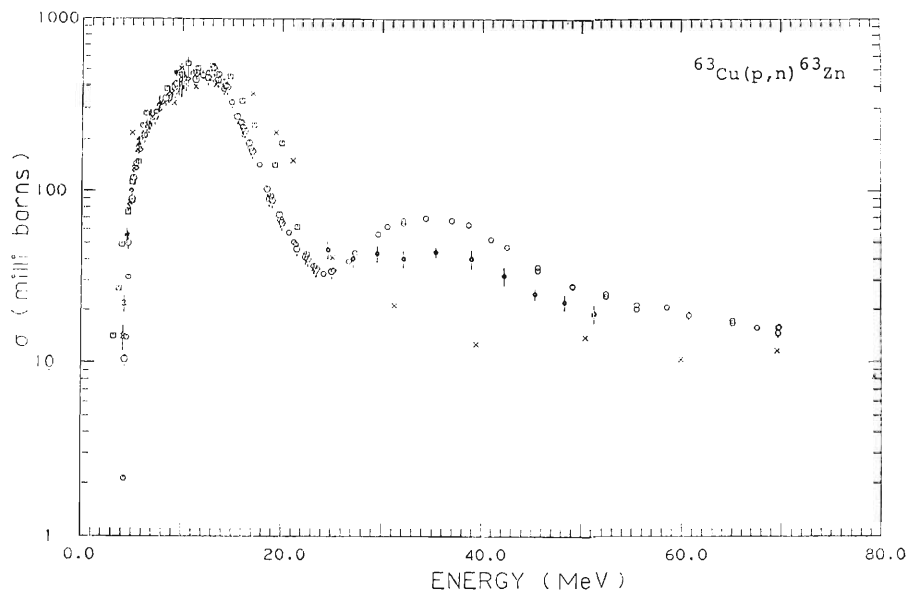


Fig. 1. Compiled cross sections for the $^{63}\text{Cu}(p, n)^{63}\text{Zn}$ reaction.

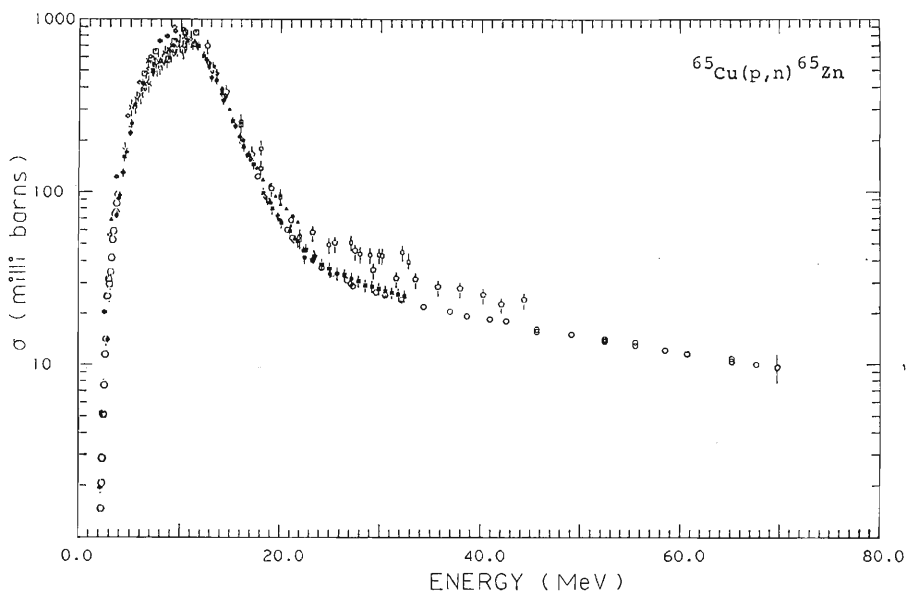


Fig. 2. Compiled cross sections for the $^{65}\text{Cu}(p, n)^{65}\text{Zn}$ reaction.

Grutter's results are smaller than Kopecky's. The data of Greene²¹⁾ and Gadioli²²⁾ are larger than those of Colle's or Grutter's results. Reinvestigation above 20 MeV are required.

References

- 1) S. N. Ghoshal: *Phys. Rev.*, **80**, 939 (1950).
- 2) J.-P. Blaser, F. Boehm, P. Marmier, and D. C. Peaslee: *Helv. Phys. Acta*, **24**, 3 (1951).
- 3) J. W. Meadows: *Phys. Rev.*, **91**, 885 (1953).
- 4) H. A. Howe: *Phys. Rev.*, **109**, 2083 (1958).
- 5) R. D. Albert and L. F. Hansen: *Phys. Rev. Lett.*, **6**, 13 (1961).
- 6) J. Wing and J. R. Huizenga: *Phys. Rev.*, **128**, 280 (1962).
- 7) H. Taketani and W. P. Alford: *Phys. Rev.*, **125**, 291 (1962).
- 8) L. F. Hansen and R. D. Albert: *Phys. Rev.*, **128**, 291 (1962).
- 9) K. F. Chackett, G. A. Chackett, and L. Ismail: *Proc. Phys. Soc.*, **80**, 738 (1962).
- 10) R. M. Humes, G. F. Deli, Jr., W. D. Ploughe, and H. J. Hansen: *Phys. Rev.*, **130**, 1522 (1963).
- 11) G. F. Dell, W. D. Ploughe, and H. J. Hausman: *Nucl. Phys.*, **64**, 513 (1965).
- 12) J. E. Cline and E. B. Nieschmidt: *Nucl. Phys.*, **A165**, 437 (1971).
- 13) M. Hille, P. Hille, M. Uhl, and W. Weisz: *Nucl. Phys.*, **A198**, 625 (1972).
- 14) E. P. Steinberg and L. Winsberg: *Phys. Rev. C*, **7**, 1410 (1973).
- 15) R. Colle, R. Kishore, and J. B. Cumming: *Phys. Rev. C*, **9**, 1819 (1974).
- 16) Y. Yoshizawa, H. Noma, T. Horiguchi, T. Katoh, S. Amemiya, M. Itoh, K. Hisatake, M. Sekikawa, and K. Chida: *Nucl. Instrum. Methods*, **134**, 93 (1976).
- 17) A. Grutter: *Nucl. Phys.*, **A383**, 98 (1982).
- 18) M. E. Seviour, L. W. Mitchell, M. R. Anderson, C. I. W. Tingwell, and D. G. Sargood: *Aust. J. Phys.*, **36**, 463 (1982).
- 19) B. W. Shore, N. S. Wall, and J. W. Irvine, Jr.: *Phys. Rev.*, **123**, 276 (1961).
- 20) I. R. Williams and C. B. Fulmer: *Phys. Rev.*, **162**, 1055 (1967).
- 21) M. W. Greene and E. Lebowitz: *Int. J. Appl. Radiat. Isotopes*, **23**, 342 (1972).
- 22) E. Gadioli, A. M. G. Strini, G. Lo Blanco, G. Strini, and G. Tagliaferri: *Nuovo Cimento A*, **22**, 547 (1974).
- 23) Z. E. Switkowski, J. C. P. Heggie, and F. M. Mann: *Aust. J. Phys.*, **31**, 253 (1978).
- 24) P. Kopecky: *Int. J. Appl. Radiat. Isot.*, **36**, 657 (1985).
- 25) R. L. Auble: *Nucl. Data Sheets*, **28**, 559 (1979).

IV-3. Present Status of a Monitor Reaction $\text{Al}(p, x)^{24}\text{Na}$

A. Hashizume, Y. Tendow, Y. Ohkubo, and K. Kitao

In obtaining integral cross-sections from experiments, there are many sources which cause errors. An important systematic error comes from the estimation of a beam flux. The beam flux is usually measured from the electric currents of an incident beam in a Faraday cup. However, without sufficient precaution, the measurement would be accompanied by an unexpected error. Part of the charge collected in the Faraday cup would be changed because secondary electrons, ions and electrons produced by the secondary electrons and/or by ionization of gas remaining in a vacuum would escape from the Faraday cup.

Instead of the absolute measurements of beam energies and currents, the cross sections are obtainable relatively to known cross sections of monitor reactions. The use of a monitor reactions also has an advantage when a Faraday cup cannot be used in such a case as for internal beams of high energy accelerators.

For the production of radioisotopes protons are most extensively used, and the monitor reaction, $^{12}\text{C}(p, pn)^{11}\text{C}$, has been studied since 1950 to increase the accuracy of the cross sections in a wide range of incident proton energies.¹⁾ This reaction has the threshold of 18.5 MeV.

Because of its relatively high threshold, other reactions are often used as monitor reactions for the reactions of which products are useful for medical applications; another reason is that aluminum or copper is a very accessible material for the target and often used as energy degrader in the stack foil method. The monitor reactions other than $^{12}\text{C}(p, pn)^{11}\text{C}$ include $\text{Al}(p, x)^{24}\text{Na}$, $^{63}\text{Cu}(p, n)^{63}\text{Zn}$, $^{65}\text{Cu}(p, n)^{65}\text{Zn}$, and about 13 kinds of other reactions.²⁾ However, since no evaluated values of cross sections are available for these reactions, it is needed to compile and evaluate these values of cross sections. As the first step we compiled the integral cross sections measured by the $^{27}\text{Al}(p, x)^{24}\text{Na}$ reaction.

The cross sections available for the $^{27}\text{Al}(p, x)^{24}\text{Na}$ reactions are plotted in Fig. 1, which shows large discrepancies from the threshold to about 70 MeV among different experiments. The disagreement still exists over the cited errors even at 80 MeV. One reason for these discrepancies could be attributed to the estimation of energies which were degraded by targets and absorbers from incident values. The

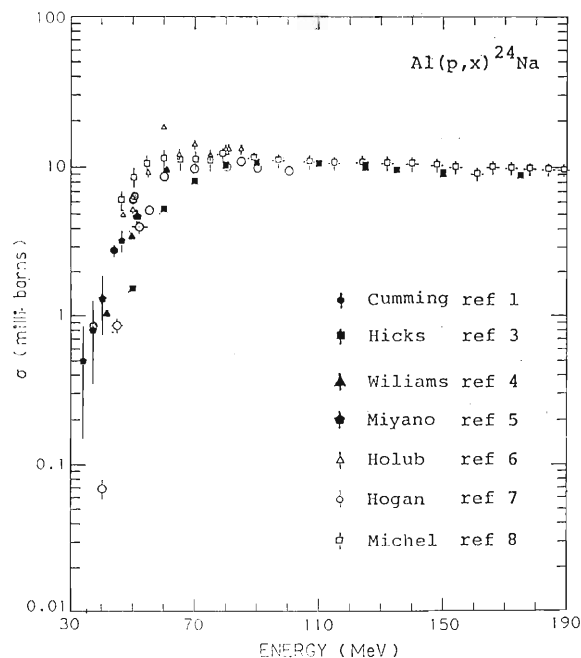


Fig. 1. Cross sections for the $\text{Al}(p, x)^{24}\text{Na}$ reaction as a function of energy.

recent values obtained by Michel *et al.*⁸⁾ are determined relatively to the cross sections of $^{27}\text{Al}(p, x)^{22}\text{Na}$. Above 100 MeV, the agreement between Michel's and Hicks' results is good, though Hicks' values³⁾ are systematically smaller than Michel's values. The results of Holub show a pronounced sharp peak at 65 MeV.⁶⁾ It is not clear whether or not the energy resolution in the experiments of Holub is better than the other experiments, because neither the beam condition nor target thickness is explicitly given.

References

- 1) J. B. Cumming: *Nucl. Phys.*, **49**, 417 (1963).
- 2) A. Hashizume: INDC (NDS)-196/GZ, 37 (1988).
- 3) H. G. Hicks, P. C. Stevenson, and W. E. Nervik: *Phys. Rev.*, **102**, 1390 (1956).
- 4) I. R. Williams and C. B. Fulmer: *Phys. Rev.*, **162**, 1055 (1967).
- 5) K. Miyano: *J. Phys. Soc. Jpn.*, **34**, 853 (1973).
- 6) R. Holub, M. Fowler, L. Yaffe, and A. Zeller: *Nucl. Phys.*, **A288**, 291 (1977).
- 7) J. J. Hogan and E. Gadioli: *Nuovo Cimento A*, **45**, 341 (1978).
- 8) R. Michel, F. Peiffer, and R. Stuck: *Nucl. Phys.*, **A441**, 617 (1985).

IV-4. On the Cross Sections for ^{77}Br Production Reactions

K. Kitao, A. Hashizume, Y. Tendow, Y. Ohkubo, and K. Sueki

One of the roles of the evaluation of nuclear reaction data is to provide the best reference for the bench mark test of computer codes on the calculation of excitation functions and to provide the basic data for estimating the optimum irradiation conditions for the cyclotron production of radionuclides. From this point of view, the status of the experimental excitation functions for the production reactions of ^{77}Br ($T_{1/2} = 56.0$ h) were discussed.

Radioactive isotopes of bromine have been considered suitable to prepare labelled radiopharmaceuticals. At present some comprehensive reviews exist on productions and applications of the isotopes. These are:

- 1) G. Stocklin: *Int. J. Appl. Radiat. Isot.*, **28**, 131-147 (1977)
- 2) S. M. Qaim and G. Stocklin: *Radiochim. Acta*, **34**, 25-40 (1983)
- 3) M. J. Welch and K. D. McElvancy: *Radiochim. Acta*, **34**, 41-46 (1986)
- 4) S. M. Qaim: *Appl. Radiat. Isot. (Int. J. Appl. Radiat. Isot. part A)*, **37**, 803-810 (1986)
- 5) B. Maziere and C. Loc'h: *Appl. Radiat. Isot. (Int. J. Appl. Radiat. Isot. part A)*, **37**, 703-713 (1986).

However, radiobromine compounds have been rarely used in hospitals and clinics in Japan.

Our first object is to prepare a complete data file for reaction cross sections concerning certain radionuclide productions. The second object is to evaluate these cross sections so as to facilitate the production maker to use them for the estimation of the yield of radionuclides concern. It is also important to find out a reaction type and an energy range to minimize the impurities. ^{77}Br is one of these radionuclides selected, and we reexamined the present status of data and compared with the results calculated by a code ALICE.

Bromine-77 can be produced directly by charged-particle reactions with arsenic, selenium or bromine, and also be obtained indirectly as the decay product of ^{77}Kr ($T_{1/2} = 77.4$ min) or the decay chain of ^{77}Rb ($T_{1/2} = 3.7$ min) \rightarrow ^{77}Kr . The spallation reactions with high-energy protons on molybdenum are also used to produce ^{77}Br . Since a method of production of carrier-free ^{77}Br by bombarding α

particles on arsenic was developed by Helus,¹⁾ various types of reactions and the target assemblies have been proposed to produce ^{77}Br and ^{77}Kr . Thick target yields and cross sections for the production of these nuclides were measured under various bombarding conditions and for target systems.²⁻²³⁾ See Table 1.

(1) Excitation functions

The $^{75}\text{As}(\alpha, 2n)^{77}\text{Br}$ reaction (^{75}As has 100% natural abundance) is most widely used for the production of ^{77}Br with bombarding energies of 28-30 MeV. The excitation functions were given by Waters *et al.*,³⁾ Nozaki *et al.*,¹³⁾ Alfassi *et al.*,¹⁷⁾ and Qaim *et al.*²⁸⁾ Figure 1 shows these data to be in good agreement in the energy range of 25 to 28 MeV, except for those Nozaki *et al.*¹³⁾ But these data would become more reliable if Alfassi had measured cross sections at energy of 20 MeV, or if Waters or Qaim had measured with energies higher than 30 MeV. Qaim *et al.*²⁸⁾ pointed out the discrepancy to be ascribed partially to the use of different target materials. In Fig. 1, theoretical cross sections calculated by using the code ALICE/Livermore/82 are also included. Qaim *et al.*²⁸⁾ have also measured cross sections of the reaction $^{75}\text{As}(\alpha, 2n)^{77\text{m}}\text{Br}$ and cross section ratios for the isomeric pair.

The excitation function for the reaction $^{79}\text{Br}(p, p2n)^{77}\text{Br}$ are difficult to measure, because, as shown in Fig. 2, the ^{79}Br nuclide is also produced from the decay of ^{77}Kr by the reaction $^{79}\text{Br}(p, 3n)$ occurring simultaneously in the bombarding process. Moreover, in proton energies higher than the threshold of the $^{81}\text{Br}(p, p4n)$ reaction, when natural bromine is used as target materials, the ^{77}Br nuclide is also produced from this reaction. For the reaction $^{81}\text{Br}(p, p4n)^{77}\text{Br}$, there is a similar situation. These data were measured by Dikšić *et al.*¹¹⁾ using the isotopically 95.06% enriched ^{79}Br and 97.81% for ^{81}Br . Dikšić *et al.*¹¹⁾ also compared cross sections for the (p, xn) and (p, pxn) reactions on ^{79}Br and ^{81}Br with some theoretical predictions by intranuclear cascade and two pre-equilibrium models followed by equilibrium evaporation. He concluded, however, that none of the three computer codes was able to reproduce all excitation functions satisfactorily.

The excitation function for the $^{79}\text{Br}(p, 3n)^{77}\text{Kr}$

Table 1. Production reactions and measured quantities.

Reaction	Measured quantities	
	Thick target yield	Excitation function
$^{75}\text{As}(\alpha, 2n)^{77}\text{Br}$	Helus ¹⁾ Nunn <i>et al.</i> ⁵⁾ Nozaki <i>et al.</i> ¹⁸⁾ Alfassi <i>et al.</i> ¹⁷⁾ Blessing <i>et al.</i> ¹⁸⁾ Dmitriev <i>et al.</i> ¹⁹⁾ Qaim <i>et al.</i> ²³⁾	Waters <i>et al.</i> ⁸⁾ Nozaki <i>et al.</i> ¹⁸⁾ Qaim <i>et al.</i> ²³⁾
$^{75}\text{As}(\alpha, 2n)^{77\text{m}}\text{Br}$	Qaim <i>et al.</i> ²³⁾	Qaim <i>et al.</i> ²³⁾
$^{77}\text{Se}(p, n)^{77}\text{Br}$	Norton <i>et al.</i> ⁶⁾ * Janssen <i>et al.</i> ¹⁵⁾ *	Janssen <i>et al.</i> ¹⁵⁾ *
$^{78}\text{Se}(p, 2n)^{77}\text{Br}$	Madhusudhan <i>et al.</i> ¹⁴⁾ * Janssen <i>et al.</i> ¹⁵⁾ *	Janssen <i>et al.</i> ¹⁵⁾ *
$^{79}\text{Br}(p, p2n)^{77}\text{Br}$	Dikšić <i>et al.</i> ⁶⁾ *	Dikšić <i>et al.</i> ⁶⁾ *
$^{81}\text{Br}(p, p4n)^{77}\text{Br}$	Dikšić <i>et al.</i> ⁶⁾ *	Dikšić <i>et al.</i> ⁶⁾ *
$\text{Br}(d, p\alpha n)^{77}\text{Br}$	Qaim <i>et al.</i> ⁷⁾	Qaim <i>et al.</i> ⁷⁾
$^{76}\text{Se}(^3\text{He}, pn)^{77}\text{Br}$	He Youfeng <i>et al.</i> ²⁰⁾ *	He Youfeng <i>et al.</i> ²⁰⁾ *
$^{77}\text{Se}(^3\text{He}, p2n)^{77}\text{Br}$	He Youfeng <i>et al.</i> ²⁰⁾	He Youfeng <i>et al.</i> ²⁰⁾ *
$\text{Se}(p, \alpha n)^{77}\text{Br}$	Dmitriev <i>et al.</i> ¹⁹⁾ Nozaki <i>et al.</i> ¹⁸⁾	Nozaki <i>et al.</i> ¹⁸⁾
$\text{Se}(d, \alpha n)^{77}\text{Br}$	Dmitriev <i>et al.</i> ¹⁹⁾	
$\text{Se}(\alpha, \alpha n)^{77}\text{Br}$	Dmitriev <i>et al.</i> ¹⁹⁾	
$\text{Mo}(p, \text{spallation})^{77}\text{Br}$	Grant <i>et al.</i> ¹⁶⁾	
$^{79}\text{Br}(p, 3n)^{77}\text{Kr}$	Dikšić <i>et al.</i> ⁶⁾ * Nozaki <i>et al.</i> ¹⁸⁾ de Jong <i>et al.</i> ⁹⁾ de Jong <i>et al.</i> ¹⁰⁾ Weinreich <i>et al.</i> ²¹⁾	Lundqvist <i>et al.</i> ¹²⁾ Nozaki <i>et al.</i> ¹⁸⁾ de Jong <i>et al.</i> ⁹⁾ Dikšić <i>et al.</i> ¹¹⁾ * Weinreich <i>et al.</i> ²¹⁾
$^{81}\text{Br}(p, 5n)^{77}\text{Kr}$	Lundqvist <i>et al.</i> ¹²⁾ Nozaki <i>et al.</i> ¹⁸⁾ de Jong <i>et al.</i> ⁹⁾	Lundqvist <i>et al.</i> ¹²⁾ Nozaki <i>et al.</i> ¹⁸⁾ de Jong <i>et al.</i> ⁹⁾ Dikšić <i>et al.</i> ⁶⁾ *
$\text{Br}(d, \alpha n)^{77}\text{Kr}$	Qaim <i>et al.</i> ⁷⁾	Qaim <i>et al.</i> ⁷⁾
$^{76}\text{Se}(^3\text{He}, 2n)^{77}\text{Kr}$	de Jong <i>et al.</i> ¹⁰⁾ He Youfeng <i>et al.</i> ²⁰⁾ *	He Youfeng <i>et al.</i> ²⁰⁾ *
$^{77}\text{Se}(^3\text{He}, 3n)^{77}\text{Kr}$	de Jong <i>et al.</i> ¹⁰⁾ He Youfeng <i>et al.</i> ²⁰⁾ *	He Youfeng <i>et al.</i> ²⁰⁾ *
$^{71}\text{Se}(^3\text{He}, 4n)^{77}\text{Kr}$	de Jong <i>et al.</i> ¹⁰⁾	
$\text{Se}(^3\text{He}, \alpha n)^{77}\text{Kr}$	He Youfeng <i>et al.</i> ²⁰⁾	
$^{76}\text{Se}(\alpha, 3n)^{77}\text{Kr}$	Blue <i>et al.</i> ²⁾ †	
$\text{Br}(\alpha, \alpha n)^{77}\text{Rb}$	Helus <i>et al.</i> ⁴⁾ †	

* enriched targets were used.

† no data given by authors.

reaction with the ^{79}Br enriched target was obtained only Dikšić.¹¹⁾ If bombarding energies are below the threshold of the $^{81}\text{Br}(p, 5n)^{77}\text{Kr}$ reaction, the excitation function on natural bromine can be used for the evaluation. Comparisons of experimental

excitation functions of this reaction are shown in Figs. 3 and 4: there are considerable disagreement between these data. In all these experiments, sodium bromide (NaBr) was used as target materials.

$^{77}\text{Se}(p, n)^{77}\text{Br}$ and $^{78}\text{Se}(p, 2n)^{77}\text{Br}$ reactions are

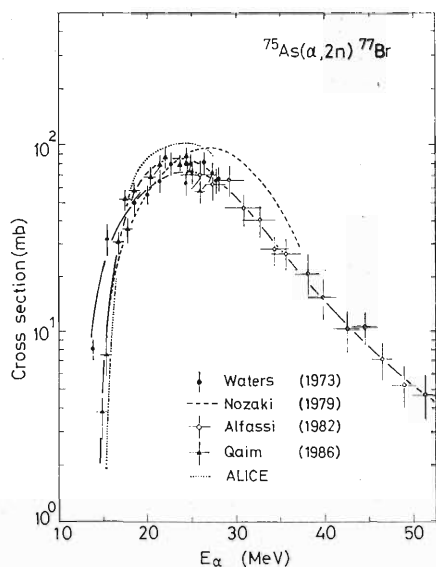


Fig. 1. A comparison of excitation functions for the reaction $^{75}\text{As}(\alpha, 2n)^{77}\text{Br}$. Included is that calculated by code ALICE/Livermore/82.

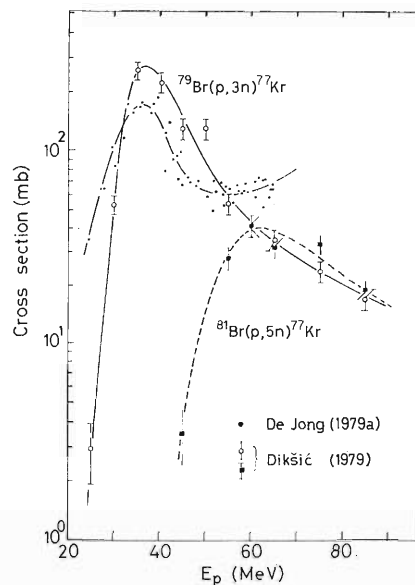


Fig. 3. A comparison of excitation functions for the $^{79}\text{Br}(p, 3n)^{77}\text{Kr}$ and the $^{81}\text{Br}(p, 5n)^{77}\text{Kr}$ reactions.

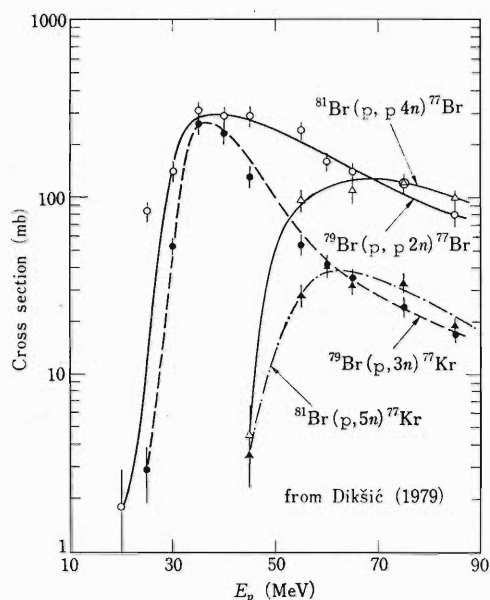


Fig. 2. Excitation functions for $^{76,81}\text{Br} + \text{proton}$ reaction.

also used practically to produce ^{77}Br . Selenium consists of many isotopes. The enriched target prevents cross contamination with other isotopes. Only one data has been reported by Janssen *et al.*¹⁵⁾

In the $\text{Se} + ^3\text{He}$ reactions enriched targets should also be used. Excitation functions for these reactions were given by He Youfeng *et al.*²⁰⁾ on enriched targets. Although the values of cross sections for $\text{Se}(^3\text{He}, xn)^{77}\text{Kr}$ reactions are comparable to those of other ^{77}Kr production reactions, de Jong *et al.*¹⁰⁾ reported that thick target yields were lower than

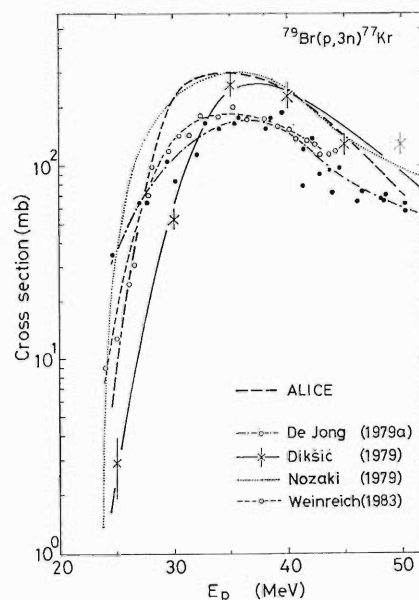


Fig. 4. A comparison of excitation functions for the reaction $^{79}\text{Br}(p, 3n)^{77}\text{Kr}$. Including is that calculated by code ALICE/Livermore/82.

other reactions as figures of one to two order. This may be due to the kind of target materials. This suggests that the kind of target materials and bombarding conditions strongly affect measurements of the cross section.

The production of ^{77}Br by the spallation process allows the preparation of a batch with larger activities. The cross sections for the spallation of molybdenum with 800-MeV proton were measured.

Table 2. Target materials used in some references.

Authors	Materials
Waters et al. ³⁾	As deposited by electric discharge on Al foil in arsenic gas.
Nozaki et al. ¹³⁾	Stacked Mg ₂ As ₂ O ₇ foils.
Alfassi et al. ¹⁷⁾	Metallic As suspended in a self-supporting polystyrene film.
Qaim et al. ²³⁾	Electrolytic deposition of arsenic on Cu-baking.

(2) Decay data

There were confusing differences among decay data used in activity measurements. The half-life of 56 h for the nuclide ⁷⁷Br has been widely used, while Blue and Benjamin²⁾ used 59 h and Blessing et al.¹⁸⁾ used 57 h. As for the γ -rays abundance of ⁷⁷Br, Dikšić et al.¹¹⁾ used 26.0% for the 239-keV γ rays, but other authors used 22.8 or 23.1 or 23.8%. Weinreich and Knieper²¹⁾ used 82.2% for the 130-keV γ ray and 39.3% for 147-keV γ ray of the nuclide ⁷⁷Kr, but all other authors used values of 87.3% and 40.9%, respectively.

(3) Conclusions

At present, the excitation functions for the production of ⁷⁷Br or ⁷⁷Kr are difficult to evaluate, because published excitation functions depend upon conditions of experiments. Because of this reason, discrepancies still exist among these values in some type of reactions. As for the decay parameters of the nuclides ⁷⁷Br or ⁷⁷Kr and those of monitor reaction products, different values are used in activity measurements in some cases. More precise measurements are necessary for those reactions.

References

- 1) F. Helus: *Radiochem. Radioanal. Lett.*, **3**, 45 (1970).
- 2) J. W. Blue and P. P. Benjamin: *J. Nucl. Med.*, **12**, 417 (1971).
- 3) S. L. Waters, A. D. Nunn, and M. L. Thakur: *J. Inorg. Nucl. Chem.*, **35**, 3413 (1973).
- 4) F. Helus, W. Maier-Borst, R. M. Lambrecht, and A. P. Wolf: Proc. 7th Int. Conf. Cyclotrons and Their Applications, *Experimentia, Suppl.*, **24**, 474 (1975).
- 5) A. D. Nunn and S. L. Waters: *Int. J. Appl. Radiat. Isot.*, **26**, 731 (1975).
- 6) M. Dikšić, J.-L. Galinier, H. Marshall, and L. Yaffe: *Int. J. Appl. Radiat. Isot.*, **28**, 885 (1977).
- 7) S. M. Qaim, G. Stocklin, and R. Weinreich: *Int. J. Appl. Radiat. Isot.*, **28**, 947 (1977).
- 8) E. F. Norton, K. Kondo, K. Karlstrom, R. M. Lambrecht, A. P. Wolf, and S. Treves: *J. Radioanal. Chem.*, **44**, 207 (1978).
- 9) D. de Jong, G. A. Brinkman, and L. Lindner: *Int. J. Appl. Radiat. Isot.*, **30**, 188 (1979).
- 10) D. de Jong, H. Kooiman, and J. Th. Veenboer: *Int. J. Appl. Radiat. Isot.*, **30**, 786 (1979).
- 11) M. Dikšić, J.-L. Galinier, H. Marshall, and L. Yaffe: *Phys. Rev. C*, **19**, 1753 (1979).
- 12) H. Lundqvist, P. Malmberg, B. Langstrom, and S. N. Chiengami: *Int. J. Appl. Radiat. Isot.*, **30**, 39 (1979).
- 13) T. Nozaki, M. Iwamoto, and Y. Itoh: *Int. J. Appl. Radiat. Isot.*, **30**, 79 (1979).
- 14) C. P. Madhusudhan, S. Treves, A. P. Wolf, and R. M. Lambrecht: *J. Radioanal. Chem.*, **53**, 299 (1979).
- 15) A. G. M. Janssen, R. L. P. van den Bosch, J. J. M. de Goeij, and H. M. J. Theelen: *Int. J. Appl. Radiat. Isot.*, **31**, 405 (1980).
- 16) P. M. Grant, R. E. Whipple, J. W. Barnes, G. E. Bentley, P. M. Wanek, and H. A. O'Brien, Jr.: *J. Inorg. Nucl. Chem.*, **43**, 2217 (1981).
- 17) Z. B. Alfassi and R. Weinreich: *Radiochim. Acta*, **30**, 67 (1982).
- 18) G. Blessing, R. Weinreich, S. M. Qaim, and G. Stocklin: *Int. J. Appl. Radiat. Isot.*, **33**, 333 (1982).
- 19) P. P. Dmitriev, M. V. Panarin, and Z. P. Dmitrieva: *At. Energ.*, **52**, 72 (1982).
- 20) He Youfeng, S. M. Qaim, and G. Stocklin: *Int. J. Appl. Radiat. Isot.*, **33**, 13 (1982).
- 21) R. Weinreich and J. Knieper: *Int. J. Appl. Radiat. Isot.*, **34**, 1335 (1983).
- 22) G. Blessing and S. M. Qaim: *Int. J. Appl. Radiat. Isot.*, **35**, 917 (1984).
- 23) S. M. Qaim, G. Blessing, and Ollig: *Radiochim. Acta*, **39**, 57 (1986).

IV-5. On the Cross Sections for $^{127}\text{I}(p, 5n)^{123}\text{Xe}$

K. Sueki and A. Hashizume

In the production of radioactive nuclides for medical use, it is necessary to select the type of reaction and to find the best condition of bombardment such as beam energy, target material, and its thickness. This is because the ratio of the activity of the interested radioactive nuclide to those of impurities is related to this bombarding conditions. If the excitation functions of these reactions were calculated, it would be of a great help to find the best condition of bombardment, in particular when all the excitation functions related to impurities were not studied experimentally. And this is often the case.

Many excitation functions have been studied experimentally and theoretically so far. However, the parameters of a computer codes have not yet been examined systematically to fit the excitation functions of the reactions which related to a wide range of elements and/or masses.

For the production of radioisotopes by using a cyclotron, the nuclear reactions of type (a, xn) are frequently employed, where a is an incident particle and x is the number of neutrons emitted. In this reaction, the particles are considered to be emitted by evaporation after passing through a compound and pre-compound process. The cross sections of this reaction type can be calculated by codes such as ALICE, STAPRE. We used the ALICE¹⁾ to calculate the cross sections for the $^{127}\text{I}(p, 5n)^{123}\text{Xe}$ reaction and compared with experimental excitation functions. In the code ALICE, the binding energies of related nucleus are calculated by the mass formula of Myers and Swiatecki.²⁾ The optical potential is calculated by giving certain fixed optical potential parameters.³⁾ Evaporation of particles and fission from compound nuclei are calculated by a statistical model. In this processes pre-equilibrium processes are treated by a hybrid model⁴⁾ where the intermediate state densities are calculated by exciton model and their average intermediate state lifetime

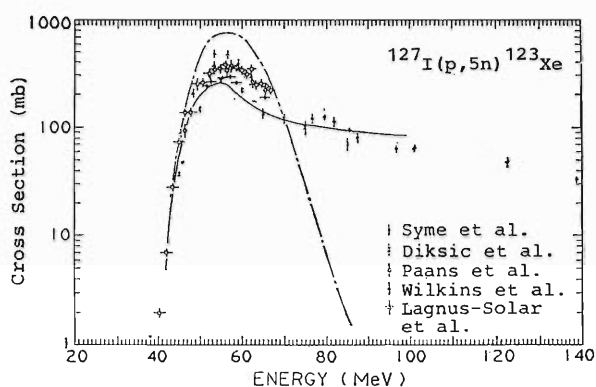


Fig. 1. Calculated (ALICE) and experimental excitation functions for proton induced reaction on ^{127}I target. The dot-dashed line represents compound-nucleus formation theory, and the dashed and solid lines the hybrid model.

was combined to the nucleon-nucleon scattering data. The level density parameter, the upper limit of angular momentum concerned, initial exciton number and some parameters of optical potential were varied to find optimum fit for the experimental excitation function. The results are shown in Fig. 1.

Although many parameters have been adjusted systematically, the absolute experimental values of cross sections in the high incident bombarding energy region, which is related mainly to the precompound process, could not be fitted very satisfactory in our first survey. Further parameter search and examination of the code related to this processes are necessary.

References

- 1) M. Blann: COO-3493-29.
- 2) W.D. Myers and W.J. Swiatecki: *Nucl. Phys.*, **81**, 1 (1966).
- 3) P. E. Hodgson: *Ann. Rev. Nucl. Sci.*, **17**, 1 (1967).
- 4) M. Blann: *Phys. Rev. Lett.*, **27**, 337 (1971); M. Blann and A. Mignerey: *Nucl. Phys.*, **A186**, 245 (1972); M. Blann: *Nucl. Phys.*, **A213**, 570 (1973).

V. DEVELOPMENT OF ACCELERATOR FACILITIES

1. Status of RIKEN Ring Cyclotron Project in 1987

H. Kamitsubo

After successful extraction of an Ar beam from RIKEN Ring Cyclotron (RRC) on December 16, 1986, it was officially permitted on January 13, 1987, to operate the machine routinely and use it for experiments. The inauguration ceremony was held on January 23, and then RRC was shut down for two months for regular inspection. Routine operation of the facility started in April, and after acceleration test and beam study of two months, preliminary experiments have been carried out. Species and energies per nucleon of ions accelerated in this period are: $^{40}\text{Ar}^{12+}$ (21 MeV/u), $^{40}\text{Ar}^{13+}$ (26 MeV/u), $^{14,15}\text{N}^{6+}$ (33.7 MeV/u), $^{65}\text{Cu}^{18+}$ (16.7 MeV/u), $^{18}\text{O}^{7+}$ (41.5 MeV/u), and $^{12}\text{C}^{5+}$ (42 MeV/u). The beam intensity ranges from several hundreds nA down to 1 nA. The energy resolution and beam bunch width were measured as $\Delta E/E < 0.16\%$ and $\tau < 400$ ps in the experimental hall E1.

At the moment only two beam lines are temporarily installed for the experiments in the experimental hall E1 (Fig. 1) where all the preliminary experiments were performed. They were classified into three groups, the first one is projectile fragmentation in the reactions $^{15}\text{N} + ^9\text{Be}$, $^{40}\text{Ar} + ^{27}\text{Al}$, and $^{65}\text{Cu} + ^9\text{Be}$, the second is fusion-like reaction $^{40}\text{Ar} + ^{181}\text{Ta}$, and the last is atomic physics measuring X rays from the $^{40}\text{Ar} + ^9\text{Be}$ reaction. In the first experiments, projectile fragments have successfully been identified from lithium to nuclei neighbouring the projectile by applying a TOF, a charge analyzing magnet, and ΔE - E counter telescopes. In the second one, energetic γ rays up to 100 MeV were observed with BaF_2 detectors. The atomic physics group measured X rays associated with radiative electron capture at several angles with respect to the beam direction. All these measurements show that the backgrounds and noises in the experimental area are very small.

The construction of the second injector, an AVF cyclotron with $K = 70$ MeV, started in April, 1987. We decided to adopt a Model 715 of SUMITOMO Heavy Industries, Ltd. (SHI) as a prototype for the design of the injector cyclotron and modified it to be equipped with external ion sources which are an ECR source for heavy ions and a duoplasmatron for

protons and deuterons. The detailed design has been finished in RIKEN and the order was placed to SHI. It is expected to be completed in March, 1988.

The design of the ECR source was carried out based on the source developed in Berkeley. Assembly of the source will begin in February, 1988.

The construction of beam transport lines to experimental halls E1, E2, E3, and E7 is under way and will be finished in March, 1988. The beam line going to the RIPS (RIKEN Projectile Fragment Separator) and to E7 branches from the main beam line at the exit of the cyclotron vault. Those going to E4, E5, and E6 will be installed after the building is completed.

This year we have started construction of the following facilities: An ion-guided isotope separator on line (IGISOL) combined with a gas-filled recoil isotope separator (GARIS) will be installed in E1 by June, 1988. Laser spectroscopy experiments are planned to measure spins, moments, and mean square charge radii of those nuclei as are separated at the IGISOL. A large scattering chamber with a multi-particle correlation spectrometer is under construction and will be installed in E2.

The beam line for the study of atomic physics is installed in E2, too. A highly-ionized-atom spectrometer, a general purpose scattering chamber, and an X-ray goniometer will be built along this beam line.

A pion spectrometer which is now set up in E1 will be moved to E3 and the study of subthreshold pion production by measuring charged pions with this spectrometer will be continued there. An irradiation system for short-lived isotope production is also installed in E3.

A slow pion and muon spectrometer with a large solid angle is under construction. This is a superconducting solenoid and will be used to measure the production rate of the low energy charged pions and muons, providing a possibility to apply RRC for very low energy muon spectroscopy. A spectrometer to measure the ion emission from metallic surface is also under construction. These two spectrometers will be installed in the room E7.

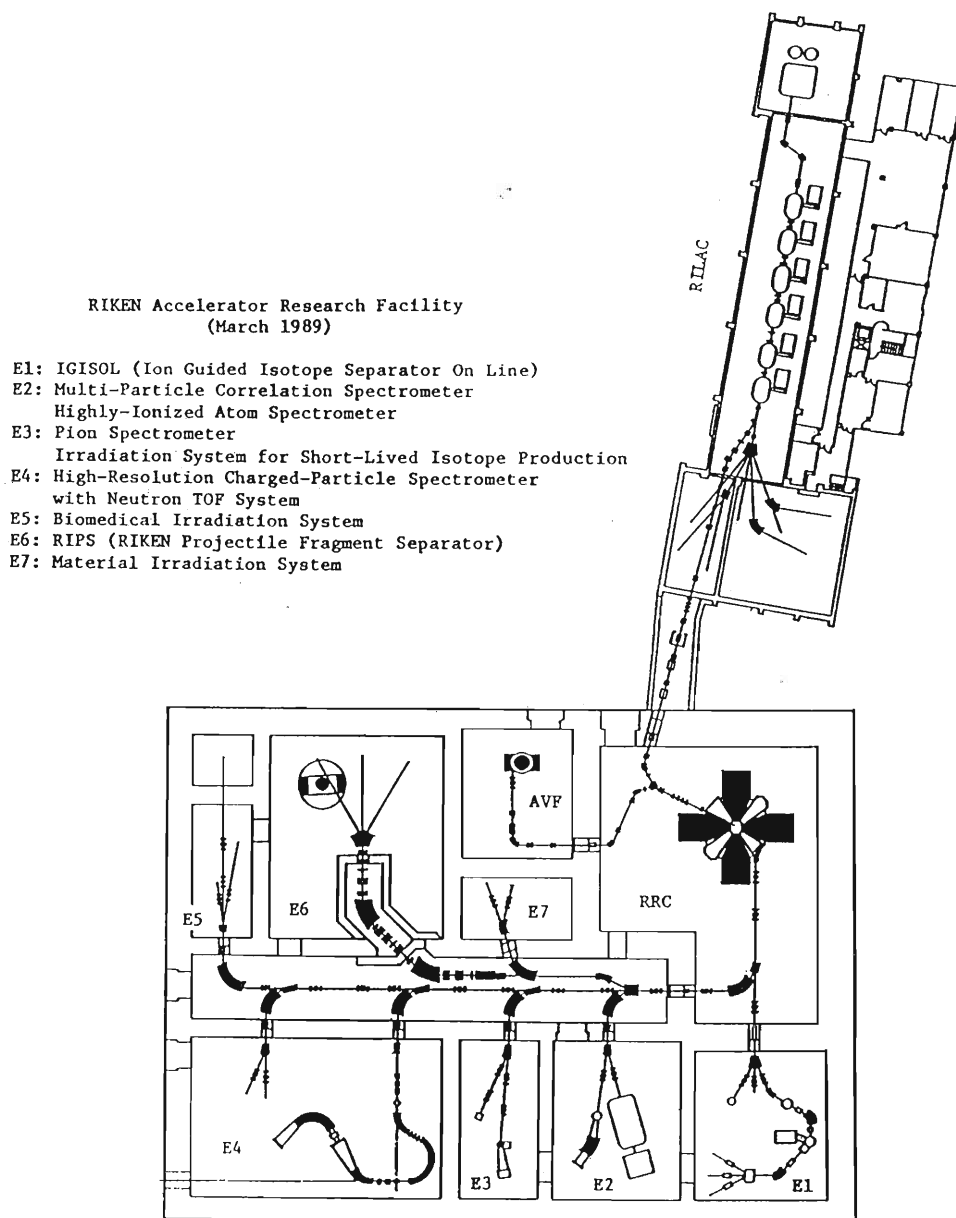


Fig. 1. Plan view of RIKEN Accelerator Research Facility.

Projectile fragmentation in heavy ion reactions is a very promising process to produce nuclei far from the stability line and also to get a "radioisotope beam." The RIPS is designed to separate the projectile fragments from an incident beam and to collect the produced isotopes having a broad spectrum of kinetic energy onto the focussing point in the room E6. It will be completed by the beginning of 1989.

A horizontal irradiation system with a wobbler magnet is installed for biomedical studies in E5. Because the room E5 will be completed in March, 1989, the system will be tentatively installed in E1.

The data acquisition system is a hierarchic multi-processor system with CAMAC interfaces. The local

processor consists of three DEC Micro VAXII's and a VAX8350. The host computer is a FACOM M-380 whose processing speed is 23 MIPS. The CAMAC crate is equipped with an auxiliary crate controller, CES2180, which works as a front-end processor of the data-taking system. The whole system is used for on-line data acquisition as well as off-line data reduction and analysis.

The design of the particle spectrograph and the beam swinger is in progress. They will be installed in E4 in 1989.

The phase III part of the building is under construction; it includes experimental rooms E4, E5, and E6, and the offices for the staffs and visitors.

V-2. Field Stability of the Sector Magnets

H. Takebe, T. Wada, M. Nagase, J. Fujita, and S. Motonaga

The first overhaul of sector magnet power supplies was done from Sept. 26 to Oct. 10, 1987. After adjustment of the power supplies by the company engineers, the current stability of a main coil power supply was checked. Stabilities of the main coil power supplies* were found within $\pm 5 \times 10^{-6}$, and the temperature of a shunt resistance was $29 \pm 0.2^\circ\text{C}$ (Fig. 1). Nevertheless, the magnetic field of the sector magnet drifted by a few tens of parts per million (Fig. 2) with a temperature drift (5°C) of the cooling water for the magnets. To reduce the field drift, an NMR** feedback system was operated by using an NMR probe and a host computer (M350/60). Figure 3 shows the field deviation measured during the machine time on November 9–11; it was within ± 2 or 3 ppm at 1 Tesla when the NMR feedback loop was turned on.

Figure 4 shows a sector magnets control system. As the NMR scanning data should be used simultaneously for three programs (a logging and graphic program, an NMR feedback (stabilizing) program, and a touch panel program), a global common memory on the M350/60 host computer was used (Fig. 4(a)). If the difference in the sector field was between $+2\mu\text{T}$ and $+100\mu\text{T}$ and dB/dt was positive, the bypass current of the M2 power supply was increased. When it exceeds $100\mu\text{T}$, or dB/dt was negative, this program was only waiting the next data (Fig. 4(b)). Thus the four sector stabilizing system was achieved independently.

The reproducibility of the sector magnet fields was measured using the CYCLING method.¹⁾ Figure 5 shows a time chart of the sector magnets operation during the machine time. At the end of the machine

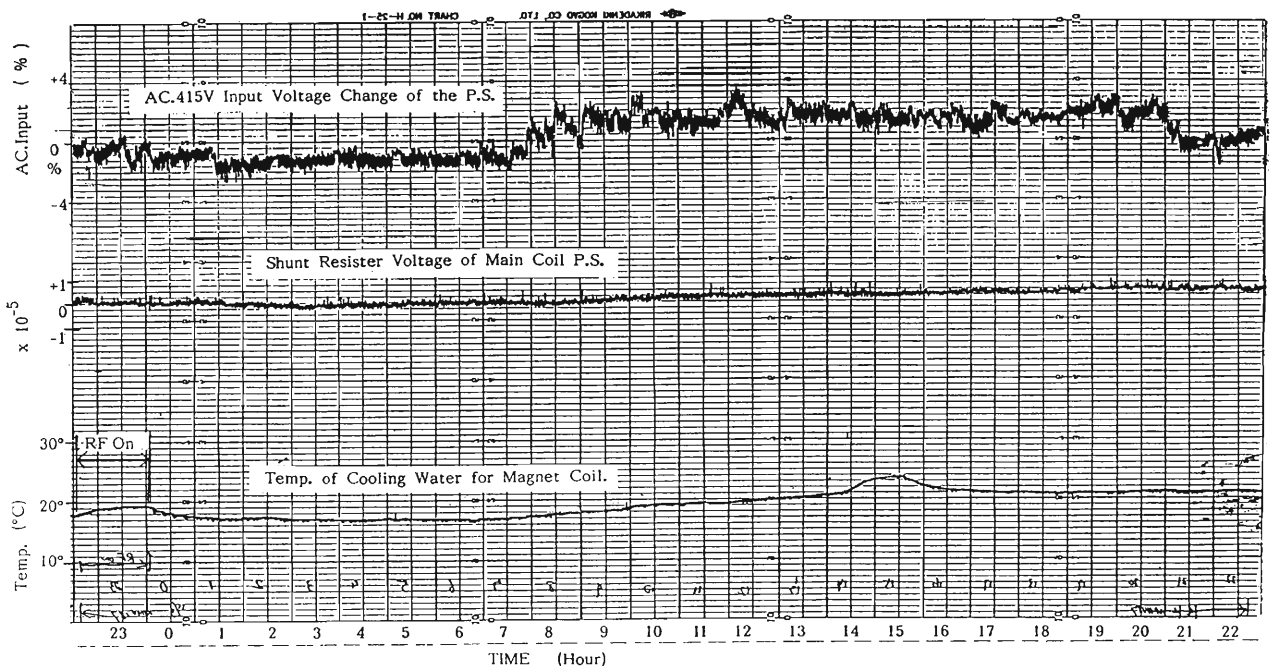


Fig. 1. Twenty-four-hour record of the shunt resistance voltage of the main coil power supply (M1), AC415 V input voltage, and a temperature for the magnets cooling water.

* DC Hi-precision power supply; IDX Corporation, Tokyo.

** NMR Magnetometer (type 1000); SENTEC Co., Ltd., Switzerland.

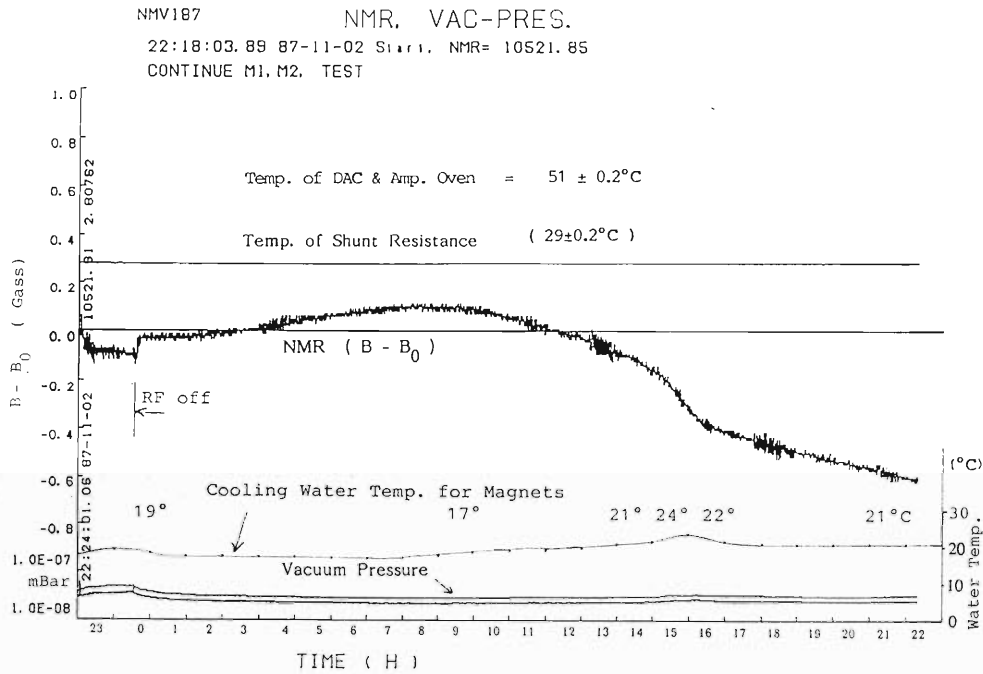


Fig. 2. Magnetic field drift of the E-sector magnet, water temperature for the magnets, and vacuum pressures of the RF chambers.

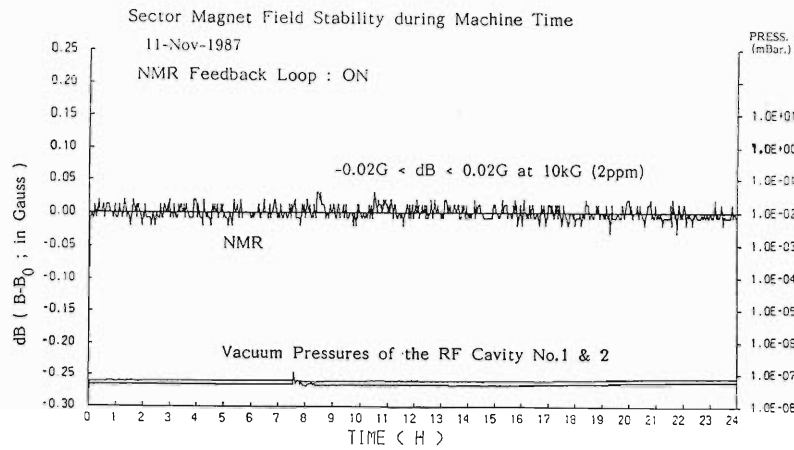
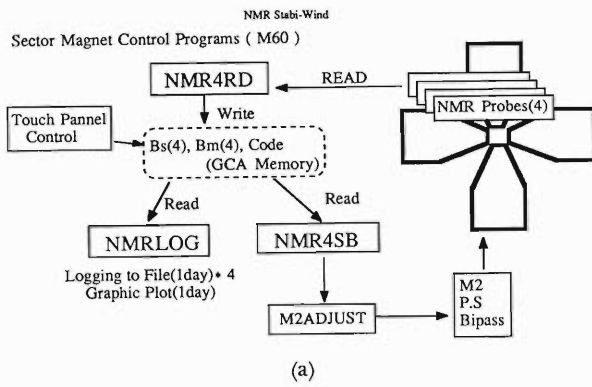


Fig. 3. Magnetic field stability of the sector magnets, which was measured during the machine time on November 9-11; it was within ± 2 ppm at 1 Tesla.

time, all the magnet currents were logged and the sectors were turned off. Next day and the day after the next, the sector magnets were excited again by using CYCLING as exited to the logged data. The

difference in the magnetic field from those of the previous days, measured by the NMRs, are shown in parentheses in Fig. 5; they were within $\pm 70 \mu\text{T}$.



NMR4SB ; Sector field stabilizing Sequence

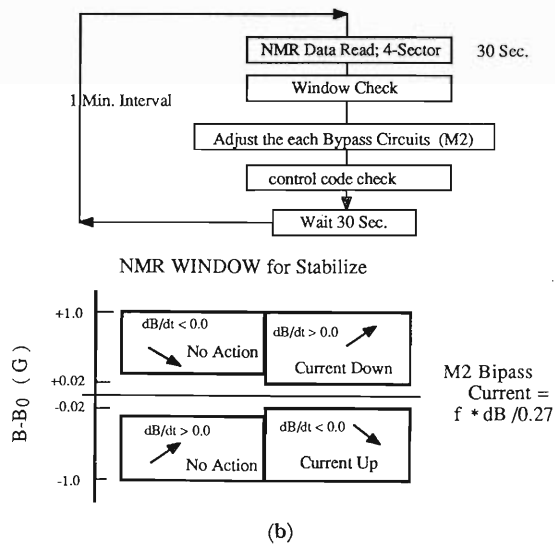


Fig. 4. Sector magnets control programs (a) and NMR feedback system for stabilizing the sector magnetic field (b).

Reproducibility of the Sector Magnet Field Level

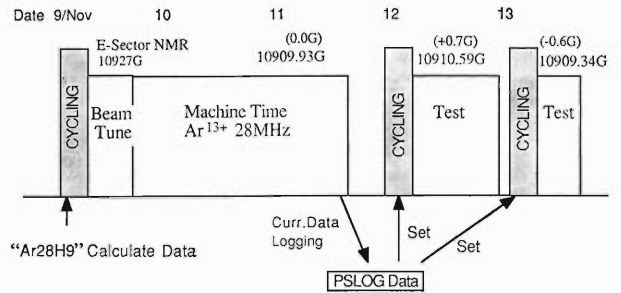


Fig. 5. Reproducibility of the sector magnet fields measured by using the CYCLING method.

Reference

- 1) H. Takebe, T. Wada, M. Nagase, S. Motonaga, and A. Goto: *RIKEN Accel. Prog. Rep.*, **20**, 172 (1986).

V-3. Applications of CIM-DIM in the Beam Diagnostic System of RIKEN Ring Cyclotron

M. Kase and I. Yokoyama

All measurements concerning the beam diagnosis at RIKEN Ring Cyclotron, except for the observation of fast signals from a probe, are made through a CIM-DIM (Communication Interface Module and Device Interface Module)¹⁾ data transfer system under control of a Mitsubishi M60 computer. The applications of DIM, in the beam diagnostic system, are divided into two groups, BDA (Beam diagnostic DIM Application) and BDI (Beam Diagnostic Interface).

A BDA circuit has been developed for a fixed purpose. Every BDA circuit is composed of a DIM board and other circuits and has its own way how to use the DIM digital I/O. Three kinds of BDA circuits are used: a profile monitor controller, a slit system controller and an emittance monitor controller.

A block diagram of the profile monitor controller (BDA-PF) is shown in Fig. 1. For the measurement of a beam profile in a beam line, the three-wire sensor is scanned on the beam area with an air cylinder.²⁾ The wire position relative to the beam axis is detected by using position sensors at the both ends of stroke and a rotary encoder. The total counter (16 bits) is reset at one of the position sensors and counts pulses from the rotary encoder. A preset counter (8 bits) provides a trigger for sample holding and data taking. After receiving a measurement command, the DIM actuates the air cylinder, takes the position and three analog data, and stores them in a memory. The DIM transmits these data to CIM by other command.

The other application of DIM (the BDI circuit) has a large flexibility compared to the BDA circuit. In the beam diagnostic system, some probes may be added or moved from one place to other depending on situations, and some new devices will be developed in the future. In these cases, electronics in the BDI application can easily be modified according to the changes.

The BDI circuit, which is built in a plug-in module (according with DIN 41494), uses DIM digital input/output as a common bus (BDI bus). The bus has 48 digital signals (6 bits for the high address, 8 bits for low address, 8 bits for input and output data, 8 bits for LAM (Look At Me), 8 bits for unit number, and 2 bits for read/write strobes).

Four power lines (+5 V, +15 V, -15 V, and +24 V) are also contained in the BDI bus. The BDI circuit has two connectors at the rear end of its board: the lower one (64 pin) connected to the BDI bus and the upper one used for connection with probes or other circuits. The circuit is readily change-

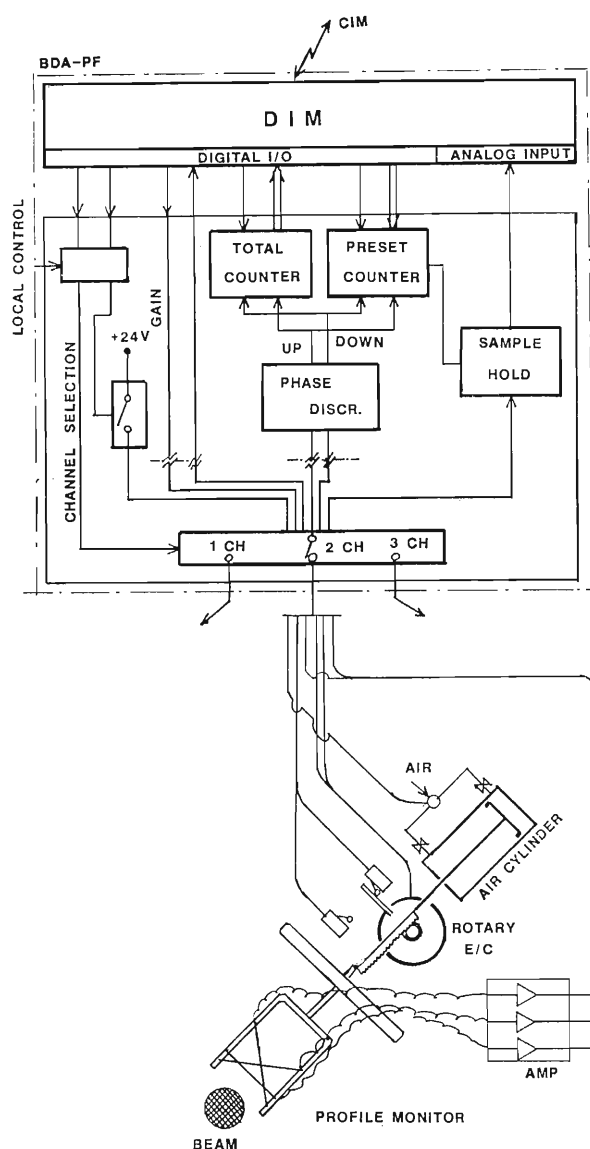


Fig. 1. Block diagram of a beam profile measurement system.

able if necessary, since there is no cable connection on its front panel.

There are two types of BDI circuits, a BDI module and a BDI unit. BDI module has a passive function under control of DIM. A maximum of 64 BDI modules can be connected to one DIM and each BDI module can be operated on 256 functions. Several kinds of BDI modules are used, such as a pneumatic driver controller, a bias supply, a vacuum system controller, an interlock circuit, and a beam current amplifier.

The circuit called the BDI unit has a micro processor in it and executes more intelligent functions than those of BDI modules. A Maximum of eight BDI units can be connected to one DIM. An example of the BDI units, BDI-RP/C (radial probe control unit), is shown in Fig. 2. The radial probes

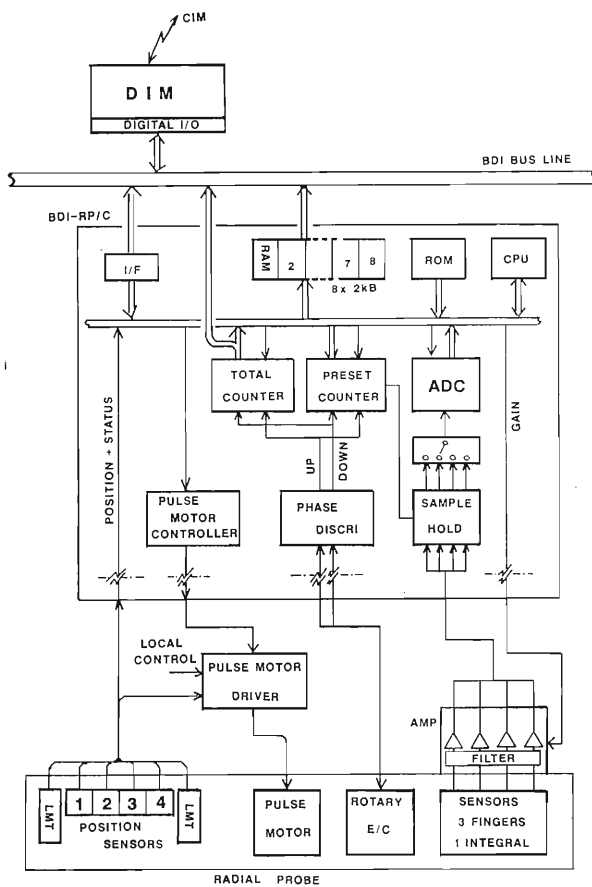


Fig. 2. Block diagram of a radial probe system.

in RIKEN Ring Cyclotron is actuated by the combination of a stepping motor and ball screw and a probe position is detected by the combination of six position sensors and a rotary encoder. After receiving a command from a DIM via the BDI bus, a processor on the BDI-RP/C starts a measurement. It actuates the probe, takes data, and stores them on one of its 2 kB memories. When one of the memories is full, BDI-RP/C makes a LAM flag to the DIM and continues the measurement using another memory. The DIM can read, at any time, the data in the fully-stored memory directly without disturbing the measurement going on. The radial probe data can, therefore, be taken step by step without waiting for the end of whole measurement.

The program in DIM and CIM is directly written into an 8 kB ROM in them. The CIM program is identical for any DIM's used in the beam diagnostic system. A main function of the CIM program is to convert the data transfer format between 8-bit serial one (CIM-DIM) and 24-bit parallel one (CIM-CAMAC).

Every DIM has a common program for the communication with CIM. Whenever a command from CIM reaches one DIM, the DIM is interrupted and this program starts. In this routine DIM checks the priority of the command, verifies it on a command list of its own, and finally sends a three-byte response back to CIM, which waits for the response for 30 ms after sending the command. The response has information about whether or not the command is acceptable, and also some message, when the command is rejected. After sending the response, the DIM start performing the command.

The other area of ROM in DIM is used for a specified program for each DIM. Four kinds of programs have been developed for the DIM used for a BDI circuits and for three types of BDA circuits.

References

- 1) T. Wada, J. Fujita, I. Yokoyama, T. Kambara, and H. Kamitsubo: *Sci. Papers I.P.C.R.*, **79**, 28 (1985); K. Shimizu, T. Wada, J. Fujita, and I. Yokoyama: 10th Int. Conf. on Cyclotron and Their Applications, East Lansing, Michigan, USA, April (1984).
- 2) M. Kase, I. Yokoyama, I. Takeshita, Y. Oikawa, M. Saito, and Y. Yano: 11th Int. Conf. on Cyclotron and Their Applications, Tokyo, Japan, Oct. (1986).

V-4. Improvement of RF Amplifier of RIKEN Ring Cyclotron

T. Fujisawa, S. Kohara, M. Saito, and Y. Chiba

The radio-frequency system of RIKEN Ring Cyclotron was installed in the cyclotron vault in August 1986 and have been working well.^{1,2)} Its performance is satisfactory for most of the frequencies, 20–45 MHz, but the maximum output power of the final amplifier is limited to be 160 kW at the frequency around 40 MHz.²⁾ This reduction in the output power is caused by the 80 MHz resonance (G1–G2 resonance) between the screen and control grids of the final tube SIEMENS RS2042SK, which is excited by a higher harmonic component of tuning frequency of 40 MHz. In order to avoid the effect of this resonance, we are trying to shift the resonance at a frequency higher than 90 MHz by improving the screen and control grid bypass capacitors. We studied performance of a few models of capacitors mounted on RS2042SK by measuring the voltage transmission ratios from the plate terminal to the screen and control grid bypass capacitors.

Figure 1 shows the cross-sectional view of RS2042SK with the bypass capacitors finally designed. The cylindrical bypass capacitors ($C_{g1} = C_{g2} = 8,700$ pF) are made of 125 μm Kapton film coated with silver paint. A pair of the capacitors is mounted in the space between the screen grid and cathode terminals in order to reduce inductance which lowers the resonant frequency. Calculation showed that this reduction of inductance (7 Ω , 4.5 cm) moves the res-

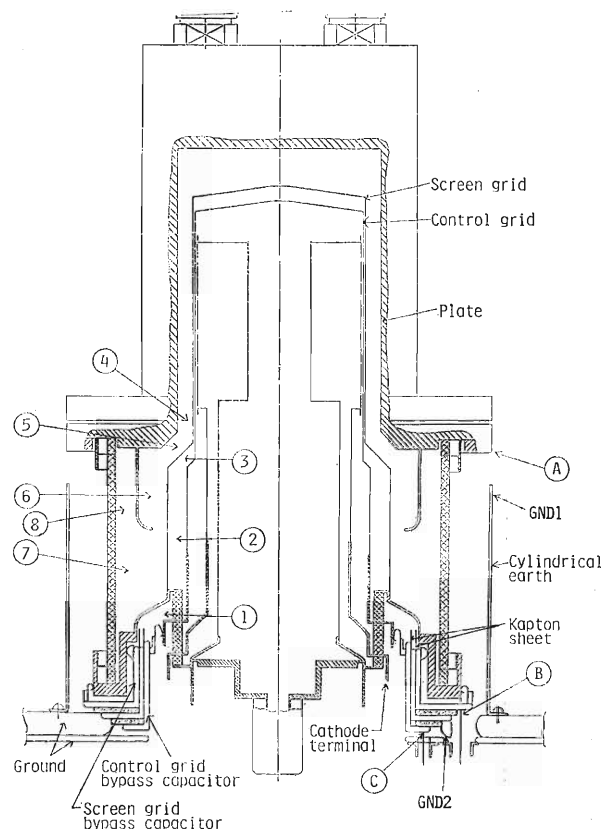


Fig. 1. Cross sectional view of the RS2042SK tetrode and improved screen and control grid bypass capacitors.

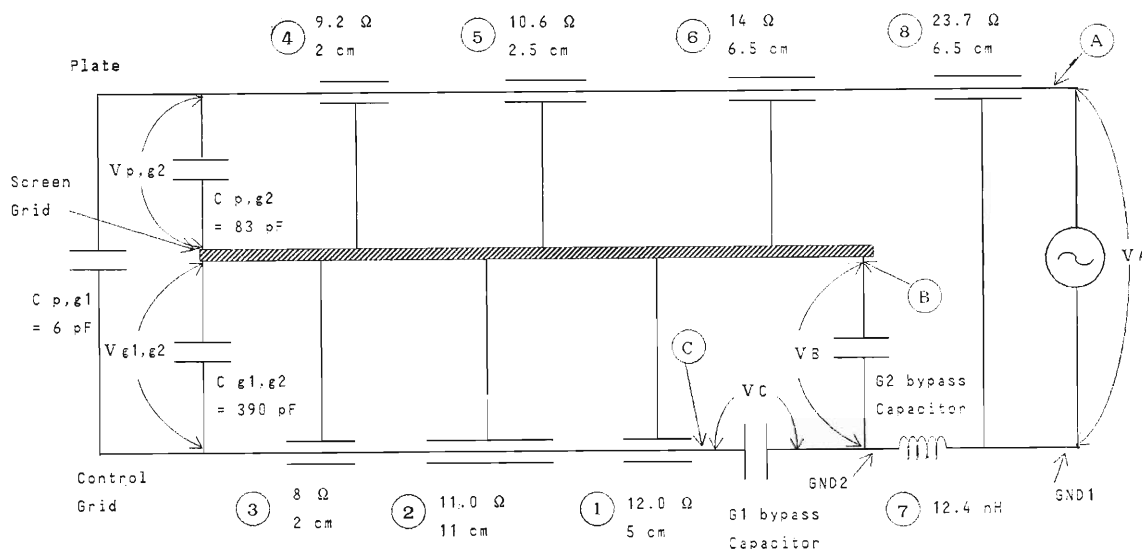


Fig. 2. Equivalent circuit of the plate, screen grid, and control grid of RS2042SK with bypass capacitors.

onance at a frequency higher than 100 MHz. A copper cylindrical earth surrounds the tube to keep the circuit a coaxial geometry and to reduce the inductance of the feeder line for a signal. An RF signal was fed to four positions between A and GND1, which are set in axial symmetry, and the voltage transmission ratios were measured at positions B and C.

Figure 2 shows an equivalent circuit for the plate, screen grid, and control grid of RE2042SK and the bypass capacitors. The numbers correspond to the positions shown in Fig. 1 and the positions A, B, and C are also shown.

Figure 3 shows the measured voltage transmission ratios together with the result calculated with the equivalent circuit. The voltages V_A , V_B , and V_C are obtained at the positions A, B, and C, respectively. The calculations are in fairly good agreement with the measurements. The resonant frequency becomes about 100 MHz, and the voltage transmission ratios are 0.012–0.014 for the screen grid bypass capacitor and 0.0014–0.002 for the control grid bypass capacitor

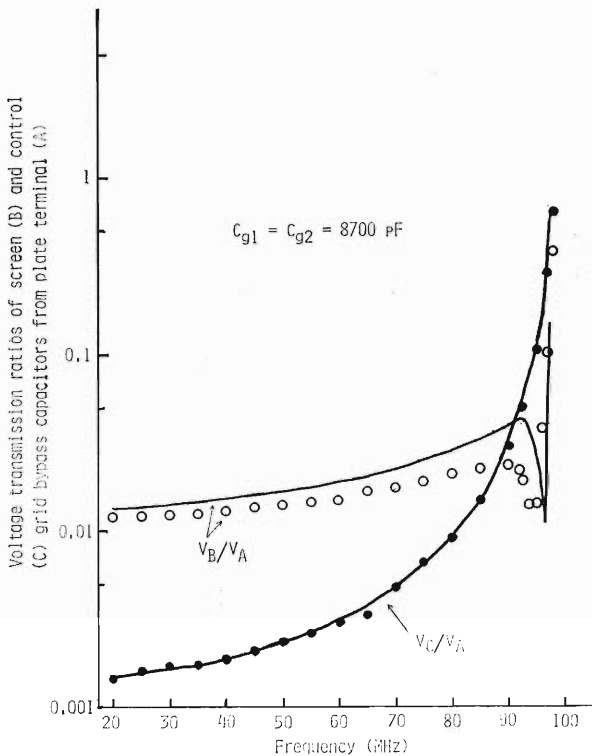


Fig. 3. Voltage-transmission ratios from the plate terminal of RS2042SK to the screen and control grid bypass capacitors. The line shows the calculation with the equivalent circuit.

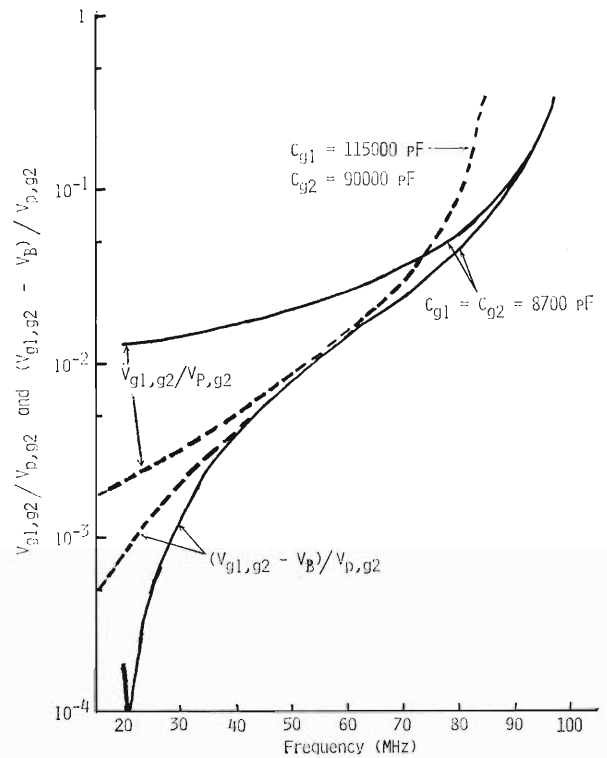


Fig. 4. Calculated ratios of $V_{g1,g2}$ to $V_{p,g2}$ and of $(V_{g1,g2} - V_B)$ to $V_{p,g2}$.

in the frequency range of 20 to 45 MHz. The voltage transmission ratios obtained, however, are not the ratios at the active area inside the tube. In order to estimate the ratios at the active area, we calculated the ratios of $V_{g1,g2}$ to $V_{p,g2}$, and of $(V_{g1,g2} - V_B)$ to $V_{p,g2}$ (See Fig. 2).

In Fig. 4, the result is shown together with a result of the bypass capacitors ($C_{g1} = 115,000$ pF and $C_{g2} = 90,000$ pF) used in the actual amplifier. It is clear that the G1-G2 resonance is moved at around 100 MHz. In the present study calculation was carried out with the computer FACOM 380 at RIKEN.

References

- 1) T. Fujisawa, K. Ogiwara, S. Kohara, Y. Oikawa, I. Yokoyama, I. Takeshita, Y. Chiba, and Y. Kumata: *Sci. Papers I.P.C.R.*, **79**, 12 (1985); T. Fujisawa, K. Ogiwara, S. Kohara, Y. Oikawa, I. Yokoyama, M. Nagase, I. Takeshita, Y. Chiba, and Y. Kumata: *Proc. 11th Int. Conf. Cyclotron and Their Applications*, Tokyo, Japan (1986).
- 2) T. Fujisawa, S. Kohara, K. Ogiwara, I. Yokoyama, M. Nagase, and Y. Chiba: *RIKEN Accel. Prog. Rep.*, **19**, 170 (1985); **20**, 167 (1986).

V-5. Effects of Magnetic Fields on a Turbomolecular Pump of 5,000//s

A. Nishide and S. H. Be

We investigated effects of magnetic fields on a turbomolecular pump of 5,000 l/s (TMP; OSAKA Vacuum, Ltd., TH5000), which is used in RIKEN Ring Cyclotron. We estimated: 1) a temperature rise of the TMP rotor installed in magnetic field distributions as shown in Fig. 1; 2) a decrease in the revolutions per second; and 3) an increase in loss on the power supply for driving TMP. Figure 1 shows that magnetic field distributions as a function of a distance from the presumptive center of TMP before installation. The distributions as shown in Fig. 1 were produced at a maximum base field, B_{\max} of 15.4 kGauss for sector magnets of the cyclotron, but the magnetic fields can be varied by adjusting the exciting current of main coils for the sector magnets.

In this experiments, the magnetic fields were continuously applied throughout an operation of TMP. For estimation of the effects of the magnetic fields on TMP, only the magnetic fields in the direction vertical to a revolution axis of TMP were considered because the magnetic fields in the direction parallel to a revolution axis caused no temperature rise of the rotor and no decrease in revolutions per second.

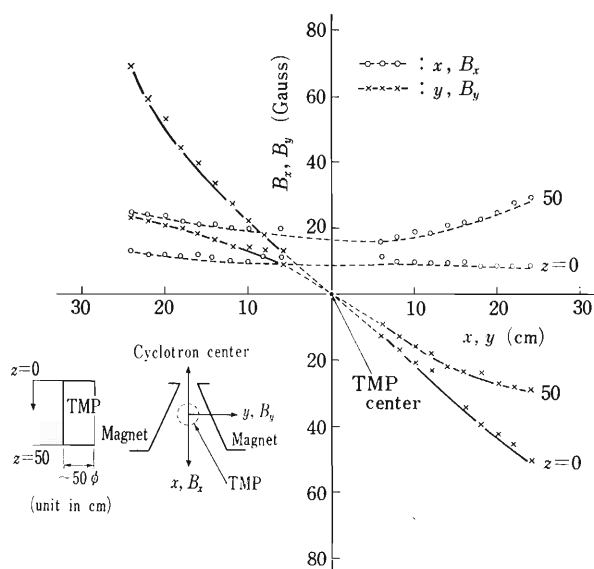


Fig. 1. Magnetic field distributions as a function of a distance from the presumptive center of TMP before TMP is installed. $Z=0$ and 50 cm correspond to positions of an uppermost part (inlet port) and lowermost one (exhaust port) of TMP, respectively.

Actually, we need to consider the effects of the magnetic fields in the parallel direction since magnetic materials are present in TMP; however, at $B_z \approx 200$ Gauss (at $B=B_{\max}$) no problem occurred.

The rotor temperature rise in the magnetic fields is indirectly estimated from an eddy current loss, P_{loss} , in blades to be proportional to the square of the magnetic field. The P_{loss} is evaluated from the difference of dissipation powers in the blades for $B=0$ and $B \neq 0$ at revolution frequency decay curves measured, not shown here, after TMP is stopped. When the revolution frequency decreases from ω to $(\omega - \Delta\omega)$ during a short time Δt , the dissipation power P is given by $I(\omega \Delta\omega) / \Delta t$. Here I is the moment of inertia. The rotor temperature rise can be obtained using both the P_{loss} , which is shown in Fig. 2, and a relation between the rotor temperature

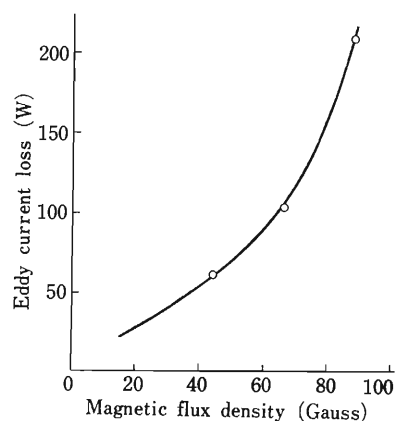


Fig. 2. Eddy current loss vs. magnetic flux density.

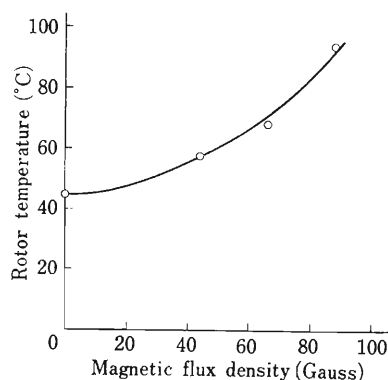


Fig. 3. Rotor temperature as a function of the magnetic flux density.

and the P_{loss} . This relation has been given by other experimental results. Figure 3 shows that the rotor temperature increases with an increase in the magnetic fields and reaches $\sim 100^\circ\text{C}$ at ~ 80 Gauss. The rotor temperature which can be allowed for TMP is $\sim 120^\circ\text{C}$.

The decrease in revolutions per second is indirectly evaluated from a difference between accelerating torques of the motor with and without the magnetic fields. In this evaluation we used a retarding torque in the magnetic fields, as shown in Fig. 4, and the accelerating torque without the magnetic field. The evaluated result, *i.e.*, the decrease in the revolutions per second is shown in Fig. 5 as a function of the magnetic field. As seen from Fig. 5, the revolutions per second decrease slightly with an increase in the magnetic fields, because the retarding force due to an eddy current induced by the magnetic fields breaks a constant torque condition under which a high frequency power of the pump motor is supplied.

The results of the rotor temperature rise and the decrease in the revolutions per second for TMP immersed in the non-uniform magnetic fields indicate, as shown in Fig. 1, that the magnetic field allowed for TMP is ~ 80 Gauss. This value corresponds to that at the position of the TMP when the maximum base field for the sector magnets is 15.4 kGauss .

A relationship between the output current of the power supply and the magnetic field, not shown here, shows that the output current increases slightly with an increase in the magnetic field up to $B = (2/3)B_{\text{max}}$, but the output current at $B > (2/3)B_{\text{max}}$ increases

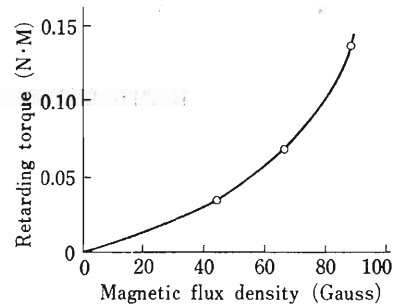


Fig. 4. Relation between retarding torque of the motor and magnetic flux density.

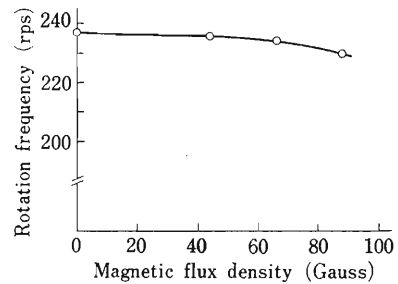


Fig. 5. Revolutions per second as a function of the magnetic flux density.

rapidly with increasing magnetic field, where B is the base field for the sector magnets. From these results, we conclude that the magnetic field allowed for the continuous operation of the TMP is ~ 30 Gauss, which corresponds to $B = (2/3)B_{\text{max}}$. The continuous operation of the TMP at $B = B_{\text{max}}$ for a short time of about 1 h will cause no damage.

V-6. Communication System for RIKEN Ring Cyclotron

H. Takebe, S. Fujita, R. Abe,* H. Akagi,* T. Wada, and T. Inamura

The RIKEN Accelerator Research Facility (RARF) consists of two injectors, a heavy ion linac-AVF cyclotron and a K540 ring cyclotron.¹⁾ RIKEN Ring Cyclotron (RRC) was completed in November 1986 and the first beam was accelerated in December. At present, the heavy ion linac (RILAC) is used as an injector for RRC. The construction of another injector, a K70 AVF cyclotron, has been started and will be completed at the end of 1989 FY. Total area of the facilities exceeds 12,000 m² and the number of the rooms will be about 80.

The communication (audio and video) system for the RARF consists of interphones/speakers, a bi-directional transceiver, a video monitors network (CATV), and a computerized voice warning system. Figure 1 shows a schematic diagram of the whole system. Some of them are installed and tested this year. Fifteen sets of small hand-free transceivers (bi-directional, headphone-mic type wireless telephones; Shinwa Comm. Co., Ltd., 410 MHz-up/450 MHz-down band) and the interphone/speakers system (AIHON Electr. Co., Ltd.) were installed in 1986. Antennas (400 MHz) for this transceivers are installed in all experiment halls, RRC vault, the control room, and the counting room. The linear accelerators vault and their control room will be installed with antennas in 1988. In-house broadcast speakers will be connected with a paging system of a new Digital PBX²⁾ system this fiscal year. A four-camera auto-scan³⁾ system and CCD color video cameras (high-resolution, low price; family use) were installed and tested this year. In 1988, ten to sixteen video cameras for power supply rooms and experiment devices will be installed and connected to video/audio remote scanning switches. Some of the selected signals are transferred to the control room, and displayed and converted to a CATV's RF frequency (Ch. 1-12) to

be broadcasted in the facility. This system is controlled by a CIM/DIM⁴⁾ system or a personal computer (PC9801 or mz-X1) with a touch panel.

Figure 2 shows a computerized voice warning system for RRC control system and a radiation safety control system. Message signals of the control (or surveillance) programs of RRC's M350/60 mini-computer⁵⁾ should give notice to operators and other staffs using voice synthesizer sounds. A hard wired interlock or warning signals of the RF system and a vacuum system are also connected to the voice synthesizer boards to give notice. There are two types of synthesizer boards, which are of a 6 kHz sampling ROM type and of an 8 or 16 kHz sampling RAM type.⁶⁾ These audio signals will also be connected to the CATV and interphone speakers (Fig. 2(a)).

The entrance to and exit from a radiation-controlled area are checked very strictly by using a personal card.⁷⁾ Users, especially unfamiliar with our facility, need some information of checking procedure to pass over a radiation safety check point (hand-foot-clothe monitors are especially difficult to use for general users) smoothly. For this purpose, a voice guide system using a voice synthesizer is adopted (Fig. 2(b)).

References

- 1) H. Kamitsubo: *RIKEN Accel. Prog. Rep.*, **20**, 160 (1986).
- 2) Digital Private Branch Exchanger: FIJITSU, FETEX-3700.
- 3) Mitsubishi Electr. Co., Ltd.: MELOOK-8.
- 4) Communication Interface Module and Device Interface Module.
- 5) T. Wada, H. Takebe, J. Fujita, T. Kambara, and H. Kamitsubo: *RIKEN Accel. Prog. Rep.*, **20**, 170 (1986).
- 6) Sankyo Electr. Co., Ltd.: ICR500Z/A, VS400A, VS800A.
- 7) I. Sakamoto, S. Fujita, T. Wada, and H. Takebe: *RIKEN Accel. Prog. Rep.*, **20**, 206 (1986).

* Sumijyu Accelerator Service, Ltd.

88-2-4, CATV-4

RRC-Communication/CATV system

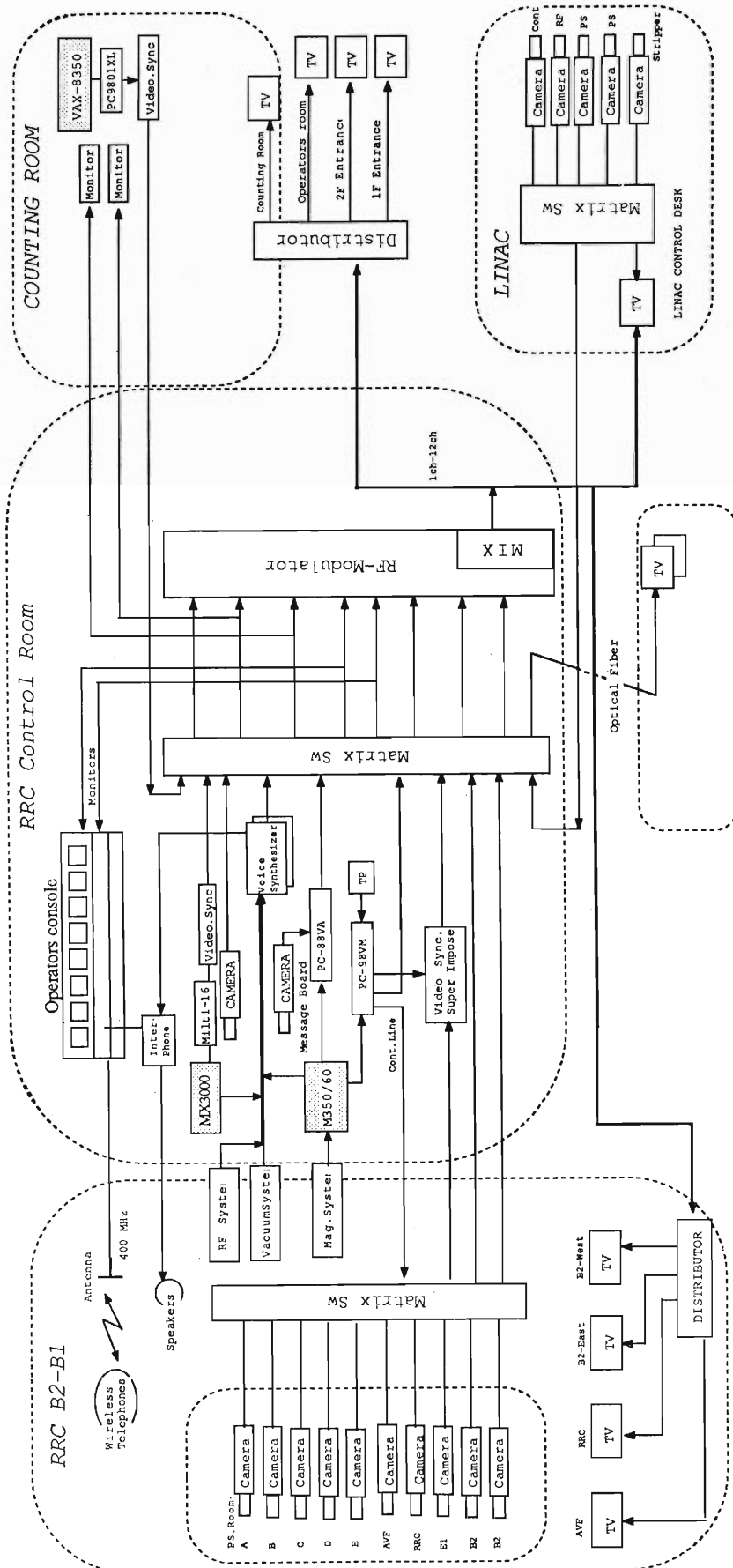


Fig. 1. Schematic diagram of the information system for RIKEN Accelerator Research Facility (ring cyclotron and linac). It consists of interphone / speakers, bidirectional transceiver, video monitors network (CATV), and computerized voice warning system.

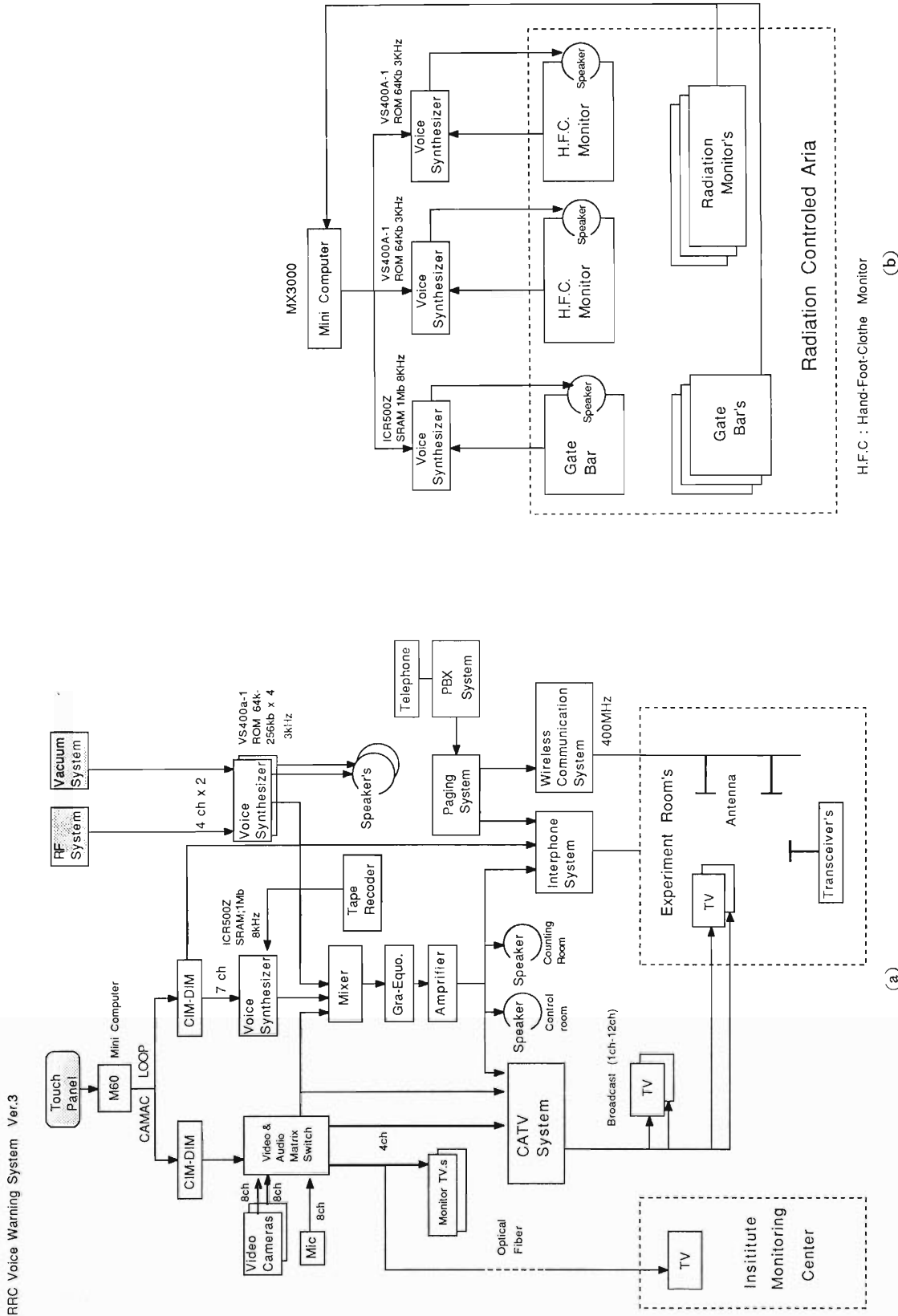


Fig. 2. Computerized voice warning system for RRC control system (a) and for a radiation safety control system (b).

V-7. Injector AVF Cyclotron for RIKEN Ring Cyclotron

A. Goto, K. Hatanaka, K. Ikegami, T. Kageyama,
M. Kase, S. Kohara, N. Nakanishi, H. Nonaka,
M. Saito, H. Takebe, and Y. Yano

An AVF cyclotron is used as an injector to get higher energies for light and light heavy ions. In coupled use with RRC, the final energies designed are 210 MeV for protons, 135 MeV/u for ^{12}C , ^{14}N , ^{16}O , 95 MeV/u for ^{40}Ar and so on. A conceptual design of the AVF cyclotron was reported elsewhere.¹⁾ At that stage the cyclotron was designed to be used not only as the injector for RRC but also as a stand-alone machine which can accelerate, for example, protons up to 60 MeV, by taking the acceleration harmonic number to be 2 and 1, respectively. Recently, however, the harmonic number of 1 was abandoned because otherwise the central region of the cyclotron will be very complicated. A model 750 PV²⁾ of Sumitomo Heavy Industries, Ltd. (SHI) was decided to be purchased and to be modified to meet the requirements for the injector as well as for external injection.

Table 1 gives the characteristics of the AVF cyclotron.

Table 1. Characteristics of the AVF cyclotron.

Number of sector	4
Sector gap	127 mm
Pole gap	300 mm
Pole diameter	1,730 mm
Extraction radius	714 mm
Maximum magnetic field	1.7 T
Maximum main coil current	1,000 A
Maximum power	150 kW
Number of trim coils	9
Number of harmonic coils	4
Magnet size	2.1 m (H) × 1.9 m (W) × 3.9 m (L)
Magnet weight	110 t
Number of dees	2
Dee angle	85 deg
Frequency	12–24 MHz
Maximum dee voltage	50 kV
Maximum RF power	30 × 2 kW
Inflector	spiral type
Main evacuation system	4,000, 6,500 l/s cryopumps 1,500 l/s turbomolecular pump
Pressure	2 × 10 ⁻⁸ Pa
Control system	Computer network and CAMAC interfaces
Acceleration harmonic number	2

tron; its layout is shown in Fig. 1 and its performance in Fig. 2. The K70 AVF cyclotron has four spiral sectors and two RF dees with an angle of 85°. The extraction radius is 714 mm. Ions from external ion sources consisting of a duoplasmatron and an ECR source are axially injected into the cyclotron and led onto the median plane with a spiral inflector. This cyclotron can accelerate ions whose m/q values are up to 4.

Construction of the AVF cyclotron started in April 1987. After magnetic field measurement, all parts

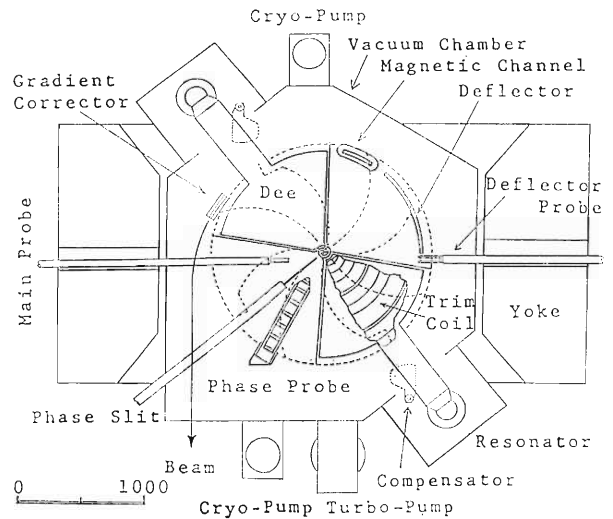


Fig. 1. Layout of the AVF cyclotron.

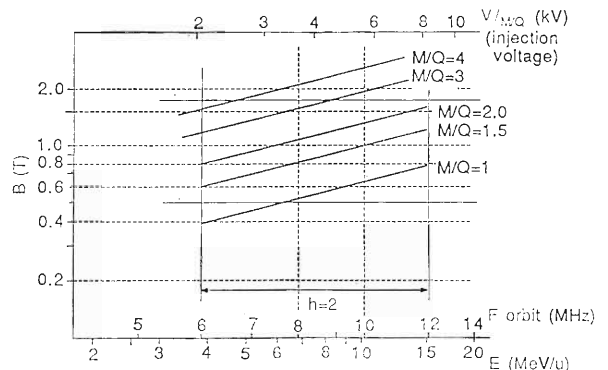


Fig. 2. Performance of the AVF cyclotron.

of the cyclotron will be assembled at the factory of SHI by the autumn of 1988 and various tests such as a leak test, a moving test, and an RF test will be made there before the installation into the cyclotron vault of RIKEN. The installation and assembly of the cyclotron at RIKEN is scheduled to be completed by the end of March 1989.

References

- 1) N. Nakanishi and T. Kageyama: *RIKEN Accel. Prog. Rep.*, **19**, 197 (1985).
- 2) K. Fujii, M. Maruyama, T. Satoh, M. Ishikawa, and S. Kadota: *Proc. 11th Int. Conf. Cyclotrons and Their Applications*, p. 626 (1986).

V-8. ECR Ion Source for an Injector AVF Cyclotron

K. Hatanaka and H. Nonaka

An ECR ion source for an AVF-Ring Cyclotron complex is now under construction. The source will be used to produce highly-charged relatively light heavy ions (up to Ar). The first beam is scheduled in April 1988. Through further one-year development, the beam from this source will be axially injected into the AVF cyclotron. The m/q value of ions which the AVF cyclotron can accept is less than 4. In the case of Ar ions, for example, the charge state must be higher than 10. If an $^{40}\text{Ar}^{13+}$ ion is accelerated with this cyclotron, the final beam energy from RRC reaches 95 MeV/u.

Main parameters of the source are listed in Table 1; its schematic view is shown in Fig. 1. The source

Table 1. Main parameters of the ECR source.

1st stage	
magnetic confinement	solenoidal field
chamber diameter	60 mm
	20 mm (quartz tube)
chamber length	250 mm
RF	10 GHz CW 1 kW max
pump	520 l/s TMP
2nd stage	
magnetic confinement	mirror+hexapole field
mirror ratio	1.4 to 1.8 (variable)
chamber diameter	100 mm
chamber length	520 mm
RF	10 GHz CW 2.5 kW max
pump	500 l/s TMP
extraction	
acceleration voltage	3 to 25 kV
suppression voltage	0 to -10 kV
extraction gap	5 to 45 mm (variable)

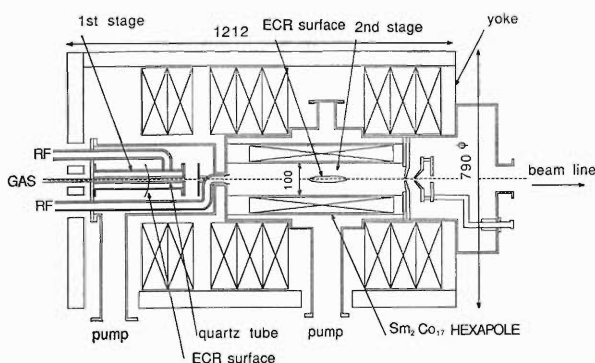


Fig. 1. Schematic drawing of the ECR source.

consists of two stages: the first stage is used for plasma filamentation and the second for production of highly charged ions. The source is provided with three gas feeding lines: two lines at the first stage and the other line at the second for gas mixing.

Principal design of our ECR source is based on the LBL ECR source,¹⁾ but the higher frequency (10 GHz) microwave is used for both the first and second stages, and stronger magnetic confinement is adopted in plasma stages.

An axial magnetic field is produced by solenoid coils, which are divided into eight sections. The currents in all eight axial field coils can independently be varied to find the optimum axial magnetic field profile. A return yoke reduces the power consumption of coils and shields X ray from the plasma chamber. In the second stage, an open $\text{Sm}_2\text{Co}_{17}$ ($B_{\text{res}}=10$ kG) hexapole magnet is set to produce a radial magnetic field. The inner diameter of the hexapole is 11 cm. Each pole is 4 cm wide, 5 cm high, and 45 cm long. The hexapole is placed inside the vacuum chamber, and each pole is enclosed in a jacket and cooled with a non-dielectric coolant. The magnetic field at the exit of the first stage is well above the resonance field for 10 GHz. This field profile gives better second stage confinement. A surface position of the ECR zone near the gas feed is easily changed by varying currents of the first two axial coils. The second stage works in the usual minimum B mode. The mirror ratio and the minimum value of the magnetic field are easily controlled by varying currents for six axial coils. The minimum field can be high enough to test the tangential field effect.²⁾ But from the magnetic pressure point of view, the B^2/μ_0 value at the extraction hole is required to be lower than that of the hexapole chamber wall: if not, the diffusion of the plasma is caused mainly to the hexapole walls and the extraction current may be reduced. The optimum mirror field may be lower for getting high extraction current than that to test the tangential field effect. The second stage plasma chamber is 10 cm in diameter and 52 cm in length. The long plasma region can reduce the magnetic field gradient at an ECR surface to about 100 G/cm, which is better for the electron acceleration by the ECR and increases the electron temperature.³⁾

10 GHz microwaves are fed into both first and second stages through circular wave guides of 27 mm in inner diameter. In the first stage, an RF power is injected radially from the high magnetic field region. By the beach effect, an RF reflection will be reduced. On the other hand, a microwave is axially fed into the second stage. For the efficient absorption of an RF power in a plasma, a plasma chamber must be a multimode cavity. It is pointed out that the chamber diameter D is more than twice as large as the RF wavelength λ .^{4,5)} In our case, D/λ is 2 in the first stage and 3.3 in the second stage. The RF signal is sent from a Gunn oscillator source, amplified with a GaAs FET amplifier, divided into two lines, and amplified with two klystron amplifiers (Thomson TV851). The RF power fed to each stage can be varied independently by using a variable attenuator. The maximum RF power is 1 kW for the first stage and 2.5 kW for the second stage. A DC cut is performed up to 25 kV with a two-fold insulation of 2-mm thick Teflon sheets. A vacuum window is made of BeO.

The pressure is expected to be about 10^{-4} Torr in the first stage cavity, and in the second stage it must be less than 10^{-6} Torr to reduce charge exchange

collisions with neutral atoms. A 500 l/s TMP is set at the first stage, and two 1,500 l/s TMP's at the second stage and in the extraction region. To avoid the diffusion of the fed gas into the wave guide, a quartz tube of 20 mm in inner diameter is used in the first stage.

The extraction voltage is varied from 3 to 25 kV according to the injection condition to the AVF cyclotron. The extraction hole is 10 mm in diameter, and the gap between the extraction hole and the extraction electrode can be changed from 5 mm to 45 mm. To reduce secondary electrons from the grounded electrode, the extraction electrode is biased at the negative suppression voltage.

References

- 1) C. M. Lyneis: Proc. 7th Workshop ECR Ion Source, p.1 (1986).
- 2) T. A. Antaya and Z. Q. Xie: Proc. 7th Workshop ECR Ion Source, p.72 (1986).
- 3) Y. Jongen: Proc. 6th Workshop ECR Ion Source, p.238 (1985).
- 4) F. Bourg, J. Debernardi, R. Geller, B. Jacquot, R. Pauthenet, M. Pontonnier, and P. Sortais: Proc. 6th Workshop ECR Ion Source, p.1 (1985).
- 5) C. M. Lyneis: Private communication.

V-9. RF Amplifier System of the Injector Cyclotron for RIKEN Ring Cyclotron

S. Kohara, M. Nagase, M. Saito, T. Kageyama, A. Goto, and T. Fujisawa

Design parameters of the RF system of the injector AVF cyclotron¹⁾ ($K=70$) for RIKEN Ring Cyclotron²⁾ (RRC) are summarized in Table 1.

A block diagram of the amplifier system is shown in Fig. 1. A master oscillator and power amplifier (MOPA) system is employed to keep synchronous operation through the whole RF system including RRC and beam bunchers. A phase adjustment system consists of two modulators: one is used so as to keep the phase difference between the two resonators zero and the other to adjust the phase of the dee voltage to the reference. The dee voltage is regulated with an amplitude modulator. A pulse modulator is employed to overcome the multipactoring phenomenon in the resonator and also helps vacuum aging.

Table 1. Design parameters of the RF system.

Number of resonators	2
RF frequency	12-23 MHz
Harmonic number	2
RF peak voltage	50 kV
Frequency stability	1×10^{-5}
Voltage stability	1×10^{-3}
Phase stability	0.5°
Extraction radius	71.4 cm
Dee angle	83°
Output power of RF amplifier	20 kW

The resonator is tuned automatically with a capacitive frequency tuner by comparing phases between a plate and a control grid voltage of the final amplifier.

A power amplifier system consists of a solid-state wide-band amplifier (500 W) and a grounded-cathode tetrode amplifier (EIMAC 4CW50,000E). A schematic diagram of the power amplifier system is shown in Fig. 2. An all-pass network³⁾ is adopted in the input circuit of 4CW50,000E; a transformer is used to match the input impedance of the all-pass network, 25Ω , to the output im-

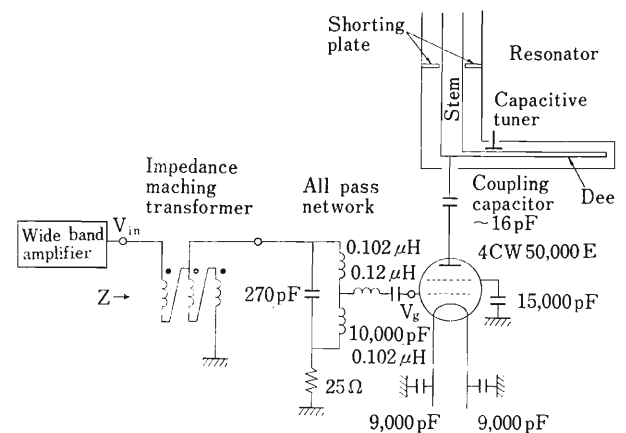


Fig. 2. Schematic diagram of the power amplifier.

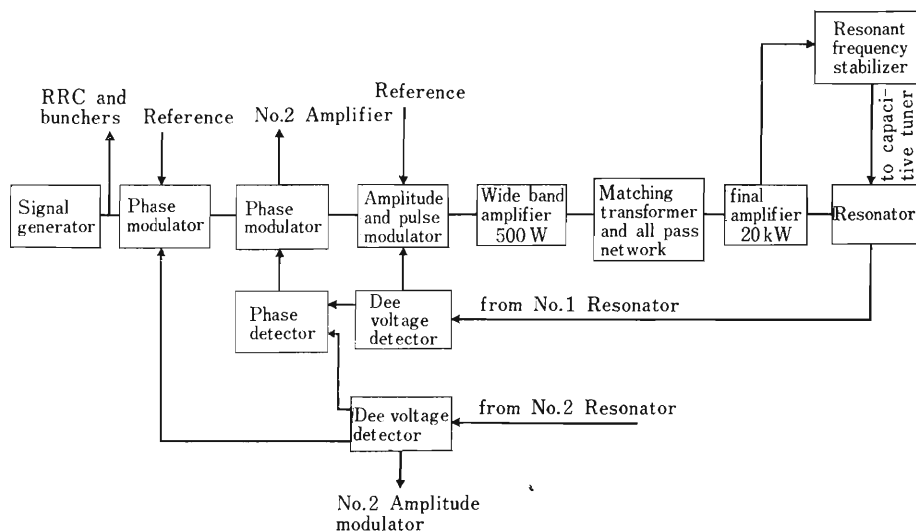


Fig. 1 Block diagram of the amplifier system.

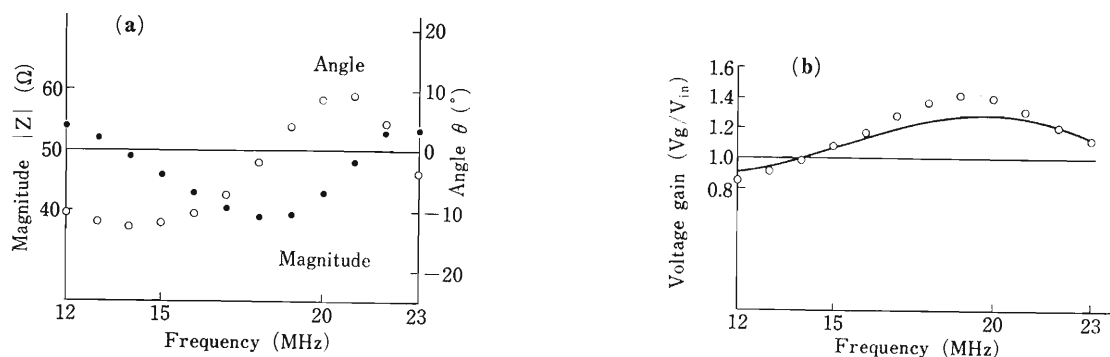


Fig. 3. (a) Input impedance ($Z=|Z|e^{j\theta}$) and (b) voltage gain (V_g/V_{in}) measured for the all-pass network combined with the impedance matching transformer. The solid line in (b) is the calculation.

pedance of the wide-band amplifier, 50 Ω . The RF control grid voltage is estimated to be 200 V for the dee voltage required. The measured input capacitance of the tube is 340 pF. The model study of several types of all-pass networks was carried out; voltage gain (V_g/V_{in}) and input impedance ($Z=|Z|e^{j\theta}$) were measured for several values of circuit parameters for each type. The results for the optimum circuit type and parameters are shown in Fig. 3. The impedance varies from 39 to 54 Ω ; the voltage standing wave ratio (VSWR)

is less than 1.3. Construction of the amplifier is in progress.

References

- 1) N. Nakanishi and T. Kageyama: *RIKEN Accel. Prog. Rep.*, **19**, 197 (1985).
- 2) H. Kamitsubo: Proc. 11th Int. Conf. Cyclotrons and Their Applications, Tokyo, p.17 (1987).
- 3) T. Fujisawa, K. Ogiwara, S. Kohara, Y. Oikawa, I. Yokoyama, I. Takeshita, Y. Chiba, and Y. Kumata: *Sci. Papers I.P.C.R.*, **79**, 12 (1987).

V-10. Production of Multicharged Heavy Ions by PIG Source of RILAC

Y. Miyazawa, M. Hemmi, T. Chiba, and M. Kase

The production of multicharged heavy-ions of elements having mass numbers from 40 (calcium) to 208 (lead) has been examined on a test bench by using sputter PIG sources of an indirectly-heated cathode type. We reported last year the production of multicharged heavy ions with mass numbers below 74.¹⁾

The M/q spectra observed for Ca, Zn, Zr, Ag, Sn, Ta, W, and Pb are shown in Figs. 1–8. Argon or xenon was used as a support and sputter gas for arc discharge of the sputter PIG source. The sputter electrodes had different shapes for respective elements as shown in Figs. 1–8. For prevention of melting good thermal contact was essential between a sputter electrode and its clamp for low melting-point metals,

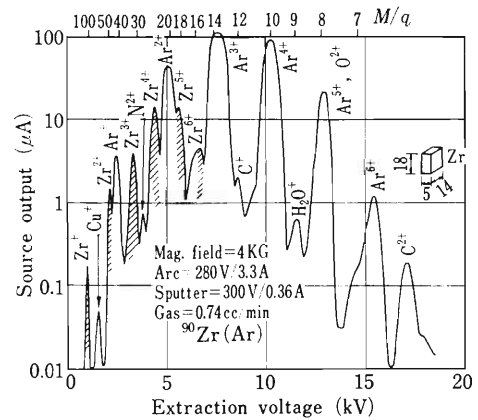


Fig. 3. M/q spectrum of Zr sputtered in argon discharge.

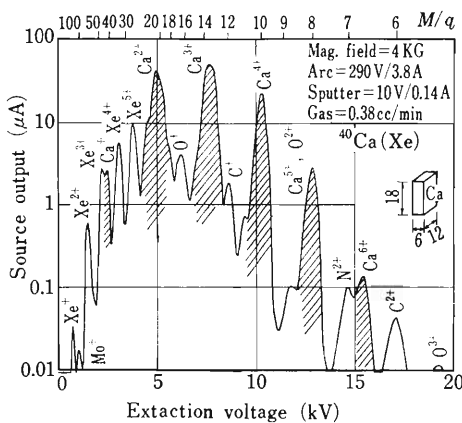


Fig. 1. M/q spectrum of Ca sputtered in xenon discharge.

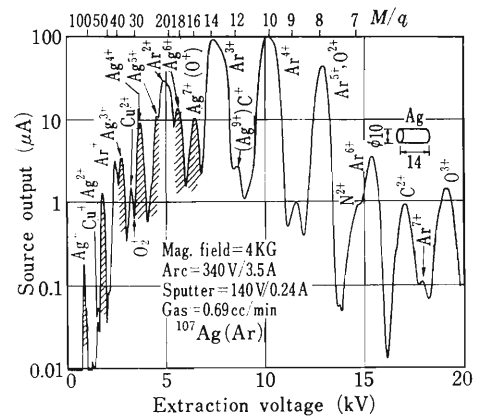


Fig. 4. M/q spectrum of Ag sputtered in argon discharge.

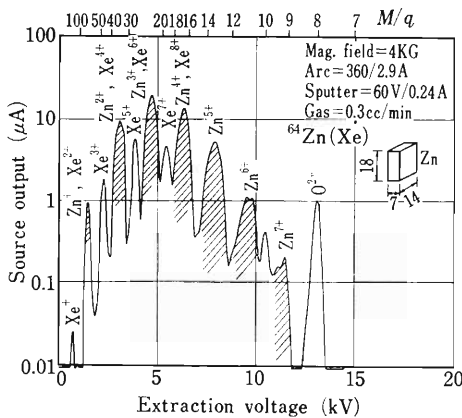


Fig. 2. M/q spectrum of Zn sputtered in xenon discharge.

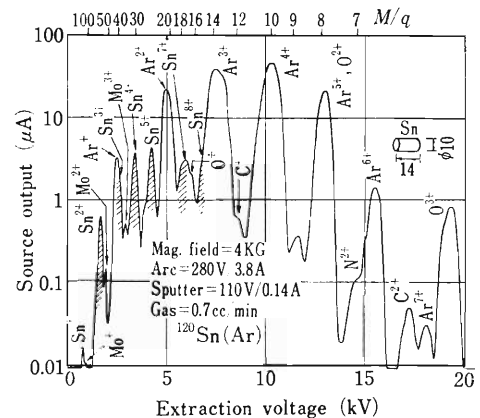
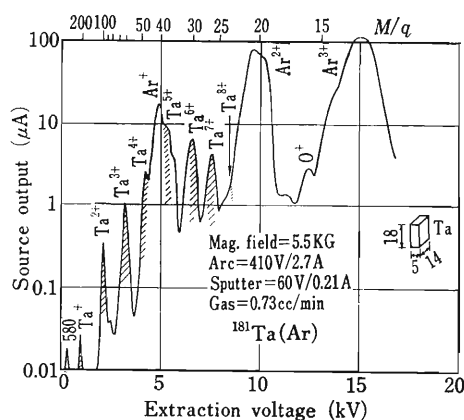
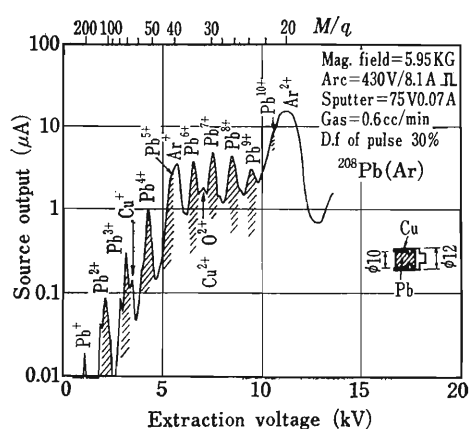
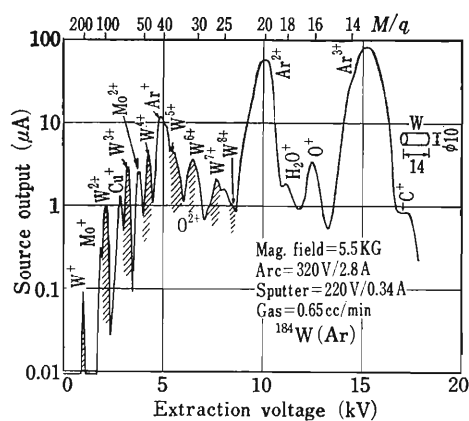


Fig. 5. M/q spectrum of Sn sputtered in argon discharge.

Table 1. Output currents of RILAC source (in $e\mu A$).

Element	Gas	Charge state									Arc
		1+	2+	3+	4+	5+	6+	7+	8+	9+	
Ca	Xe	2	40	50	22	—	0.14				DC
//	//	—	—	10	7	2	0.7	0.06	—		pulse
Zn	//	—	10	20	13	5	1	0.2			DC
Zr	Ar	0.17	1.5	3.8	14	13	4	—			//
Ag	//	0.18	1.2	3.4	9	10	14	8	—		//
Sn	//	0.02	0.6	—	3.6	4.2	—	3	—		//
//	//	—	0.1	—	0.8	1.3	—	1	0.3		pulse
Ta	//	0.02	0.3	1	2	—	6	4	—		DC
//	//	—	0.02	0.1	0.25	—	1.2	1.3	1		pulse
W	//	0.1	1	3	4	4	3.5	2	0.5		DC
Pb	//	0.02	0.1	0.3	1	—	3.6	4.8	4.3	1.5	pulse

* Gases used to support arc-discharge.

Fig. 6. M/q spectrum of Ta sputtered in argon discharge.Fig. 8. M/q spectrum of Pb sputtered in argon discharge. Arc discharge was operated at pulse with a duty factor of 0.3.Fig. 7. M/q spectrum of W sputtered in argon discharge.

such as Zn, Sn, and Pb. The sputter electrodes were machined to final dimensions except for Pb, which was prepared by molding.

Table 1 lists the output currents obtained with the ion sources. In the present experiment, we succeeded in detecting Ca^{7+} , Zn^{7+} , Zr^{6+} , Ag^{7+} , Sn^{8+} , Ta^{8+} , W^{8+} , Pb^{9+} . The dashed line in table shows the lower limit of the charge to mass ratios of ions which can be accepted by RILAC.

Reference

- 1) Y. Miyazawa, M. Hemmi, T. Chiba, and M. Kase: *RIKEN Accel. Prog. Rep.*, **20**, 195 (1986).

V-11. Development of an LCE Ion-Source

T. Kobayashi, T. Urai, and H. Sakairi

Figure 1 shows the LCE (lithium charge exchange) ion-source equipped originally to our TANDETRON. This ion source comprises a duoplasmatron ion source, an einzel lens, and a lithium-vapor cell. The positive ions produced by arc discharge in the duoplasmatron were converted to negative ions by double charge exchange in the lithium-vapor cell shown in Fig. 2.

In this cell the heater wires of the furnace being installed in a vacuum chamber, the loaded lithium is rapidly contaminated or oxidized by degassing the heaters. The heaters, on the other hand, are corroded by the lithium vapor faster than in a good vacuum. Such interference resulted in shorten-

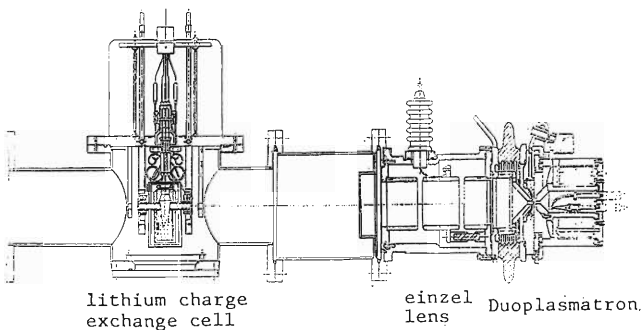


Fig. 1. Original LCE ion-source.

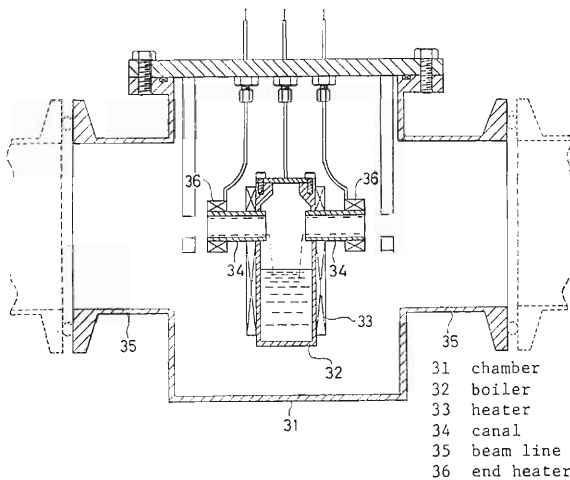


Fig. 2. Original (inner heating) LCE cell.

ing of the lifetimes of the loaded lithium and heaters. Moreover, use of the heaters in a vacuum requires a special terminal structure, expensive in preparation. In a new cell developed in our laboratory shown in Fig. 3, these problems were settled by winding heater wires outside the vacuum chamber to separate lithium from the heaters.

Another disadvantage occurs on the former cell

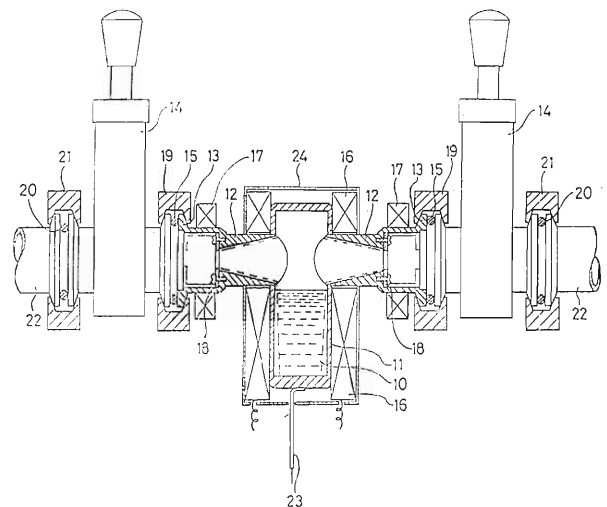


Fig. 3. New (outer heating) LCE cell.

Table 1. Comparison of the original charge exchange cell with the new one.

	Original, inner heating type	New, outer heating type
Difficulty in maintenance	large	small
Work for lithium loading	2 persons × 1 h	1 person × 0.5 h
Difficulty in operation	large	small
Start-up time	greater than 3 h	about 1 h
Interval of lithium loading	1 week	about 5 weeks
Stability	not so good	improved
Intensity of He ⁻		
Average	200 nA	500 nA
Maximum	1.5 μA	2.6 μA

when it is reassembled to the beam line after reloaded with lithium in argon atmosphere in a glove box. As the cell is equipped no gate valves it requires the greatest care not to expose the lithium to air in bringing the cell from the glove box to the beam line. The new cell, however, has a compact structure and is allowed to be set gate valves at both ends of

canal without any alteration of beam optics. This improvement makes easy in reassembling the cell.

The performances of the original and new cells are compared in Table 1. The beam intensity and the interval of lithium loading increased evidently and the maintenance became easier; the beam stability was also improved.

V-12. 6 GeV SOR Project

M. Hara and H. Kamitsubo

In the fiscal year 1987, RIKEN was given funds for technical research for the construction of a large synchrotron radiation facility and started research and development for a next-generation synchrotron radiation source.

The goals of this facility should:

- (1) be composed of a great number of long straight sections for undulators and wigglers;
- (2) provide high-brilliance photon beams (10^{17} photons/s mA mm² mrad² 0.1% b.w.); and
- (3) have long beam lines and ample space for experiments.

In designing the facility, future expansion is also taken into consideration. This facility is composed of a main storage ring, a booster synchrotron, a 1.5 GeV pre-injector linac, positron production linacs and others.

This year we have started the basic design, in which main efforts are laid on the lattice design. The main parameters of the ring should be determined from the requirements of users. Although user groups have not been fully organized yet, the energy is tentatively determined to be 6 GeV. The main photon sources are expected to be insertion devices as shown in Fig. 1. For stable photon beams, positron beams are to be stored and a full-energy injection system should be adopted. The storage ring is designed to

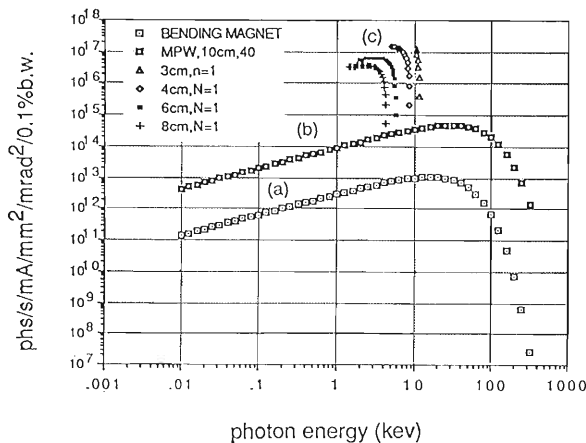


Fig. 1. Spectral brilliance of the 6 GeV synchrotron radiation source (a), $B_0=0.8$ T, dipole magnet; (b), $B_0=1.5$ T, $\lambda_u=10$ cm, total length 4 m multi-pole wiggler; (c), Undulator radiation, total length 4 m, fundamental mode, $B_r=1.25$ T, minimum gap=12 mm. Fundamental modes for $\lambda_u=3$ cm, 4 cm, 6 cm, 8 cm are shown.

satisfy the following conditions:

- (1) low emittance operation with ε_x less than 10 nm·rad;
- (2) a great number of long straight sections (7 m) for insertion devices;
- (3) a large dynamic aperture sufficient for injection;
- (4) having flexibility in the lattice configuration; and
- (5) being easy to construct.

For the 6 GeV storage ring, we have intensively investigated the double bend achromatic (Chasman-Green type) lattice which consists of two bending magnets, ten quadrupole magnets, and seven sextupole magnets per unit cell.¹⁾ The characteristics of accelerators, a storage ring, and a radiation source are listed in Tables 1–3. A low-emittance ring with many

Table 1. Accelerators.

Positron production linacs	200 MeV + 250 MeV
Electron (positron) linac	1.5 GeV
Synchrotron	6 GeV
Source ring	6 GeV

Table 2. Source ring characteristics.

Particle	electron, positron
Energy	6 GeV
Currents	100 mA
Bending magnet	0.8 T
Bending radius	25 m
Circumference	1,069.2 m
Periodicity	36
Energy width	0.001
Emittance horizontal	8.2 nm rad
Vertical	0.8 nm rad (10% coupling)
Harmonic number	1,800
rf Frequency	504.7 MHz
Bunch	single bunch, 25 n

Table 3. Light source.

Insertion devices	
Number of sources	30
Length of straight sections	7 m
Beam size horizontal	0.43 mm
Vertical	0.09 mm
Beam divergence horizontal	0.02 mrad
Vertical	0.01 mrad
Bending magnet source	
Number of source	(30)
Beam size horizontal	0.15 mm
Vertical	0.14 mm
Beam divergence horizontal	
Vertical	0.005 mrad

long dispersion-free straight sections can be obtained only by using strong quadrupole fields, thus resulting in high tune values and large natural chromaticities. The chromaticity should be corrected with sextupole magnets in the dispersive sections. The use of sextupole magnets, however, produces amplitude-dependent tunes, which make a beam unstable by driving harmful resonances and make a dynamic aperture small. In order to get rid of these harmful effects, additional sextupole magnets (harmonic sextupoles) are introduced. We analyzed the modified betatron motion with the sextupole magnets by a canonical perturbation theory. Using a tracking code, we intensively surveyed the electron behavior in the DFA lattice configuration, and found the lattice with a sufficiently large dynamic aperture. The betatron functions and the dispersion function of one of the lattice candidates are shown in Fig. 2, and the calculated dynamic aperture is shown in Fig. 3.

The synchrotron lattice was also investigated. A booster synchrotron was used to raise energy from 1.5 to 6 GeV for full energy injection to the storage ring. A simple FODO-type lattice¹⁾ with four dispersion-

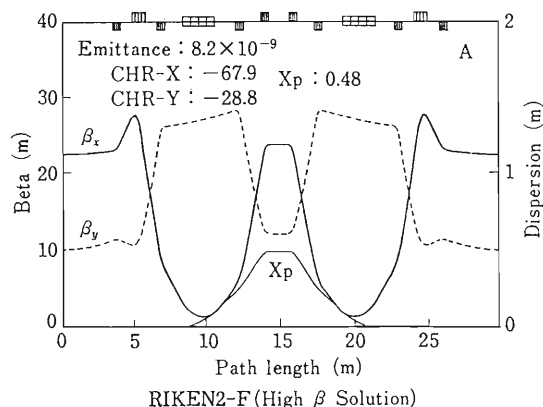


Fig. 2. Betatron functions and dispersion function for one of the lattice candidates (RIKEN 2-F high β).

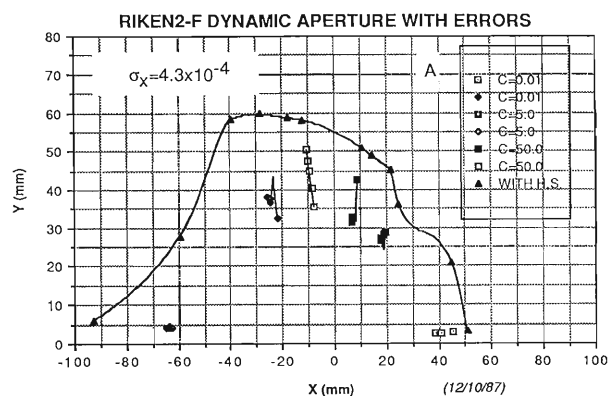


Fig. 3. An example of the calculated dynamic apertures (RIKEN 2-F).

Table 4. Booster synchrotron characteristics.

Energy	1.5–6 GeV
Lattice type	FODO
Circumference	342.145 m
Double rf system	504.7 MHz, 28.02 MHz
Number of cells	36
Number of straight sections	4
Emittance ϵ_x at 6 GeV	2.7×10^{-7} mrad

free sections was adopted. The dispersion is suppressed by removing a dipole magnet. Injection elements, extraction elements, and RF cavities are arranged in these dispersion-free straight sections. Although vertical tune can be adjusted in a wide range, horizontal tune can be changed only within a narrow range. This can be improved by allowing slight dispersion at the straight section. Chromaticity can be corrected using two families of sextupoles. A large dynamic aperture was obtained even with magnetic field and misalignment errors. For efficient injection, two RF system is under investigation. The main parameters are listed in Table 4. A beam flow is also investigated for two types of operations (e^- and e^+). Details are presented in this report.²⁾

The design of the RF system, the magnet system, and the vacuum system is also in progress. The RF parameters of the storage ring and the synchrotron are specified. The type of a cavity resonator has not been determined yet. We have many technical problems remaining unsolved. A test cavity was fabricated and subjected to investigation. Storage ring magnets were designed by using a computer code TRIM. The design of proto-types for dipole and quadrupole magnets was almost completed.

The design study of the vacuum system of the 6 GeV source ring was also performed. Very high synchrotron radiation power and its density make the vacuum system design difficult. In order to protect the vacuum system from high radiation power, crotches and absorbers are adopted, and basically the surface of the vacuum chamber is not directly exposed to the radiation. The crotch is located just downstream near the bending magnet and is equipped with three pumps (NEG, SIP, TSP) to trap photo-induced outgasses. Analysis to simulate the heat flow within the crotch was made by using finite-element models and was presented in this report.³⁾ The vacuum chamber of the main ring was investigated. For the materials of the chamber, stainless steel and aluminum are the candidates and are under investigation. As for the cross sectional shapes of the chamber, we are considering an antechamber type adopted at Argonne (APS). The pumping system is based on the NEG strips in the antechamber, a titanium sublimation pump, and a sputtering ion pump. Since we must use many vacuum components for the system, their reliability is very important. In order

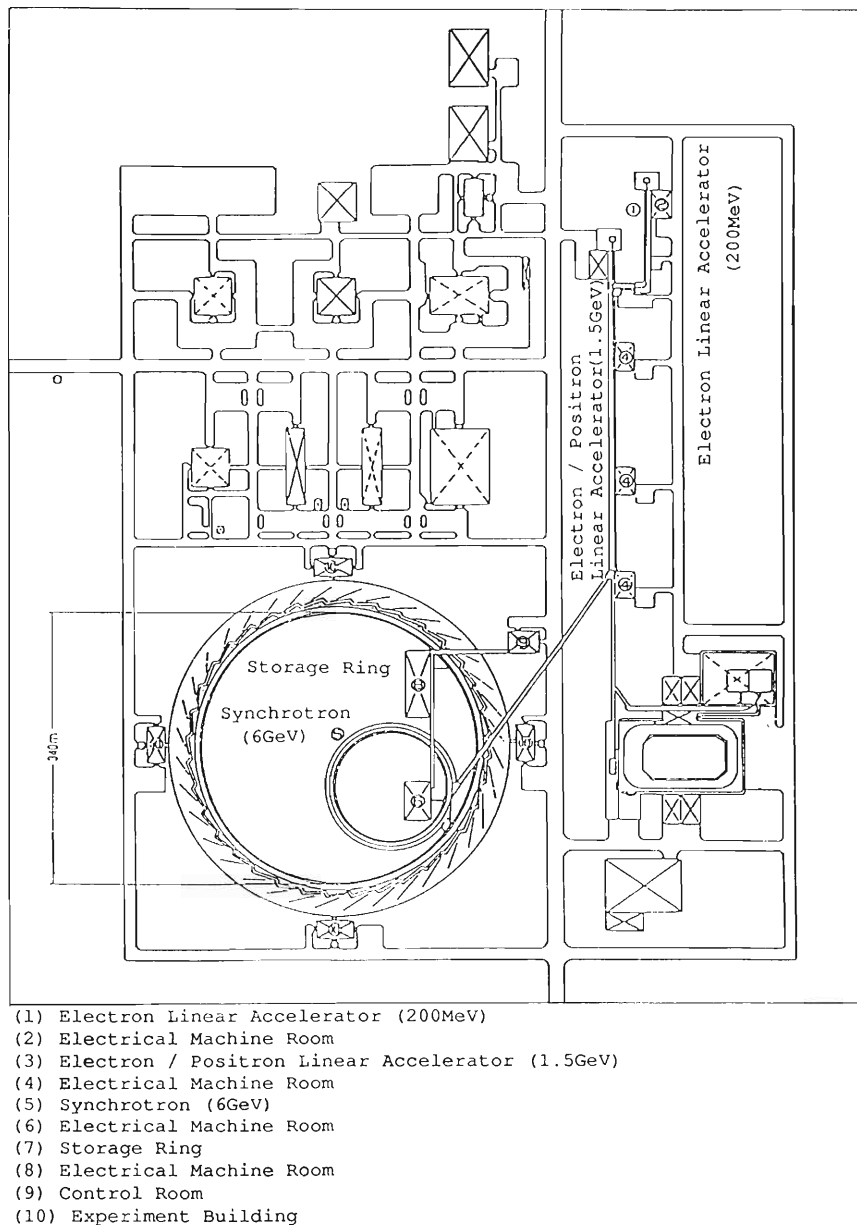


Fig. 4. An example of facility arrangements.

to investigate the performance characteristics of various vacuum components, a test device consisting of extruded aluminum alloy chambers were constructed.

In parallel with the design work, we have been granted the Special Coordination Funds for Promoting Science and Technology to construct a multipole wiggler at the Photon Factory of National Laboratory for High Energy Physics (KEK-PF) in cooperation with the KEK-PF group. This year we designed a 27-poles wiggler and the front end of the beam line, which were installed at the straight section between the bending magnets, B12 and B13, of the 2.5 GeV electron storage ring of KEK-PF.⁴⁾ The design was completed and are under construction.

At present, construction site has not been decided yet. The configuration of the facilities depends much

on the site. The site will be selected within 1988. In order to grasp an image, an example of the arrangement is shown in Fig. 4.

We have many research and development problems in constructing the synchrotron radiation source and will need three years for research and development from 1987 followed by five years for construction.

References

- 1) H. Tanaka, R. Nagaoka, and M. Hara: p.225 in this report.
- 2) H. Miyade, K. Yoshida, K. Tsumaki, and M. Hara: p.233 in this report.
- 3) Y. Morimoto, S. Yokouchi, H. Sakamoto, and S.H. Be: p.247 in this report.
- 4) S. Anami, H. Kitamura, Y. Kamiya, and T. Nakajima: Photon Factory Activity Report 1984/85, p.6.

V-13. Design of the Booster Synchrotron Lattice

K. Tsumaki, K. Yoshida, H. Tanaka, R. Nagaoka, and M. Hara

The booster synchrotron was designed under the specifications shown in Table 1. The synchrotron lattice has four super periodicity, and the lattice of a super period consists of normal cells and a straight section where a dispersion function is suppressed by a missing dipole (Fig. 1). The straight section is used for setting injection, extraction elements, and rf cavities.

Only two families of quadrupole magnets QF and QD are used to make the system simple. In this case, the stability region of betatron oscillation is represented by a necktie diagram, but the condition that the straight section must be a dispersion free section restricts the operational region and the possible region is only on the solid line as shown in Fig. 2. When the operating point moves on the solid line, the tune changes as shown in Fig. 3, from which one can see that the horizontal tune can be changed only from 10.2 to 10.45, while the vertical tune can be changed from 3.4 to 12.1. However, if a small value of dispersion function at the straight section is permitted, the horizontal fractional tune is easily changed to the upper half region (0.5–1.0). When the maximum value of the dispersion function at the straight section

is 0.1 m, the solution is represented by the dotted line in Fig. 2, and the fractional tune moves to the upper half as shown by the dotted line in Fig. 3.

For simplicity, a operating point is so chosen that the quadrupole magnets QF and QD have the same strength. The betatron function and the energy dispersion function are shown in Fig. 4, and the major parameters are shown in Table 2.

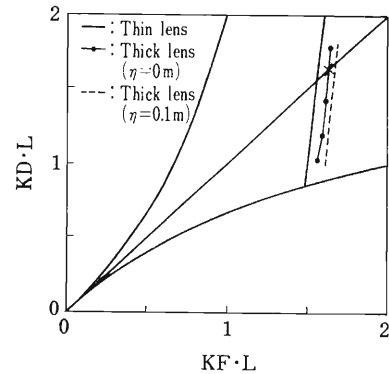


Fig. 2. Operational region on the necktie diagram. X, Operating point: $KF = B' \cdot l_q / B \rho$; l_q , Length of quadrupole magnet; L , Distance between the two adjacent quadrupole magnet.

Table 1. Specifications of the booster synchrotron.

Item	Specification
Acceleration energy	1.5–6 GeV
Magnet lattice	FODO
Number of straight section	4
Number of cell	36

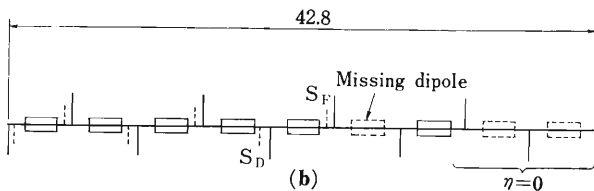
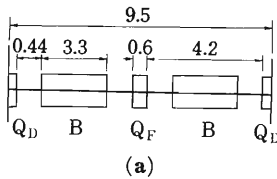


Fig. 1. (a) Normal FODO cell (B, bending magnet; QF and QD, quadrupole magnets). (b) Lattice configuration of 1/2 superperiod (SF and SD, sextupole magnet).

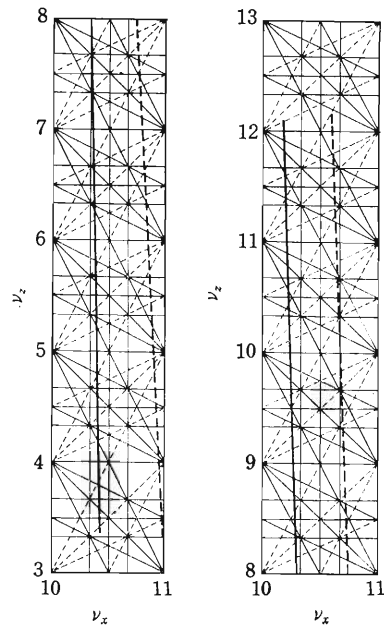


Fig. 3. Possible operating region on the tune diagram. —, $\eta = 0 \text{ m}$; ---, $\eta = 0.1 \text{ m}$.

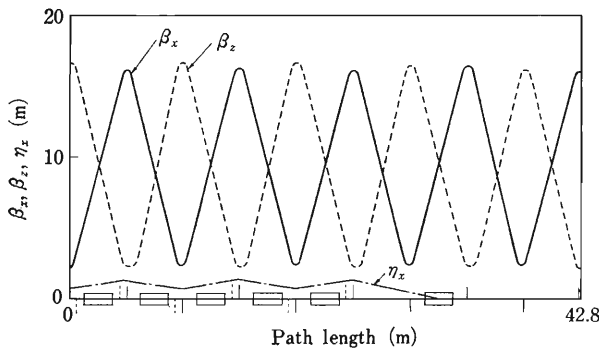


Fig. 4. Betatron and energy dispersion function.

Table 2. Major parameters of the booster synchrotron.

Energy E (GeV)	6
Maximum bending field B (T)	0.8
Strength of quadrupole magnet KF (m)	0.343
KD (m)	0.343
Tune ν_x	10.232
ν_z	10.419
Momentum compaction α	0.015
Circumference C (m)	342.145
Natural chromaticity ζ_x	-14.2
ζ_z	-14.3
Energy loss UO (MeV/rev)	4.59
Damping time τ_x (ms)	3.0
τ_z (ms)	3.0
τ_θ (ms)	1.5
Emittance ε (π mrad)	2.7×10^{-7}
Harmonic number h	576
R.F. voltage V_{rf} (MV)	9
R.F. frequency f_{rf} (MHz)	504.7

To avoid the head-tail instability, the chromaticity correction is applied by means of two families of sextupoles SF and SD, and the resulting dynamic aperture was calculated by the particle tracking for the following three cases: (1) no error, (2) with errors, and (3) with momentum deviation. In case of errors, the tracking was done under the conditions shown in Table 3. The results are shown in Fig. 5. The dynamic apertures of all three cases were larger than the aperture of a vacuum chamber, and no problems were found.

When the strength of dipole magnet fields is changed, the sextupole fields are induced due to the

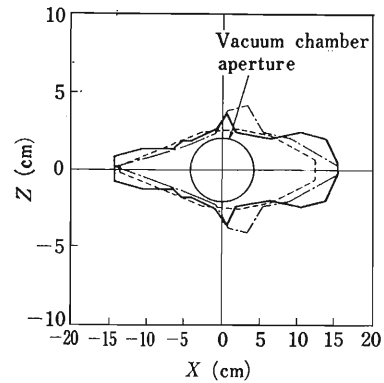
Fig. 5. Dynamic aperture. —, no error; ---, with errors; - · -, $\delta p/p=1\%$.

Table 3. Tracking condition for the case of errors.

Error		Strength
Bending magnet	Field uniformity $\delta B/B$	$\pm 1 \times 10^{-3}$
	Rotation error $\delta\theta$ (mrad)	0.5
Quadrupole magnet	Setting error $\delta x, \delta z$ (mm)	0.1
	Field gradient error $\delta K/K$	1×10^{-3}
	Skew $\delta\theta$ (mrad)	1

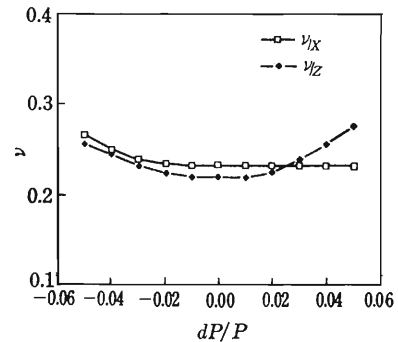


Fig. 6. Momentum dependence of tune.

eddy currents in the vacuum chamber. However, the chromaticity generated by this effect is of the acceptable order of 1 at most for the slow change in the magnetic field of a bending magnet.

The momentum dependence of tune is shown in Fig. 6. For the particles, the energy deviation of which is within $\pm 2\%$, the tune variations were less than 0.005; this is quite acceptable.

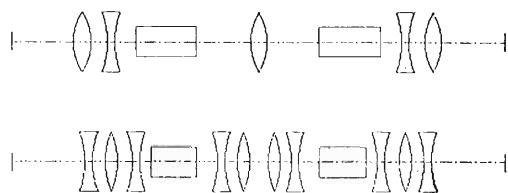
V-14. Lattice Design for a 6 GeV Storage Ring

H. Tanaka, R. Nagaoka, and M. Hara

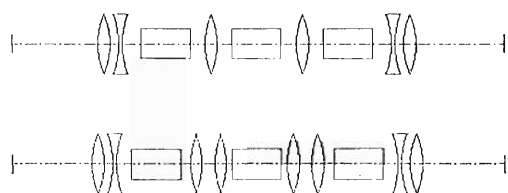
The lattice design for a 6 GeV storage-ring was studied. Following performance conditions are required for this lattice.

- a dispersion-free long straight section (about 6–7 m)
- low emittance (≤ 10 nmrad)
- tunability of β configuration at the straight section
- a large dynamic aperture even with practical errors
- operation flexibility

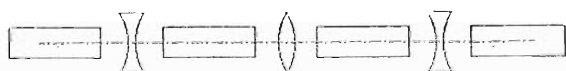
CHASMAN GREEN (Double Bend Achromat)





TBA (Triple Bend Achromat)



FODO



 : Bending Magnet

 : Focusing Quadrupole Magnet


 : Defocusing Quadrupole Magnet

Fig. 1. Lattice types for a low-emittance ring.

Most efforts are concentrated in optimizing these requests which frequently conflict with each other.

There are three typical lattice types (Fig. 1) for a low-emittance ring. The most suitable type of lattice must be selected as a 6 GeV low-emittance lattice among these candidates after careful investigation and comparison. As a first step to make comparison among three lattice types, a Chasman Green (CG) lattice was studied in detail along a following design flow.

CG Lattice design flow

Step-1 According to the doubly achromat conditions, a dispersive area structure (drift arrangement and quadrupole magnets strength) is decided.

Step-2 Based on constraints[†] for drift arrangement, a dispersion free area structure is decided.

Step-3 Twiss parameter matching is made with the computer code SYNCH on many different conditions of β_x and β_y at the straight section remarking a location of the crossing point of β_x and β_y at a dispersive area and emittance. (From the viewpoint of chromaticity correction, it is better that the crossing point of β_x and β_y is located between two chromaticity correction sextupoles).

Step-4 Tune and emittance are adjusted. Concerning tune, a workpoint is selected carefully to avoid first- and third-order resonances driven by sextupoles.

Step-5 Coefficients of amplitude dependent tune-shift are checked. If coefficients are bigger than criteria, go back to Step-2.

Step-6 Harmonic sextupoles and chromaticity correction sextupoles are optimized to suppress the resonance driving term.

Step-7 Dynamic aperture is calculated in both ideal case (no error) and practical case (including errors) with a computer code RACE-TRACK, and behavior of dynamic aperture is analyzed.

[†] Constraints of drift arrangement in our case

- long drift sections (about 1 m) are obtained at both side of bending magnet for crotch and bumper magnet of injection;
- 0.2 m is taken as a minimum drift section between two magnets; and
- a dispersion free straight section = 7.0 m

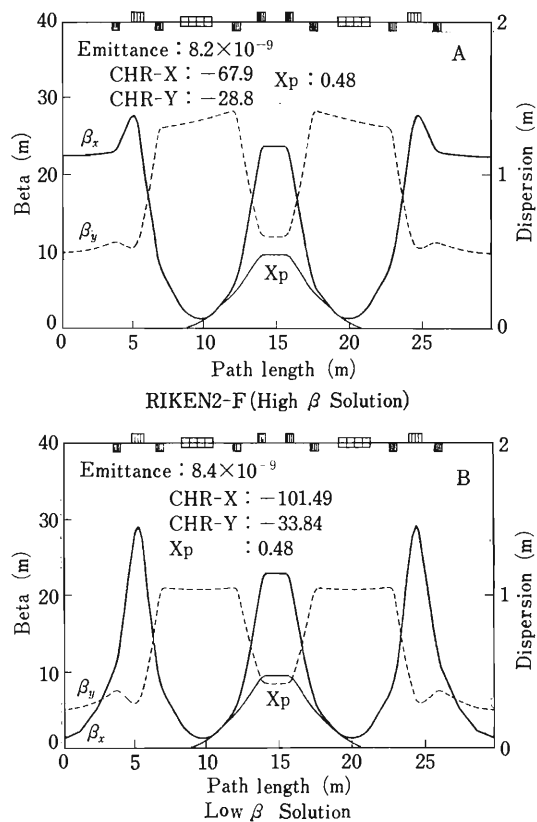


Fig. 2. RIKEN tentative CG lattice candidates (1). CHR-X and Y represent horizontal and vertical chromaticity, respectively; and X_p represents horizontal dispersion.

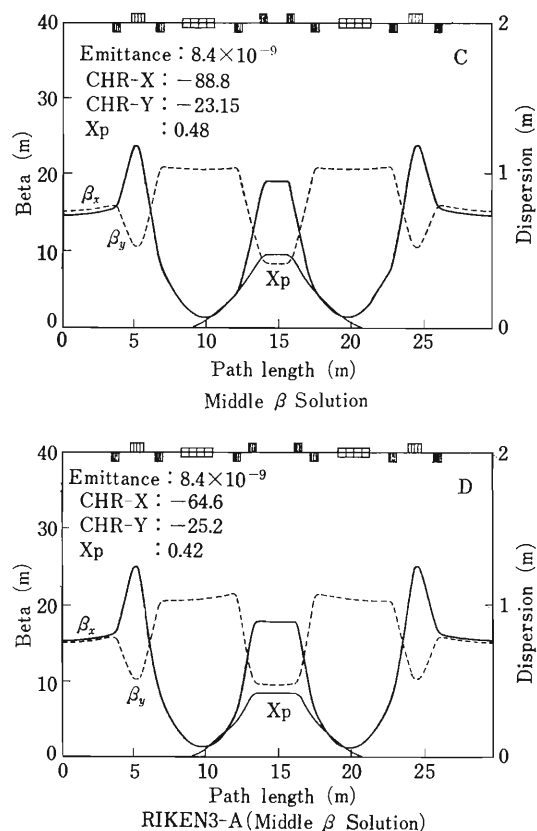


Fig. 3. RIKEN tentative CG lattice candidates (2). CHR-X and Y represent horizontal and vertical chromaticity, respectively; and X_p represents horizontal dispersion.

RIKEN tentative CG lattice candidates for high β , low β , and middle β designed along the CG lattice design flow described above and lattice parameter are shown in Figs. 2 and 3 and Table 1. The number of cells is determined from the viewpoint of request of emittance (≤ 10 nmrad). The length of a unit cell and circumference are 29.7 m and 1,069.2 m respectively. Quadrupole doublet in the dispersive area is adopted to adjust a dispersion value and also a quadrupole triplet in a dispersion free area is adopted to adjust β configuration at the straight section and tune per cell.

The tune diagram is shown in Fig. 4, from which fetal resonance lines driven by sextupoles ($\nu_x = 36 N$, $3\nu_x = 36 N$, $\nu_x \pm 2\nu_y = 36 N$) are found to be far from working points.

The dynamic aperture corresponding to each lattice candidate is shown in Figs. 5 and 6 with other ones which were presented by ESRF and APS. Tracking condition for dynamic aperture calculation is shown in Table 2. In spite that RIKEN tentative lattice

Table 1. Ring parameters of RIKEN tentative CG lattice candidates.

Beam energy	6.0 GeV
Beam current	$1 \geq 100$ mA
Natural emittance	$8.2 \times 10^{-9} - 8.4 \times 10^{-9}$
Circumference	1,069.2 m
Cell No.	36
Length of cell	29.7 m
Length of straight section	7.0 m
Damping time (Horizontal)	9.3 ms
(Energy)	4.7 ms
Bending radius	25.0 m

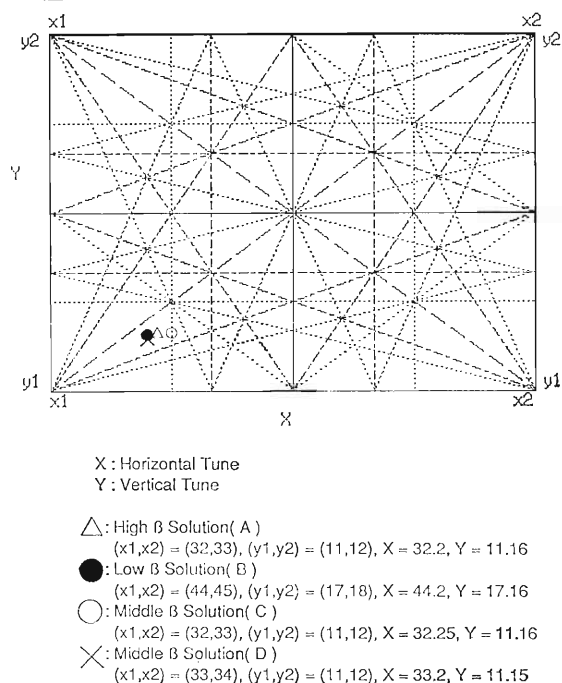


Fig. 4. RIKEN tentative lattice tune diagram.

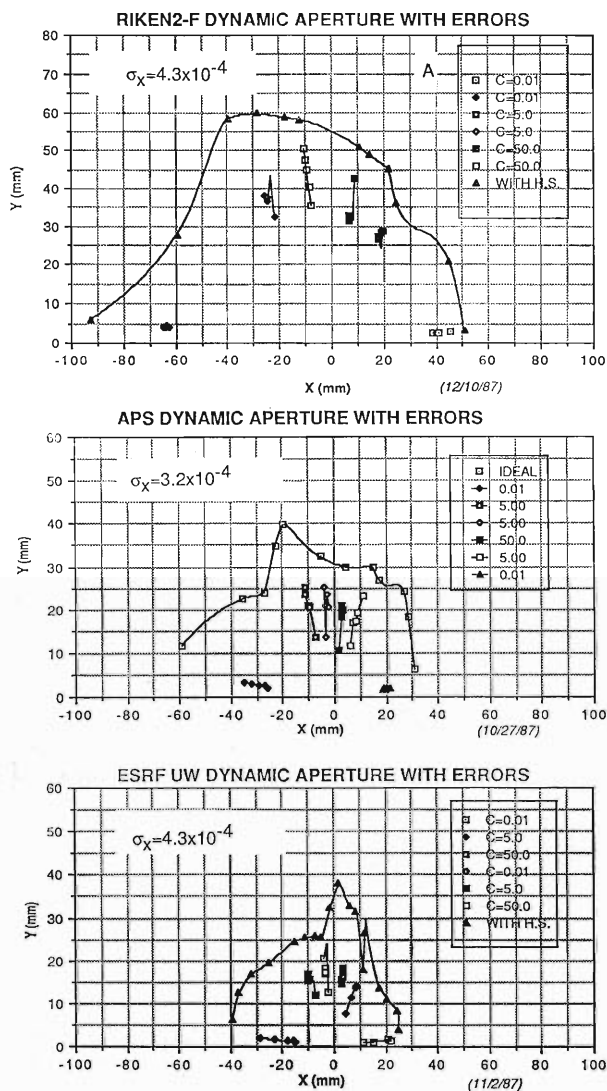


Fig. 5. Comparison of dynamic aperture among three lattice.

Table 2. Tracking condition for dynamic aperture calculation.

(1) Tracking code	: RACETRACK
(2) Turn No.	: 500 turn
(3) Tracking initial condition	: $X'=0, Y'=0$
(4) Tracking particle No.	: 1 particle
(5) Error condition	
(a) Error input style	: random
(b) Kind of error	
Misalignment at Q magnet	5×10^{-5} m
Bending field error (dB/B)	2.5×10^{-4}
Bending tilt error	2.5×10^{-4} rad
.....	
Gradient error	
(d(DB/DX)/(DB/DX))	2.5×10^{-4}
Q magnet tilt error	5.0×10^{-4} rad
(6) In the case that errors are distributed in the ring, tracking is done without COD correction	

candidates have emittance of lower than 10 nmrad, they have a large dynamic aperture ($>$ about $50\sigma_x$) even in both ideal case (no error) and practical case (including errors). It will be studied whether the dynamic aperture is sufficient for beam injection and

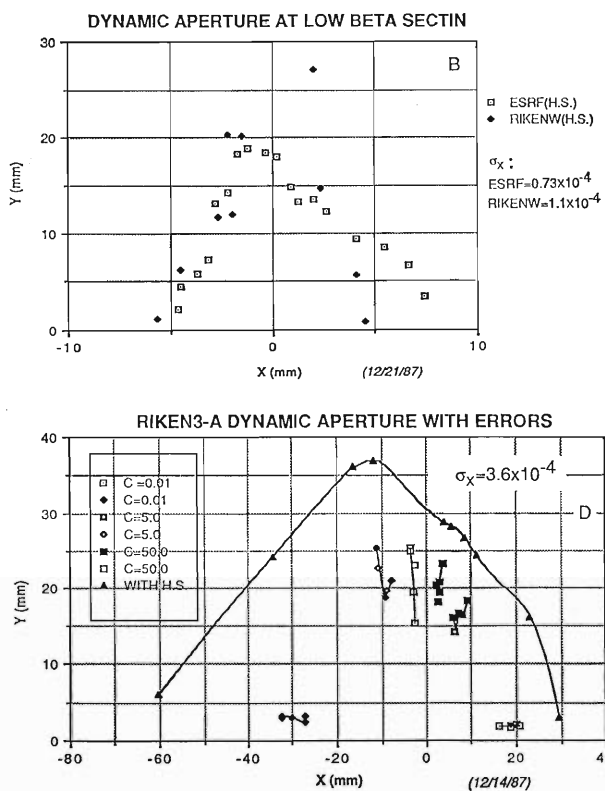


Fig. 6. Dynamic aperture of RIKEN tentative CG lattice candidates.

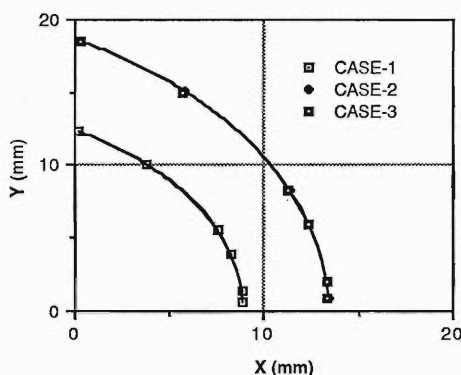


Fig. 7. An example of dynamic aperture recovery by COD correction.

for the ring installed many insertion devices and distributed multipole magnet errors and other different conditions.

In a real ring, COD is corrected with a monitor and corrector system, so the dynamic aperture is expected to have a certain value between ideal and practical case according to the level of COD correction. The COD correction is simulated by RACETRACK and its result is shown in Fig. 7. With COD correction, the dynamic aperture is almost recovered. It is ascertained from the present results that COD correction by a monitor and corrector system is very important for a low emittance ring.

V-15. Chromaticity Correction in the Low-Emittance Chasman-Green Lattice

R. Nagaoka, H. Tanaka, and M. Hara

The “dedicated” storage rings should be able to accumulate, in general, a low-emittance beam for a long period of the operation time. Due to the following relation, however, the low-emittance and the large stability of the motion cannot be simply met simultaneously: The low-emittance condition necessarily demands a large value of the horizontal betatron tune ν_x , since the emittance is roughly proportional to third power of the inverse tune. This implies the presence of strong quadrupole magnets, which in turn calls for stronger sextupole magnets to correct the larger linear chromaticity. In Fig. 1 is shown the momentum dependence of the betatron tunes in the absence of the linear chromaticity correction. With the sextupole magnets, the large amplitude betatron motions of the particles are greatly influenced by their non-linear fields and in many cases become quite unstable due to harmful resonances driven by these elements.

To recover the stability of the betatron motion, analysis must be made of the motion under sextupole fields. Since sextupole fields enter the equation of motion as quadratic, one can no longer rely on the usual linear optics theory. Here, we follow what is called the “canonical perturbation theory” to describe the modified betatron motion perturbed by the sextupoles.^{1,2)}

When the sextupole potential enters as a perturbation to the Hamiltonian system, the action variable

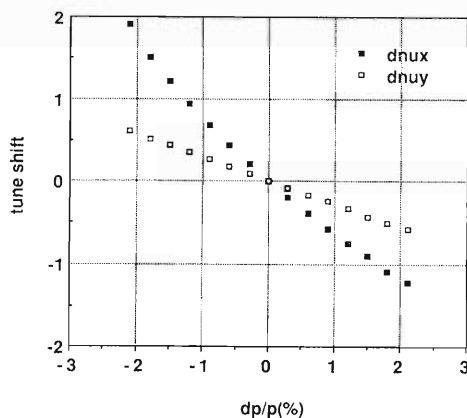


Fig. 1. Momentum dependence of the betatron tunes without chromaticity correction.

becomes no longer an invariant. The spirit of the canonical perturbation theory is to perform systematic transformation of the canonical variables so that the action becomes approximately an invariant. Within the first-order formulation, one then finds the following “amplitude-dependent tune shift formulae.”

$$\Delta\nu_{xc} = C_{11} \cdot 2J_x + C_{12} \cdot 2J_y \quad (1)$$

$$\Delta\nu_{yc} = C_{21} \cdot 2J_x + C_{22} \cdot 2J_y \quad (2)$$

where ν_{uc} ($u = x, y$) is the tune per cell, $\Delta\nu_{uc}$ is the corresponding shift, and J_u denotes the action variable. Coefficients C_{ij} ($i, j = 1, 2$) can be expressed analytically. Using the harmonic expansion, the expression for C_{11} reads, for example,²⁾

$$C_{11} = -18 \cdot \sum_{m=-\infty}^{\infty} \left(\frac{A_{3m}^2}{3\nu_{xc} - m} + \frac{3A_{1m}^2}{\nu_{xc} - m} \right) \quad (3)$$

It is worth noting that coefficients A_{jm} ($j = 1$ or 3) depend on the sum of strength and location of the sextupole magnets. Remaining C_{ij} have similar expressions. One finds that the larger the C_{ij} , the greater will be the tune shifts leading to unstable betatron motions. Amplitude dependent tune shifts are sensitive to the resonances induced by the sextupoles as seen in Eq. 3.

Figure 2 illustrates the configuration of the Chasman-Green (CG) type lattice which is under consideration. Important point is that, as suspected from the shape of β_x , horizontal tune per cell comes close

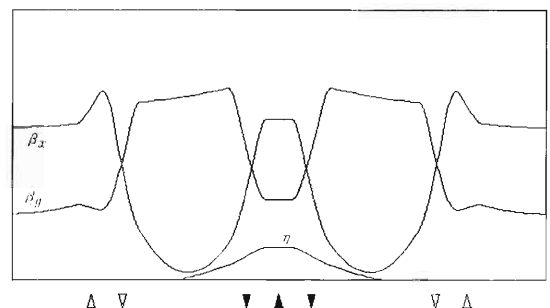


Fig. 2. Beta and dispersion functions for Chasman-Green cell. Dark triangles indicate chromaticity correcting sextupoles, and white ones the harmonic sextupoles.

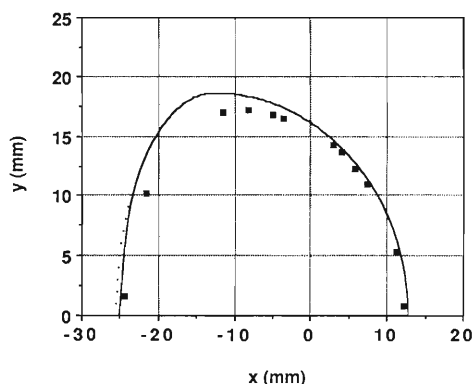


Fig. 3. Comparison of the theory and tracking in the dynamic aperture calculations. No harmonic sextupoles are included.

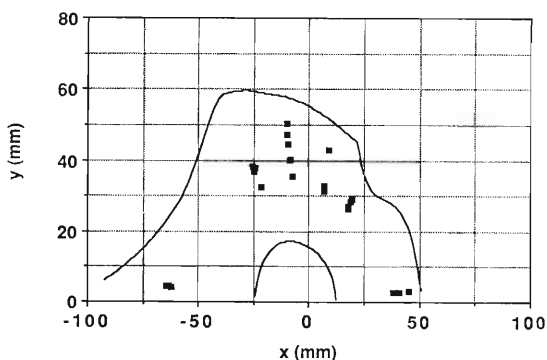


Fig. 4. Dynamic aperture obtained from tracking a particle over 500 turns. Outer and inner curve represent results with and without the harmonic sextupoles, respectively. Dark squares are those including random errors.

to unity which results from achieving the low-emittance. Under such circumstances, we can expect tune shifts to be dominated by the resonances $\nu_{xc} = 1$, and $3\nu_{xc} = 3$, which are of the order one and three, respectively. In fact, this was verified from the numerical analysis. Dominance of the above two components can also be realized from Fig. 3 where comparison of the dynamic aperture is made between the theory and tracking. Prediction of the theory is based on the simplified Hamiltonian which only takes account of the contributions of the above resonances.

Knowing the origin of the instability and that they are much localized, it may be possible to recover the stability by adding few families of sextupoles in the lattice so as to cancel the harmful effect. Two families of "harmonic sextupoles" as they are called are tried in our case (see Fig. 2). Although the locations of these magnets are another freedom, they

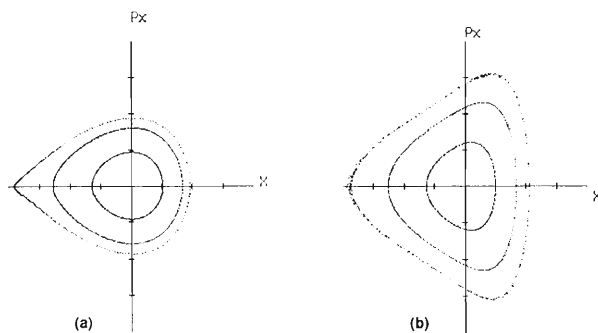


Fig. 5. Phase space of the horizontal betatron motion calculated at the straight section. (a): without harmonic sextupoles, (b): with harmonic sextupoles.

were fixed in our present case study and their strengths were numerically searched to minimize the magnitudes of the coefficients C_{ij} ($i, j = 1, 2$). In most cases, the strengths converged at moderate values, whereby the resultant magnitudes of C_{ij} were reduced roughly by the order of two. We show in Fig. 4 the dynamic aperture obtained after optimizing the harmonic sextupoles. One observes a drastic improvement of the stability. Also demonstrated is the tracking result for five machines including random errors. (Field error of 0.025%, and as much as 0.05 mm of quadrupole magnet misalignment are taken into account.) In the result shown, the dynamic aperture is still adequately large even with errors. According to our analysis, however, the behavior of the ring against errors has a deep connection with the properties of the ideal lattice and is certainly a subtle problem. We believe further study is required on this subject. Typical changes of the phase space behavior before and after the correction are displayed in Fig. 5. Characteristic shapes of the curves indicate that before correction, the horizontal motion is ruled by the first-order resonance, while it disappears after correction and the motion is affected by resonances of the third-order.

To sum up, we have been able to restore the stability of the betatron motion by the aid of two families of harmonic sextupoles. Routine for optimization relied greatly on the specific situation met with the low-emittance CG lattice. We have interest to extend the analysis to other type of lattices and we hope to do so in future.

References

- 1) H. Wiedemann: PEP-220, 1976.
- 2) E. A. Crosbie: ANL-HEP-CP-87-21.

V-16. Design Study of the Magnets for a Storage Ring

S. Motonaga, T. Kasahara, and Y. Yamagishi

A storage ring is designed with a Double Bend Achromat Chasman Green Lattice.¹⁾ It is aimed at the storage of electrons with an energy of 6 GeV injected from a synchrotron.²⁾ The magnet lattice consists of 36 unit cells, each composed of 2 dipole magnets and 10 quadrupole magnets in the principal, and 7 sextupole magnets used for the chromaticity correction; thus total amount of the magnets constituting the magnet lattice is 72 dipole magnets, 360 quadrupole magnets, and 252 sextupole magnets. The orbit characteristics of the storage ring are given elsewhere in this progress report.¹⁾ The aperture of the magnet required for a good flat field is 70 mm in the horizontal (X) and 30 mm in the vertical direction. The requirement for field quality of the dipole and quadrupole magnets is serious to get a good beam.¹⁾ Guidelines of the required field quality are given in Table 1.

In order to design these magnets, we carried out numerical calculations of magnetic fields by using the program code TRIM. Figure 1 shows the cross sectional views of the dipole and quadrupole magnets designed to be optimum. The parameters used in these calculations are given in Fig. 1. Ten quadrupole

Table 1. Required field quality of the dipole and quadrupole magnets.

Magnet	Dipole magnet	Quadrupole magnet
Field strength	0.8 T	15 T/m, 14 T/m, 10 T/m
Gap distance or bore radius	0.062 m	0.04 m
Bending radius	24.98 m	
Bending angle	5	
Uniformity		
Field strength or gradient	$\Delta B_{(X)}/B_{(X=0)} < 1.5 \times 10^{-4}$	$\Delta G_{(X)}/G_{(X=0)} < 1 \times 10^{-8}$
	$X = \pm 37$ mm	$X = \pm 35$ mm
	$Y = \pm 14$ mm	$Y = \pm 14$ mm
Effective length of field	$\Delta Bl_{(X)}/Bl_{(X=0)} < 2 \times 10^{-4}$	$\Delta Gl_{(X)}/Gl_{(X=0)} < 2.5 \times 10^{-8}$

$\Delta B_{(X)}/B_{(X=0)}$, $\Delta G_{(X)}/G_{(X=0)}$ indicate variations in field strength and field gradient, respectively, $\Delta Bl_{(X)}/Bl_{(X=0)}$, $\Delta Gl_{(X)}/Gl_{(X=0)}$ also indicate variations in integrated field strength (effective field length) and integrated field gradient, respectively.

magnets in a unit cell were divided into three groups according to their field strength and core length. The cross sections of these magnets are identical.

For the dipole magnet we calculated various pole widths, shim geometries, and the optimum geometry

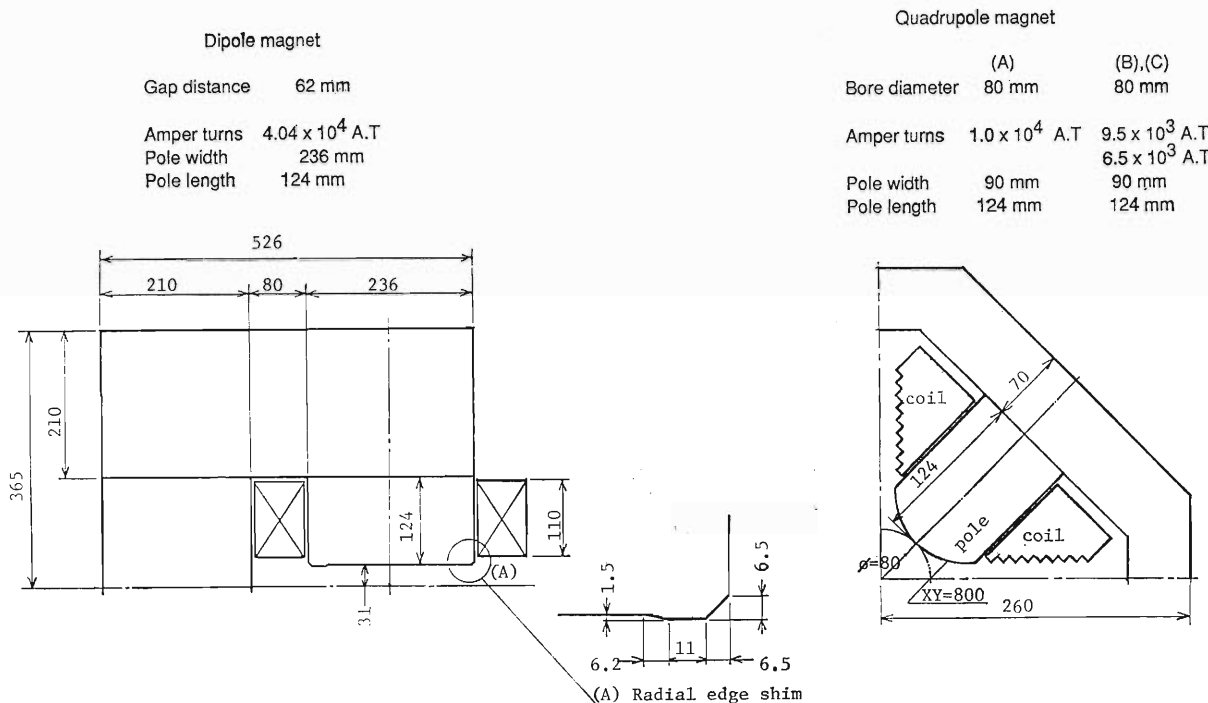


Fig. 1. Cross sectional views of the dipole and quadrupole magnets for the calculation.

which gives a desired field distribution. The magnet is of the C-shaped rectangular type as shown in Fig. 1. The pole is flat over the horizontal range of ± 104.3 mm and has radial shims of 1.5 mm in thickness at both ends. The ratio of cross-sectional area of the yoke to that of the pole base is 0.89. The ampere-factor, which indicates the degree of saturation of the iron core, is 1.25 percent at $=0.81$ T. Calculated radial field distributions normalized at the center of the dipole magnet are shown in Fig. 2. The flat field region within a radial variation $\Delta B/B = 1.0 \times 10^{-4}$ is expected over an aperture of $X = \pm 60$ mm and $Y = \pm 15$ mm.

As the first step for choosing the optimum pole profile, the calculation carried out on the quadrupole magnet having a completely four-fold symmetry as shown in Fig. 1.

In order to enlarge a flat field gradient region and to suppress higher multipole fields, the pole profile is shaped along a hyperbola. Radial field distributions calculated for the quadrupole magnets are shown in Fig. 3a. The field gradient of 15 T/m is achieved at a magnetomotive force of 1.0×10^4 ampere turns per pole; this magnetomotive force is 5% higher than the value calculated by assuming infinite permeability. This difference shows that the effect of saturation in the iron core is large at this field gradient; therefore, a yoke width will be wider by more than 10% of this design. The magnetomotive force of 1.0×10^4 A. T is adequate at the real magnet. Figure 3b shows the variation in field gradient in the radial direction for two pole widths of 80 mm and 90 mm. The distributions of the field gradient are normalized at a radius of 25 mm, because the calculation introduces a field

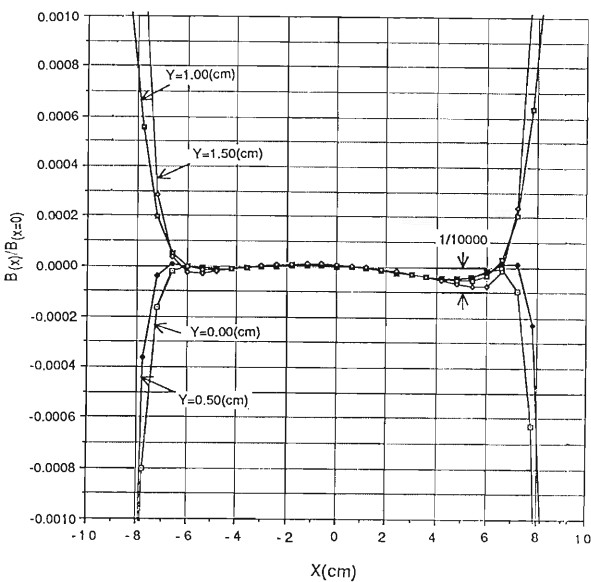


Fig. 2. Calculated radial field distribution of the dipole magnet. Field distribution is normalized at the center ($x=0$).

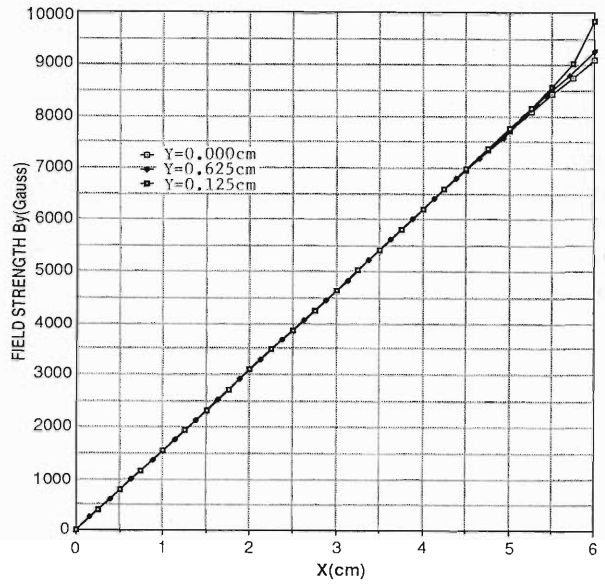


Fig. 3a. Calculated radial field distribution of the quadrupole magnet.

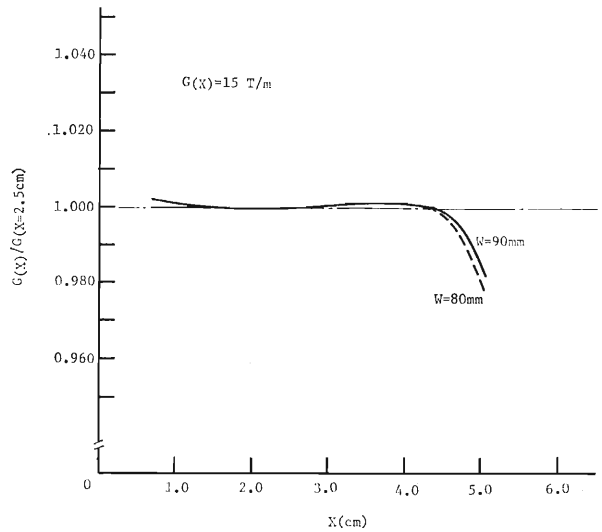


Fig. 3b. Variation of calculated field gradient of the quadrupole magnet for the pole widths of 80 mm and 90 mm.

error at the central region caused by mesh plots of the TRIM.³⁾ Difference in the field quality can not be distinguished in both cases of the pole width considering the accuracy of the calculation. The flat region of the field gradient is wide enough. The radial variation in the field gradient at 15 T/m is shown in Fig. 4. The pole has a hyperbolic shape and a width of 90 mm. The flat region of the field gradient within 1.0×10^{-3} is expected over an elliptical area of $X = \pm 35$ mm and $Y = \pm 12.5$ mm.

As described above, the geometry of the quadrupole magnet used in the calculation is completely four-fold symmetry. In the real quadrupole and sextupole magnets, however, a vacuum chamber having an antechamber will be installed as shown in Fig. 5a.

The top and bottom halves of the quadrupole magnet are jointed through a non-magnetic metal as shown in Fig. 5a. Therefore, the structure is not completely four-fold symmetric, magnetic flux does not cross the median plane of return yoke, and unwanted dipole and higher multipole fields will increase in the quadrupole and sextupole fields. However, from the calculation carried out by assuming the structure as shown in Fig. 5b, the variation in the field gradient was found almost the same as that for the completely symmetric structure. The detailed design

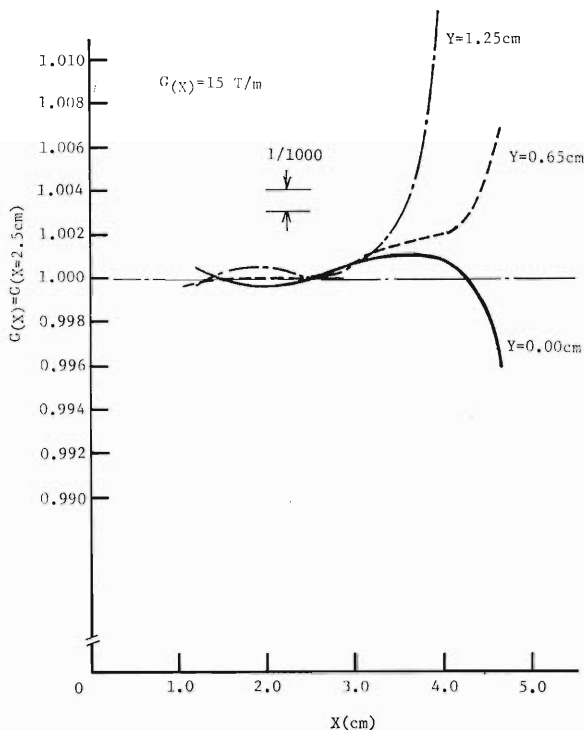


Fig. 4. Variation of calculated field gradient of the quadrupole magnet at 15 T/m.

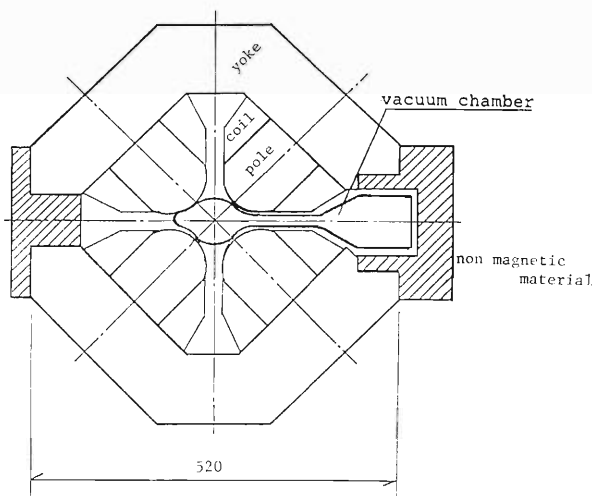


Fig. 5a. Cross sectional view of the quadrupole magnet in which a vacuum chamber with an antechamber is installed.

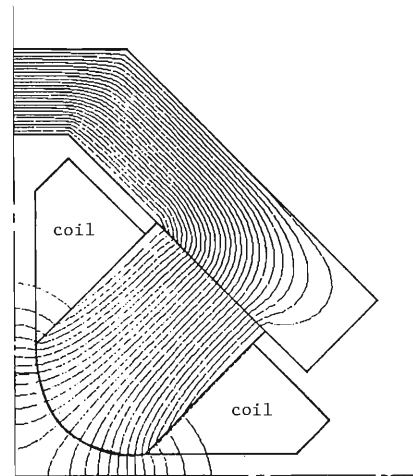


Fig. 5b. Cross sectional view of the quadrupole magnet for calculation. The yoke core at the median plane is removed.

Table 2. Specifications of the prototypes of dipole and quadrupole magnets.

	Dipole magnet	Quadrupole magnet
Core length	2,114 mm	865 mm
Gap distance	62 mm	80 mm
Pole length	124 mm	124 mm
Pole width	236 mm	90 mm
Magnet height	730 mm	500 mm
Magnet width	526 mm	610 mm
Amper turns	4.04×10^4 A.T	1×10^4 A.T
Conductor	11.5 × 17.5 mm, 5 mm	6 × 6 mm, 3 mm
Redistance	0.018 ohm at 40°C	0.4 ohm at 45°C
Max current	900 A	140 A
Max. voltage	16.3 V	55 V
Consumption power	15 kW	7.5 kW

and calculation are now in progress to achieve a required field with various asymmetric constructions.

Precise estimation of the effective length of a field, necessary for beam dynamics, should take the end effect of the magnet into account. Effective lengths at various radii are different due to the end effect. Their variation will be corrected based on the results obtained from iterative measurements of the field with various end shims.

The design of prototypes for dipole and quadrupole magnets has been almost finished. Investigation of the field property and development of the techniques for the field correction will be carried out on these magnets. The main specifications of these magnets are given in Table 2. The magnetic field will be measured by using flip and rotating coils for fast and accurate measurement. The design of the measurement system is now in progress.

References

- 1) H. Tanaka, R. Nagaoka, and M. Hara: p.225 in this report.
- 2) M. Hara and H. Kamitsubo: p.220 in this report.
- 3) K. Egawa: Proc. Semin. High Energy Accelerator, OHO'85, 2-1 (1985).

V-17. The Overall Beam Flow of the 6 GeV SOR

H. Miyade, K. Yoshida, K. Tsumaki, and M. Hara

The overall beam flow of the 6 GeV SOR was investigated. Two types of operations are expected. One is the case in which electrons are used (e^- -mode), and the other, positrons are used (e^+ -mode). Table 1 shows main specifications of the 6 GeV SOR.

Eight electron pulses are produced with an electron gun at 60 Hz. Each pulse is 15 ns long. The current is 170 mA for the e^- -mode and 3.5 A for the e^+ -mode. It is expected that the efficiency from the electron gun to the electron linac is 60%.^{1,2)}

In the e^- -mode electrons are accelerated with an electron linac up to 1.5 GeV, injected into a syn-

chrotron through a septum magnet during the 1/6 s flat bottom, accelerated up to 6 GeV in 1/3 s at the constant rate of 13.5 GeV/s (15.4 keV per turn), and extracted during the 1/6 s flat top; the cycle is 1 Hz. Since the injection method is of one-turn, a kicker magnet with a duration time of less than 120 ns is used.

In the e^+ -mode, electrons from the gun are accelerated up to an appropriate energy and hit a positron converter, where positron pulses are produced. The conversion efficiency is assumed to be 0.5%.^{1,2)} The positrons are accelerated with a positron linac up to 1.5 GeV and injected into the synchrotron. The scheme of injection, acceleration, and extraction is the same as in the e^- -mode.

To avoid radioactivation due to high energy beams from the linac both in the e^- -mode and in the e^+ -mode, the beam loss at the injection into the synchrotron is desired to be as low as possible. In the e^+ -mode the beam current from the linac is lower than in the e^- -mode. Therefore, the synchrotron has two RF systems. One is a high frequency system (504.7 MHz) and the other is a low one. The low one makes a bucket wide so that it is possible to inject the beam with good efficiency.^{1,3)} With this method the efficiency of the injection into the synchrotron is expected to be 95%.¹⁾ The low frequency will be either 28.04 MHz or 42.06 MHz. Figure 1 shows the longitudinal separatrices for the

Table 1. Main specifications of the 6 GeV SOR.

Electron gun	
Energy	150 keV
Pulse length	15 ns
Pulses/cycle	8
Current	170 mA (e^- -mode) 3.5 A (e^+ -mode)
Pulse rate	60 Hz
Linac	
Energy	1.5 GeV
Current	100 mA (e^- -mode) 10 mA (e^+ -mode)
Frequency	2.856 GHz
Synchrotron	
Injection energy	1.5 GeV
Extraction energy	6 GeV
Current	10 mA (e^- -mode) 1.0 mA (e^+ -mode)
Circumference	342.144 m
RF frequency	
Low	28.04 or 42.06 MHz
High	504.7 MHz
Harmonic No.	
Low	32 or 48
High	576
Acceleration cycle	1 Hz
Duration time of kicker magnet	<120 ns
Bunches/cycle	8
Storage ring	
Energy	6 GeV
Current	100 mA
Circumference	1,069.2 m
RF frequency	504.7 MHz
Harmonic No.	1,800
No. of bunches	1, 25 × N
Accumulation time	1 min (e^- -mode) 10 min (e^+ -mode)

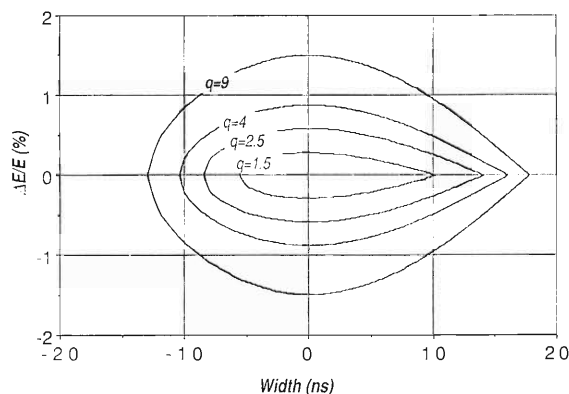


Fig. 1. Separatrices of the low frequency system at $E_B = 1.5$ GeV with various q . The frequency is 28.04 MHz. At $q = 2.5$ the bucket width is 22.5 ns and the height ($\Delta E/E_N$) is 0.58%.

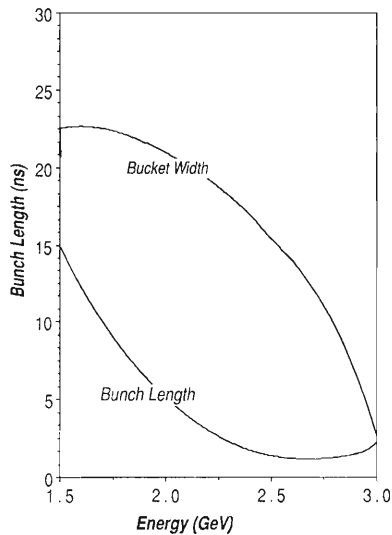


Fig. 2. Decrease in the bunch length by radiation damping. The behavior of bucket width is also shown. This bucket is of the 28.04 MHz frequency system. In the area of this figure the bunch length decreases faster than the decrease in the bucket width.

28.04 MHz frequency system at $E_B = 1.5$ GeV (E_B is the beam energy). On the basis that the relative deviation of beam energy ($\Delta E/E_B$) is 0.6%,¹⁾ the overvoltage (q) at injection should exceed 2.5.

During acceleration the bunch length is decreased by radiation damping. Its behavior is shown in Fig. 2. In this calculation, $q = 2.5$ at the injection ($E_B = 1.5$ GeV) and the constant increasing rate of the peak voltage (1,950 kV/s) were assumed. When the bunch length is short enough to fit the bucket of the high one, the high frequency system is turned on and the low one is turned off. The bucket width of the high one is about 2 ns. From Fig. 2 it is found that the bunch length is less than 2 ns at $E_B \approx 2.3$ GeV.

After acceleration, the electron (or positron) bunches are extracted from the synchrotron and injected into a storage ring; the efficiency of the injection is expected to be 50%.^{1,2)} The number of bunches in the storage ring is a multiple of 25. In order to accumulate the beam up to 100 mA, it takes about 1 min for the e^- -mode and 10 min for the e^+ -mode.

References

- 1) 7 GeV Advanced Photon Sources: Conceptual Design Report, ANL-87-15, April (1987).
- 2) European Synchrotron Radiation Facility: Foundation Phase Report, Feb. (1987).
- 3) A. Febel and G. Hemmie: Proc. 11th Int. Conf. High Energy Accelerators, Geneva, Switzerland, July 7-11, 1980, p. 43 (1980).

V-18. RF System for the 6 GeV SOR

T. Yoshiyuki, T. Kusaka, and M. Hara

The RF (radio frequency) systems designated for the 6 GeV SOR are classified into RF systems of a storage ring, a booster synchrotron, and linacs. In this report we represent the RF systems of the storage ring and the booster synchrotron.

(1) Storage ring RF system

The RF system of the storage ring provides adequate accelerating voltage to compensate for the energy loss due to synchrotron radiation from the dipole magnets and insertion devices. There will be an additional loss due to the excitation of parasitic modes by the beam. The peak RF voltage must be in excess of the amount needed to make up these losses and to provide overvoltage for an adequate beam lifetime. The RF system is also the major factor in determining the bunch length.

The RF parameters are listed in Table 1. The nominal frequency of operation for the storage ring RF system is 504.7 MHz. At 6 GeV beam energy, the energy loss per turn due to synchrotron radiation emission from the dipoles amounts to 4.6 MeV. The additional loss component due to the insertion devices depends on the exact distribution of undulators or wigglers and their characteristics finally applied. Here, the estimation for the maximum loss component due to insertion devices is based on one example of the

Table 1. RF parameters of the storage ring.

Beam energy	6 GeV
Circumference	1,069.2 m
Bending radius	25 m
Momentum compaction factor	1.86×10^{-4}
Radio frequency	504.7 MHz
Harmonic number	1,800
Synchrotron radiation loss per turn	4.6 MeV
Energy loss for insertion devices	2.1 MeV
Parasitic energy loss per 100 mA	0.3 MeV
Nominal RF voltage	7 MV
Maximum RF voltage	10 MV
Shunt impedance	23.5 M Ω /m
Quantum lifetime	1.6×10^6 h
Number of cells	20
Synchrotron frequency	2.48 kHz
Radiation damping time	4.66×10^{-8} s
Synchrotron phase angle	44.4 deg
Beam current	100 mA
Beam power	700 kW
Cavity power	710 kW
Klystron power	1 MW
Number of klystrons	2

Table 2. Characteristics of the cavities for the representative storage ring.

	Cell length (m)	Shunt impedance (M Ω /m)	(M Ω per cell)	Cavity power (kW per cell)
APS*	0.425	26.4	11.23	36
ESRF**	0.426	26.6	11.31	25
PETRA**	0.4	22	8	25
PF*	0.3	29	8	30
RIKEN	0.3	23.5	7.05	36

* single-cell cavity, ** 5-cell cavity

design for a set of undulators and wigglers. The total energy loss is estimated at 2.1 MeV. This energy loss can be compared with other similar facilities; ESRF¹⁾ in which a total loss per turn due to a full operational set of insertion devices is 1.5 MeV and APS²⁾ in which this loss is 1.2 MeV. Other energy losses due to cavities and vacuum chambers are evaluated to be 0.3 MeV. These would make the total loss 7 MeV per turn. The operation RF voltage required would then be 7 MV. The peak voltage would be 10 MV to get a sufficiently long quantum lifetime. The overvoltage factor of 1.43 gives a relative energy acceptance $\Delta E_{rf}/E_0$ of $\pm 2.4\%$. When a beam energy spread σ_e/E_0 is 3×10^{-3} , a relative "bucket" size $\Delta E_{rf}/\sigma_e$ is 8.0, from which a quantum lifetime is evaluated at 10^6 h.

The RF power is calculated from the shunt impedance of the cavities, the cell number, and the beam current. The shunt impedance of the cavities is 23.5 M Ω /m, which can be compared with other representative facilities in the world. Table 2 shows the characteristics of the cavities for the representative storage rings. In this RF system cavities have 20 cells. The RF power dissipation per cell is 36 kW and the total cavity power is 710 kW. The beam power at the nominal storage ring current of 100 mA is 700 kW. The total power consumed in the storage ring is 1.41 MW. The RF generator should supply the sum of the beam power, the cavity power, and reflected power which depends on the cavity coupling coefficient. The generator power, therefore, needs at least about 2 MW. Klystrons rated for 1 MW output at 504.7 MHz are available. In total two 1 MW klystrons are required for 20 cells.

In the structure of RF cavity we examine two types: one is a single-cell cavity which is used on

the Photon Factory and SRS (Daresbury) and is proposed to use on APS, and another is a multi-cell cavity which is used on PEP (Stanford), PETRA (Hamburg), and LEP (CERN) and is proposed to use on ESRF. To select the type of cavity we are presently testing the model cavity used as both single-cell cavity and multi-cell cavity.³⁾

Besides the fundamental RF system a higher harmonic RF system may be combined with it and used to provide additional Landau damping or to lengthen the bunches if required for added stability. From now on, we will further investigate this RF system about the RF parameters and the structure of cavities.

(2) Booster synchrotron RF system

The booster synchrotron has two accelerating systems. The first, a low frequency system, is used to capture electron or positron bunches from the linac and accelerate electrons or positrons from 1.5 GeV, accelerating energy of the linac, to more than 2 GeV. After that, a high frequency system is used to

accelerate them to 6 GeV, beam energy in the storage ring.

A list of parameters for the high frequency system is given in Table 3. The frequency is the 576th harmonic of the revolution frequency. Since this RF system will also make use of 504.7 MHz, it would be favorable if the same RF cavities would be used as those for the storage ring. The maximum RF voltage required for acceleration, synchrotron radiation loss, and adequate longitudinal bucket size is given as 9 MV. At the maximum voltage of 9 MV a quantum lifetime is calculated at 10 min and the overvoltage factor at 1.8. The shunt impedance of the cavities is the same value, 23.5 M Ω /m, as the storage ring, so more than 15 cells in the cavities needed in this case is about 770 kW. Consequently, the use of one 1 MW klystron identical to the ones used for the storage ring is expected. The RF power the use of one 1 MW klystron identical to the ones used for the storage ring is expected. The RF power from the klystron is divided equally among the 15 cells.

The subharmonic frequency of the low frequency RF system is 28.0 or 42.1 MHz. The exact dynamics and maximum RF voltage required for this low frequency system have not been determined at this report. Nevertheless, the harmonic number of both rings and their circumferences have been adjusted for such a subharmonic system. The harmonic number of the low frequency system is, therefore, fixed at 32 or 48.

Table 3. Parameters of 504.7 MHz RF system in the booster synchrotron.

Beam energy	6 GeV
Circumference	342.144 m
Bending radius	25 m
Radio frequency	504.7 MHz
Harmonic number	576
Synchrotron radiation loss per turn	4.6 MeV
Nominal RF voltage	5 MV
Maximum RF voltage	9 MV
Shunt impedance	23.5 M Ω /m
Quantum lifetime	>600 s
Number of cells	15
Cavity power	770 kW
Beam power	<50 kW
Klystron power	1 MW
Number of klystrons	1

References

- 1) European Synchrotron Radiation Facility: Foundation Phase Report, Feb. (1987).
- 2) 7 GeV Advanced Photon Source: Conceptual Design Report, ANL-87-15, April (1987).
- 3) T. Kusaka, T. Yoshiyuki, N. Kawasaki, and M. Hara: p. 237 in this report.

V-19. Design of the RF Test Cavity for the 6 GeV SOR Ring

T. Kusaka, T. Yoshiyuki, N. Kawasaki,* and M. Hara

In the 6 GeV SOR ring, it is desired for accelerating cavities to make a stable and efficient acceleration. For this purpose, it is important to study the characteristics of the cavities at resonant frequencies. Computer programs are available to design the structure of cavities. However, they are limited in the cavity structure and the resonant modes which can be calculated. Therefore, it is necessary to fabricate a test cavity and evaluate its electromagnetic properties. In this report, the design of the model cavity for low power tests by using numerical programs is described.

In Advanced Photon Source, single-cell cavities are proposed for the storage ring, while multi-cell cavities are designed in European Synchrotron Radiation Facility.^{1,2)} In order to compare them, a model cavity has been designed to operate in both single-cell mode and multi-cell mode. Figure 1 shows the structure of the cavity in a 3-cell mode. The single-cell cavity, on the other hand, is assembled by using a center cell and two end plates. Each cell has the re-entrant structure and the noses help concentrate the electric field in the beam axis. The cell lengths are of a half wavelength long. In a multi-cell mode, cells are coupled together magnetically with off-axis slots. The cavity is excited through the coupling loop located in the center cell. Three other ports are prepared for a frequency tuner and damping couplers which suppress higher-order modes.

The cross section of the half cell is shown in Fig. 2. The gap length g , the nose angle θ , the nose radius r , and the disk thickness t are chosen as design pa-

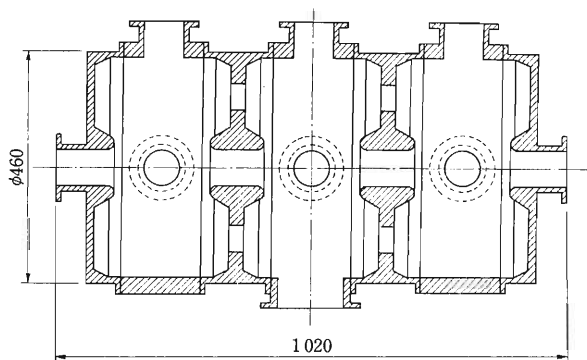


Fig. 1. Structure of the test cavity in a 3-cell mode.

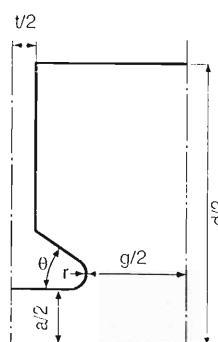


Fig. 2. Design parameters.

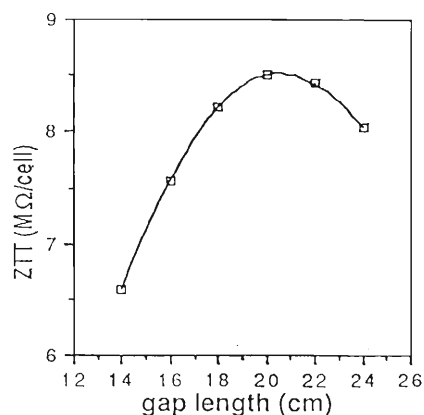


Fig. 3. Variation in shunt impedance as a function of the gap length.

rameters. The accelerating frequency is set to 500 MHz, and the cavity diameter d is adjusted. The beam aperture a , which is decided by injection conditions, is now set to 10 cm ϕ . The characteristics of the cavity are calculated by a program, SUPERFISH. Figure 3 shows the shunt impedance Z_{TT} as a function of the gap length when the values of the remaining parameters are fixed. The shunt impedance should be increased for efficient acceleration as far as the beam stability is kept. The optimum shunt impedance exists for the gap length of about 20.6 cm. The reason why the optimum value exists is that the Q value increases with the gap length, but the transit time factor decreases. Similarly, the dependences of the shunt impedance upon the other parameters are calculated. The optimum nose angle and the optimum disk thickness are searched under the condition that the values of the other parameters are

* College of Humanities and Sciences, Nihon University.

Table 1. Specification of test cavity.

Operating frequency	500 MHz
Number of cells	3
Material	Aluminium
Cell diameter	437 mm
Gap length	200 mm
Q (single cell)	32,000
ZTT (single cell)	7.4 M Ω

constant. The best disk thickness is thought to give the maximum ratio of the cavity volume to the surface area. The smaller nose radius produces the larger shunt impedance, but it should be designed to avoid voltage breakdown because of a higher value of electrical field gradient.

Table 1 shows the specification of the test cavity based on the above calculations. The cavity is made of aluminium because of high electric conductivity and handling convenience. Overall machining accuracy should be better than 0.1 mm for the purpose of tuning the resonant frequency. The Q value and the shunt impedance are given for the single-cell cavity in the accelerating mode. Higher-order modes with axially-symmetric fields can be calculated as well as the fundamental mode. Several patterns of electric field, which are calculated by a computer code HAX, are shown in Fig. 4 (a) through (d). Higher-order modes cause the beam energy loss and the bunched beam instabilities. The longitudinal and transverse impedances of higher-order modes should be suppressed to avoid the bunched beam instabilities.³⁾

The following items will be studied by using the test cavity.

- (1) the comparison between the single-cell cavity and the multi-cell cavity;
- (2) the optimization of the cavity structure;
- (3) the measurement of the characteristics of the

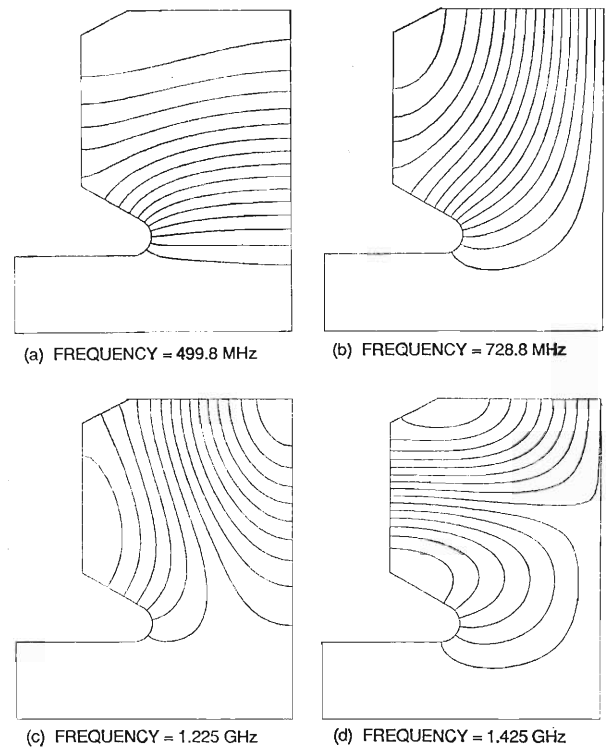


Fig. 4. Plots of electric field at several resonant frequencies.

cavity in resonant modes; and

- (4) the test of the input coupler, the frequency tuner and the damping coupler.

References

- 1) 7 GeV Advanced Photon Source: Conceptual Design Report, ANL 87-15, April (1987).
- 2) European Synchrotron Radiation Facility: Foundation Phase Report, Feb. (1987).
- 3) Y. Yamasaki, K. Takata, and S. Tokumoto: KEK 80-8, August (1980).

V-20. Vacuum Chamber for the 6 GeV Storage Ring

S. H. Be, Y. Morimoto, H. Sakamoto, and S. Yokouchi

The vacuum chamber, a ring of about 340 m in diameter, consists of two chambers with different shapes and two types of absorbers. To minimize synchrotron radiation (SR)-induced desorption as well as thermal outgassing, we are considering to use new aluminum-alloy chamber extrusions (A6063 T6) with a slot-isolated antechamber.

In the slot-isolated antechamber, the feature of the slot is to prevent the circulating electron beam from coupling to the lower-frequency modes of the antechamber. However, higher-frequency electromagnetic fields in the range above 15.9 GHz¹⁾ of the cutoff frequency for the 1 cm-slot penetrate into the antechamber and their power is stored there. At present the power is not estimated quantitatively, but in the operation of TRISTAN ($e^+ e^-$ collider), it was found that (1) the wires of electric connection present in the chamber of sputter ion pump, which is separated from beam chambers by the slits of 10 mm \times 50 mm, are cut by melting,²⁾ and (2) in higher-frequency electromagnetic fields, conductors discharge even when they are ceramic-insulated, ultimately leading to breakdown.³⁾ These findings indicate that the thermal loading to non-evaporable getter (NEG) strips due to the power of higher frequency modes gives rise to an increase in bulk NEG temperature. In the storage ring this temperature change occurs repeatedly because of repetitive operation of the storage ring and would give a deleterious effect⁴⁾ to the NEG strips by causing thermal fatigue.

The development of the thermal fatigue effects

causes the peel-off of gettering powder; the peel-off strongly depends on temperature and duration of NEG activation. Consequently, the lifetime of the NEG strips will be limited, becoming short. To avoid this deleterious effect on the NEG strips and discharge between the NEG strips and ceramics for supporting the NEG strips, a new vacuum chamber is proposed for use in the straight sections.

(1) Vacuum chamber for the straight sections

The vacuum chamber consists of an electron beam chamber and an antechamber and cross-sectional view of it is shown in Fig. 1. The antechamber structure with a slit-isolated pump chamber differs from that planned for the Advanced light source by Lawrence Berkeley Laboratory, or for the Advanced photon source by Argonne National Laboratory, and consists of two portions: a portion for inserting NEG strip pumps and the other for the passage of synchrotron radiation. The former is separated from the latter by a wall with slits for pumping. The important feature of our new vacuum chamber prevents a deleterious effect on the NEG strips due to thermal fatigue.

At present effects of photons and their associated photo-electrons on the NEG performance are not clear; no one knows whether or not photons and their associated photo-electrons are injurious to the getter performance. At least our antechamber structure with a slit-isolated pump chamber can reduce interaction of the NEG strips with photons and their associated photo-electrons.

(2) Bending magnet vacuum chamber

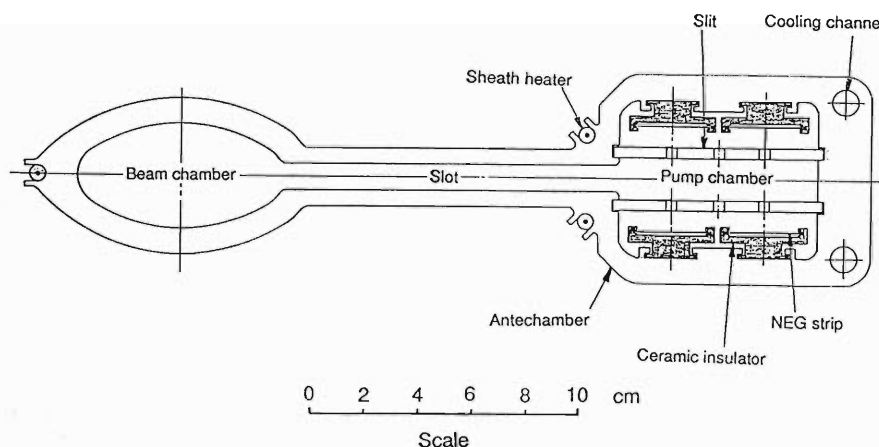


Fig. 1. Cross-sectional view of the vacuum chamber for the straight sections.

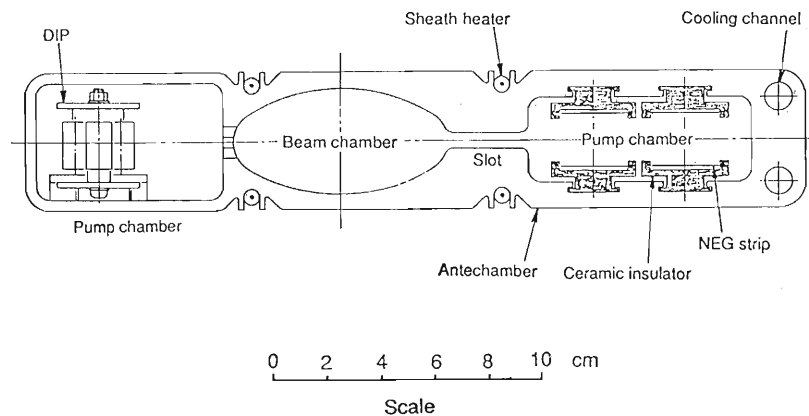


Fig. 2. Cross-sectional view of the bending magnet vacuum chamber.

The cross-sectional view of the vacuum chamber is shown in Fig. 2.

Much of the gas produced by the localized SR-induced desorption as well as thermal desorption at the absorbers placed downstream and upstream of the bending magnet is pumped out with lumped pumps, but part of the gas is suspected to diffuse into the bending chamber throughout the antechamber.

We therefore install a distributed ion pump (DIP) and a NEG strip pump on opposite sides of the electron beam chamber as shown in Fig. 2. These pumps evacuate not only gases desorbed from the bending magnet chamber but also assure efficient removal of gases which permeates from the crotch and absorber locations and results in low operating pressure in the electron beam chamber.

The same antechamber structure with slit-isolated pump chamber as in the straight chambers cannot be used in the bending magnet chambers, because of the narrow gap between bending magnet poles. DIP is to be the main pumping source for the bending magnet vacuum chambers.

Since the discussions on the chambers described above are qualitatively, quantitative studies are needed to determine which type antechamber is more appropriate for the storage ring from the point of view of higher-frequency modes and photons.

(3) Bakeout of the chamber and its cooling

The vacuum chambers shown in Figs. 1 and 2 contain a cooling and a baking channels. In our vacuum chambers part (~ 1 kW) of SR light that passes out through the slot, without being intercepted at the crotch (C) as shown in Fig. 3 and absorber (SA), intercepts a part (~ 3 m) of the back side of the slot, but only in the dispersion region of the lattice between the two bending magnets (BM1, BM2). The corresponding power deposition at the back side of the slot is ~ 300 W/m. Besides this power deposition, the power due to NEG activation must also be taken into consideration. To achieve temperature sufficient for the NEG activation, a

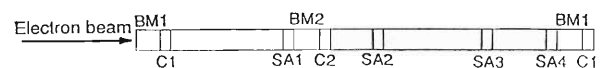
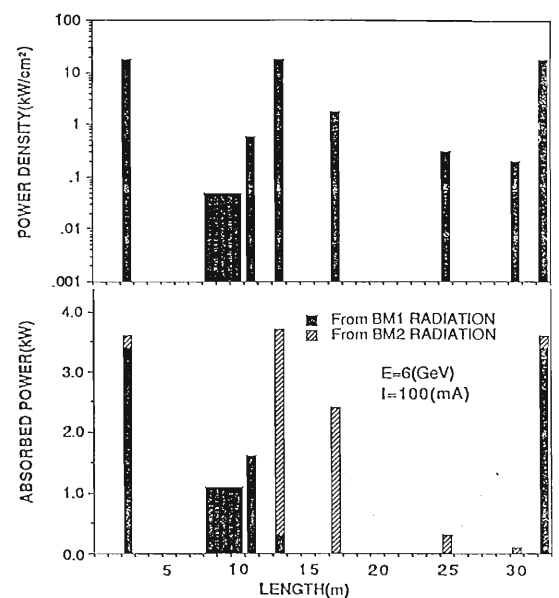


Fig. 3. Absorbed power and power density.

heating current of 110 A is required and the corresponding power dissipation is 4×990 W/m larger than 300 W/m. These thermal loads can easily be removed by a cooling water system, which is designed for loads up to 5 kW/m. This can be achieved by flowing water at ~ 2 m/s in two channels of 10 mm-diameter.

The chamber is baked out by inserting flexible sheathed heaters into baking channels, which bring the chamber temperature up to 150°C . The chamber is thermally insulated with kapton films.

References

- 1) R. L. Kustom, G. L. Nicholls, S. L. Kramer, T. K. Khoe, and J. M. Cook: ANL-HEP-CP-87-19.
- 2) H. Mizuno: private communications.
- 3) H. Ishimaru: private communications.
- 4) J. L. Cecchi, S. A. Cohen, and J. J. Sredniawsky: *J. Vac. Sci. Technol.*, **17**, 294 (1980).

V-21. Pumping System for the 6 GeV SOR

S. Yokouchi, Y. Morimoto, H. Sakamoto, and S.H. Be

The pumping system of the 6 GeV SOR storage ring must maintain a pressure of the order of 10^{-10} Torr to achieve a beam lifetime of about 20 h. The gas load in the vacuum system depends on the SR-induced gas desorption and thermal desorption. The gas load due to this SR-induced gas desorption decreases with an increasing in an integrated photon flux, which is directly related to the circulating electron beam:¹⁾ The gas load, Q , decreases with the integrated electron beam current, D (Ah), *i.e.*, $Q = 1.9 \times 10^{-4} D^{-2/3}$ Torr l/s for 0.1 A at 6 GeV. This means that at the start of ring operation a larger pumping system is needed because of the very high SR-induced desorption, but a smaller pumping system is enough after depleting the chamber wall with increasing the D . We consider 10 Ah as the D in the following discussions. In the planned 6 GeV ring, the SR-induced total gas load after 10 Ah dose is 4.1×10^{-5} Torr l/s , and the total thermal gas load is 3.1×10^{-5} Torr l/s . In estimating the thermal gas load, we consider an extruded aluminum alloy as the chamber material and assumed that its outgassing rate is 5×10^{-12} Torr l/s cm^2 . In our case, the inner surface area of the chamber is 6.1×10^6 cm^2 ; thus, the total gas load in our ring is 7.2×10^{-5} Torr l/s .

Figure 1 shows the pumping system per cell of the ring. For this total gas load, the total pumping speed necessary to achieve a pressure of 1×10^{-10} Torr at the beam chamber is 29,100 l/s per cell. In this estimation, for the case of the antechamber the slot conductance was considered of course. The actual total pumping speed of our pumping system, which consists of non-evaporable getter (NEG) strips, a sputter-ion pump (SIP), and a titanium sublimation pump (TSP), and a titanium sublimation pump

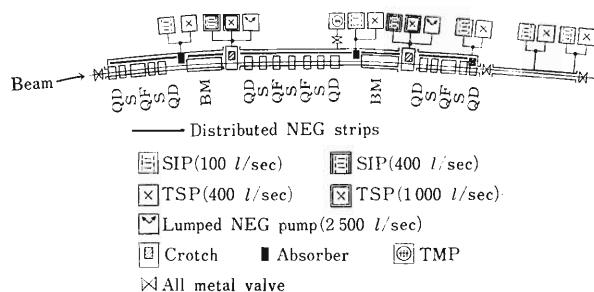


Fig. 1. Pumping system of the 6 GeV SOR storage ring per cell.

(TSP) installed in the chambers, is 30,900 l/s per cell (see Fig. 1).

The NEG material is a 84%Zr-16%Al alloy, which is suitable for pumping active gases, but not for methane or noble gases. The alloy reacts with the active gases such as CO, CO₂, N₂, O₂, H₂O, forming stable chemical compounds, while hydrogen is sorbed reversibly. NEG needs a heat treatment called "activation," which makes a thin surface layer, formed on the surface by exploding to air or by venting to atmospheric pressure, diffuse into the bulk. The temperature for this activation depends on a kind of NEG, and the activation for NEG (St 101) to be used in the 6 GeV ring is performed at 700°C. After the activation NEG develops its pumping characteristics, which depends on the amounts and molecular species of the gases and also on the temperature of NEG. The pumping speed of NEG decreases gradually with pumpdown time because of saturation of the getter surfaces. Therefore, NEG must be heated repeatedly to recover the pumping speed. For this purpose, the CERN Laboratory made experiments and found that a few minutes of heating at 400°C is sufficient for recovering the pumping speed.²⁾ This operation is referred to as "conditioning." Distributed NEG strips are installed in the antechamber, as shown in Fig. 2, and thereby all of the SR-induced gas molecules are pumped before they have a chance to bounce into the beam chamber, and the thermally desorbed gas molecules are pumped uniformly in the chamber. The pumping speed of the NEG strips at an operating temperature of 25°C is 900 l/s m for H₂ and CO. The sorption capacity for H₂ is sufficient to keep practical "conditioning" intervals of about 5 months in the ring operation at

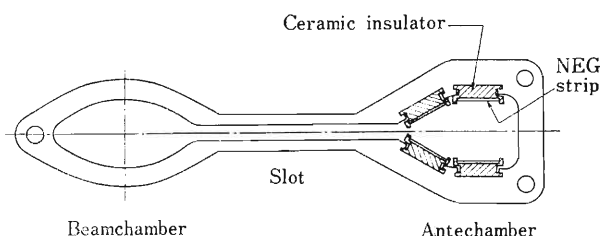


Fig. 2. Cross section of the vacuum chamber with NEG strips. SR from beam strikes surface of the antechamber and induces gas molecules.

1×10^{-9} Torr. Since sorption of H_2 gas is reversible, the lifetime of the NEG strips is estimated at more than 20 y. On the other hand, since CO gas is not sorbed reversibly but also forms stable chemical compounds, the lifetime for CO is estimated at two or three years even if conditioning is repeated several hundred times. Therefore, additional titanium sublimation pumps (TSP) are required for pumping reactive gases such as CO and CO_2 except H_2 gas.

TSP can pump active gases by sorbing into the sublimated fresh titanium film on the chamber surface, but not methane or noble gases. As consumed, the getter material must be exchanged every 1 or 2 y. The NEG strip and TSP are limited to only reactive gases, and noble gases and CH_4 are not pumped. Therefore, additional sputter-ion pumps (SIP) are to be installed.

SIP has ability to pump out both active and noble gases, and the pump current can be used as an indication of local pressure.

By locating lumped NEG pumps, SIP and TSP near the crotch and absorber (details of which will be described in this progress report by Y. Morimoto *et al.*), almost all the SR-induced gas molecules are pumped out before they have a chance to bounce around in the beam chamber. At the section of an insertion device, which will be constructed in the future, only beamchamber instead of the antechamber is planned to be used, and SIP and TSP are installed.

Our main pumping system is based on the NEG

strip and a feature of the pumping system is a mixed pumping one which consists of NEG strip, SIP, and TSP.

As a roughing pump, turbo molecular pumps are under consideration and will be used for pumping the chambers before the SIP, TSP, and NEG pump start up. Further, TMP's are also used for bakeout of the chambers and the activation and conditioning of NEG.

All metal gate valves with an RF contact are mounted for isolating the chambers at each end of the cell. By closing them each cell can be pumped independently after venting to atmospheric pressure and subjected to leak check.

Bellows with RF fingers are used for compensating misalignments during installation of the chambers, valves, *etc.* and thermal expansion during ring operation and bakeout.

The all metal gate valves and bellows are to be specially designed to minimize the RF impedance; development of valves and bellows with smoother, simpler, and more conductive wall is strongly required.

Aluminum gaskets are used for connection of the flanges.

References

- 1) ESRF, Foundation Phase Report, Chap. II (1987).
- 2) H. P. Reinhard: "The Vacuum System of LEP," Proc. IX IVC-V ICSS, Madrid (1983).

V-22. Vacuum Test Device for Preliminary Experiments on the 6 GeV SOR

S. Yokouchi, Y. Morimoto, H. Sakamoto, and S. H. Be

We constructed an experimental device consisting of extruded aluminum alloy chambers as shown in Fig. 1 to investigate characteristics of various vacuum components and materials, which will be used in the 6 GeV ring; they include characteristics of pumps, outgassing rates from chamber materials and other materials in the vacuum, and reliabilities of components such as valves, bellows, and gauges. A photograph of the device is shown in Fig. 2.

The device consists of three cylindrical chambers, and vacuum seals between flanges of the chambers are made by using aluminum gaskets. The individual chambers can be isolated with two gate valves, and an orifice of 5 mm in diameter was mounted between the chambers 1 and 2. On each outside surface of the chambers, sheath heaters were welded for baking the chambers at 150°C, and chromel-almel thermo-

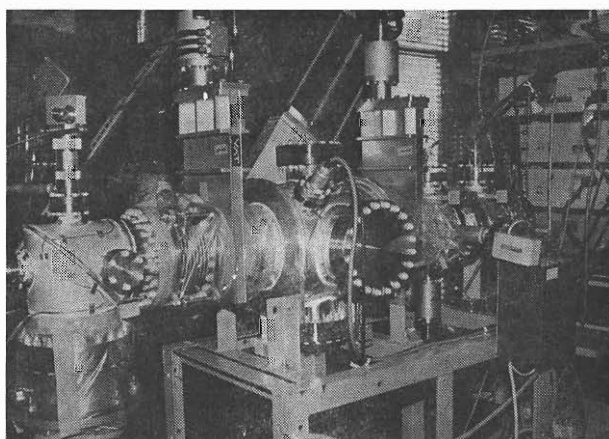


Fig. 2. Photograph of the device with test instruments.

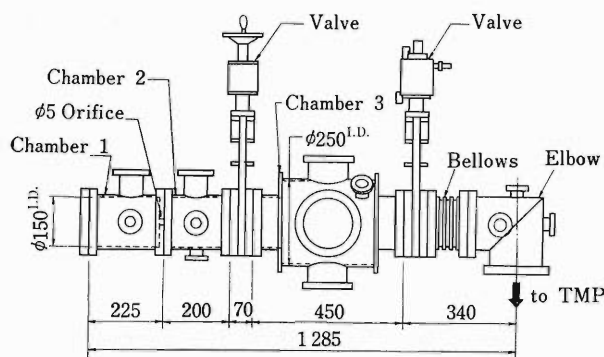


Fig. 1. Outline of the device.

couples were also attached for measuring temperature of the chambers.

Figure 3 shows a schematic diagram of the device with test instruments. As seen from Fig. 3, in the chamber 1, a Bayard-Alpert (BA) nude gauge (BAG1), a BA normal gauge (BAG2), and a variable leak valve (VLV) for introducing gases were installed. In the chamber 2, a BA nude gauge (BAG3), a spinning rotor gauge (SRG) for calibration of ionization gauges and a quadrupole mass analyzer (QMA) for analyzing residual gases were installed. In the chamber 3, a sputter ion pump (SIP), a titanium sublimation pump (TSP), and non-evaporable getter (NEG) strips, all of which will be used in the 6 GeV ring, are installed. Thus we can in-

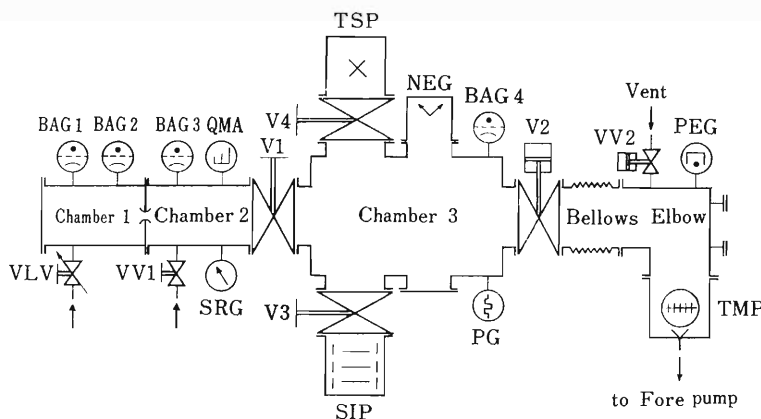


Fig. 3. Schematic diagram of the device with test instruments.

investigate the pumping characteristics of each pump and a mixed pumping system consisting of two pumps or three by opening or closing the gate valves V3 and V4.

At the present time, the chambers have been evacuated for about 470 h with only 300 l/s turbo molecular pump without baking the chambers, and the outgassing rate of the chamber 1 as a function of pumpdown time is shown in Fig. 4. Fluctuation of data after about 40 h in this figure is due to the variation in the pressure caused by the change in ambient temperature. The pressure after about 40 h

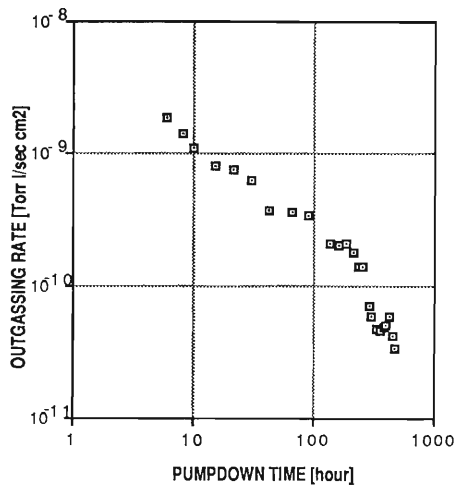


Fig. 4. Outgassing rate of the extruded aluminum alloy chamber.

was about 1×10^{-7} Torr. The outgassing rate Q was obtained from $Q = C \times (P_1 - P_2) / A$ Torr l/s cm², where C is the conductance (2.28 l/s) of the orifice, P_1 the pressure in the chamber 1, P_2 that in the chamber 2, and A the inner surface area (1,715 cm²) of the chamber 1. Further, the pressures in the chamber 1 and chamber 2 after 470 h pumping are 5.5×10^{-8} Torr and 3.0×10^{-8} Torr, respectively. From this figure, we can find that the outgassing rate after 470 h pumping is 3.3×10^{-11} Torr l/s cm², and this is a reasonable value as the outgassing rate of the extruded aluminum alloy chamber without bakeout.

We plan to carry out following investigations using the test device described above:

- 1) Thermal outgassing rate of various materials which will be used in the 6 GeV ring
- 2) Surface treatment for reducing the outgassing rates from the various materials
- 3) Outgassing rate of a model chamber for the 6 GeV ring
- 4) Outgassing rates of the materials bombarded with electron beams
- 5) Pump
 - a) Characteristics of the NEG strip (or pump), SIP, and TSP
 - b) Vacuum performance of the mixed pumping system
 - c) Practical pumping characteristics after pumps are installed in the model chamber of the 6 GeV ring

V-23. Synchrotron Radiation Power Distribution at the 6 GeV SOR

Y. Morimoto, H. Sakamoto, S. Yokouchi, and S. H. Be

Synchrotron radiation (SR) power distributions along the 6 GeV SOR storage ring are calculated to estimate thermal problems of a vacuum chamber and its outgassing rates. The dominant outgassing rate in the storage ring is due to an SR-induced desorption rather than a thermal one. In general, the rate of SR-induced desorption is 10 to 100 times larger than the thermal outgassing rate at the initial operation. The SR power distribution is determined by a shape of the vacuum chamber or its size, and positions of the crotch and strip absorber where most of the SR power produced in bending magnets (BM) is deposited. The SR power, P_r in kW, is given by $P_r = 26.6E^3BI$, where E is the electron energy in GeV, B the magnetic field in T, and I the electron current in A. In the design parameters of $E = 6$ GeV, $B = 0.8$ T, and $I = 0.1$ A, the total SR power from 72 BM in our storage ring corresponds to about 460 kW. Thus the SR power emitted from each BM becomes approximately 6.4 kW.

As shown in Fig. 1, to prevent vacuum chambers from receiving such a high SR power, crotches, C1 and C2, are positioned just downstream of BM1 and BM2, respectively, and strip absorbers, SA1, SA2, and SA3, in front of BM2, an insertion device (ID), and BM1, respectively. The crotches and absorbers are used for the same purpose, but their structures are different. The structure of the crotch is more complicated than that of the absorber because of its higher power absorption.

The calculated SR power distributions including power densities along the storage ring are shown in Fig. 2. In Table 1, numerical values of those shown in Fig. 2 are given. The crotches, C1 and C2, intercept the greater part of SR except that to the experimental facility and the electron beam passageway. The crotch consists of a water-cooled copper

unit which absorbs thermal load from SR, and highly concentrated pumps for evacuating gases desorbed with SR in this region. Details of the crotches are described in this progress report by Morimoto *et al.* Approximately 50% (3.4 kW) of each SR power from BM1 and BM2 is absorbed at the C1 and C2, respectively.

SR power absorbed at SA3 depends on a shape

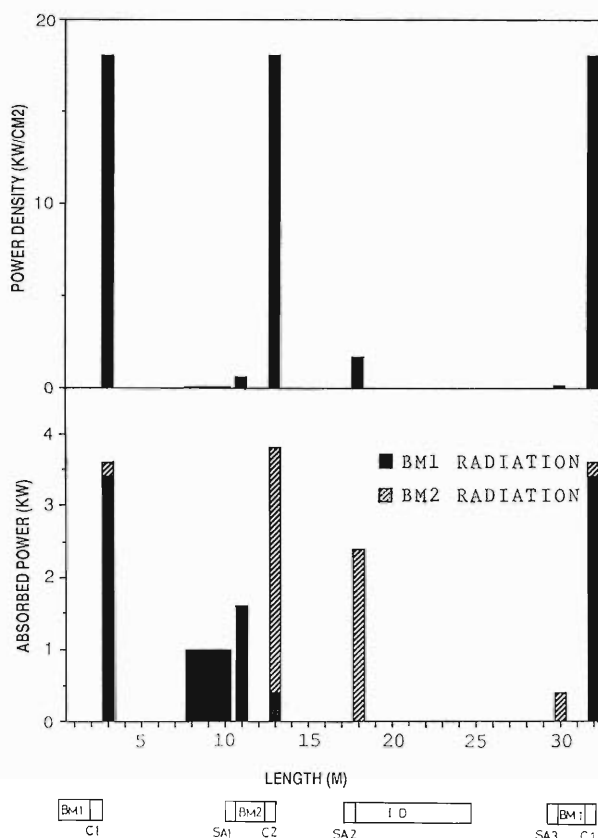


Fig. 2. Absorbed power and power density in the chamber for ID.

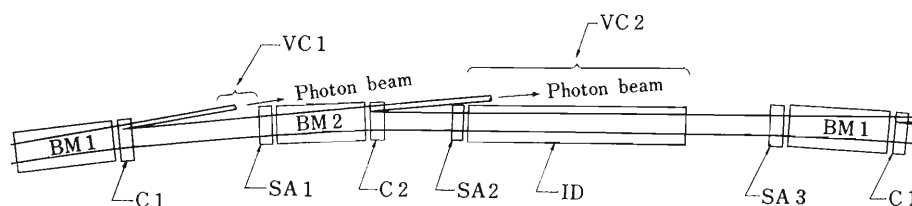


Fig. 1. Schematic of the cell of the 6 GeV storage ring.

Table 1. Absorbed power and power density. The values in parentheses are for the chamber without ID.

Area	% Absorbed	Absorbed power (kW)	Power density (kW/cm ²)
a) BM1 Radiation			
C1	52.7	3.4	18.0
VC1	16.6	1.1	0.05
SA1	25.2	1.6	0.6
C2	5.5	0.3	0.3
Total	100.0	6.4	
b) BM2 Radiation			
C2	52.7	3.4	18.0
SA2	37.7	2.4	1.7
VC2	0.0 (5.6)	0.0 (0.3)	0.0 (0.05)
SA3	6.8 (1.2)	0.4 (0.1)	0.2 (0.2)
C1	2.8	0.2	0.1
Total	100.0	6.4	

and size of the chamber mounted in a straight section (VC2). In the chamber for ID, the percentage of

the power absorbed at SA3 is 6.8% (0.4 kW) of the SR power from BM2 and that in the chamber without ID is 1.2% (0.1 kW). The difference in these percentages comes from that in the latter a part of SR is intercepted with the chamber before SR reaches SA3, but in the former not so. A part of SR from BM1 also strikes the vacuum chamber in front of SA1(VC1), and a small percentage of the SR power from BM1 and BM2 is caught up by the following crotch.

The power density of less than 2 kW/cm² can be absorbed by the normal absorber such as a water-cooled copper plate or cylinder, or cooling channels mounted in the vacuum chamber, but for the high power density of 18 kW/cm² as in our cases, a specially designed absorber is required for the crotch. The design of the crotch which absorbs high power density and evacuates large SR-induced gas load is one of most severe and urgent problems in the vacuum system of the 6 GeV SOR.

V-24. Crotch Design for the 6 GeV SOR

Y. Morimoto, S. Yokouchi, H. Sakamoto, and S. H. Be

We made conceptual design of a new type crotch having a structure in which photo-electrons produced by photons and reflected photons are trapped. Synchrotron Radiation (SR)-induced outgasses from the crotch are pumped locally with three different pumps: a lumped non-evaporable getter (NEG) pump, a sputter-ion pump (SIP), and a titanium-sublimation pump (TSP). A bird's eye view of the crotch is shown in Fig. 1. The main chamber made of copper consists of two rooms: one is for an electron beam passageway, which is fabricated so that it matches a cross section of an electron beam chamber, and the other is for trapping of photo-electrons, photons, and SR-induced outgas. A slit in front of the trapping room is for the SR beam pass. The pumps, *i.e.*, a NEG pump, a SIP, and a TSP are mounted to the trapping room. Thus, almost all the SR-induced outgasses are pumped before they have a chance to bounce around in the electron beam chamber. Cooling is achieved by flowing water through four channels

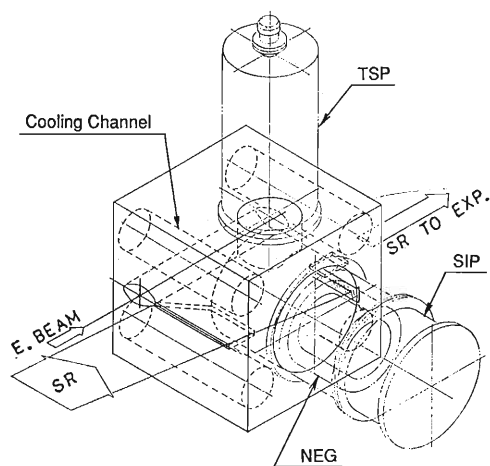


Fig. 1. Bird's eye view of the crotch.

provided in the main chamber.

The crotch is a component used for intercepting the SR beam from the bending magnet except that to an experimental facility and evacuating gases desorbed with SR in this region as described before.

The positions which the crotches are considered to be located in the 6 GeV storage ring are shown in Fig. 2. The crotches are located just down stream of the bending magnets, and photon beam lines are separated from the electron beam chamber behind the crotches. A distance between the crotch and the end of the bending magnet is approximately 50 cm.

The SR power from the bending magnet is concentrated into a smaller vertical angle ($\sim 1/\gamma$), thus resulting in significantly great power densities at the impinging surfaces; here γ is the ratio of an electron beam energy to the electron rest mass energy. For the design parameters of 6 GeV and 100 mA, the SR power and its power density for the crotch are 3.4 kW and 18.0 kW/cm², respectively. The absorption of such high power density is a severe technological problem.

For a detailed study and analysis to optimize configuration of the crotch and for assessment of its vacuum benefits, we are developing computer programs to analyze temperature and stress distributions due to specific power input. The results of computer simulation is to be confirmed by tests for actual configurations using an electron and an SR beam.

As a first step, for simulation of the heat flow within the crotch thermal analysis was made using a finite element method program MARK-CDC on the same configurations and conditions as CESR (Cornell Electron Storage Ring).¹⁾ The simulation model and conditions are shown in Fig. 3. This model consists of beryllium and copper, and a beryl-

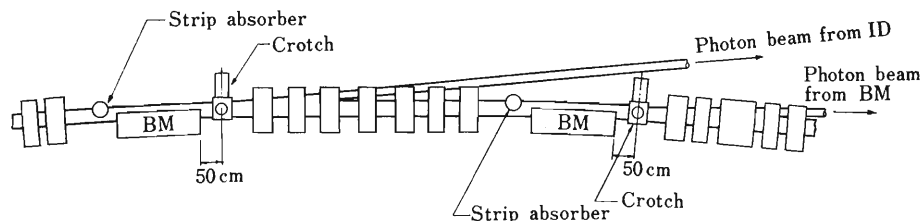


Fig. 2. Schematic of the cell of a 6 GeV storage ring.

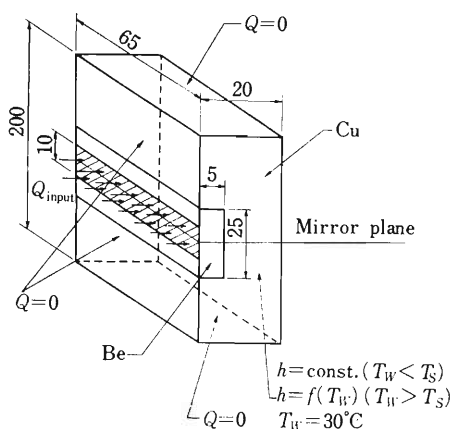


Fig. 3. Simulation model and conditions for heat flow computation.

lium piece is used to diffuse heat load. Heat input of 6.5 kW is uniformly distributed over a strip of 1 cm wide and 6.5 cm long and is deposited just on the surface (power density = 1 kW/cm²). Boundary conditions are set to allow heat transfer to occur only at the back side, along which cooling-water flows, and insulate the other surface. The heat flux per unit area, Q in W/m², at the water-cooled back side is given by

$$Q = h(T_w - T_c) \quad (1)$$

$$Q = 1,970 \exp(2P/8.69 \times 10^6)(T_w - T_s)^2 \quad (2)$$

where h is the heat transfer coefficient in W/cm²K, T_w the wall temperature in K, T_c the water temperature in K, P the water pressure in N/m² absolute, and T_s the boiling point in K at pressure P . Equation 1 can be applied only to the forced convection heat-transfer condition. When the wall temperature is higher than the water boiling temperature, Eq. 2 for the fully developed nucleate boiling is used in addition to Eq. 1. The nucleate boiling causes heat-transfer extremely greater than that of the forced convection; but we must pay attention to the reduction of heat-transfer properties due to the film boiling, which is caused by excessive heat flux through the wall-water interface. Figure 4 shows the calculations for the model illustrated in Fig. 3, assuming $h = 1.2$ W/cm². K and $T_c = 30^\circ\text{C}$. The results are in good agreement with Cornell's one.

Since this simulation model is the one for the experiments using a electron beam welder, the power density is not so high. No calculations for SR of a high power density was carried, because heat input conditions are not clear. The difference between the

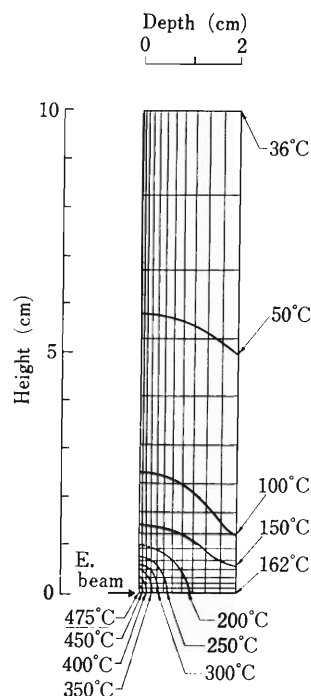


Fig. 4. Computed temperature distribution by an electron beam.

power deposition with an electron beam and that with SR is that, in the former, heat is deposited on the surface, while in the latter, SR penetrates considerably into the materials, especially low atomic number materials such as beryllium and thereby the heat power is distributed in a large volume. Therefore we must determine the distributions of input heat load in the materials to simulate the model for SR. The study of the heat input conditions for SR is under way.

The total gas load in the crotch is 3.5×10^{-7} Torr l/s (SR-induced gas load = 3.3×10^{-7} Torr l/s after 10 A. hr beam condition, and thermal gas load = 2.3×10^{-8} Torr l/s at 120°C). Thus, the overall effective pumping speed required for an operational pressure of 1×10^{-10} Torr is 3,500 l/s. In the crotch, a 2,500 l/s NEG pump, a 400 l/s SIP, and a 1,000 l/s TSP will be installed. This total pumping speed is high enough to achieve a required pressure.

The detailed design of the new crotch is scheduled to be completed by the end of April, 1988, and a heating test using an electron beam will be performed with a prototype model.

Reference

- 1) D. M. Mills, D. H. Bilderback, and B. W. Batterman: *IEEE Trans. Nucl. Sci.*, **NS-26**, 3854 (1979).

V-25. Design of the Front End of the Beam Line at the KEK Photon Factory

Y. Morimoto, S. H. Be, M. Hara, and S. Sato*

The project for the analysis and estimation technology of high performance material by a new beam technique was started in April, 1986. This project is financed out of the Special Coordination Funds for Promoting Science and Technology, which is provided by Science and Technology Agency. A new beam line BL-13 is constructed at the KEK Photon Factory as a part of this project. RIKEN takes charge of the construction of a multi-pole wiggler (MPW) and the front end of a beam line. Details of MPW are described by Sasaki *et al.* in this volume.

Two major considerations must be taken into account in the design of the front end of the beam line: (1) vacuum protection of the components of the storage ring against vacuum failure in the experimental area and (2) power absorption of synchrotron radiation (SR) from MPW and the bending magnet (BM) except that to experimental area.

A layout of the various components of the BL-13 a beam line for MPW is shown in Fig. 1. All components are set along a line extended to the straight section of the ring where MPW is located. Vacuum protection is achieved with an acoustic delay line (ADL), a fast closing valve (FCV), and an isolation valve. ADL is used to delay rapid propagation of a pressure front caused by vacuum failure. FCV is closed by a pneumatic actuator with a closing time of less than 12 ms, but sealing performance of FCV is not perfect. Therefore, the isolation valve is to be successively closed within a few seconds after closing FCV. A water cooled absorber is installed to prevent

the valves and a beam shutter from overheating due to SR. Three masks limit a SR beam to a size of the aperture which is necessary for transporting an SR beam to the experimental area. The apertures

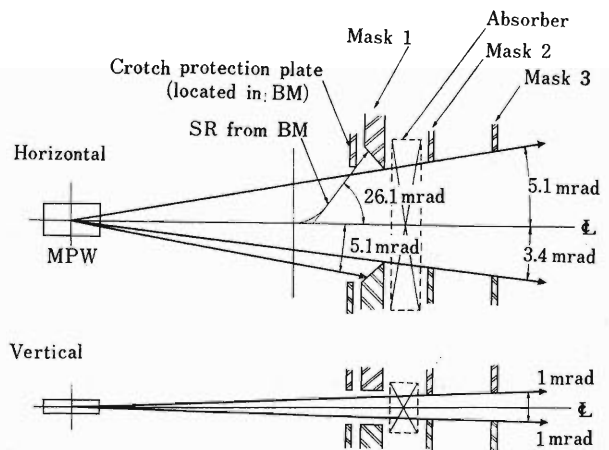


Fig. 2. SR beam from MPW.

Table 1. Absorbed power and power density. P_{ab} is the absorbed power in kW and W_{ab} the power density in kW/cm². Power densities are the values at the surfaces perpendicular to SR.

	from MPW		from BM		MPW+BM	
	P_{ab}	W_{ab}	P_{ab}	W_{ab}	P_{ab}	W_{ab}
Absorber	7.0	3.5	0.2	0.9	7.2	4.4
Mask 1	1.4	3.8	0.5	1.1	1.9	4.9
Mask 2	0.0	0.0	0.1	0.6	0.1	0.6
Mask 3	0.0	0.0	0.1	0.3	0.1	0.3

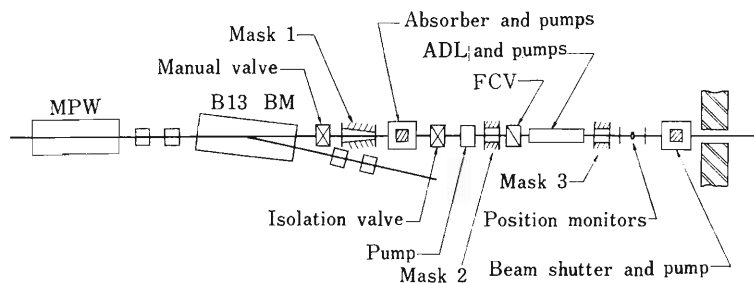


Fig. 1. Schematic layout of the front end of BL-13.

* Photon Factory, National Laboratory for High Energy Physics.

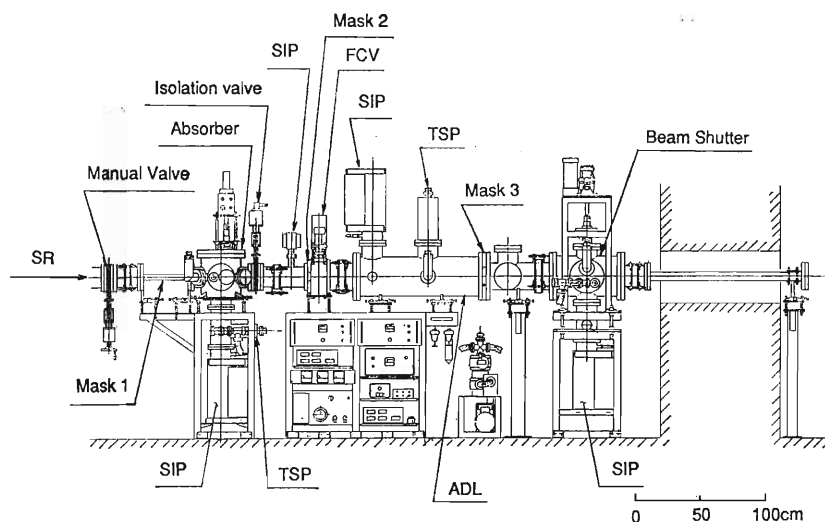


Fig. 3. Schematic assembly of the front end of BL-13.

for a SR beam, and absorbed powers and power densities deposited on a absorber and masks for the design parameters of 2.5 GeV and 350 mA are shown in Fig. 2 and Table 1, respectively. A beam shutter made of a stainless steel block of 16 cm in width, 8 cm in height, and 40 cm in thickness is operated with a hydrostatic pressure cylinder and is installed for personnel protection from radiation caused by beam loss during injection. Final assembly of BL-13 is shown in Fig. 3. Vacuum chambers including main components are made of stainless steel and evacuated below 2×10^{-10} Torr after baking at 250°C using three 110 l/s sputter-ion pumps (SIP) and two 5,500 l/s titanium-sublimation pumps (TSP). A 170 l/s turbomolecular pump is used as a roughing pump.

On the base of the method given by Okano and Tominaga,¹⁾ we made an analysis to simulate the transit time in ADL. A simulation model is shown in Fig. 4. Calculations were made on the assumptions that the flow rate through an orifice is determined by the pressures on both sides of the orifice and that the gas flow which blow straight through the orifice is negligibly small. The pressure of each segment, P_i , is given by

$$V_i(dP_i/dt) = C_{i-1}(P_{i-1} - P_i) - C_i(P_i - P_{i+1}) - S_i P_i \quad (1)$$

$$V_0(dP_0/dt) = -C_0(P_0 - P_i) \quad (2)$$

where C_i is the conductance of the orifice, V_i the volume of each segment, S_i the pumping speed of an auxiliary pump, P_0 and V_0 the pressure and the volume of a reservoir, respectively, and P_{N+1} and V_{N+1} the pressure and volume of the main vacuum system of a storage ring. V_{N+1} is assumed to be infinitely large and P_{N+1} is fixed at the initial pressure of the storage ring.

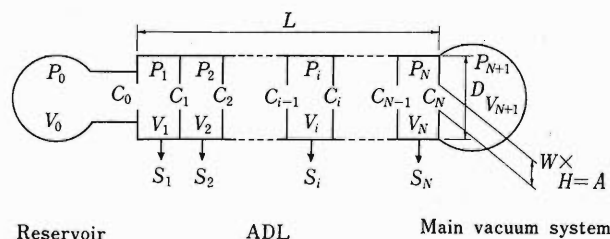


Fig. 4. Simulation model of a N-segmented ADL.

The increasing rate of pressure for each segment at a given time is calculated from Eqs. 1 and 2. The pressure after considerably short time intervals, Δt is determined by

$$(P_i)_{at+\Delta t} = (P_i)_{at} + (dP_i/dt)_{at} \Delta t \quad (3)$$

In this manner, the increases in pressure were numerically calculated. Gas molecules in each segment of ADL were assumed to be in thermal equilibrium with the wall, and the conductance of the orifice was calculated all in air at 293 K.

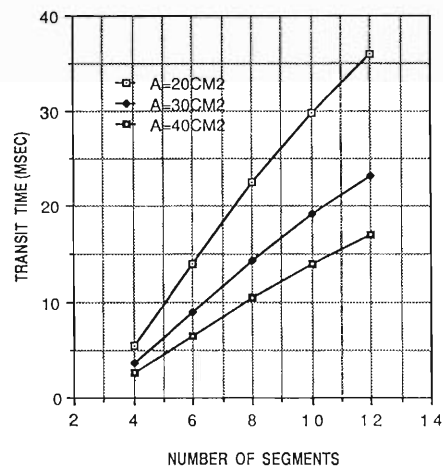


Fig. 5. Relation between the transit time and number of segments.

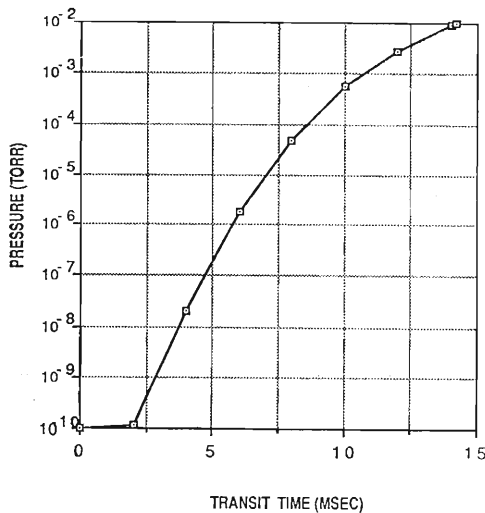


Fig. 6. Pressure increase in the last segment.

Figure 5 shows a relationship between the transit time to reach 1×10^{-2} Torr in the last segment and the number of the segments as parameter of the orifice area A . Initial conditions for calculation are: $P_0 = 760$ Torr at $t = 0$, P_1 to $P_N = 1 \times 10^{-10}$ Torr, $V_0 = 60$ l, $L = 90$ cm, and $D = 28.9$ cm. All segments have an equal volume. Pumps are applied only to the

$N/2$ 'th and N 'th segment with the effective pumping speeds of 5,300 l/s and 102 l/s, respectively. The calculated transit times increase with increasing number of segments and/or decreasing orifice area.

Figure 6 shows the pressure increase in the last segment of the finally designed ADL. In this calculation, the orifice area of 39 cm² was used. Ten segments have irregular volumes owing to pumps installed. The transit time to reach 1×10^{-3} Torr in the last segment is approximately 12 ms, which is long enough. In an actual beam line, since the transit time in components other than ADL is further added to that in ADL, the realistic one becomes longer than 12 ms and thereby the pressure in the last segment is expected to be less than 1×10^{-3} Torr. The calculated results show that the FCV can be closed before the pressure front reaches the storage ring.

The construction of BL-13 including a control system is scheduled to be completed by the end of August, 1988, and experiments using BL-13 will be started at the beginning of 1989.

Reference

- 1) T. Okano and G. Tominaga: *Jpn. J. Appl. Phys.*, **20**, 1729 (1981).

V-26. Construction of a Multipole Wiggler, B13MPW, at KEK-PF

S. Sasaki, M. Hara, S. Yamamoto,* T. Shioya,* and H. Kitamura*

A multipole wiggler is under construction at the Photon Factory of the National Laboratory for High Energy Physics, KEK-PF. This insertion device, B13MPW, will be installed at the straight section between the bending magnets, B12 and B13, of the 2.5 GeV electron storage ring of the PF. It will provide with highly intense synchrotron radiation in the X-ray region for the diffraction and absorption experiments.

The maximum magnetic field, B_{\max} , of 1.5 T is required so that a sufficient flux of photon beam up to 10 keV may be obtained. The critical photon energy corresponding to the 1.5-T magnetic field is 6.2 keV. The hybrid configuration of magnetic and core materials was adopted in order to realize such a high field. As shown in Fig. 1, each magnetic pole is composed of a permendur core and Nd-Fe-B permanent magnets having the residual magnetic field of 1.2 T, the coercive force of 17 kOe, and the maximum energy product of 35 MGOe.

The number of the magnetic poles was determined to be 27 for the B13MPW from the conditions: (1) the minimum gap width of 27 mm, (2) the period length of the magnetic field of 180 mm, and (3) the available length of the straight section of about 3 m. Therefore about thirty times higher flux of a photon beam is expected around 5 keV photon energy compared with that of the bending magnet radiation. The designed parameters are listed in Table 1. Figure

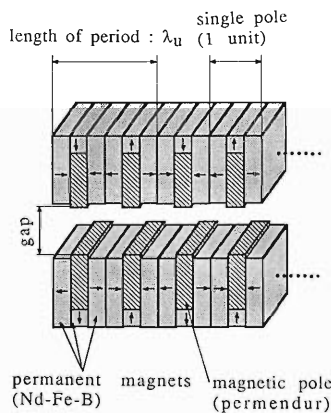


Fig. 1. Schematic structure of the hybrid configuration of the multipole wiggler, B13MPW.

* Photon Factory, National Laboratory for High Energy Physics.

Table 1.

Minimum gap	27 mm
Period length of the magnetic field	180 mm
Width of the magnetic pole	150 mm
Number of poles	27
Maximum magnetic field	1.5 T
Maximum K -value	25
Maximum load	13 tf

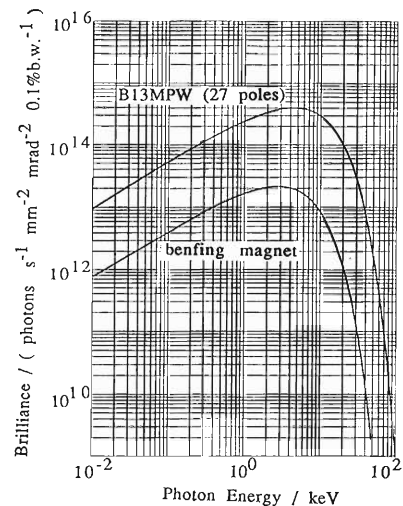


Fig. 2. Spectrum of the multipole wiggler, B13MPW, calculated on the basis of the parameters listed in Table 1 and the beam parameters of the PF ring ($\sigma_x=1.7$ mm, $\sigma_y=0.22$ mm, $\sigma_x'=0.15$ mrad, $\sigma_y'=0.024$ mrad).

2 shows the spectrum calculated by using the parameters listed in Table 1 and the beam parameters of the PF ring.

Magnetic properties of a single pole was measured using a mirror image method. The results show that our design of the magnet yields the satisfactory magnetic properties including maximum field strength of 1.49 T at the gap of 27 mm.

Each magnetic pole is mounted on I-beams of the supporting frame so as to generate an alternating magnetic field of 1.5 T with the period length of 180 mm. Since an electron travels sinusoidally in such a field, the geometrical conditions as well as the performance of the magnetic poles are very important for the characteristics of the radiation from the device. The schematic view of the overall structure is shown in Fig. 3.

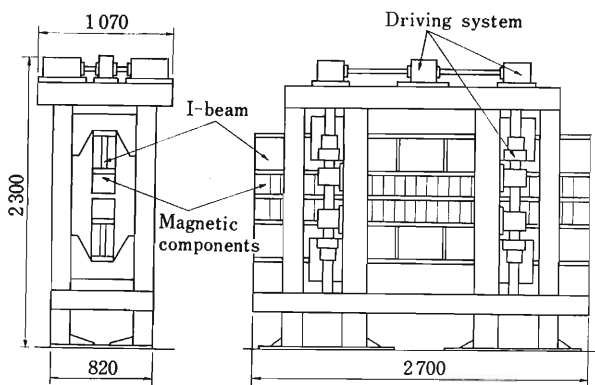


Fig. 3. Schematic view of the multipole wiggler, B13MPW.

In the design process of the support frame, the heavy load of 13 tf generated by the magnetic field was considered. The required specifications were; (1) the machining accuracy is high enough: the degree of straightness of the I-beams should be within

$50 \mu\text{m}/\text{m}$ and the parallelism of the two beams should be at most $20 \mu\text{m}$ over the full length of the beams of 2,700 mm. (2) The strain of each beam should be less than $15 \mu\text{m}$ by the magnetic force and the self weights. (3) The gap should be controlled with the accuracy of $5 \mu\text{m}$ over the moving range of the gap from 27 mm to 250 mm.

The gap width between upper and lower poles can be adjusted by changing the inter I-beam distance by the driving system. The techniques used for numerically controlled machines are applied to the driving system. The operation of the device will be controlled by a computer placed at the operating room of the storage ring with a GPIB interface.

This project is being performed by the Insertion Device Group of KEK-PF and the Design Group at Synchrotron Radiation Facility Planning Section at RIKEN under the auspices of the Special Coordination Funds for Promoting Science and Technology by the Science and Technology Agency.

VI. RADIATION MONITORING

1. Leakage-Radiation Measurements in the Cyclotron Building

I. Sakamoto, S. Fujita, and I. Kohno

In October 1987 leakage radiation was measured at various points in the cyclotron building, when a target placed in the beam course No. 2 was bombarded with 40 MeV helium ions at a beam intensity of $0.4 \mu\text{A}$.

γ -Ray dose rates were measured with an ionization chamber survey meter, and dose-equivalent rates for fast neutrons and slow neutrons were measured with a "rem meter."* The results are shown in Fig. 1.

The leakage doses measured from April 1986 to December 1987 with γ ray and neutron film badges placed at two positions on the underground passage (point A and B in Fig. 1) are shown in Table 1.

The operation of the cyclotron was discontinued on according to the scheduled from August 1986 to January 1987.

Of the dose values at point A measured every month, the maximum total dose of 1,810 mrem was observed in June 1986, when the values for γ rays and thermal neutrons and fast neutrons were 1,280, 130, and 400 mrem, respectively.

The high fast-neutron doses observed at point A in April, May, and June 1986 were 200, 100, and 400 mrem, respectively. These increases in neutron dose were due mainly to activation analysis and radio-isotope production carried out for these periods.

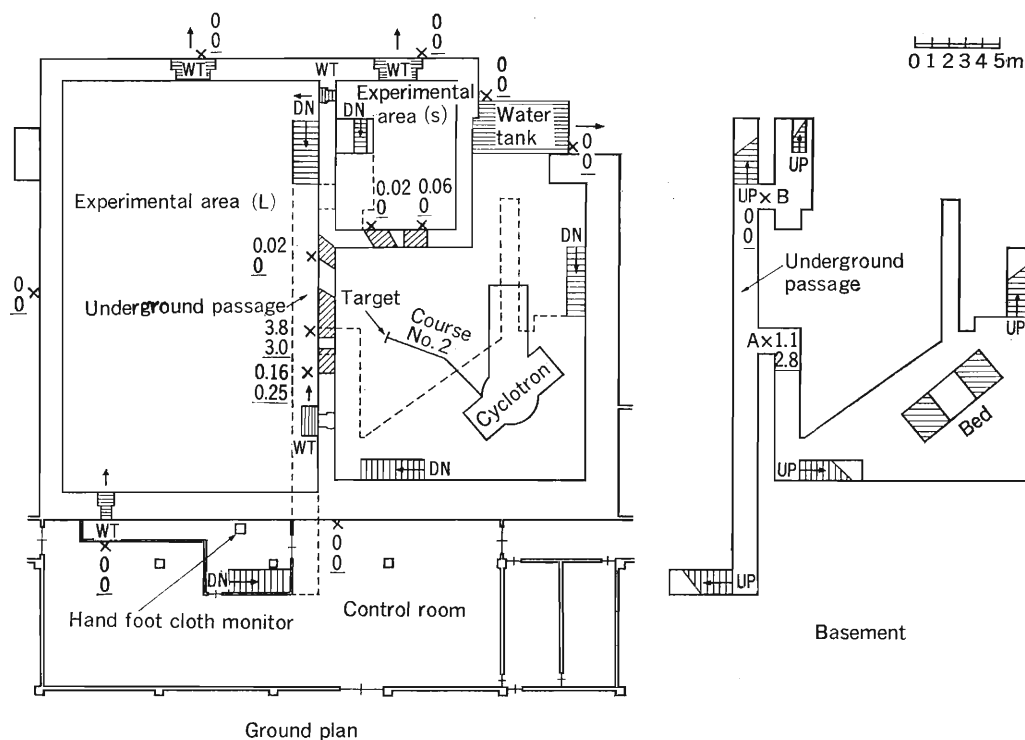


Fig. 1. Leakage-radiation (neutrons and γ rays) in the cyclotron building.

Operating conditions	Dose unit
E_α : 40 MeV	γ ray : mR/h
Beam course : No. 2	Neutron : mrem/h (under line)
Target : Ir	

* A Neutron Dose Rate Meter 2202 manufactured by AB Atomenergi, Sweden.

Table 1. Leakage-radiation dose (in mrem) in the underground passage of the cyclotron building from April 1986 to December 1987.

Month	Point A*				Point B*			
	γ rays (mrem)	Thermal neutrons (mrem)	Fast neutrons (mrem)	Total (mrem)	γ rays (mrem)	Thermal neutrons (mrem)	Fast neutrons (mrem)	Total (mrem)
4.86'	230	30	200	460	10	0	50	60
5	210	30	100	340	0	0	10	10
6	1,280	130	400	1,810	30	0	100	130
7	0	0	0	0	0	0	0	0
8	0	0	0	0	0	0	0	0
9	0	0	0	0	0	0	0	0
10	0	0	0	0	0	0	0	0
11	0	0	0	0	0	0	0	0
12	0	0	0	0	0	0	0	0
1.87'	0	0	0	0	0	0	0	0
2	30	0	10	40	0	0	10	10
3	0	0	0	0	0	0	0	0
4	0	0	0	0	0	0	0	0
5	310	40	0	350	0	0	10	10
6	550	0	10	560	0	0	0	0
7	220	20	20	260	0	0	10	10
8	0	0	0	0	0	0	0	0
9	280	10	20	310	0	0	0	0
10	320	10	40	370	0	0	10	10
11	70	10	0	80	0	0	0	0
12	0	0	0	0	0	0	0	0
Total	3,500	280	800	4,580	40	0	200	240

* See Fig. 1.

VI-2. Routine Monitoring of the Cyclotron, RILAC, and TANDETRON

I. Sakamoto, S. Fujita, M. Yanokura, T. Kobayashi, O. Kurihara,
T. Katou, M. Miyagawa, S. Kagaya, S. Shinohara, and I. Kohno

The present report describes the results of routine radiation monitoring carried out for the cyclotron, RILAC, and TANDETRON from April 1986 to December 1987. Because of unexpected contaminations found in the hot laboratory and experimental area in the cyclotron building in August 1986, the cyclotron and RILAC were stopped compulsorily for three months. The radioactive nuclide found by γ -ray spectrometry was ^{210}Pb . The decontamination and repairs of the hot laboratory were performed from August 1986 to January 1988. RILAC was put back in operation in the middle of November, 1986. The operation of the cyclotron was discontinued on account of long scheduled shutdown from August 1986 to January 1987.

Aspects of the leakage radiation from the cyclotron are described in a succeeding report.¹⁾

(1) Residual activities of the cyclotron

In August 1987, the dose rates due to residual activities of the machine were measured 23 days after the scheduled shutdown; the result are shown in Table 1. The external exposure doses for two workers during replacement of the septum were 25 and 28 mrem.

(2) Contamination in the cyclotron building

The surface contamination has been kept below $10^{-5} \mu\text{Ci}/\text{cm}^2$ on the floors of the cyclotron building. The radioactive nuclides found by γ -ray spectrometry were ^{183}Re , ^{65}Zn , and ^{185}Os in the cyclotron vault and the experimental areas, and ^{77}Br , ^{65}Zn , and ^{137}Cs in the hot laboratory and chemical laboratories. The contamination was wiped off twice a year. Immediately after this decontamination, the activities on the floor of most of the above places were reduced below $10^{-7} \mu\text{Ci}/\text{cm}^2$.

When radioactive substances were handled in the

hot laboratory and chemical laboratories, the air in a draft chamber was activated. The air in the draft chamber was exhausted; and the radioactivity in the exit was found $10^{-12} \mu\text{Ci}/\text{cm}^3$.

(3) Drainage

The radioactivities in drain water from the cyclotron and the linac buildings were found to be of the order of 10^{-8} – $10^{-5} \mu\text{Ci}/\text{cm}^3$. The total activity in aqueous effluents was about $490 \mu\text{Ci}$, in which the main radioactive nuclide was ^{77}Br , the radioactivity was about $470 \mu\text{Ci}$, and the other nuclides found by γ -ray spectrometry were ^{75}Se , ^{137}Cs , ^{51}Cr , ^{56}Co , and ^{57}Co .

(4) Radiation monitoring for RILAC and TANDETRON

The leakage radiation during operation of RILAC was measured in the outside the linac building every three months. No leakage of γ rays and neutrons from the linac building was detected. No contamination due to residual activities was found on the floor of control area and conditioning air in the linac building.

X-ray monitoring was carried out for TANDETRON, when a rutile (TiO_2) target was bombarded with 2.1 MeV B^{2+} ions of 0.2 nA, the maximum irradiation dose rates measured around TANDETRON was 1.2 mR/h. No leakage X-rays were detected around the target chamber and outside TANDETRON room.

(5) Personnel monitoring

The external exposure dose to personnel were measured by using γ ray and neutron film badges. The dose received by accelerator workers from April 1986 to December 1987 are shown in Tables 2 and 3. The collective γ -ray doses to all workers from April 1986 to March 1987 and from April to December 1987 were 1,160 and 180 man-mrem, respectively. The collective dose owing to thermal and fast neutron exposures was under the detection limit. The collective dose to the workers from April 1986 to March 1987 increased to 122% of the value in the preceding period.

In August 1986, ^{210}Pb intakes occurred to two workers who checked up a contaminated substance with a radioisotope in the hot laboratory. The amount of intake in the operation was assessed by

Table 1. Dose rates of residual activities.

Location	Dose rate (mR/h)
ca. 1 cm apart from septum (with a cover (Pb 3 mm), before replacement of septum)	100
ca. 1 cm apart from septum holder (with a cover (Pb 3 mm), before replacement of septum)	80

Table 2. Annual external exposure doses received by RIKEN accelerator workers from April 1986 to March 1987.

Workers	Number of persons				Collective dose (mrem)
	Dose undetectable	10-100 (mrem)	>100 (mrem)	Total (mrem)	
Cyclotron operators	9	0	0	9	0
Linac operation and maintenance groups	7	3	0	10	30
Nuclear physicists	16	1	0	17	50
Accelerator physicists	9	3	0	12	90
Physicists in other fields	25	3	0	28	60
Nuclear chemists	4	4	3	11	930
Radiation chemists	6	0	0	6	0
Biological chemists	9	0	0	9	0
TANDETRON workers	11	0	0	11	0
Health physicists	6	0	0	6	0
Total	102	14	3	119	1,160

Average annual dose per person, 9.7 mrem; Maximum individual annual dose, 370 mrem.

Table 3. External exposure doses received by RIKEN accelerator workers from April to December 1987.

Workers	Number of persons				Collective dose (mrem)
	Dose undetectable	10-100 (mrem)	>100 (mrem)	Total (mrem)	
Ring cyclotron operation and maintenance groups	6	0	0	6	0
Cyclotron operators	4	1	0	5	60
Linac operation and maintenance groups	9	1	0	10	30
Nuclear physicists	16	0	0	16	0
Accelerator physicists	14	1	0	15	30
Physicists in other fields	26	1	0	27	30
Nuclear chemists	6	1	0	7	20
Radiation chemists	4	1	0	5	10
Biological chemists	8	0	0	8	0
TANDETRON workers	9	0	0	9	0
Health physicists	6	0	0	6	0
Total	108	6	0	114	180

Average dose per person, 1.6 mrem; Maximum individual dose, 60 mrem.

using the equation as recommended by ICRP²⁾ for the workers from the ²¹⁰Pb concentration in feces. The internal exposure dose of the workers were 4.2 rem and 0.3 rem. The workers were subjected to periodic medical examination, but showed no abnormal signs.

Commissioning of RIKEN Ring Cyclotron started in April 1987, and its operation and maintenance

groups were organized.

References

- 1) I. Sakamoto, S. Fujita, and I. Kohno: p.254 in this report.
- 2) Recommendations of the International Commission on Radiological Protection Report of Committee II on Permissible Dose for Internal Radiation (1959); ICRP Publication 2, Pergamon Press, Oxford (1960).

VI-3. Radiation Monitoring at RIKEN Ring Cyclotron Facility

S. Fujita, I. Sakamoto, T. Inamura, and H. Kamitsubo

The Radiation Safety Control System (RSCS) has been in steady operation since it was installed.¹⁾ Figure 1 shows the layout of RIKEN Ring Cyclotron facility and its indoor monitoring positions. Commissioning of RIKEN Ring Cyclotron started in April 1987; and radiation monitoring has been continuously and automatically performed by the RSCS. The beam line available for experiments was in the experimental vault E1 only. Here we shall present a typical example recorded.

(1) Leakage radiation

In July, an experiment was carried out with a ⁶⁵Cu beam of 16.7 MeV/u in the E1 experimental vault; the beam current was 100 nA. Figure 2 shows day variations in dose rates recorded on radiation monitors: (a) RIKEN Ring Cyclotron vault and (b) the experimental vault E1. The dose rate recorded on July 20 shows that a beam was accelerated (Fig. 2(a)), but no leakage γ rays and neutrons were recorded in the E1 vault (Fig. 2(b)). The dose rates on July 21–22 show that the beam was guided into the E1 vault; accordingly, the radiation

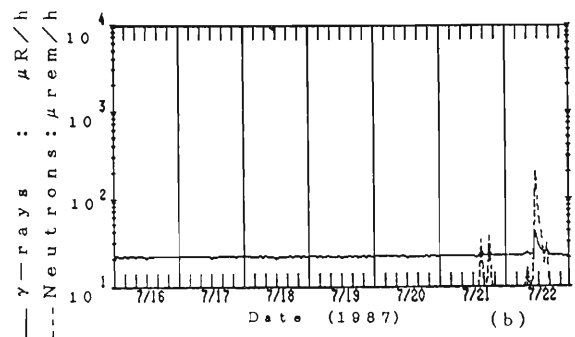
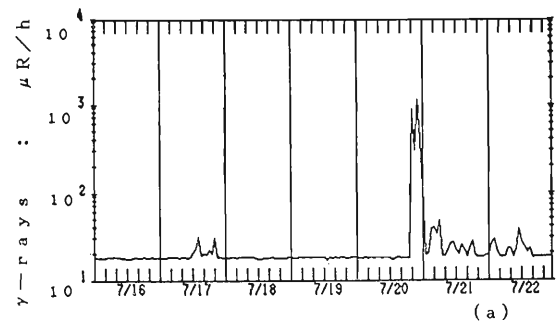
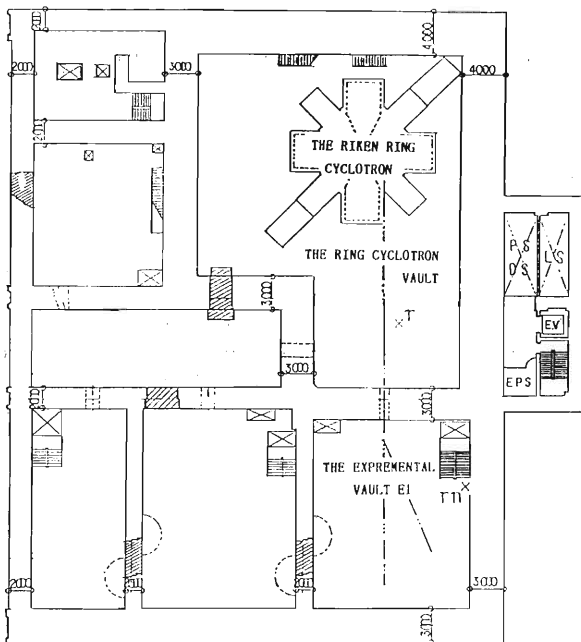


Fig. 2. Day variations in the radiation level measured in RIKEN Ring Cyclotron facility. Detectors are: (a), an ionization chamber in RIKEN Ring Cyclotron vault; (b), an ionization chamber and a BF₃ counter in the experimental vault E1.



Q12345 m

Fig. 1. Layout of RIKEN Ring Cyclotron facility as of 1987. Monitoring positions are denoted by x.

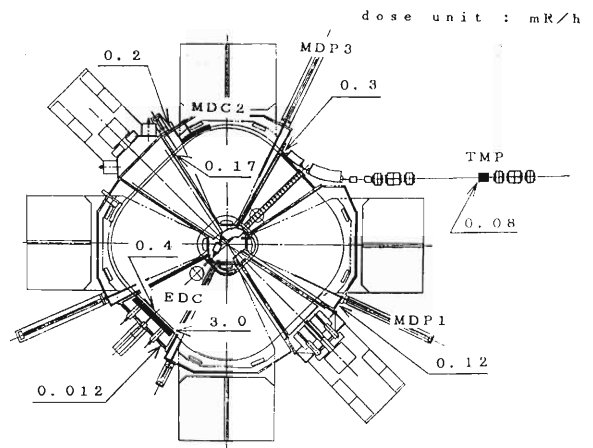


Fig. 3. Detection points around RIKEN Ring Cyclotron. EDC, an electrostatic deflection channel; MDC2, a magnetic deflection channel; MDP1, a main differential probe 1; MDP3, a main differential probe 3; and TMP, a turbo-molecular pump.

level in the cyclotron vault (a) suddenly decreased and the neutron dose rate in the E1 vault sharply increased (b).

No leakage γ rays and no neutrons from RIKEN Ring Cyclotron and E1 vaults were detected since commissioning.

(2) Residual activities

On September 7-8, days after experiment, the dose rates due to residual activities of the machine

were measured with a NaI scintillation survey meter. The results are shown in Fig. 3. The maximum dose rate was observed to be 3.0 mR/h at EDC, an electrostatic deflection channel of the beam extraction region.

Reference

- 1) I. Sakamoto, S. Fujita, T. Wada, and M. Takebe: *RIKEN Accel. Prog. Rep.*, **20**, 206 (1986).

VII. LIST OF PUBLICATIONS

1. Accelerator development and accelerator physics

- 1) H. Kamitsubo: "Progress in RIKEN Ring Cyclotron Project," Proc. 11th Int. Conf. Cyclotrons and Their Applications, Tokyo, Oct. 1986, p. 17 (1987).
- 2) I. Kohno, K. Ogiwara, S. Fujita, K. Ikegami, T. Kageyama, S. Kohara, and H. Takebe: "RIKEN 160 cm Cyclotron," Proc. 11th Int. Conf. Cyclotrons and Their Applications, Tokyo, Oct. 1986, p. 46 (1987).
- 3) Y. Miyazawa, M. Hemmi, T. Inoue, T. Kambara, M. Yanokura, M. Kase, T. Kubo, E. Ikezawa, Y. Chiba, and I. Tanihata: "Operation of RILAC at RIKEN," Proc. 11th Int. Conf. Cyclotrons and Their Applications, Tokyo, Oct. 1986, p. 50 (1987).
- 4) A. Goto, H. Takebe, S. Motonaga, K. Hatanaka, Y. Yano, T. Wada, and N. Nakanishi: "Isochronous Fields for RIKEN Ring Cyclotron," Proc. 11th Int. Conf. Cyclotrons and Their Applications, Tokyo, Oct. 1986, p. 292 (1987).
- 5) T. Fujisawa, K. Ogiwara, S. Kohara, Y. Oikawa, I. Yokoyama, M. Nagase, I. Takeshita, Y. Chiba, and Y. Kumata: "Radio Frequency System of the RIKEN Ring Cyclotron," 11th Int. Conf. Cyclotrons and Their Applications, Tokyo, Oct. 1986, p. 329 (1987).
- 6) M. Hara, T. Wada, K. Mitomori, and F. Kikuchi: "Three Dimensional Analysis of RF Electromagnetic Field by the Finite Element Method," Proc. 11th Int. Conf. Cyclotrons and Their Applications, Tokyo, Oct. 1986, p. 337 (1987).
- 7) K. Ikegami, S. Nakajima, Y. Oikawa, I. Takeshita, S. Motonaga, and S.H. Be: "Vacuum System for the RIKEN Ring Cyclotron," Proc. 11th Int. Conf. Cyclotrons and Their Applications, Tokyo, Oct. 1986, p. 392 (1987).
- 8) T. Wada, H. Takebe, J. Fujita, T. Kambara, and H. Kamitsubo: "Control System of the RIKEN Ring Cyclotron," Proc. 11th Int. Conf. Cyclotrons and Their Applications, Tokyo, Oct. 1986, p. 407 (1987).
- 9) M. Nagase, H. Takebe, T. Wada, and K. Shimizu: "Program for Controlling Magnet Power Supplies of the RIKEN Ring Cyclotron," Proc. 11th Int. Conf. Cyclotrons and Their Applications, Tokyo, Oct. 1986, p. 410 (1987).
- 10) M. Kase, I. Yokoyama, I. Takeshita, Y. Oikawa, M. Saito, and Y. Yano: "Beam Diagnostic Equipments for RIKEN Ring Cyclotron and Its Beam Lines," Proc. 11th Int. Conf. Cyclotrons and Their Applications, Tokyo, Oct. 1986, p. 443 (1987).
- 11) Y. Yano, A. Goto, K. Hatanaka, H. Takebe, and S. Motonaga: "Beam Injection and Extraction System of RIKEN Ring Cyclotron," Proc. 11th Int. Conf. Cyclotrons and Their Applications, Tokyo, Oct. 1986, p. 470 (1987).
- 12) N. Nakanishi, T. Kageyama, and H. Kamitsubo: "AVF-Cyclotron as an Injector for RIKEN Ring Cyclotron," Proc. 11th Int. Conf. Cyclotrons and Their Applications, Tokyo, Oct. 1986, p. 511 (1987).
- 13) K. Hatanaka, T. Inamura, Y. Yano, A. Goto, M. Kase, and H. Kamitsubo: "Beam Transport System for RIKEN Ring Cyclotron," Proc. 11th Int. Conf. Cyclotrons and Their Applications, Tokyo, Oct. 1986, p. 523 (1987).
- 14) T. Shikata, N. Nakanishi, S. Fujita, and T. Kosako: "Shielding Calculation of Neutrons for the RIKEN Ring Cyclotron Facility," Proc. 11th Int. Conf. Cyclotrons and Their Applications, Tokyo, Oct. 1986, p. 538 (1987).
- 15) T. Kambara: "Control System of the RIKEN Heavy-Ion Linear Accelerator," *Reports I.P.C.R.* (in Japanese), **62**, 88 (1986).
- 16) K. Ikegami, S. Nakajima, S.H. Be, N. Ohsako, K. Morimoto, T. Kikuchi, and S. Morishita: "Design and Performance Characteristics of Refrigerator-Cooled Cryopumps for the RIKEN Ring Cyclotron," *Vacuum*, **38**, 99 (1987).

2. Nuclear physics and nuclear instrumentation

- 1) E. Minehara, M. Oshima, S. Kikuchi, T. Inamura, A. Hashizume, and H. Kumahara: "Signature Dependence Observed for M1 Transitions between Rotational Levels Based on an $f_{7/2}$ Single-Particle State in ^{163}Dy ," *Phys. Rev. C*, **35**, 858 (1987).
- 2) T. Ichihara, H. Sakaguchi, M. Nakamura, T. Noro, H. Sakamoto, H. Ogawa, M. Yosoi, M. Ieiri, N. Isshiki, Y. Takeuchi, and S. Kobayashi: "Effect of Inelastic Excitation on the Elastic Scattering of Alpha Particles from $^{144,148,150,152,154}\text{Sm}$ at 120 MeV," *Phys. Rev. C*, **35**, 931 (1987).
- 3) H. Sakai, N. Matsuoka, T. Saito, A. Shimizu, M. Tosaki, M. Ieiri, K. Imai, A. Sakaguchi,

- and T. Motobayashi: "Transverse Polarization Transfer $D_{NN}(0^\circ)$ Measurements for the (p, n) Reactions on ^{58}Ni and ^{90}Zr at $E_p = 80$ MeV," *Phys. Rev. C*, **35**, 1280 (1987).
- 4) T. Ichihara, H. Sakaguchi, M. Nakamura, M. Yosoi, M. Ieiri, Y. Takeuchi, H. Togawa, T. Tsutsumi, and S. Kobayashi: "Inelastic Proton Scattering Exciting the γ -Vibrational Band in Deformed Nuclei ($152 \leq A \leq 192$) at 65 MeV and the Systematics of the Hexadecapole (Y_{42}) Strength of the γ -Vibration," *Phys. Rev. C*, **36**, 1754 (1987).
 - 5) H. Sakai, N. Matsuoka, T. Noro, T. Saito, A. Shimizu, M. Tosaki, M. Ieiri, K. Imai, A. Sakaguchi, Y. Takeuchi, and T. Motobayashi: "A Neutron Polarimeter for the (p, n) Reaction at $E_p = 50$ –80 MeV," *Nucl. Instrum. Methods A*, **257**, 279 (1987).
 - 6) K. Ieki, N. Hoshino, M. Iwase, H. Ohnuma, Y. Takahashi, and H. Orihara: "A Liquid-Helium Scintillator as a Fast-Neutron Polarimeter," *Nucl. Instrum. Methods A*, **262**, 323 (1987).
 - 7) K. Morita, T. Inamura, T. Nomura, J. Tanaka, H. Miyatake, M. Fujioka, T. Shinozuka, M. Yoshii, H. Hama, K. Taguchi, K. Sueki, Y. Hatsukawa, K. Furuno, and H. Kudo: "An Ion-Guide Isotope Separator On-Line at INS," *Nucl. Instrum. Methods B*, **26**, 406 (1987).
 - 8) H. Katsuragawa, T. Minowa, M. Shimazu, and T. Inamura: "Electron-Ion Coincidence Method for Ultrasensitive Detection of Atoms," *Nucl. Instrum. Methods B*, **26**, 440 (1987).
 - 9) M. Matsuo and K. Matsuyanagi: "Microscopic Description of Anharmonic Gamma-Vibrations by Means of the Selfconsistent-Collective-Coordinate Method. III," *Prog. Theor. Phys.*, **78**, 591 (1987).
 - 10) M. Matsuo: "Microscopic Analysis of the Hexadecapole Strengths to the Gamma-Vibrational Bands," *Prog. Theor. Phys.*, **78**, 609 (1987).
 - 11) H. Kawakami, K. Nisimura, T. Ohishima, S. Sibata, Y. Shoji, I. Sugai, K. Ukai, T. Yasuda, N. Morikawa, N. Nogawa, T. Nagafuchi, T. Suzuki, F. Naito, H. Taketani, M. Iwahashi, K. Hisatake, M. Fujioka, Y. Fukushima, T. Matsuda, and T. Taniguchi: "An Upper Limit for the Mass of Electron Anti-Neutrino from the INS Experiment," *Phys. Lett. B*, **51**, 198 (1987).
 - 12) S. Hirezaki, T. Kajima, K.-I. Kubo, H. Toki, and I. Tanihata: "Pionic Atoms of Unstable Nuclei," *Phys. Lett. B*, **194**, 20 (1987).
 - 13) H. Ohsumi, H. Ejiri, T. Shibata, K. Okada, Y. Nagai, and T. Motobayashi: "Continuum Spectra of Neutrons Following the $^{90}\text{Zr}(\alpha, \alpha')$ Reaction," *Nucl. Phys. A*, **469**, 507 (1987).
 - 14) S. Yamaji, H. Hofmann, and R. Samhammer: "Selfconsistent Transport Coefficients for Average Collective Motion at Moderately High Temperatures," *Nucl. Phys. A*, **475**, 487 (1987).
 - 15) K. Sato and S. Yoshida: "Studies of Nuclear Second Moments for Pre-Equilibrium Nuclear Reaction Theories," *Z. Phys. A*, **327**, 421 (1987).
 - 16) S. Kubota, T. Motobayashi, J. Ruan (Gen), T. Murakami, J. Kasagi, and T. Shimizu: "Response of Barium-Fluoride Plastic Scintillator to Light Particles and Particle Identification," *IEEE Trans. Nucl. Sci.*, **NS-34**, 438 (1987).
 - 17) Y. Nojiri, K. Matsuta, T. Minamisono, K. Sugimoto, K. Takeyama, H. Hamagaki, S. Nagamiya, K. Omata, Y. Shida, I. Tanihata, T. Kobayashi, S. Matsuki, S. Shimoura, J. R. Alonso, G. Krebs, and T. J. M. Symons: "Online Isotope Separation of Projectile Fragments Produced in Relativistic Heavy-Ion Reactions," *Hyperfine Interact.*, **35**, 1019 (1987).
 - 18) K. Asahi: "Physics Using Secondary Beams," *Butsuri* (in Japanese), **42**, 799 (1987).
3. Atomic and solid-state physics
 - 1) T. Watanabe and K. Hino: "Radiative Processes in High-Energy Ion-Atom Collisions," *Nucl. Instrum. Methods A*, **262**, 29 (1987).
 - 2) H. Iwai, I. Shimamura, and T. Watanabe: "Irregularities in the Differential and Integral Cross Sections for Ion-Atom Collision in the Plane-Wave Born Approximation," *Nucl. Instrum. Methods A*, **262**, 37 (1987).
 - 3) H. Tawara, T. Tonuma, T. Matsuo, M. Kase, H. Kumagai, and I. Kohno: "Multiply Charged Atomic Ions Produced through Coulomb Explosions in Heavy Ion Impact," *Nucl. Instrum. Methods A*, **262**, 95 (1987).
 - 4) M. Kimura, N.F. Lane, K. Fujima, and H. Sato: "Theory of Ion-Surface Collisions; Case Study of He^+ Projectile Ion," *Nucl. Instrum. Methods A*, **262**, 114 (1987).
 - 5) Y. Kanai, Y. Awaya, T. Kambara, M. Kase, H. Kumagai, T. Mizogawa, and K. Shima: "Charge-State Distribution Measurements of Heavy Ions," *Nucl. Instrum. Methods A*, **262**, 128 (1987).
 - 6) T. Mizogawa, Y. Awaya, T. Kambara, Y.

- Kanai, M. Kase, H. Kumagai, P. H. Mokler, and K. Sima: "Target Thickness Dependence of Projectile Ar K X-Rays L-shell Non-equilibrium," *Nucl. Instrum. Methods A*, **262**, 141 (1987).
- 7) M. Uda, O. Benka, K. Fuwa, K. Maeda, and Y. Sasa: "Chemical Effects in PIXE Spectra," *Nucl. Instrum. Methods B*, **22**, 5 (1987).
 - 8) H. Tawara, T. Tonuma, K. Baba, T. Matsuo, M. Kase, T. Kambara, H. Kumagai, and I. Kohno: "Multiply Charged Ion Production through Coulomb Explosion of Molecular Ions in Heavy Ion-Molecule Collisions," *Nucl. Instrum. Methods B*, **23**, 203 (1987).
 - 9) K. Hino and T. Watanabe: "Cross Sections of Relativistic Radiative Electron Capture by the Use of Strong-Potential Born Calculation," *Phys. Rev. A*, **36**, 581 (1987).
 - 10) T. Tonuma, T. Matsuo, M. Kase, T. Kambara, H. Kumagai, S. H. Be, and I. Kohno: "Slow-Recoil Ne^{q+} Ions Produced by 1.05 MeV/amu Ne^{q+} ($q=2, 6, 8-10$) and Ar^{q+} ($q=4, 10, 12, 14$) Ion Impact: Evidence of Inner-Shell Electron Transfer in Highly Charged Recoil-Ion Production," *Phys. Rev. A*, **36**, 1941 (1987).
 - 11) N. Sakai and H. Sekizawa: "Magnetic-Electron Compton Profiles of Ferromagnetic Fe and Ferrimagnetic Mn Ferrite," *Phys. Rev. B*, **36**, 2164 (1987).
 - 12) A. Koyama, O. Benka, Y. Sasa, H. Ishikawa, and M. Uda: " Z_2 -Dependence of Peak Energies of Loss Electrons Back-Scattered from Target for He^+ Impact," *Phys. Rev. B*, **36**, 4535 (1987).
 - 13) K. Hino and T. Watanabe: "Angular Distribution and Linear-Polarization Correlation of Photons Induced by the Relativistic Electron Capture Process," *Phys. Rev. A*, **36**, 5862 (1987).
 - 14) I. Hashimoto, H. Yorikawa, H. Mitsuya, H. Yamaguchi, K. Takaiishi, T. Kikuchi, K. Furuya, E. Yagi, and M. Iwaki: "Annealing Behavior of Krypton-Implanted Aluminum, I. Diffraction Effects from Krypton Bubbles," *J. Nucl. Mater.*, **149**, 69 (1987).
 - 15) Y. Higashiguchi, Y. Suzuki, E. Yagi, M. Narui, and H. Kayano: "Effect of Helium on the Deformation Mode for Ti-7.5 Al Alloy," *J. Nucl. Mater.*, **149**, 328 (1987).
 - 16) I. Hashimoto, H. Yorikawa, H. Mitsuya, H. Yamaguchi, K. Furuya, E. Yagi, and M. Iwaki: "Annealing Behavior of Krypton-Implanted Aluminum, II. SEM Study on Surface Structure during Emission of Krypton Atoms," *J. Nucl. Mater.*, **150**, 100 (1987).
 - 17) K. Asai, F. Ambe, S. Ambe, T. Okada, and H. Sekizawa: "An Investigation on the After-Effects of $^{111}\text{In}(\rightarrow^{111}\text{Cd})$ EC Decay in $\alpha\text{-Fe}_2\text{O}_3$," *Hyperfine Interact.*, **34**, 277 (1987).
 - 18) K. Asai, T. Okada, and H. Sekizawa: "Super-transferred Hyperfine Magnetic Fields at $^{111}\text{Cd}(\leftarrow^{111}\text{In})$ in Ferrimagnetic Oxides with the Spinel Structure," *Hyperfine Interact.*, **34**, 435 (1987).
 - 19) Y. Fukai, K. Watanabe, and E. Yagi: "Nature and Some Consequences of Stress-Induced States of Hydrogen in b.c.c. Metals," *J. Less-Common Metals*, **130**, 202 (1987), (Extended Abstract).
 - 20) E. Yagi, S. Nakamura, T. Kobayashi, F. Kano, K. Watanabe, Y. Fukai, and T. Osaka: "Lattice Location Study of H in Ta by the Channeling Method," *J. Less-Common Metals*, **130**, 207 (1987), (Extended Abstract).
 - 21) T. Kambara, Y. Awaya, M. Kase, H. Kumagai, H. Shibata, and T. Tonuma: "REC X-Rays for ^3He and ^4He Targets," *J. Phys. Soc. Jpn.*, **56**, 1907 (1987).
 - 22) N. Sakai: "Simulation of Compton Double Scatterings of Circularly Polarized γ -Rays by Magnetic Electrons," *J. Phys. Soc. Jpn.*, **56**, 2477 (1987).
 - 23) Y. Awaya: "Recent Studies on Atomic Physics at RIKEN Accelerators," *JAERI-M*, **87-134**, 70 (1987).
 - 24) K. Ando, Y. Awaya, S. Kohmoto, H. Kumagai, T. Tonuma, and S. Tsurubuchi: "Spectrum and Lifetime of Highly Ionized Aluminum," *JAERI-M*, **87-134**, 84 (1987).
 - 25) R. Schuch, Y. Awaya, T. Kambara, T. Mizogawa, Y. Kanai, H. Shibata, and K. Shima: "Measurement of Impact Parameter Dependent Probabilities and Total Cross Sections for Target K-Shell Ionization by He^+ Ions," *Z. Phys. D-At. Mol. Clusters*, **4**, 339 (1987).
 - 26) K. Nagamine, T. Matsuzaki, K. Ishida, Y. Hirata, Y. Watanabe, R. Kadono, Y. Miyake, K. Nishiyama, S. E. Jones, and H. R. Maltrud: "Muonic X-Ray Measurement on the μ^- Sticking Probability for Muon Catalyzed Fusion in Liquid d-t Mixture," *Muon Catalyzed Fusion*, **1**, 137 (1987).
 - 27) A. Ohsaki, T. Watanabe, K. Nakanishi, and K. Iguchi: " μ^- -Transfer Cross Sections from (μ^-d) or (μ^-t) to t and α in High Velocity Region Using Classical Trajectory Monte Carlo Method," *Muon Catalyzed Fusion*, **1**, 245 (1987).
 - 28) T. Mizogawa, Y. Awaya, Y. Itoh, T. Kambara, Y. Kanai, T. Koizumi, S. Ohtani, K. Okuno, H. Shibata, S. Takagi, and S. Tsuru-

- buchi: "Charge State Distribution of Ions Extracted from a Compact EBIS," *Mass Spectrosc.*, **35**, 1 (1987).
- 29) Y. Awaya, K. Hino, A. Hitachi, Y. Kanai, K. Kawatsura, K. Kuroki, H. Vogt, Y. Yamazaki, and T. Watanabe: "Photon Angular Distribution of the Relativistic Electron Capture," Lecture Notes of Third Workshop on High-Energy Ion-Atom Collision Process, Springer-Verlag, p. 185 (1987).
 - 30) T. Nozaki, M. Uda, and E. Yagi: "Analysis of Impurities in Metals by Particle Accelerators," *Tetsu to Hagane* (in Japanese), **73**, 41 (1987).
 - 31) E. Yagi: "Lattice Location Study on Kr in Al by the Channelling Method," *Phys. Status Solidi A*, **104**, K13 (1987).
 - 32) N. Shimakura, N. Toshima, T. Watanabe, and H. Tawara: "Final (n, l) State-Resolved Electron Capture by Multiply Charged Ions from Neutral Atoms," IPPJ-AM-Report, IPPJ-AM-54, Inst. Plasma Phys., Nagoya Univ., p. 62 (1987).
 - 33) T. Watanabe: "Atomic and Molecular Research Using High Brightness and Strong Intensity Radiation Sources," Proc. Workshop Future Prospect of the Research Study Using Intense and Bright Synchrotron Radiation in VUV and Soft X-Ray Region (National Laboratory for High Energy Physics, Oho, Ibaraki, Japan), (in Japanese), p. 98 (1987).
 - 34) E. Yagi, F. Kano, S. Nakamura, M. Iwaki, and T. Osaka: "Defect-Impurity Interaction in Sn- or Ni-Implanted Aluminum," *Mater. Sci. Forum*, **15-18**, 605 (1987).
 - 35) T. Minowa, H. Katsuragawa, K. Nishiyama, M. Shimazu, and T. Inamura: "Novel Highly Sensitive Coincidence Detection Method for Resonance Ionization Signals," *J. Appl. Phys.*, **61**, 436 (1987).
 - 36) N. Shimakura, H. Sato, M. Kimura, and T. Watanabe: "Electron Capture Process in Collisions of O^{6+} with He Using Travelling Molecular Orbital Method," *J. Phys. B: At. Mol. Phys.*, **20**, 1801 (1987).
 - 37) H. Kawakami, K. Nisimura, T. Ohshima, S. Sibata, Y. Shoji, I. Sugai, K. Ukai, T. Yasuda, N. Morikawa, N. Nogawa, T. Nagafuchi, T. Suzuki, F. Naito, H. Taketani, M. Iwahashi, K. Hisatake, M. Fujioka, Y. Fukusima, T. Matsuda, and T. Taniguchi: "Precise Measurement of Ag KLL Auger-Spectrum," *Phys. Lett. A*, **121**, 414 (1987).
 - 38) T. Watanabe: "Report on International Conference on Atomic Physics and Few-Body Systems; Emphasis on Atomic Physics," *J. At. Energy Soc. Jpn.* (in Japanese), **29**, 34 (1987).
4. Radiochemistry, radiation chemistry and radiation biology
 - 1) M. Uda, K. Maeda, Y. Sasa, H. Kusuyama, and Y. Yokode: "An Attempt to Diagnose Cancer by PIXE," *Nucl. Instrum. Methods B*, **22**, 184 (1987).
 - 2) K. Maeda, Y. Yokode, Y. Sasa, H. Kusuyama, and M. Uda: "Multielemental Analysis of Human Thyroid Glands Using Particle Induced X-Ray Emission (PIXE)," *Nucl. Instrum. Methods B*, **22**, 188 (1987).
 - 3) Y. Sasa, K. Maeda, and M. Uda: "Application of PIXE and Diffraction Analysis to Ancient Remains," *Nucl. Instrum. Methods B*, **22**, 426 (1987).
 - 4) K. Maeda, Y. Sasa, M. Maeda, and M. Uda: "Diagnosis of River Pollution by PIXE," *Nucl. Instrum. Methods B*, **22**, 456 (1987).
 - 5) H. Nagai, S. Hayashi, M. Aratani, T. Nozaki, M. Yanokura, and I. Kohno: "Reliability, Detection Limit and Depth Resolution of the Elastic Recoil Measurement of Hydrogen," *Nucl. Instrum. Methods B*, **28**, 59 (1987).
 - 6) T. Nozaki, Y. Itoh, S. Hayashi, and Q. Qiu: "Utilization of Deuterium and ^{15}N as Activable Tracers in Solid State Sciences," *J. Radioanal. Nucl. Chem.*, **112**(1), 47 (1987).
 - 7) H. Fukushima, T. Kimura, H. Hamaguchi, T. Nozaki, Y. Itoh, and Y. Ohkubo: "Routine Determination of Light Elements by Charged-Particle Activation Analysis," *J. Radioanal. Nucl. Chem.*, **112**(2), 415 (1987).
 - 8) T. Nozaki: "Charged Particle Activation Analysis of Light Impurity Elements in Semiconductor Materials," Proc. 11th Int. Conf. Cyclotrons and Their Applications, Tokyo, Oct. 1986, p. 579 (1987).
 - 9) I. Kaneko, K. Eguchi-Kasai, T. Takahashi, T. Kosaka, and K. Nakano: "Beamport and Irradiation Chamber of the RIKEN Cyclotron for Biological Samples," 11th Int. Conf. Cyclotrons and Their Applications, Tokyo, Oct. 1986, p. 633 (1987).
 - 10) K. Eguchi-Kasai, T. Kosaka, I. Kaneko, T. Takahashi, A. Maruhashi, and K. Nakano: "Cell Death and DNA Lesion Caused by Accelerated Charged Particles," 11th Int. Conf. Cyclotrons and Their Applications, Tokyo, Oct. 1986, p. 667 (1987).
 - 11) T. Seguchi, T. Sasuga, W. Kawakami, M. Hagiwara, I. Kohno, and H. Kamitsubo: "Proton Irradiation Effects on Organic Polymers," Proc. 11th Int. Conf. Cyclotrons

- and Their Applications, Tokyo, Oct. 1986, p. 669 (1987).
- 12) T. Takahashi, F. Yatagai, T. Katayama, S. Konno, K. Takahashi, Y. Takayanagi, K. Nakano, and I. Kaneko: "Calculation of Dose around the Trajectory of an Ion and Interpretation of Inactivation Cross Sections of Microorganisms," *J. Radiat. Res.*, **28**, 71 (1987).
 - 13) K. Eguchi-Kasai, T. Kosaka, I. Kaneko, T. Takahashi, A. Maruhashi, and K. Nakano: "Induction of Non-Repairable DNA Strand Breaks by N-ion Beams," *J. Radiat. Res.*, **28**, 213 (1987).
 - 14) S. Ambe: "Adsorption Kinetics of Sb(V) Ions onto α -Fe₂O₃ Surfaces from an Aqueous Solutions," *Langmuir*, **3**, 489 (1987).
 - 15) K. Kimura: "Roles of Electronic Excited States in Irradiation Effect of Heavy Ion," *Radiat. Chem.* (in Japanese), **44**, 42 (1987).
 - 16) K. Eguchi, T. Inada, M. Yaguchi, S. Satoh, and I. Kaneko: "Induction and Repair of DNA Lesions in Cultured Human Melanoma Cells Exposed to a Nitrogen-Ion Beam," *Int. J. Radiat. Biol.*, **52**, 115 (1987).
 - 17) T. Takahashi, K. Eguchi, A. Hashizume, and T. Inada: "Data Requirements in Heavy Ion Radiotherapy — Considerations on Available Physical Quantities —," Proc. Advisory Group Meeting on Nuclear and Atomic Data for Radiotherapy and Related Radiobiology, IAEA Panel Proc. Ser. STI/PUB/741, p. 367 (1987).
 - 18) I. Kaneko: "Basic Researches for Cancer Therapy with Heavy Charged Particles — DNA Lesions and Their Repair in Human Melanoma Cells," *Rep. Mochida Mem. Found. Med. Pharm. Res.*, **3**, 241 (1987).
 - 19) T. Takahashi, F. Yatagai, T. Katayama, T. Doke, and H. Ohashi: "The Inactivation of Microorganisms by Different Heavy Ions," Proc. 1986 Int. Symp. Biological Sciences in Space (eds. S. Watanabe *et al.*), MYU Research, Tokyo, p. 365 (1987).
- Extraction System of RIKEN Ring Cyclotron," 11th Int. Conf. Cyclotrons and Their Applications, Tokyo, Oct. (1986).
- 3) K. Hatanaka, T. Inamura, Y. Yano, A. Goto, M. Kase, and H. Kamitsubo: "Beam Transport System for RIKEN Ring Cyclotron," 11th Int. Conf. Cyclotrons and Their Applications, Tokyo, Oct. (1986).
 - 4) Y. Miyazawa, M. Hemmi, T. Inoue, T. Kambara, M. Yanokura, M. Kase, T. Kubo, E. Ikezawa, Y. Chiba, and I. Tanihata: "Operation of RILAC at RIKEN," 11th Int. Conf. Cyclotrons and Their Applications, Tokyo, Oct. (1986).
 - 5) K. Ikegami, S. Nakajima, Y. Oikawa, I. Takeshita, S. Motonaga, and S.H. Be: "Vacuum System for the RIKEN Ring Cyclotron," 11th Int. Conf. Cyclotrons and Their Applications, Tokyo, Oct. (1986).
 - 6) T. Shikata, N. Nakanishi, S. Fujita, and T. Kosako: "Shielding Calculation of Neutrons for the RIKEN Ring Cyclotron Facility," 11th Int. Conf. Cyclotrons and Their Applications, Tokyo, Oct. (1986).
 - 7) K. Ikegami, S. Nakajima, Y. Oikawa, I. Takeshita, and S.H. Be: "Vacuum System for the RIKEN Ring Cyclotron," 11th Int. Conf. Cyclotrons and Their Applications, Tokyo, Oct. (1986).
 - 8) F. Kikuchi, M. Hara, and T. Wada: "Development of a Finite Element Code for 3-D Analysis of Electromagnetic Waves," Workshop Fundamental Studies of Numerical Computations of MHD Problems and Confinement of Plasmas by Tokamak Type Devices, Enoshima, Jan. (1987).
 - 9) A. Goto, T. Fujisawa, I. Takeshita, T. Urai, Y. Ikegami, and Y. Yamada: "Beam Buncher in the Injection Beam Transport System of the RIKEN Ring Cyclotron," 42th Annu. Meeting Phys. Soc. Jpn., Nagoya, Mar. (1987).
 - 10) S. Motonaga, Y. Yano, A. Goto, K. Hatanaka, M. Kase, T. Wada, H. Takabe, and H. Kamitsubo: "Beam Acceleration Test of the RIKEN Ring Cyclotron," 42th Annu. Meeting Phys. Soc. Jpn., Nagoya, Mar. (1987).
 - 11) M. Kase and I. Yokoyama: "Beam Diagnostic Equipment in the RIKEN Ring Cyclotron," 24th Eur. Cyclotron Progress Meeting, Nice, May (1987).
 - 12) Y. Yano: "Commissioning of the RIKEN Ring Cyclotron," 24th Eur. Cyclotron Progress Meeting, Nice, May (1987).
 - 13) M. Kase and I. Yokoyama: "Beam Diagnostic System in the RIKEN Ring Cyclotron,"

(Papers Presented at Meetings)

1. Accelerator development and accelerator physics
 - 1) M. Nagase, H. Takebe, T. Wada, and K. Shimizu: "Program for Controlling Magnet Power Supplies of the RIKEN Ring Cyclotron," 11th Int. Conf. Cyclotrons and Their Applications, Tokyo, Oct. (1986).
 - 2) Y. Yano, A. Goto, K. Hatanaka, H. Takebe, and S. Motonaga: "Beam Injection and

- 6th Symp. Accelerator Science and Technology, Tokyo, Oct. (1987).
- 14) T. Inamura: "Ring Cyclotron Project at RIKEN," RIKEN-IN2P3 Symp. Heavy-Ion Collisions, Shimoda, Oct. (1987).
 - 15) A. Goto: "Status of the RIKEN Ring Cyclotron," 1987 Fall Meeting Phys. Soc. Jpn., Utsunomiya, Oct. (1987).
 - 16) F. Kikuchi, M. Hara, and T. Wada: "A Finite Element Method for 3-D Analysis of Cavity Resonators," Int. Symp. Modeling and Simulation of Distributed Parameter Systems, Hiroshima, Oct. (1987).
 - 17) T. Fujisawa, K. Ogiwara, S. Kohara, Y. Oikawa, I. Yokoyama, M. Nagase, and Y. Chiba: "Radio Frequency System of the RIKEN Ring Cyclotron," 3rd Jpn.-China Jt. Symp. Accelerators for Nuclear Science and Their Applications, Wako, Nov. (1987).
 - 18) Y. Yano: "Initial Operation of RIKEN Ring Cyclotron," 3rd Jpn.-China Jt. Symp. Accelerators for Nuclear Science and Their Applications, Wako, Nov. (1987).
 - 19) H. Takebe, T. Wada, M. Kase, T. Kambara, and H. Kamitsubo: "Control System of the RIKEN Ring Cyclotron," Control System Workshop, Tsukuba, Nov. (1987).
2. Nuclear physics and nuclear instrumentation
- 1) K. Asahi: "Spectroscopy of Unstable Nuclei with LISE and RIB," INS Symp. Clustering Aspects in Nuclear Physics and Prospects in Intermediate- and High-Energy Heavy-Ion Physics, Tokyo, Jan. (1987).
 - 2) K. Asahi: "Summary of Experiments Using Radioactive Beam Course," Workshop Experiments at RIKEN Ring Cyclotron, Tokyo, Jan. (1987).
 - 3) M. Oshima, E. Minehara, S. Ichikawa, H. Iimura, T. Inamura, A. Hashizume, and H. Kusakari: "E2 Transition Probabilities of the Ground-State Rotational Band in $^{161,163}\text{Dy}$," 42th Annu. Meeting Phys. Soc. Jpn., Nagoya, Mar. (1987).
 - 4) K. Omata, T. Kobayashi, T. Shimoura, K. Sugimoto, I. Tanihata, K. Takeyama, N. Takahashi, Y. Nojiri, and O. Yamakawa: "Projectile Fragmentation of ^{11}Li , ^8He , ^6He at 0.8 GeV/A," 42th Annu. Meeting Phys. Soc. Jpn., Nagoya, Mar. (1987).
 - 5) S. Yamaji and N. Yoshinaga: "Dipole Moment of ^{222}Ra as a System of $\text{Pb} + ^{14}\text{C}$ Molecular Configuration," 42th Annu. Meeting Phys. Soc. Jpn., Nagoya, Apr. (1987).
 - 6) T. Suzuki: "Neutrino Mass Studied by Measuring Tritium Beta-Decay with an Iron Free Beta-Ray Spectrometer," 11th Int. Conf. Particle and Nuclei (PANIC '87), Kyoto, Apr. (1987).
 - 7) I. Tanihata: "Nuclear Structure Studies Using High-Energy Radioactive Beams," 11th Int. Conf. Particle and Nuclei (PANIC '87), Kyoto, Apr. (1987).
 - 8) K. Nagamine, T. Matsuzaki, K. Ishida, Y. Hirata, Y. Watanabe, R. Kadono, Y. Miyake, K. Nishiyama, S. E. Jones, and H. R. Maltrud: "Direct Observation of α -Sticking Probability in Muon Catalyzed ($\text{dt}\mu$)-Fusion with X-Ray Method," Int. Symp. Muon Catalyzed Fusion, Leningrad, U.S.S.R., May (1987).
 - 9) T. Sano, T. Doke, J. Kikuchi, K. Masuda, and T. Takahashi: "Liquid Xenon Photoionization Detector," 1987 Fall Meeting Phys. Soc. Jpn., Sendai, Sep. (1987).
 - 10) I. Tanihata: "Nuclear Structure Studies Using Beams of Radioactive Nuclei," 5th Int. Conf. Nuclei Far from Stability, Rosseau Lake, Canada, Sep. (1987).
 - 11) K. Asahi, M. Ishihara, T. Shimoda, T. Fukuda, N. Takahashi, K. Katori, K. Hanakawa, T. Itahashi, Y. Nojiri, T. Minamisono, N. Ikeda, S. Shimoura, and A. Nakamura: "Production of Spin Polarized ^{15}C in Heavy-Ion Reaction and Measurement of g -Factor for the $1/2^+$ Ground State," 5th Int. Conf. Nuclei Far from Stability, Rosseau Lake, Canada, Sep. (1987).
 - 12) T. Inamura: "Progress in Research at RIKEN Ring Cyclotron Facility," 1987 Fall Meeting Phys. Soc. Jpn., Utsunomiya, Oct. (1987).
 - 13) H. Harada, J. Kasagi, T. Murakami, K. Yoshida, T. Inamura, and T. Kubo: "The Rotational Band in Odd Mass ^{111}Sn ," 1987 Fall Meeting Phys. Soc. Jpn., Utsunomiya, Oct. (1987).
 - 14) K. Yoshida, J. Kasagi, H. Hama, H. Harada, H. Takeuchi, M. Sakurai, K. Ieki, T. Kubo, and M. Ishihara: "High Energy γ Rays Observed in $^{181}\text{Ta} + ^{40}\text{Ar}$ Reaction at 21 MeV/nucleon," 1987 Fall Meeting Phys. Soc. Jpn., Utsunomiya, Oct. (1987).
 - 15) K. Asahi, M. Ishihara, T. Shimoda, T. Fukuda, N. Takahashi, K. Katori, K. Hanakawa, T. Itahashi, Y. Nojiri, T. Minamisono, N. Ikeda, S. Shimoura, and A. Nakamura: "Study of Spin Polarized Nuclei Using Heavy Ion Reaction," RIKEN-IN2P3 Symp. Heavy-Ion Collisions, Shimoda, Oct. (1987).
 - 16) I. Tanihata: "Nuclear Structure Studies Using Beams of Radioactive Nuclei," RIKEN-

- IN2P3 Symp. Heavy-Ion Collisions, Shimoda, Oct. (1987).
- 17) T. Motobayashi: "(d, ^2He) Reactions by Polarized Deuteron," RIKEN-IN2P3 Symp. Heavy-Ion Collisions, Shimoda, Oct. (1987).
 - 18) A. Hitachi, A. Yunoki, T. Doke, and T. Takahashi: "The Scintillation and Ionization Yield in the Presence of Quenching in Liquid Argon," 12th Int. Conf. Atomic Collisions in Solids, Okayama, Oct. (1987).
 - 19) T. Kubo: "RIKEN Projectile-Fragment Separator RIPS," 1987 Fall Meeting Phys. Soc. Jpn., Utsunomiya, Oct. (1987).
 - 20) T. Murayama: "Arrangements for RIS at RIKEN Ring Cyclotron," Symp. Lasers in Nuclear Physics, Osaka, Dec. (1987).
 - 21) T. Inamura: "Lasers in Nuclear Physics," Symp. Lasers in Nuclear Physics, Osaka, Dec. (1987).
 - 22) K. Asahi: "Beta Decays of High Isospin Nuclei," INS Symp. Nuclear Physics in Japan Hadron Project, Tokyo, Dec. (1987).
 - 23) K. Asahi: "Recent Results from GANIL," Symp. Clustering Aspects in Nuclear Structures and Reactions, Osaka, Dec. (1987).
 - 24) K. Asahi: "Spectroscopy of Neutron-Rich Nuclei," INS Workshop Studies of Nuclear Reactions at Intermediate Energies Using 4π Spectrograph, Tokyo, Dec. (1987).
3. Atomic and solid-state physics
- 1) Y. Awaya, T. Watanabe, K. Ando, T. Kambara, M. Kase, H. Kumagai, Y. Kanai, and K. Shima: "The Charge Distribution of Swift Heavy Ions Passing through Solids," Symp. Interactions between Ion-Beams and Solids, Tokyo, Jan. (1987).
 - 2) T. Mizogawa, Y. Awaya, T. Kambara, M. Kase, H. Kumagai, Y. Kanai, and K. Shima: "Charge Distribution of High-Velocity Heavy Ion after Passing through Solid Target," Symp. Interaction between Ion-Beam and Solids, Tokyo, Jan. (1987).
 - 3) E. Yagi: "Lattice Location Study on Hydrogen in Metals by Means of Heavy Ion Channeling Method," Symp. Interactions between Ion Beam and Solids, Tokyo, Jan. (1987).
 - 4) K. Fujima, T. Watanabe, and K. Mima: "X-ray Emission Spectra of High and Dense Si Plasma," Symp. Atomic Processes in Laser Induced Implosion Plasma, Okayama, Jan. (1987).
 - 5) T. Kambara: "Impact Parameter Dependence of K-Shell Vacancy Production for Solid and Gas Targets," Energetic Atomic Collisions, Oberstdorf, W. Germany, Jan. (1987).
 - 6) Y. Awaya, "Recent Studies on Atomic Physics at RIKEN Accelerators," 2nd Jt. Semin. Atomic Physics, Solid State Physics and Material Sciences in the Energy Region of Tandem Accelerators, Tokai, Jan. (1987).
 - 7) K. Hino and T. Watanabe: "Radiative Processes in Ion-Atom Collisions," US-Jpn. Jt. Semin. Interactions of Highly Ionized Atoms by Ion-Atom Collisions, Kobe, Mar. (1987).
 - 8) I. Shimamura, M. Iwai, and T. Watanabe: "Irregularities in the Cross Sections for Discrete Excitation in Ion-Atom Collisions Calculated in the Plane-Wave Born Approximation," US-Jpn. Jt. Semin. Interactions of Highly Ionized Atoms by Ion-Atom Collisions, Kobe, Mar. (1987).
 - 9) H. Tawara, T. Tonuma, T. Matsuo, M. Kase, T. Kambara, H. Kumagai, and I. Kohno: "Multiply Charge Atomic Ion Production through Coulomb Explosions by Heavy Ion Impact," US-Jpn. Jt. Semin. Interactions of Highly Ionized Atoms by Ion-Atom Collisions, Kobe, Mar. (1987).
 - 10) Y. Kanai, Y. Awaya, T. Kambara, M. Kase, H. Kumagai, T. Mizogawa, and K. Shima: "Charge State Distribution Measurements of Heavy Ions at RIKEN," US-Jpn. Jt. Semin. Interactions of Highly Ionized Atoms Produced by Ion-Atom Collisions, Kobe, Mar. (1987).
 - 11) T. Mizogawa, Y. Awaya, T. Kambara, Y. Kanai, M. Kase, H. Kumagai, P. H. Mokler, and K. Shima: "Target Thickness Dependence of Projectile Ar K X-Rays—L-Shell Non-Equilibrium," US-Jpn. Jt. Semin. Interactions of Highly Ionized Atoms Produced by Ion-Atom Collisions, Kobe, Mar. (1987).
 - 12) K. Ishida, T. Matsuzaki, Y. Hirata, Y. Miyake, Y. Watanabe, and K. Nagamine: "Muon Transfer Reaction to Helium Impurity in Liquid Hydrogen II," 42th Annu. Meeting Phys. Soc. Jpn., Nagoya, Mar. (1987).
 - 13) K. Nishiyama, H. Katsuragawa, T. Minowa, M. Shimazu, and T. Inamura: "Resonance Ionization Spectroscopy of Tl Atomic Beam," 42th Annu. Meeting Phys. Soc. Jpn., Nagoya, Mar. (1987).
 - 14) H. Katsuragawa, K. Nishiyama, T. Minowa, M. Shimazu, and T. Inamura: "Resonance Ionization Spectroscopy of Ta Atoms," 42th Annu. Meeting Phys. Soc. Jpn., Nagoya, Mar. (1987).
 - 15) Y. Kanai, Y. Awaya, T. Kambara, M. Kase, H. Kumagai, T. Mizogawa, and K. Shima: "Charge-State Distribution of Heavy Ions after Single Close Collisions," 42th Annu. Meet-

- ing Phys. Soc. Jpn., Nagoya, Mar. (1987).
- 16) E. Yagi, H. Sakairi, A. Koyama, and R. R. Hasiguti: "Isochronal Annealing of Proton- or α -Irradiated Cu_3Au at Low Temperatures," 42th Annu. Meeting Phys. Soc. Jpn., Nagoya, Mar. (1987).
 - 17) N. Sakai and T. Okada: "Mössbauer Spectrometer Using Piezoelectric Actuators," 42th Annu. Meeting Phys. Soc. Jpn., Nagoya, Mar. (1987).
 - 18) T. Matsuzaki, K. Ishida, Y. Hirata, Y. Watanabe, Y. Miyake, R. Kadono, K. Nagamine, H. R. Maltrud, and S. E. Jones: "Fundamental Experiment for Muon Catalyzed Fusion II," 42th Annu. Meeting Phys. Soc. Jpn., Nagoya, Mar. (1987).
 - 19) X.-W. Liu, Q.-C. Ma, J.-F. Cheng, X.-X. Zhang, Y.-Y. Liu, and T. Watanabe: "Calculation of Cross Section for $\mu^+ + (\mu^-p) \rightarrow (\mu^+\mu^-) + p$," 42th Annu. Meeting Phys. Soc. Jpn., Nagoya, Mar. (1987).
 - 20) T. Watanabe: "Radiative Processes Induced by Ion-Atom Collisions," Jt. Workshop Atomic-Molecular Physics and Heavy-Ion Nuclear Reaction, Tanashi, Mar. (1987).
 - 21) K. Aono, M. Iwaki, and S. Namba: "Ion Implantation in CaF_2 (II)," RIKEN Symp. '18th Symp. Ion Implantation and Submicron Fabrication,' Wako, Mar. (1987).
 - 22) Y. Awaya, K. Hino, T. Kambara, Y. Kanai, K. Komaki, K. Kuroki, I. Shimamura, and Y. Yamazaki: "Study of Atomic Collisions by Using Relativistic Heavy Ions," Workshop Experiments and Experimental Facilities at SIS/ESR, Darmstadt, W. Germany, Mar. (1987).
 - 23) K. Nagamine: "Muon Catalyzed Fusion with Pulsed Muons: Present and Future," Int. Sch. Fusion Reactor Technology, Erice, Italy, Apr. (1987).
 - 24) T. Matsuzaki, K. Ishida, Y. Hirata, R. Kadono, and K. Nagamine: "Muonic X-ray Measurement on the μ^- Transfer Process in Liquid D_2 to ^4He Impurity," Int. Symp. Muon Catalyzed Fusion, Leningrad, U.S.S.R., May (1987).
 - 25) E. Yagi: "Lattice Location Study of Impurities by Means of Channeling Method," 24th Meeting Isotope Research in Science and Technology, Tokyo, Jun. (1987).
 - 26) S. Karashima and T. Watanabe: "Electron Stripping Cross Sections from Multiply Charged Ions by Neutral Atoms Using BEA and Born Approximation Method," 15th Int. Conf. Physics of Electronic and Atomic Collisions, Brighton, England, Jul. (1987).
 - 27) T. Mizogawa, Y. Awaya, T. Kambara, Y. Kanai, M. Kase, H. Kumagai, P. H. Mokler, and K. Shima: "Study of K-, L- and M-Shell Equilibration Processes of 50 MeV Argon Ions in Carbon Foils," 15th Int. Conf. Physics of Electronic and Atomic Collisions, Brighton, England, Jul. (1987).
 - 28) T. Kambara, Y. Awaya, T. Mizogawa, H. Kumagai, Y. Kanai, K. Shima, H. Shibata, and R. Schuch: "Measurement of Impact Parameter Dependent Probabilities for K-Shell Ionization in Ar-Ca and Ar-Cu Collisions," 15th Int. Conf. Physics of Electronic and Atomic Collisions, Brighton, England, Jul. (1987).
 - 29) S. Reusch, Y. Awaya, T. Kambara, P. H. Mokler, D. J. McLaughlin, A. Müller, R. Schuch, and M. Schultz: "Resonant Transfer and Excitation (RTE) in $^{32}\text{Ge}^{20+} \rightarrow \text{H}_2$ Collisions," 15th Int. Conf. Physics of Electronic and Atomic Collisions, Brighton, England, Jul. (1987).
 - 30) Y. Kanai, Y. Awaya, T. Kambara, M. Kase, H. Kumagai, B. Liu, T. Mizogawa, and K. Shima: "Charge State Measurements of Heavy Ions Scattered by Gas and Solid Targets," 15th Int. Conf. Physics of Electronic and Atomic Collisions, Brighton, England, Jul. (1987).
 - 31) H. Tawara, T. Tonuma, T. Matsuo, M. Kase, H. Kumagai, and I. Kohno: "Multiply Charged Atomic and Their Initial Kinetic Energy through Coulomb Explosions of Multiply Molecular Ions Produced in Energetic, Heavy Ion Collisions," 15th Int. Conf. Physics of Electronic and Atomic Collisions, Brighton, England, Jul. (1987).
 - 32) K. Hino and T. Watanabe: "Gauge Invariance on Radiative Process Caused by Ion-Atom Collisions," 15th Int. Conf. Physics of Electronic and Atomic Collisions, Brighton, England, Jul. (1987).
 - 33) K. Hino and T. Watanabe: "Cross Sections for Relativistic Radiative Electron Capture by the Strong-Potential Born Calculation," 15th Int. Conf. Physics of Electronic and Atomic Collisions, Brighton, England, Jul. (1987).
 - 34) Y. Awaya, H. Hino, T. Kambara, T. Watanabe, A. Hitachi, Y. Kanai, H. Vogt, K. Kuroki, and Y. Yamazaki: "Radiative Electron Capture Process," 10th Int. Semin. Ion-Atom Collisions, Frankfurt, W. Germany, Jul. (1987).
 - 35) K. Aono, M. Iwaki, and S. Namba: "Luminescence during Eu-Implantation into Calcium Fluoride," Radiation Effects in In-

- sulators-4, Lyon, France, Jul. (1987).
- 36) Y. Awaya, K. Hino, A. Hitachi, Y. Kanai, K. Kawatsura, K. Kuroki, H. Vogt, Y. Yamazaki, and T. Watanabe: "Angular Distribution of REC X Rays," 3rd Workshop High-Energy Ion-Atom Collision Processes, Debrecen, Hungary, Aug. (1987).
 - 37) T. Tonuma, T. Matsuo, M. Kase, T. Kambara, H. Kumagai, S. H. Be, I. Kohno, and H. Tawara: "Multiple Ionization by Energetic Heavy Ion Collisions—An Evidence of the Innershell Electron Transfer in Highly Charged Recoil Ion Production," 3rd Workshop High-Energy Ion-Atom Collision Processes, Debrecen, Hungary, Aug. (1987).
 - 38) H. Iwai, I. Shimamura, and T. Watanabe: "Anomalous Behavior of Cross Sections Appeared in Ion-Atom (Ion-Ion) Collisions," UK-Jpn. Semin. Theory of Atomic Collisions, Egham, England, Aug. (1987).
 - 39) K. Hino and T. Watanabe: "Photon Emission Processes Induced by Ion-Atom Collisions," UK-Jpn. Semin. Theory of Atomic Collisions, Egham, England, Aug. (1987).
 - 40) N. Sakai: "A New Mössbauer Transducer Using Piezoelectric Bimorph Actuators," Int. Conf. Appl. Mössbauer Effect, Melbourne, Aug. (1987).
 - 41) T. Okada, N. Sakai, K. Asai, Y. Toba, and T. Yamada: "⁵⁷Fe Mössbauer Study on YBa₂Cu_{3-x}Fe_xO_{7-y}," Int. Conf. Applications of the Mössbauer Effect, Melbourne, Australia, Aug. (1987).
 - 42) Y. Sakamoto, H. Oyama, and K. Yano: "Erosion of Graphite by Very Low Energy Hydrogen Atoms," 8th Int. Symp. Plasma Chemistry, Tokyo, Aug. (1987).
 - 43) T. Matsuzaki, K. Ishida, Y. Hirata, R. Kadono, and K. Nagamine: "Photon Transition of the Excited Bound State in (μ^-d ⁴He) Mesomolecule Accompanied with ($\mu^-d + ^4\text{He} \rightarrow \mu^- ^4\text{He} + d$) Process," 1987 Fall Meeting Phys. Soc. Jpn., Utsunomiya, Sep. (1987).
 - 44) K. Ishida, T. Matsuzaki, Y. Hirata, R. Kadono, and K. Nagamine: "Photon Emission from Excited Bound State of Muonic Molecule dHe μ^- ," 1987 Fall Meeting Phys. Soc. Jpn., Sendai, Sep. (1987).
 - 45) S. Karashima, K. Hino, and T. Watanabe: "Charge State of Relativistically High Velocity Heavy Ions in Matter," 1987 Fall Meeting of Phys. Soc. Jpn., Sendai, Sep. (1987).
 - 46) K. Nishiyama, H. Katsuragawa, T. Minowa, S. Kawamura, H. Sonobe, M. Shimazu, and T. Inamura: "Resonance Ionization Spectroscopy of Neutral Atoms Produced by Lasers," 1987 Fall Meeting Phys. Soc. Jpn., Sendai, Sep. (1987).
 - 47) A. Koyama, H. Ishikawa, Y. Sasa, O. Benka, and M. Uda: "High Charge Effects on Electron Excitations in Metal Targets for Ar¹²⁺ Impact Compared with Those for He²⁺ Impact," 1987 Fall Meeting Phys. Soc. Jpn., Sendai, Sep. (1987).
 - 48) A. Koyama, H. Ishikawa, and Y. Sasa: "Energy Spectra of Al-LVV Auger Electrons Induced by Grazing Angle Incident Fast Heavy Ion Impact," 1987 Fall Meeting Phys. Soc. Jpn., Sendai, Sep. (1987).
 - 49) E. Yagi: "Behavior of Kr Atoms in Aluminum," 1987 Fall Meeting Phys. Soc. Jpn., Sendai, Sep. (1987).
 - 50) F. Itoh, Y. Sakurai, K. Suzuki, N. Shiotani, N. Sakai, H. Kawata, Y. Amemiya, and M. Ando: "High Resolution Compton Profiles of Al," 1987 Fall Meeting Phys. Soc. Jpn., Sendai, Sep. (1987).
 - 51) E. Yagi: "Lattice Defects and μ SR," 28th Meeting Lattice Defects, Fukushima, Sep. (1987).
 - 52) K. Ishida, T. Matsuzaki, and K. Nagamine: "Towards the Application of RIKEN Ring Cyclotron to Solid State Physics with Nuclear Methods," 28th Meeting Lattice Defects, Fukushima, Sep. (1987).
 - 53) S. M. Younger, A. K. Harrison, K. Fujima, and D. Griswold: "Computational Studies of High Energy Density Plasmas," 6th APS Top. Conf. Atomic Processes in High Temperature Plasmas and Int. Conf./Workshop Radiative Properties on Hot Dense Matter, Santa Fe, U.S.A., Sep. (1987).
 - 54) K. Hino and T. Watanabe: "Instantaneous X-Ray Emission Induced by Ion-Atom Collision," 14th Int. Conf. X-Ray and Inner-Shell Processes, Paris, France, Sep. (1987).
 - 55) K. Hino and T. Watanabe: "Angular Distribution and Linear Polarization of X-Rays Induced by Radiative Electron Capture," 12th Int. Conf. Atomic Collisions in Solids, Okayama, Oct. (1987).
 - 56) S. Karashima, K. Hino, and T. Watanabe: "Charge Equilibrium of Relativistic Heavy Ions in Matter," 12th Int. Conf. Atomic Collisions in Solids, Okayama, Oct. (1987).
 - 57) K. Ando, S. Kohmoto, Y. Awaya, T. Tonuma, H. Kumagai, and S. Tsurubuchi: "Beam-Foil Experiments on Lifetime and Spectra of Highly Ionized Aluminum Ions," 12th Int. Conf. Atomic Collisions in Solids, Okayama, Oct. (1987).
 - 58) K. Fujima, H. Adachi, and M. Kimura:

- "The Charge Transfer Collision between a Low Energy Ion and the Solid Surface," 12th Int. Conf. Atomic Collisions in Solids, Okayama, Oct. (1987).
- 59) K. Shima, T. Kakita, E. Nakagawa, M. Yamanouchi, T. Momoi, Y. Awaya, T. Mizogawa, and Y. Kanai: "Projectile Atomic Number Dependence of Equilibrium Charge States for 1 and 2 MeV/u Ions Passing through Carbon Foil," 12th Int. Conf. Atomic Collisions in Solids, Okayama, Oct. (1987).
 - 60) T. Mizogawa, Y. Awaya, T. Kambara, Y. Kanai, M. Kase, H. Kumagai, and K. Shima: "Charge Equilibrium Process of 50 MeV Ar Ions in C Foils," 12th Int. Conf. Atomic Collision in Solids, Okayama, Oct. (1987).
 - 61) A. Koyama, H. Ishikawa, and Y. Sasa: "Energy Spectra of Al-LVV Auger Electrons Induced by Grazing Angle Incident Fast Heavy Ion Impact," 12th Int. Conf. Atomic Collisions in Solids, Okayama, Oct. (1987).
 - 62) A. Koyama, H. Ishikawa, Y. Sasa, O. Benka, and M. Uda: "Depression of Yields of Low Energy Secondary Electrons Induced by Impact of Heavy Ions with High Electric Charges," 12th Int. Conf. Atomic Collisions in Solids, Okayama, Oct. (1987).
 - 63) A. Koyama, H. Ishikawa, Y. Sasa, O. Benka, and M. Uda: "High Charge Effects on Electron Excitations in Metal Targets for Ar¹²⁺ Impact Compared with Those for He²⁺ Impact," 12th Int. Conf. Atomic Collisions in Solids, Okayama, Oct. (1987).
 - 64) E. Yagi, M. Iwaki, K. Tanaka, I. Hashimoto, and H. Yamaguchi: "Behaviour of Krypton Atoms in Aluminium," 12th Int. Conf. Atomic Collisions in Solids, Okayama, Oct. (1987).
 - 65) E. Yagi, T. Kobayashi, S. Nakamura, F. Kano, K. Watanabe, Y. Fukai, and T. Matsumoto: "Hydrogen Trapping by Substitutional Impurities in NbMo_{0.03} Alloys as Observed by the Channeling Method," 12th Int. Conf. Atomic Collisions in Solids, Okayama, Oct. (1987).
 - 66) S. Nakamura, E. Yagi, T. Osaka, and M. Iwaki: "Lattice Disorder and Behavior of Implanted Atoms in In-Implanted TiO₂ (Rutile)," 12th Int. Conf. Atomic Collisions in Solids, Okayama, Oct. (1987).
 - 67) K. Kobayashi: "N Ion Beam Induced Recrystallization of AlN_x Films," 12th Int. Conf. Atomic Collisions in Solids, Okayama, Oct. (1987).
 - 68) Y. Awaya: "Measurements of REC X-rays for 20.4 MeV/u Ar Ions on Be Target," RIKEN Symp. '8th Symp. Atomic Collisions by Using Accelerators, Int. Symp. Dynamic Interactions of Charged Particles with Solids,' Wako, Oct. (1987).
 - 69) B. Sulik: "Simple Projectile and Target Scaling in the Description of Multiple Ionization," RIKEN Symp. '8th Symp. Atomic Collisions by Using Accelerators, Int. Symp. Dynamic Interactions of Charged Particles with Solids,' Wako, Oct. (1987).
 - 70) T. Kambara: "Measurement of Impact Parameter Dependent Probabilities for K-Shell Ionization in Ar-Ca and Ar-Cu Collisions," RIKEN Symp. '8th Symp. Atomic Collisions by Using Accelerators, Int. Symp. Dynamic Interactions of Charged Particles with Solids,' Wako, Oct. (1987).
 - 71) A. Koyama: "Energy Spectra of Al-LVV Auger Electrons Induced by Grazing Angle Incident Fast Heavy Ion Impact," RIKEN Symp. '8th Symp. Atomic Collisions by Using Accelerators, Int. Symp. Dynamic Interactions of Charged Particles with Solids,' Wako, Oct. (1987).
 - 72) K. Hino: "Theory of Relativistic Radiative Electron Capture," RIKEN Symp. '8th Symp. Atomic Collisions by Using Accelerators, Int. Symp. Dynamic Interactions of Charged Particles with Solids,' Wako, Oct. (1987).
 - 73) I. Kohno: "Application of RIKEN 160 cm Cyclotron," Int. Symp. Applications of Ion Beams Produced by Small Accelerators, Jinan, China, Oct. (1987).
 - 74) K. Aono, M. Iwaki, and S. Namba: "Luminescence during Ion-Implantation into CaF₂," 1987 Fall Meeting Jpn. Soc. Appl. Phys., Nagoya, Oct. (1987).
 - 75) Y. Awaya: "Introduction of Some Experimental Proposals for RRC," RIKEN Symp. Studies of Solid State Physics and Materials, Atomic Processes, Nuclear Chemistry, and Biology and Medical Science by Using Ring Cyclotron, Wako, Nov. (1987).
 - 76) Y. Awaya: "On the Organization of Non-Nuclear Study Group at RRC," RIKEN Symp. Studies of Solid State Physics and Materials, Atomic Processes, Nuclear Chemistry, and Biology and Medical Science by Using Ring Cyclotron, Wako, Nov. (1987).
 - 77) Y. Kanai: "Beam Line and Facilities for Studies of Atomic Physics at RRC," RIKEN Symp. Studies of Solid State Physics and Materials, Atomic Processes, Nuclear Chemistry, and Biology and Medical Science by Using Ring Cyclotron, Wako, Nov. (1987).
 - 78) Y. Awaya: "The Test Experiment made at RRC," RIKEN Symp. Studies of Solid State

- Physics and Materials, Atomic Processes, Nuclear Chemistry, and Biology and Medical Science by Using Ring Cyclotron, Wako, Nov. (1987).
- 79) T. Kambara and K. Ando: "Experiments at RRC Planned by Atomic Processes Laboratory," RIKEN Symp. Studies of Solid State Physics and Materials, Atomic Processes, Nuclear Chemistry, and Biology and Medical Science by Using Ring Cyclotron, Wako, Nov. (1987).
 - 80) K. Nishiyama, H. Katsuragawa, T. Minowa, S. Kawamura, H. Sonobe, M. Shimazu, and T. Inamura: "Resonance Ionization Spectroscopy with Laser Ablation," 1987 Fall Meeting Spect. Soc. Jpn., Kyoto, Nov. (1987).
 - 81) T. Watanabe and K. Hino: "Photon Emission Processes Induced by Ion-Atom Collisions," Natl. Symp. Scattering Theory and Its Applications, Culcatta, India, Dec. (1987).
 - 82) T. Watanabe, A. Ohsaki, K. Nakanishi, and K. Iguchi: "Classical-Trajectory Monte Carlo Calculation for Collision Processes of Coulomb-Interacting Three-Body Systems," Natl. Symp. Scattering Theory and Its Applications, Culcatta, India, Dec. (1987).
 - 83) T. Watanabe: "Atomic Processes in X-Ray Laser Development Research," Symp. Atomic Collisions, Kalyani, India, Dec. (1987).
4. Radiochemistry, radiation chemistry, and radiation biology
- 1) T. Seguchi, T. Sasuga, W. Kawakami, M. Hagiwara, I. Kohno, and H. Kamitsubo: "Proton Irradiation Effects on Organic Polymers," 11th Int. Conf. Cyclotrons and Their Applications, Tokyo, Oct. (1986).
 - 2) T. Takahashi, S. Konno, F. Yatagai, K. Takahashi, Y. Takayanagi, T. Tabata, and R. Ito: "Calculation of Dose around the Trajectory of an Ion and Its Application (2)," 34th Spring Meeting Jpn. Soc. Appl. Phys., Tokyo, Mar. (1987).
 - 3) S. Ambe, T. Okada, and F. Ambe: "*In situ* Emission Mössbauer Spectra of $^{119}\text{Sb}^{5+}$ and $^{57}\text{Co}^{2+}$ Adsorbed on $\alpha\text{-Fe}_2\text{O}_3$ with a Macro-Amount of Sb^{5+} ," 54th Natl. Meeting Chem. Soc. Jpn. (Spring), Tokyo, Apr. (1987).
 - 4) T. Takahashi, F. Yatagai, T. Katayama, and T. Kasuya: "Inactivation of *B. subtilis* Spores by Heavy Ions Using Solid State Nuclear Track Detectors," 5th Meeting Solid State Nuclear Track Detectors, Tokyo, Apr. (1987).
 - 5) K. Kimura, T. Ueno, K. Kanai, T. Nishina, A. Fundo, and M. Kataoka: "Decay Measurement of Sub ns Resolution of Photoemission Induced by Heavy-Ion Irradiation," 42th Annu. Meeting Phys. Soc. Jpn., Nagoya, Apr. (1987).
 - 6) T. Nozaki, Y. Itoh, and Q. Qiu: "Dissolution of Hydrogen and Nitrogen in Silicon," Int. Conf. Methods and Applications of Radio-analytical Chemistry, Conna, Hawaii, Apr. (1987).
 - 7) F. Ambe, S. Ambe, and T. Okada: "Chemical States of $^{57}\text{Co}^{2+}$ and $^{119}\text{Sb}^{5+}$ on $\gamma\text{-Fe}_2\text{O}_3$ and NiFe_2O_4 Surfaces," 13th Int. Hot Atom Chemistry Symp., Yamanaka, May (1987).
 - 8) S. Ambe, F. Ambe, T. Okada, I. Tanaka, S. Nasu, and F. E. Fujita: "Mössbauer Study of the Chemical States of $^{119}\text{Sn} \xrightarrow{\text{EC}} ^{119}\text{Sb}$ Electrodeposited on Gold Surface," 13th Int. Hot Atom Chemistry Symp., Yamanaka, May (1987).
 - 9) K. Asai, F. Ambe, S. Ambe, T. Okada, and H. Sekizawa: "TDFAC Studies of the After-Effects of $^{111}\text{In} \rightarrow ^{111}\text{Cd}$ EC Decay in $\alpha\text{-Fe}_2\text{O}_3$ and Other Inorganic Compounds," 13th Int. Hot Atom Chemistry Symp., Yamanaka, May (1987).
 - 10) K. Kimura: "Roles of Electronic Excited States in Radiation Effect of Heavy Ions," 3rd Semin. Radiation Chemistry, Tokyo, May (1987).
 - 11) K. Kimura: "High-Density Excitation by Heavy Ions: Track-Depth Resolved Emission Spectra and Decays along the Path of Ions Impinging into Helium at 400 Torr and 5 K," 3rd China-Jpn. Bilateral Symp. Radiation Chemistry, Changchun, China, Jun. (1987).
 - 12) I. Kaneko, K. Eguchi-Kasai, and K. Nakano: "Oxygen Effect on DNA Double Strand Breaks in Human Melanoma Cells Induced by Alpha Particles," 3rd Workshop Heavy Charged Particles in Biology and Medicine, Darmstadt, W. Germany, Jul. (1987).
 - 13) I. Kaneko, K. Eguchi-Kasai, T. Takahashi, T. Kosaka, and K. Nakano: "Beam Port and Irradiation Chamber of the RIKEN Ring Cyclotron for Biological Samples," 3rd Workshop Heavy Charged Particles in Biology and Medicine, Darmstadt, W. Germany, Jul. (1987).
 - 14) I. Kaneko, K. Eguchi-Kasai, and T. Takahashi: "Cell Biology at RIKEN Accelerator," 3rd Workshop Heavy Charged Particles in Biology and Medicine, Darmstadt, W. Germany, Jul. (1987).
 - 15) T. Takahashi, F. Yatagai, T. Katayama, I. Kaneko, and T. Tabata: "Effect of Heavy Ions on Microorganisms—Track Structure Theories and Single Particle Experiment—,"

- 3rd Workshop Heavy Charged Particles in Biology and Medicine, Darmstadt, W. Germany, Jul. (1987).
- 16) K. Kimura: "The dE/dx Dependence of High-Density Excitation by Heavy-Ion, Studied by Track-Depth Resolved Emission Spectra and Decay on Rare Gas," 8th Int. Congr. Radiation Research, Edinburgh, U.K., Jul. (1987).
 - 17) T. Takahashi, F. Yatagai, S. Konno, T. Tabata, and R. Ito: "Calculation of Dose around the Trajectory of an Ion and Its Application, 8th Int. Congr. Radiation Research, Edinburgh, U.K., Jul. (1987).
 - 18) H. Kusuyama, K. Okada, T. Kawai, K. Maeda, Y. Sasa, and M. Uda: "Elemental Analysis of Thinly Sliced Renal Cancer by PIXE," 16th Annu. Meeting Soc. Trace Metal Metabolism Research of Jpn., Tokyo, Jul. (1987).
 - 19) S. Ambe and F. Ambe: "Mössbauer Emission Study of Recoil ^{119}Sb and $^{119\text{m}}\text{Te}$ Atoms after p- and Alpha-Reactions in SnS and SnSe," Int. Conf. Applications of the Mössbauer Effect, Melbourne, Aug. (1987).
 - 20) K. Maeda, Y. Sasa, M. Maeda, H. Kusuyama, and M. Uda: "Application of PIXE to Biological Materials in a Daily Life," 12th Int. Symp. Hosei Univ., Application of Ions in Material Science, Tokyo, Sep. (1987).
 - 21) K. Kimura, N. Hamada, F. Imai, T. Nakamura, and T. Yoshida: "Simultaneous Measurement of Ion-Track Scintillation Using a Bundle Fiber and One-Dimensional Photo-detector," 1987 Fall Meeting Phys. Soc. Jpn., Sendai, Sep. (1987).
 - 22) Y. Itoh, T. Nozaki, H. Fukushima, Y. Mochizuki, T. Masui, and T. Abe: "Diffusion Constant of Nitrogen in Silicon Measured by ^{15}N Activable Tracer Method," 48th Fall Meeting Jpn. Soc. Appl. Phys., Nagoya, Sep. (1987).
 - 23) T. Takahashi: "Biological Effects of HZE Particles," 1st Annu. Meeting Jpn. Phys. Soc. Biol. Sci. in Space, Tokyo, Sep. (1987).
 - 24) I. Kaneko, K. Eguchi-Kasai, T. Kosako, A. Maruhashi, and K. Nakano: "Oxygen Effect of α -Particles on Human Melanoma Cells," 46th Annu. Meeting Jpn. Cancer Assoc., Tokyo, Sep. (1987).
 - 25) S. Ambe, F. Ambe, T. Okada, and H. Sekizawa: "Emission Mössbauer Spectra of ^{151}Gd Adsorbed on YIG Surface," 31st Symp. Radiochemistry, Fukuoka, Oct. (1987).
 - 26) F. Ambe, S. Ambe, and T. Okada: "*In situ* and *Ex situ* Emission Mössbauer Spectra of $^{57}\text{Co}^{2+}$ and $^{119}\text{Sb}^{5+}$ Adsorbed on $\gamma\text{-Fe}_2\text{O}_3$ and NiFe_2O_4 Surfaces," 31st Symp. Radiochemistry, Fukuoka, Oct. (1987).
 - 27) M. Aratani, M. Yanokura, I. Sugai, and H. Kato: "Heavy-Ion Probe Backscattering Analysis Applied to the Study for Preparation of Self-Supporting Carbon Film," 31st Symp. Radiochemistry, Fukuoka, Oct. (1987).
 - 28) Y. Kobayashi, M. Katada, H. Sano, T. Okada, K. Asai, N. Sakai, S. Ambe, and F. Ambe: "Mössbauer Spectroscopic Studies of Ruthenium Compounds (II)," 31st Symp. Radiochemistry, Fukuoka, Oct. (1987).
 - 29) S. Ambe: "Adsorption of No-Carrier-Added $^{119}\text{Sb}^{5+}$ onto Metal Oxide Surfaces," 31st Symp. Radiochemistry, Fukuoka, Oct. (1987).
 - 30) H. Kumagai, K. Eguchi, Y. Hatanaka, T. Takahashi, I. Kaneko, and T. Kanai: "Dosimetry at the Biology Course of RIKEN Ring Cyclotron," 1987 Fall Meeting Jpn. Soc. Appl. Phys., Nagoya, Oct. (1987).
 - 31) K. Kimura, T. Yoshida, N. Hamada, F. Imai, and T. Nakamura: "Simultaneous One-Dimensional Photo-Counting of Ion Track Using a Bundle Fiber," 30th Conf. Radiation Chemistry, Nagoya, Oct. (1987).
 - 32) T. Sako, K. Sasaki, S. Imai, Y. Ohmura, Y. Noguchi, S. Tazawa, Y. Itoh, and T. Nozaki: "Determination of Carbon and Boron in GaAs," Annu. Meeting Anal. Chem. Soc. Jpn., Kumamoto, Oct. (1987).
 - 33) T. Takahashi, F. Yatagai, T. Katayama, and I. Kaneko: "Biological Effects of Heavy Charged Particles in Cosmic Rays and Experimental Programme of our Group," 46th Space Environmental Monitoring Group Meeting, Wako, Oct. (1987).
 - 34) T. Takahashi, T. Katayama, F. Yatagai, S. Konno, I. Kaneko, T. Kasuya, T. Doke, and H. Ohashi: "The Inactivation of Bacterial Spores by a Single Heavy Ion and Preparation for Experiments in the Spacecraft," 30th Annu. Meeting Jpn. Radiat. Res. Soc., Tokyo, Dec. (1987).
 - 35) K. Eguchi-Kasai, I. Kaneko, T. Kosaka, K. Nakano, and A. Maruhashi: "Effects of Heavy Charged Particles on DNA in Mammalian Cells," 30th Annu. Meeting Jpn. Radiat. Res. Soc., Tokyo, Dec. (1987).
 - 36) T. Kosaka, I. Kaneko, and K. Eguchi-Kasai: "Potentially Lethal Damage Sensitive to Hypotonic Solution and DNA Double Strand Breaks," 30th Annu. Meeting Jpn. Radiat. Res. Soc., Tokyo, Dec. (1987).

VIII. LIST OF OUTSIDE USERS AND THEIR THEMES

(Jan.–Dec. 1987)

- | | |
|--|---|
| 1) H. Fukushima
"Radiochemical Analysis of ^{16}O , ^{14}N ,
and ^{12}C in Si Crystal and GaAs" | Japan Chemical Analysis Center |
| 2) T. Hayashi and A. Ohnishi
"Radiation Damage of Cover Glass
for a Solar Cell" | Institute of Space and Astronautical Science |
| 3) S. Yoshida
"Radiation Damage of GaAs
Solar Cells" | Mitsubishi Electric Co., Ltd. |
| 4) H. Ueyama
"Radiation Damage of Si
Crystal Solar Cells" | Sharp Co., Ltd. |
| 5) M. Watanabe and K. Ueno
"Improvement of Thyristors by
Proton Irradiation" | Fuji Electric Corporate R & D, Ltd. |
| 6) H. Akiyama
"Improvement of Thyristors
by Proton Irradiation" | LSI Lab., Mitsubishi Electric Co., Ltd. |
| 7) T. Abe and K. Tomii
"Improvement of Thyristors
by Proton Irradiation" | Semiconductor R & D Lab.,
Matsushita Electric Work Co., Ltd. |
| 8) K. Toriyama
"Study of Single Event Upset in
Microprocessors by Bombarding
^{14}N and ^{12}C Particles" | Mitsubishi Electric Co., Ltd. |
| 9) T. Kikuchi and K. Yamazaki
"Study of Single Event Upset in
Microprocessors by Bombarding
^{14}N and ^{12}Ne Particles" | Nippon Electric Co., Ltd. |
| 10) K. Yamamoto and I. Yoshii
"Study of Single Event Upset in
Microprocessors by Bombarding
^{14}N and ^{40}Ar " | Semiconductor R & D Lab., Toshiba Co., Ltd. |
| 11) Y. Fujita
"Calibration of Space Environment
Monitor Carried on a Satellite
with Proton and α Particles" | Meisei Electric Co., Ltd. |
| 12) T. Suematsu
"Effects of the Proton Irradiation
on Cable Materials" | Fujikura Co., Ltd. |

IX. LIST OF SEMINARS

(Jan.–Dec. 1987)

- 1) Y. R. Shimizu, Kyushu Univ. (Fukuoka), 16 January
“Recent Topics on High Spin Nuclear Structure”
- 2) F. P. Calaprice, Princeton Univ. (U.S.A.), 22 January
“Narrow Resonance Optical Pumping NMR and Possible Searches for Nuclear Elastic Dipole Moments”
- 3) M. Ieiri, Kyoto Univ. (Kyoto), 22 January
“Polarimeter and Polarization Transfer in Deuteron Break-up Reaction”
- 4) H. Utsunomiya, Texas A & M Univ. (U.S.A.), 5 February
“Width of the Fragment Momentum Distribution in Peripheral Nucleus-Nucleus Collisions”
- 5) Z. Yizhong, Institute for Atomic Energy (China), 10 February
“Semimicroscopic Optical Potential Based on Some Effective Interactions from Non-Relativistic to Relativistic”
- 6) M. Namiki, Waseda Univ. (Tokyo), 10 March
“Measurements in the Quantum Mechanics”
- 7) K. Valli, Univ. Jyväskylä (Finland), 17 March
“Gas Flow in Ion Guide”
- 8) H. J. Mang, Tech. Univ. Munich (W. Germany), 24 March
“RPA Calculations for the Low-Lying Collective States of ^{164}Er ”
- 9) M. Fujiwara, RCNP, Osaka Univ. (Osaka), 7 April
“New Interest in Nuclear Discrete States”
- 10) Y. Terrien, CEN Saclay (France), 14 April
“Inelastic Process in Intermediate Nucleon-Nucleon Scattering”
- 11) J. Gosset, CEN Saclay (France), 14 April
“Correlation Measurements of Intermediate Heavy Ion Reaction by 4π -TPC Counter”
- 12) A. Gelberg, Univ. Köln (W. Germany), 14 April
“F-Spin Symmetry and M1 Transitions”
- 13) M. Blann, Univ. California (U.S.A.), 27 April
“Nuclear De-Excitation Processes Following Heavy-Ion Collisions”
- 14) T. Shibata, CERN (Switzerland), 28 April
“Low Energy Anti-Proton Experiments by LEAR”
- 15) J. P. Schiffer, Argonne National Lab. (U.S.A.), 30 April
“Crystalline Beams”
- 16) M. Nishimura, RCNP, Osaka Univ. (Osaka), 14 May
“M1 Form Factor in the Region of Low Momentum Transfer”
- 17) T. Marumori, Univ. Tsukuba (Ibaraki), 19 May
“Theory of Large-Amplitude Collective Motions”
- 18) Y. Masuda, KEK (Ibaraki), 2 June
“P and T Invariance in Nuclei — Experiments Using Polarized Low Energy Neutron —”
- 19) S. Iwasaki, Univ. Chiba (Chiba), 9 June
“Rotational Bands of Sn”
- 20) O. Yamakawa, KEK (Ibaraki), 25 June
“Data Acquisition System for TOPAZ Detector”
- 21) K. Koyama, Inst. of Space and Astronautical Science (Tokyo), 30 June
“Formation of Elements in Space”
- 22) D. C. Hoffman, Univ. California (U.S.A.), 3 July
“The LEAD to Explore the Region of Neutron-Rich Heavy Element Isotopes”
- 23) H. Togawa, Kyoto Univ. (Kyoto), 10 July
“Development of Data Acquisition System Using Some Front-End Processors”
- 24) J. Tanaka, Hitachi, Ltd. (Tokyo), 10 July
“RF Power Source”
- 25) H. Nishimura, LBL (U.S.A.), 13 July
“Introduction to Particle Tracking for a Synchrotron Radiation Source in the Next

Generation”

- 26) H. Nishimura, LBL (U.S.A.), 14 July
“Introduction to the Theory and Practice of Particle Tracking”
- 27) K. Koshigiri, Osaka Kyoiku Univ. (Osaka), 14 July
“Nuclear β -Decay and Axial Charge”
- 28) P. J. Nacher, Laboratoire de Physique de l'ENS (France), 17 July
“Polarizing ^3He Nuclei by Laser Optical Pumping”
- 29) H. Nishimura, LBL (U.S.A.), 20 July
“Advance Light Source Project at LBL”
- 30) Y. Hirata, Kitasato Univ. (Tokyo), 24 July
“Soliton-Antisoliton Pair Creation in Strong External Fields”
- 31) S. Lunardi, Univ. Padova (Italy), 4 September
“Shape Coexistence at High Spin in the $N=78$ Nuclei ^{140}Sm and ^{142}Gd ”
- 32) Y. Fujia, Fudan Univ. (China), 8 September
“Scientific Activity at Fudan Univ. and Institute of Nuclear Research Shanghai”
- 33) T. Kamei, Univ. Tsukuba (Ibaraki), 9 September
“On the Accelerators”
- 34) Y. Yamazaki, KEK (Ibaraki), 9 September
“RF System of KEK PF and TRISTAN”
- 35) K. Satoh, Tokyo Inst. Technol. (Tokyo), 11 September
“Electromagnetic Characteristics of I-H Type

Linear Accelerator”

- 36) P. G. Hansen, Aarhus Univ. (Denmark), 21 September
“Nuclei Far From Stability: Past, Present and Future”
- 37) H. Hofmann, Tech. Univ. Munich (W. Germany), 22 October
“On a Nuclear Transport Theory for Slow Collective Motion”
- 38) M. Ichimura, Univ. Tokyo (Tokyo), 27 October
“Excitation of τ - σ Modes in Quasi-Free Scattering”
- 39) M. Matsuzaki, Kyoto Univ. (Kyoto), 5 November
“Triaxial Deformation and Electromagnetic Transitions at High Spin”
- 40) K. Hirata, KEK (Ibaraki), 6 November
“Introduction to Beam Tracking”
- 41) K. Nomoto, Univ. Tokyo (Tokyo), 24 November
“Supernova and Formation of Heavy Elements”
- 42) H. Duohui, Univ. Sci. Tech. (Hefei China), 30 November
“Status of HESYRL Project”
- 43) T. Kobari, Hitachi, Ltd. (Ibaraki), 10 December
“Photon-Stimulated Desorption from Vacuum Chamber”
- 44) H. Aiba, Kyoto Univ. (Kyoto), 16 December
“Microscopic Description of Large-Amplitude Quadrupole Motions”

X. LIST OF PERSONNEL

Members of the Board

AMBE Fumitoshi 安部文敏	AWAYA Yohko 栗屋容子
CHIBA Yoshiaki 千葉好明	HASHIZUME Akira 橋爪 朗
INAMURA Takashi 稲村 卓	ISHIHARA Masayasu 石原正泰*
KAMITSUBO Hiromichi 上坪宏道	KANEKO Ichiro 金子一郎
KATSUMATA Koichi 勝又紘一	KIRA Akira 吉良 爽
KOHNO Isao 河野 功	KURIHARA Osamu 栗原 修
MATSUOKA Masaru 松岡 勝	NAKAMINE Kanetada 永嶺謙忠
SAKURAI Akira 桜井 成	TABATA Yoshio 田畑嘉雄
TAKAMI Michio 高見道生	TANIHATA Isao 谷畑勇夫
WATANABE Tsutomu 渡部 力	

* Chairman

Cyclotron Operation and Maintenance Group

FUJITA Shin 藤田 新	IKEGAMI Kumio 池上九三男
KAGEYAMA Tadashi 影山 正	KOHARA Shigeo 小原重夫
KOHNO Isao 河野 功	OGIWARA Kiyoshi 荻原 清
TAKEBE Hideki 武部英樹	

Linac Operation and Maintenance Group

CHIBA Yoshiaki 千葉好明	HEMMI Masatake 逸見政武
IKEZAWA Eiji 池沢英二	INOUE Toshihiko 井上敏彦
KAMBARA Tadashi 神原 正	KASE Masayuki 加瀬昌之
KUBO Toshiyuki 久保敏幸	MIYAZAWA Yoshitoshi 宮沢佳敏
YANOKURA Minoru 矢野倉 実	

Scientific and Engineering Personnel

Cosmic Ray Laboratory

IMAI Takashi 今井 喬	KOHNO Tsuyoshi 河野 毅
MUNAKATA Kazuoki 宗像一起	

(Visitors)

HASEBE Nobuyuki 長谷部信行 (Fac. Gen. Educ., Ehime Univ.)
 MURAKAMI Hiroyuki 村上浩之 (Fac. Sci., Rikkyo Univ.)
 NAGATA Katsuaki 永田勝明 (Fac. Eng., Tamagawa Univ.)
 NAKAMOTO Atsusi 中本 淳 (Fac. Sci., Rikkyo Univ.)
 YANAGIMACHI Tomoki 柳町朋樹 (Fac. Sci., Rikkyo Univ.)

(Student)

KASHIWAGI Toshisuke 柏木利介 (Sci. Eng. Res. Lab., Waseda Univ.)

Cyclotron Laboratory

BE Suck Hee 裴 碩喜

FUJITA Jiro 藤田二郎

GOTO Akira 後藤 彰

HATANAKA Kichiji 畑中吉治

INAMURA Takashi 稲村 卓

KAMITSUBO Hiromichi 上坪宏道

KOHARA Shigeo 小原重夫

MATSUO Masayuki 松尾正之

MOTONAGA Shoshichi 元永昭七

NAGASE Makoto 長瀬 誠

NAKANISHI Noriyoshi 中西紀喜

SAITO Motozo 齊藤始三

SHIKATA Takashi 四方隆史

TAKEBE Hideki 武部英樹

TOYAMA Mitsuru 遠山 満

YAMAJI Shuhei 山路修平

YOKOYAMA Ichiro 横山一郎

FUJISAWA Takashi 藤沢高志

FUJITA Shin 藤田 新

HARA Masahiro 原 雅弘

IKEGAMI Kumio 池上九三男

KAGEYAMA Tadashi 影山 正

KARASAWA Takashi 唐沢 孝

KOHNO Isao 河野 功

MORITA Kosuke 森田浩介

NAGAOKA Ryutaro 長岡隆太郎

NAKAJIMA Shunji 中島諄二

OGIWARA Kiyoshi 荻原 清

SASAKI Shigeki 佐々木茂樹

SHIMIZU Kazuo 清水和男

TAKESHITA Isao 竹下勇夫

WADA Takeshi 和田 雄

YANO Yasushige 矢野安重

(Visitors)

ANAYAMA Hiroshi 穴山 汎 (Reliability Cent. for Electronic Components of Japan)

CHOE Byung-Ha 趙 炳夏 (KAIST, Korea)

EGUCHI-KASAI Kiyomi 江口(笠井)清美 (Inst. Basic Med. Sci., Univ. Tsukuba)

EJIRI Hiroyasu 江尻宏泰 (Dep. Phys., Osaka Univ.)

FUKUMOTO Sadayoshi 福本貞義 (KEK)

FURUNO Kohei 古野興平 (Inst. Phys. Tandem Accel. Cent., Univ. Tsukuba)

GOKA Tateo 五家建夫 (NASDA)

HARADA Kichinosuke 原田吉之助 (Nippon Energy K.K.)

HARADA Minoru 原田 稔 (Reliability Cent. for Electronic Components of Japan)

HAYASHI Nobuyuki 林 伸行 (Electro Tech. Lab.)

HIRAKI Akio 平木昭夫 (Fac. Eng., Osaka Univ.)

IKEGAMI Hidetsugu 池上榮胤 (RCNP, Osaka Univ.)

INOUE Makoto 井上 信 (RCNP, Osaka Univ.)

ISOYA Akira 磯矢 彰 (Sch. Sci., Tokai Univ.)

IWAMOTO Akira 岩本 昭 (Japan Atomic Energy Res. Inst.)

IWASHITA Yoshihisa 岩下芳久 (Inst. Chem. Res., Kyoto Univ.)

KADOYA Shingo 角矢真吾 (Japan Gasoline Co.)

KANEKO Kumetaro 金子彖太郎 (Inst. Nucl. Study, Univ. Tokyo)

KASAI Shunichi 河西俊一 (Japan Atomic Energy Res. Inst.)

KATORI Kenji 鹿取謙二 (Dep. Phys., Osaka Univ.)

KATSURAGAWA Hidetsugu 桂川秀嗣 (Dep. Phys., Toho Univ.)

KIKUCHI Fumio 菊地文男 (Coll. Arts Sci., Univ. Tokyo)

KOBAYASHI Shinsaku 小林辰作 (Dep. Phys., Kyoto Univ.)

KOHMOTO Susumu 河本 進 (Univ. Electro-Commun.)

KONDO Michiya 近藤道也 (RCNP, Osaka Univ.)
 KOSAKO Toshiso 小佐古敏莊 (Atomic Energy Res. Cent., Univ. Tokyo)
 KOWATA Mitsuyoshi 小綿光喜 (Reliability Cent. for Electronic Components of Japan)
 KUDO Hisaaki 工藤久昭 (Dep. Chem., Niigata Univ.)
 KUSAKA Takuya 日下卓也 (Kobe Steel, Ltd.)
 MALLIK Chaturanan (V.E.G. Cent., B.A.R.C., India)
 MATSUKI Seishi 松木征史 (Inst. Chem. Res., Kyoto Univ.)
 MINOWA Tatsuya 箕輪達哉 (Dep. Phys., Toho Univ.)
 MIURA Iwao 三浦岩 (RCNP, Osaka Univ.)
 MIYADE Hiroki 宮出宏紀 (Sumitomo Heavy Ind., Ltd.)
 MIYATAKE Hiroari 宮武宇也 (Fac. Sci., Osaka Univ.)
 MORIMOTO Yoshihide 森本佳秀 (Kobe Steel, Ltd.)
 MORIO Atsuo 森尾篤夫 (Reliability Cent. for Electronic Components of Japan)
 MURAYAMA Toshiyuki 村山利幸 (Tokyo Univ. Mercantile Marine)
 NAGAMIYA Shoji 永宮正治 (Dep. Phys., Univ. Tokyo)
 NAKAHARA Hiromichi 中原弘道 (Dep. Chem., Tokyo Metropolitan Univ.)
 NAKAI Koji 中井浩二 (KEK)
 NAKAJIMA Kazuhisa 中島一久 (KEK)
 NAKAMURA Shinya 中村慎也 (Reliability Cent. for Electronic Components of Japan)
 NAKAMURA Takashi 中村尚司 (Cyclotron Radioisot. Cent., Tohoku Univ.)
 NOMURA Toru 野村亨* (Inst. Nucl. Study, Univ. Tokyo)
 NONAKA Hideki 野中英生 (Sumitomo Heavy Ind., Ltd.)
 ODERA Masatoshi 小寺正俊* (Sci. Eng. Res. Lab., Waseda Univ.)
 ONISHI Naoki 大西直毅 (Dep. Phys., Coll. Gen. Educ., Univ. Tokyo)
 OTA Shigemi 太田滋生 (KEK)
 SAKAMOTO Hiroyuki 坂本浩幸 (Ishikawajima-Harima Heavy Ind., Co., Ltd.)
 SAKAMOTO Isao 坂本勲 (Electro Tech. Lab.)
 SAKURADA Yuzo 桜田勇三 (ULVAC Co.)
 SASUGA Tsuneo 貴家恒男 (Japan Atomic Energy Res. Inst.)
 SATO Kenichi 佐藤憲一 (Div. Phys., Tohoku Coll. Pharm.)
 SHIMANO Yosuke 島野洋介 (NASDA)
 SHIMAZU Mitsuyoshi 島津備愛 (Dep. Phys., Toho Univ.)
 SHINOZUKA Tsutomu 篠塚勉 (Cyclotron Radioisot. Cent., Tohoku Univ.)
 SHIRAISHI Haruki 白石春樹 (Natl. Res. Inst. Metals)
 SUEKI Keisuke 末木啓介 (Inst. Nucl. Study, Univ. Tokyo)
 SUNAGA Hiromi 須永博美 (Japan Atomic Energy Res. Inst.)
 TAKEGOSHI Hidekuni 竹腰秀邦 (Inst. Chem. Res., Kyoto Univ.)
 TAKEMASA Tadashi 武政尹士 (Dep. Phys., Saga Univ.)
 TAKIGAWA Noboru 滝川昇 (Dep. Phys., Tohoku Univ.)
 TAMAGAKI Ryoza 玉垣良三 (Dep. Phys., Kyoto Univ.)
 TANAKA Hitoshi 田中均 (Japan Gasoline Co.)
 TANAKA Jinichi 田中仁市 (Inst. Nucl. Study, Univ. Tokyo)
 TANAKA Koki 田中幸基 (Nippon Steel Corp.)
 TASAKA Shigeki 田坂茂樹 (Fac. Educ., Gifu Univ.)
 TOMIMASU Takio 富增多喜夫 (Electro Tech. Lab.)
 TORIZUKA Kanji 鳥塚莞爾 (Fac. Med., Kyoto Univ.)
 TSUKIJI Masaru 築地優 (NEC Corp.)
 TSUMAKI Koji 妻木孝治 (Hitachi, Ltd.)

TSUNEMOTO Hiroshi 恒元 博 (Natl. Inst. Radiol. Sci.)
 VALLI Kalevi (Dep. Phys., Jyvaskyla Univ., Finland)
 WAKISHIMA Susumu 脇島 進 (Reliability Cent. for Electronic Components of Japan)
 WANG Zhen (Inst. Mod. Phys., Acad. Sin., China)
 WATANABE Hiroshi 綿鍋博志 (Electro Tech. Lab.)
 YAMASU Kazushige 弥益和重 (Mitsubishi Heavy Ind., Ltd.)
 YAMAZAKI Takashi 山崎 魏 (RCNP, Osaka Univ.)
 YOKOUCHI Shigeru 横内 茂 (Osaka Vacuum, Ltd.)
 YOSHIDA Katsuhisa 吉田克久 (Mitsubishi Electric, Co.)
 YOSHIDA Nobuaki 吉田宣章 (Dep. Phys., Univ. Tokyo)
 YOSHIDA Shiro 吉田思郎 (Dep. Phys., Tohoku Univ.)
 YOSHINAGA Naotaka 吉永尚孝 (Comput. Cent., Univ. Tokyo)
 YOSHIYUKI Takeshi 吉行 健 (Toshiba, Co.)

* Visiting Professor

(Students)

ARAI Toshiyuki 新井利幸 (Fac. Sci., Toho Univ.)
 HARADA Hideo 原田秀郎 (Dep. Phys., Tokyo Inst. Technol.)
 KASAHARA Tatsuya 笠原達也 (Fac. Sci. Eng., Chuo Univ.)
 KAWASAKI Noriko 川寄紀子 (Coll. Hum. Sci., Nihon Univ.)
 KOIKE Yuji 小池裕司 (Dep. Phys., Univ. Tokyo)
 KOJIMA Toshiyuki 小島智之 (Fac. Sci. Eng., Chuo Univ.)
 YAMAGISHI Yoshinori 山岸義徳 (Fac. Sci. Eng., Chuo Univ.)
 YOSHIDA Minoru 吉田 稔 (Coll. Hum. Sci., Nihon Univ.)

Linear Accelerator Laboratory

CHIBA Toshiya 千葉利哉	CHIBA Yoshiaki 千葉好明
HEMMI Masatake 逸見政武	INOUE Toshihiko 井上敏彦
KAMBARA Tadashi 神原 正	KASE Masayuki 加瀬昌之
KUBO Toshiyuki 久保敏幸	KUMAGAI Hidekazu 熊谷秀和
MIYAZAWA Yoshitoshi 宮沢佳敏	NAKAGAWA Takahide 中川孝秀
SUZUKI Takeshi 鈴木 健	TAKEUCHI Sachiko 竹内幸子
TANIHATA Isao 谷畑勇夫	TONUMA Tadao 戸沼正雄
YANOKURA Minoru 矢野倉 実	

(Visitors)

FUJIWARA Ichiro 藤原一郎 (Inst. Atomic Energy, Kyoto Univ.)
 ITO Noriaki 伊藤憲昭 (Dep. Cryst. Mater., Nagoya Univ.)
 KIKUCHI Jun 菊地 順 (Sci. Eng. Res. Lab., Waseda Univ.)
 LIU Wei Ping 柳 丕平 (Inst. Atomic Energy, China)
 NONAKA Hideki 野中英生 (Sumitomo Heavy Ind., Ltd.)
 SUGAWARA Masahiko 菅原昌彦 (Fundam. Sci., Chiba Inst. Technol.)
 YAMAGUCHI Hiromi 山口裕美 (Sci. Eng. Res. Lab., Waseda Univ.)

(Student)

FUKUDA Mitsunori 福田光順 (Fac. Sci., Tokyo Inst. Technol.)
 ITO Tatsuya 伊藤達也 (Sci. Eng. Res. Lab., Waseda Univ.)

Radiation Laboratory

ASAHI Koichiro 旭 耕一郎	GONO Yasuyuki 郷農靖之
HASHIZUME Akira 橋爪 朗	ICHIHARA Takashi 市原 卓
ISHIHARA Masayasu 石原正泰	IZUMO Koichi 出雲光一
KONNO Satoshi 金野 智	TAKAHASHI Tan 高橋 旦
TENDO Yoshihiko 天道芳彦	

(Visitors)

ABE Yasuhisa 阿部恭久 (Res. Inst. Fundam. Phys., Kyoto Univ.)
 ADACHI Minoru 足立 實 (Dep. Appl. Phys., Tokyo Inst. Technol.)
 ANDO Yoshiaki 安藤嘉章 (Dep. Phys., Rikkyo Univ.)
 DOKE Tadayoshi 道家忠義 (Sci. Eng. Res. Lab., Waseda Univ.)
 ENDO Saburo 遠藤三郎 (Fac. Eng., Sci. Univ. Tokyo)
 FUJIOKA Manabu 藤岡 学 (Dep. Phys., Tohoku Univ.)
 HAMA Hiroyuki 浜 広幸 (Dep. Phys., Tokyo Inst. Technol.)
 HASEGAWA Takeo 長谷川武夫 (Inst. Nucl. Study, Univ. Tokyo)
 HITACHI Akira 月出 章 (Sci. Eng. Res. Lab., Waseda Univ.)
 ICHIMURA Munetake 市村宗武 (Coll. Gen. Educ., Univ. Tokyo)
 IEKI Kazuo 家城和夫 (Fac. Sci., Rikkyo Univ.)
 KASAGI Jirota 笠木治郎太 (Fac. Sci., Tokyo Inst. Technol.)
 KATO Norihisa 加藤哲久 (Dep. Phys., Kyushu Univ.)
 KATO Seigo 加藤静吾 (Fac. Lib. Arts, Yamagata Univ.)
 KATORI Kenji 鹿取謙二 (Fac. Sci., Osaka Univ.)
 KAWAKAMI Hirokane 川上宏金 (Inst. Nucl. Study, Univ. Tokyo)
 KITAO Kensuke 喜多尾憲助 (Natl. Inst. Radiol. Sci.)
 KOBAYASHI Hisanobu 小林久信 (Fac. Eng., Saitama Univ.)
 KOHNO Toshiyuki 河野俊之 (Natl. Inst. Radiol. Sci.)
 KUBONO Sigeru 久保野 茂 (Inst. Nucl. Study, Univ. Tokyo)
 KUBOTA Shinzou 窪田信三 (Fac. Sci., Rikkyo Univ.)
 KUSAKARI Hideshige 草刈英榮 (Fac. Educ., Chiba Univ.)
 LEE Sang Mu 李 相茂 (Inst. Phys., Univ. Tsukuba)
 MASUDA Kimiaki 増田公明 (Sch. Sci. Eng., Waseda Univ.)
 MOTOBAYASHI Tohru 本林 透 (Fac. Sci., Rikkyo Univ.)
 MURAKAMI Takeshi 村上 健 (Dep. Phys., Tokyo Inst. Technol.)
 NAGAI Yasuki 永井泰樹 (Fac. Sci., Tokyo Inst. Technol.)
 NAGASHIMA Yasuo 長島泰夫 (Dep. Phys., Univ. Tsukuba)
 NAKAYAMA Shintarou 中山信太郎 (Coll. Gen. Educ., Univ. Tokushima)
 OHNUMA Hajime 大沼 甫 (Fac. Sci., Tokyo Inst. Technol.)
 OHSUMI Hideaki 大隅秀晃 (Fac. Sci., Osaka Univ.)
 ORIHARA Hikonojo 織原彦之丞 (Cyclotron and Radioisot. Cent., Tohoku Univ.)
 OYAIZU Mitsuhiro 小柳津充広 (Inst. Nucl. Study, Univ. Tokyo)
 RUAN (GEN) Jian-zhi 阮 建治 (Dep. Phys., Rikkyo Univ.)
 SAKAGUCHI Harutaka 坂口治隆 (Dep. Phys., Kyoto Univ.)
 SHIBAMURA Eido 柴村英道 (Saitama Coll. Health)
 SHIMIZU Hajime 清水 肇 (Fac. Sci., Tokyo Inst. Technol.)
 SHIRATO Shoji 白土鈔二 (Dep. Phys., Rikkyo Univ.)
 SUGAWARA Masahiko 菅原昌彦 (Fundam. Sci., Chiba Inst. Technol.)
 TAKAHASHI Noriaki 高橋憲明 (Coll. Gen. Educ., Osaka Univ.)

TAKIGAWA Noboru 滝川 昇 (Dep. Phys., Tohoku Univ.)
 TOKI Hiroshi 土岐 博 (Dep. Phys., Tokyo Metropolitan Univ.)
 YAMAYA Takashi 山屋 堯 (Dep. Phys., Tohoku Univ.)
 YASUE Masaharu 安江正治 (Inst. Nucl. Study, Univ. Tokyo)
 YOSHIZAWA Yasukazu 吉沢康和 (Dep. Phys., Hiroshima Univ.)

(Students)

ASHIKAGA Kinya 足利欣哉 (Sch. Sci. Eng., Waseda Univ.)
 FUJIWARA Hideaki 藤原英明 (Inst. Phys., Univ. Tsukuba)
 FUKUDA Mitsunori 福田光順 (Fac. Sci., Tokyo Inst. Technol.)
 FUNATSU Yoshinori 船津義徳 (Fac. Sci., Kyushu Univ.)
 HWANG Han Yull 黄 翰悦 (Dep. Phys., Yonsei Univ., Korea)
 ICHINOSE Hideo 市之瀬秀夫 (Grad. Sch. Sci. Eng., Waseda Univ.)
 ITO Tatsuya 伊藤達也 (Grad. Sch. Sci. Eng., Waseda Univ.)
 IWASA Naohito 岩佐直仁 (Dep. Phys., Rikkyo Univ.)
 JEONG S. C. 鄭 淳讚 (Inst. Phys., Univ. Tsukuba)
 KOGUCHI Masanari 高口雅成 (Dep. Appl. Phys., Tokyo Inst. Technol.)
 MIZOTA Takeshi 溝田武志 (Inst. Phys., Univ. Tsukuba)
 OGIWARA Masahiro 荻原正弘 (Dep. Phys., Rikkyo Univ.)
 OGIWARA Mitsuhiko 荻原光彦 (Inst. Phys., Univ. Tsukuba)
 OKUMURA Susumu 奥村 進 (Inst. Phys., Univ. Tsukuba)
 OKUMURA Yasuaki 奥村泰明 (Sch. Sci. Eng., Waseda Univ.)
 ONO Yoichi 小野陽一 (Fac. Educ., Chiba Univ.)
 PU Y. H. 蒲 越虎 (Inst. Phys., Univ. Tsukuba)
 SAKURAI Mikio 桜井幹夫 (Dep. Phys., Tokyo Inst. Technol.)
 SANO Toshio 佐野俊夫 (Grad. Sch. Sci. Eng., Waseda Univ.)
 SHIBUYA Shinji 渋谷真二 (Dep. Phys., Rikkyo Univ.)
 TAKEUCHI Hiroki 竹内宏喜 (Dep. Phys., Tokyo Inst. Technol.)
 TAMURA Akitoshi 田村彰敏 (Grad. Sch. O-okayama, Tokyo Inst. Technol.)
 UTSUMI Motoharu 内海資元 (Grad. Sch. Sci. Eng., Waseda Univ.)
 YOSHIDA Koichi 吉田光一 (Fac. Sci., Tokyo Inst. Technol.)

Atomic Processes Laboratory

ANDO Kozo 安藤剛三	AWAYA Yohko 粟屋容子
HINO Kenichi 日野健一	KAMBARA Tadashi 神原 正
KANAI Yasuyuki 金井保之	NISHIDA Masami 西田雅美
SHIMAMURA Isao 島村 勲	WATANABE Tsutomu 渡部 力

(Visitors)

FUJIMA Kazumi 藤間一美 (Dep. Phys., Chuo Univ.)
 HARA Shunsuke 原 俊介 (Dep. Phys., Univ. Tsukuba)
 HITACHI Akira 月出 章 (Inst. Sci. Technol., Waseda Univ.)
 ISHII Keishi 石井慶之 (Dep. Eng. Sci., Kyoto Univ.)
 ISOZUMI Yasuhito 五十棲泰人 (Radioisot. Res. Cent., Kyoto Univ.)
 ITO Shin 伊藤 真 (Radioisot. Res. Cent., Kyoto Univ.)
 ITOH Yoh 伊東 陽 (Fac. Sci., Josai Univ.)
 IWAI Masahiro 岩井正博 (Theor. Div., Inst. Mol. Sci.)

KARASHIMA Shosuke 唐島照介 (Dep. Electron. Eng., Tokyo Univ. Sci.)
 KAWATSURA Kiyoshi 川面澄 (Japan Atomic Energy Res. Inst.)
 KIMURA Mineo 季村峯生 (Argonne Natl. Lab.)
 KOIKE Fumihiro 小池文博 (Sch. Med., Kitasato Univ.)
 KOIZUMI Tetsuo 小泉哲夫 (Dep. Phys., Rikkyo Univ.)
 KOYAMA Naoto 小山直人 (Dep. Eng. Phys., Univ. Electro-Commun.)
 KUROKI Kenro 黒木健郎 (Natl. Res. Inst. Police Sci.)
 LIU Bing 劉泳 (Inst. Mod. Phys., Acad. Sin., China)
 MATSUO Takashi 松尾崇 (Dep. Pathol., Tokyo Med. Dent. Univ.)
 MATSUZAWA Michio 松澤通生 (Dep. Eng. Phys., Univ. Electro-Commun.)
 MIZOGAWA Tatsumi 溝川辰巳 (Fac. Sci., Saitama Univ.)
 MUKHERJEE Sunil Chandra (Dep. Theor. Phys., Indian Assoc. for Cultiv. Sci.)
 OHSAKI Akihiko 大崎明彦 (Inst. Mol. Sci.)
 OHTANI Shunsuke 大谷俊介 (Inst. Plasma Phys., Nagoya Univ.)
 OKUNO Kazuhiko 奥野和彦 (Dep. Phys., Tokyo Metropolitan Univ.)
 SATO Hiroshi 佐藤浩史 (Dep. Phys., Ochanomizu Univ.)
 SATO Kuninori 佐藤国憲 (Inst. Plasma Phys., Nagoya Univ.)
 SCHUCH Reinhold (Oak Ridge Natl. Lab.)
 SHIBATA Hiromi 柴田裕美 (Res. Cent. Nucl. Sci. Technol., Univ. Tokyo)
 SHIMA Kunihiko 島邦博 (Tandem Accel. Cent., Univ. Tsukuba)
 SHIMAKURA Noriyuki 島倉紀之 (Gen. Educ. Dep., Niigata Univ.)
 STOLTERFOHT Nikolaus (Hahn-Meitner-Inst. Kernforschung, Berlin)
 SULIK Bela (Inst. Nucl. Res., Hung. Acad. Sci. (ATOMKI))
 TAKAGI Shoji 高木祥示 (Dep. Phys., Toho Univ.)
 TAWARA Hiroyuki 俵博之 (Inst. Plasma Phys., Nagoya Univ.)
 TSURUBUCHI Seiji 鶴淵誠二 (Fac. Technol., Tokyo Univ. Agric. Technol.)
 URAKAWA Junji 浦川順治 (Natl. Lab. High Energy Phys.)
 VOGT Hans G. (Phys. Inst., Univ. Heidelberg)
 WHELAN Colm T. (Univ. Coll. London)
 YAMAZAKI Yasunori 山崎泰規 (Res. Lab. Nucl. Reactor, Tokyo Inst. Technol.)

(Student)

NISHIMURA Hisashi 西村久 (Dep. Phys., Tokai Univ.)

Metal Physics Laboratory

ISHIDA Katsuhiko 石田勝彦	KOYAMA Akio 小山昭雄
MATSUZAKI Teiichiro 松崎禎市郎	NAGAMINE Kanetada 永嶺謙忠
SHIOTANI Nobuhiro 塩谷亘弘	YAGI Eiichi 八木栄一

(Students)

ISHIKAWA Hiroshi 石川浩 (Fac. Sci., Sci. Univ. Tokyo)
 KANO Fumihisa 鹿野文寿 (Sch. Sci. Eng., Waseda Univ.)
 NAKAMURA Shiho 中村志保 (Sch. Sci. Eng., Waseda Univ.)

Magnetic Materials Laboratory

ASAI Kichizo 浅井吉蔵	OKADA Takuya 岡田卓也
-------------------	-------------------

SAKAI Nobuhiko 坂井信彦

(Visitor)

YAMADAYA Tokio 山田谷時夫 (Fac. Lit. Sci., Yokohama City Univ.)

(Student)

TOBA Yoshikazu 鳥羽良和 (Fac. Sci., Toho Univ.)

Plasma Physics Laboratory

ISHIBE Yukio 石部行雄

ISHII Shigeyuki 石井成行

OKAZAKI Kiyohiko 岡崎清比古

OYAMA Hitoshi 大山等

SAKAMOTO Yuichi 坂本雄一

YANO Katsuki 矢野勝喜

(Visitors)

SUGIYAMA Kazuo 杉山和夫 (Fac. Eng., Saitama Univ.)

YAMASHINA Toshiro 山科俊郎 (Fac. Eng., Hokkaido Univ.)

Semiconductor Laboratory

(Visitor)

AONO Keiko 青野桂子 (Coll. Lib. Arts, Kitasato Univ.)

Inorganic Chemistry Laboratory

DAI Yisheng 戴義生 (Inst. Opt. Electron., Acad. Sin., China)

Solid-State Chemistry Laboratory

KOBAYASHI Masayoshi 小林雅義

MAEDA Kuniko 前田邦子

SASA Yoshihiko 佐々嘉彦

TAKAMI Michio 高見道生

(Visitors)

ISHII Keizo 石井慶造 (Cyclotron Radioisot. Cent., Tohoku Univ.)

KUSUYAMA Hiroyuki 楠山弘之 (Saitama Med. Sch.)

MUKOUYAMA Takashi 向山毅 (Inst. Chem. Res., Kyoto Univ.)

UDA Masayuki 宇田応之 (Dep. Mater. Sci., Waseda Univ.)

(Student)

MAEDA Haruka 前田はるか (Dep. Eng., Tokyo Univ.)

Radiochemistry Laboratory

AMBE Fumitoshi 安部文敏

AMBE Shizuko 安部静子

ARATANI Michi 荒谷美智

ITOH Yoshiko 伊東芳子

IWAMOTO Masako 岩本正子

NOZAKI Tadashi 野崎正

OHKUBO Yoshitaka 大久保嘉高

(Visitors)

ENDO Kazutoyo 遠藤和豊 (Fac. Sci., Tokyo Metropolitan Univ.)
 FUKUSHIMA Hiroto 福嶋浩人 (Japan Chemical Analysis Cent.)
 IMAI Masato 今井正人 (Komatsu Electronic Metals Co., Ltd.)
 IMURA Ryo 井村亮 (Cent. Res. Lab., Hitachi, Ltd.)
 KATADA Motomi 片田元己 (Fac. Sci., Tokyo Metropolitan Univ.)
 KATO Hajime 加藤一 (Fac. Educ., Yamanashi Univ.)
 KIMURA Toshimasa 木村敏正 (Japan Chemical Analysis Cent.)
 MOCHIZUKI Yasuhiro 望月康弘 (Hitachi, Ltd.)
 OOHIRA Shigeo 大平重男 (Nikkei Techno Res. Co., Ltd.)
 SAITO Kazuo 斉藤和男 (Toshiba Corp., R & D Cent.)
 SUEHIRO Makiko 末広牧子 (Tokyo Metropolitan Geriatric Hospital)
 SUGAI Isao 菅井勲 (Inst. Nucl. Study, Univ. Tokyo)
 SUZUKI Ryo 鈴木良 (Cent. Res. Lab., Hitachi, Ltd.)
 WATANABE Yasuo 渡辺裕夫 (Fac. Sci., Tokyo Metropolitan Univ.)
 YATSURUGI Yoshifumi 八剣吉文 (Komatsu Electronic Metals Co., Ltd.)

(Students)

KOBAYASHI Yoshio 小林義男 (Fac. Sci., Tokyo Metropolitan Univ.)
 KUBO Kenya 久保謙哉 (Fac. Sci., Univ. Tokyo)
 QUI Qi 邱齐 (Res. Lab. Nucl. React., Tokyo Inst. Technol.)
 YU Byon Gon 俞炳坤 (Res. Lab. Nucl. React., Tokyo Inst. Technol.)

Radiation Chemistry Laboratory

KIMURA Kazuie 木村一字

(Visitor)

ITO Yasuo 伊藤泰男 (Res. Cent. Nucl. Sci. Technol., Univ. Tokyo)

(Students)

FUNDOH Atsushi 分銅淳至 (Dep. Phys., Chuo Univ.)
 HAMADA Naoki 浜田直樹 (Dep. Phys., Chuo Univ.)
 HARA Korehisa 原是久 (Dep. Phys., Chuo Univ.)
 IIDA Tsuyoshi 飯田剛 (Dep. Phys., Chuo Univ.)
 IMAI Satoshi 今井聡 (Dep. Phys., Chuo Univ.)
 KANAI Koichi 金井浩一 (Dep. Phys., Chuo Univ.)
 KATAOKA Masayoshi 片岡将克 (Dep. Phys., Chuo Univ.)
 NAKAMURA Tetsuya 中村哲也 (Dep. Phys., Chuo Univ.)
 NISHINA Takuya 仁科卓也 (Dep. Phys., Chuo Univ.)
 UENO Takao 上野貴男 (Dep. Phys., Chuo Univ.)
 YOSHIDA Tatsuya 吉田達也 (Dep. Phys., Chuo Univ.)

Radiobiology Laboratory

KANEKO Ichiro 金子一郎

NAKANO Kazushiro 中野和城

(Visitors)

BAVERSTOCK Keith F. (Radiobiol. Unit, Med. Res. Counc., U.K.)
 EGUCHI-KASAI Kiyomi 江口(笠井)清美 (Inst. Basic Med. Sci., Univ. Tsukuba)
 MARUHASHI Akira 丸橋 晃 (Inst. Clin. Med., Univ. Tsukuba)
 SUZUKI Keiji 鈴木啓司 (RI Cent., Fac. Med., Yokohama City Univ.)
 WATANABE Masami 渡辺正己 (RI Cent., Fac. Med., Yokohama City Univ.)
 YAMASHITA Shoji 山下昌次 (Natl. Saitama Hospital)

(Students)

KOSAKA Toshiyuki 小坂俊之 (Dep. Vet. Radiol., Nihon Univ.)
 SUZUKI Masao 鈴木雅雄 (Fac. Sci., Rikkyo Univ.)

Safety Control Affairs Office

KAGAYA Satoru 加賀屋 悟	KATOU Takeo 加藤武雄
KURIHARA Osamu 栗原 修	MATSUZAWA Yasuhide 松沢安秀
MIYAGAWA Makoto 宮川真言	SAKAMOTO Ichiro 坂本一郎
SAWA Hiroshi 澤 宏	SHINOHARA Shigemi 篠原茂己
USUBA Isao 薄葉 勲	

Beam Analysis Center

IWAKI Masaya 岩木正哉	KOBAYASHI Takane 小林 峰
SAKAIRI Hideo 坂入英雄	

(Visitor)

FUJIHANA Takanobu 藤花隆宣 (Advanced Technology Inc.)

(Student)

KOBAYASHI Kenzo 小林健三 (Fac. Eng. Sci., Osaka Univ.)

Laser Science Research Group

NAMBA Susumu 難波 進

AUTHOR INDEX

- ABE Ryo 阿部 亮 2, 207
ADACHI Hirohiko 足立裕彦 45
ADACHI Minoru 足立 實 21, 161
AGEMATSU Takashi 上松 敬 141
AIHARA Toshimitsu 藍原利光 3
AKAGI Hiroyasu 赤木宏安 2, 207
AMBE Fumitoshi 安部文敏 92, 96, 131, 133, 163
AMBE Shizuko 安部静子 96, 131, 133, 135, 163
ANDO Kozo 安藤剛三 62, 63
ANDO Yoshiaki 安藤嘉章 9
ANNE Rene 11
AONO Keiko 青野桂子 106
AONO Masakazu 青野正和 112
ARAI Eiichi 新井栄一 123
ARATANI Michi 荒谷美智 125, 126
ASAHI Koichiro 旭 耕一郎 11, 21, 161, 163, 180
ASAI Kichizo 浅井吉蔵 92, 93, 98, 133
AWAYA Yohko 粟屋容子 62, 67, 69, 71, 73, 76, 78, 80, 82
BAZIN Daniel 11
BE Suck Hee 裴 碩喜 84, 205, 239, 241, 243, 245, 247, 249
BENKA Oswald 87
BIMBOT René 11
BURKE Philip G. 53
CHIBA Toshiya 千葉利哉 216
CHIBA Yoshiaki 千葉好明 3, 203
DAI Yisheng 戴 義生 105
DOKE Tadayoshi 道家忠義 19, 152
EGUCHI-KASAI Kiyomi 江口(笠井)清美 145
EKUNI Katsuaki 江国克昭 17
FANG Xushan 方 緒珊 39
FUJIHANA Takanobu 藤花隆宣 105
FUJIMA Kazumi 藤間一美 45, 55
FUJIOKA Manabu 藤岡 学 155
FUJISAWA Takashi 藤沢高志 203, 214
FUJITA Jiro 藤田二郎 198
FUJITA Shin 藤田 新 5, 207, 254, 256, 258
FUJIWARA Hideaki 藤原英明 9
FUKAI Yuh 深井 有 109
FUKUDA Hiroshi 福田 宏 57
FUKUDA Mitsunori 福田光順 11, 21, 161, 180
FUKUSHIMA Hiroto 福嶋浩人 123, 124
FURUNO Kohei 古野興平 155
FUSE Masaharu 布施雅治 180
GONO Yasuyuki 郷農靖之 11
GOTO Akira 後藤 彰 2, 210, 214
GOTOH Eiichiro 後藤栄一郎 180
GUILLEMAUD-MUELLER D. 11
HAMA Hiroyuki 浜 広幸 8, 155
HAMADA Naoki 浜田直樹 137
HARA Masahiro 原 雅弘 220, 223, 225, 228, 233, 235, 237, 249, 252
HARA Shunsuke 原 俊介 57
HARADA Hideo 原田秀郎 7, 8
HARADA Shigenobu 原田重信 158
HASEBE Hiroo 長谷部裕雄 3
HASEBE Nobuyuki 長谷部信行 19, 152
HASHIMOTO Iwao 橋本 巖 101
HASHIZUME Akira 橋爪 朗 15, 185, 186, 190, 191, 195
HATANAKA Kichiji 畑中吉治 2, 164, 210, 212
HATORI Satoshi 羽鳥 聡 13
HATSUKAWA Yuichi 初川雄一 155
HAYAKAWA Shun-ichiro 早川俊一郎 164
HEMMI Masatake 逸見政武 3, 216
HINO Ken-ichi 日野健一 32, 35, 37, 41, 69
HIRATA Yoshihiro 平田嘉裕 64
HITACHI Akira 月出 章 67, 69
HOFMANN Helmut 31
HOSONO Kazuhiko 細野和彦 13
ICHIHARA Takashi 市原 卓 11, 21, 149, 164
IEKI Kazuo 家城和夫 8, 9, 164
IKEDA Nobuo 池田信夫 158
IKEGAMI Kumio 池上九三男 5, 210
IKEZAWA Eiji 池沢英二 3
IMAI Satoshi 今井 聡 137
IMAI Takashi 今井 喬 152
INAMURA Takashi 稲村 卓 7, 15, 149, 155, 174, 176, 207, 258
INOUE Toshihiko 井上敏彦 3
ISHIDA Katsuhiko 石田勝彦 64, 170, 172
ISHIHARA Masayasu 石原正泰 8, 9, 11, 13, 21, 63, 161, 164, 168, 180
ISHIHARA Takeshi 石原 武 57
ISHIKAWA Hiroshi 石川 浩 87, 89
ISHIKAWA Toshiyuki 石川俊行 2
ISSHIKI Hiroshi 一色 博 2
ITO Tatsuya 伊藤達也 19
ITOH Yoshiko 伊東芳子 123, 124
IWAI Masahiro 岩井正博 59
IWAKI Masaya 岩木正哉 101, 103, 105, 106, 107, 112
IWASA Naohito 岩佐直仁 9
IZUMO Koichi 出雲光一 143
JEONG S. C. 鄭 淳讚 9
KADONO Ryosuke 門野良典 64

- KADOTA Yoshinori 角田佳績 124
- KAGAYA Satoru 加賀屋 悟 256
- KAGEYAMA Tadashi 影山 正 5, 210, 214
- KAMBARA Tadashi 神原 正 71, 73, 78, 80, 82
- KAMITSUBO Hiromichi 上坪宏道 116, 196, 220, 258
- KANAI Yasuyuki 金井保之 67, 69, 73, 76, 78, 80, 82
- KANEKO Ichiro 金子一郎 143, 145, 147
- KANO Fumihisa 鹿野文寿 109
- KARASHIMA Shosuke 唐島照介 41
- KASAGI Jirota 笠木治郎太 7, 8, 11
- KASAHARA Tatsuya 笠原達也 230
- KASE Masayuki 加瀬昌之 2, 3, 73, 76, 82, 201, 210, 216
- KASHIWAGI Toshisuke 柏木利介 152
- KASUYA Takahiro 粕谷敬宏 143
- KATADA Motomi 片田元己 133
- KATAYAMA Toshiko 片山敏子 143
- KATO Seigo 加藤静吾 164, 166
- KATOU Takeo 加藤武雄 256
- KATSURAGAWA Hidetsugu 桂川秀嗣 176, 178
- KAWANISHI Shunichi 河西俊一 139
- KAWASAKI Noriko 川崎紀子 237
- KAWATSURA Kiyoshi 川面 澄 67
- KIKUCHI Jun 菊地 順 19, 152
- KIKUCHI Shiro 菊地士郎 15
- KIMURA Kazuie 木村一字 137
- KIMURA Mineo 季村峯生 45, 55
- KITAMURA Hideo 北村英男 252
- KITAO Kensuke 喜多尾憲助 185, 186, 190, 191
- KOBAYASHI Kenzo 小林健三 105
- KOBAYASHI Takane 小林 峰 6, 105, 109, 112, 218, 256
- KOBAYASHI Toshio 小林俊雄 17
- KOBAYASHI Yoshio 小林義男 133
- KOGUCHI Masanari 高口雅成 21, 161
- KOHARA Shigeo 小原重夫 5, 203, 210, 214
- KOHMOTO Susumu 河本 進 62, 63
- KOHNO Isao 河野 功 5, 118, 139, 141, 254, 256
- KOHNO Tsuyoshi 河野 毅 152
- KONNO Satoshi 金野 智 143
- KOSAKA Toshifumi 小坂俊文 145
- KOYAMA Akio 小山昭雄 87, 89
- KUBO Toshiyuki 久保敏幸 7, 8, 11, 19, 21, 164, 168
- KUBONO Shigeru 久保野 茂 164
- KUDO Hisaaki 工藤久昭 155
- KUMAGAI Hidekazu 熊谷秀和 19, 21, 62, 73, 82, 84, 161, 180, 183
- KURIHARA Osamu 栗原 修 256
- KUROKI Kenro 黒木健郎 67, 69
- KUSAKA Takuya 日下卓也 235, 237
- KUSAKARI Hideshige 草刈英榮 15
- KUSUYAMA Hiroyuki 楠山弘之 127
- LEE S. M. 李 相茂 9
- LIU Lon Chang 劉 龍章 23
- LIU Wei Ping 柳 丕平 19
- LIU Yaoyang 劉 輝陽 39, 47
- MA Qianchen 馬 干乘 39, 47
- MAEDA Kazushige 前田和茂 164
- MAEDA Kuniko 前田邦子 120, 127, 129
- MAEDA Masaru 前田 勝 127
- MARUHASHI Akira 丸橋 晃 145
- MATSUMOTO Takehiko 松本武彦 109
- MATSUMOTO Yoshiyasu 松本吉泰 174
- MATSUO Masayuki 松尾正之 29
- MATSUO Takashi 松尾 崇 84
- MATSUOKA Nobuyuki 松岡伸行 13
- MATSUZAKI Masayuki 松崎昌之 15
- MATSUZAKI Teiichiro 松崎禎市郎 64, 170, 172
- MATVEENKO A. V. 57
- McLAUGHLIN D. J. 71
- MINEHARA Eisuke 峰原英介 15
- MINOWA Tatsuya 箕輪達哉 176, 178
- MIYADE Hiroki 宮出宏紀 233
- MIYAGAWA Makoto 宮川真言 256
- MIYATAKE Hiroari 宮武宇也 155
- MIYAZAWA Yoshitoshi 宮沢佳敏 3, 216
- MIZOGAWA Tatsumi 溝川辰巳 73, 76, 78, 80, 82
- MIZOTA Takeshi 溝田武志 9
- MOCHIZUKI Yasuhiro 望月康弘 123
- MOKLER P. H. 71
- MORIMOTO Yoshihide 森本佳秀 239, 241, 243, 245, 247, 249
- MORITA Kosuke 森田浩介 155, 158
- MOTOBAYASHI Tohru 本林 透 9, 13, 152, 164
- MOTONAGA Shoshichi 元永昭七 198, 230
- MUELLER Alex C. 11
- MUKHERJEE Sunil Chandra 43
- MÜLLER A. 71
- MUNAKATA Kazuoki 宗像一起 152
- MURAKAMI Hiroyuki 村上浩之 9, 13, 19, 152
- MURAKAMI Takeshi 村上 健 7
- MURAKAMI Yoshio 村上義雄 158
- MURAYAMA Toshiyuki 村山利幸 9, 174
- NAGAI Yasuki 永井泰樹 155, 158
- NAGAMINE Kanetada 永嶺謙忠 64, 170, 172
- NAGAOKA Ryutaro 長岡隆太郎 223, 225, 228
- NAGASE Makoto 長瀬 誠 198, 214
- NAGASHIMA Yasuo 長島泰夫 9
- NAGATA Katsuaki 永田勝昭 152
- NAKAGAWA Takahide 中川孝秀 19

- NAKAMOTO Atsushi 中本 淳 152
 NAKAMURA Shiho 中村志保 107, 109
 NAKAMURA Takashi 中村尚司 164
 NAKAMURA Tetsuya 中村哲也 137
 NAKANISHI Noriyoshi 中西紀喜 210
 NAKANO Kazutoshi 中野和城 145
 NAMBA Susumu 難波 進 105, 106
 NISHIDA Yoshihiko 西田善彦 27
 NISHIDE Akihiko 西出昭彦 205
 NOBLE Cliff J. 53
 NOMURA Toru 野村 亨 155, 158
 NONAKA Hideo 野中英生 2, 210, 212
 NORO Tetsuo 野呂哲夫 13
 NOZAKI Tadashi 野崎 正 123, 124, 126, 185
 OGIWARA Kiyoshi 荻原 清 5
 OGIWARA Masahiro 荻原正弘 9
 OHKI Tomonori 大木智則 3
 OHKUBO Yoshitaka 大久保嘉高 23, 163, 185, 186,
 190, 191
 OHNUMA Hajime 大沼 甫 164
 OKADA Takuya 岡田卓也 93, 96, 98, 131, 133
 OKAMURA Hiroyuki 岡村弘之 13
 OKIHANA Akira 沖花 彰 13
 OKUMURA Susumu 奥村 進 9
 ORIHARA Hikonojo 織原彦之丞 164
 OSAKA Toshiaki 大坂敏明 107
 OSHIMA Masumi 大島真澄 15
 OTSUKA Shozo 大塚省三 2
 OTSUKI Masayoshi 大槻昌義 176
 OYAIZU Mitsuhiko 小柳津充広 158
 OYAMA Hitoshi 大山 等 114
 PU Y. H. 蒲 越虎 9
 RUAN (GEN) Jian-zhi 阮 建治 9
 REUSCH S. 71
 SAITO Kazuo 齊藤和男 125
 SAITO Motozo 齊藤始三 203, 210, 214
 SAITO Takane 齊藤高嶺 13
 SAKAI Hideyuki 酒井英行 13
 SAKAI Nobuhiko 坂井信彦 92, 93, 133
 SAKAIRI Hideo 坂入英雄 6, 112, 218
 SAKAMOTO Hiroyuki 坂本浩幸 239, 241, 243, 245,
 247
 SAKAMOTO Ichiro 坂本一郎 254, 256, 258
 SAKAMOTO Yuichi 坂本雄一 114
 SAKURAI Mikio 桜井幹夫 8
 SAMHAMMER R. 31
 SANO Hirotoshi 佐野博敏 133
 SASA Yoshihiko 佐々嘉彦 87, 89, 120, 127, 129
 SASAKI Shigeki 佐々木茂樹 252
 SASUGA Tsuneo 貴家恒男 139
 SATO Hiroshi 佐藤 竝 17
 SATO Hiroshi 佐藤浩史 55
 SATO Kenichi 佐藤憲一 25
 SATO Sigeru 佐藤 繁 249
 SATOH Shinichi 佐藤眞一 13
 SCHMIDT-OTT Wolf Dieter 11
 SCHUCH Reinhold 71, 80
 SCHULZ M. 71
 SEGUCHI Tadao 瀬口忠男 139
 SEKIZAWA Hisashi 関沢 尚 96, 98
 SHIBUYA Shinji 渋谷真二 9
 SHIMA Kunihiro 島 邦博 73, 80, 82
 SHIMAMURA Isao 島村 勲 49, 51, 53
 SHIMAUCHI Masaaki 島内正昭 27
 SHIMAZU Mitsuyoshi 島津備愛 176, 178
 SHIMIZU Hajime 清水 肇 164
 SHIMOURA Susumu 下浦 亨 17
 SHINOHARA Shigemi 篠原茂己 256
 SHINOZUKA Tsutomu 篠塚 勉 155
 SHIOYA Tatsuro 塩屋達郎 252
 SHIRATO Shoji 白土鈔二 9
 SUEKI Keisuke 末木啓介 155, 185, 191, 195
 SUGIMOTO Kenzo 杉本健三 17
 SULIK Bela 78
 SUNAGA Hiromi 須永博美 141
 SUZUKI Keiji 鈴木啓司 147
 SUZUKI Masao 鈴木雅雄 147
 SUZUKI Takeshi 鈴木 健 19
 TAGUCHI Kazuhiro 田口和博 155
 TAKAHASHI Tan 高橋 旦 143, 145
 TAKAMI Michio 高見道生 174
 TAKEBE Hideki 武部英樹 2, 5, 198, 207, 210
 TAKEMASA Tadashi 武政尹士 27
 TAKEUCHI Hiroki 竹内宏喜 8
 TANAKA Hitoshi 田中 均 223, 225, 228
 TANAKA Jinichi 田中仁市 155, 158
 TANAKA Koki 田中幸基 103, 116
 TANAKA Ryuichi 田中隆一 141
 TANIHATA Isao 谷畑勇夫 17, 19, 21, 168
 TAWARA Hiroyuki 俵 博之 84
 TENDOW Yoshihiko 天道芳彦 185, 186, 190, 191
 TOBA Yoshikazu 鳥羽良和 93
 TONUMA Tadao 戸沼正雄 62, 84
 TORII Yoshinari 鳥居良成 158
 TORIYAMA Tamotsu 鳥山 保 155, 158
 TOYOKAWA Hidenori 豊川秀訓 164
 TSUMAKI Koji 妻木孝治 223, 233
 TSURUBUCHI Seiji 鶴淵誠二 62

UDA Masayuki 宇田 応之 87, 120, 127, 129
URAI Teruo 浦井輝夫 6, 218
VALLI Kalevi 155, 158
VOGT Hans 67, 69, 76
WADA Takeshi 和田 雄 149, 198, 207
WATANABE Kenji 渡辺健次 109
WATANABE Masami 渡辺正己 147
WATANABE Tsutomu 渡部 力 32, 35, 37, 39, 41, 43, 47
WHELAN Colm T. 49
YAGI Eiichi 八木栄一 6, 101, 103, 107, 109, 116
YAMADAYA Tokio 山田谷時夫 93, 98
YAMAGISHI Yoshinori 山岸義徳 230
YAMAGUCHI Hiromi 山口裕美 19
YAMAGUCHI Hiroshi 山口 博 125
YAMAGUCHI Hiroyuki 山口弘之 101
YAMAJI Shuhei 山路修平 31
YAMAMOTO Shigeru 山本 樹 252
YAMAZAKI Yasunori 山崎泰規 67, 69
YANAGIMACHI Tomoki 柳町朋樹 19, 152
YANO Katsuki 矢野勝喜 114
YANO Yasushige 矢野安重 2, 210
YANOKURA Minoru 矢野倉 実 3, 19, 114, 125, 126, 163, 256
YASUE Masaharu 安江正治 164
YATAGAI Fumio 谷田貝文夫 143
YOKOUCHI Shigeru 横内 茂 239, 241, 243, 245, 247
YOKOYAMA Ichiro 横山一郎 201
YOSHIDA Hiroshi 吉田浩司 164
YOSHIDA Katsuhisa 吉田克久 223, 233
YOSHIDA Kenichiro 吉田謙一郎 127
YOSHIDA Kenzo 吉田健三 141
YOSHIDA Koichi 吉田光一 7, 8
YOSHIDA Shiro 吉田思郎 25
YOSHIDA Tatsuya 吉田達也 137
YOSHII Masahito 吉井正人 155
YOSHIYUKI Takeshi 吉行 健 235, 237
YU Byong Gon 俞 炳坤 126
ZHANG Xixiang 張 錫祥 39, 47

RIKEN Accelerator Progress Report

理化学研究所加速器年次報告 第21巻 (1987)

印刷 昭和63年(1988)10月25日

発行 昭和63年(1988)10月30日

発行者 理化学研究所

代表者 小 田 稔

〒351-01 埼玉県和光市広沢2番1号

電話 (0484) 62-1111

編集者 理化学研究所加速器運営委員会

製作 財団法人 学会誌刊行センター

〒113 東京都文京区弥生2丁目4番16号

印刷所 有限会社 学 術 製 版

〒105 東京都港区東新橋2丁目9番11号

定価 5,000円

理化学研究所

埼玉県 和光市 広沢